THE UNIVERSITY OF MANITOBA

A NUMERICAL FORECAST MODEL USING BICUBIC SPLINES ON A TELESCOPING GRID

by

G. V. PRICE

A THESIS

SUBMITTED TO THE FACULTY OF GRADUATE STUDIES

IN PARTIAL FULLFILMENT OF THE REQUIREMENTS FOR THE DEGREE

OF MASTER OF SCIENCE

DEPARTMENT OF MECHANICAL ENGINEERING

WINNIPEG, MANITOBA

OCTOBER, 1972

SUMMARY

A two-level numerical forecast model is proposed in which bicubic polynomial splines are used to fit the spatial variations of the dependent variable fields on a variable area telescoping grid. The spline method generates spatial derivatives which inherently represent a form of smoothing of the slope estimates generated by finite difference methods; the telescoping grid is constructed to ensure computational stability at high latitudes without the need of high frequency filters, spatial staggering of the dependent variables and complex flux calculations.

Thirty-six hour numerical forecasts using the proposed model and using a 1969 version of the Mintz-Arakawa model are compared between themselves and the real weather. The spline method is shown to have advantages over the finite difference method in terms of decreased phase lag and lower root-mean-square forecast error. Computation time is decreased by a factor of 1/3 due to the telescoping nature of the grid, and there is no decrease in forecast accuracy in the fine grid region arising from the surrounding coarse grid region.

Extensions to the model are developed through the derivation of a generalized spline based on continuity of curvature and a numerical forecast technique using weighted residual methods.

Acknowledgements

The author would like to thank Dr. A. K. Macpherson and Dr. J. Tinkler for advice in preparing this thesis. Financial support from the National Research Council of Canada in the form of a studentship is acknowledged with thanks. The Computer Centre at the University of Manitoba provided the necessary computer facilities. Finally, thanks are due to Mrs. D. Miller, Mrs. L. McLuckie and Mrs. B. Price for carefully typing this thesis and supplying drafting assistance.

Table of Contents

NOMENCLATURE

t	=	time
x	=	coordinate to the east
y	=	coordinate to the west
P	=	pressure
P_s	=	surface pressure
P_T	=	pressure at the base of the stratosphere, 200 mb
ζ	=	$P_s - P_T$
σ	=	$(P - P_T)/\zeta$, normalized pressure
u,v	=	horizontal wind components in the x and y directions, respectively
T	=	temperature
θ	=	potential temperature
q	=	mixing ratio (mass of water vapour/mass of dry air)
ϕ	=	geopotential
ϕ_s	=	surface geopotential
Θ	=	longitude
Φ	=	latitude
$\Delta\Theta$	=	longitude grid spacing in the Mintz-Arakawa model
$\Delta\Phi$	=	latitude grid spacing in the Mintz-Arakawa model
δ	=	extent of the polar cap, in radians of latitude
m,n	=	metrics
A	=	mean radius of the earth
u^*	=	$n\zeta u$, flux in the x direction
v^*	=	$m\zeta v$, flux in the y direction
Z	=	$mn\zeta$
a	=	specific volume

ρ = density

C_p = specific heat at constant pressure

R = gas constant for dry air

K = R/C_p

P^* = standard pressure, 1000 mb.

λ = level (altitude) sign parameter

F_x, F_y = x and y components of the horizontal friction force per unit mass

H = heating rate per unit mass

E = evaporation rate

C = precipitation rate

ψ, Ψ = represents any dependent variable

Δt = time step interval

B = the number of time steps between energy source calculations

i,j = general indexing pair specifying the grid point

N = the number of rows of grid points in the y direction

M_j = the number of grid points in the x direction on latitude circle j

d_j = grid point spacing on the j'th latitude circle

V = resultant velocity

S = $S(x)$ or $S(x,y)$, the equation for the cubic spline curve fit or the bicubic spline surface fit.

$u_i, u_{i,j}$ = $S(x_i)$ or $S(x_i,y_j)$

$P_i, P_{i,j}$ = $\frac{\partial S(x_i)}{\partial x}$ or $\frac{\partial S(x_i,y_j)}{\partial x}$, slope at the grid point in the x direction

$q_{i,j}$ = $\frac{\partial S(x_i,y_j)}{\partial x}$, slope at the grid point in the y direction

$s_{i,j}$ = $\frac{\partial^2 S}{\partial x \partial y}(x_i,y_j)$, cross derivative

$P_i, P_{i,j}$ = $\frac{\partial^2 S}{\partial x^2}(x_i)$ or $\frac{\partial^2 S}{\partial x^2}(x_i, y_j)$

$Q_{i,j}$ = $\frac{\partial^2 S}{\partial y^2}(x_i, y_j)$

$S_{i,j}$ = $\frac{\partial^4 S}{\partial x^2 \partial y^2}(x_i, y_j)$

h_i = $x_i - x_{i-1}$

k_j = $y_j - y_{j-1}$

λ_i = $h_{i+1} / (h_i + h_{i+1})$

μ_i = $h_i / (h_i + h_{i+1})$ = $1 - \lambda_i$

u_p, v_p, V_p, Θ_p = expressions used in defining the polar boundary condition for the horizontal wind components

$a, b, \beta_i, XS, US, D_i, C_i^*, \lambda_i^*, \mu_i^*, \lambda_i^{**}, \mu_i^{**}$ = constants and expressions used in defining the generalized spline based on continuity of curvature

$a, b, c, \xi, \bar{h}, h_i$ = expressions used in interpolation method A

f_1, f_2, h_i = expressions used in interpolation method B

RMSE = 36 hour forecast root-mean-square error relative to the true weather at 36 hours

$RMSE_i$ = average of RMSE along longitude line i

$RMSE_j$ = average of RMSE around latitude circle j

RMSC = the root-mean-square change in the true weather over the 36 hour forecast period

$RMSC_i$ = average of RMSC along longitude line i

$RMSC_j$ = average of RMSC around latitude circle j

Glossary

balanced wind: Applying the assumption of non-divergent quasi-horizontal flow in which the horizontal velocity field is expressed in terms of a stream function, and other assumptions, the vector equation of motion may be reduced to the "balance equation". This equation involves the stream function and geopotential as dependent variables. Under certain conditions, with a known distribution of geopotential, the balance equation may be solved for the stream function. The velocity field obtained from the stream function is called a balanced wind.

barotropic: A barotropic atmosphere is one in which the surfaces of constant pressure are also surfaces of constant density and temperature.

computational mode: The computational mode is the portion of the solution of the difference equation which has no physical counterpart in the true solution of the differential equation.

filtered equation models: A numerical forecast model in which the governing equations are differentiated first and then numerically solved is termed a filtered equation model.

geopotential: The work done in moving a unit mass from mean sea level to some elevation above sea level is called the geopotential of that level.

grid points: These are points on the numerical forecast grid at which values of the dependent variables are estimated at discrete time intervals throughout the forecast.

latitudinal: The latitudinal direction is the south-north direction on the earth, perpendicular to the latitude circles.

longitudinal: The longitudinal direction is the west-east direction on the earth's surface, perpendicular to the longitude circles.

nine point difference operator: This denotes a finite difference expression involving values of the dependent variables at nine grid points.

node point: see grid point

numerical explosion: A numerical forecast is said to explode numerically when the magnitudes of the dependent variables exceed the allowable limits of computer storage.

mixing ratio: A measure of moisture content, the mixing ratio is the mass of water vapour per unit mass of dry air.

potential temperature: If a parcel of gas at temperature T and pressure P is brought adiabatically to standard pressure (1000 mb), the resulting temperature in the parcel is called the potential temperature.

phase lag: The position in longitude of the large scale meteoroligical waves in the numerical forecast is compared to the position of the waves in the true weather. The difference between the two positions is termed the phase lag of the numerical forecast.

physical mode: The physical mode refers to that portion of the solution of the difference equation which has a physical counterpart in the true solution of the differential equation.

primitive equation models: A numerical forecast model in which the governing equations are numerically solved in their usual form is termed a primitive equation model.

surface geopotential: This is the geopotential at the surface of the earth.

wave number n: The number of complete meteorological waves around a latitude circle is the wave number.

1. INTRODUCTION

Weather prediction by numerical methods deals with the numerical solution of the hydrodynamic and thermodynamic equations governing atmospheric flow. Such a solution involves an enormous number of arithmetic and logical operations for which reason electronic computers are now used. The basic principles underlying numerical weather prediction were discovered early in this century. At the time, it was recognized that the non-linear system of equations did not possess an analytic solution. Also, initial data defining the state of the atmosphere was inadequate. The first attempt to solve this system of equations using numerical methods was made by L.F. Richardson in 1921. His results were in considerable error and interest in numerical weather prediction declined. However, with the advent of the electronic computer in the 1940's, numerical forecasting was revived. The first successful numerical prediction was made by J. Charney in 1949. From this point on, the science developed rapidly and models with varying numbers of restrictions on the flow were studied by numerous research groups in many countries.

It is a common practice to classify numerical forecast models into one of two basic categories based on the form of the governing differential equations (Haltiner and Martin (1), Haltiner (2)). In primitive equation (PE) models*, the governing equations are numerically solved in their usual form, whereas in filtered equation (FE) models, the governing equations are differentiated first and then solved numerically. The

---

* Refer to the Glossary for definitions of common meteorological terms.

PE models permit all types of wave motions (both long and short waves), while the FE models permit only the long meteorologically significant wave motions called Rossby waves. The earlier numerical forecast models are of the filtered type since they are the simplier model form (containing approximations which are only true on the average over long periods of time) and require considerably less computation time. This shorter computation time for FE models compared to PE models arises from the longer time steps and fewer dependent variables and equations in PE models. With the increase in computational speed of computers, it becomes feasible to investigate the more sophisticated PE models.

Numerical forecast models are primarily used for general circulation studies and short term weather prediction. In general circulation studies, the forecast usually begins with an atmosphere at rest and extends over a long period of time (several months). However, in short term weather prediction, the forecast begins with real weather data defining the initial state of the atmosphere and extends over a short period of time (up to a week). Three PE general circulation models which have been in operation for several years are a multi-level model developed by Smagorinsky at the Geophysical Fluid Dynamics Laboratory, U.S.A. (Smagorinsky (3,4), Smagorinsky, Manabe and Holloway (5), and others), a two level model developed by Mintz and Arakawa at UCLA (Mintz (6), Langlois and Kwok (7), and a multi-level model developed by Kasahara and Washington (8) at the National Center for Atmospheric Research, U.S.A. These models are being applied only in a limited fashion to short term forecasting. The Smagorinsky model shows promising results with real weather data for short term forecasts up to a week in duration (p.77 of ref 2), however the computation time

is too long for operational purposes. Similarly, the Mintz-Arakawa model is being applied with some success to short term predictions (Kesel and Winninghoff (9), Price (10)). Two short term forecast models which have been in use for many years are an operational barotropic model developed by Shuman and Vanderman (11) and a six level PE short term forecast model developed by Shuman and Hovermale (12). In addition, many other short term forecast models are in use in various countries for both operational and experimental purposes.

Three major steps may be identified in the formulation of a numerical weather prediction model. The first step is to choose a system of hydrodynamic and thermodynamic equations, in terms of a suitable coordinate system, in order to explain mathematically the motion in the atmosphere. The relevant equations are Newton's second law of motion, the first law of thermodynamics, the equation of state for a perfect gas, and laws expressing conservation of dry air and water vapour. Next, it is necessary to approximate the continuous dependent variable fields by discrete values of the variables at specified nodes or grid points in the forecast region. This selection of the forecast grid is of major importance in determing the forecast resolution, accuracy, and computation time. The final step is to obtain an approximate numerical solution to the governing equations at the specified grid points, thereby advancing the dependent variable fields in time. In this thesis, emphasis will be placed on the second and third steps in the formulation of the forecast model: the selection of a forecast grid and the method used to solve the governing differential equations.

1.1 The Method of Solution of the Governing Differential Equations

Consider first the method used to solve the governing differential equations. In the majority of numerical forecast models, finite difference methods are used to obtain an approximate solution to the system of partial differential equations. The basic approximation in finite difference methods is to replace the continuous variables by discrete variables which vary stepwise by finite increments in space and time. Whereas the behavior of the continuous variables is governed by the system of differential equations, the behavior of the discrete variables is governed by a system of difference equations. Hence, a difference equation is simply the finite difference representation of a differential equation; and the solution of the difference equation yields an approximate solution to the differential equation at specified points in space and at discrete intervals in time. Associated with the numerical solution of the system of difference equations are a number of errors, primarily truncation error and discretization or computational error (Smith (13), Forsythe and Wasow (14)). The truncation error in the difference equation arises from representing the spatial derivatives in the differential equation by the first few terms in a Taylor series expansion of the derivative, in terms of specified values of the variable at adjacent nodes or grid points. This error depends on both the size of the finite space increment and the wavelength of the continuous field being estimated (Gates (15)). The most widely used procedure is the central space difference, which may be illustrated in the case of the first derivative of a continuous function f as (ref 15, 13)

$$\frac{\partial f}{\partial x} \simeq \frac{f(x + \Delta x) - f(x - \Delta x)}{2\Delta x} \quad , \tag{1.1}$$

where x denotes a typical spare variable and Δx is the grid point interval. The truncation error of this approximation is in the order of $(\Delta x)^2$. Other frequently used estimates for the first derivative are the forward difference and backward difference,

$(f(x + \Delta x) - f(x))/\Delta x$ and $(f(x) - f(x - \Delta x))/\Delta x$,

respectively. The error in these approximations is in the order of Δx. The difference between the difference equation as a whole and the differential equation which it represents is called the truncation error of the difference equation.

The second error, discretization error, is the error in the exact numerical solution of the difference equation (Smith (13)). If ϕ represents the exact solution of the partial differential equation, and ϕ_D represents the exact solution of the difference equation, then the discretization error is $\phi - \phi_D$. The solution method is convergent if ϕ_D approaches ϕ as Δx, Δt become infinitisimally small. Here, Δx and Δt denote the finite space and time increments respectively. Closely associated with the discretization error is the computational stability of the difference scheme; that is, the time variation of the discretization error (Crandal (16), Kurihara (17)). Fundamentally, whenever $\Delta t/\Delta x$ becomes larger than some critical value, the computational mode in the numerical solution tends to grow in time and eventually destroys the physical mode. The physical mode refers to that portion of the solution of the difference equation which has a physical counterpart in the true solution of the differential equation; the computational mode is the remaining portion of the solution of the difference equation and has no physical counterpart in the true solution of the differential equation. Since there is no analytic solution to the governing partial

differential equations for atmospheric flow, it is customary to examine the stability of this corresponding linearized version of the governing equations, with constant coefficients (the von Neumann stability condition, Kasahara (18)). To simplify the analysis further, a common approximation is to check the stability of the difference equations considering only one factor at a time (ref 18). For example, to examine the stability of the difference scheme for a typical advective term in the thermodynamic equation, one may examine the linear one dimensional advection equation for temperature, T,

$$\frac{\partial T}{\partial t} + c \frac{\partial T}{\partial x} = 0 \quad , \tag{1.2}$$

where c is a constant (the zonal wind speed). Haltiner (pp. 18-25 of ref 2) shows that the difference scheme for equation 1.2 using central differences for both time and space, is computationally stable provided $c\Delta t/\Delta x \leq 1$. This means that the computational mode in the numerical solution approaches 0 as time increases, provided $c\Delta t/\Delta x \leq 1$. However, if forward time and central space differences are used, this difference scheme is computationally unstable for all values of $\Delta t/\Delta x$. It is interesting to note that the case of forward time and forward space differences is computationally unstable when $c>0$ and computationally stable when $c<0$. This corresponds to the so-called "upstream differencing" technique, in which a stable differencing scheme is obtained when the space differencing is in the opposite direction to the wave motion (Gosman, et.al. (19)). In addition to the computational stability of the difference scheme, it is necessary to consider the degree of phase lag and amplitude distortion of the physical mode of the numerical solution. For example, although the difference scheme using central

finite differences in space and time for the one-dimensional advection equation 1.3 is computationally stable when $c\Delta t/\Delta x \leq 1$, the physical mode exhibits a phase lag and smaller amplitude when compared to the true solution.

The accuracy and stability characteristics of ten different finite difference schemes are discussed by Grammeltvedt (20) using the primitive equations in a barotropic fluid; with primary emphasis on the effects of the spatial differencing on the forecast. With an analytic wave for the initial condition, the analysis shows that the quadratic conservative difference schemes (or schemes which conserve both the first and second moments of the dependent variables) and total energy conservative difference schemes (or schemes which conserve the sum of available potential plus kinetic energy) are more stable than the other second order conservative schemes. However, the most stable schemes are those in which the advective terms are calculated using nine point spatial finite differences and therefore contain a form of smoothing, and the generalized Arakawa scheme which conserves mean vorticity, mean kinetic energy, and mean square vorticity in nondivergent flow. The most commonly used methods to suppress computational instabilities are to include artificial viscosity terms in the difference equations, or to write the finite difference equations in a form which conserves certain statistical moments (usually of quadratic form) of the dependent variables (ref 20). The Smagorinsky general circulation model (ref 3,4, 5) uses finite differences which conserve momentum and total energy. Therefore, the Smagorinsky model requires lateral eddy viscosity terms to suppress the nonlinear computational instabilities inherent in the difference scheme, but Mintz (6) feels that this may have the undesirable

side effect of excessively damping the meteorologically significant wave motions. However, the Mintz-Arakawa general circulation model (ref 6,7,10) uses finite differences due to Arakawa which are both quadratic conservative and total energy conservative schemes. Therefore, the differencing in the Mintz-Arakawa model is inherently nonlinearly computationally stable without the use of explicit frictional dissipation. Of the short term prediction models, Shuman's scheme (ref 11) calculates the advective terms using a nine point difference operator which should yield the most stable forecast due to its smoothing effect (ref 20).

In addition to the space differencing scheme, the form of time differencing employed has a strong effect on stability. This was mentioned briefly in the discussion of computational stability, where, for example, it was noted that forward differencing in time is unstable whereas central differencing in time is conditionally stable (provided $c\Delta t/\Delta x \leq 1$). The stability characteristics of several implicit, explicit and iterative time differencing schemes were examined by Kurihara (17) using a linear system of equations. Of the methods investigated, the two stage leapfrog-trapezoidal method shows the most promise since it has little damping and little phase retardation effect on the physical mode, with strong damping of the spurious computational mode, for $c\Delta t/\Delta x < \sqrt{2}$. However, being a two stage scheme, it requires twice the computation time of the simple centered difference time differencing scheme (also called the centered leapfrog explicit scheme), which itself has no change in amplitude of both the physical and computational modes with only moderate acceleration of the physical mode. Therefore, the simple centered leapfrog explicit scheme is used in most models.

In the Mintz-Arakawa model, a modified Matsuno time integration (Matsuno (21), pp. 105-110 of ref 10) is employed. The original three stage Matsuno scheme gives strong damping of the high frequency waves (which are usually spurious). However, the modification used in the Mintz-Arakawa model essentially reduces the Matsuno method to a two stage Euler-backward scheme discussed by Kurihara (17). This scheme has no computational mode, with moderate selective damping and large phase acceleration of the physical mode.

In this thesis, a numerical forecast model is proposed in which double cubic polynomial spline functions are used to fit the spatial variation of the dependent variable fields, thereby eliminating the need for finite differencing in space to estimate the spatial derivatives. The cubic spline $S(x)$ of interpolation to the ordinates u_i at mesh locations x_i, i,...M, is a piecewise continuous function defined as a cubic polynomial in each interval $x_{i-1} \leq x \leq x_i$ having continuous first and second derivatives (Ahlberg, Nilson and Walsh (22), Greville (23)). The generalization to two dimensions to obtain the double cubic (or bicubic) spline is straightforward. There are several reasons for proposing that the use of double cubic polynomial splines may be an improvement over finite difference methods in estimating spatial derivatives.

Firstly, cubic polynomial splines are an effective tool in the processes of numerical interpolation, differentiation, integration, and curve fitting (pp. 42-52 of ref 22). In particular, the slope estimates returned by a spline curve fit inherently represent a form of smoothing of the slope estimates returned by standard forward, backward or central finite differences. In the numerical forecast models developed up to

this point, complex differencing schemes are necessary to obtain a smoothed slope estimate. For example, the Shuman model (ref 12) uses nine point difference estimates (a form of smoothing) to obtain estimates for the advective terms; and the Mintz-Arakawa model (Langlois and Kwok (7), Price (10)) was complex, multi-point difference estimates for the spatial slopes. These complex and somewhat arbitrary smoothing schemes used in finite difference methods are not required when the double cubic spline is used to estimate the first derivatives, due to the inherent "smoothed" nature of the spline curve fit. It should be mentioned that this does not hold true for the second derivative. Rather, the finite difference estimate of the second derivative given by Newton's second divided difference (a three point operator in one-dimension) represents a smoothing of the spline estimates for the second derivative (p.44 of ref 22). In order to employ the spline method to obtain good "smoothed" second derivative estimates, it is necessary to do a spline fit to the first derivatives, with the first derivative itself obtained from a previous spline fit. Ahlberg, Nilson and Walsh (p.44 or ref 22) discuss this "spline-on-spline" method of obtaining smoothed second derivatives.

A second reason for proposing the use of a spline function to obtain slope estimates, in place of finite difference methods, is the minimum norm property, or Holladay's theorem, for cubic splines (p.3 of ref 22). This theorem states that for any function $f(x) \in C^{2*}$ satisfying $f(x_i) = u_i$, $i = 1,\ldots M$, the integral of $|f''(x)|^2$ over the interval (x_1, x_M) is a minimum when $f(x) = S(x)$, provided $S''(x_1) = S''(x_M) = 0$.

---

* $f(x)$ and its first two derivatives are continuous.

Since this integral is often a good approximation to the integral of the square of the curvature for a curve $y = f(x)$, Holladay's theorem is often called the minimum curvature property. This follows from the definition of curvature, $f''(x)^2/(1 + f'(x)^2)^{3/2}$, which is approximately equal to $f''(x)^2$ when $f'(x)<<1$. Therefore, of all the possible curve fits having continuous first and second derivatives, the smoothest is the cubic spline curve fit since it has the minimum curvature (providing slopes are not excessively large).

A third appealing characteristic of the double cubic spline is its inherent flexibility in the application to a forecast grid with varying grid interval. Providing the grid expansion is smooth, there are no difficulties in applying bicubic splines on an expanding grid. Ahlberg (24) discusses a problem in curve fitting with splines when the physical spacing between grid points changes significantly in a limited region. The example cited is the case of monotonic increasing data with alternately large, then small, then large grid point spacing. A small local spike appears in the otherwise monotonic spline curve fit. Although this small spike has little obvious effect on the curve fit, its effect on the slope estimate at the node where the grid point spacing changes abrubtly is devastating (since the spike is located at this grid point). It is therefore important to use a smoothly expanding grid if splines are to be used to estimate the spatial derivatives.

Finally, it should be mentioned that the theory of double cubic splines depends largely on the theory of the one dimensional cubic spline. Ahlberg, Nilson and Walsh (pp. 235-264 of ref 22), de Boor (25) and Ahlberg, Nilson and Walsh (26) discuss many properties of the double cubic spline, such as the minimum curvature property, best approximation

property, existence, uniqueness, and others. In addition, Ahlberg, Nilson and Walsh (26) present a derivation of the double cubic spline in terms of nodal values of the second derivative; and de Boor (25) presents a computation scheme for the double cubic spline in terms of nodal values of the first derivative. The treatment of the double cubic spline in terms of nodal values of the first derivative is preferred here since the purpose of using bicubic splines in this application to numerical weather prediction is to obtain good estimates of the spatial first derivatives for the dependent variable fields.

It is possible to make a direct comparison between the different conservative properties of the spatial finite difference schemes and the corresponding properties of cubic splines. In deciding whether or not a specific finite difference scheme is either conservative or quadratic conservative, a comparison is made between the spatially integrated forms of the difference equation and differential equation for the property under consideration (momentum, kinetic energy, thermal energy, and others). If the two integrated forms are similar, then the difference scheme conserves the property represented by the difference equation. Differences between the two integrated forms usually arise from the truncated nature of the difference expressions. Now, bicubic splines are piecewise analytic cubic polynomial functions with continuous first and second derivatives. The third derivative is not continuous and the fourth and higher derivatives vanish. Despite the continuous nature of the cubic spline, the differential equations are only solved at the grid points; and only the nodal* values of the

---

* The terms node point and grid point are used interchangeably in this thesis.

dependent variables are advanced in time. Therefore, similar to a finite difference method, it is possible to write a difference equation for the dependent variables at each node using the bicubic spline estimates for the slope of the variable fields. By matrix inversion, the spline slope at the node may be expressed in terms of all the nodal values of the dependent variable in the row or column in the direction of the slope (p.42 of ref 22). For example, if the west-east slope of the temperature field is desired at node i^* on a latitude circle, and if the nodes are separated by 5° longitude on this latitude circle, then the cubic spline estimate of this slope becomes

$$\left(\frac{\partial T}{\partial x}\right)_{i^*} = \sum_{i=1}^{72} \alpha_i T_i \quad , \tag{1.3}$$

where the values for α_i, i = 1,...72 are obtained by matrix inversion of the spline coefficient matrix. The substitution of equation 1.3 into the difference equation and integration of the resulting equation over all the spatial dimensions is a complicated calculation but may be performed. It is therefore possible to determine the conservative and quadratic conservative properties of the proposed bicubic spline method. This analysis will not be performed in this thesis due to the length of the calculation when testing for quadratic conservative properties. It is felt that the cubic spline scheme will show energy and momentum conservative properties; however, it is doubtful that the cubic spline will also show quadratic conservative properties, especially on a variable area grid.

1.2 The Selection of the Forecast Grid

The first factor to consider in the selection of a forecast grid is the uniformity of the grid's resolution over the surface of the earth. If a forecast with equal emphasis at all regions of the earth is desired, then each grid cell on the map projection should represent approximately the same physical area on the earth. In the majority of the numerical forecast models formulated to date, the system of difference equations has been solved on a uniform square or rectangular grid system. However, certain resolution problems arise when such a grid is applied in the coordinate systems convenient to numerical weather forecasting. For example, in the frequently used polar stereographic projection (used in models by Smagorinsky, Manabe and Holloway (5), Shuman and Hovermale (12), and many others), the map scale factor varies from 1 at the pole to 2 at the equator.* This means that 1 unit of distance on the earth's surface maps into 1 unit and 2 units at the pole and equator respectively on the polar stereographic projection. Therefore, a square grid on the stereographic projection gives double the resolution at low latitudes than it does at high latitudes, representing a marked over-resolution of low latitude regions. The opposite resolution problem occurs in the Mercator map projection used in the models by Smagorinsky (3, 4) and Shuman and Vanderman (11), as well as in the projection used in the Mintz-Arakawa model (pp. 31-38 of ref 7, pp. 83-90 of ref 10). Here, longitude maps linearly into the west-east coordinate on the projection. This means that 1 unit of distance in the west-east direction on the earth's surface maps into 1 unit at the equator and 4 units at 76° of

---

* The map scale factor is derived on p.174 of Price (10) and on p.175 of Haltiner and Martin (1).

latitude on the projection: a square or rectangular grid on this projection constitutes severe over-resolution at high latitudes. One consequence of this over-resolution in the Mintz-Arakawa model is the growth of spurious short waves traveling in the longitudinal (west-east) direction at high latitudes. These short waves are removed through the use of an averaging operation which gradually increases in strength as latitude increases.

An interesting approach to the computational drawback of over-resolution near the poles is made by Grimmer and Shaw (27). Two methods are used: firstly, the time step is varied latitudinally on a grid with constant longitudinal grid interval; and secondly, the longitudinal grid interval is varied latitudinally in a constant time step scheme. Using a barotropic PE model with analytic initial data consisting of a wave number four in the horizontal velocity and geo-potential fields, the first method is stable and shows good agreement (except for a slight phase lag) with the analytic solution for the case of non-divergent barotropic flow. The stability of this method may be in part due to a degree of time smoothing inherent in the variable time step method. However, the second method gives a solution which rapidly departs from the analytic solution, especially at high latitudes. This is expected since for this initial condition (wave number four at both high and low latitudes), there are too few grid points to adequately resolve the wave at high latitudes (fewer than nine grid points per wave length) whereas at low latitudes, the wave is adequately resolved (greater than nine grid points per wave length). The forecast results from the second method show negligible wave motion at high latitudes with realistic wave motion at low latitudes.

Several researchers are experimenting with grids giving uniform resolution over the entire earth. Kurihara and Holloway (28) are trying a general circulation PE model formulated in spherical coordinates by the "box method"; and the network of grid points used in this model forms a nearly uniform grid resolution over the entire earth. Further, preliminary experiments are being performed using triangular or geodesic grids with uniform resolution over the earth. Williamson (29) and Sadourny et.al. (30) integrate the barotropic vorticity equation on a spherical geodesic grid using analytic initial data. Their numerical forecasts are nonlinearly computationally stable, since the difference schemes used conserve vorticity, kinetic energy and the square of vorticity. Williamson (31) and Sadourny and Morel (32) further extend the use of this grid to a primitive equation barotropic model; and Williamson finds his results to be superior to the results from Kurihara's homogeneous spherical grid system (ref 33). Experiments with non-uniform triangular grids which serve as a transition from fine grid to coarse grid regions are being made also by Winslow (34) and Williamson (35).

A second point to consider in the selection of a forecast grid is whether or not the grid resolution should be varied in order to obtain higher forecast resolution in regions of primary interest. For example, if the purpose of performing the numerical forecast is to obtain a short term forecast for North America, it would be inefficient to perform a global forecast with equal grid resolution over the entire earth. One may identify two approaches to the problem of obtaining efficient numerical forecasts in limited regions of interest: either construct a limited area forecast model for the region of interest, or formulate a

variable area model with increasing grid spacing as distance from the region of interest increases (a telescoping grid). The major problem with limited area prediction models is the selection of boundary conditions, primarily for the east and west boundaries of the region. Although the telescoping grid scheme does not have the boundary condition problems of the limited area grid, it does have increased complexities in the computation scheme due to the expanding grid intervals. Also, there may be some as yet unforseen difficulties in the form of spurious growth of meteorological features due solely to the expanding grid. Gerrity and McPherson (36) discuss the results from twenty-four hour numerical forecasts performed with real weather initial data on a limited area fine-mesh PE barotropic model. Although constant lateral boundary conditions are used over the forecast period, the predictions compare favorably with those from operational barotropic and baroclinic models. The constant lateral boundary conditions prohibit the running of much longer forecasts on their limited area grid. A variable grid design to obtain increased resolution in the center of the forecast domain is studied by Anthes (37). The grid is applied in a free surface model of an inviscid, incompressible fluid vortex confined to a rectangular domain. The results show a slight (less than 1%) increase in total energy after two thousand time steps. A simple finite difference scheme with non-constant intervals is also discussed by Sundqvist and Veronis (38). This grid, applied to a few simple boundary layer flow problems, shows distinct advantages in improved resolution in the regions of interest.

A third point to consider in the selection of the forecast grid is whether the grid should be staggered or unstaggered. A staggered

grid is one in which not all the dependent variables are carried at the same grid points. Spatial staggering is a common practice in finite difference models as a technique for reducing the effective grid length. The effective grid length is the distance between grid points entering into a finite difference expression. For example, the effective grid length of the central finite difference operator equation 1.1 is $2\Delta x$. It is desirable to have the effective grid length as small as possible in order to maximize the number of grid points which resolve the smallest significant meteorological wave (thereby improving its phase speed). Two basic forms of staggering are possible. A spatial staggering occurs when not all the dependent variables are carried at the same grid points. The grid in the Mintz-Arakawa model is an example of this (p.31 of ref 7, p.84 of ref 10). Also it is possible to have a time staggering in which the variables are carried at different grid points depending on whether the time is an even or odd multiple of the time interval Δt. The grid in a model by Phillips (39) is an example of time staggering.

In this thesis, a numerical forecast model is proposed in which the forecast grid is an expanding grid with basic expansions of two types superimposed on each other. The first grid expansion is required to maintain the physical distance between grid points on latitude circles approximately equal to some distance greater than the minimum distance required for computational stability; and the second grid expansion is used to decrease the number of grid points in regions which are not of primary interest (a telescoping grid).

Consider first the basic expansion of the first type. It was mentioned earlier that when there are no particularly important regions of interest in the forecast domain, it is desirable to have a uniform

grid resolution over the entire forecast region. This basic uniformity of resolution is ensured by the grid expansion of the first type. With grid points lying on the latitude circles, this expansion essentially means that as latitude increases, the number of grid points on each latitude circle decreases in order to maintain a constant physical distance between the grid points on the earth's surface. This grid is an improvement over the square or rectangular grids used on the Mercator and polar stereographic map projections. Also, this first grid expansion results in a grid very similar to the grid used by Kurihara and Holloway (28) using the so-called "box method"; and is similar to the second grid used by Grimmer and Shaw (27). Although Grimmer and Shaw have forecast problems with their grid using a wave number four at all latitudes as initial data, it is felt that these problems will not be apparent here due to the full spectrum of wave present at all latitudes in the real weather initial data used in this application.

Consider next the basic grid expansion of the second type, to be superimposed onto the first grid expansion. It was mentioned earlier that there are two methods of emphasizing a region of interest in the forecast domain: either construct a limited area forecast model or use a telescoping grid with increasing grid interval as distance increases from the region of interest. This results in a high resolution forecast in the region of interest without expending an unduly large amount of computational time in generating a high resolution forecast elsewhere. Problems with the lateral boundary conditions in limited area models make them only useful for very short term predictions, unless a variable boundary condition is maintained through a coarse grid global

model executed simultaneously with the limited area model. However, even when a variable boundary condition is maintained, the smaller grid lengths in the limited area grid region will result in faster phase speeds of the meteorological waves inside the limited area region compared to the phase speeds in the external coarse grid region. Hence, problems in matching at the boundaries will occur as time proceeds. For these reasons, the telescoping grid is preferred over the limited area grid and a telescoping method is used as the grid expansion of the second type in the model proposed in this thesis. Having decided on a region of interest and a grid resolution within this region, the smooth grid expansion of type two is applied successively to grid points outside of the region of interest. The most important characteristic of this telescoping method is the smooth transition between regions of changing grid size, as well as a smooth matching at the poles and equator. This expansion is more generalized than the expansions used by Anthes (37) and Sundqvist and Veronis (38). Also, inherent characteristics of the bicubic polynomial splines make them readily adaptable to an expanding grid, and problems should not occur providing the expansion is smooth.

The final consideration in the formulation of the forecast grid for the proposed model is whether or not the dependent variables should be spatially staggered. With bicubic splines, the slope estimates of the variable fields are equally accurate whether they are obtained at the grid points, the center of the grid lines, or the center of the grid cells. Therefore, there is no reason to stagger the dependent variables and an unstaggered forecast grid is used in the proposed model.

1.3 The Proposed Forecast Model

The use of double cubic polynomial spline functions in solving the system of partial differential equations and the selection of a telescoping forecast grid having superimposed grid expansions are the most important characteristics of the numerical forecast model proposed in this thesis. These characteristics distinguish this model from the current forecast models which use conventional grid systems and finite difference methods to solve the system of equations. The advantages of the polynomial spline method and the telescoping grid system have been discussed earlier in the Introduction. It remains, however, to evaluate these methods in comparison to finite difference and conventional grid methods through the execution of numerical forecast experiments.

To complete the definition of the proposed forecast model, it is necessary to select the following additional model features: a system of governing partial differential equations, a method of extrapolating the dependent variables in time, and a method of generating the heat, moisture and friction source terms. These features are of minor importance here since emphasis in this study is placed on the polynomial spline method and the telescoping grid system. The selection of the additional features is arbitrary, but is here chosen to be the same as in a current model which uses the finite difference method on a conventional grid so that effective comparison may be made.

The model selected for comparison purposes is the two-level Mintz-Arakawa general circulation model (ref 7, 10). This model uses a complex finite differencing scheme to solve the system of partial differential equations, with a regular square grid on a map projection similar to the Mercator projection. Also, in order to obtain computational

stability, this model requires several special techniques, such as high frequency filters, spatial staggering of the dependent variables, and complex flux calculations. The Mintz-Arakawa model is convenient to use as a comparison model for three reasons: it has only two levels of resolution in the vertical and therefore requires less computation time than some of the multi-level models in use today; the finite differencing and regular square grid used are representative of the differencing schemes and grids used in modern numerical weather prediction models; and this model illustrates several of the special techniques required for computational stability when the forecast grid severely over-resolves the high latitude regions.

The proposed forecasting model will be applied to a thirty-six hour northern hemisphere forecast and its performance will be compared with the Mintz-Arakawa model and the real weather.

2. The Mintz-Arakawa (1969) Model

A thorough description of the Mintz-Arakawa (1969) numerical weather prediction model may be found in two earlier reports by the author (ref 10 and 40). The following brief description of the essential features of the model is based on the two earlier reports.

2.1 The Basic Equations in x, y, σ, t Coordinates

The two level Mintz-Arakawa model uses the hydrodynamic and thermodynamic equations written in a cartesian x, y, σ, t coordinate system. The x and y axes are transformed from the s_1 and s_2 curvilinear coordinate curves which lie respectively along latitude and longitude circles on the earth's surface. The vertical parameter σ is a pressure coordinate normalized with respect to surface pressure. Hence, σ takes on values between unity at the earth's surface and 0 at the two hundred mb level. The fundamental geometric nature relating the orthogonal curvilinear s_1, s_2 surface (of the earth) to the cartesian x, y plane (map projection in which the governing equations are solved) is described by the metrics m and n (pp.68, 88, 89 of ref 10), given by

$$m = \frac{ds_1}{dx} \quad , \tag{2.1a}$$

$$n = \frac{ds_2}{dy} \quad , \tag{2.1b}$$

$$ds_1 = A \cos\Phi d\Theta \quad , \tag{2.2a}$$

$$ds_2 = A \, d\Phi . \tag{2.2b}$$

The elements ds_1 and ds_2 represent elements of arc length (or physical distance) along the s_1 and s_2 coordinate curves respectively, and the

elements dx and dy represent elemental changes in the map coordinates x and y. In the Mintz-Arakawa model, a linear mapping is used to relate the coordinates x and y to longitude (Θ) and latitude (Φ). This applies to all the regions except for the polar caps, in which the mapping of y into Φ is modified to account for a larger latitude grid spacing (δ) compared to the latitude grid spacing in the remainder of the field ($\Delta\Phi$). This results in the following metric expressions for the Mintz-Arakawa model (p.89 of ref 10):

$$m = A\,\Delta\Theta\cos\Phi \quad , \tag{2.3a}$$

$$n = A\,\Delta\Phi, \quad 90 - \delta > |\Phi| \quad , \tag{2.3b}$$

$$= A\ \ \delta, \quad 90 - \delta < |\Phi| < 90. \tag{2.3c}$$

The third independent variable, σ, is a normalized vertical parameter defined by the relation (p.41 of ref 10)

$$\sigma = \frac{P - P_T}{\zeta} \quad , \tag{2.4}$$

$$\zeta = P_S - P_T \quad , \tag{2.5}$$

P_S = surface pressure, variable,

P_T = pressure at the top of the troposhere, 200 mb.

In this two level model, flow in the upper half of the troposphere ($0 < \sigma < 1/2$) is represented by conditions at the level $\sigma = 1/4$ and flow in the lower half of the troposphere ($1/2 < \sigma < 1$) is represented by conditions at level $\sigma = 3/4$. The dependent variables carried at levels one and three are shown in Figure 2.1. Note that the two horizontal wind components (u, v) as well as the temperature (T) are carried at both levels one and three, while all the moisture (q) is assumed to be carried by the lower level only. Also, the pressure at each grid point on any σ level is determined from the single dependent

variable ζ, by equation 2.4.

In the coordinate system defined by equations 2.1 to 2.5, the governing hydrodynamic and thermodynamic equations become (pp.60-83 of ref 10):

(a) the two horizontal equations of motion,

$$\frac{\partial}{\partial t}(Zu) + \frac{\partial}{\partial x}(u^* u) + \frac{\partial}{\partial y}(v^* u) + \lambda u_2 \dot{S} - G\zeta v + n\left[\frac{\partial}{\partial x}(\zeta\phi) + (\sigma\zeta a - \phi)\frac{\partial \zeta}{\partial x}\right] = -ZF_x \quad , \tag{2.6}$$

$$\frac{\partial}{\partial t}(Zv) + \frac{\partial}{\partial x}(u^* v) + \frac{\partial}{\partial y}(v^* v) + \lambda v_2 \dot{S} + G\zeta u + m\left[\frac{\partial}{\partial y}(\zeta\phi) + (\sigma\zeta a - \phi)\frac{\partial \zeta}{\partial y}\right] = -ZF_y \quad , \tag{2.7}$$

(b) the thermodynamic equation,

$$\frac{\partial}{\partial t}(ZT) + \frac{\partial}{\partial x}(u^* T) + \frac{\partial}{\partial y}(v^* T) - \frac{\sigma a}{C_P}\left[\zeta\frac{\partial Z}{\partial t} + u^*\frac{\partial \zeta}{\partial x} + v^*\frac{\partial \zeta}{\partial y}\right] + \lambda(P/P^*)^K \theta_2 \dot{S} = ZH/C_P \quad , \tag{2.8}$$

(c) the continuity equation,

$$\frac{\partial Z}{\partial t} + \frac{\partial u^*}{\partial x} + \frac{\partial v^*}{\partial y} + \lambda\dot{S} = 0 \quad , \tag{2.9}$$

(d) the moisture balance equation,

$$\frac{\partial}{\partial t}(Zq) + \frac{\partial}{\partial x}(u^* q) + \frac{\partial}{\partial y}(v^* q) = 2\,nmg\,(E - C). \tag{2.10}$$

Equations 2.6 to 2.9 are applied at both the upper ($\sigma = 1/4$) and lower ($\sigma = 3/4$) levels, and equation 2.10 is only applied at the lower level ($\sigma = 3/4$). The symbols used in these equations are defined in the list of nomenclature at the beginning of the thesis. In addition, the following equations are useful in explaining the relationships existing between the dependent variables:

$$Z = mn\zeta \quad , \tag{2.11a}$$

$$u^* = n\zeta u \quad , \tag{2.11b}$$

$$v^* = m\zeta v \quad , \tag{2.11c}$$

$$\dot{S} = 2mn\zeta \left(\frac{d\sigma}{dt}\right)_2 \quad , \tag{2.11d}$$

$$G = mnf - u\left(\frac{dm}{dy}\right) \quad , \tag{2.11e}$$

$$\theta = T(P^*/P)^K. \tag{2.11f}$$

The parameter λ, appearing in equations 2.6 to 2.9, is used to indicate the sign of a term according to

$$\lambda = \begin{array}{l} +1 \text{ if } \sigma = 1/4, \text{ upper level,} \\ -1 \text{ if } \sigma = 3/4, \text{ lower level.} \end{array} \tag{2.11g}$$

The potential temperature (θ) and horizontal wind components (u, v) at level $\sigma = 2/4$ are interpolated from the corresponding values at levels $\sigma = 1/4$ and 3/4 in a fashion ensuring conservation of the first and second moments of potential temperature and conservation of horizontal momentum. The resulting interpolation formulas are

$$\theta_2 = 1/2\ (\theta_1 + \theta_3) \quad , \tag{2.11h}$$

$$u_2 = 1/2\ (u_1 + u_3) \quad , \tag{2.11i}$$

$$v_2 = 1/2\ (v_1 + v_3) \quad . \tag{2.11j}$$

Also, the geopotential of the lower and upper levels is calculated in a fashion ensuring conservation of total energy (kinetic plus potential). This gives the following equations for the geopotential:

$$\phi_1 = \phi_S + 1/2\ C_P\ \theta_2\ (P_3^K - P_1^K)/P^{*K} + 1/2\ \zeta(\sigma_3 a_3 + \sigma_1 a_1) \quad , \tag{2.11k}$$

$$\phi_3 = \phi_S - 1/2\ C_P\ \theta_2\ (P_3^K - P_1^K)/P^{*K} + 1/2\ \zeta\ (\sigma_3\ a_3 + \sigma_1\ a_1). \quad (2.11\ell)$$

2.2 Space and Time Finite Differencing

In the Mintz-Arakawa model the differential equations 2.6 to 2.10 are horizontally finite differenced on a rectangular grid (pp.84 of ref 10) with equispaced grid lines mapped from the latitude and longitude circles. The mapping of longitude into x is linear, resulting in the same number of grid points (M) around each latitude circle at all latitudes. Since the circumference of each latitude circle decreases as latitude increases, this grid severely over-resolves the high latitude regions. This over-resolution is partially compensated for by chosing a piecewise linear mapping of latitude into y, with the latitudinal spacing of grid lines at the poles, δ, taken to be greater than the latitudinal spacing of grid lines at all lower latitudes, $\Delta\phi$. This gives equidistant grid points on the map projection in both longitude and latitude except for the polar cap. Also, this simplifies the task of approximating the horizontal derivatives in equations 2.6 to 2.10 by finite differences. The Mintz-Arakawa model employs a complex set of finite difference approximations for these spatial derivatives. This results in a form of smoothing of the finite difference slope estimates. To aid in the differencing scheme, the dependent variables in the Mintz-Arakawa model are spatially staggered. The velocity components, u and v, are carried at grid points (the corners of grid cells), the state parameters such as ζ, q and T are carried at the center of grid cells, the flux u^* is carried at the midpoint of vertical grid sides, and the flux v^* is carried at the midpoint of horizontal grid sides. The resulting set of difference

equations used in estimating the spatial derivatives in equation 2.6 to 2.10 are given by Price (pp.89-104 of ref 10) and will not be listed here.

With suitable finite difference expressions approximating the spatial derivatives, equations 2.6 to 2.10 may be used to advance the dependent variables in time. The time extrapolation scheme used in the Mintz-Arakawa model is a modified Matsuno two stage time differencing scheme (Matsuno (21), Price (pp.105-110 of ref 10)), and is the same as the two-stage Euler-backward differencing scheme discussed by Kurihara (17). This scheme may be illustrated by examining a representative equation in the set 2.6 to 2.10, abreviated as

$$\frac{\partial}{\partial t} Z\Psi = F_\Psi + S_\Psi. \tag{2.12}$$

Here, Ψ takes on the values unity, q, T, u and v; S_Ψ represents all terms arising from the heat, moisture and friction source terms H, (E - C) and F respectively; and F_Ψ represents all the remaining terms in the equation. Since the source terms S_Ψ vary slowly with time, they are neglected at most time steps and are only applied at every B'th time step in one large increment. In the first stage of each time step, a forward difference approximation yields the first estimate for $\Psi(t + \Delta t)$ according to

$$Z^* = Z(t) + F_1(t)\ \Delta t,\ \Psi^* = \frac{Z\Psi(t) + F_\Psi\ (t)\ \Delta t}{Z^*}\ , \tag{2.13a}$$

where S_Ψ has been neglected. In the second stage of the time differencing, a backward difference approximation results in the revised estimates for $\Psi(t + \Delta t)$ according to

$$Z^{**} = Z(t) + F_{1*}(t)\Delta t \quad , \quad \Psi^{**} = \frac{Z\Psi(t) + F_{\Psi*}(t)\Delta t}{Z^{**}} . \tag{2.13b}$$

If the time $t + \Delta t$ is not an integer multiple of $B\Delta t$, then the source terms are not included in the differencing, and the dependent variables at time $t + \Delta t$ are assigned the values

$$Z(t + \Delta t) = Z^{**} \quad , \quad \Psi(t + \Delta t) = \Psi^{**} . \tag{2.13c}$$

However, if the time $t + \Delta t$ is an integer multiple of $B\Delta t$, then the source terms are incorporated through a third stage in the differencing scheme. Firstly, the temperatures are adjusted to ensure that the atmosphere is dry adiabatically stable (p.109 of ref 10). Then with the dry adiabatically stable atmosphere characterized by the state parameters Ψ^{***}, the source term contributions are incorporated through a backward difference approximation using the extended time interval $B\Delta t$. This third or source stage results in the value

$$\Psi(t + \Delta t) = \Psi^{**} + S_{\Psi***}(t)\ B\Delta t/Z(t + \Delta t). \tag{2.13d}$$

2.3 Techniques to Aid Stability

The Mintz-Arakawa model is a finite difference model on a projection whose physical counterpart exhibits considerable shrinking between grid points as distance from the pole decreases (the metric m decreases as latitude increases). It is necessary to employ several special techniques in order to avoid computational instabilities on such a grid using a finite difference scheme. One technique has already been mentioned, namely carrying the individual dependent variables at different locations in the grid cells (a space staggered grid).

A second technique used in this model to avoid instabilities is to estimate the fluxes (u^*, v^*) and the pressure gradient terms

$\partial\zeta\phi/\partial x$, $\partial\zeta\phi/\partial y$, $(\sigma\zeta a - \phi)\ \partial\zeta/\partial x$, $(\sigma\zeta a - \phi)\ \partial\zeta/\partial y$ in the momentum equation according to different methods, depending on whether it is the first or second stage of the time step, or whether the time is an even or odd multiple of Δt. In the first stage of all time steps the fluxes and pressure gradient terms are estimated by centered symmetrical finite difference approximations. However, in the second stage of the time steps, the terms are estimated by uncentered non-symmetric finite difference estimates (pp.110-113 of ref 10): down-left uncentered estimates are used if time is an odd multiple of Δt, and up-right uncentered estimates are used if time is an even multiple of Δt. The term down-left means the difference expression uses values of the variable to the left and below the point where the flux or derivative is being calculated. A similar interpretation applies to the term up-right.

A third technique used in the Mintz-Arakawa model to avoid instabilities is to employ an averaging operator designed to damp out high frequency waves (short waves) travelling around latitude circles (in the longitudinal direction) at high latitudes. These spurious short waves arise from the shortening of the physical distance between grid points on the latitude circles as latitude increases. Subsequently, computational instability develops when the grid spacing becomes too small in comparison to the time step interval. The averaging operation is applied to the flux u^* and the pressure gradient terms $\partial\zeta\phi/\partial x$ and $(\sigma\zeta a - \phi)\ \partial\zeta/\partial x$ in the covariant component (u component) of the momentum equation. The averaging technique (p.114 of ref 10) is illustrated for the flux u^*. Define

$$D(y) = \Delta\Phi/(\Delta\Theta\cos\Phi) \quad , \tag{2.14a}$$

$$A(y) = \frac{1}{8}\,(D(y) - 1)/D^{*}(y) \quad , \tag{2.14b}$$

where $D^{*}(y)$ is the largest integer not greater than $D(y)$. Then,

$$u^{*(n)}(x,y) = u^{*(n-1)}(x,y) + A(y)\left[u^{*(n-1)}(x+1,y) - 2u^{*(n-1)}(x,y) + u^{*(n-1)}(x-1,y)\right] . \tag{2.14c}$$

This averaging expression is applied $D^{*}(y)$ times with n taking on the values $1,2,\ldots,D^{*}(y)$. The term $u^{*(0)}(x,y)$ denotes the value of $u^{*}(x,y)$ before any averaging is performed. On the completion of the averaging, $u^{*(0)}(x,y)$ is replaced by its averaged value, $u^{*(D^{*}(y))}(x,y)$. Although relatively weak in low and middle latitudes, this averaging operator shows a rapid increase in strength as latitude increases above 60° (or below -60°).

Finally, it is necessary to make additional special considerations at the poles. M cell centers map into each pole in the Mintz-Arakawa model. Since the state parameters ζ, q and T are carried at the cell centers, unique values for these parameters at each pole may be obtained by averaging the parameters over the M cell centers constituting each pole. A further problem, the vanishing of metric m at the poles, causes Z to vanish, thereby invalidating equations 2.13a to d. This is remedied by artificially assigning the value of metric m at latitudes north of $(90 - \delta/2)$ degrees to be equal to the metric evaluated at latitude $(90 - \delta/2)$, with a similar treatment at the south pole. It is also necessary to redefine the flux u^{*} carried at the mid-points of the M vertical grid sides crossing each pole, since a longitudinal flux at the north or south pole is physically meaningless. In the Mintz-Arakawa model, this is done by applying conservation of mass to the polar cap as a whole and solving for a ficticious set of u^{*} values for each pole. Finally, artificial latitudinal fluxes from regions "north of the north

pole" arise in the finite difference equations for the dependent variables in the polar cap. Such artificial fluxes are physically meaningless and are neglected when they arise.

2.4 Heat, Moisture and Friction Sources

The energy inputs in the Mintz-Arakawa model include the heating function H, moisture source or sink Q, and friction dissipation F. Four contributions to the heating function are taken into account: incoming solar radiation, long wave radiation exchange by the different atmosphere levels and from the earth to each level, upward transport of sensible heat from the earth's surface into the lower level air, and the release of latent heat when precipitation occurs. Evaporation from oceans is the only source of moisture in the model, and two mechanisms for condensation are accounted for: large scale precipitation and convective precipitation. From the amount and type of precipitation, a fractional cloud cover amount is calculated. The two sources of friction accounted for in the model are surface friction acting on the lower layer, and a horizontal shear stress acting on the interface between the upper and lower layers. A detailed description of the individual heat and moisture sources in the Mintz-Arakawa model is given by Price (40), and the friction contributions are described by Price (pp.99-103 of ref. 10).

3. The Proposed Forecast Model: Bicubic Polynomial Splines on a Variable Area Telescoping Grid

3.1 The Basic Equations in x, y, σ, t Coordinates

The basic equations of thermodynamics and hydrodynamics used in the Mintz-Arakawa model (equations 2.6 to 2.10) are representative of the many available classical systems of equations used in modern numerical weather prediction models. The x, y, σ, t coordinate system is appealing since the entire earth is readily mapped in this coordinate system (with but two singularities at the poles) and the earth's surface itself becomes the $\sigma = 1$ coordinate surface. For these reasons, as well as to facilitate the comparison of the polynomial spline method and telescoping grid of the proposed model with the finite difference method and conventional grid of the Mintz-Arakawa model, the governing equations in the proposed model are chosen to be the same as those in the Mintz-Arakawa model (equations 2.6 to 2.10). Further, only a two-level version of the model is studied in order to save computation time.

A very simple linear mapping is used to relate the cartesian map coordinates x and y to longitude Θ and latitude Φ respectively. Chosing x and y also to denote longitude and latitude, then

$$x = \Theta \, 180/\pi \quad , \qquad y = \Phi \, 180/\pi \quad , \tag{3.1}$$

where Θ and Φ are in radians, and x and y denote distance on the projection expressed in degrees of longitude and latitude. Hence, the bounds of the northern hemisphere forecast region are the lines $x = -180.0$, $x = +180.0$, $y = 90.0$ and $y = YS$, corresponding respectively to the 180° West meridian, 180° East meridian, north pole and southern boundary line located a few degrees (YS) south of the equator. Having selected suitable units for the x and y coordinates it is now

possible to solve for the metrics m and n in the proposed forecast model. Applying equations 2.1 and 2.2 along with 3.1, there results the values

$$dx = d\theta\ 180/\pi \quad , \qquad dy = d\Phi\ 180/\pi \quad , \tag{3.2}$$

$$m = \frac{ds_1}{dx} = \pi A \cos\Phi\ /180 \quad , \tag{3.3a}$$

$$n = \frac{ds_2}{dy} = \pi A\ /180 \quad . \tag{3.3b}$$

Since the flux v^* is required at the north pole, it is necessary to have a nonzero value for m at the pole (m_p). This is approximated by taking

$$m_p = m(y_2) \quad , \tag{3.3c}$$

where y_2 is the latitude of the first row of grid points lying just south of the north pole. This artificial value for the metric m at the pole is in keeping with the method used to assign values for the dependent variables at the pole. This is further discussed in Section 3.2.3.

3.2 The Variable Area Telescoping Grid

A double subscript indexing notation (subscripts i, j) is used to locate any node (grid point) in the forecast region. Subscript j denotes the latitude circle on which the node is located. This subscript takes on the values between 1 at the north pole and N at the southern boundary latitude circle y = YS. Subscript i denotes the position of the node on the latitude circle. The first node on each latitude circle (at all latitudes) is at x = - 177.5, and it is assigned the subscript i = 1. Subsequent nodes around the latitude circle in the direction of x increasing are assigned the subscripts $i = 2,3,\ldots$ to M_j, where the number of nonrepeating nodes on the j'th

latitude circle is M_j.

3.2.1 Two Grid Expansion Forms

The variable area telescoping grid in the proposed forecast model has two forms of grid expansion superimposed on each other. The first grid expansion is required to maintain the physical distance between grid points on latitude circles greater than or equal to some minimum distance required for computational stability; and the second grid expansion is used to decrease the number of grid points in regions which are not of primary interest.

In the first expansion, since the physical length of each latitude circle decreases as latitude increases, the number of nodes on the latitude circle must also decrease. The range of coordinate x on each latitude circle remains constant (360.0) at all latitudes. Hence, fewer nodes on the latitude circle results in an increase (expansion) in spacing between the nodes $x_{1,j}, x_{2,j}, \ldots x_{Mj,j}$. This expansion increases as latitude y_j increases. The physical distance between M_N equispaced nodes on latitude circle y_N (lying closest to the equator) is

$$d_N = (2\pi A \cos y_N)/M_N \quad , \tag{3.4}$$

where A is the mean radius of the earth. The interval d_N is selected to be the minimum physical distance between adjacent nodes on any latitude circle. In other words, the distance d_N is used in selecting a suitable time step for the computationally stable time extrapolation scheme. It is therefore necessary to have $d_j \geq d_N$, where d_j is the physical distance between M_j equispaced nodes on latitude y_j. With d_j given by

$$d_j = (2 \pi AA \cos y_j)/M_j \quad , \tag{3.5}$$

then the selection

$$M_j = \text{largest integer} \leq M_N \cos y_j / \cos y_N \quad , \tag{3.6a}$$

$$M_1 = M_2 \quad , \tag{3.6b}$$

$$M_N = \text{arbitrary} \tag{3.6c}$$

ensures that $d_j \geq d_N$ for $j = 1,\ldots N$. The resolution throughout the forecast region is very uniform since the spacing d_j at any latitude is less than $100/M_j$% larger than d_N*. Equation 3.6b is a necessary approximation to accommodate the pole. It will be discussed later in this chapter.

The second grid expansion results in an increase in the grid point spacing as distance away from the region of interest increases. In this fashion the amount of computation time spent in generating good resolution forecasts in regions of little concern is considerably reduced, without sacrificing resolution in the region of primary interest. The method used to generate this expanding or telescoping grid is discussed in Appendix 2. The most important characteristic of the method is the smooth transition between regions of increasing grid size and regions of decreasing grid size, as well as a smooth matching with the fixed north pole and southern boundary line YS.

---

* This result may be verified in the following fashion:

let $M_j^* = M_N \cos y_j / \cos y_N$,

d_j = equation 3.5 ,

$d_N = 2\pi AA \cos y_j / M_j^*$;

then the % difference between d_j and d_N becomes $100\left(\frac{d_j - d_N}{d_N}\right)$

or $\frac{100}{M_j}(M_j^* - M_j) \leq \frac{100}{M_j}$ since $M_j^* - M_j < 1$.

3.2.2 Grids Used in the Numerical Forecasts

The four grids A, B, C and D used in the numerical forecasts are given in Figures 3.1 to 3.4 respectively. Grid A (Figure 3.1) has a 5° latitude, 5° longitude grid, with a 12.5° polar cap (the spacing between rows j = 1 and j = 2 is 12.5°). Nodes are indicated by the symbols × , the numbers immediately adjacent to the grid along the top and right hand side denote longitude and latitude respectively, in degrees, and the column of numbers from 1 to 18 along the right hand side denotes the row numbers. In this grid, N = 18 and M_j = 72, j = 1, ...N. The grid interval in grid B, Figure 3.2, is double that of grid A. In all other respects grid B is of the same nature as grid A. Grid C, Figure 3.3, is formed by imposing the basic expansion of type one on grid A. In order to maintain a constant physical distance between nodes on all latitude circles in this grid, the number of nodes around each latitude circle must decrease as latitude increases. In increasing order, from high to low latitude, the terms M_j take on the values M_j = 15,15,21,27,33,38,43,48,53,57,60,63,66,68,70,71,72,72 as j increases from 1 to 18. The final grid used in the numerical forecast experiments is the telescoping grid, grid D (Figure 3.4). This grid is generated by superimposing the expansion of type two on grid C, which already had a basic expansion of type one. In this second expansion the grid expansion factors in the x and y axes directions respectively (see Appendix 2 and Figure A2.1) are EX = 1.1 and EY = 1.04. The expansion is centered about the point (XP, YP) = (95, 50) located close to Winnipeg, Canada.

The region of interest corresponds to a three grid cell or 1000 mile wide band extending eleven grid cells or 3500 miles across

North America. Within this region of interest, the grid cells are of the minimum size required for computational stability at that latitude. The grid then expands monotonously as distance away from the region of interest increases. In increasing order, from high to low latitude, the terms M_j take on the values M_j = 17,17,22,25,28,30,31,33,34,35,36,37,38, 38,39,39 as j increases from 1 to 16. In Figure 3.4, the expansion in the y direction is shown by a crowding of latitude lines at high and low latitudes, with equispaced grid point rows on the figure.

There are no difficulties in applying bicubic polynomial splines on an expanding grid, provided the grid expansion is smooth. Ahlberg (24) reports problems in curve fitting when the physical spacing changes significantly in a limited region. Essentially, when the grid point spacing in a one-dimensional region containing four grid points is alternately very large, very small, then very large, the resulting spline fit to a monotonic increasing ordinate shows a local maximum followed by a local minimum. This results in a very small local spike in an otherwise monotonic spline curve fit. The spike is very local and usually small (barely perceptible). In the application of splines in the proposed forecast model, a good estimate of slopes is desired. Although a small local spike has little obvious effect on the curve fit, it has a devastating effect on the derivative at the node where the grid spacing changes too abrubtly. Hence a smoothly expanding grid is essential.

3.2.3 Assigning Dependent Variables at the Pole and Equator

In the proposed model, the dependent variables are advanced in time at nodes on the latitude circles $j = 2$ to $j = N - 1$ (see Figure 3.1, in which $N = 18$). This may be compared to the Mintz-Arakawa model, in

which the dependent variables are advanced in time on all the latitude circles $j = 1$ to $j = N$. Several special techniques are required to ensure a conservative differencing scheme at the pole in the Mintz-Arakawa model. These special techniques are not required in the proposed model since the north pole (latitude circle $j = 1$) is not independently advanced in time. The x-component of the bicubic spline is readily applied along each of the latitude circles $j = 2$ to $j = N - 1$ since the dependent variables are periodic in x. However, the y component of the spline surface must be applied along the longitude lines $i = 1$ to $i = M_j$ from $j = 1$ (north pole) to $j = N$ (south boundary just south of the equator). It is therefore necessary to generate values for the dependent variables at the nodes on the polar and equatorial latitude circles, $j = 1$ and $j = N$ respectively.

The latitude circle $j = 1$ corresponds to the north pole, a singular point. It is proposed that a suitable set of unique dependent variables at the pole may be chosen to be representative of the dependent variables in the polar cap (carried at nodes on latitude circle $j = 2$). The variables in question are u, v, T, q, ζ, ϕ and v*, of which v* and ϕ depend on the others. Note that since the y derivatives of u* are absent from the differential equations, it is not necessary to generate u* at the pole. This may be compared to the artificial u* fluxes in the Mintz-Arakawa model at the pole, required to ensure conservation of mass and momentum in the differencing scheme used to update the polar dependent variables. In the proposed model, a unique polar value for variable $\Psi = \zeta$, q, T or ϕ is obtained by the averaging

$$\Psi_{i,1} = \frac{1}{M_2} \sum_{k=1}^{M_2} \Psi_{k,2} , \qquad i = 1,\ldots M. \tag{3.7}$$

A unique nonzero horizontal wind at the pole is obtained by first referencing all horizontal winds at nodes (i, 2), i = 1,...M_2 in terms of horizontal axes with the y axis aligned along the Greenwich meridian (0° longitude), next averaging these winds to obtain a unique horizontal wind at the pole, and finally finding the local components of this wind in terms of local horizontal axes at nodes (i, 1), i = 1, ...M_1. In terms of horizontal axes at the Greenwich meridian, the unique polar horizontal wind components are

$$u_p = \frac{1}{M_2} \sum_{k=1}^{M_2} V_{k,2} \cos \Theta_{k,2} \quad , \tag{3.8a}$$

$$v_p = \frac{1}{M_2} \sum_{k=1}^{M_2} V_{k,2} \sin \Theta_{k,2} \quad , \tag{3.8b}$$

where $$V_{i,2} = (u_{i,2}^2 + v_{i,2}^2)^{\frac{1}{2}} \quad , \; i = 1,...M_2, \tag{3.8c}$$

$$\Theta_{i,2} = \tan^{-1} (v_{i,2}/u_{i,2}) + x_{i,2} \quad , \; i = 1,...M_2. \tag{3.8d}$$

Then the local components of this polar wind, in terms of local horizontal axes located at nodes (i, 1) i = 1,...M_1, become

$$u_{i,1} = V_p \cos(\Theta_p - x_{i,1}) \quad , \; i = 1,...M_1 \quad , \tag{3.9a}$$

$$v_{i,1} = V_p \sin(\Theta_p - x_{i,1}) \quad , \; i = 1,...M_1 \quad , \tag{3.9b}$$

where $$V_p = (u_p^2 + v_p^2)^{\frac{1}{2}} \quad , \tag{3.9c}$$

$$\Theta_p = \tan^{-1} (v_p/u_p) \quad . \tag{3.9d}$$

The flux v^* at the pole is generated using equations 2.11c, 3.3c and 3.9b.

The pole now has realistic unique values of the dependent variables. It is important to recognize that this data at the pole is not independently updated in time, since no time extrapolation expressions are written for nodes along the latitude circle j = 1 making up the pole.

Rather, the pole depends solely on the average state of the polar cap as defined by the dependent variables around latitude circle j = 2. The polar data is required only to serve as a realistic boundary condition on the y component of the bicubic spline data fit.

Values for the dependent variables on the latitude circle j = N, just south of the equator, are assigned from corresponding data points on the latitude circle j = N - 1, just north of the equator. A mirror image symmetry arrangement is used for the dependent variables Ψ = u, T, ζ and q, according to

$$\Psi_{i,N} = \Psi_{i,N-1} \quad , \quad i = 1,\ldots M_1. \tag{3.10a}$$

An anti-symmetric boundary condition is imposed on the y component of the horizontal wind, thereby preventing cross equatorial flow. Hence,

$$v_{i,N} = - v_{i,N-1} \quad , \quad i = 1,\ldots M_1 \quad . \tag{3.10b}$$

Again, this equatorial data is required only to serve as a realistic boundary condition on the y component of the bicubic spline data fit. It is not independently advanced in time.

3.3 Bicubic Polynomial Splines

3.3.1 The Spline Based on Continuity of Second Derivative

It is proposed that bicubic polynomial splines be used to estimate the horizontal derivatives in the system of governing equations 2.6 to 2.10. Consider the rectangular mesh $x_1 < x_2 < \ldots < x_M$, $y_1 > y_2 > \ldots > y_N$ with prescribed ordinates u_{ij} at mesh points (x_i, y_j), i = 1,...M; j = 1,...N. The double cubic or bicubic spline of interpolation to the ordinates u_{ij} at mesh locations (x_i, y_j) is a piecewise continuous function defined as a double cubic polynomial in each rectangle $x_{i-1} \leq x \leq x_i$, $y_{j-1} \geq y \geq y_j$, with continuous first derivatives and

cross derivative at all points in the rectangular mesh. Ahlberg, Nilson and Walsh (26) describe the construction of a periodic two-dimensional cubic spline S(x, y) over rectangular elements. This spline is expressed in terms of prescribed ordinates $u(x_i, y_j)$ and generated second and fourth derivatives $\partial^2 S/\partial x^2$ $\partial^2 S/\partial y^2$ and $\partial^4 S/\partial x^2 \partial y^2$ at x_i, y_j. Since one basic aim of applying double cubic splines to fit meteorological data fields is to obtain best estimates of the first derivatives at data points, it is more convenient to construct the spline S(x,y) in terms of prescribed ordinates u_{ij} and generated first and cross derivatives p_{ij}, q_{ij} and s_{ij} representing, respectively, $\partial S/\partial x$, $\partial S/\partial y$ and $\partial^2 S/\partial x \partial y$ at x_i, y_j. In Appendix 1, the double cubic spline S(x,y) is derived in terms of u_{ij}, p_{ij}, q_{ij} and s_{ij}. In the proposed model, it is not necessary to generate all the coefficients in the double cubic piecewise continuous spline field. Rather, only the nodal values of the first two derivatives, p_{ij} and q_{ij} are generated.

3.3.2 Boundary Conditions on the Spline

The possible boundary conditions on the bicubic spline data fit are discussed in Appendix 1. The boundary conditions on the x-component of the bicubic spline cause no problems since the field is periodic in x. However, a certain degree of judgement is required in selecting the boundary conditions on the y component of the spline. Nodal values at the ends of the spline in the y direction are known, since they are generated from equations 3.7, 3.9a, 3.9b, 3.10a and 3.10b. However, an additional piece of information is required at the ends, generally in the form of a specified first or second derivative.

This information is straight forward at the equator, where a symmetry boundary condition is assumed. The equator lies at the center

of grid cells between latitude circles $j = N - 1$ and $j = N$. The slope on the spline surface and the corresponding value of the spline between two nodes are given by equations A1.42a,c in Appendix 1. For the symmetrical dependent variables (equation 3.10a), $\partial S/\partial y$ must vanish on the equator. Setting equation A1.42c to zero yields

$$q_{i,N} = - q_{i,N-1} \quad . \tag{3.11a}$$

For the anti-symmetric v compenent of the horizontal wind (equation 3.10b), $S(x,y)$ must vanish on the equator. Setting equation A1.42a to zero yields

$$q_{i,N} = q_{i,N-1} \quad . \tag{3.11b}$$

At the pole, however, it is a question of how rigidly should the bicubic spline surface be restrained by an end condition affecting the slope. For example an end condition having little or no influence on the slope of the spline surface fit at the pole is undesirable. With such an unrestrained end condition there is no coupling between the slopes of the spline surface along the different longitude lines meeting at the pole. Computational stability with any particular time step requires the slope resolution at nodes in the field be less than some maximum value. This is a logical corollary of the stability requirement that the grid interval be greater than some minimum value, and the larger the grid interval, the poorer the slope resolution. Hence, some coupling between the slopes along longitude lines meeting at the pole is required to decrease the overall polar slope resolution to a value at least representative of the slope resolution in the remainder of the field. Increasing the coupling is therefore a restraining influence on the spline surface fit at the pole. The possible end conditions which exert this restraining influence include specifying the slope or second

derivative at the pole, or specifying the second derivative at a ficticious point "north of the north pole" (equations A1.25 to A1.28 in Appendix 1).

End conditions of the form $q_{i,1} = q_{i,2}$ or $Q_{i,1} = Q_{i,2}$ are ruled out as having too unrestrained an influence on the spline surface fit. Here, the symbol Q represents $\partial^2 S/\partial y^2$ (similar to having q represent $\partial S/\partial y$). The end condition involving a specified second derivative at a ficticious point "north of the north pole" permits some control on the restraining influence of the end condition on the spline surface fit. However, at this stage in the analysis, it is felt that such control is not required and this end condition is eliminated. This leaves a selection of one of two possible end conditions:

$$q_{i,1} = 0 \quad , \quad \text{or} \tag{3.12a}$$

$$Q_{i,1} = 0 \quad . \tag{3.12b}$$

In the standard atmosphere, the temperature and pressure fields are radially symmetric about the pole, and both end conditions 3.12a and 3.12b are satisfied. However, in the real atmosphere there is generally a large deviation from radial symmetry. Of the two end conditions, specifying the first derivative is a more restrictive influence on the spline surface fit than is specifying the second derivative. Therefore, equation 3.12b is the preferred end condition, and it is used in the proposed forecast model. The other end condition is tested in the preliminary numerical forecast experiments.

3.3.3 A Generalized Spline Based on Curvature

It has been mentioned that the cubic spline based on continuity of the second derivative exhibits the minimum curvature property when curve fitting data with small slopes. This property does not apply when

the slope is large. In order to accommodate rapidly changing data with few data points, it was decided to derive a generalized cubic spline based on continuity of the approximate curvature at points located between the data nodes.

The need for such a generalized spline becomes apparent from an examination of the nature of the cubic spline curve fit in cases of rapidly changing data. Preliminary experiments with the cubic spline based on continuity of the second derivative have shown that when there is a sudden change in the curvature nature between two regions in the field, the spline slope estimates at the nodes oscillate about the true slopes, with a decreasing percentage error as distance from the junction between the two regions increases. In Table 3.1, six sets of sample data are given to illustrate the consequence of abrubtly changing curvature on the spline data fit. In data sets one to three, the region $x < x_4$ corresponds to a sinusoidal test function and the region $x > x_5$ corresponds to a straight line of three different slopes. Data sets four and five are cases of two straight lines meeting at a point between x_4 and x_5. The sixth and final data set corresponds to a sinusoidal test function over the entire interval. The true derivative p_{it} is obtained by differentiating the analytic test function u(x); the spline derivative estimates p_{is} are formed by fitting a one-dimensional cubic spline to the known ordinates u_i at nodes x_i for all i ; and, the % error in p_{is} is calculated relative to the true slope p_{it}. From this table it is seen that there are significant oscillations in the spline curve fit at the junction between regions of abrubtly changing curvature, while the accuracy of the spline curve fit is very high (less than 0.1% error) in regions of slower changing curvature. This illustrates the

type of problem which may be encountered when using the cubic spline based on continuity of the second derivative to curve fit data which has abrubt changes in curvature. A generalized spline based on curvature (rather than the second derivative) is proposed as an alternative to the problem of curve fitting rapidly changing data.

The general cubic spline based on continuity of the approximate curvature is derived in a similar fashion to the cubic spline based on continuity of the second derivative (Appendix 1). The derivations differ primarily in the continuity requirement. Where the simple cubic spline employs the continuity of second derivative constraint (equations A1.19 to A1.23 in Appendix 1), the generalized cubic spline employs a continuity of curvature constraint,

$$\frac{1}{\beta_i} S''(x_i - ah_i) = \frac{1}{\beta_{i+1}} S''(x_i + bh_{i+1}) \quad , \tag{3.13a}$$

$$\beta_i = (1 + S'^{2}_{fi})^{3/2} \quad , \tag{3.13b}$$

$$S'_{fi} = \left(\frac{u_i - u_{i-1}}{h_i}\right) \frac{XS}{US} \quad . \tag{3.13c}$$

$$h_i = x_i - x_{i-1} \quad , \tag{3.13d}$$

$$XS, US = \text{nondimensionalizing factors} \quad , \tag{3.13e}$$

$$o \leq a \leq 1 \quad , \quad o \leq b \leq 1 \quad . \tag{3.13f}$$

Here, equation 3.13a expresses continuity of the approximate curvature between the points $x_i - ah_i$ and $x_i + bh_{i+1}$. These points are generally not grid points since a and b are generally nonzero. Also, the curvature is only approximate since S'_{fi} is a finite difference estimate for the slope at $x_i - ah_i$, not the true spline slope. If the true spline slope (equation A1.17) were used in place of S'_{fi}, equation 3.13a would become nonlinear. The solution of a nonlinear system of

algebraic equations is very difficult and therefore not practical in this application. The additional factor XS/US appearing in equation 3.13c is required to scale the ordinate u and abscissa x to be independent of the units used, and to make S'_{fi} of the same order of magnitude as the number "1" appearing in equation 3.13b. This is necessary since β_i is nonlinear in S'_{fi}, and the numerical value of the ratio β_i/β_{i+1} in equation 3.13a should be independent of the units used. For example. if u_{i+1}, u_i, u_{i-1}, x_{i+1}, x_i, x_{i-1} have the values 200°K, 196°K, 206°K, 100 ft, 96 ft, 101 ft respectively, then with no scaling factors (XS/US = 1.0), there results the slopes S'_{fi+1} = 1°K/ft, S'_{fi} = 2°K/ft giving $\beta_{i+1}/\beta_i = 0.252$. However, if the units of x are changed from feet to inches, then S'_{fi+1} = 1/12°K/in., S'_{fi} = 1/6°K/in. and $\beta_{i+1}/\beta_i = 1.0$. This is discussed further in the actual numerical experiments.

With S"(x) given by equation A1.18, the continuity requirement 3.13a becomes

$$\frac{2p_{i-1}(1-3a)}{\beta_i h_i} + \frac{4p_i(1-\frac{3}{2}a)}{\beta_i h_i} - \frac{6(u_i - u_{i-1})(1-2a)}{\beta_i h_i^2} \qquad (3.14)$$

$$= -\frac{4p_i(1-\frac{3}{2}b)}{\beta_{i+1} h_{i+1}} - \frac{2p_{i+1}(1-3b)}{\beta_{i+1} h_{i+1}} + \frac{6(u_{i+1} - u_i)(1-2b)}{\beta_{i+1} h_{i+1}^2} \quad ,$$

or $$\lambda_i^* p_{i-1} + 2p_i + \mu_i^* p_{i+1} = c_i^* \quad , \; i = 2,3,\ldots M-1 \quad , \qquad (3.15)$$

where $$c_i^* = 3\lambda_i^{**} \frac{(u_i - u_{i-1})}{h_i} + 3\mu_i^{**} \frac{(u_{i+1} - u_i)}{h_{i+1}} \quad , \qquad (3.16a)$$

$$\lambda_i^* = \beta_{i+1} h_{i+1} (1-3a)/D_i \quad , \qquad (3.16b)$$

$$\mu_i^* = \beta_i h_i (1-3b)/D_i \quad , \qquad (3.16c)$$

$$\lambda_i^{**} = \beta_{i+1} h_{i+1} (1 - 2a)/D_i \quad , \tag{3.16d}$$

$$\mu_i^{**} = \beta_i h_i (1 - 2b)/D_i \quad , \tag{3.16e}$$

$$D_i = (1 - \tfrac{3}{2}a)\, \beta_{i+1} h_{i+1} + (1 - \tfrac{3}{2}b)\, \beta_i h_i \quad , \tag{3.16f}$$

provided at least one of a or b is not 2/3. Since there is no advantage in using a different from b in this application, a and b are assigend the same value. In the discussion which follows, let A denote the coefficient matrix for the left hand side of the system of equations 3.15 written for the periodic case ($p_0 = p_M$, $p_1 = p_{M+1}$). If a = 2/3, the multipliers of p_i, i = 1,...M, become zero and the main diagonal of the coefficient matrix A vanishes. Hence, although the system of equations has a unique solution (since the terms c_i^* are not 0 and the det(A) $\neq$ 0 for M > 4), the solution may not be obtained by conventional pivotal numerical methods because the system of equations is not diagonally dominant (p.425 of ref 41). Also, this solution is only of minor interest since the zero main diagonal in matrix A results in double the effective grid length, thereby reducing the accuracy of the phase speeds predicted for the short meteorological waves. The role of the effective grid length is briefly discussed in the Introduction. In the second case of interest, a = 1/2, the homogeneous system ($c_i^* = 0$ for all i) which results has a unique solution since det(A) $\neq$ 0; and the solution is the trivial solution $p_i = 0$ for all i (p.384 of ref 42). This spline curve fit with zero slopes at all the grid points represents the maximum possible smoothing of the slope estimates. Values of a between 2/3 and 1/2 represent varying degrees of the characteristics of the two extremes and are of little practical importance. A third case occurs when a = 1/3 and XS = 0. The system then reduces to a simple central finite difference scheme

$$p_i = \lambda_i \frac{(u_i - u_{i-1})}{h_i} + \mu_i \frac{(u_{i+1} - u_i)}{h_{i+1}} \quad , \quad i = 2,\ldots M, \tag{3.17a}$$

where $$\lambda_i = \frac{h_{i+1}}{h_i + h_{i+1}} \quad , \quad \mu_i = \frac{h_i}{h_i + h_{i+1}} \quad . \tag{3.17b}$$

Similar to the bicubic splines in Appendix 1, the factors λ_i and μ_i give a weighting of the finite difference estimates to account for the varying grid interval. The values of a between 1/2 and 1/3 give varying degrees of smoothing or damping of the slope estimates, with an increase in smoothing as a approaches 1/2. Finally, when a = 0 and XS = 0, the system 3.15 reduces to the system A1.21 in Appendix 1 used to define the original cubic spline based on continuity of the second derivative. Of major interest in this study is the inter-relationship between finite differences and cubic splines. Since the former occurs when a = 1/3, XS = 0 and the latter occurs when a = 0, XS = 0, the range of values of a which are of most interest are $0 \lesssim a \lesssim 1/3$.

3.4 The Forecast Procedure Using Bicubic Splines on the Telescoping Grid

The governing partial differential equations (2.6 to 2.10) are of the form

$$\frac{\partial}{\partial t} Z\psi = A_{\psi x} + B_{\psi y} \tag{3.18}$$

where the terms $A_{\psi x}$ and $B_{\psi y}$ represent all terms involving first derivatives in x and y respectively in the ψ differential equation, ψ taking on the values unity, u, v, ζ, q and T. The time extrapolation scheme for $Z\psi$ is applied using equation 3.18 at all the nodes j = 2,... N-1; i = 1,...M_j. The dependent variables at the pole (j = 1) and on the latitude circle just south of the equator (j = N) are not extrapolated in time, since they are generated from data on latitude circles

$j = 2$ and $j = N-1$. In the proposed forecast model, suitable values for $A_{\psi x}$ and $B_{\psi y}$ are generated from a cubic spline surface fit to the dependent variable fields. There is no problem in generating $A_{\psi x}$ in this fashion since the variably spaced grid points lie on latitude circles. However a conventional cubic spline data fit in the y direction is not possible unless the dependent variables are aligned along longitude lines. It is seen from Figures 3.3 and 3.4 that this is not the case, since one or two types of expansion have been imposed on the grid. This problem is circumvented in the following fashion. First, the dependent variables are interpolated from nodes on the expanding grid to nodes on an underlying rectangular grid having grid points aligned along longitude circles. Next, the dependent variables on the underlying grid are fit by cubic splines in the y direction, thereby generating $B_{\psi y}$ at all nodes on the underlying grid. Finally, the $B_{\psi y}$ values on the underlying grid are back interpolated to the expanding grid. With $A_{\psi x}$ and $B_{\psi y}$ known at grid points on the expanding grid, $\partial Z\psi/\partial t$ becomes known and the time differencing proceeds according to equations 2.13a,b at nodes on the expanding grid.

Grid A (Figure 3.1) is a suitable underlying grid for the expanding grid C (Figure 3.3). It is seen from the figures that grid A meets the requirement of having grid points aligned along longitude lines. The method by which dependent variables at nodes on the expanding grid are interpolated to nodes on the underlying grid will be referred to as interpolation method A. Since the interpolation is in the direction of finer resolution, a quadratic interpolation using intermediate data formed by linear interpolation is used. With reference to Figure 3.5, the method is to use the known ordinates at nodes x_1, x_2, x_3 and x_4 to

estimate a value for the ordinate at point x^* lying between x_2 and x_3. Linear interpolation is first used to assign values to the ordinate at points $x_{1.5}$, $x_{2.5}$ and $x_{3.5}$ lying at the midpoint of the grid intervals.

$$\psi_{i+.5} = \frac{1}{2}(\psi_i + \psi_{i+1}) \tag{3.19}$$

A quadratic interpolation is now possible using the ordinate values at $x_{1.5}$, $x_{2.5}$ and $x_{3.5}$. The interpolation polynomial is constructed using Neuton's interpolation formula with divided differences (p.171 of ref 43). Hence,

$$\psi(x^*) = \psi_{1.5} + (x^* - x_{1.5})\, f_{1.5,2.5} + (x^* - x_{1.5})(x^* - x_{2.5})\, f_{1.5,2.5,3.5} \quad , \tag{3.20a}$$

where

$$f_{i,j} = (\psi_i - \psi_j)/(x_i - x_j) \quad , \tag{3.20b}$$

$$f_{i,j,k} = (f_{j,k} - f_{i,j})/(x_k - x_i) \quad . \tag{3.20c}$$

Then the following interpolation formula results:

$$\psi(x^*) = a\psi_{1.5} + b\psi_{2.5} + c\psi_{3.5} \tag{3.21a}$$

where

$$a = \xi\bar{\eta}^2(\xi - 1)/(1 + \bar{\eta}) \quad , \tag{3.31b}$$

$$b = (\xi\bar{\eta} + 1)(1 - \xi) \quad , \tag{3.21c}$$

$$c = \xi(1 + \xi\bar{\eta})/(1 + \bar{\eta}) \quad , \tag{3.21d}$$

$$\xi = \frac{x^* - (x_2 + h_3/2)}{.5(h_3 + h_4)} \quad , \tag{3.21e}$$

$$\bar{\eta} = (h_3 + h_4)/(h_3 + h_2) \quad , \tag{3.31f}$$

$$h_i = x_i - x_{i-1} \quad . \tag{3.21g}$$

The method by which variables on the underlying grid are back interpolated to the expanding grid will be referred to as interpolation method B. Since the interpolation is in the direction of coarser resolution, especially at high latitudes, a weighted averaging

technique will be used. With reference to Figure 3.6, the method is to evaluate ψ_{i*} on the expanding grid using equal contributions from all nodes lying within range R on the underlying grid and using smaller weighted contributions from nodes x_{i1-1} and x_{i2+1} lying just outside of R. The resulting interpolation formula is

$$\psi_{i*} = \frac{\sum_{k=i1}^{i2} \psi_k + f_1\psi_{i1-1} + f_2\psi_{i2+1}}{i2 - i1 + f_1 + f_2} \quad , \tag{3.22a}$$

where $$f_1 = d_1/h_{i1} \quad , \qquad f_2 = d_2/h_{i2+1} \quad , \tag{3.22b}$$

$$h_i = x_i - x_{i-1} \quad . \tag{3.22c}$$

It is important to note that this scheme is only used in generating the terms in $B_{\psi y}$ (equation 3.18) used in the time extrapolation scheme; this method is not applied to any of the dependent variables in the model.

It is also worth noting that both interpolation methods A and B are numerical quadrature methods. Although a polynomial spline method may be potentially more accurate in interpolation, it is not used here for several reasons. Firstly, the major reason for using splines in this thesis is to obtain best estimates for the slopes of the dependent variable fields at the grid points. This was discussed in the Introduction where it was pointed out that a spline estimate of the slope has several inherently better characteristics than a finite difference slope estimate. Secondly, the interpolation methods A and B discussed above are important but not critical in this model, since these interpolation methods only enter into the calculation of $B_{\psi y}$ in equation 3.18. The more critical calculation of $A_{\psi x}$, which strongly determines the meteorological wave speeds, is performed directly using polynomial splines without any intermediate interpolation. Also, stability problems are

primarily concerned with spurious short waves travelling in the west-east direction, and the calculation of $B_{\psi y}$ has little influence on this. The third reason for the use of the quadrature interpolation methods A and B is the saving in computation time without a marked decrease in accuracy compared to the spline interpolation method. Essentially, the two important characteristics of interpolation methods A and B which must be realized are that the methods be reasonably accurate and fast.

4. Numerical Experiments and Forecast Results

4.1 Real Weather Initial and Verification Data: 0000 GMT February 2,1970 and 1200 GMT February 3,1970

Input data required to begin forecasts using the proposed model and the comparison Mintz-Arakawa model consists of the following parameters specified at each grid point in the forecast domain:

1. T_{oc}, ocean temperature required in calculating the heat sources H_1 and H_3.
2. ϕ_s, surface geopotential, determined from land elevations by equations 2.11k and 2.11ℓ.
3. Z, determined from the surface pressure P_s by equations 2.5 and 2.11a.
4. q_3, mixing ratio at the $\sigma = 3/4$ level only.
5. $u_1, u_3; v_1, v_3$, x and y components of the horizontal wind at the $\sigma = 1/4$ and $\sigma = 3/4$ levels.
6. T_1, T_3, temperature at the $\sigma = 1/4$ and $\sigma = 3/4$ levels respectively.

The mean northern hemisphere ocean temperatures for February were obtained from the U. S. Navy Marine Climatic Atlas of the World (ref.44). Values for the temperature, height, and 2 horizontal components of a balanced wind corresponding to the heights, for the 1000, 850, 700, 500, 300, 200 and 100 mb surfaces, and dew point values at 850, 700 and 500 mb were obtained from the Central Analysis Office of the Canadian Department of Transport, Dorval, Quebec. This data was supplied for 2805 grid points of a Polar Stereographic projection of the northern hemisphere for the month of February, 1970. Although surface elevations may be readily obtained from standard topographical atlases, the author was unable to obtain ground surface pressures, making it necessary to obtain an alternative set of data for ϕ_s and P_s. Approximations for ϕ_s and P_s suitable for short term weather predictions were obtained by setting the 1000 mb surface to be the ground surface at the beginning of the forecast. Therefore,

1. The surface pressure was initially 1000 mb at all grid points.

2. The surface elevation was the height of the initial 1000 mb surface.

3. The $\sigma = 3/4$ and $\sigma = 1/4$ surfaces initially coincided with the 800 and 400 mb surfaces respectively.

4. Values for T, u and v at the 800 and 400 mb levels, and dew point at the 800 mb level were obtained by linear interpolation from the nearest pressure levels at which this data was known. The data was then interpolated from grid points on the stereographic projection to grid points on the map projection used in the proposed model.

5. The mixing ratio q_3 was obtained from the dew point by using steam tables. Alternatively, the Clausius-Clapeyron equation could have been used to obtain the vapour pressure P_v corresponding to the dew point, and the mixing ratio would then have been calculated from

$$q_3 = 0.622\ P_v/(P - P_v)\ .$$

The numerical forecasts all begin with real weather data for 0000 GMT February 2, 1970, compiled in the fashion mentioned above. For convenience, the term "0 hour data" is used to refer to this real weather data for 0000 GMT February 2, 1970. This initial data is presented in Figures 4.1 to 4.8 in the form of contour maps containing the following information: isotachs for the horizontal wind on the lower (800 mb) and upper (400 mb) surfaces (10 m/sec contour spacing), isotherms on the 800 and 400 mb surfaces (10^{o} K spacing), mixing ratio contours at the 800 mb level (contour spacing is 3.0, in units of g H_2O /g dry air x 10^{-3}), surface pressure (mb), and elevation contours for the 800 and 400 mb surfaces (200 m contour spacing). In a similar fashion the 36 hour verification data (real weather for 1200 GMT, February 3, 1970) is presented in Figures 4.9 to 4.16.

As a guide to locating those regions in each variable field where the true weather is changing at a rapid rate, a weather change parameter d_ψ is defined:

$$d_\psi = \psi_{t0} - \psi_{t36} + 1000 , \qquad (4.1)$$

where ψ_{t0} = true value of the variable ψ at 0 hours,

ψ_{t36} = true value of the variable ψ at 36 hours.

The contour lines labelled 1000 denote regions where there has been no change in the value of ψ over the 36 hour period. With d_ψ defined by equation 4.1, it is possible to generate contour maps for each dependent variable field showing regions where the weather has changed the least and the most. Weather change contour maps for the 36 hour period are given in Figures 4.17 to 4.22. Actual details of the true weather change over the 36 hour forecast period are discussed in Chapter 5, in connection with the evaluation of forecast performance of the proposed model.

4.2 Preliminary Numerical Experiments

Several preliminary attempts were made to generate a stable numerical forecast using the bicubic spline method on a regular rectangular 5^o latitude, 5^o longitude grid (grid A, Figure 3.1), with filters and averaging operators to remove spurious short waves at high latitudes. This model will be referred to as model P. It has some characteristics of the proposed forecast model and some characteristics of the Mintz-Arakawa model, since the proposed model uses the bicubic spline method and the Mintz-Arakawa model uses a regular rectangular grid with several filters and special techniques to obtain stability (see Section 2.3). The preliminary numerical experiments were performed in order to determine the nature of the special techniques required on a Mintz-Arakawa grid to obtain a stable forecast, and to investigate the effects of different boundary conditions on the cubic spline at the north pole.

In the first experiment (P1), model P was applied with an 8.5^o

polar cap (8.5^{o} interval between the pole and latitude circle j=2) and boundary condition 3.12a at the pole. In this experiment, no averaging operators or special techniques were used to improve the computational stability, and the resulting numerical forecast was computationally unstable (exploded numerically) in less than 1/2 hour of forecast time. This indicates a definite need for special techniques to control the computational stability of the numerical forecast on a Mintz-Arakawa grid.

In the second experiment (P2), model P1 was altered by applying the Mintz-Arakawa averaging operator 2.14c to the pressure gradient terms in the x component of the momentum equation. This is but one of several special techniques used in the Mintz-Arakawa model to obtain a stable forecast (see Section 2.3). However, the resulting numerical forecast was unstable after 20 hours of forecast time. The 20 hour upper level flow conditions (horizontal winds, temperatures and surface elevations (geopotential)) and surface pressure are given by contour maps in Figures 4.23 to 4.26. Since the forecast reached 20 hours of forecast time before exploding numerically at the pole, a considerable improvement has been realized over model P1. However, there remains room for improvement.

A first attempt to improve stability at the pole was made by using a 12.5^{o} polar cap in place of the 8.5^{o} polar cap model P2. This decrease in grid resolution at the pole is an improvement since the Mintz-Arakawa grid inherently has the undesirable characteristic of severely over-resolving the high latitude regions. The results at 26 hours from this third numerical experiment (P3) are given in Figures 4.27 to 4.30. These results show some improvement over model P2 since the forecast reached 26 hours of forecast time before exploding numeri-

cally at the pole and over Asia. It is emphasized at this point that the only special technique used to aid stability in the forecast up to this point is the Mintz-Arakawa averaging operation 2.14c. In the Mintz-Arakawa model itself, several other techniques and special considerations are employed at the pole to obtain stability (see Section 2.3).

In the fourth experiment (P4), additional averaging operations were imposed on model P3. The one-dimensional 3-point averaging operator

$$\psi_i^f = \psi_i + \tfrac{1}{2}\,(\lambda_i\psi_{i-1} - \psi_i + \mu_i\psi_{i+1}) \qquad (4.2)$$

was applied in a fashion limited to the smoothing of all fields requiring the evaluation of x and y derivatives. In all other competitions, including the time extrapolation scheme 2.13a and 2.13b, the field was used in its unsmoothed form. Hence, the averaging operation is a stabilizing influence on the slope calculation, a critical step in the forecast procedure, without unduly influencing the remaining calculations. The Mintz-Arakawa averaging operator 2.14c and the above 3-point averaging operator 4.2 are very similar since equation 4.2 may be obtained from equation 2.14c by replacing the factor A(y) with 1/4, and by using $\lambda_i = \mu_i = 1/2$ (the values for a constant grid). Results from this numerical forecast after the full 36 hour period are presented in Figures 4.31 to 4.34. There is a considerable improvement in this forecast over model P3 since the 36 hour forecast was obtained. However, instabilities still remain in the forecast field over Asia and at the pole.

At this point it was decided to improve the boundary condition for the y component of the bicubic spline at the pole. Preliminary experiments with cubic splines have shown that when there is a sudden

change in the function's curvature between two regions in the field, the spline slope estimates at the nodes oscillate about the true slope, with a decreasing percentage error as distance from the junction between the two regions increases. This problem in curve fitting with the bicubic spline was discussed in Section 3.3.3 (see Table 3.1). Since the state parameters at the pole are average values for the polar cap, they may differ significantly from parameters close to the pole on the individual longitude lines meeting at the pole. It is possible then to have a data fit situation similar to the junction regions for the curves tabulated in Table 3.1. Therefore, a further modification to effect a partial decoupling of the pole may improve the forecast.

For the fifth experiment (P5) the pole was not carried explicitly as a boundary condition for the spline, thereby partially decoupling the pole from the remainder of the forecast domain. With the notation y_0, y_1 and y_2 respectively representing the values 90.0, 82.5 and 77.5, the dependent variables serving as boundary conditions on the y component of the bicubic spline were assigned values along the line $y_1 = 82.5$ according to

$$\psi_{i,1} = \frac{1}{3}\left(\psi_{i+1,2} + \psi_{i,2} + \psi_{i-1,2}\right) \tag{4.3a}$$

for $\psi = \zeta, q_3, T$; and

$$\psi_{i,1} = a\psi_{i,0} + b\psi_{i,2} + c\psi_{i,3} , \tag{4.3b}$$

for $\psi = u, v$. The following notation is used in the above equations:

$$a = 1 - \nu(1 + \varepsilon) , \tag{4.4a}$$

$$b = \nu(1 + \varepsilon) + \varepsilon k_1/k_3 , \tag{4.4b}$$

$$c = -\varepsilon k_1/k_3 , \tag{4.4c}$$

$$k_i = y_i - y_{i-1} . \tag{4.4d}$$

For the indicated values of y_0, y_1 and y_2, the parameters a, b and c

take on the values 0.2285, 1.2000 and -0.4285 respectively. Equation 4.3a is a relaxed form of the old polar boundary condition 3.7, and equation 4.3b is a quadratic estimate for $\psi_{i,1}$ using the three nearest nodal values along a longitude line. The value $\psi_{i,0}$ in equation 4.3b is the polar value for the horizontal wind given by equations 3.9a and b. Finally, the boundary condition A1.27,A1.28 specifying the second derivative at a point y_0 outside of the spline curve fit region was used. With this second derivative set to zero, the following end condition was obtained:

$$\frac{\partial \psi_1}{\partial y} = - 0.846153 \frac{\partial \psi_2}{\partial y} + 1.846153 \left(\frac{\psi_2 - \psi_1}{y_2 - y_1} \right) \qquad (4.5)$$

The boundary conditions 4.3a to 4.5 were used to replace the previous boundary conditions 3.7 to 3.8d and 3.12a used in the fourth experiment, P4. Results from this fifth experiment (P5) are presented in Figures 4.35 to 4.38. This forecast was also unstable at 36 hours, although to a lesser degree than the previous experiments. In this case the pole itself appears as the source of the instability, and the instability over Asia is considerably reduced. Therefore, partially decoupling the pole has some good effects and some bad effects on the forecast.

Since both firmly coupled and partially decoupled pole boundary conditions failed to induce stability at high latitudes, it was necessary to investigate other sources of instabilities.

A sixth numerical experiment (P6) was performed to remove the possibility that the instabilities are due to the use of bicubic splines. In this experiment a moderately coupled polar boundary condition (3.12b) and a simple central finite difference scheme (3.17) were used. This is similar to the Mintz-Arakawa model in that finite differences are used

to estimate derivatives on a grid with constant latitude and longitude grid intervals. However, model P6 does not use the staggered space grid, complex finite differences, special methods of calculating fluxes, and other special techniques to obtain stability used in the Mintz-Arakawa model. The basic results from this experiment at 36 hours are presented in Figures 4.39 to 4.42. Again the forecast is found to be unstable at high latitudes with an instability developing over Asia. The time variations of the longitudinal mean values of the surface pressure and upper level (400 mb) dependent variables for the 36 hour forecast period are given in Figures 4.43 to 4.46. The longitudinal mean $\bar{\psi}_j$ for variable ψ_{ij} is the mean value of ψ around the latitude circle $y = y_j$, according to

$$\bar{\psi}_j = \frac{1}{M_j} \sum_{i=1}^{M_j} \psi_{i,j} \quad , \tag{4.6}$$

where $y_1 = 90.0$, $y_2 = 77.5$, $y_3 = 72.5$, ... , $y_{17} = 2.5$, $y_{18} = -2.5$. In the longitudinal mean figures, the numbers along the right hand side of each figure denote the latitude circle (j) for which the longitudinal mean curve was generated. It is seen from these figures that the forecast is stable in the most part, since the instabilities at the pole and over Asia have not appreciably altered the longitudinal mean curves. The oscillations in these curves are present even in stable forecasts, and they will be discussed in Section 5.1. Some indication of the instabilities do begin to appear in the gradual rise of the longitudinal means for the upper level velocity at high latitudes (j = 2 to 5 in Figure 4.43). This effect is not apparent in the remaining longitudinal mean curves.

Both the boundary conditions at the pole and the use of bicubic splines have been ruled out as sources of the instabilities in the

numerical experiments to this point. As a final experiment (P7), the possibility of computational instability due to the shrinking of the physical distance between grid points on the earth as latitude increases was investigated by repeating the forecast P6, except using a grid with double the grid interval (10^{o} latitude, 10^{o} longitude grid). The grid used is shown in Figure 3.2 and is called grid B. Results from this forecast after 36 hours are given in the form of contour maps of the variable fields (Figures 4.47 to 4.54), error contour maps for the dependent variables (Figures 4.55 to 4.60), and longitudinal mean curves for the dependent variables over the 36 hour forecast period (Figures 4.61 to 4.68). Error contour maps are a comparison of the difference between the forecast fields and true weather fields at 36 hours, according to the definition of local error,

$$e_{\psi} = \psi_{f36} - \psi_{t36} + 1000 , \qquad (4.7)$$

where ψ_{f36} = the forecast value of the variable ψ at 36 hours,

ψ_{t36} = the true value of the variable ψ at 36 hours,

evaluated at each node in the field. On the error contour map, the lines labled 1000 denote the lines where the forecast field exactly agrees with the true 36 hour weather. In general the forecast is poor due to its large phase lag relative to the phase speed observed in the true weather. Also there is a strong tendency to damp out significant features in the fields and not resolve features which would appear in a finer grid model. This is shown in the comparison of Figure 5.55 with Figure 4.9. Despite these flaws, the forecast is definitely stable, a characteristic which earlier experiments did not have. Since stability was obtained on a coarse grid and not on a finer grid version of the same model, the instability problem may be attributed in the most part to the shrinking

of the physical distance between grid points on a constant latitude, constant longitude interval grid. Further discussion of the results from model P7 is included in Chapter 5, in connection with the evaluation of forecast performance for all the numerical experiments.

4.3 36 Hour Forecast Results Using Splines on a Telescoping Grid

As discussed in Section 3, the proposed forecast model uses the bicubic polynomial spline method on an expanding or telescoping grid having superimposed basic expansions of two types. Hereafter, this model will be referred to as model ST. All the necessary boundary conditions as well as the proposed forecast procedure are also discussed in Section 3. It is emphasized here that model ST does not employ any of the several special techniques (Sections 2.2 and 2.3) used in the Mintz-Arakawa model to obtain a stable forecast. Several numerical forecasts were performed using modified versions of model ST to illustrate fundamental characteristics of the method.

The first 36 hour forecast performed was an application of model ST limited to an expanding grid having only one basic expansion (grid C, Figure 3.3). This forecast model will be called S. The forecast was performed to demonstrate that the use of a grid having a basic expansion of Type 1 produces a stable 36 hour forecast without the necessity of resorting to the special techniques (averaging, space staggered grid, complicated flux estimates, and others) used in the Mintz-Arakawa model. Results from this forecast in the form of contour maps, error maps and variations with time of the longitudinal means are given in Figures 4.69 to 4.90. The forecast shows good resolution and is definitely stable, without excessive overdamping of strong features. Further discussion of this forecast is given in Section 5, where it is evaluated.

The second 36 hour forecast performed using a modified version of model ST had a grid with an expansion of Type 1 (grid C), but used central finite differences (3.17) in place of bicubic splines to estimate the derivatives. This forecast, to be referred to as model F, was performed to demonstrate the advantages and disadvantages of bicubic splines compared to finite differences in estimating derivatives. As with model S, it was not necessary to resort to special techniques to obtain stability, since grid C was used. Results at 36 hours from this forecast in the form of contour maps of the dependent variable fields are given in Figures 4.91 to 4.98. Model F is similar to model S in that the forecast shows good resolution and is definitely stable without excessive overdamping of strong features. However, all the fields show a distinct phase lag to the forecast from model S. Since both forecasts lag the real weather(this is shown by the 400 mb geopotential fields in Figures 5.49 to 5.52), model S using bicubic splines shows a distinct advantage over model F using finite differences. Further discussion is given in Chapter 5.

The third 36 hour forecast performed was to run model ST as it was designed: using the bicubic polynomial spline method on a telescoping grid having superimposed expansions of two types. The grid used for this forecast is grid D, Figure 3.4. Like the previous two forecasts it was not necessary to employ special techniques to obtain stability. The forecast results in the form of contour and error maps of the dependent variables, as well as variations of the longitudinal means with time during the forecast, are given in Figures 4.99 to 4.120. Of particular interest in this forecast is the reduction of computer time (1/3 that of model S) without sacrificing resolution and accuracy

in the region of primary interest (North America for grid C). The forecast shows good resolution and phase speed of the large scale meteorological waves over North America, with somewhat poorer resolution and phase speed in the expanded grid regions over Europe. This forecast is compared with others in Chapter 5.

The fourth forecast was to run a modified model ST on a grid with an expansion of Type 1 (grid C, Figure 3.1), using the new bicubic spline 3.15 based on continuity of curvature. The values of parameters a and XS selected were

$$a = 0.222222 , \tag{4.8a}$$

$$XS = 0.0 . \tag{4.8b}$$

In this fashion the derivative estimates are exactly intermediate between central finite difference estimates (a = 1/3) and estimates from cubic splines based on continuity of the second derivative (a = 0). This follows from equations 3.15 and 3.16f, for which if a = b and XS = 0, the sum of contributions by λ^* and μ^* to the slope at node i is (1 - 3a)/(1 - 1.5a). This must equal unity if a = 0 ($\lambda + \mu = 1$, spline based on continuity of second derivative) and must equal zero if a = 1/3 (central finite differences). The intermediate value is (1 - 3a)/(1 - 1.5a) = 1/2; and solving for a yields equation 4.8a. Note that when $a \neq 0$ and XS = 0, equation 3.15 becomes the condition for continuity of second derivative at points in the elements other than node points. This model is referred to as model C1. Forecast results at 36 hours in the form of contour maps of the dependent variables are given in Figures 4.121 to 4.128. On the whole the forecast shows characteristics of both models S and F. This comparison will be discussed in Chapter 5.

The final forecast performed was to repeat the previous forecast using splines based on curvature, with the selection of suitable

non-zero values for the scaling factors. In this experiment (C2), the scaling factors XS for the x direction, YS for the y direction and US for the dependent variable were selected to be

$$US = \psi_{max} - \psi_{min} , \tag{4.9a}$$

$$XS = 20.0 , \tag{4.9b}$$

$$YS = 20.0 . \tag{4.9c}$$

This selection was based on the aim of keeping S'_{fi} (equation 3.13b,c) near unity and independent of the units used. On a latitude circle with grid interval $\Delta = 5^{o}$, the shortest wave of meteorological significance would be approximately 8 grid intervals long.* If this wave extended between the maximum and the minimum values of the dependent variable in the field, the approximate maximum slope to be expected would be $(\psi_{max} - \psi_{min})/4$. Equating this maximum slope multiplied by the scale factors to unity yields

$$\frac{XS}{US} \frac{(\psi_{max} - \psi_{min})}{4\Delta} = 1 . \tag{4.10}$$

This is satisfied by the selection 4.9a,b,c for $\Delta = 5^{o}$. Results from model C2 after 7 hours are given in Figures 4.129 to 4.132. A strong numerical explosion (or instability) is present in each of the dependent variable fields. The numerical explosion originated at the equator, and propagated into the field in the form of a broad band. Of particular interest is the fact that despite a strong, broad explosion band through the middle of the forecast field, the remaining regions of the forecast

---

* Haltiner and Martin (1) discuss the dynamics of atmospheric waves on pp. 308-386. With n denoting the wave number (the number of complete waves around a latitude circle), then the longitudinal scale of long waves and short waves in mid-latitudes corresponds approximately to n=5 and n=10 respectively (p. 335 of ref.1). Therefore, on a 5^{o} grid, a wave which is 8 grid intervals in length corresponds to a wave number n=9, representing approximately the shortest wave of meteorological significance.

are very stable. This is remarkable since the numerical explosion is of such a strong nature. In the contour plots, whenever V, T or P_s are outside the ranges $V < 100$ m/sec, $210 < T < 320^{o}$ K or $900 < P_s < 1100$ mb, the plot prints out the extremes of the interval considered. Hence, the row of numbers 100 along the top of the upper level resultant horizontal wind contour plot (Figure 4.129) indicates that at the pole, the winds exceed 100 m/sec. However, this strong instability does not seem to affect regions either side of the explosion band. The explanation for this explosion is based on the reduction of coupling between individual nodes in the field, produced by the factor β_i in the numerator of the continuity of curvature equation 3.13a. In particular, at the equator, a frequently occurring natural phenomenon is to have the variables on the latitude circle $j = N - 1$ differing substantially from the variables on the next latitude circle $j = N - 2$. With the symmetry boundary condition, there results a situation as in Figure 4.133, with the slope on one side of y_{N-1} differing substantially from the slope on the other side. Taking the slope between y_{N-1} and y_{N-2} to be a typical large value, $(\psi_{max} - \psi_{min})/2\Delta$, then with YS = 20 the values of β become $\beta_{N-1} = 8$ and $\beta_N = 1$. The effect of these factors is to remove node y_{N-1} away from node y_N by a factor 8 times the grid spacing, as far as the influence of R_1 on R_2, or vice versa, is concerned. This decoupling effectively prevents the regions from unduly influencing each other. If R_2 begins to rise relative to R_1, it will feel little or no restraining influence from the lower values of the variable at y_{N-2}, and the more it rises, the less restraining influence it will feel from R_1. Similarly, if R_2 begins to explode numerically, region R_1 will feel little bad effects from the explosion adjacent to it. This accounts for the slow propagation of the broad expansion band into the rest of the

field. The explosion began at selected points along the equator, and spread the 16 grid intervals towards the pole at about the same rate as it fanned out in the east and west directions. It is therefore apparent that the use of decoupling in the form of a spline based on curvature, with non-zero scaling factors XS and YS, results in an unstable forecast due to the influence of the artificial boundary condition at the equator. The instability may be lessened or removed by using smaller scaling factors XS and YS, or preferably by removing the artificial equator boundary condition by performing global forecasts.

5. Evaluation and Comparison of the 36 Hour Numerical Forecasts

The first method used to evaluate the accuracy of models S, F, ST and C1, as well as the results from numerical experiment P7, is based on the calculation of the root mean square error in the 36 hour forecast, denoted RMSE. This is the forecast error relative to the true 36 hour weather: the calculation is performed along latitude circles, longitude lines, and for the field as a whole. The error of dependent variable at node i,j is defined by

$$e_{ij} = (\psi_{t36} - \psi_{f36})_{ij} , \tag{5.1}$$

where ψ_{t36} = the true value of the variable at 36 hours,

ψ_{f36} = the forecast value for the variable at 36 hours.

Therefore, expressions for the RMSE of the ψ forecast at 36 hours around latitude circle i, longitude line j and for the field as a whole are, respectively,

$$RMSE_j = \left(\frac{1}{M} \sum_{i=1}^{M} e_{ij}^2 \right)^{\frac{1}{2}} , \tag{5.2}$$

$$RMSE_i = \left(\frac{1}{N} \sum_{j=1}^{N} e_{ij}^2 \right)^{\frac{1}{2}} , \tag{5.3}$$

$$RMSE = \left(\frac{1}{MN} \sum_{i=1}^{M} \sum_{j=1}^{N} e_{ij}^2 \right)^{\frac{1}{2}} . \tag{5.4}$$

In general, the lower the RMSE the better the forecast. It is instructive in the evaluation of model performance to compare the RMSE against the root mean square of the true weather change, denoted RMSC. The true weather change at node ij for dependent variable ψ is defined by

$$c_{ij} = (\psi_{t36} - \psi_{t0})_{ij} . \tag{5.5}$$

Values for the RMSC of the ψ field around latitude circle j, longitude line i, and for the field as a whole, denoted respectively $RMSC_j$, $RMSC_i$,

and RMSC, are defined in a fashion similar to equations 5.2 to 5.4 .

When the RMSE > RMSC, the question arises as to what advantage has been obtained by performing the forecast, since the error in the 36 hour forecast exceeds the change in the true weather. It is true that when this happens one cannot have excessive confidence in the forecast. It would appear that when the error is greater than the true change it would be better (less error) to take the initial weather and use it as the forecast at 36 hours. However, there are other factors to consider, one being that the forecast data is only interpreted from contour plots. Since only general trends are apparent from a contour map, the local forecast deviations from the true weather are of little consequence, provided the general trends in the true weather are properly forecast. Generally the lower the RMSE, the better the numerical forecast predicts the large scale trends in the real weather: this comparison holds true even when RMSE > RMSC. In light of this, the RMSC is used as the standard for comparison of the forecast RMSE. A forecast will be considered good when RMSE < RMSC, and it will be considered poor when RMSE > RMSC.

The second method used in this thesis to estimate the forecast model's performance is to follow individual features in the forecast as they move from their initial position to their 36 hour forecast position. In this fashion it is possible to evaluate average phase speeds of recognizable portions of the large scale meteorological waves. Due to the human element involved in such a calculation, there is naturally some error in the analysis. For this reason several features of the waves are monitored and an average phase speed is calculated, in an attempt to reduce the error in the mean phase speeds reported. This second method generally correlates well with the comparison of RMSE against

RMSC, with moderately good phase speeds (greater than 1/2 the observed true phase speed) occurring when RMSE < RMSC.

For comparison purposes, the Mintz-Arakawa model, referred to as model MA, was used to generate a forecast over the same 36 hour period from the same initial conditions. A detailed description of the accuracy of this forecast is given in Price (56), and the forecast characteristics are summarized in Section 5.1. It is unnecessary to perform detailed descriptions of this nature for the results from the proposed forecast model ST, and modified models S, F, and C1, since they follow immediately from the comparison of these forecasts against the Mintz-Arakawa results. For convenience, a summary of the symbols used to represent each forecast model is given in Table 5.1 .

5.1 Comparison Data: The Mintz-Arakawa Model

The 1969 version of the Mintz-Arakawa numerical general circulation model was used to generate a forecast for the northern hemisphere for the 36 hour period 0000 GMT February 2, 1970 to 1200 GMT February 3, 1970. A grid spacing of 5^{o} was used for both latitude and longitude ($\Delta\Theta = \Delta\Phi = 5^{o}$), along with a 15^{o} polar cap ($\delta = 15^{o}$). The number of distinct primary grid points in the x and y directions were 72 and 17 giving a total of 1224 distinct primary grid points. To ensure computational stability a time step of six minutes was used (Δt = 360 sec). The results from this forecast are given in Figures 5.1 to 5.20 in the form of contour maps for the dependent variables, error contour maps, and variations with time of the longitudinal (zonal) means of the dependent variables. The longitudinal mean curves for the Mintz-Arakawa model are indexed with the equator index = 1 and the north pole index = N; however, the corresponding curves for the proposed model

have the north pole index = 1 and the equator index = N. A detailed description and evaluation of the 36 hour forecast was given by Price (pp. 129 to 168 of ref.10). In summary, the results of this forecast when compared with the true weather are listed below.

1. Surface Pressure, PS.
   a) PS increased as latitude increased.
   b) The time variation of the zonal mean surface pressure developed a periodic variation (period of 13 to 14 hours), with low latitude curves antisymmetric to high latitude curves (Figure 5.20).

2. 800 and 400 mb Resultant Velocity, V1 and V2 respectively.
   a) The time variation of the zonal mean of V1 had very short period oscillations (Figure 5.15).
   b) A fair forecast of the middle latitude V2 wind belt was obtained for wind speeds > 20 m/sec.
   c) The time variation of the zonal mean of V2 exhibited regular oscillations with a 13 to 14 hour period (Figure 5.16).

3. 800 mb Temperature, T1.
   a) In the vicinity of strong troughs and ridges, the forecast field travelled at approximately 1/2 the speed of the true field and the troughs and ridges were of similar shape to those in the true field.
   b) In the vicinity of weak troughs and ridges, the forecast field was of the same shape and speed as the true field.
   c) T1 was over-estimated in equatorial regions by approximately the same amount ($> 5^{o}$) it was under-estimated in polar regions.

4. 400 mb Temperature, T2.
   a) T2 was forecast better than T1.
   b) In the vicinity of medium to weak troughs and ridges, a good forecast of the speed and shape of the temperature field was obtained.
   c) In the vicinity of strong troughs, the forecast field travelled at approximately 1/2 the speed of the true field and had large shape errors.
   d) T2 was over-estimated in equatorial regions by small amounts ($> 5^{o}$ usually).
   e) Fairly constant zonal mean temperature curves (weak oscillations only) were obtained except for the low and high latitude curves which exhibited slight increases and decreases in temperature, respectively (Figure 5.17).

5. 800 mb Geopotential, $\phi 1$.
   a) It is difficult to follow the movement of the individual troughs and ridges.
   b) The positions of the highs and lows were forecast correctly; however, shapes were distorted.
   c) This is not a useful contour map for analysis due to the use of a large contour interval.

6. 400 mb Geopotential, $\phi 2$.
   a) $\phi 2$ was forecast better than $\phi 1$.
   b) The forecast field generally travelled at approximately 2/3 the speed of the true field and had a similar shape.
   c) The largest forecast shape error and phase lag occurred in the vicinity of strong troughs and ridges.
   d) The forecast falling of highs and rising of lows was greater than observed, but the forecast position of the highs and lows agreed with the observed positions.
   e) Fairly constant zonal mean geopotential curves (weak oscillations only) were obtained except for low and high latitude curves which respectively exhibited slight increases and decreases in elevation (Figure 5.19).

7. 800 mb Mixing Ratio, Q1.
   a) In most regions the forecast field moved 1/2 as fast as the true field and had larger ridges.
   b) Fairly constant zonal mean curves having small oscillations were obtained with a zonal mean increase for curve 1 (equator) of 0.0005 (Figure 5.18).

5.2 Overall Performance of the Models

An overall estimate of the forecast accuracy for models ST, S, F, C1 and P7 is obtained by comparing the RMSE for each dependent variable against both the RMSC in the true field and the RMSE of the comparison Mintz-Arakawa model. The RMSE values for each dependent variable in each of the 36 hour forecasts are tabulated in Table 5.2. For notation in the table and the discussion hereafter the symbols V1, T1, $\phi 1$ and Q1 respectively represent the resultant horizontal wind speed, temperature, geopotential, and moisture content for the 800 mb level. Similarly, the 400 mb level resultant horizontal wind, temperature and geopotential are represented by the symbols V2, T2 and $\phi 2$. These may be distinguished from the local values of the variables on the $\sigma = n/4$ surface, which are denoted by u_n, v_n, T_n, ϕ_n; $n = 1,3$; and q_3.

To facilitate the comparison of RMSE against RMSC, a % difference is calculated according to

$$d\% = \frac{RMSE - RMSC}{RMSC} \times 100\% \ . \qquad (5.6)$$

The % difference for each RMSE value is also included in Table 5.2 .

A comparison of d% for models S and P7 relative to model MA is given in Table 5.3a; and a comparison of d% for models C1, F and ST relative to model S is given in Table 5.3b. From the tables it is apparent that all of the models, including the comparison model MA, generally have RMSE > RMSC for all fields. The only exceptions are the T2 fields by models S, C1, F and ST, and the V1 field by model ST. Model S shows distinct advantages over model MA, in that d% for S is consistently from 1/4 to 3/4 of the corresponding values for MA. This shows that the combination of the bicubic spline method on a grid having a basic expansion of Type 1, with no filters or special techniques to aid stability, gives a better 36 hour forecast for the sample day chosen than does the Mintz-Arakawa model, consisting of a complex finite difference method on a grid with constant latitude and longitude intervals and numerous techniques to aid stability.

The additional techniques used in model MA over and above averaging operations are definitely required for stability, since it was not possible to obtain a stable forecast when these techniques were omitted (see the preliminary forecast P6). Model P7, using finite differences on a course (10^{o}) Mintz-Arakawa grid, with only filters to aid stability, yields a stable but poorer forecast than both models MA and S. Therefore the solution to the stability problem on a Mintz-Arakawa grid may be solved by using a coarser grid. However, the corresponding forecast is of little use due to poor resolution and lack of accuracy.

An overall estimate of the relative performance of bicubic splines, finite differences, and the new spline based on curvature is obtained by comparing the RMSE for models S, F and C1. Model S shows

improvement over F for $\phi 2$ and T1; and model F shows improvement over S for T2 and Q1. Both models give approximately the same results for V1, V2 and $\phi 1$. Therefore, on the whole, it is difficult to decide from this data whether splines are better or worse than finite differences. Since the geopotential ϕ is often of more interest than the other variables, it would appear that model S would be slightly preferable to F. It will remain to look at the distribution of error with latitude and longitude, as well as the mean phase speeds of the large scale meteorological waves, in order to evaluate the performance of the bicubic spline method compared to finite differences.

Model C1 generally yields results intermediate to those of S and F. This is expected due to the selection of the constants a and XS in equation 3.13 using the values given in equations 4.8a,b.

Except for T1 and $\phi 2$, model ST shows improvement over S on the whole. This is not expected since ST uses a grid with poorer resolution in a portion of the forecast domain than does S. However, for this test forecast, the coarse grid portion of grid D used in model ST lies over Europe, a region where the observed true weather change is very small, without strong troughs and ridges. In such a region it is not necessary to have fine resolution to resolve the meteorological fields adequately, and a coarse grid may yield better results than a fine grid. This point will be further illustrated in the discussion on the forecast error distribution with longitude.

5.3 Distribution of Forecast Error with Latitude and Longitude

The distribution of forecast error with latitude, $RMSE_j$, $j=1,\ldots N$, is given in figures 5.21 to 5.34 for the models S, F, ST and MA. Also included in the figures is the distribution of the true

weather change with latitude, $RMSC_j$, j=1,...N. The RMSE for latitude circle j is $RMSE_j$, given by equation 5.2; and the RMSC for latitude circle j is $RMSC_j$, calculated similarly.

Figures 5.21 to 5.27 give the RMSE distribution with latitudes for models MA and S, along with the RMSC distribution with latitude for the true weather. To facilitate the analysis of these figures, Table 5.4 gives an evaluation of the mean difference between RMSE and RMSC in three latitude belts and at the pole and equator. In addition the adjectives poor (P) and good (G) are used to describe this difference, with poor implying RMSE > RMSC and good implying RMSE < RMSC. It is seen from the figures and table that model S gives a good forecast in general at middle latitudes, with poorer performance at high and low latitudes. However, model MA yields a poor forecast at all latitudes, with middle latitudes somewhat better than high and low latitudes. Both models give very poor estimates at the equator, and model MA is somewhat better than model S at the pole.

More specifically, at high latitudes, S is better than MA for all variables except T2, for which both models give approximately the same results; at middle latitudes, S is significantly better than MA for all variables; and at low latitudes, S is better or the same as MA for all variables except $\phi 2$, for which S is poorer than MA. Therefore in the majority of the field, model S gives a better forecast than model MA. However, at the pole, although S is better than MA for V2 and T1, it gives poor results for the remaining variables so that in general model MA gives a better polar forecast than model S. Both models give poor forecasts at the equator, with S better than MA for $\phi 2$ and poorer for T2.

Figures 5.28 to 5.34 give the RMSE distribution with latitude for models S, F and ST. To facilitate the analysis of these figures, Table 5.5 gives an evaluation of the mean differences between the $RMSE_j$ of models F and ST with the $RMSE_j$ of model S at different latitudes.

Comparing models F and S first, it is seen that at the pole, model F forecasts $\phi 1$ and $\phi 2$ better and T1 and V2 worse than model S. Therefore, the previously mentioned differences between models MA and S at the pole appear in part due to the use of finite differences in the former and bicubic splines in the latter. For high latitudes, S is generally better than F for all variables except T2 and Q1. This also correlates well with the generally better performance of model S over MA at high latitudes, as discussed in Section 5.2, and shows that the use of splines over finite differences is part of the reason why S is better than MA at high latitudes. In middle latitudes, $\phi 1$, $\phi 2$ and T1 are forecast better by S and the remaining variables are forecast better by F. Since the geopotential is often of more interest than the other variables, the spline method would appear slightly preferable to finite differences at middle latitudes. At low latitudes and the equator, the forecast using splines (S) is either the same or poorer than the forecast using finite differences (F). Therefore it would be preferable to use finite differences at low latitudes.

This comparison between models S and F may also be made individually for each dependent variable field. The best forecast for the velocity fields V1 and V2 would be to use splines at high latitudes and finite differences at all other latitudes. The lower level temperature T1 is forecast better using splines for all latitudes except at the equator. However the upper level temperature T2 and lower level

moisture Q1 are forecast better by finite differences than by splines at all latitudes. Finally, the geopotential fields $\phi 1$ and $\phi 2$ are forecast better at the pole by finite differences, and better or the same by splines at all other latitudes. Therefore the use of splines over finite differences would depend on which fields are of most interest.

Comparing models ST and S next, it is seen that the differences between the two models vary considerable in the different latitude regions and for the different dependent variables. In general, however, ST appears better than S at the equator at low latitudes. It will be shown that differences between ST and S depend more on longitude than on latitude.

The distribution of forecast error with longitude, $RMSE_i$, $i=1,...M$, is given in Figures 5.35 to 5.48. Also included in the figures is the distribution with longitude of the true weather change, $RMSC_i$, $i=1,...M$. The RMSE for longitude line i is $RMSE_i$, given by equation 5.3; and the RMSC for longitude line i is $RMSC_i$ calculated similarly. In these figures, the longitude x_i corresponding to longitude line i is given by

$$x_i = -182.5 + 5i \ , \ i=1,...72 \ . \qquad (5.7)$$

This corresponds to the location of the nodes on the latitude circles in grid A, Figure 3.1 .

Figures 5.35 to 5.41 give the RMSE distribution with longitude for models MA and S, along with the RMSC distribution with longitude for the true weather. It is seen from the figures that in regions of fast changing weather (large values of $RMSC_i$), model S gives a good forecast for V1, T2, Q1 and $\phi 2$, since $RMSE_i < RMSC_i$, and a poor forecast for V2, T1 and $\phi 1$, since $RMSE_i > RMSC_i$. This may be compared to

model MA which gives a good forecast for $\phi 2$ and V1 and a poor forecast for the remaining variables in regions of fast changing weather. Both models give poor forecasts ($RMSE_i > RMSC_i$) in regions of slower changing weather (lower values of $RMSC_i$). Generally, the $RMSE_i$ curves for model MA have larger amplitude oscillations than the corresponding curves for model S. Also, there is less spread between the $RMSE_i$ curves of models MA and S (no definite pattern, Figures 5.35 to 5.41) than between the $RMSE_j$ curves of the same models (definite pattern, Figures 5.21 to 5.27). This indicates that the models differ primarily in their error distribution with latitude.

Figures 5.42 to 5.48 give the RMSE distribution with longitudes for models S, F and ST. Both models S and F have similar distributions, in that both are highly oscillatory with alternating regions in which they overshoot each other. Generally, T1 is forecast better by splines (S) than by finite differences (F), especially in the regions of fast changing weather, $i < 21$; and in the remainder of the field, both models are approximately the same. A systematically better forecast is also given by splines over finite differences for the geopotentials $\phi 1$ and $\phi 2$. However T2 and Q1 are forecast better using finite differences than by splines, especially for $i > 40$. Both models forecast V1 and V2 approximately the same. Therefore, the RMSE distribution with longitude for models S and F agree well with the overall RMSE values for the forecast field discussed in Section 5.2 .

Comparing the longitudinal RMSE distributions for models S and ST, it is seen that ST gives the same or slightly poorer a forecast than S in regions $i < (20 \text{ to } 40)$, for T1, T2, Q1 and $\phi 1$. However for the same fields in regions $i > (24 \text{ to } 40)$, model ST gives a systematically better forecast than model S. For V1, V2 and $\phi 2$, models ST and S

have one model better than the other in alternating regions, the average being approximately the same RMSE for both models. The region $i < (24 \text{ to } 40)$ corresponds to a region of fast changing weather on the fine grid portion of the expanding grid (Figure 3.4, grid D). Also the region $i > (24 \text{ to } 40)$ corresponds to a region of slower changing weather on the coarser grid portion of the expanding grid. It is seen that on the fine grid portion of grid D, models S using grid C and ST using grid D have similar grid resolutions, and both models give similar RMSE distribution curves with longitude. This is a good characteristic of model ST since it shows that good forecast accuracy is maintained in the region of primary interest, the fine grid portion of the field, despite the presence of a coarser grid with poorer resolution surrounding the fine grid region. In the coarse grid portion of grid D, model ST (using grid D) gives a better forecast than model S (using grid C). This is not expected since usually, the poorer the resolution the poorer the forecast. However, in this particular case, the region of poorer resolution on grid D corresponds to a slow changing region in the true weather. Under these conditions, poor resolution need not yield a poorer forecast since fewer grid points are capable of adequately resolving the dependent variables. This appears to be the case since model ST gives a better forecast than model S in the region $i > (24 \text{ to } 40)$.

5.4 Phase Speeds of the Numerical Forecasts

The second method used to evaluate the numerical forecasts is to compare average phase speeds of the more easily recognized features on the large scale meteorological waves, calculated from the initial positions and 36 hour forecast positions of the features. In order to reduce the error in the mean phase speed, several features in each forecast are

monitored and an average phase speed is calculated. This analysis is only performed for the temperature and geopotential fields, since the large scale meteorological waves in these fields have well defined troughs and ridges which may be easily distinguished in their initial and final positions. The features are less easily distinguished in the moisture and velocity fields and hence the possibility of error would erase any credence in the comparison between the models. The evaluation of mean phase speed is performed along the 45^{o} latitude circle, since the forecast at middle latitudes is of greater importance than high and low latitude forecasts. Different phase speeds would arise from the evaluation of mean phase speed along other latitude lines.

A tabulation of the position in longitude of easily distinguished troughs (T) and ridges (R) along the 45^{o} latitude circle for the temperature and geopotential fields is given in Tables 5.6 and 5.7 . The forecast phase speed expressed as a percentage of the true phase speed is given in Table 5.8 . It is seen from the tables that all the forecast models have a phase speed smaller than the corresponding phase speeds in the real weather. This is a frequent characteristic of numerical weather prediction models. Model S has phase speeds closest to the true phase speed. The upper level speeds for T2 and $\phi 2$ by model S exceed those by model MA by over 15% of the true weather phase speed, whereas the differences between the phase speeds of the two models for T1 and $\phi 1$ are under 10% of the true phase speed. Therefore, model S gives a better forecast than model MA at middle latitudes, in terms of better phase speeds of the large scale meteorological waves. This agrees with the previously discussed differences in RMSE at middle latitudes for models S and MA (Section 5.3, Table 5.4, and Figures 5.23, 5.24. 5.26

and 5.27).

Model F consistently has lower phase speeds for the temperature and geopotential fields than model S. This shows a distinct advantage of the use of bicubic splines (model S) over central finite differences (model F) for middle latitude forecasting.

It also appears from Table 5.8 that model ST has lower phase speeds than model S. This is true on the average due to the influence of the slower phase speed in the coarse grid portion of grid D. However, for the majority of the strong troughs and ridges appearing in the fine grid portion of grid D, models S and ST both yield almost identical phase speeds at middle latitudes. This is consistent with the earlier result that models S and ST have similar variations of RMSE with longitude on the fine grid portion of grid D ($i < 24$ to 40).

Finally, model P7 is seen to have the largest phase lag of all the models. This arises from the combination of using a coarse (10^{o} latitude, 10^{o} longitude grid interval) version of the Mintz-Arakawa grid, along with simple central finite differences and only averaging operations to aid stability. This may be compared to model MA which uses a fine (5^{o} latitude, 5^{o} longitude grid interval) version of the Mintz-Arakawa grid, along with the complex finite differences and several special techniques to aid stability. The phase speeds for model MA are considerably better than those for model P7 due to the increased resolution and greater complexity of model MA.

6. Extension of the Forecast Model Using Weighted Residual Numerical Techniques

A broad class of numerical methods used in solving propagation problems in applied mechanics is the method of weighted residuals (abbreviated MWR). Crandal (pp. 147-154, 371-376 of ref. 16) and Finlayson and Scriven (45) give a good description of the MWR technique. Essentially the method is to construct a trial solution in the form of analytic expressions (approximating functions) with either undetermined parameters or undetermined functions of a single variable. It is possible to solve for the undetermined parameters by restricting the trial solution to satisfy the given differential equation over some interval in space and time. With this procedure one obtains a fairly uniform degree of accuracy over an extended interval in time. The basic idea of MWR in two dimensions is discussed in Appendix 3. Essentially the only differences between the different schemes are in the methods of selecting the weighting functions w_q used in solving for the undetermined parameters. Four weighted residual methods corresponding to different weighting functions are discussed in Appendix 3. These are the collocation method, subdomain method, Galerkin method and least-squares method.

Weighted residual methods leave considerable room for engineering analysis and judgement, primarily in selecting approximating functions and deciding which solution modes are most probable. The choice of approximating functions is crucial to the accuracy of the final solution. Usually several sets of approximating functions are admissable and it is not possible to select one set as the best. One simplification frequently used is to exclude time dependence from the

approximating function. Also any symmetry properties of the system should be exploited in the selection, although Finlayson and Scriven (p. 738 of ref. 45) suggest there are no systematic methods of doing this. For finite regions of interest it is common to select the trial functions ϕ_q as the Q lowest members of a polynomial or trigonometric series expansion in the variables χ_q and t (Snyder, Spriggs and Stewart (46), Finlayson and Scriven (p. 738 of ref. 45), Lowe (47)). If the region of interest is an unbounded domain, Lowe (47) suggests the trial functions be chosen to exhibit the same expotential order as the asymptotic variation of the dependent variables. Whatever the case, selecting approximating functions remains dependent on the user's intuition and experience. This is often considered a major disadvantage of MWR.

It is the opinion of several authors (Snyder, Spriggs and Stewart (46), Johansen (48), Lowe (47)) that the Galerkin method is superior to other weighted residual methods, primarily because it permits closer contact with the physical problem. It is the only MWR which uses the approximate solution directly (taking the weighting functions equal to the approximating functions) in reducing the equation residual. Furthermore, several proofs of convergence are available for specific applications of the Galerkin method (p. 740 of ref. 45) while convergence proofs for other MWR are lacking. Recently the Galerkin method has been successfully applied to nonlinear engineering problems. Lowe (47) applied the Galerkin method with expotential trial functions to boundary layer flow problems (Blasius flow over a flat plate, free convection over a flat vertical isothermal plate, and others). The application of Galerkin's method to nonlinear ordinary differential equations is approached in a different manner by Johansen (48). By choosing the approximating functions to contain terms generally

associated with solutions of linear equations Johansen effectively uses the Galerkin method as a linearization technique. One advantage of this over conventional linearization techniques is that the original nonlinear equation is unaltered, rather the solution parameters alone are selected to distribute the linear approximation over the domain of interest. Partial differential equations similar to those encountered in the meteorological forecast problem have been successfully treated by several authors. Snyder, Spriggs and Stewart (46) apply the Galerkin method to a transport process in a finite domain, with the flow governed by equations of motion and continuity. Macdonald (49) considers the steady laminar boundary layer equation for incompressible flow. Finally, Zienkiewicz and Parekh (50) make an important contribution by formulating the transient field problem (of the type encountered in heat conduction) in terms of the finite element approach using the Galerkin method. This is of importance since they chose to define the approximating functions in a piecewise continuous fashion over finite elements of the solution domain, and then apply the Galerkin criteria in selecting the unknown time dependent portion of the trial function.

In the treatment by Zienkiewicz and Parekh (50) the finite element approach is combined with the Galerkin criteria for a simple partial differential equation. In Appendix 3, it is shown how the meteorological forecast problem may be treated in a similar way: application of a weighted residual method with piecewise continuous double cubic polynomial spline approximating functions defining the spatial variation of the dependent variables, and undetermined functions of time defining the behavior in time of the dependent variables. By resorting to spline functions one is able to obtain high resolution without the need for a high order polynomial or trigonometric series fit. Essential features

of this extended model are listed below.

1. The trial solution is of double cubic spline nature for all $t \geq 0$.

2. The degree of approximation of the trial solution to a double cubic spline may be adjusted as desired.

3. There is a minimum number of undetermined functions per dependent variable field per node.

4. The undetermined functions (nodal values of the dependent variables) are expressed in terms of orthogonal polynomials in time.

5. The subdomain weighted residual method is employed to distribute the equation residual (error) over each element in space.

6. The Galerkin weighted residual method is employed to distribute the equation residual, weighted by Legendre polynomials, over an interval T in time.

7. The final system of equations to be solved numerically is a non-linear system of simultaneous algebraic equations.

8. The method is applied to advance nodal values of the dependent variables an interval T in time.

9. The method may be repeated over and over again to obtain a forecast of any desired length (subject to numerical stability).

Development of a forecast model along the lines of the above model could prove to be a powerful new approach to the numerical weather prediction problem.

7. Conclusions

A two level numerical forecast model was proposed (model ST) in which bicubic polynomial splines are used to fit the spatial variations of the dependent variable fields on a variable area telescoping grid. The grid has superimposed basic expansions of two types. The first expansion is required to maintain the physical distance between grid points on the latitude circles greater than or equal to some minimum distance required for computational stability. The second grid expansion is used to decrease the number of grid points in regions which are not of primary interest thereby reducing the computation time required to obtain a good resolution forecast in a region of interest.

The model used for comparison purposes to evaluate the performance of model ST was a 1969 version of the Mintz-Arakawa numerical general circulation model. Comparison of the results of the two models was facilitated by employing the same governing differential equations, time extrapolation scheme, and heat, moisture and friction source terms for both models. Several hemispheric numerical forecasts were performed with a single set of real weather initial and verification data for a 36 hour period, using modified versions of model ST in order to illustrate basic characteristics of the model.

One fundamental advantage of model ST is the natural computational stability of the expanding grid. Complicated special techniques are not required to obtain a stable forecast on this grid, whereas numerous special techniques are required for stability on the conventional constant latitude, constant longitude interval grid. Preliminary experiments were performed to illustrate the stability problem on a constant 5^{o} interval grid. When no special techniques were used to improve stability, the forecast was unstable in less than 1/2 hour, and

when filters and averaging operators were used to remove spurious short waves at high latitudes, the forecast reached 36 hours with several instabilities increasing in strength. The Mintz-Arakawa model achieves stability on a constant interval grid through the use of filters and averaging operators to remove spurious short waves travelling longitudinally at high latitudes, special methods of evaluating the fluxes, spatial staggering of the dependent variables, and complex finite difference estimates. None of these techniques are used in model ST.

A second advantage of the telescoping grid used in model ST is the reduction in computation time by using a coarser grid over regions of little concern, without sacrificing resolution and forecast accuracy in the finer grid region of primary interest. It was demonstrated from the numerical forecasts performed that the forecast accuracy in the fine grid region of primary interest is not in the least part altered, in either the phase speed of the large scale meteorological waves or in the forecast root-mean-square error (RMSE) due to the presence of a coarse grid of poorer resolution surrounding the region of interest. However, in the region of little interest, in which fewer grid points are used to resolve the dependent variable fields, the forecast accuracy is altered in terms of an increased phase lag and decreased resolution of fine features in the field. With grid expansion factors of 1.10 and 1.04 for the x and y axes directions respectively, and a region of interest extending 3500 miles by 1000 miles over North America, the resulting forecast was performed in 1/3 the computation time of the forecast on a constant grid having the same resolution as in the region of interest. This saving in computation time is of major economic benefit in producing practical numerical forecasts.

The third major advantage of model ST is due to the use of bicubic polynomial splines in place of central finite differences to estimate the spatial derivatives. These benefits are manifest in improved phase speeds of the large scale meteorological waves at middle and high latitudes. The improvements at low latitudes were marginal or non-existant. The geopotential fields and lower level temperature forecasts were improved on the whole by the use of bicubic splines in place of central finite differences. For the remaining dependent variables, bicubic splines were an improvement at the pole and high latitudes, whereas central finite differences gave the better forecast at middle and low latitudes. An additional feature of the forecast using splines was a lower RMSE in regions of fast changing weather.

Finally, model ST was found to give a good forecast in general at middle latitudes, with poorer forecast performance at high and low latitudes. At most latitudes model ST gave a better forecast in terms of larger phase speeds of the meteorological waves and lower RMSE than the comparison Mintz-Arakawa model. Both models had large forecast errors at low latitudes and the equator, and the Mintz-Arakawa forecast was somewhat better than model ST at the pole. The general improvement of model ST over the Mintz-Arakawa model was due both to the use of bicubic splines in place of finite differences, and to the use of an expanding grid of a nature requiring no special techniques to obtain stability.

Extensions of the forecast model were also discussed in some detail. A generalized spline based on continuity of curvature was derived, and forecasts with this spline were performed. One selection of parameters gave a spline theoretically intermediate between the bicubic spline based on continuity of second derivative and

central finite differences. Results from this forecast were in general intermediate between the results from the forecast S using splines based on second derivative and the forecast F using central finite differences. A second selection of parameters gave a spline based on curvature for which the numerical forecast proved to be unstable at 7 hours of forecast time. It was determined that the instability arose from the interaction of the new spline and the artificial equatorial boundary condition. This generalized spline based on curvature requires further research in order to determine its full potential in numerical weather prediction models.

Further extensions of the model using weighted residual numerical techniques were also discussed in detail, but no numerical forecasts were performed using them. It is felt that the development of a forecast model with these techniques could prove to be a powerful new approach to the numerical weather prediction problem.

APPENDIX 1: Single and Double Cubic Polynomial Splines

Single Cubic Polynomial Splines

Consider the interval $x_1 \leq x \leq x_M$, subdivided into M-1 intervals by the points $x_2, x_3, \ldots x_{M-1}$, with $x_1 < x_2 < \ldots < x_{M-1} < x_M$. Associated with each point x_i is a prescribed ordinate u_i. The single cubic spline S(x) of interpolation to values u_i at mesh locations x_i is a piecewise continuous function defined as a cubic polynomial in each interval $x_{i-1} \leq x \leq x_i$, i = 2,3,...M. In addition the cubic spline S(x) is defined to have continuous first and second derivatives ($S(x) \in C^2$). Therefore S(x) satisfies

$$S(x_i-) = S(x_i+) = u_i, \tag{A1.1}$$

$$S'(x_i-) = S'(x_i+) = p_i, \tag{A1.2}$$

$$S''(x_i-) = S''(x_i+) = P_i. \tag{A1.3}$$

for i = 2,3,...M-1, with a prime denoting differentiation with respect to x. Since S(x) is a polynomial of degree 3, S'(x) and S''(x) are of degrees 2 and 1 respectively. In each interval $x_{i-1} \leq x \leq x_i$, the cubic spline S(x) may be expressed in terms of either the nodal values u_i, u_{i-1}, p_i, p_{i-1} or the nodal values u_i, u_{i-1}, P_i, P_{i-1}. Since one major purpose of using splines to fit the data field is to obtain good estimates of the first derivative at data points, it is more convenient to construct the spline in terms of the slopes p_i rather than the second derivatives P_i. The first step in constructing S(x) in terms of p_i is to write a second degree polynomial expression for S'(x) on $x_{i-1} \leq x \leq x_i$ in a fashion ensuring continuity of S'(x). Such an expression is

$$S'(x) = p_{i-1}\,(a_1x^2 + a_2x + a_3) + p_i\,(b_1x^2 + b_2x + b_3) + c_1x^2 + c_2x + c_3. \tag{A1.4}$$

Continuity of $S'(x)$ requires

$$a_1 x_i^2 + a_2 x_i + a_3 = 0,$$

$$b_1 x_i^2 + b_2 x_i + b_3 = 1,$$

$$c_1 x_i^2 + c_2 x_i + c_3 = 0,$$

$$a_1 x_{i-1}^2 + a_2 x_{i-1} + a_3 = 1,$$

$$b_1 x_{i-1}^2 + b_2 x_{i-1} + b_3 = 0,$$

$$c_1 x_{i-1}^2 + c_2 x_{i-1} + c_3 = 0.$$

With these restrictions on the constants $a_1, a_2, \ldots$, the expression for $S'(x)$ may be simplified to

$$S'(x) = p_{i-1}\,(x - x_i)(a_1 x + a_4) + p_i\,(x - x_{i-1})(b_1 x + b_4) + c_1\,(x - x_i)(x - x_{i-1}), \tag{A1.5}$$

where

$$a_1 x_{i-1} + a_4 = -1/h_i, \tag{A1.6}$$

$$b_1 x_i + b_4 = 1/h_i, \tag{A1.7}$$

and

$$h_i = x_i - x_{i-1}. \tag{A1.8}$$

Integrating $S'(x)$ with respect to x yields

$$S(x) = p_{i-1}\,(a_1 x^3/3 + (a_4 - a_1 x_i)\,x^2/2 - x_i a_4 x + a_5) + p_i\,(b_1 x^3/3 + (b_4 - b_1 x_{i-1})\,x^2/2 - x_{i-1} b_4 x + b_5) + c_1\,(x^3/3 - (x_i + x_{i-1})\,x^2/2 + x_i x_{i-1} x + c_5). \tag{A1.9}$$

Continuity of $S(x)$ requires

$$a_1 x_i^3/3 + (a_4 - a_1 x_i)\,x_i^2/2 - x_i^2 a_4 + a_5 = 0, \tag{A1.10}$$

$$b_1 x_i^3/3 + (b_4 - b_1 x_{i-1})\,x_i^2/2 - x_i x_{i-1} b_4 + b_5 = 0, \tag{A1.11}$$

$$c_1\,(x_i^3/3 - (x_i + x_{i-1})\,x_i^2/2 + x_i^2 x_{i-1} + c_5) = u_i, \tag{A1.12}$$

$$a_1 x_{i-1}^3/3 + (a_4 - a_1 x_i)\, x_{i-1}^2/2 - x_i x_{i-1} a_4 + a_5 = 0, \qquad \text{(A1.13)}$$

$$b_1 x_{i-1}^3/3 + (b_4 - b_1 x_{i-1})\, x_{i-1}^2/2 - x_{i-1}^2 b_4 + b_5 = 0, \qquad \text{(A1.14)}$$

$$c_1\, (x_{i-1}^3/3 - (x_i + x_{i-1})\, x_{i-1}^2/2 + x_i x_{i-1}^2 + c_5) = u_{i-1}. \qquad \text{(A1.15)}$$

Equations A1.6, A1.10 and A1.13 are three simultaneous equations in three unknowns a_1, a_4 and a_5. Solving for a_1, a_4 and a_5:

$$a_1 = 3/h_i^2,$$

$$a_4 = -1/h_i - 3x_{i-1}/h_i^2,$$

$$a_5 = -\, x_i^2 x_{i-1}/h_i^2.$$

In a similar fashion equations A1.7, A1.11 and A1.14 are solved for the unknowns b_1, b_4 and b_5 to give

$$b_1 = 3/h_i^2,$$

$$b_4 = 1/h_i - 3x_i/h_i^2,$$

$$b_5 = -\, x_i x_{i-1}^2/h_i^2.$$

Finally solving equations A1.12 and A1.15 for c_1 and c_5 gives

$$c_1 = -\, 6\, (u_i - u_{i-1})\, /h_i^3,$$

$$c_5 = \frac{x_i^3}{6} - \frac{x_i^2 x_{i-1}}{2} - \frac{u_i h_i^3}{6\,(u_i - u_{i-1})}.$$

With the above expressions for constants a_1, a_4, a_5, b_1, b_4, b_5, c_1 and c_5, the equations for $S(x)$ and $S'(x)$ (A1.9 and A1.5 respectively) become

$$S(x) = \frac{p_{i-1}}{h_i^2}\,(x - x_i)^2(x - x_{i-1}) + \frac{p_i}{h_i^2}\,(x - x_{i-1})^2(x - x_i)$$

$$+ \frac{u_{i-1}}{h_i^3}\,(x - x_i)^2(h_i + 2(x - x_{i-1})) + \frac{u_i}{h_i^3}\,(x - x_{i-1})^2(h_i - 2(x - x_i)), \qquad \text{(A1.16)}$$

$$S'(x) = \frac{p_{i-1}}{h_i^2}\,(x - x_i)(3x - x_i - 2x_{i-1}) + \frac{p_i}{h_i^2}\,(x - x_{i-1})(3x - x_{i-1} - 2x_i)$$

$$- \frac{6}{h_i^3} (u_i - u_{i-1})(x - x_i)(x - x_{i-1}). \qquad \text{(A1.17)}$$

S(x) given by equation A1.16 is a piecewise continuous cubic polynomial with continuous first derivatives on $x_1 \leq x \leq x_M$. The unknown slopes p_i, $i = 1,2,\ldots$ are determined by imposing on S(x) the final restrictions of continuity of S"(x). Differentiating A1.17 yields

$$S''(x) = \frac{2p_{i-1}}{h_i^2} (3x - 2x_i - x_{i-1}) + \frac{2p_i}{h_i^2} (3x - 2x_{i-1} - x_i)$$

$$- \frac{6}{h_i^3} (u_i - u_{i-1})(2x - x_i - x_{i-1}). \qquad \text{(A1.18)}$$

The second derivative at node x_i may be written in terms of the spline from below ($x < x_i$) or above ($x > x_i$).

$$S''(x_i-) = \frac{2p_{i-1}}{h_i} + \frac{4p_i}{h_i} - \frac{6\,(u_i - u_{i-1})}{h_i^2},$$

$$S''(x_i+) = \frac{-4p_i}{h_{i+1}} - \frac{2p_{i+1}}{h_{i+1}} + \frac{6\,(u_{i+1} - u_i)}{h_{i+1}^2}. \qquad \text{(A1.19)}$$

Continuity of S"(x) at x_i requires

$$\frac{1}{h_i} p_{i-1} + 2\left(\frac{1}{h_i} + \frac{1}{h_{i+1}}\right) p_i + \frac{1}{h_{i+1}} p_{i+1} = \frac{3\,(u_i - u_{i-1})}{h_i^2} + \frac{3\,(u_{i+1} - u_i)}{h_{i+1}^2} \qquad \text{(A1.20)}$$

In more convenient notation,

$$\lambda_i p_{i-1} + 2p_i + \mu_i p_{i+1} = c_i, \quad i = 2,3,\ldots M-1, \qquad \text{(A1.21)}$$

where

$$\lambda_i = \frac{h_{i+1}}{h_i + h_{i+1}}, \qquad \mu_i = 1 - \lambda_i, \qquad \text{(A1.22)}$$

$$c_i = 3\lambda_i \frac{(u_i - u_{i-1})}{h_i} + 3\mu_i \frac{(u_{i+1} - u_i)}{h_{i+1}}, \quad i = 2,3,\ldots M-1. \qquad \text{(A1.23)}$$

Equation A1.21 forms a system of M-2 equations in M unknown slopes p_1, $p_2,\ldots p_M$. For the system to be determinate, additional end conditions must be specified.

For the periodic spline ($S^{(p)}(x_i) = S^{(p)}(x_M)$, p = 0,1,2) equation A1.21 may in addition be written for the point i = M. Since the spline is periodic then $u_M = u_1$, $p_M = p_1$, $u_{M+1} = u_2$, $p_{M+1} = p_2$ and the system of M-1 equations in M-1 unknowns $p_2, p_3, \ldots p_M$ becomes determinate.

For the nonperiodic spline two additional end conditions must be specified. The end conditions may be written in the form

$$\begin{aligned} 2p_1 + \mu_1 p_2 &= c_1 , \quad \text{at } x_1 , \\ \lambda_M p_{M-1} + 2p_M &= c_M , \quad \text{at } x_M . \end{aligned} \tag{A1.24}$$

Provided suitable values for the coefficients μ_1, c_1, λ_M, c_M are prescribed, equations A1.21 and A1.24 form a determinate system (M equations in the M unknown slopes $p_1, p_2, \ldots p_M$). The end conditions may be specified slopes (u_1' and u_M' prescribed), then

$$\mu_1 = \lambda_M = 0 , \quad c_1 = 2u_1' , \quad c_M = 2u_M' , \tag{A1.25}$$

or specified second derivatives (u_1'' and u_M'' prescribed), then

$$\begin{aligned} \mu_1 &= \lambda_M = 1, \\ c_1 &= \frac{3\,(u_2 - u_1)}{h_2} - \frac{h_2}{2}\,u_1'' , \\ c_M &= \frac{3\,(u_M - u_{M-1})}{h_M} + \frac{h_M}{2}\,u_M'' . \end{aligned} \tag{A1.26}$$

A final choice of end conditions for the nonperiodic spline could be to specify zero second derivatives at some specified points x_0 and x_{M+1} (outside of the interval $x_1 \leq x \leq x_M$ over which the spline is constructed), with the restriction that the curves over $x_0 \leq x \leq x_1$ and $x_M \leq x \leq x_{M+1}$ be cubic arcs. The locations of points x_0 and x_{M+1} are specified by assigning values to the parameters λ_0 and μ_{M+1} according to

$$\lambda_0 = \frac{x_1 - x_0}{x_2 - x_0} , \qquad \mu_{M+1} = \frac{x_M - x_{M+1}}{x_{M-1} - x_{M+1}} . \tag{A1.27}$$

Then the coefficients μ_1, c_1, λ_M, c_M take on the values

$$\mu_1 = \frac{2\ (2\lambda_0 + 1)}{\lambda_0 + 2}\ , \qquad c_1 = \frac{6\ (u_2 - u_1)(1 + \lambda_0)}{h_2\ (2 + \lambda_0)}\ ,$$
$$\lambda_M = \frac{2\ (2\mu_{M+1} + 1)}{\mu_{M+1} + 2}\ , \qquad c_M = \frac{6\ (u_M - u_{M-1})(1 + \mu_{M+1})}{h_M\ (2 + \mu_{M+1})}\ . \tag{A1.28}$$

In the nonperiodic case the system of equations to be solved (for the unknown slopes $p_1,\ldots p_M$) is of the form

$$\begin{aligned}
b_1 v_1 + c_1 v_2 &= d_1\ , \\
a_2 v_1 + b_2 v_2 + c_2 v_3 &= d_2\ , \\
&\cdots\cdots\cdots\cdots \\
a_i v_{i-1} + b_i v_i + c_i v_{i+1} &= d_i\ , \\
&\cdots\cdots\cdots\cdots \\
a_{n-1} v_{n-2} + b_{n-1} v_{n-1} + c_{n-1} v_n &= d_{n-1}\ , \\
a_n v_{n-1} + b_n v_n &= d_n\ .
\end{aligned} \tag{A1.29}$$

There are n equations in n unknowns v_i, $i = 1,\ldots n$. This tridiagonal system is readily solved by an efficient Gaussian elimination algorithm (p.441 of Carnahan, Luther and Wilkes (52) or p.14 of Ahlberg, Nilson and Walsh (22)). The solution is

$$\begin{aligned}
v_n &= \gamma_n\ , \\
v_i &= \gamma_i - c_i v_{i+1} \,/\, \beta_i,\ i = n-1, n-2, \ldots 2, 1,
\end{aligned} \tag{A1.30}$$

where the β's and γ's are determined from the recursion formulas

$$\beta_1 = b_1\ ,\ \beta_i = b_i - \frac{a_i c_{i-1}}{\beta_{i-1}}\ ,\quad i = 2,3,\ldots n,$$
$$\gamma_1 = \frac{d_1}{\beta_1}\ ,\ \gamma_i = \frac{d_i - a_i \gamma_{i-1}}{\beta_i}\ ,\quad i = 2,3,\ldots n. \tag{A1.31}$$

In the periodic case the system of equations to be solved (for the unknown slopes $p_2, p_3, \ldots p_M$) is of the form

$$
\begin{aligned}
b_1 v_1 + c_1 v_2 + \qquad\qquad\qquad\qquad + a_1 v_n &= d_1 \,, \\
a_2 v_1 + b_2 v_2 + c_2 v_3 \qquad\qquad\qquad\qquad &= d_2 \,, \\
\cdots\cdots\cdots\cdots\cdots & \\
a_i v_{i-1} + b_i v_i + c_i v_{i+1} \qquad\qquad &= d_i \,, \\
\cdots\cdots\cdots\cdots\cdots & \\
a_{n-1} v_{n-2} + b_{n-1} v_{n-1} + c_{n-1} v_n &= d_{n-1} \,, \\
c_n v_1 + \qquad\qquad\qquad\qquad + a_n v_{n-1} + b_n v_n &= d_n \,,
\end{aligned}
\tag{A1.32}
$$

n equations in n unknowns v_i, i = 1,...n. The algorithm to solve this system of equations is given by Ahlberg, Nilson and Walsh (p.15 of reference 22). The solution is

$$
\begin{aligned}
v_n &= \frac{d_n - c_n \delta_1 - a_n \delta_{n-1}}{b_n + c_n \alpha_1 + a_n \alpha_{n-1}} \,, \\
v_i &= \alpha_i v_n + \delta_i \,, \quad i = 1,2,\ldots n-1,
\end{aligned}
\tag{A1.33}
$$

where the α's and δ's are determined from the recursion formulas

$$
\begin{aligned}
&\alpha_n = 1, \quad \alpha_i = -\frac{c_i \alpha_{i+1}}{\beta_i} + \mu_i \,, \quad i = n-1, n-2, \ldots 2, 1, \\
&\mu_1 = -\frac{a_1}{\beta_1} \,, \quad \mu_i = -\frac{a_i \mu_{i-1}}{\beta_i} \,, \quad i = 2,3,\ldots n, \\
&\delta_n = 0 \,, \quad \delta_i = -\frac{c_i \delta_{i+1}}{\beta_i} + \gamma_i \,, \quad i = n-1, n-2, \ldots 2, 1,
\end{aligned}
\tag{A1.34}
$$

β_i , γ_i are given by equation A1.31.

Double Cubic Polynomial Splines

The theory of double cubic splines depends largely on the theory of one dimensional cubic splines. Consider the rectangular mesh $x_1 < x_2 < \ldots < x_M$, $y_1 > y_2 > \ldots > y_N$ with prescribed ordinates u_{ij} at mesh points x_i, y_j, i = 1,...M, j = 1,...N. The lines $x = x_1$, $x = x_M$, $y = y_1$, $y = y_N$ correspond respectively to the 180° west meridian, 180° east meridian, north pole and southern boundary line. The double cubic

spline $S(x,y)$ of interpolation to values u_{ij} at mesh locations x_i, y_j is a piecewise continuous function defined as a double cubic polynomial in each rectangle $(x_{i-1} \leq x \leq x_i,\ y_{j-1} \geq y \geq y_j)$, $i = 2,\ldots M$, $j = 1,\ldots N$. The spline $S(x,y)$ will be constructed periodic in the x direction, since meteorological fields repeat after 360° rotation around the earth, and with specified boundary conditions in the y direction. Let

$$h_i = x_i - x_{i-1} > 0, \qquad k_j = y_j - y_{j-1} < 0. \tag{A1.35}$$

Along the line $y = y_j$, the one-dimensional spline of interpolation to the ordinates u_{ij}, $i = 1,\ldots M$ may be written from equation A1.16 as

$$S(x,y_j) = p_{i-1,j}\frac{(x - x_i)^2(x - x_{i-1})}{h_i^2} + p_{i,j}\frac{(x - x_{i-1})^2(x - x_i)}{h_i^2} + \frac{u_{i-1,j}}{h_i^3}(x - x_i)^2(h_i + 2(x - x_{i-1})) + \frac{u_{i,j}}{h_i^3}(x - x_{i-1})^2(h_i - 2(x - x_i)). \tag{A1.36}$$

The slopes $p_{i,j}$, $i = 1,\ldots M$ are obtained by solving the system of equations A1.21 written for the periodic spline case. One-dimensional splines of the form A1.36 may be written for each line $y = y_j$, $j = 1,\ldots N$. Therefore, at any x (not necessarily a node point x_i, $i = 1,\ldots M$), the ordinate $S(x,y_j)$ is given by equation A1.36 and one may construct the following one-dimensional cubic spline of interpolation in y to the ordinates $S(x,y_j)$, $j = 1,\ldots N$ (equation A1.16 with x, p_i, u_i and h_i replaced by y, $q_j(x)$, $S(x,y_j)$ and k_j respectively):

$$S(x,y) = q_{j-1}(x)\frac{(y - y_j)^2(y - y_{j-1})}{k_j^2} + q_j(x)\frac{(y - y_{j-1})^2(y - y_j)}{k_j^2} + \frac{S(x,y_{j-1})}{k_j^3}(y - y_j)^2(k_j + 2(y - y_{j-1})) + \frac{S(x,y_j)}{k_j^3}(y - y_{j-1})^2(k_j - 2(y - y_j)). \tag{A1.37}$$

In equation A1.37, it remains to evaluate the terms $q_j(x)$, $q_{j-1}(x)$. The

slopes $q_{i,j}$, j = 1 to N are obtained by solving the system of equations A1.21 written for the nonperiodic spline case. This process is repeated at all i giving a matrix of evaluated slopes ($q_{i,j}$; i = 1, ...M; j = 1,...N). One may them form the following expression for $q_j(x)$ by constructing a one-dimensional spline of interpolation in x to the slopes $q_{i,j}$, i = 1,...M (equation A1.16 with p_i and u_i replaced by $s_{i,j}$ and $q_{i,j}$ respectively):

$$q_j(x) = s_{i-1,j}\frac{(x - x_i)^2(x - x_{i-1})}{h_i^2} + s_{i,j}\frac{(x - x_{i-1})^2(x - x_i)}{h_i^2} \qquad \text{(A1.38)}$$

$$+ \frac{q_{i-1,j}}{h_i^3}(x - x_i)^2(h_i + 2(x - x_{i-1})) + \frac{q_{i,j}}{h_i^3}(x - x_{i-1})^2(h_i - 2(x - x_i)).$$

In equation A1.38 the terms $s_{i,j}$ are obtained by solving the system of equations A1.21 written for the periodic case in x, with p_i and u_i replaced by $s_{i,j}$ and $q_{i,j}$ respectively. Finally substituting A1.38 and A1.36 into A1.37, the double cubic spline of interpolation to u_{ij}, i = 1, ...M; j = 1,...N becomes

$$\begin{aligned} S(x,y) = {} & ae\ s_{i-1,j-1} - af\ s_{i,j-1} + ag\ q_{i-1,j-1} + al\ q_{i,j-1} \\ & - be\ s_{i-1,j} + bf\ s_{i,j} - bg\ q_{i-1,j} - bl\ q_{i,j} \\ & + ce\ p_{i-1,j-1} - cf\ p_{i,j-1} + cg\ u_{i-1,j-1} + cl\ u_{i,j-1} \\ & + de\ p_{i-1,j} - df\ p_{i,j} + dg\ u_{i-1,j} + dl\ u_{i,j}, \\ & x_{i-1} \leq x \leq x_i,\ y_{j-1} \leq y \leq y_j \text{ for } i = 2,...M,\ j = 2,...N, \end{aligned} \qquad \text{(A1.39)}$$

where the following notation has been used:

$$\begin{aligned} n &= y - y_{j-1}, & m &= x - x_{i-1}, \\ \eta &= n / k_j, & \xi &= m / h_i, \\ a &= (1 - \eta)^2 n, & e &= (1 - \xi)^2 m, \\ b &= (1 - \eta)\,\eta\, n, & f &= (1 - \xi)\,\xi\, m, \\ c &= (1 - \eta)^2 (2\eta + 1), & g &= (1 - \xi)^2 (2\xi + 1), \\ d &= \eta^2 (3 - 2\eta), & l &= \xi^2 (3 - 2\xi). \end{aligned} \qquad \text{(A1.40)}$$

Equation A1.39 may be differentiated with respect to x and y to yield expressions for the first derivatives and cross derivative of the spline surface. It is often necessary to have good estimates of a function and its derivatives at the mid-points of horizontal and vertical grid sides as well as at the center of the element. Such estimates are readily obtained from the double cubic spline A1.39. At the mid-point of horizontal grid sides, $(x,y) = (x_i - h_i/2,\ y_j)$ or simply the point $i - \frac{1}{2}, j$,

$$
\begin{aligned}
S_{i-\frac{1}{2},j} &= \frac{h_i}{8}\,(p_{i-1,j} - p_{i,j}) + \tfrac{1}{2}\,(u_{i-1,j} + u_{i,j}) \ , \\
\frac{\partial S_{i-\frac{1}{2},j}}{\partial x} &= -\tfrac{1}{4}\,(p_{i-1,j} + p_{i,j}) + \frac{3}{2h_i}\,(u_{i,j} - u_{i-1,j}) \ , \\
\frac{\partial S_{i-\frac{1}{2},j}}{\partial y} &= \frac{h_i}{8}\,(s_{i-1,j} - s_{i,j}) + \tfrac{1}{2}\,(q_{i-1,j} + q_{i,j}) \ , \\
\frac{\partial S_{i-\frac{1}{2},j}}{\partial x \partial y} &= -\tfrac{1}{4}\,(s_{i-1,j} + s_{i,j}) + \frac{3}{2h_i}\,(q_{i,j} - q_{i-1,j}).
\end{aligned}
\qquad \text{(A1.41)}
$$

At the mid-point of vertical grid sides, $(x,y) = (x_i, y_j - k_j/2)$ or simply the point $i,\ j-\frac{1}{2}$,

$$
\begin{aligned}
S_{i,j-\frac{1}{2}} &= \frac{k_j}{8}\,(q_{i,j-1} - q_{i,j}) + \tfrac{1}{2}\,(u_{i,j-1} + u_{i,j}) \ , \\
\frac{\partial S_{i,j-\frac{1}{2}}}{\partial x} &= \frac{k_j}{8}\,(s_{i,j-1} - s_{i,j}) + \tfrac{1}{2}\,(p_{i,j-1} + p_{i,j}) \ , \\
\frac{\partial S_{i,j-\frac{1}{2}}}{\partial y} &= -\tfrac{1}{4}\,(q_{i,j-1} + q_{i,j}) + \frac{3}{2k_j}\,(u_{i,j} - u_{i,j-1}), \\
\frac{\partial^2 S_{i,j-\frac{1}{2}}}{\partial x \partial y} &= -\tfrac{1}{4}\,(s_{i,j-1} + s_{i,j}) + \frac{3}{2k_j}\,(p_{i,j} - p_{i,j-1}).
\end{aligned}
\qquad \text{(A1.42)}
$$

Finally at the cell center, $(x,y) = (x_i - h_i/2,\ y_j - k_j/2)$ or simply the point $i - \frac{1}{2},\ j - \frac{1}{2}$,

$$S_{i-\frac{1}{2},j-\frac{1}{2}} = \frac{h_i k_j}{16}\,(s_{i-1,j-1} - s_{i,j-1} - s_{i-1,j} + s_{i,j}) + \frac{k_j}{16}\,(q_{i-1,j-1}$$

$$+ q_{i,j-1} - q_{i-1,j} - q_{i,j}) + \frac{h_i}{16}\,(p_{i-1,j-1} - p_{i,j-1} + p_{i-1,j} - p_{i,j})$$

$$+ \tfrac{1}{4}\,(u_{i-1,j-1} + u_{i,j-1} + u_{i-1,j} + u_{i,j}) \quad , \qquad \text{(A1.43a)}$$

$$\frac{\partial S_{i-\frac{1}{2},j-\frac{1}{2}}}{\partial x} = \frac{k_j}{32}\,(s_{i,j} + s_{i-1,j} - s_{i-1,j-1} - s_{i,j-1}) + \frac{3k_j}{16h_i}\,(q_{i,j-1}$$

$$- q_{i-1,j-1} + q_{i-1,j} - q_{i,j}) - \frac{1}{8}\,(p_{i-1,j-1} + p_{i,j-1} + p_{i-1,j} + p_{i,j})$$

$$+ \frac{3}{4h_i}\,(u_{i,j-1} - u_{i-1,j-1} + u_{i,j} - u_{i-1,j}) \quad , \qquad \text{(A1.43b)}$$

$$\frac{\partial S_{i-\frac{1}{2},j-\frac{1}{2}}}{\partial y} = \frac{h_i}{32}\,(s_{i,j-1} - s_{i-1,j-1} + s_{i,j} - s_{i-1,j}) - \frac{1}{8}\,(q_{i-1,j-1}$$

$$+ q_{i,j-1} + q_{i-1,j} + q_{i,j}) + \frac{3h_i}{16k_j}\,(p_{i,j-1} - p_{i-1,j-1} + p_{i-1,j} - p_{i,j})$$

$$+ \frac{3}{4k_j}\,(u_{i-1,j} + u_{i,j} - u_{i-1,j-1} - u_{i,j-1}) \quad , \qquad \text{(A1.43c)}$$

$$\frac{\partial^2 S_{i-\frac{1}{2},j-\frac{1}{2}}}{\partial x \partial y} = \frac{1}{16}\,(s_{i-1,j-1} + s_{i,j-1} + s_{i-1,j} + s_{i,j}) + \frac{3}{8h_i}\,(q_{i-1,j-1}$$

$$- q_{i,j-1} + q_{i-1,j} - q_{i,j}) + \frac{3}{8k_j}\,(p_{i-1,j-1} + p_{i,j-1} - p_{i-1,j} - p_{i,j})$$

$$+ \frac{9}{4k_j h_i}\,(u_{i-1,j-1} - u_{i,j-1} - u_{i-1,j} + u_{i,j}) \quad . \qquad \text{(A1.43d)}$$

APPENDIX 2: The Telescoping Grid

In the numerical forecast model developed in this thesis, piecewise bicubic polynomial functions (double cubic splines) are used to fit the two-dimensional data fields. For this reason it is convenient to use either a constant area or smoothly expanding rectangular grid.

A point on the earth's surface is located by the coordinates (x,y), specifying longitude and latitude respectively in degrees. Hence the forecast region on the x,y plane is the rectangle $-180.0 \leq x \leq 180.0$, $YS \leq y \leq 90.0$, where YS = 0.0 (equator) for a northern hemisphere grid and YS = - 90.0 (south pole) for a full earth grid. To avoid the problem of carrying grid point data along the line y = 90.0 (north pole, a singular point), it was decided to first generate a preliminary grid having the north pole as a grid line and then use the centers of grid cells in the preliminary grid as grid points in the final grid. The preliminary grid itself is determined entirely by the following set of adjustable parameters:

1. XP, YP = longitude, latitude of a center of interest about which the rectangular grid expands uniformly.
2. NX, NY = the number of grid rectangles of constant size centered about the point of interest, in the x and y directions respectively. The region containing grid rectangles of constant size is termed the region of interest, since it locates a region on the earth in which a forecast of good accuracy and high resolution is desired.
3. DX, DY = the grid spacing (in degrees) in the region of interest, in the x and y directions respectively.

4. EX, EY = the grid expansion factors applying outside the region of interest, in the x and y directions respectively.

The role which the above parameters play in generating the preliminary grid may be seen by examining Figure A2.1. This figure shows sample grid lines for both the x and y directions. It is seen that both the x and y grid lines expand uniformly as distance from the point (XP,YP) increases. However, special consideration is required to ensure that the x grid meshes smoothly at the point XXP (located 180° east or 180° west of point XP) and that the y grid meshes smoothly at both the north pole and the southern boundary point YS.

Figure A2.1 shows the x and y grid lines corresponding to the first generation of the preliminary grid. The parameter d_0 determines the form of special treatment required to ensure a smooth x grid in in the vicinity of point XXP. Four cases may be considered:

1. $d_0 < d_1 - DX/2$ The x grid is generated over again using $NX_{new} = NX_{old} + NN$ where NN is the largest integer $\leq (d_0/DX) + 1$. In the new grid the points x_{-1} and x_1 are set to coincide with XXP. If $d_1 > d_2$, then the new grid expands smoothly up to XXP from both sides and is satisfactory. However if $d_1 < d_2$ the grid does not smoothly expand up to XXP and should be regenerated using $NX_{new} = NX_{old} + NN - 1$ to give a satisfactory grid.
2. $d_1 - DX/2 < d_0 < d_1 + DX/2$ A satisfactory grid may be obtained by slight adjustments in the position of points x_{-1} and x_1. Let $x_{-1\ new} = x_{-2} + XM$ and $x_{1\ new} = x_2 - XM$, where $XM = (x_2 - x_{-2})/3$. If $d_1 > d_2$, the new grid expands smoothly up to XXP and is satisfactory. However if $d_1 < d_2$, then case 1 is applied.

3. $d_1 + DX/2 < d_0 < 2d_1$ The grid is generated over again using $NX_{new} = NX_{old} + MM$ where MM is the largest integer $\leq (d_0 - d_1)/DX + \frac{1}{2}$. This new grid is then adjusted as in case 2.

4. $2d_1 < d_0 < (2d_1)$ EX The point XXP is set to be a grid point.

The y grid must mesh smoothly at both the north pole (y = 90) and the southern boundary point YS (YS = -90 if the grid is global, 0 if the grid is hemispheric). A smooth meshing with the north pole is obtained by shifting the entire y grid north or south until the nearest generated y grid point coincides with the pole. This results in a small shift in YP, the y coordinate of the center of interest. It then remains to adjust the position of points y_1 and y_2 (see Figure A2.1) in order that YS becomes a grid point and the grid expands smoothly up to YS. Let the distance from y_3 to YS be denoted by D.

$$D = a + b + c = y_3 - YS \quad . \tag{A2.1}$$

Two cases may be considered:

1. If $D/3 > d$, $a > 0$ it is possible to expand a grid from y_3 to YS using an expansion factor less than EY but greater than 1. To make the expansion smooth the grid expansion factor will be decreased gradually in proceeding from y_3 to YS, with the grid lengths c, b and a taking on the values $(EY - \delta)d$, $(EY - 2\delta)(EY - \delta)d$ and $(EY - 3\delta)(EY - 2\delta)(EY - \delta)d$ respectively. Substituting these expressions for a, b and c into equation A2.1 gives a cubic equation in the unknown parameter δ .

$$6\delta^3 - (2 + 11EY)\delta^2 + (1 + 3EY + 6\,EY^2)\delta + (D/d - EY\,(1 + EY + EY^2)) = 0 \quad . \tag{A2.2}$$

Using δ given by the real root of equation A2.2 (the two conjugate imaginary roots of equation A2.2 are neglected), the

grid lengths a, b, c are evaluated and the points y_2, y_1 located in such a fashion that the y grid expands smoothly to mesh with the southern boundary point YS.

2. If D/3 < d, a > 0 the y grid is generated over again using $NY_{new} = NY_{old} + NN$ where NN is the largest integer $\leq$ (a/DY) + 1. In the new grid the position of points y_1 and y_2 is adjusted as in case 1.

Having constructed the preliminary grid as described above, the final grid is formed by using the centers of grid cells in the preliminary grid as grid points in the final grid.

APPENDIX 3: Extension of the Model: Galerkin and Subdomain Methods

The basic idea of the method of weighted residuals (abbreviated MWR) may be illustrated by considering a differential equation governing the behaviour of dependent variable $\Psi(\chi,t)$ in domain S bounded by curve C. Here, χ represents two space dimensions and t denotes time. Following Finlayson and Scriven (46),

$$\frac{\partial \Psi}{\partial t} + D(\Psi) = 0 \quad , \tag{A3.1}$$

where D denotes a general differential operator involving spatial derivatives only. The initial and boundary conditions respectively are

$$\begin{aligned} \Psi(\chi,0) &= \Psi_0 \quad , \quad \chi \text{ in } S \quad , \\ \Psi(\chi,t) &= f_s(\chi,t) \quad , \quad \chi \text{ on } C, \; t \geq 0 \quad . \end{aligned} \tag{A3.2}$$

A trial solution $\Psi^*(\chi,t)$ is constructed in terms of prescribed approximating functions $\phi_q(\chi,t)$ and undetermined functions of a single variable $C_q(t)$, $q = 1,\ldots Q$.

$$\Psi^*(\chi,t) = \sum_{q=0}^{Q} C_q(t)\, \phi_q(\chi,t) \quad . \tag{A3.3}$$

Often the approximating functions are selected subject to $\phi_1(\chi,t) = f_s(\chi,t)$, $\phi_q(\chi,t) = 0$, $q = 2,\ldots Q$, χ on S . Then $C_1(t) \equiv 1$, $C_q(t)$ may take on any values, and the trial function $\Psi^*(\chi,t)$ will inherently satisfy the boundary conditions. The degree to which the trial function Ψ^* satisfies the differential equation and initial condition is measured by the qquation residual R and initial residual R_0 which are defined as

$$\begin{aligned} R(\Psi^*) &= \frac{\partial \Psi^*}{\partial t} - D(\Psi^*) \quad , \quad t > 0 \quad , \\ R_0(\Psi^*) &= \Psi_0 - \sum_{q=0}^{Q} C_q(0)\, \phi_q(\chi,0) \quad , \quad \chi \text{ in } S \; . \end{aligned} \tag{A3.4}$$

If $\Psi^*(\chi,t)$ was the exact solution to equations A3.1 and A3.2, the residuals A3.4 would be identically zero. The method of weighted residuals approximates this exact solution case by setting the weighted integral

of the residuals to zero.

$$< w_q ; R(\Psi^*) > = 0 \quad , \tag{A3.5}$$

$$< w_q ; R_0(\Psi^*) > = 0 \quad , \tag{A3.6}$$

$$< w,v > = \int_S wv dS \quad . \tag{A3.7}$$

Equation A3.5 forms a system of Q first order ordinary differential equations in the unknown functions $C_q(t), q = 1,...Q$, with Q initial conditions given by A3.6. Solving the system A3.5, A3.6 for the coefficients $C_q(t)$ and substituting these coefficients into equation A3.3 yields an approximate solution to equations A3.1 and A3.2 by the MWR technique.

The MWR scheme in which undetermined functions $C_q(t)$, $q = 1,...Q$ are used in forming the approximate solution is equivalent to replacing the continuous propagation problem by a propagation problem with a finite number of degrees of freedom. As the number Q of approximation functions increases, the number of permitted degrees of freedom increases and the approximate solution approaches the true solution.

There are numerous methods of selecting the weighting functions w_q, each giving rise to a specific numerical method (ref 45,46,49). The following are examples of numerical methods arising from the different weighting functions:

Collocation - $$w_q = \delta(\chi_q - \chi) \quad , \tag{A3.8}$$

Subdomain - $$w_q = 1 \ , \ \chi \text{ in } S_q \quad , \quad w_q = 0 \ , \ \chi \text{ not in } S_q \quad , \tag{A3.9}$$

Galerkin - $$w_q = \phi_q \quad , \tag{A3.10}$$

Least-squares - $$w_q = \frac{\partial R(\Psi^*)}{\partial C_q} \quad . \tag{A3.11}$$

In the collocation method the differential equation is satisfied exactly

at Q collocation points χ_q, q = 1,...Q. Hence the weighting function is the unit impulse or Dirac delta $\delta(\chi_q - \chi)$ which vanishes everywhere except at $\chi = \chi_q$ and satisfies $\int_{-\infty}^{+\infty}\delta(\chi - \chi_q)d\chi = 1$. The subdomain criterion A3.9 results in the differential equation being satisfied on the average in Q subdomains S_q, q = 1,...Q in domain S. The earliest MWR, the Galerkin method, takes the weighting functions w_q equal to the approximating functions ϕ_q, thereby forcing the residual to be orthogonal to the approximating functions. If the set of approximating functions spans all degrees of freedom of the system (forms a complete set of functions) then the residual, orthogonal to the approximating functions, must vanish. Finally the least-squares method A3.11 corresponds to minimizing the mean square residual with respect to coefficients C_q.

In meteorology the system of governing differential equations is of the form

$$\frac{\partial \Psi_n}{\partial t} + \sum_{j,k=1}^{N} \left(a^n_{jk}\, \Psi_k \frac{\partial \Psi_j}{\partial x} + b^n_{jk}\, \Psi_k \frac{\partial \Psi_j}{\partial y} + c^n_{jk}\, \Psi_j\, \Psi_k\right) + \sum_{j=1}^{N} f^n_j(x,y)\, \Psi_j + g^n(x,y) = 0,\ n = 1,2...N, \tag{A3.12}$$

where x,y = spatial coordinates;

$\Psi_n = \Psi_n(x,y,t)$, the n^{th} dependent variable, n = 1,2...N;

$a^n_{jk}, b^n_{jk}, \ldots g^n$ = known functions of x and y.

Similar to equation A3.3 the trial solution Ψ^*_n is constructed in terms of Q prescribed approximating functions $\phi_q(x,y)$ and undetermined functions of a single variable $d_q(t)$. In this application, however, the functions $\phi_q(x,y)$ will be polynomials of a spline nature, defined to be piecewise continuous on all elements. Hence,

$$\Psi_n^{*e} = \sum_{q=1}^{Q} d_q^{ne}(t)\, \phi_q^{ne}(x,y) \ , \tag{A3.13}$$

where the superscript e implies the terms are defined piecewise, element by element, and superscript n denotes the dependent variable. With E denoting the total number of elements in the domain of interest then e = 1,2,...E. Substituting A3.13 into A3.12, there results the system of equations

$$\sum_{q=1}^{Q} \phi_q^{ne}(x,y)\, \frac{d}{dt}\,(d_q^{ne}(t)) + \sum_{j,k=1}^{N} \sum_{p,q=1}^{Q} h_{jkpq}^{ne}(x,y)\, d_q^{je}(t)\, d_p^{ke}(t) + \ldots = 0, \tag{A3.14}$$

$$\text{or} \quad R^{ne}(x,y,t,\underset{\sim}{d}(t), \frac{d}{dt}\,(\underset{\sim}{d}(t))) = 0, \ n = 1,\ldots N. \tag{A3.15}$$

For each element e there are N equations of the form A3.15 in NQ unknowns. Sufficient equations to form a determinate system are obtained by applying the weighted residual criterion A3.5.

$$< w_q^{ne} \ , \ R^{ne} > = 0, \ n = 1,\ldots N \ , \tag{A3.16}$$

$$q = 1,\ldots Q \ ,$$

$$\text{where} \quad < a,b > = \iint_e abdxdy. \tag{A3.17}$$

The integration in the inner product A3.17 is performed over element e alone. For each element e there are NQ equations of the form A3.16, giving in the entire solution domain a total of NQE equations in NQE unknown functions $d_q^{ne}(t)$, q = 1,...Q; n = 1,...N; e = 1,...E.

At this point it is necessary to consider the choice of trial functions $\phi_q^{ne}(x,y)$, undetermined functions $d_q^{ne}(t)$ and weighting functions $w_q^{ne}(x,y)$. It is proposed that the approximating functions be double cubic polynomial splines, piecewise continuous element by element. Equation A1.39 in Appendix 1 expresses the double cubic spline on element e in terms of sixteen nodal values u_{ij}, p_{ij}, q_{ij}, s_{ij}, ... and corresponding polynomial coefficients d1, df, b1, bf,... .

In adapting the notation of Appendix 1 to the notation here, the terms u, p, q, s represent respectively Ψ_n, $\frac{\partial \Psi_n}{\partial x}$, $\frac{\partial \Psi_n}{\partial y}$, $\frac{\partial^2 \Psi_n}{\partial x \partial y}$. It is therefore natural to select the sixteen polynomial coefficients d1, df, ... to be approximating functions, with the nodal values u, p, ... taken to be initial values of the variable coefficients $d_q^{ne}(t)$. With reference to equations A1.39 and A1.40 the following expressions are obtained:

$$\begin{aligned}
&\phi_1^{ne} = ae = (1 - \eta)^2 n (1 - \xi)^2 m \ , \\
&\vdots \\
&\phi_{16}^{ne} = d1 = \eta^2 (3 - 2\eta)\ \xi^2 (3 - 2\xi) \ , \\
&d_1^{ne}(t) = S_{i-1,j-1}(t) \quad , \quad d_1^{ne}(0) = S_{i-1,j-1}(0) \quad , \\
&\vdots \\
&d_{16}^{ne}(t) = u_{ij}(t) \quad , \quad d_{16}^{ne}(0) = u_{ij}(0) \quad .
\end{aligned} \tag{A3.18}$$

In this fashion the trial solution Ψ_n^{*e} on element e (given by equation A3.13) is defined in terms of Q = 16 trial functions ϕ_q and undetermined functions of a single variable $d_q^{ne}(t)$. All of the functions $d_q^{ne}(t)$, q = 1,2,...Q for element e are not unique to that element since each corner of e is common to three other elements. With each dependent variable field having four degrees of freedom per node point (namely u(t), p(t), q(t), s(t)) then each element also has four degrees of freedom on the average, and only four applications of the weighted residual criterion A3.16 need be performed. This is equivalent to replacing Q by Q/4 in A3.16. It now remains to select the four weighting functions w_q^{ne}, q = 1,...Q/4 (where Q = 16). A straight forward application of the Galerkin method ($w_q^{ne}(x,y) = \phi_q^{ne}(x,y)$) is not possible since there are sixteen trial functions and only four weighting functions. The trial functions are of four types: coefficients of

either u(t), p(t), q(t) or s(t) at the nodes. Weighting functions representative of each type of trial function may be formed by summing the trial functions of each type. This gives

$$\begin{aligned} w_1^{ne}(t) &= 1 \quad , \\ w_2^{ne}(t) &= m(1-\xi)(1-2\xi) \quad , \\ w_3^{ne}(t) &= n(1-\eta)(1-2\eta) \quad , \\ w_4^{ne}(t) &= mn(1-\xi)(1-\eta)(1-2\xi)(1-2\eta) \quad . \end{aligned} \tag{A3.19}$$

This weighted residual scheme employing trial and undetermined functions A3.18 and weighting functions A3.19 will be referred to as method A. This scheme reduces equation A3.16 to a nonlinear system of first order ordinary differential equations of the type

$$A_z \frac{d}{dt} (\underset{\sim}{d}(t)) = B \quad , \tag{A3.20}$$

where z = NEQ/4, $\underset{\sim}{d}$ is a z element vector carrying the terms $d_q^{ne}(t)$, A is a zxz band matrix with band width NQ, and B is a zxz band matrix with linear and nonlinear terms involving $d_q^{ne}(t)$.

The major drawback of method A is the difficulty in solving equation A3.20. It would be impractical to store matricies A and B due to their large order. Hence a matrix algebra solution is impossible. If A were the identity matrix I a Runge Kutta solution could be used to solve for the vector $\underset{\sim}{d}(t)$. However, A is not I, and it would be impractical to employ matrix methods to replace A by I in A3.20. One must conclude that although a solution to A3.20 could be attempted in theory, such a solution would be impractical. A second characteristic of method A is that the dependent variable fields do not remain of a spline nature as time progresses, despite the use of initial values $d_q^{ne}(0)$ generated by spline techniques. This arises from permitting four

degrees of freedom per node point for each dependent variable field (in other words, for each dependent variable at each node the values u(t), p(t), q(t) and s(t) vary independently of each other for all $t > 0$). Therefore a saving in the number of unknown functions per dependent variable field per node point could be realized by forcing p(t), q(t) and s(t) to be some function of u(t), $t \geq 0$. This gives rise to a second method, to be referred to as method B.

The number of permitted degrees of freedom for each dependent variable at each node may be reduced from four to one by forcing the trial solution A3.13 to be of double cubic spline shape for all $t \geq 0$. In this case the values p(t), q(t) and s(t) depend on u(t) according to equation A1.21 (in Appendix 1) written respectively for the periodic, nonperiodic and periodic case with u(t) replaced by q(t). An alternative form of expressing the dependence of p(t), q(t) and s(t) on u(t) is to write

$$p_{ij}(t) = \sum_{i^*=1}^{I} b_{iji^*} u_{i^*j}(t) \quad , \tag{A3.21a}$$

$$q_{ij}(t) = \sum_{j^*=1}^{J} c_{ijj^*} u_{ij^*}(t) \quad , \tag{A3.21b}$$

$$s_{ij}(t) = \sum_{i^*=1}^{I} \sum_{j^*=1}^{J} d_{iji^*j^*} u_{i^*j^*}(t) \quad . \tag{A3.21c}$$

In equations A3.21a,b,c, the coefficient vectors $\underset{\sim}{b}$, $\underset{\sim}{c}$, $\underset{\sim}{d}$ are obtained by taking the inverse of the coefficient matrix of the system of equations A1.21 written for the periodic and nonperiodic cases, and the limits I, J denote the number of grid points in the x and y directions respectively. Substituting equations A3.21a,b,c, along with the trial and undetermined functions A3.18 into the trial solution A3.13 yields

$$\psi_n^{*e}(x,y,t) = \sum_{q=1}^{Q} \sum_{i=1}^{I} \sum_{j=1}^{J} a_{ijq}^{e} \, \psi_{nij}(t) \, \phi_q(x,y) \quad . \tag{A3.22}$$

All of the coefficients a, b, c, d are characteristic of the grid and are generated only once, at the beginning of the forecast. Further, these coefficients decrease rapidly as distance from element e increases. For example, the inverse of the coefficient matrix of A1.21 for the periodic case with equidistant grid points results in the values

$$\begin{aligned}
b_{i,j,i} &= 0.5773504 \ , \\
b_{i,j,i-1} &= b_{i,j,i+1} = -\ 0.1547006 \ , \\
b_{i,j,i-2} &= b_{i,j,i+2} = \ \ 0.0414519 \ , \\
b_{i,j,i-3} &= b_{i,j,i+3} = -\ 0.0111070 \ , \\
b_{i,j,i-4} &= b_{i,j,i+4} = \ \ 0.0029761 \ , \\
b_{i,j,i-5} &= b_{i,j,i+5} = -\ 0.0007974 \ , \\
&\ \ \vdots \\
b_{i,j,i-35} &= b_{i,j,i+35} = -\ 0.5935 \times 10^{-20} \ .
\end{aligned} \tag{A3.23}$$

Therefore if only the seven terms centered around node i,j were retained in the summation A3.21a, the derivative $p_{ij}(t)$ would be in error by less than 1% of the value it would have had if all I terms were retained in the summation. Restricting the summation overindicies i and j to less than seven terms each considerably reduces the number of terms in A3.21a,b,c, without significant loss of accuracy. Substituting A3.22 into A3.12, there results the system of equations

$$R^{ne}(x,y,t, \psi_{nij}(t), \frac{d}{dt}(\psi_{nij}(t))) = 0 \quad , \quad \begin{matrix} n = 1 \text{ to } N, \\ e = 1 \text{ to } E, \end{matrix} \tag{A3.24}$$

in the NE unknowns ψ_{nij}, n = 1 to N, i = 1 to I, j = 1 to J (note that E = IJ). A determinate system of equations formed by applying the

weighted residual criterion A3.5 with weighting function $w_q^{ne} = 1$ (subdomain method).

$$< 1 , R^{ne} > = 0 \quad , \qquad n = 1 \text{ to } N, \qquad e = 1 \text{ to } E. \tag{A3.25}$$

This weighted residual scheme consisting of undetermined functions A3.21, double cubic spline trial solution A3.22, equation residual A3.24 and subdomain MWR criteria A3.25 will be referred to as method B. The major advantage of method B over method A is the reduced number of degrees of freedom for each dependent variable at each node. This results in fewer undetermined functions to compute. Also, method B forces the field to retain a double cubic spline shape at all times, a desired characteristic since the initial data is spline fitted and splines readily permit the use of a variable area grid. With the number of terms in A3.22 left to the judgement of the user, one may chose to experiment by initially using a crude spline fit and then increasing the number of terms to learn the effect of the accuracy of the spline trial function on the solution obtained. Equation A3.25 reduces to a system of equations of the form A3.20, with z = NE. Similar to method A, the major disadvantage of method B is the difficulty in solving the resulting system of equations. It is with this drawback in mind that a third method is constructed by adding a slight modification to method B.

Several characteristics of method B are appealing: the trial solution is of double cubic spline nature for all $t \geq 0$, the degree of approximation of the trial solution to a double cubic spline may be adjusted as desired, there is a minimum number of undetermined functions (one degree of freedom per dependent variable field per node), and the subdomain weighted residual method is employed to distribute the

equation residual (error) over each element. It now remains to remove the drawbacks of trying to solve a difficult system of ordinary differential equations of the form A3.20. This may be accomplished by expressing the undetermined functions $\Psi_{nij}(t)$ in terms of orthogonal polynomials in time. Then, using the Galerkin or some other MWR, the unknown coefficients in the polynomial for $\Psi_{nij}(t)$ could be generated. Hence, form

$$\Psi_{nij}(t) = \sum_{k=1}^{K} a_{nijk} P_k(t) \quad . \tag{A3.26}$$

A suitable selection for the polynomials $P_k(t)$ would be Legendre polynomials. With the transformation $x = (2t/T) - 1$, Legendre polynomials $P(x)$, orthogonal over $-1 \leq x \leq 1$, are transformed to be orthogonal over $0 \leq t \leq T$. Therefore,

$$\begin{aligned} P_1(t) &= 1 \ , \\ P_2(t) &= 2\tau - 1 \ , \\ P_3(t) &= 6\tau^2 - 6\tau + 1 \ , \\ P_4(t) &= 20\tau^3 - 30\tau^2 + 12\tau - 11 \ , \\ &\vdots \end{aligned} \tag{A3.27a}$$

where $$\tau = t/T \tag{A3.27b}$$

and $$\begin{aligned} \int_0^T P_n(t)\, P_m(t) &= \frac{T}{2n-1} \quad , \quad m = n \ , \\ &= 0 \quad , \quad m \neq n \ . \end{aligned} \tag{A3.27c}$$

Substituting A3.26 and A3.22 into A3.12 results in the system of equations

$$R^{ne}(x,y,t, a_{nijk}) = 0 \quad , \quad \begin{matrix} n = 1 \text{ to } N, \\ e = 1 \text{ to } E, \end{matrix} \tag{A3.28}$$

in the NEK unknowns a_{nijk}, $i = 1$ to I, $j = 1$ to J, $k = 1$ to K and $n = 1$ to N. This system A3.28 is converted to a determinate system of equations by application of the weighted residual criteria

$$< R^{ne}, P_k >^{*} = 0 \quad , \qquad e = 1 \text{ to } E,$$
$$n = 1 \text{ to } N, \tag{A3.29}$$
$$k = 2 \text{ to } K \text{ or } 1 \text{ to } (K-1).$$

The inner product is now defined to combine the subdomain weighted residual criteria in space with the Galerkin weighted residual method in time. This gives

$$< a,b >^{*} = \iiint_{e}\int_{0}^{T} ab \; dx \; dy \; dt \quad . \tag{A3.30}$$

It is seen that the orthogonality of Legendre's polynomials will lead to considerable simplification in the system of equations A3.29. By using the limits k = 1 to K in system A3.29, one could obtain K equations for each dependent variable field on each element. However, in this case, with $\Psi_{nij}(t)$ represented by A3.26, it is necessary to add a restriction on the coefficients a_{nijk} in order that $\Psi_{nij}(0)$ satisfies prescribed initial conditions. Since $P_k(0) = (-1)^{k+1}$, then

$$\Psi_{nij}(0) = \sum_{k=1}^{K} (-1)^{k+1} a_{nijk} \quad , \quad n = 1 \text{ to } N,$$
$$i = 1 \text{ to } I, \tag{A3.31}$$
$$j = 1 \text{ to } J.$$

Therefore, K equations for each dependent variable on each element are obtained by writing equation A3.29 for k = 1 to (K - 1) or k = 2 to K and by imposing the initial condition A3.31 to supply the final equation. Equations A3.29 and A3.31 together form a determinate system of NEK equations in the NEK unknown coefficients a_{nijk}, n = 1 to N, i = 1 to I, j = 1 to J, k = 1 to K (where i = 1 to I and j = 1 to J is equivalent to e = 1 to E). This system is a nonlinear system of simultaneous algebraic equations. Two common methods of obtaining an approximate solution to such a system are the Newton Rapson method and

the method of steepest descent (for example see Forsythe and Moler (pp.132-136 of ref 53) and Hildebrand (pp.443-451 of ref 54)). An alternative solution procedure used successfully by Macdonald (50) in his solution of the incompressible boundary layer equations via the Galerkin technique is a method of parameter variation. This method is described in detail in a paper by Deist and Sefor (55).

This final weighted residual method will be referred to as method C. It has all the advantages of method B, with the additional advantage of reducing to a system of simultaneous nonlinear algebraic equations whose solution may be obtained by conventional techniques. The essential features of method C may be summarized as follows:

1. The trial solution is of a double cubic spline nature for all $t \geq 0$.

2. The degree of approximation of the trial solution to a double cubic spline may be adjusted as desired.

3. There is a minimum number of undetermined functions per dependent variable field per node.

4. The undetermined functions (nodal values of the dependent variables) are expressed in terms of orthogonal polynomials in time.

5. The subdomain weighted residual method is employed to distribute the equation residual (error) over each element in space.

6. The Galerkin weighted residual method is employed to distribute the equation residual, weighted by Legendre polynomials, over an interval T in time.

7. The final system of equations to be solved numerically is a nonlinear system of simultaneous algebraic equations.

8. The method is applied to advance nodal values of the dependent variables an interval T in time.

9. The method may be repeated over and over again to obtain a forecast of any desired length (subject to numerical stability).

The speed of obtaining a solution to the system of algebraic equations of method C may be greatly improved by supplying a good starting estimate for the coefficients a_{nijk}. One method of obtaining good starting estimates for these coefficients will be briefly illustrated for the K = 3 case. Extension to other values of K may be readily performed. From equations A3.26 and A3.27,

$$\Psi_{nij}(0) = a_{nij1} - a_{nij2} + a_{nij3} \quad ,$$

$$\frac{d}{dt}\Psi_{nij}(t)_{t=0} = \frac{1}{T}(2\,a_{nij2} - 6\,a_{nij3}) \quad , \qquad \text{(A3.32)}$$

$$\frac{d^2}{dt^2}\Psi_{nij}(t)_{t=0} = \frac{12}{T^2}\,a_{nij3} \quad .$$

If initial values for Ψ_{nij} and its first two time derivatives were known, then the system A3.32 could be solved for starting estimates of the coefficients a_{nijk}, k = 1 to 3. This would then be repeated for each dependent variable (n = 1 to N) at each node point (i = 1 to I, j = 1 to J). The value of $\Psi_{nij}(0)$ is known from prescribed initial conditions. An estimate of $(d\,\Psi_{nij}/dt)_{t=0}$ is obtained by solving for $d\,\Psi_{nij}/dt$ at t = 0 in equation A3.12. In this equation, the initial values of all dependent variables are known at the nodes, and spatial derivatives of the dependent variables are evaluated by a double cubic spline fit to the initial data fields. This is similar to the methods used to estimate spatial derivatives in the model discussed in the body of this thesis. Finally, an estimate of $(d^2\,\Psi_{nij}/dt^2)_{t=0}$ is obtained by differentiating equation A3.12 with respect to time, solving for $d^2\,\Psi_{nij}/dt^2$, and evaluating all the remaining terms using their prescribed or previously generated initial values. In this calculation, values for $\frac{\partial}{\partial x}$ or $\frac{\partial}{\partial y}$ of $\frac{d\Psi}{dt}$nij are obtained by forming a double cubic spline fit to the initial values of $\frac{d\Psi}{dt}$nij obtained in the previous step.

It is recognized that calculating starting estimates of the unknown coefficients a_{nijk} by the method illustrated above is essentially a K^{th} order forward differencing scheme in time. If this scheme alone were used to advance the dependent variable fields the numerical solution would prove unstable in a short time. Since this forward differencing would be used to return only starting estimates of the undetermined coefficients a_{nijk}, it should have no effect on the stability of the numerical scheme using the subdomain and Galerkin weighted residual methods.

REFERENCES

1. Haltiner, G.J., and Martin, F.L., Dynamical and Physical Meteorology, New York, Toronto, London: McGraw-Hill Book Co., 1957, 470 pp.

2. Haltiner, G.J., Numerical Weather Prediction, Navy Weather Research Facility 30-0768-142, Building R-48 Naval Air Station, Norfolk, Virginia, July 1968, 88 pp.

3. Smagorinsky, J., "On the Numerical Integration of the Primitive Equations of Motion for Baroclinic Flow in a Closed Region", Monthly Weather Review, Vol.86, No.12, December 1958, pp. 457-466.

4. Smagorinsky, J., "General Circulation Experiments with the Primitive Equations. I. The Basic Experiment", Monthly Weather Review, Vol.91, No.3, March 1963, pp.99-164.

5. Smagorinsky, J., Manabe, S., and Holloway, J.L., "Numerical Results From a Nine-Level General Circulation Model of the Atmosphere", Monthly Weather Review, Vol93, No.12, December 1965, pp.727-768.

6. Mintz, Y., "Very Long-Term Global Integration of the Primitive Equations of Atmospheric Motion: An Experiment in Climate Simulation", Amer. Met. Soc. Meteorological Monographs, Vol.8, No.30, 1968, pp.20-36.

7. Langlois, W.E., and Kwok, H.C.W., Description of the Mintz-Arakawa Num. Circulation Model, Numerical Simulation of Weather and Climate Technical Report No. 3, Department of Meteorology, University of California, Los Angeles, 1969, 95 pp.

8. Kasahara, A., and Washington, W.M., "NCAR Global General Circulation Model of the Atmosphere", Monthly Weather Review, Vol.95, No.7, July 1967, pp.389-402.

9. Kessel, P.G., and Winninghoff, F.J., "Fleet Numerical Weather Central's Four-Processor Primitive Equation Model", Fleet Numerical Weather Central, Monterey, 1970 (unpublished manuscript).

10. Price, G.V., Numerical Weather Prediction Models: An Introduction to Phillips (1956) Model & A Further Description of the Mintz-Arakawa Model following Langlois and Kwok (1969) with a 36 hour Numerical Forecast using Real Weather Data and a comparison with 20 hour Numerical Forecasts using two Barotropic Models, Technical Report ER25.16, Department of Mechanical Engineering, University of Manitoba, Winnipeg, Canada, August 1971, 194 pp.

11. Shuman, F.G., and Vandermann, L.A., "Difference Systems and Boundary Conditions for the Primitive Equation Barotropic Forecast", Monthly Weather Review, Vol.94, No.5, May 1966, pp.329-335.

12. Shuman, F.G., and Hovermale, J.B., "An Operational Six-Layer Primitive Equation Model", J. of Applied Meteorology, Vol.7, No.4, August 1968, pp.525-547.

13. Smith, M.G., Introduction to the Theory of Partial Differential Equations, London: D. VanNostrand Co. Ltd., 1967, 214 pp.

14. Forsythe, G.E., and Wasow, W.R., Finite Difference Methods for Partial Differential Equations, New York: J. Wiley, 1960, 440 pp.

15. Gates, W.L., "The Reduction of Truncation Error by Extrapolation Techniques", Monthly Weather Review, Vol.89, No.4, April 1961, pp.115-124.

16. Crandall, S.H., Engineering Analysis, New York: McGraw-Hill Book Co., 1956, 417 pp.

17. Kurihara, Y., "On the Use of Implicit and Iterative Methods for the Time Integration of the Wave Equation", Monthly Weather Review, Vol.93, No.1, January 1965, pp.33-46.

18. Kasahara, A., "On Certain Finite Difference Methods For Fluid Dynamics", Monthly Weather Review, Vol.93, No.1, January 1965, pp.27-31.

19. Gosman, A.D., et.al., Heat and Mass Transfer in Recirculating Flows, London, New York: Academic Press, 1969, 338 pp.

20. Grammeltvedt, A., "A Survey of Finite-Difference Schemes for the Primitive Equations for a Barotropic Fluid", Monthly Weather Review, Vol. 97, No.5, May 1969, pp.384-404.

21. Matsuno, T., "A Finite Difference Scheme for Time Integration of Oscillatory Equations with Second Order Accuracy and Sharp Cut-off for High Frequencies", J. Meteorological Soc. of Japan, Vol.44, No.1, February 1966, pp.85-88.

22. Ahlberg, J.H., Nilson, E.N., and Walsh, J.L., The Theory of Splines and their Application, New York: Academic Press, 1967, 284 pp.

23. Greville, T.N.E., "Spline Functions, Interpolation, and Numerical Quadrature", Mathematical Methods for Digital Computers, Vol.2, by A. Ralston and H.S. Wilf, New York: John Wiley and Sons, 1967, pp.156-163.

24. Ahlberg, J.H., "The Spline Approximation as an Engineering Tool", Computer Aided Engineering, Proceedings of the Symposium Held at the University of Waterloo, May 11-13, 1971, pp.1-18.

25. deBoar, C., "Bicubic Spline Interpolation", J. of Mathematics and Physics, Vol. 41, 1962, pp.212-218.

26. Ahlberg, J.H., Nilson, E.N., and Walsh, J.L., "Extremal, Orthogonality, and Covergence Properties of Multi-diminensional Splines", J. of Mathematical Analysis and Applications, Vol.12, 1965, pp.27-48.

27. Grimmer, M., and Shaw, D.B., "Energy-Preserving Integrations of the Primitive Equations on the Sphere", Quart. J. Roy. Meteor. Soc., Vol.93, No.397, July 1967, pp.337-349.

28. Kurihara, Y., and Holloway, J.L., "Numerical Integration of a Nine-Level Global Primitive Equation Model Formulated by the Box Method", Monthly Weather Review, Vol.95, No.8, August 1967, pp.337-349.

29. Williamson, D.L., "Integration of the Barotropic Vorticity Equation on a Spherical Geodesic Grid", Tellus, Vol.20, No.4, November 1968, pp.642-653.

30. Sadourny, R., Arakawa, A., and Mintz, Y., "Integration of the Non-divergent Barotropic Vorticity Equation with an Icosahedral-Hexagonal Grid for the Sphere", Monthly Weather Review, Vol.96, No.6, June 1968, pp.351-356.

31. Williamson, D.L., "Integration of the Primitive Barotropic Model over a Spherical Geodesic Grid", Monthly Weather Review, Vol. 98, No.7, July 1970, pp.512-520.

32. Sadourny, R., and Morel, P., "A Finite-Difference Approximation of the Primitive Equations for a Hexagonal Grid on a Plane", Monthly Weather Review, Vol.97, No.6, June 1969, pp.439-445.

33. Kurihara, Y., "Numerical Integration of the Primitive Equations on a Spherical Grid", Monthly Weather Review, Vol.93, No.7, July 1965, pp.399-415.

34. Winslow, A.M., "Numerical Solution of the Quasilinear Poisson Equation is a Nonuniform Triangle Mesh", J. of Computational Physics, Vol.2, 1967, pp.149-172.

35. Williamson, D., "Numerical Integration of Fluid Flow Over Triangle Grids", Monthly Weather Review, Vol.97, No.12, December 1969, pp.885-895.

36. Gerrity, J.P., and McPherson, R.D., "Development of a Limited Area Fine-Mesh Prediction Model", Monthly Weather Review, Vol.97, No.9, September 1969, pp.665-669.

37. Anthes, R.A., "Numerical Experiments with a Two-Dimensional Horizontal Variable Grid", Monthly Weather Review, Vol.98, No.11, November 1970, pp.810-882.

38. Sundqvist, H., and Veronis, G., "A Simple Finite-Difference Grid With Non-Constant Intervals", Tellus, Vol.22, No.1, 1970, pp.26-31.

39. Phillips, N.A., "Numerical Integration of the Hydrostatic System of Equations with a modified Version of the Eliassen Finite-Difference Grid", Tellus, Vol.10, 1958, pp.109-120.

40. Price, G.V., A Description of the Energy Inputs to the Mintz-Arakawa Numerical General Circulation Model, Technical Report ER25.15, Department of Mechanical Engineering, University of Manitoba, Winnipeg, Canada, July 1971, 79 pp.

41. Ralston, A., A First Course in Numerical Analysis, New York: McGraw-Hill Book Co., 1965, 578 pp.

42. Kreysig, E., Advanced Engineering Mathematics, 2nd ed., New York: John Wiley and Sons, Inc., 1967, 898 pp.

43. Froberg, C.-E., Introduction to Numerical Analysis, Addison-Wesley Publishing Company, Reading, Massachusetts, 1964, 340 pp.

44. U.S. Navy Marine Climatic Atlas of the World, Volume 1: North Atlantic Ocean, Navaer 50-1C-528, Volune 2: North Pacific Ocean, Navaer 50-1C-529, Published by Direction of the Chief of Naval Operations, 1 July, 1956.

45. Finlayson, B.A., and Scriven, L.E., "The Method of Weighted Residuals - A Review", Applied Mechanics Review, Vol.19, No.9, 1966, pp.735-748.

46. Snyder, L.J., Spriggs, T.W. and Stewart, W.E., "Solution of the Equations of Change by Galerkin's Method", American Institute for Chemical Engineering Journal, Vol.10, 1964, pp.535-540.

47. Lowe, P.A., "The Method of Galerkin Applied to Boundary-Layer Flow Problems", Development in Mechanics, Vol.5. Proceedings of the 11th Midwestern Mechanics Conference, 1969, pp.59-76.

48. Johansen, P.R., "Numerical Application of Galerkin's Method to Nonlinear Engineering Problems", Computer Aided Engineering, Proceedings of the Symposium Held at the University of Waterloo, May 11-13, 1971, pp.251-265.

49. Macdonald, D.A., "Solution of the Incompressible Boundary Layer Equations via the Galerkin-Kantorovich Technique", J. Inst. Maths Applics, Vol.6, 1970, pp.115-130.

50. Zienkiewicz, O.C., and Parekh, C.J., "Transient Field Problems: Two-Dimensional and Three-Dimensional Analysis by Isoparametric Finite Elements", International J. for Numerical Methods in Engineering, Vol.2, 1970, pp.61-71.

51. Carnahan, B., Luther, H.A., and Wilkes, J.O., Applied Numerical Methods, New York: J. Wiley and Sons, 1969, 604 pp.

52. Forsythe, G., and Moler, C., Computer Solution of Linear Algebraic Systems, Englewood Cliffs: Prentice Hall, 1967, 148 pp.

53. Hildebrand, F.B., Introduction to Numerical Analysis, New York: McGraw-Hill Book Co., 1956, 511 pp.

54. Deist, F.H., and Sefor, L., "Solution of Systems of Nonlinear Equations by Parameter Variation", Computer Journal, Vol.10, 1967, pp.78-82.

Table 3.1: Spline Curve Fitting Between Regions of Abruptly Changing Curvature

	i	1	2	3	4	5	6	7	8
	x_i	0	5	10	15	20	25	30	35
1.	u_i	-7.483	-10.88	5.434	9.458	10.00	10.00	10.00	10.00
	p_{it}	1.066	1.391	1.128	0.429	0.0	0.0	0.0	0.0
	p_{is}	1.065	1.388	1.133	0.407	-0.022	0.006	-0.002	0.000
	% error	0.059	0.188	-0.458	5.205	-	-	-	-
2.	u_i	-7.483	-10.88	5.434	9.458	5.000	15.00	25.00	35.00
	p_{it}	1.066	1.391	1.128	0.429	2.000	2.000	2.000	2.000
	p_{is}	1.082	1.323	1.375	-0.494	0.344	2.444	1.881	2.032
	% error	-1.569	4.845	-21.88	215.2	82.80	-22.19	5.945	-1.593
3.	u_i	-7.483	-10.88	5.434	9.458	-1.250	-3.750	-6.250	-8.750
	p_{it}	1.066	1.391	1.128	0.429	-0.500	-0.500	-0.500	-0.500
	p_{is}	1.091	1.290	1.497	-0.952	-1.698	-0.179	-0.586	-0.477
	% error	-2.395	7.206	-32.75	321.8	-239.7	64.23	-17.2	4.611
4.	u_i	145.0	155.0	165.0	175.0	175.0	165.0	155.0	145.0
	p_{it}	2.000	2.000	2.000	2.000	-2.000	-2.000	-2.000	-2.000
	p_{is}	2.014	1.947	2.196	1.268	-1.268	-2.196	-1.947	-2.014
	% error	-0.704	2.628	-9.808	36.60	36.60	-9.808	2.628	-0.704
5.	u_i	-36.25	-38.75	-41.25	-43.75	-43.75	-41.25	-38.75	-36.25
	p_{it}	-0.500	-0.500	-0.500	-0.500	0.500	0.500	0.500	0.500
	p_{is}	-0.504	-0.487	-0.549	-0.317	0.317	-0.549	-0.487	0.504
	% error	-0.704	2.628	-9.808	36.60	36.60	-9.808	2.628	-0.704
6.	u_i	96.62	53.05	5.311	-37.32	-67.35	-80.30	-75.42	-55.45
	p_{it}	-7.665	-9.453	-9.329	-7.472	-4.386	-0.771	2.629	5.176
	p_{is}	-7.662	-9.451	-9.327	-7.471	-4.386	-0.772	2.628	5.174
	% error	0.031	0.024	0.020	0.017	0.009	-0.081	0.055	0.346

1. Sinusoid ($x \lesssim x_4$) meets with a straight line ($x \gtrsim x_5$, slope = 0.0).
2. Sinusoid ($x \lesssim x_4$) meets with a straight line ($x \gtrsim x_5$, slope = 2.0).
3. Sinusoid ($x \lesssim x_4$) meets with a straight line ($x \gtrsim x_5$, slope = -0.5).
4. Straight line ($x \lesssim x_4$, slope = 2.0) meets with a straight line ($x \gtrsim x_5$, slope = -2.0).
5. Straight line ($x \lesssim x_4$, slope = -0.5) meets with a straight line ($x \gtrsim x_5$, slope = 0.5).
6. Sinusoid, $x_1 \lesssim x \lesssim x_8$.

Table 5.1: Summary of Forecast Model Notation and Figures.

Model	Description	Figures
ST	the proposed forecast model in its entirety, using the bicubic spline method on a telescoping grid having superimposed expansions of two types (grid D, Figure 3.4)	4.99-4.120
S	a modified form of model ST, using the bicubic spline method on a grid having the expansion of Type 1 only (grid C, Figure 3.3)	4.69-4.90
F	a modified form of model ST, using central finite differences in place of bicubic splines, on a grid having the expansion of Type 1 only (grid C, Figure 3.3)	4.91-4.98
C1	a modified form of model ST, using the new spline based on continuity of curvature with a = 0.222222 and XS = 0.0 in place of bicubic splines, on a grid having the expansion of Type 1 only (grid C, Figure 3.3)	4.121-4.128
P7	a preliminary experiment using finite differences on a MA grid with 10^{o} grid interval and smoothing operators (grid B, Figure 3.2)	4.47-4.68
MA	the Mintz-Arakawa numerical forecast model: forecast on a 5^{o} latitude, 5^{o} longitude grid	5.1-5.20

Table 5.2: Overall Forecast Performance

	V1	V2	T1	T2	Q1	ϕ1	ϕ2
RMSC	5.380	6.032	4.493	2.754	1.363	68.45	100.80
RMSE-MA	6.178	8.606	6.330	3.183	1.833	95.57	106.22
d%	14.8	42.6	41.0	15.5	34.5	39.6	5.39
RMSE-S	5.584	7.493	5.845	2.728	1.526	82.06	102.95
d%	3.80	24.2	30.2	-0.94	12.0	19.9	2.14
RMSE-C1	5.533	7.517	5.947	2.605	1.465	82.65	102.23
d%	2.84	24.6	32.4	-5.40	7.5	20.8	1.42
RMSE-F	5.531	7.478	6.167	2.584	1.434	83.08	108.00
d%	2.81	24.0	37.4	-6.17	5.2	21.4	7.15
RMSE-ST	5.065	6.954	5.857	2.487	1.415	78.30	102.74
d%	-5.85	15.2	30.4	-9.70	3.8	14.4	1.93
RMSE-P7	5.784	8.669	6.771	3.167	1.462	83.00	136.49
d%	7.50	43.7	50.7	15.0	7.3	21.2	35.4

Units: V1, V2 - m/sec
T1, T2 - ^{o}K
ϕ1, ϕ2 - m
Q1 - g H_2O / g dry air x 10^{-3}

$$d\% = \frac{RMSE - RMSC}{RMSC} \times 100\%$$

Table 5.3a: Comparison of d% for Models S and P7 Relative to MA

Factor = the factor which d% of model MA must be multiplied by to yield d% for the indicated model.

	Factor	
Variable	S	P7
V1	1/4	1/2
V2	1/2	1
T1	3/4	1¼
T2	neg.	1
Q1	1/3	1/4
ϕ1	1/2	1/2
ϕ2	2/5	7

Table 5.3b: Comparison of d% for Models C1, F and ST Relative to S

Difference = the difference between d% of model S and d% for the indicated model. The adjectives better (b) and worse (w) describe whether the indicated model has a lower or higher value of d% compared to that of S.

	Difference		
Variable	C1	F	ST
V1	b,0.96	b,0.99	b,9.65
V2	w,0.4	b,0.2	b,9.0
T1	w,2.2	w,7.2	w,0.2
T2	b,4.46	b,5.23	b,8.76
Q1	b,2.5	b,6.8	b,8.2
ϕ1	w,0.9	w,1.5	b,5.5
ϕ2	b,0.72	w,5.01	b,0.21

Table 5.4: Comparison of Models S and MA Against the True Weather Change: Mean Differences at Different Latitudes

a) Model S

Variable	Pole	High Lat.	Middle Lat.	Low Lat.	Equator
V1	1.0 P	0.7 P	-1.3 VG	1.3 P	3.1 VP
V2	-0.4 G	2.5 P	-0.2 G	3.6 VP	1.6 VP
T1	1.5 P	0.7 P	-0.8 VG	4.1 VP	7.2 VP
T2	2.7 VP	0.6 P	-1.6 VG	2.5 VP	3.9 VP
Q1	0	0	-0.15 G	0.39 P	1.05 VP
ϕ1	-15 G	5 P	20 P	30 VP	45 VP
ϕ2	25 VP	-9 G	-25 VG	57 VP	103 VP

b) Model MA

Variable	Pole	High Lat.	Middle Lat.	Low Lat.	Equator
V1	-0.9 G	1.3 VP	-0.8 G	2.5 VP	2.7 VP
V2	0	5.0 VP	0.8 P	4.6 VP	1.6 VP
T1	3.2 VP	1.4 P	0.2 P	4.1 VP	6.8 VP
T2	2.1 VP	0.6 P	-1.2 VG	3.5 VP	4.8 VP
Q1	0	0.23 P	0.14 P	0.85 VP	1.05 VP
ϕ1	-27 VG	20 VP	40 VP	31 VP	45 VP
ϕ2	-45 VG	7 P	-9 G	40 VP	74 VP

Difference = $RMSE_j - RMSC_j$

Pole, $j = 1$, $\Phi = 90^o$
High Latitudes, $j = 2\text{-}6$, $\Phi = 80\text{-}55^o$
Middle Latitudes, $j = 7\text{-}11$, $\Phi = 55\text{-}30^o$
Low Latitudes, $j = 12\text{-}16$, $\Phi = 30\text{-}5^o$
Equator, $j = 17,18$, $\Phi = 0^o$

Units: V1,V2 - m/sec
T1,T2 - ^oK
ϕ1,ϕ2 - m
Q1 - g H_2O / g dry air x 10^{-3}

Adjectives: Poor(P), Very Poor(VP), Good(G), Very Good(VG),
Poor = $RMSE_j$ $RMSC_j$,
Good = $RMSE_j$ $RMSC_j$.

Table 5.5: Comparison of Models F and ST Against S: Mean Differences at Different Latitudes

a) Model F

Variable	Pole	High Lat.	Middle Lat.	Low Lat.	Equator
V1	0.2	0.5	-0.4	-0.2	-1.0
V2	0.4	0.7	-0.6	-0.2	0.4
T1	2.4	0.6	0.6	0.2	-0.1
T2	0	-0.1	-0.1	-0.2	-0.5
Q1	0	0	-0.03	-0.1	-0.5
ϕ1	-15	2	2	0	0
ϕ2	-40	9	10	0	0

b) Model ST

Variable	Pole	High Lat.	Middle Lat.	Low Lat.	Equator
V1	-1.0	0.1	-0.6	-0.4	-2.2
V2	1.0	-0.9	-0.6	0.2	-2.0
T1	1.4	0.1	0.1	-0.5	0
T2	-0.7	-0.1	-0.2	-0.1	-1.0
Q1	0	0.1	0.02	-0.17	-0.85
ϕ1	-5	-7	-11	-6	-5
ϕ2	-3	-9	10	-3	5

Difference = $RMSE_j$, specified model - $RMSE_j$, model S

Pole, $j = 1$, $\Phi = 90^o$
High Latitudes, $j = 2\text{-}6$, $\Phi = 80\text{-}55^o$
Middle Latitudes, $j = 7\text{-}11$, $\Phi = 55\text{-}30^o$
Low Latitudes, $j = 12\text{-}16$, $\Phi = 30\text{-}5^o$
Equator, $j = 17,18$, $\Phi = 0^o$

Units: V1,V2 - m/sec
T1,T2 - ^oK
ϕ1,ϕ2 - m
Q1 - g H_2O / g dry air x 10^{-3}

Table 5.6: Temperature Phase Speeds at 45° Latitude

a) Lower Level Temperature (800 mb, T1), Position in Degrees Longitude

Model	T	R	T	R	T	R	T	T	R	Mean Phase Speed
0 Hour	-165	-143	-105	-80	-55	-15	25	132	-185	
36 Hour True	-130	-115	-88	-55	-35	-5	30	132	-155	18.9
MA	-145	-124	-95	-70	-40	-5	18	138	-170	10.9
S	-142	-118	-95	-70	-48	0	18	135	-168	11.5
F	-150	-125	-95	-68	-50	-5	24	140	-180	9.1
ST	-143	-118	-92	-68	-48	-12	22	135	-180	9.7
P7	-162	-138	-95	-75	-52	-6	32	145	-180	6.8

b) Upper Level Temperature (400 mb, T2), Position in Degrees Longitude

Model	T	R	T	R	T	R	T	R	Mean Phase Speed
0 Hour	-162	-135	-103	-82	-58	-18	9	-180	
36 Hour True	-138	-120	-93	-63	-43	-4	23	-155	17.0
MA	-148	-125	-93	-65	-45	-5	19	-160	13.3
S	-140	-118	-93	-60	-40	-5	21	-165	16.1
F	-145	-121	-93	-65	-45	5	20	-170	14.3
ST	-138	-120	-95	-60	-45	0	18	-180	13.6
P7	-155	-135	-105	-75	-55	5	15	-192	4.0

T = Trough

R = Ridge

Phase Speed = Longitude position of the feature at 36 hours - Longitude position of the feature at 0 hours

Table 5.7: Geopotential Phase Speeds at 45° Latitude

a) Lower Level Geopotential (800 mb, $\phi 1$), Position in Degrees Longitude

Model	R	T	R	T	R	R	T	T	Mean Phase Speed
0 Hour	-173	-153	-128	-95	-65	-18	62	154	
36 Hour True	-140	-130	-108	-82	-48	-8	68	175	17.9
MA	-170	-148	-123	-92	-63	-13	72	157	4.5
S	-170	-148	-120	-92	-55	-14	75	156	6.0
F	-170	-149	-124	-92	-55	-10	72	158	5.7
ST	-170	-148	-122	-92	-55	-13	70	163	6.1
P7	-170	-153	-128	-90	-58	-15	80	161	5.4

b) Upper Level Geopotential (400 mb, $\phi 2$), Position in Degrees Longitude

Model	R	T	R	T	R	T	R	T	R	T	Mean Phase Speed
0 Hour	-180	-163	-131	-100	-73	-50	-15	28	98	148	
36 Hour True	-148	-130	-113	-87	-52	-35	-5	30	105	157	16.0
MA	-162	-145	-122	-91	-58	-37	-5	22	106	145	9.1
S	-162	-138	-119	-87	-51	-41	-5	25	107	150	11.7
F	-168	-146	-123	-88	-62	-42	-7	25	104	143	7.4
ST	-163	-138	-117	-88	-53	-41	-10	25	100	146	9.9
P7	-165	-156	-135	-95	-54	-33	2	15	116	154	8.7

T = Trough

R = Ridge

Phase Speed = Longitude position of the feature at 36 hours - Longitude position of the feature at 0 hours

Table 5.8: Comparison of Phase Speeds at 45° Latitude: % of True Phase Speed

Model	T1	T2	$\phi 1$	$\phi 2$
MA	58	78	25	57
S	61	95	34	73
F	48	84	32	46
ST	51	80	34	62
P7	36	24	30	54

$$\% \text{ of True Phase Speed} = \frac{\text{Forecast Phase Speed}}{\text{True Phase Speed}} \times 100\%$$

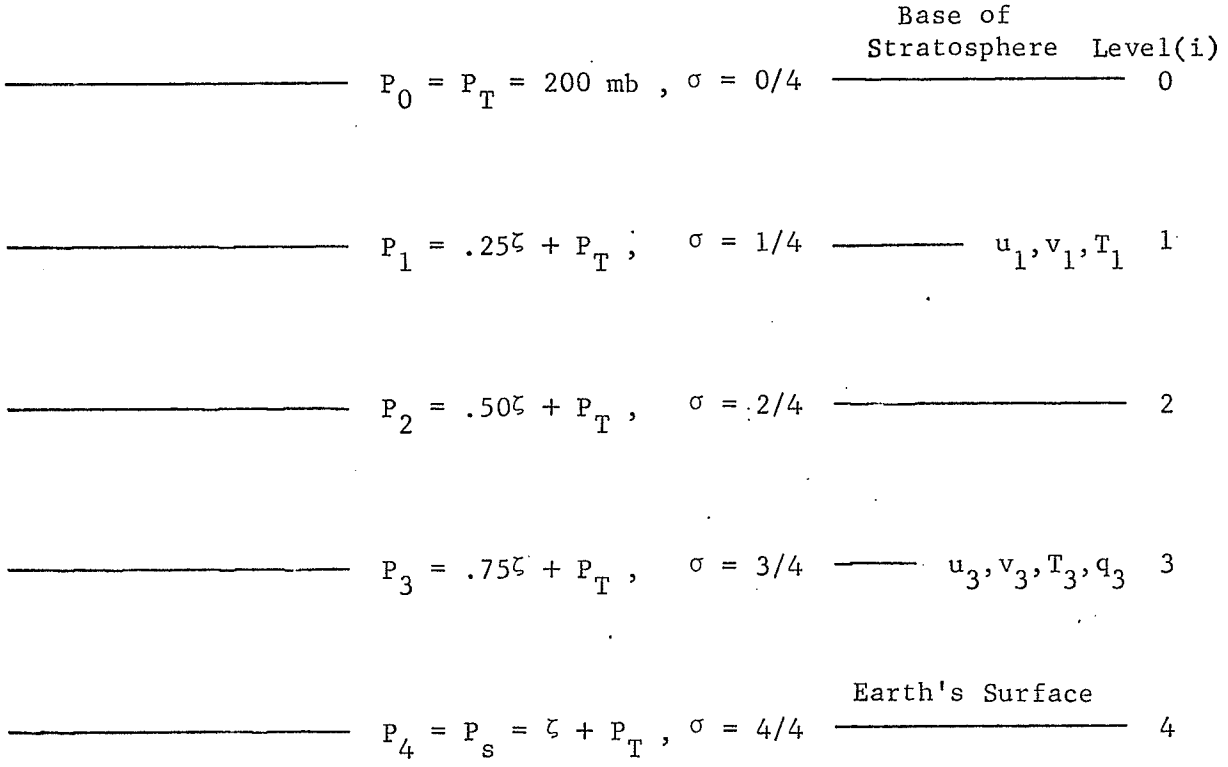

Figure 2.1: Vertical Resolution

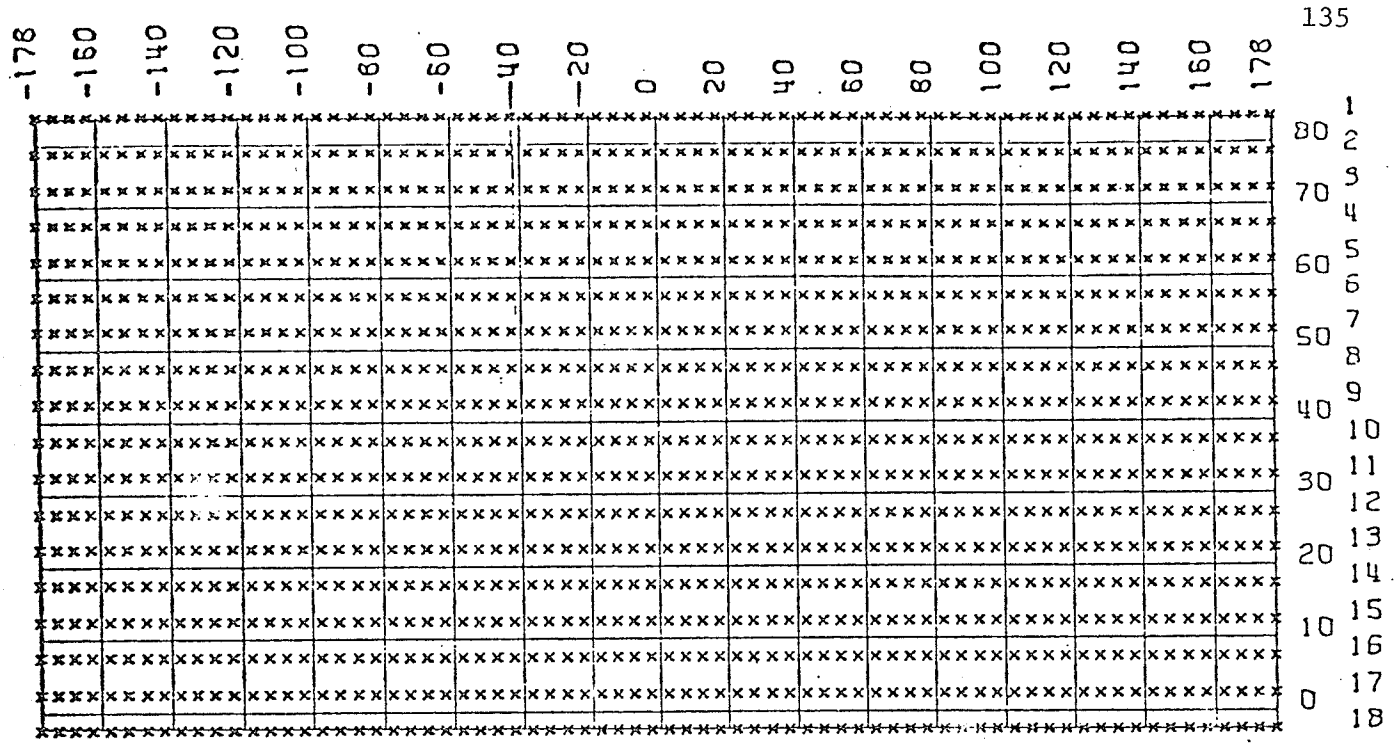

Figure 3.1: Forecast Grid A, $\Delta x = \Delta y = 5^{o}$, $\delta = 12.5^{o}$

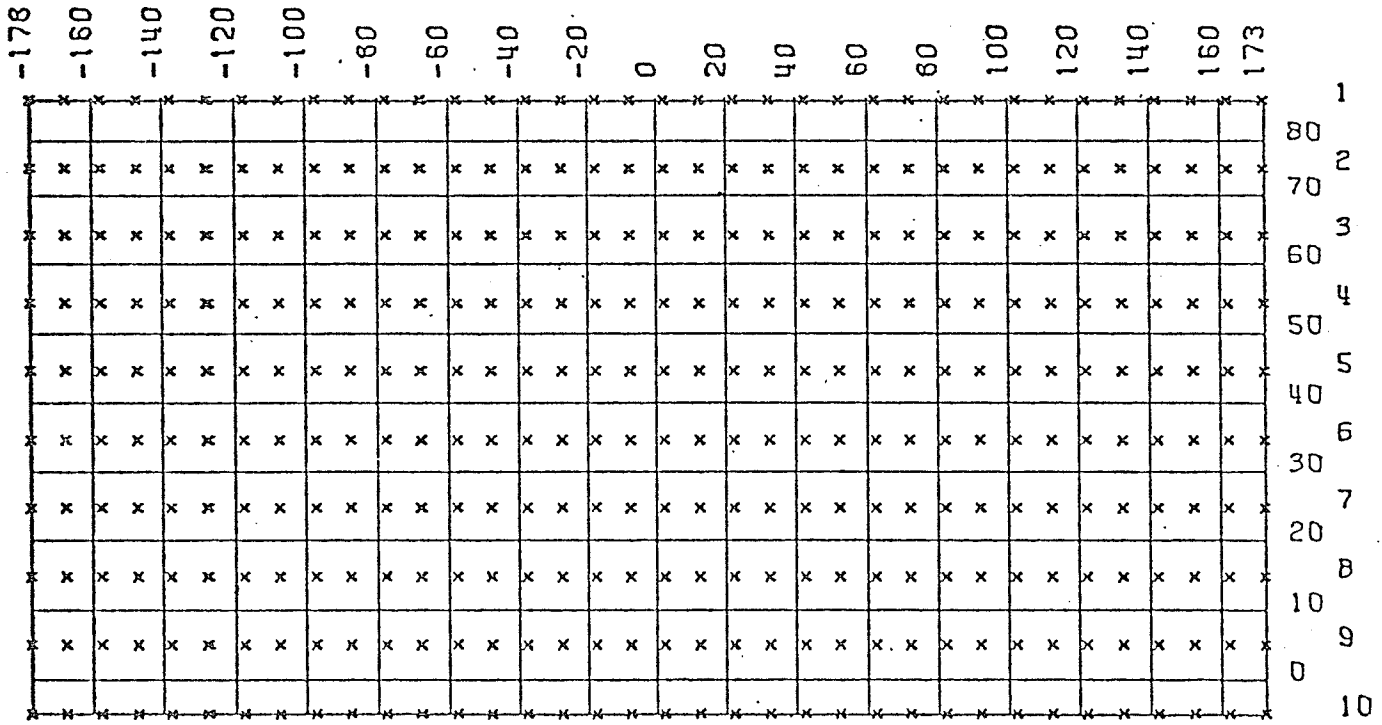

Figure 3.2: Forecast Grid B, $\Delta x = \Delta y = 10^{o}$, $\delta = 15^{o}$

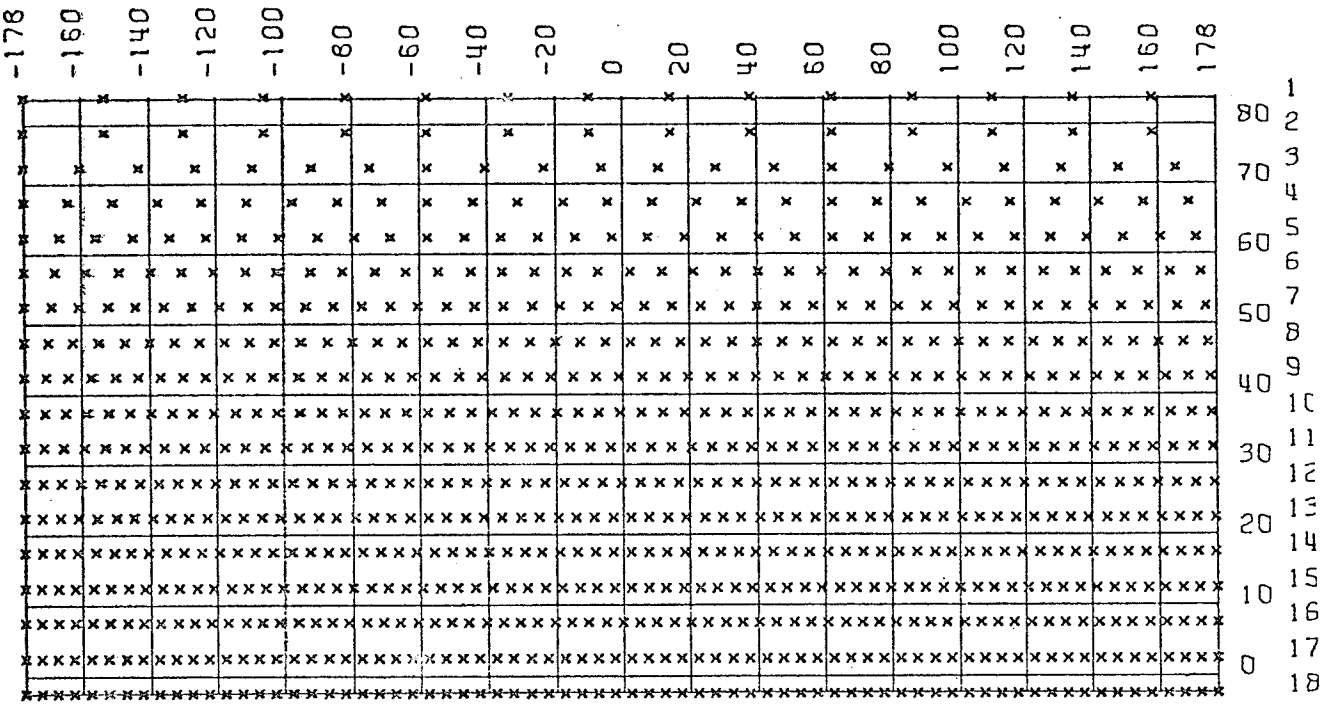

Figure 3.3: Forecast Grid C, expansion type 1 on Grid A

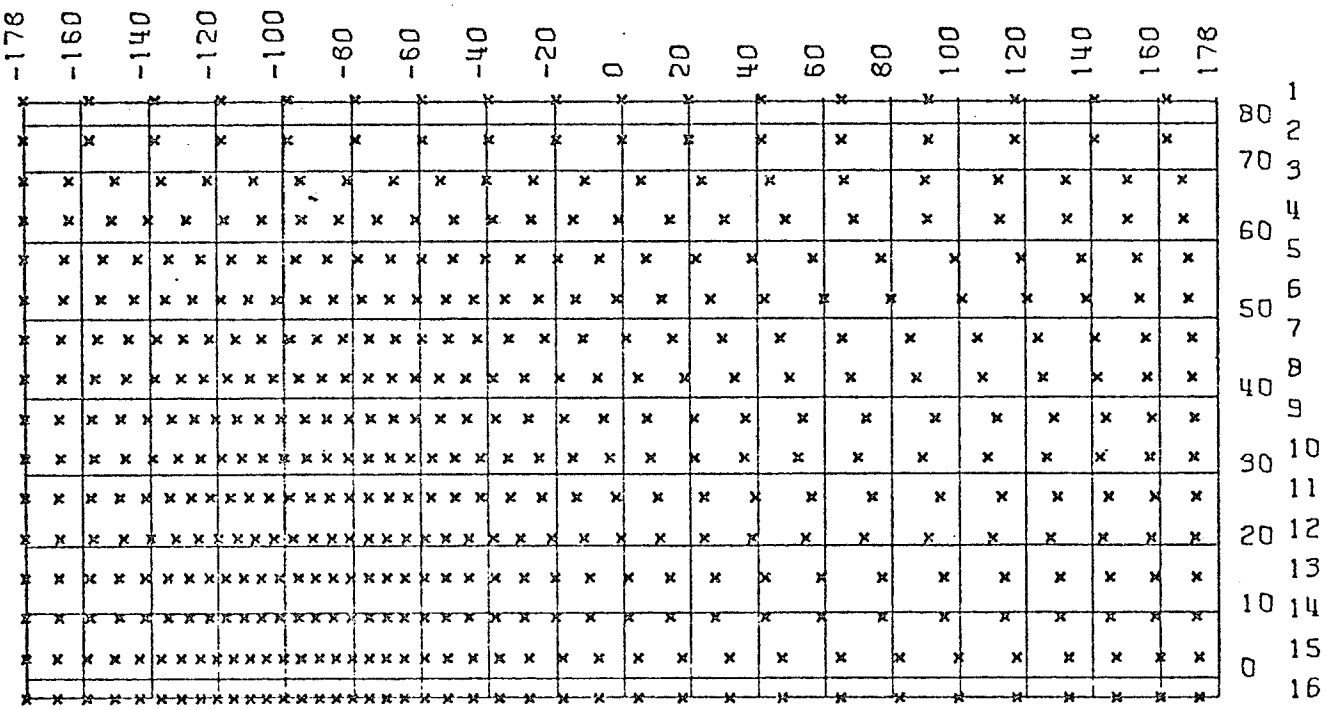

Figure 3.4: Forecast Grid D, expansion type 2 on Grid C

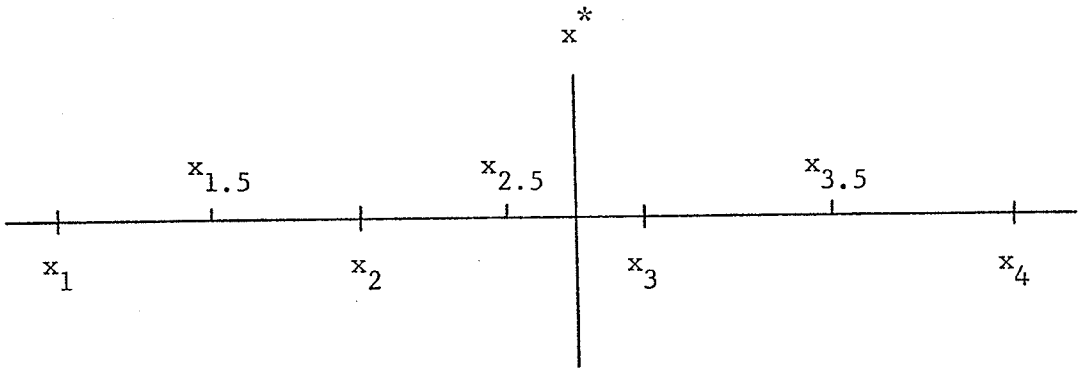

Figure 3.5: Interpolation Method A

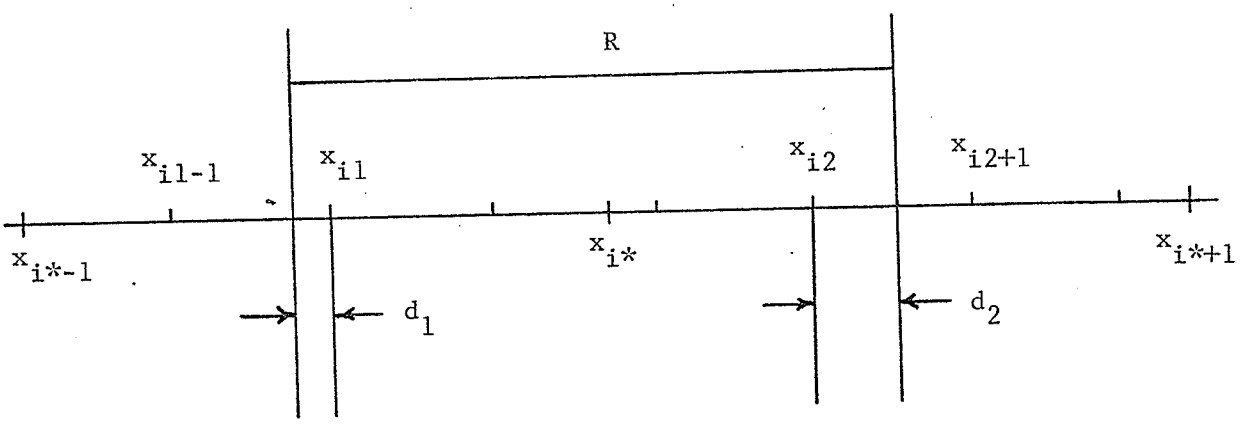

Figure 3.6: Interpolation Method B

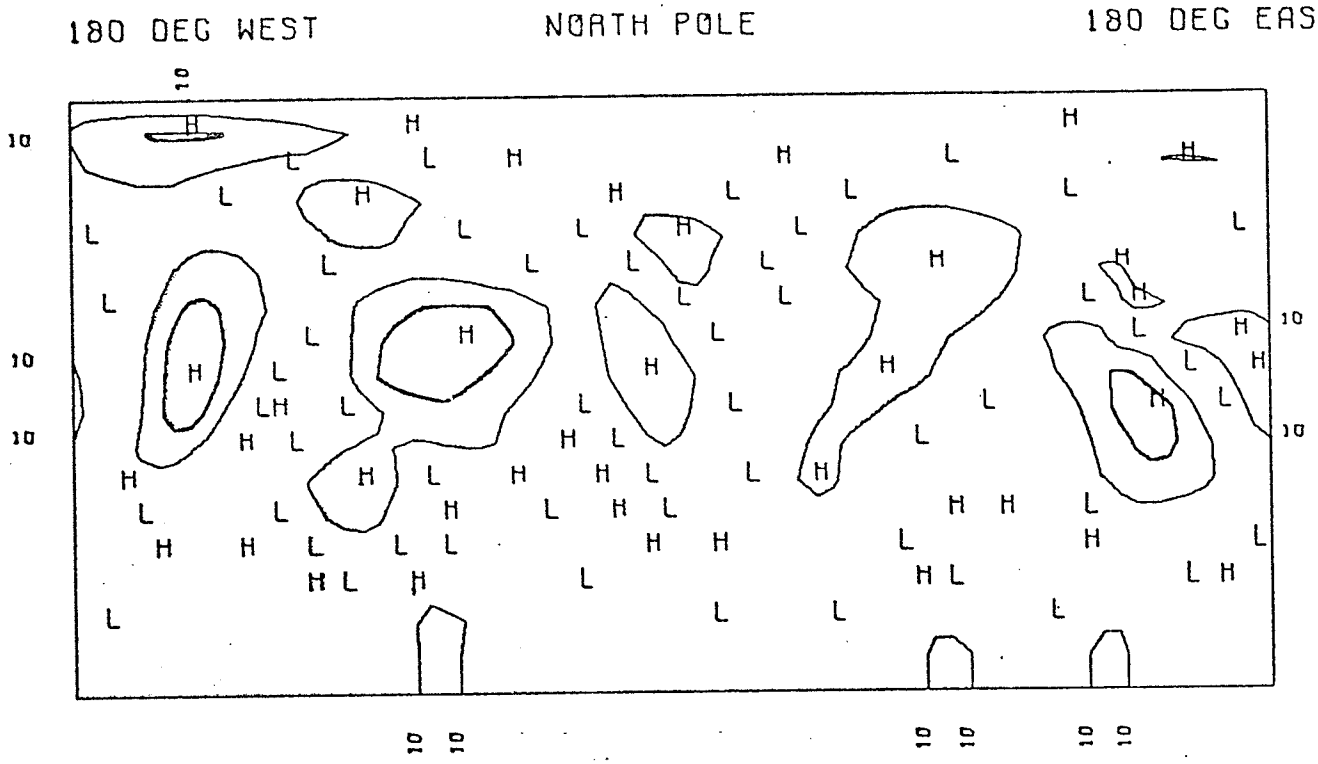

Figure 4.1: 800 mb Resultant Velocity Isotachs (m/sec), 0 hour

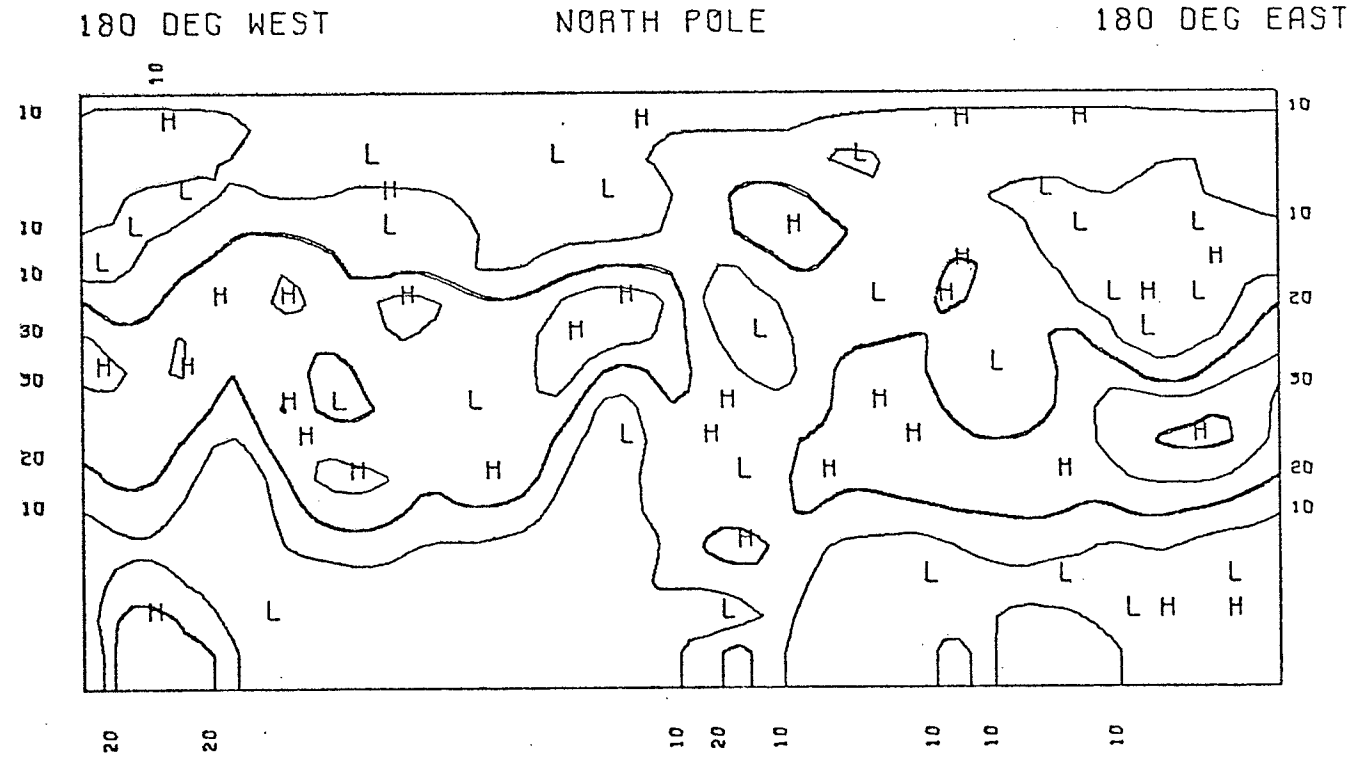

Figure 4.2: 400 mb Resultant Velocity Isotachs (m/sec), 0 hour

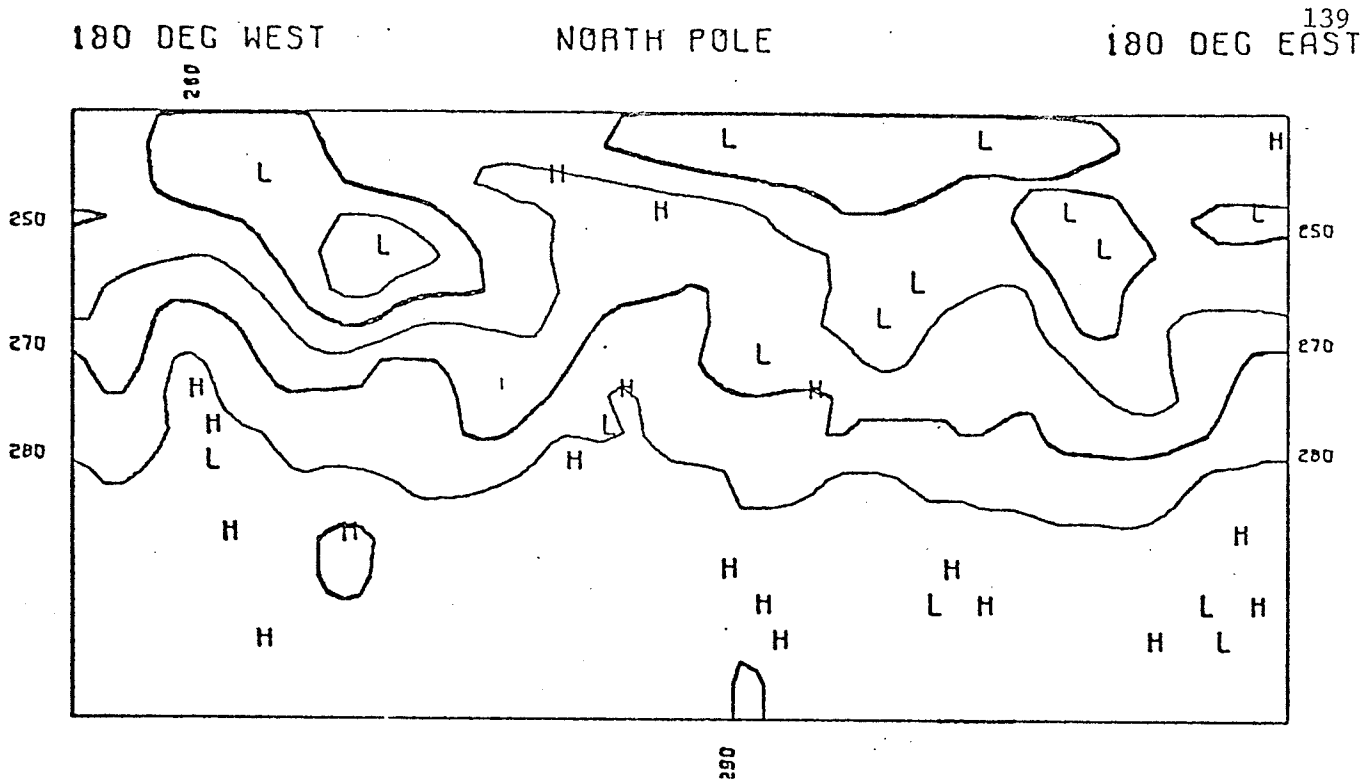

Figure 4.3: 800 mb Temperature (^{o}K), 0 hour

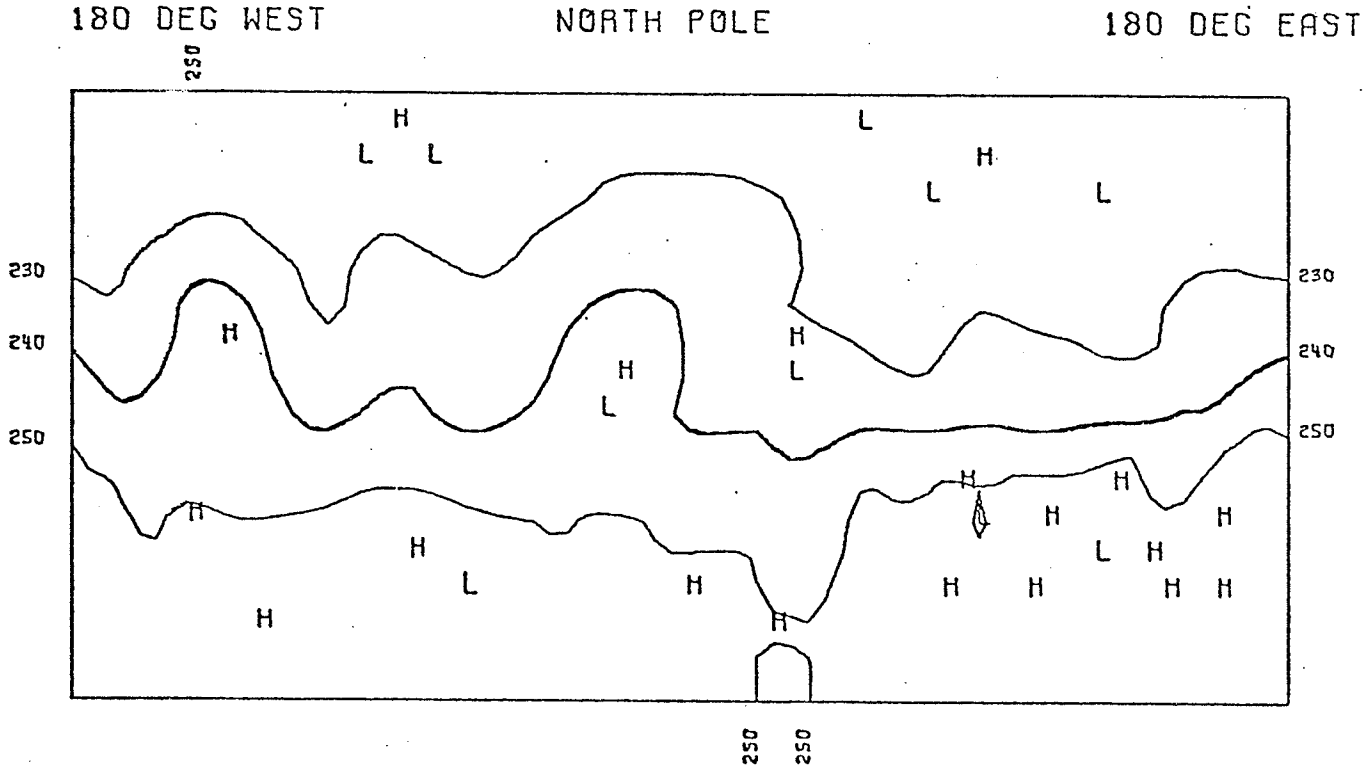

Figure 4.4: 400 mb Temperature (^{o}K), 0 hour

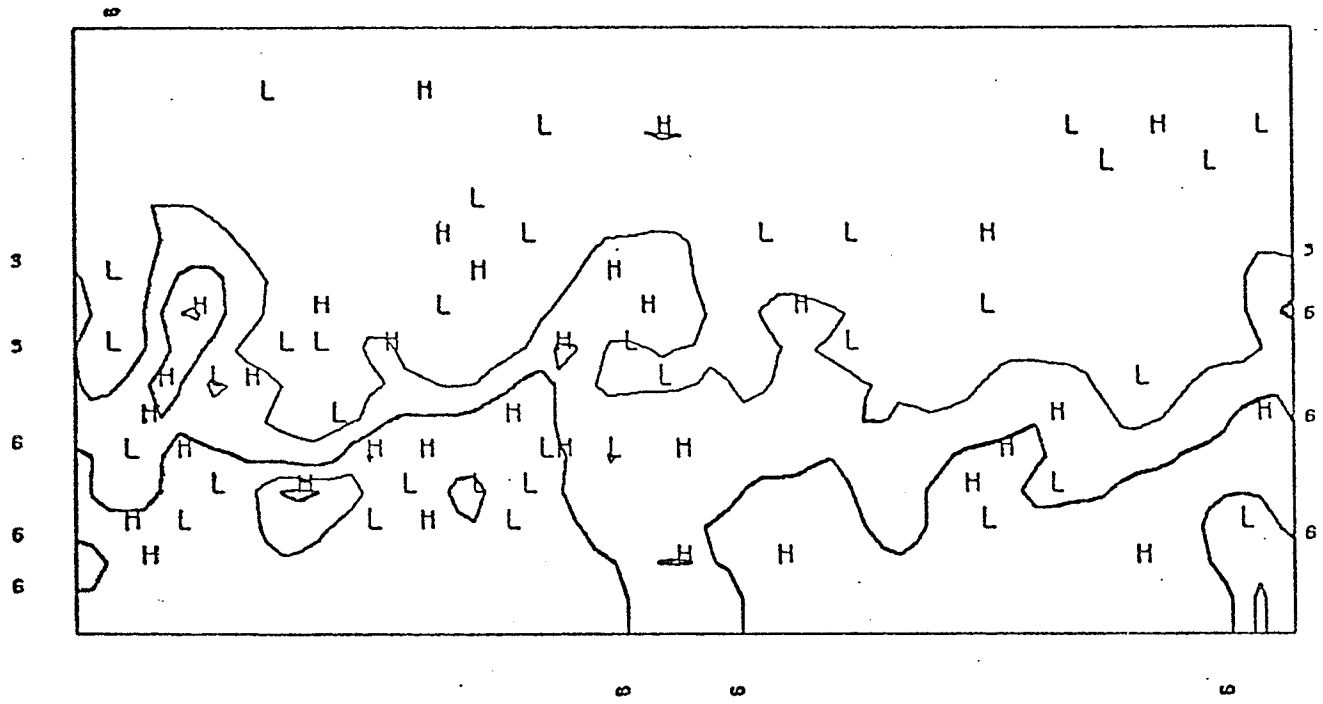

Figure 4.5: 800 mb Moisture (g H_2O/g dry air x 10^{-3}) , 0 hour

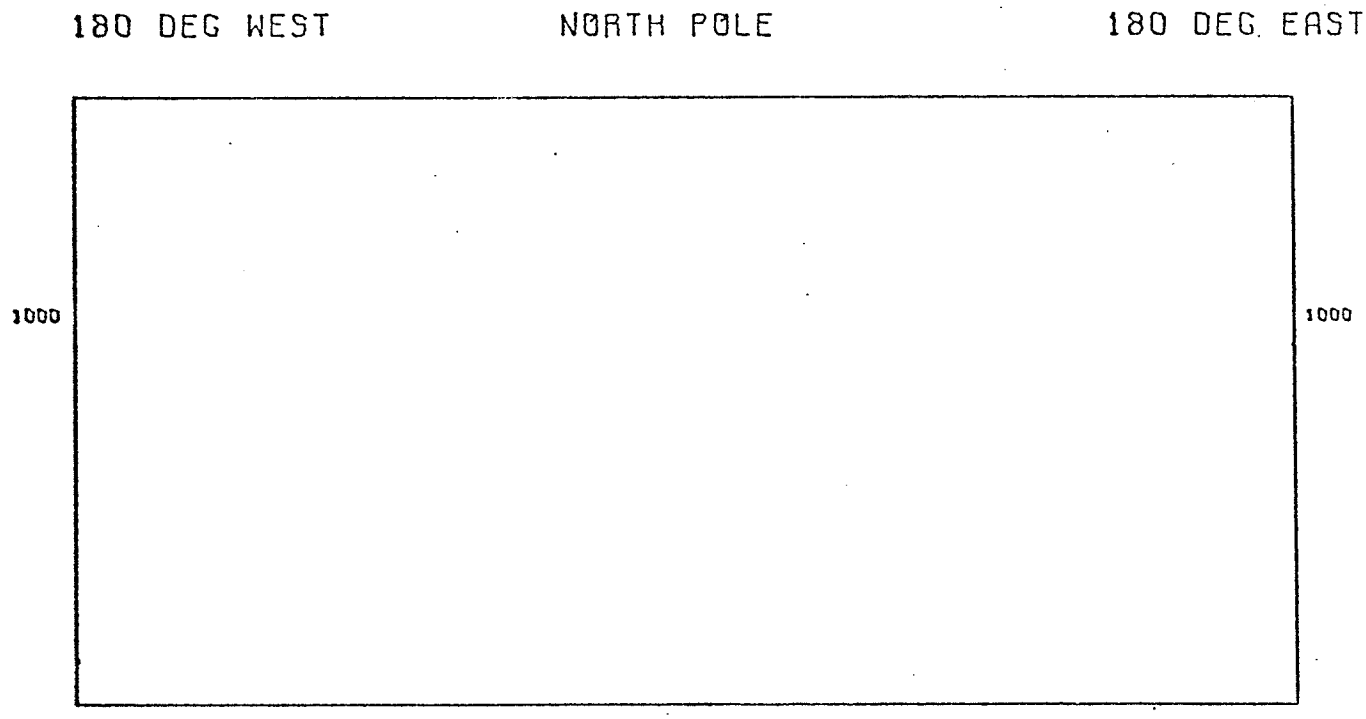

Figure 4.6: Surface Pressure (mb), 0 hour

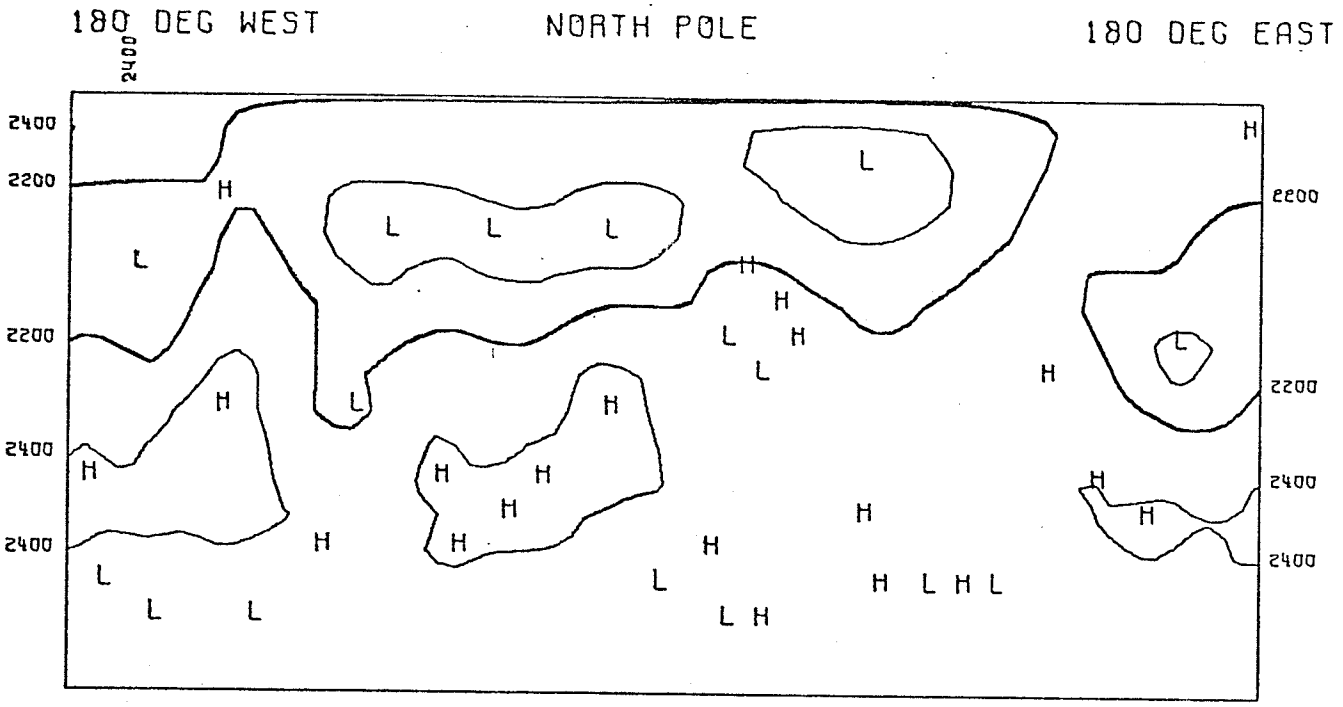

Figure 4.7: 800 mb Geopotential (m), 0 hour

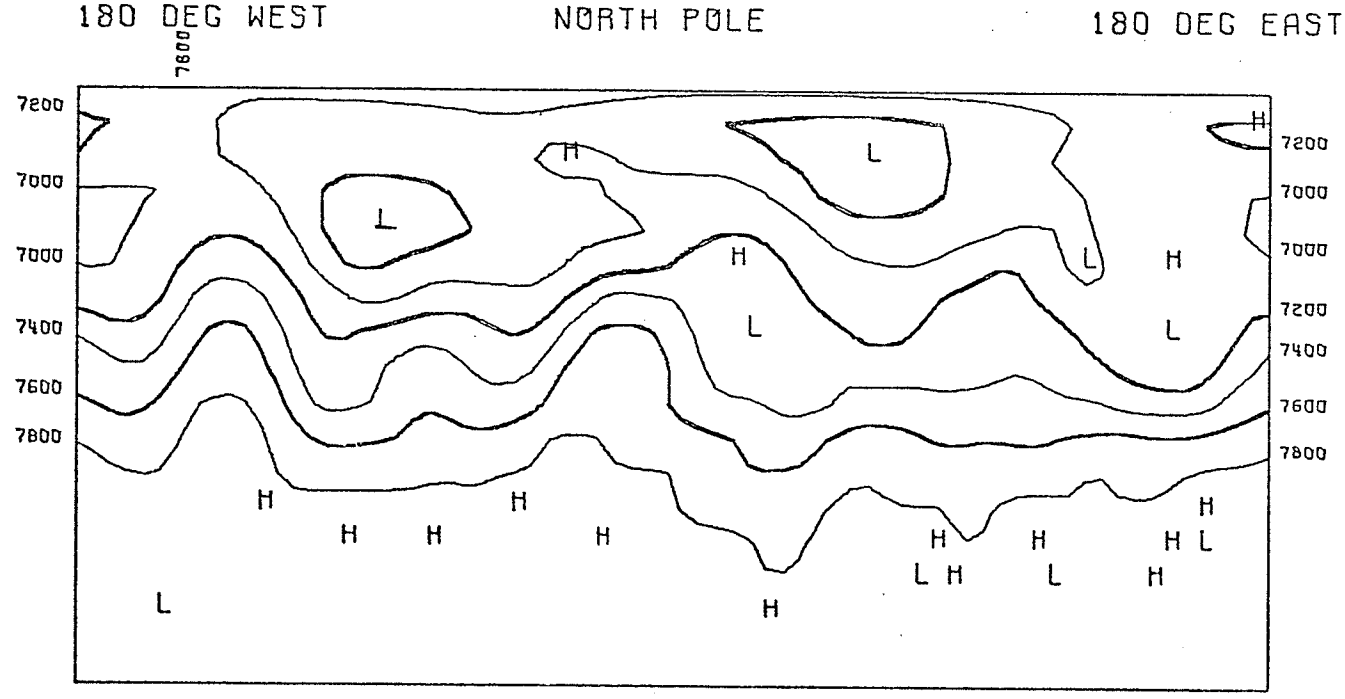

Figure 4.8: 400 mb Geopotential (m), 0 hour

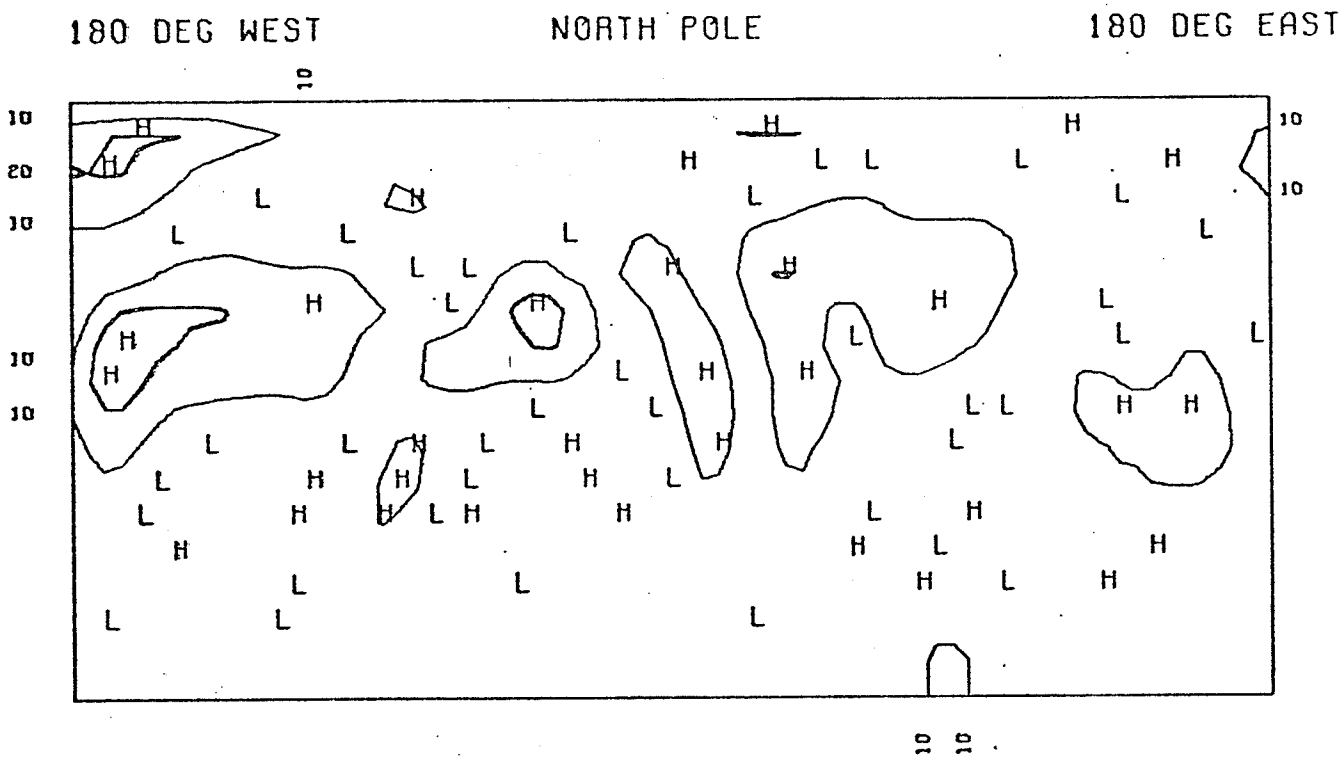

Figure 4.9: 800 mb Resultant Velocity Isotachs (m/sec), 36 hour true

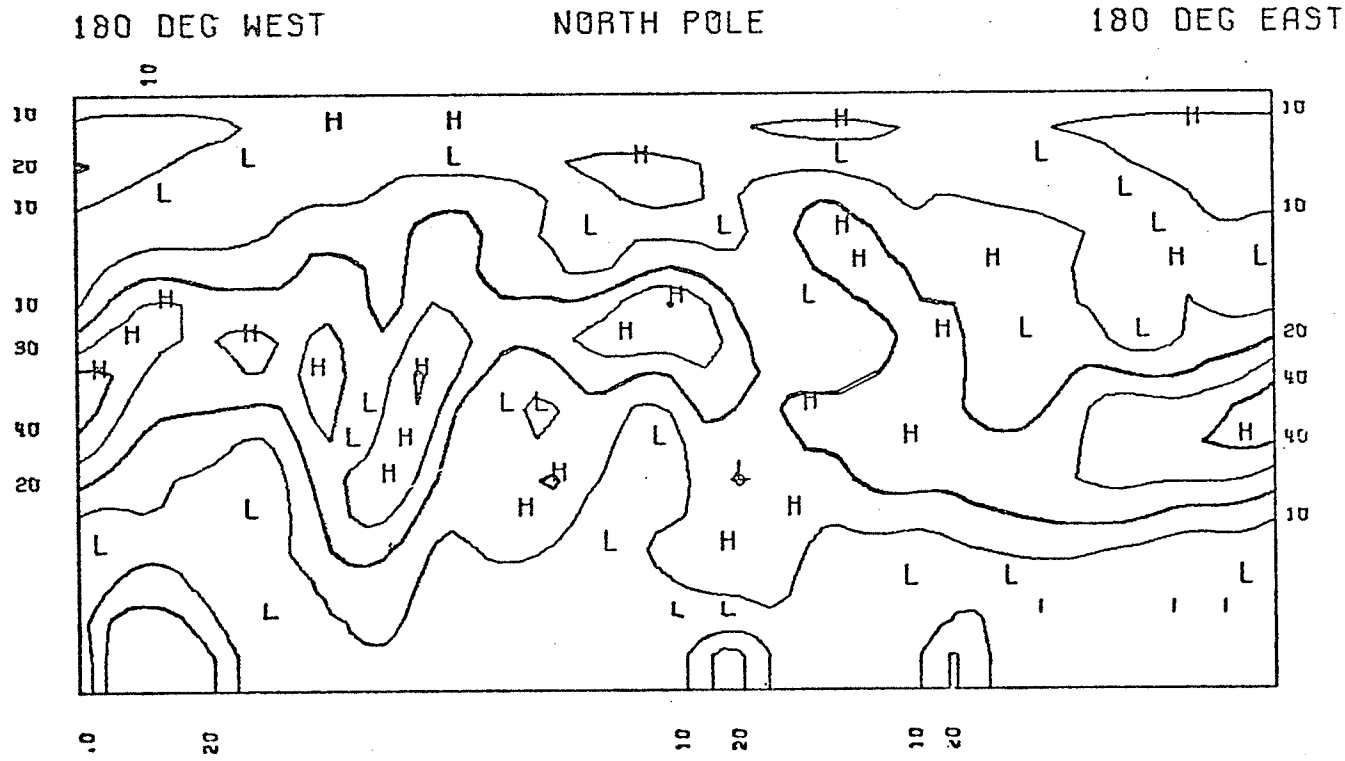

Figure 4.10: 400 mb Resultant Velocity Isotachs (m/sec), 36 hour true

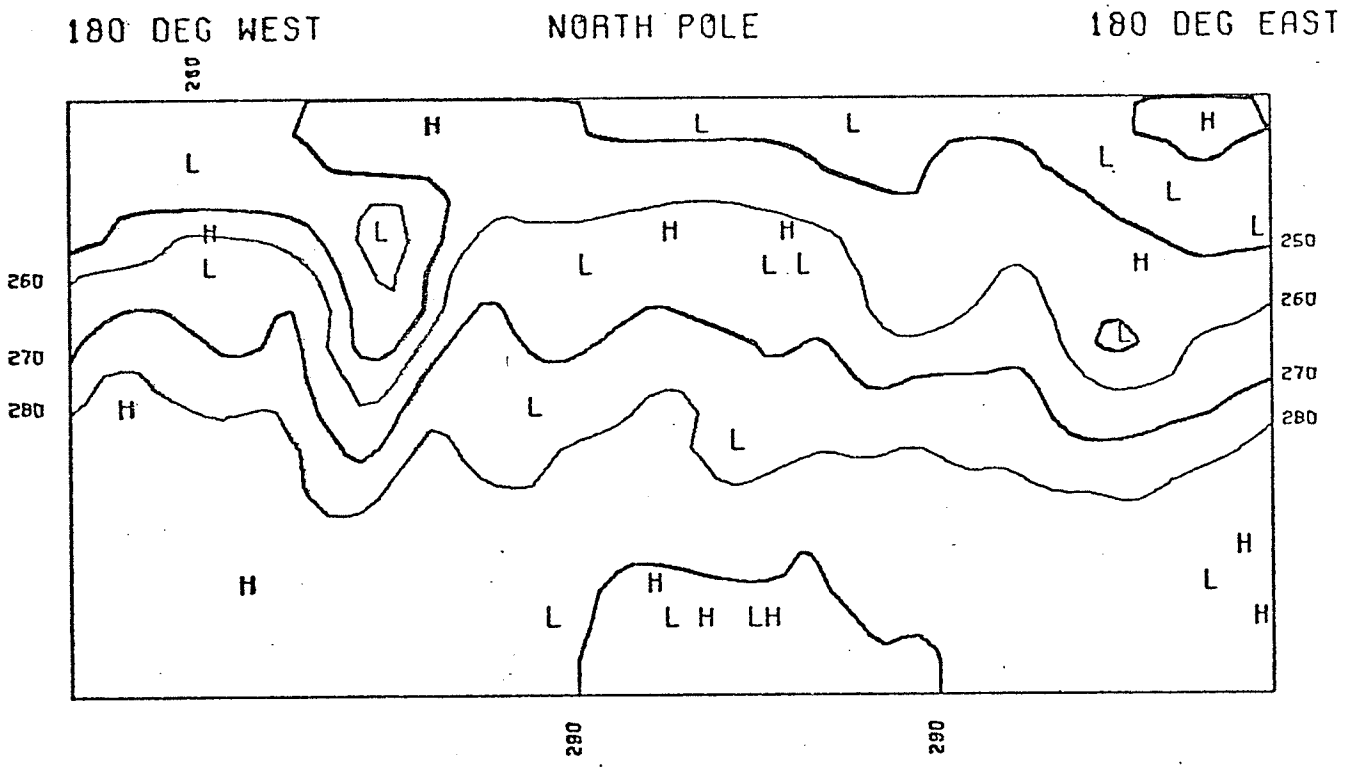

Figure 4.11: 800 mb Temperature (^{o}K), 36 hour true

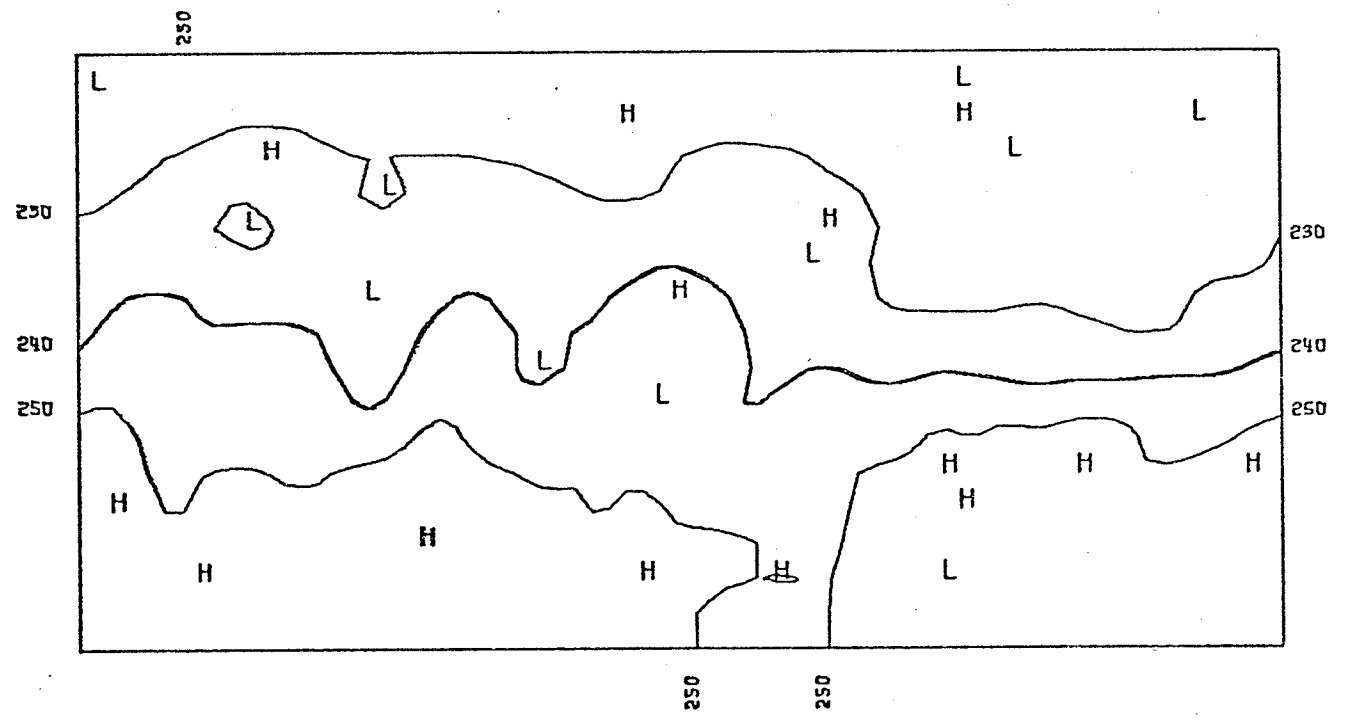

Figure 4.12: 400 mb Temperature (^{o}K), 36 hour true

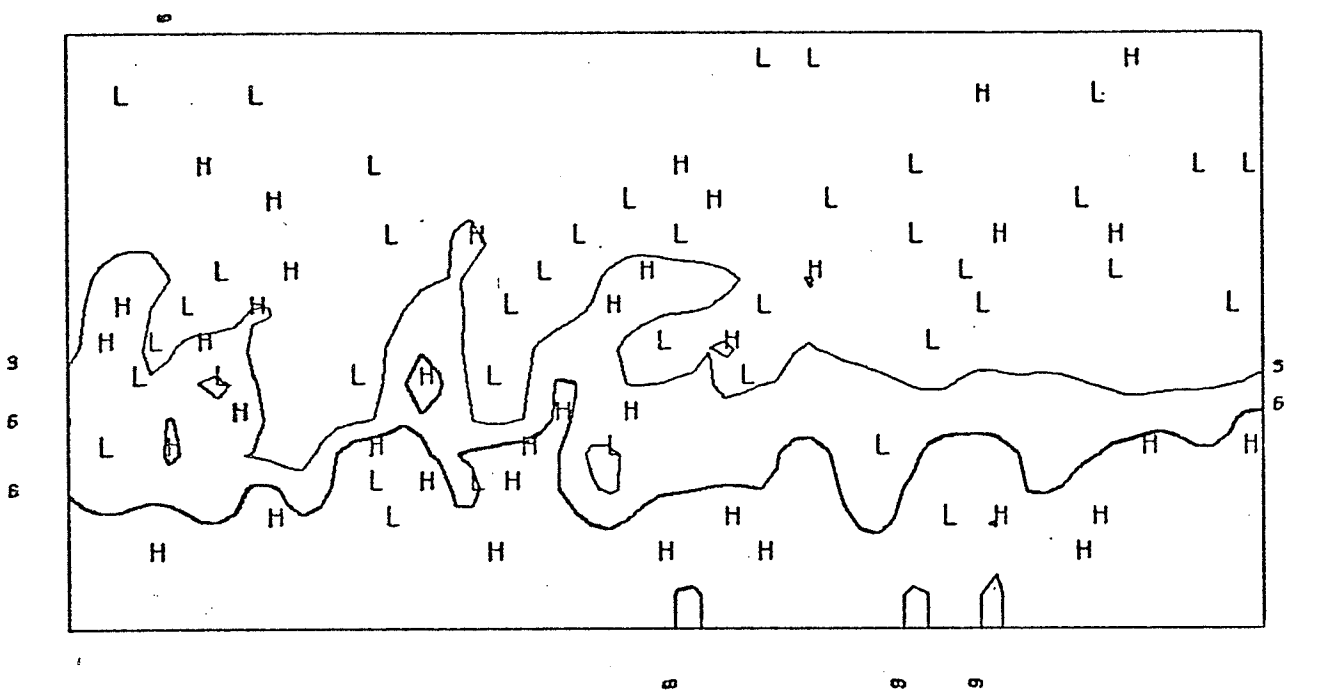

Figure 4.13: 800 mb Moisture (g H_2O/g dry air x 10^{-3}), 36 hour true

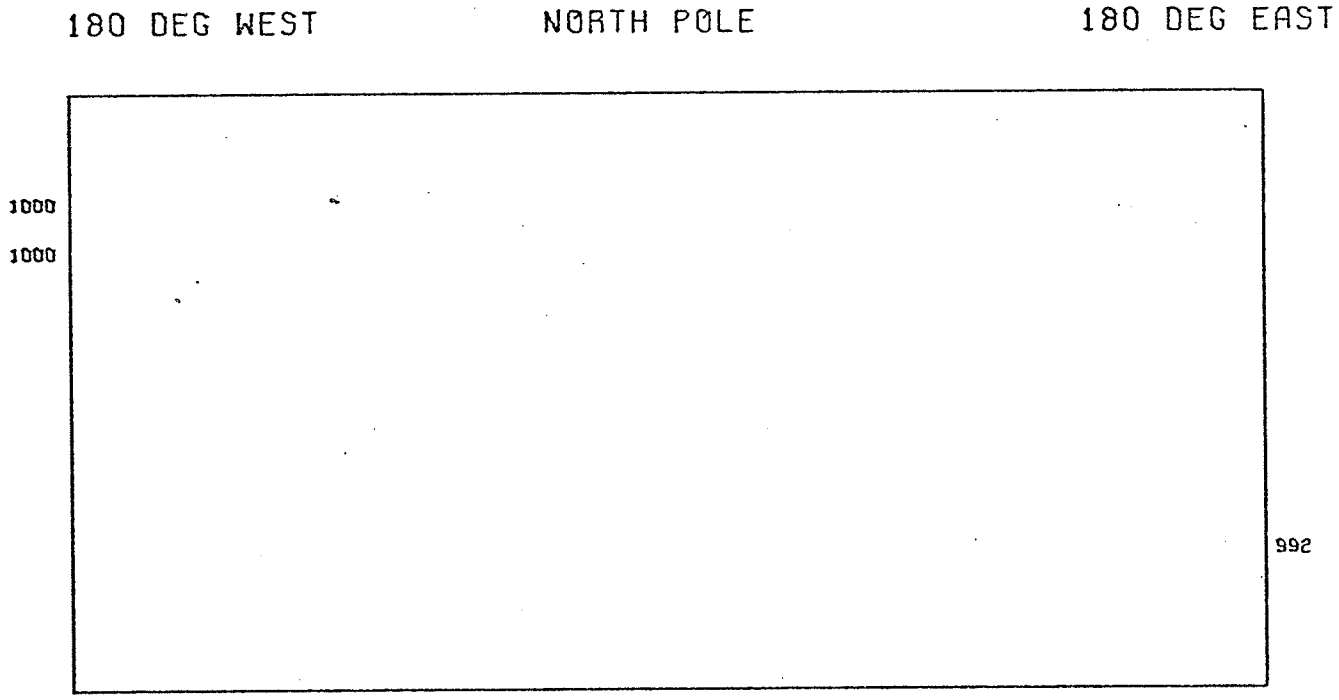

Figure 4.14: Surface Pressure (mb), 36 hour true

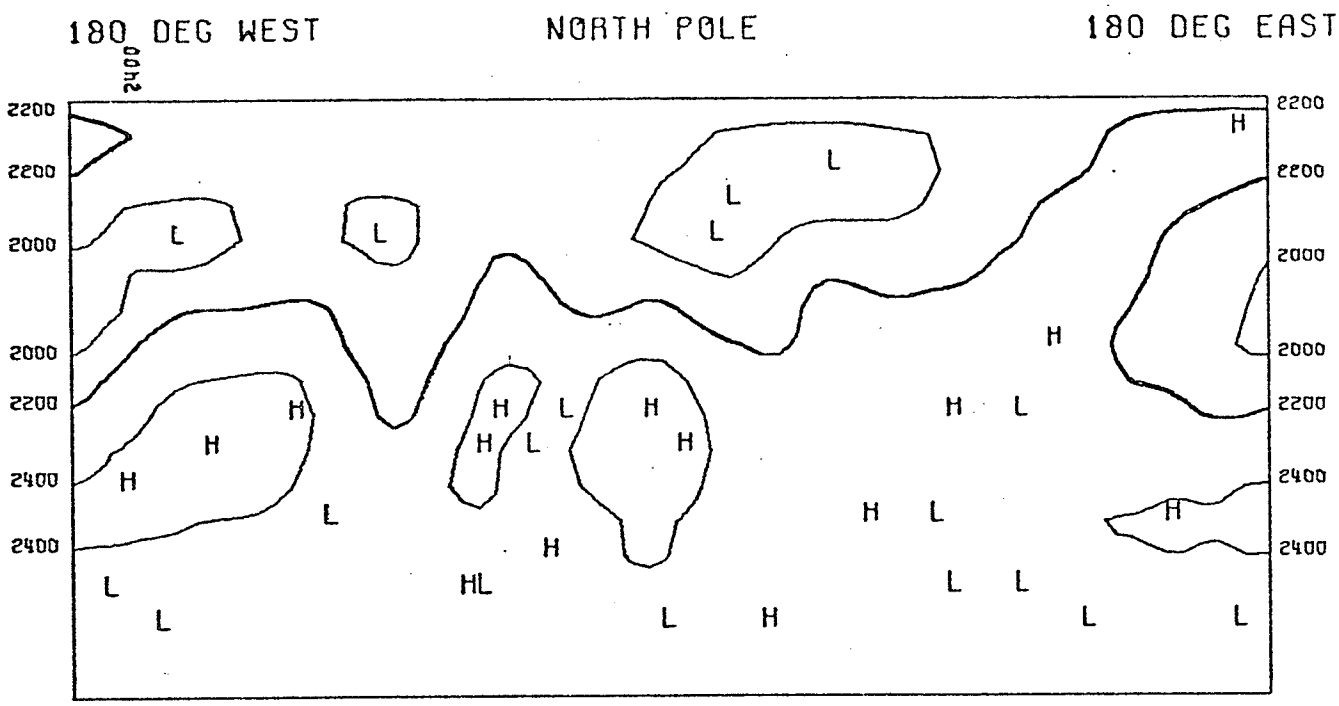

Figure 4.15: 800 mb Geopotential (m), 36 hour true

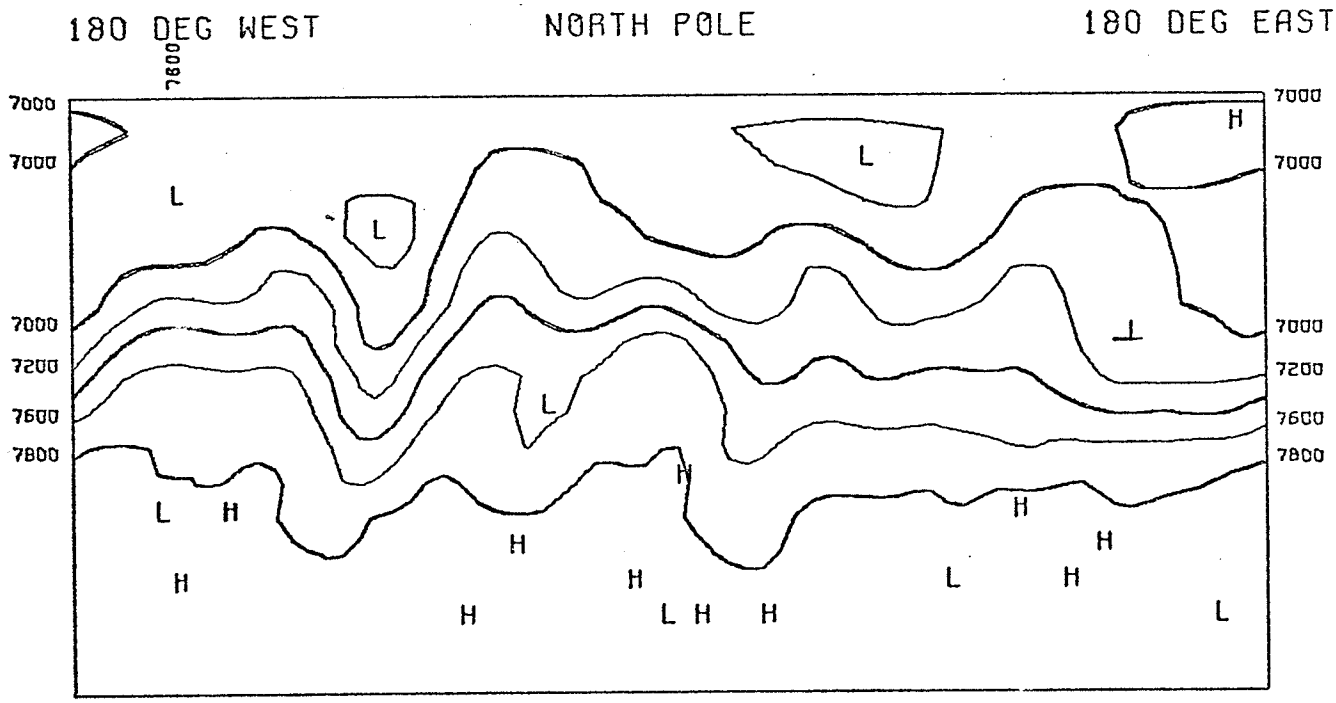

Figure 4.16: 400 mb Geopotential (m), 36 hour true

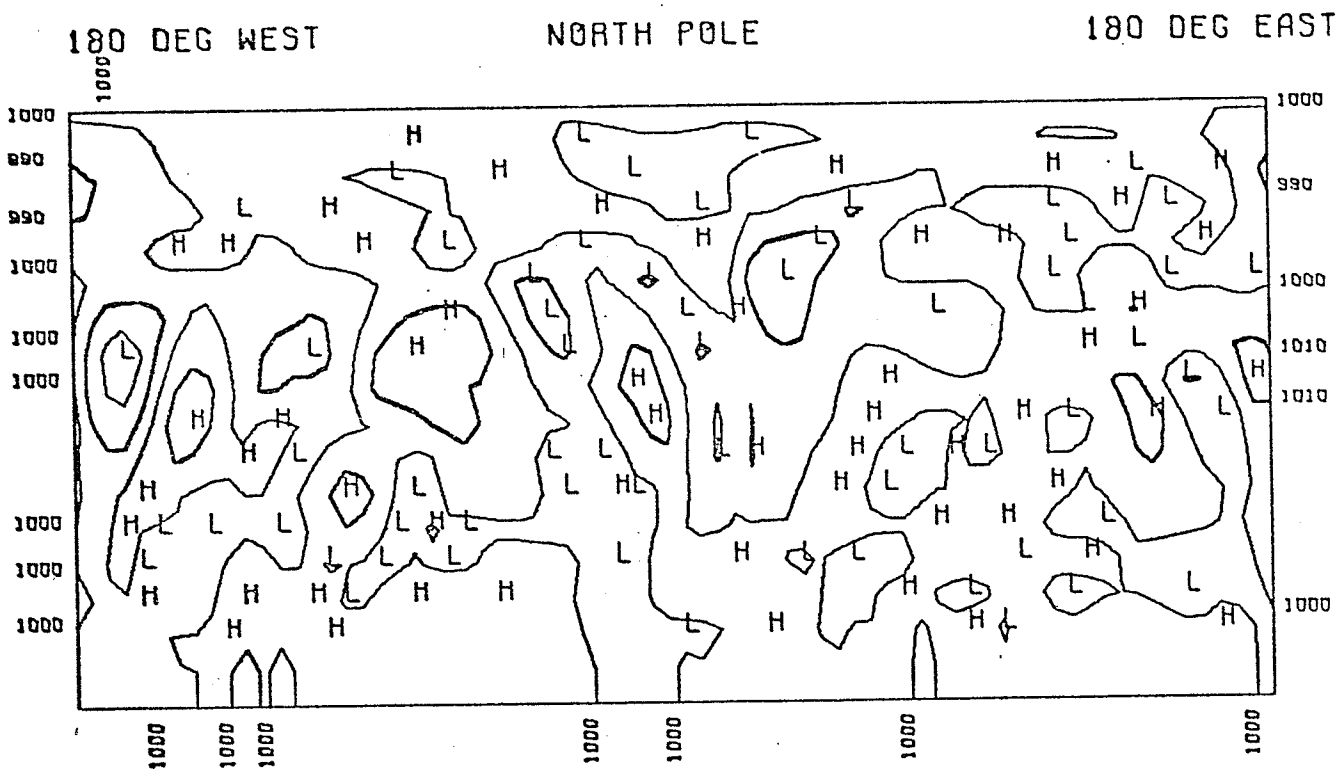

Figure 4.17: 800 mb Resultant Velocity Isotachs (m/sec), 0-36 hour change

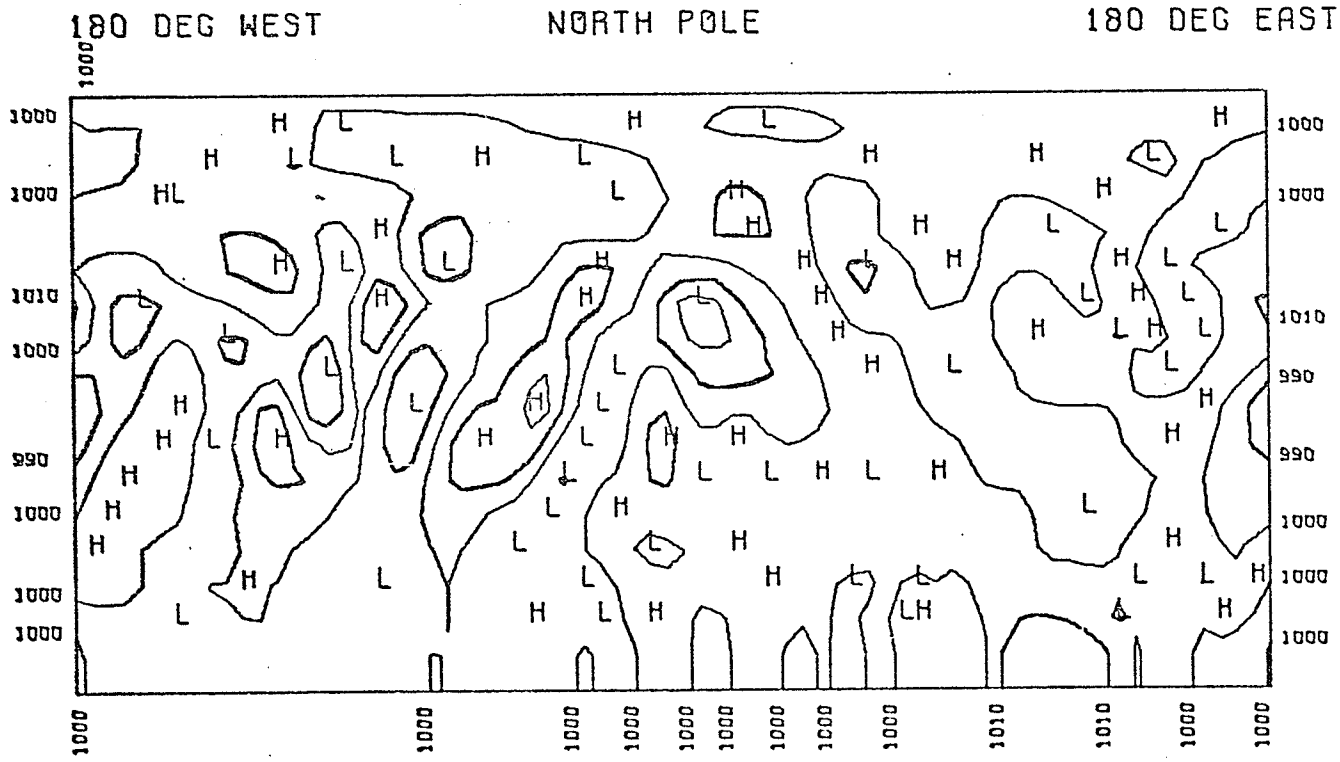

Figure 4.18: 400 mb Resultant Velocity Isotachs (m/sec), 0-36 hour change

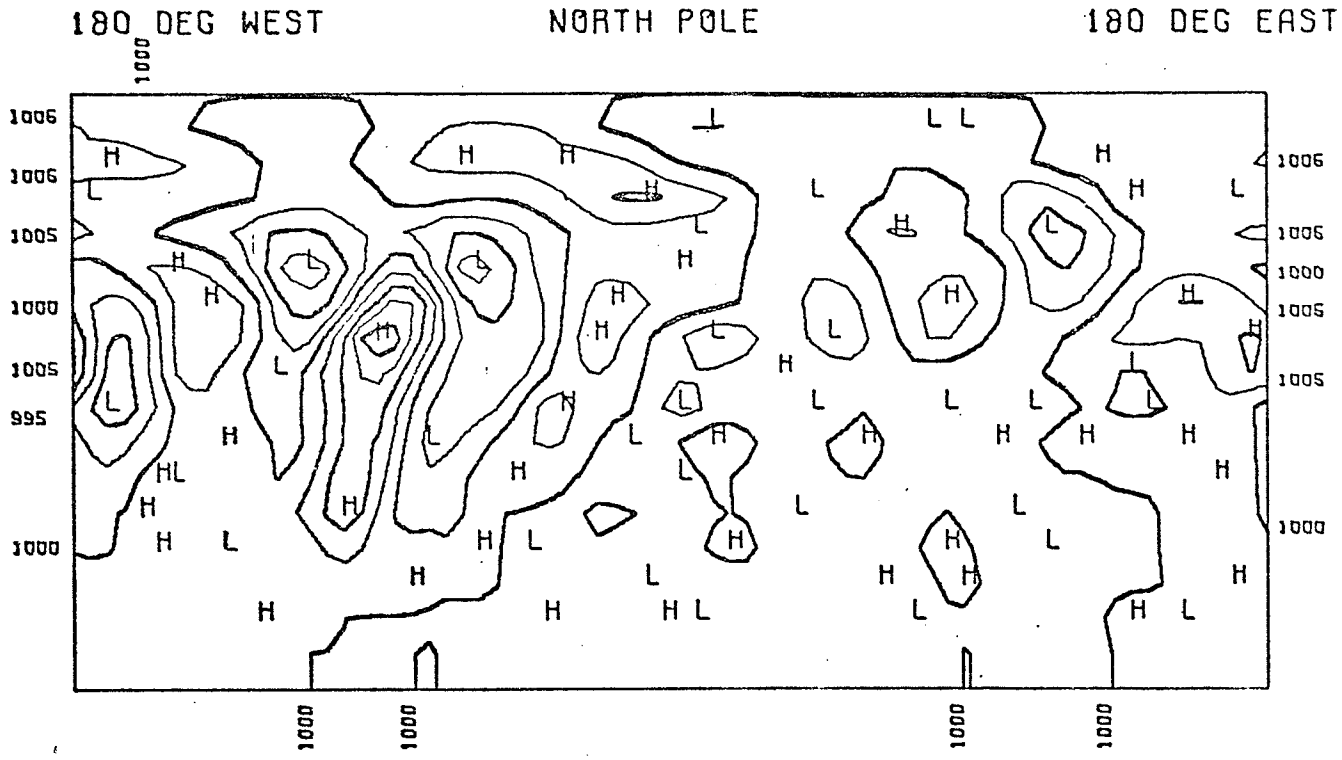

Figure 4.19: 800 mb Temperature (^{o}K), 0-36 hour change

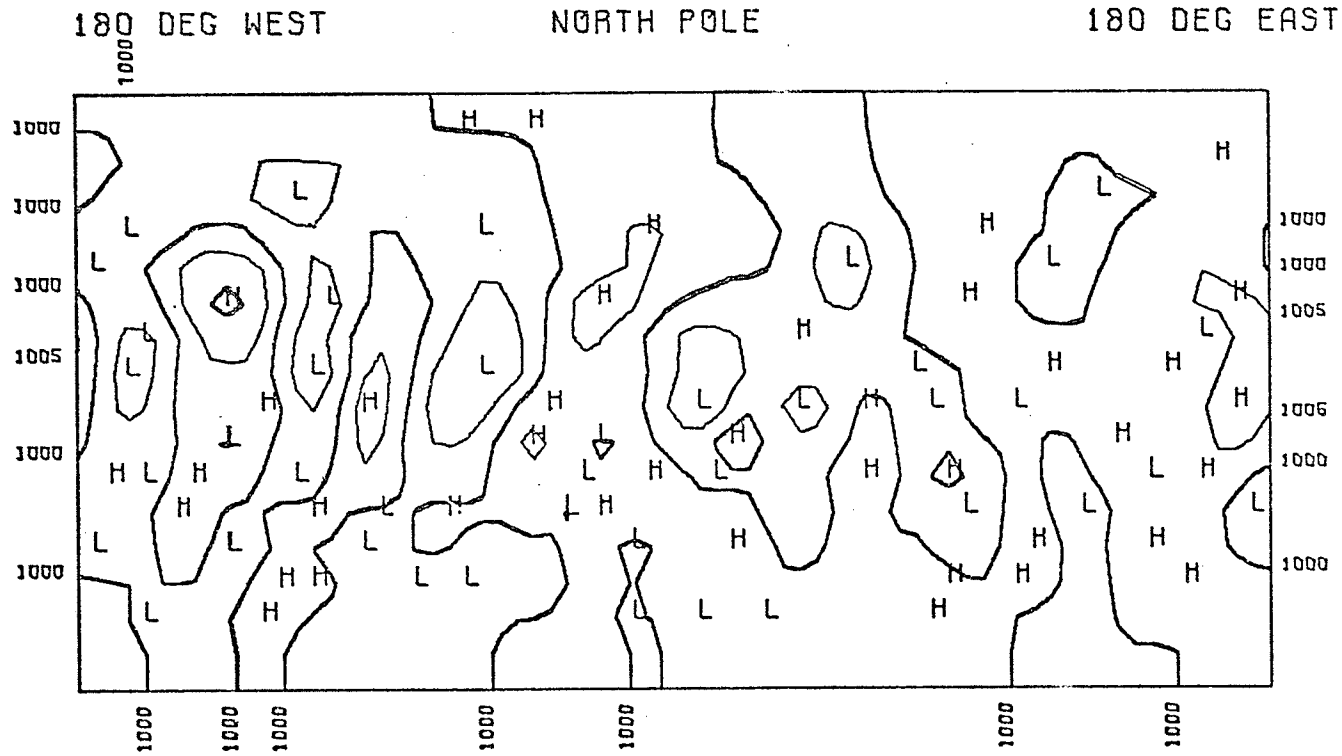

Figure 4.20: 400 mb Temperature (^{o}K), 0-36 hour change

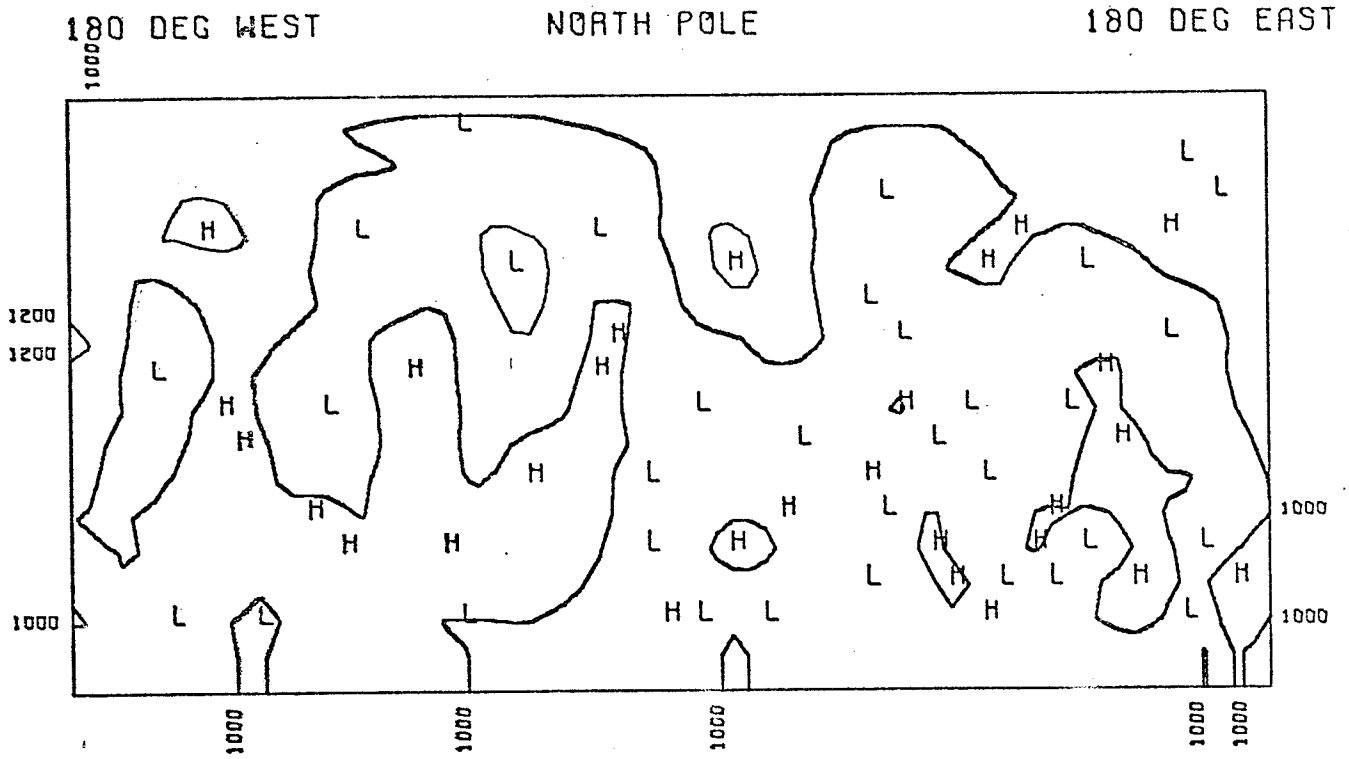

Figure 4.21a: 800 mb Geopotential (m), 0-36 hour change

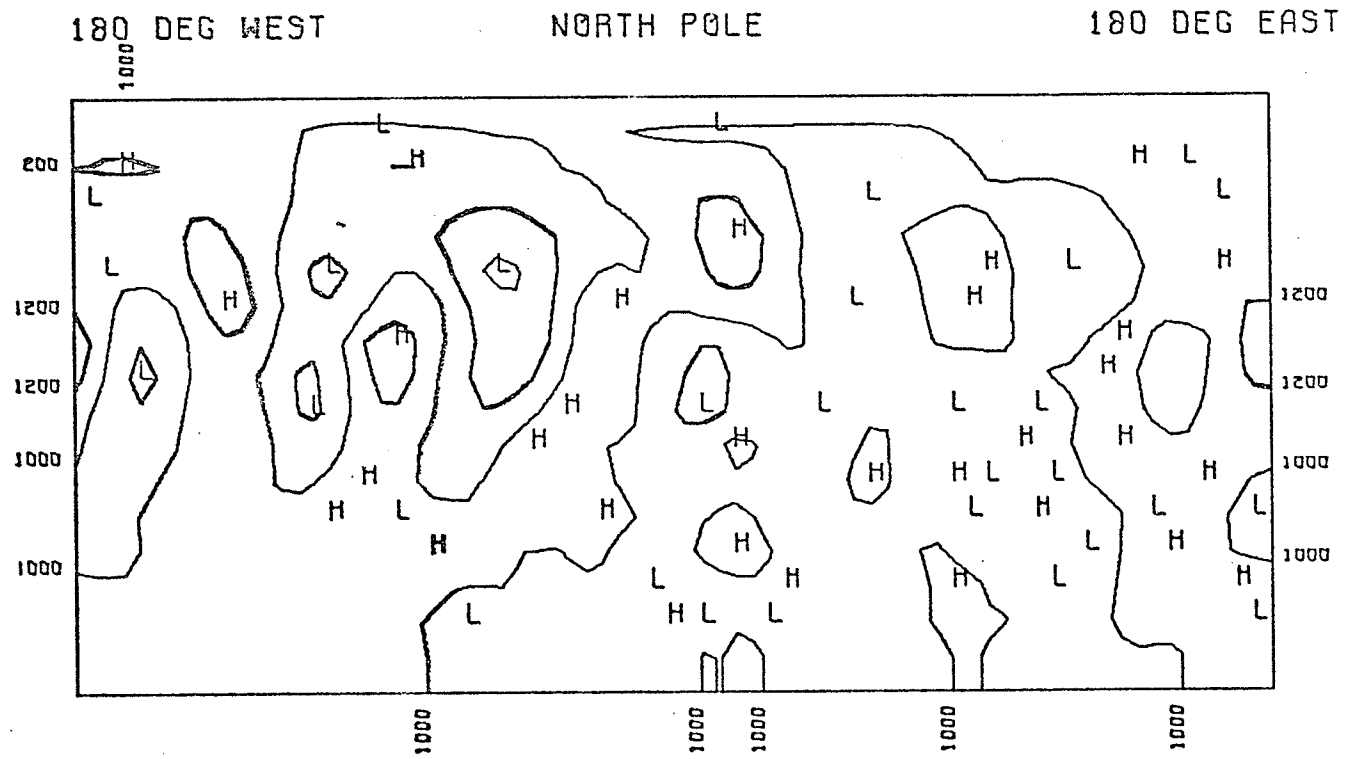

Figure 4.21b: 400 mb Geopotential (m), 0-36 hour change

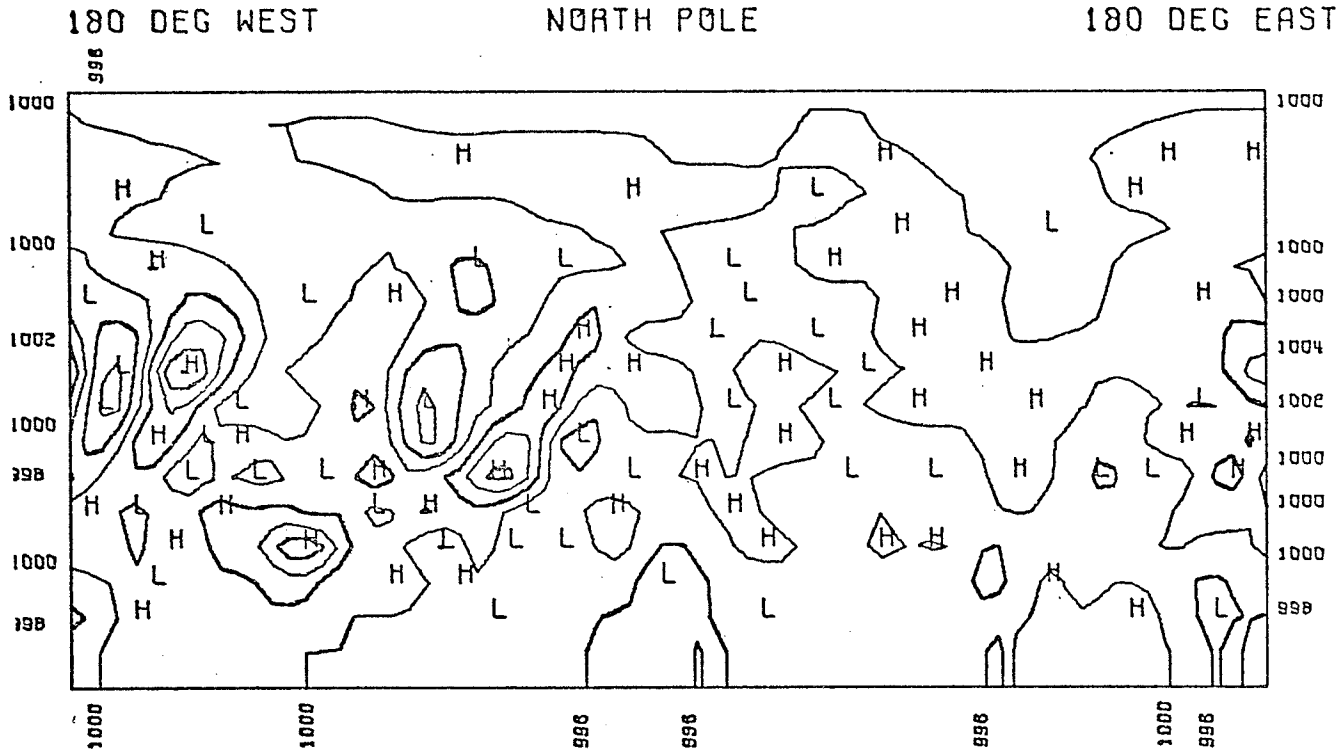

Figure 4.22: 800 mb Moisture (g H_2O/g dry air x 10^{-3}), 0-36 hour change

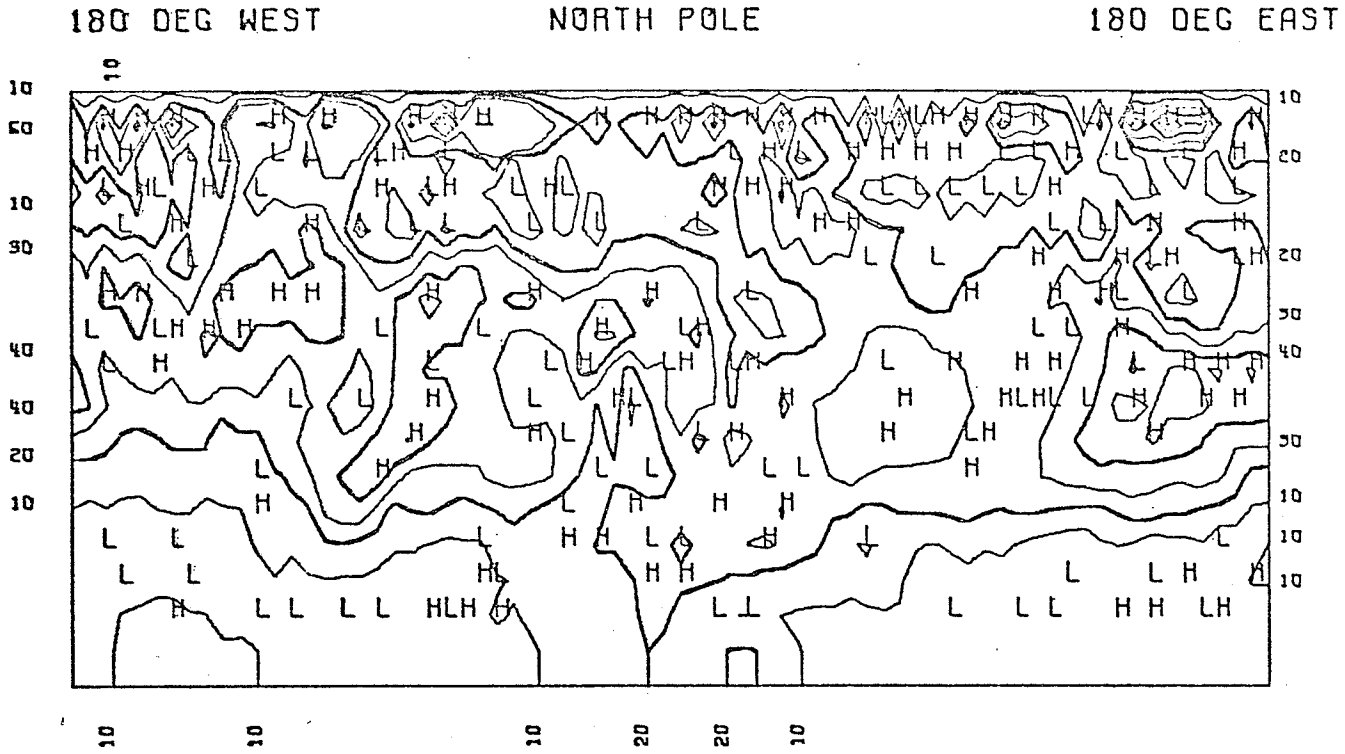

Figure 4.23: 400 mb Resultant Velocity Isotachs (m/sec), model P2, 20 hour

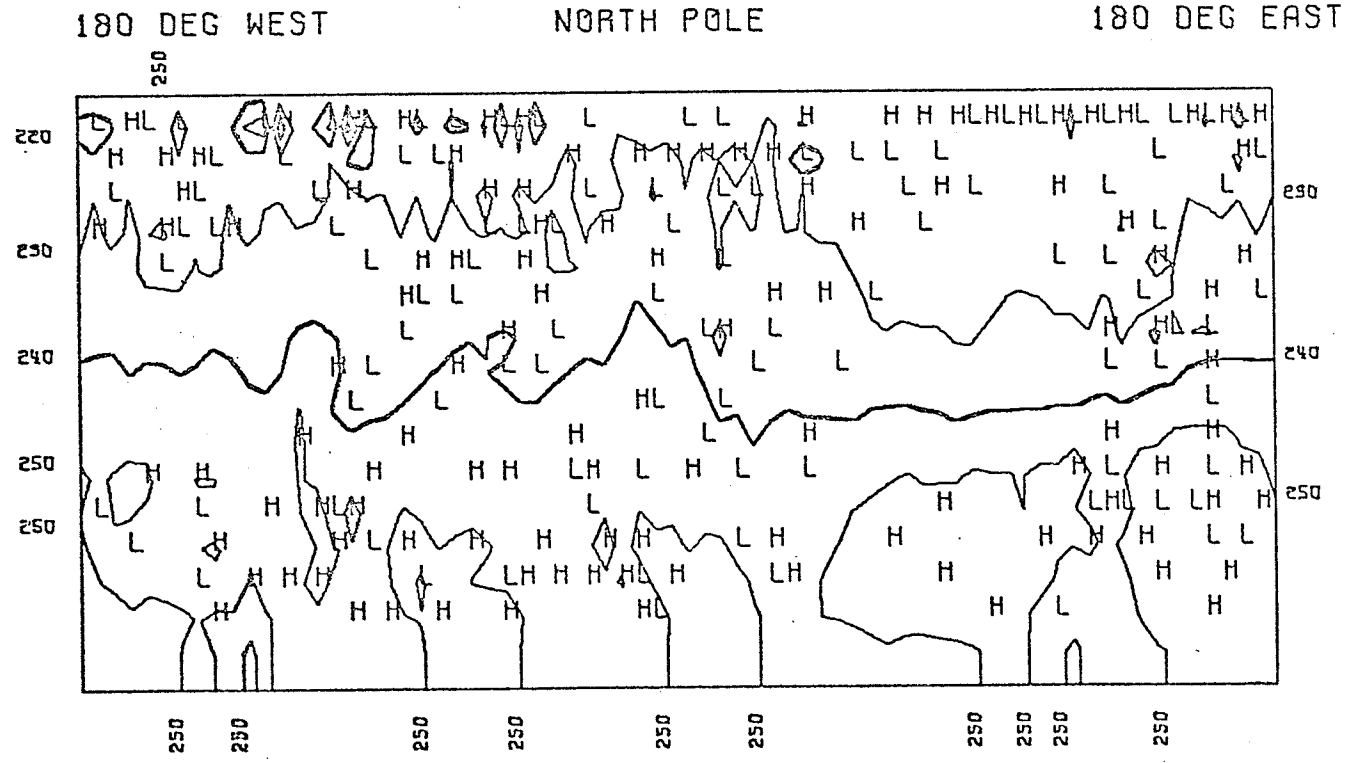

Figure 4.24: 400 mb Temperature (^{o}K), model P2, 20 hour

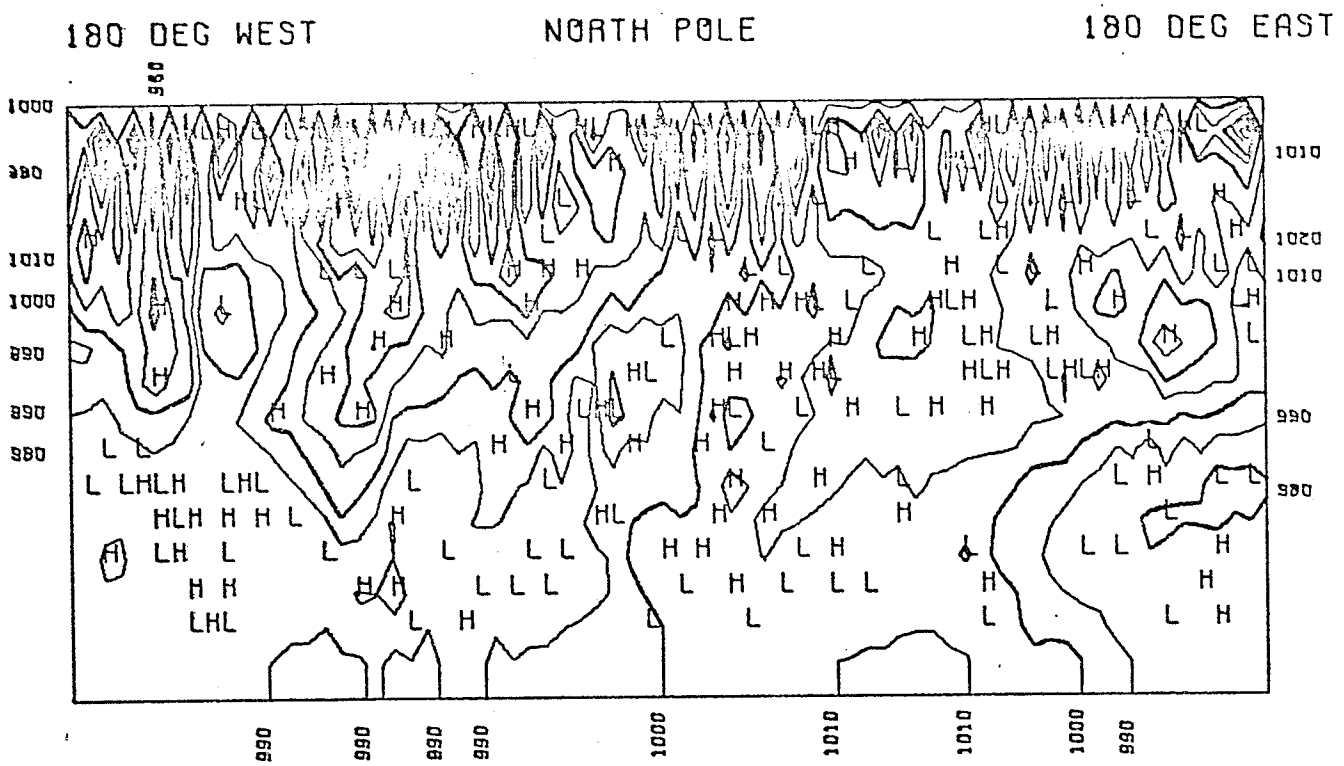

Figure 4.25: Surface Pressure (mb), model P2, 20 hour

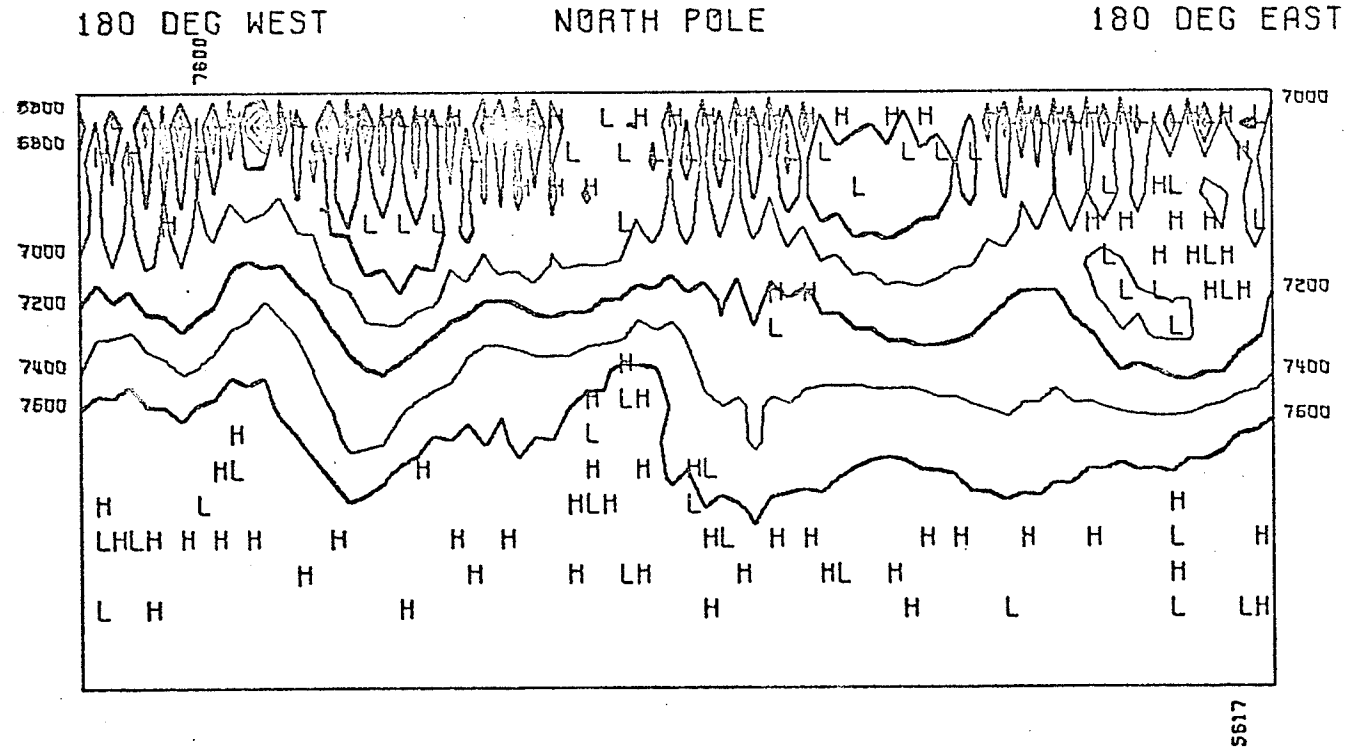

Figure 4.26: 400 mb Geopotential (m), model P2, 20 hour

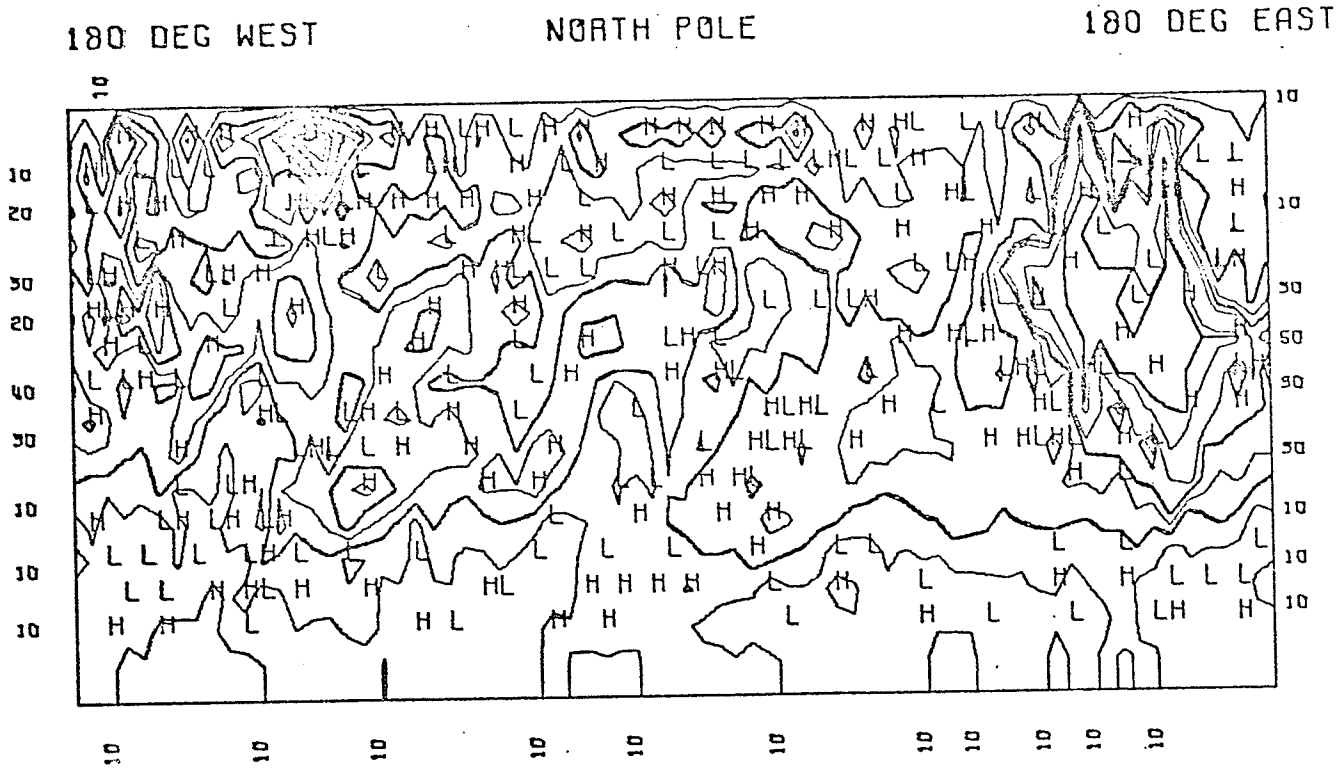

Figure 4.27: 400 mb Resultant Velocity Isotachs (m/sec), model P3, 26 hour

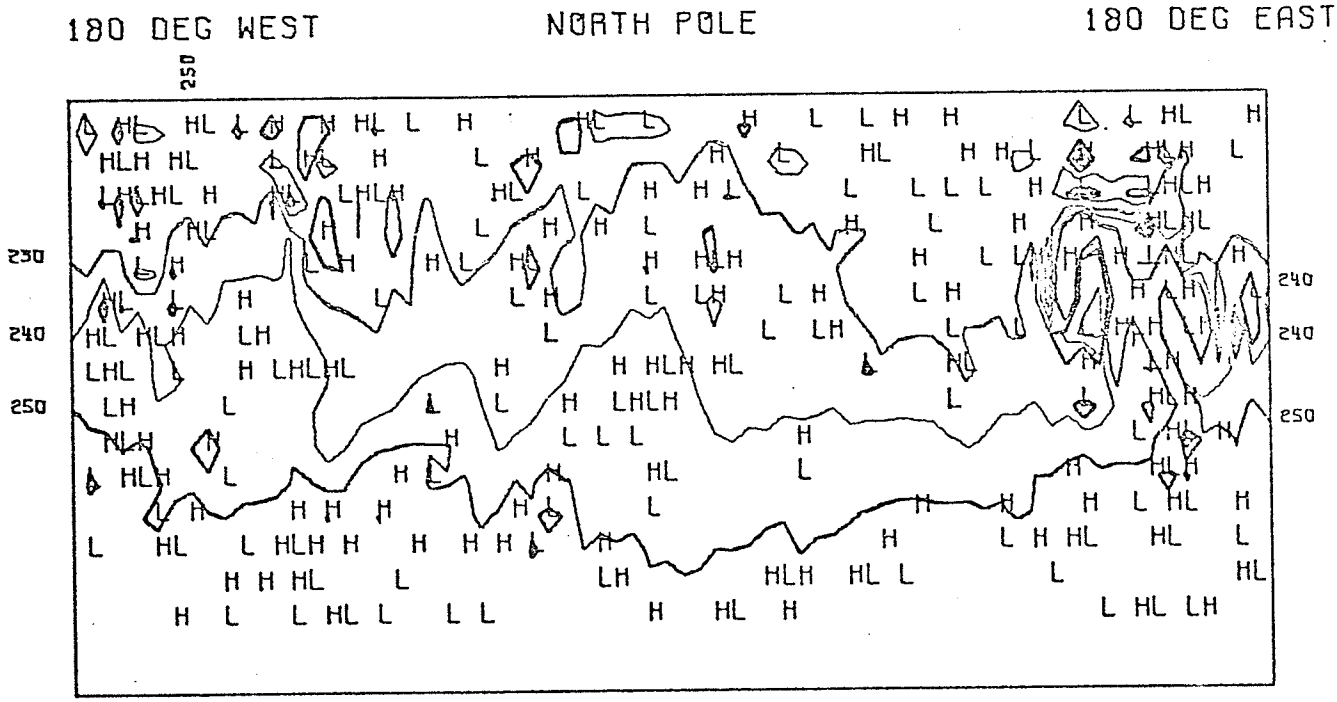

Figure 4.28: 400 mb Temperature (^{o}K), model P3, 26 hour

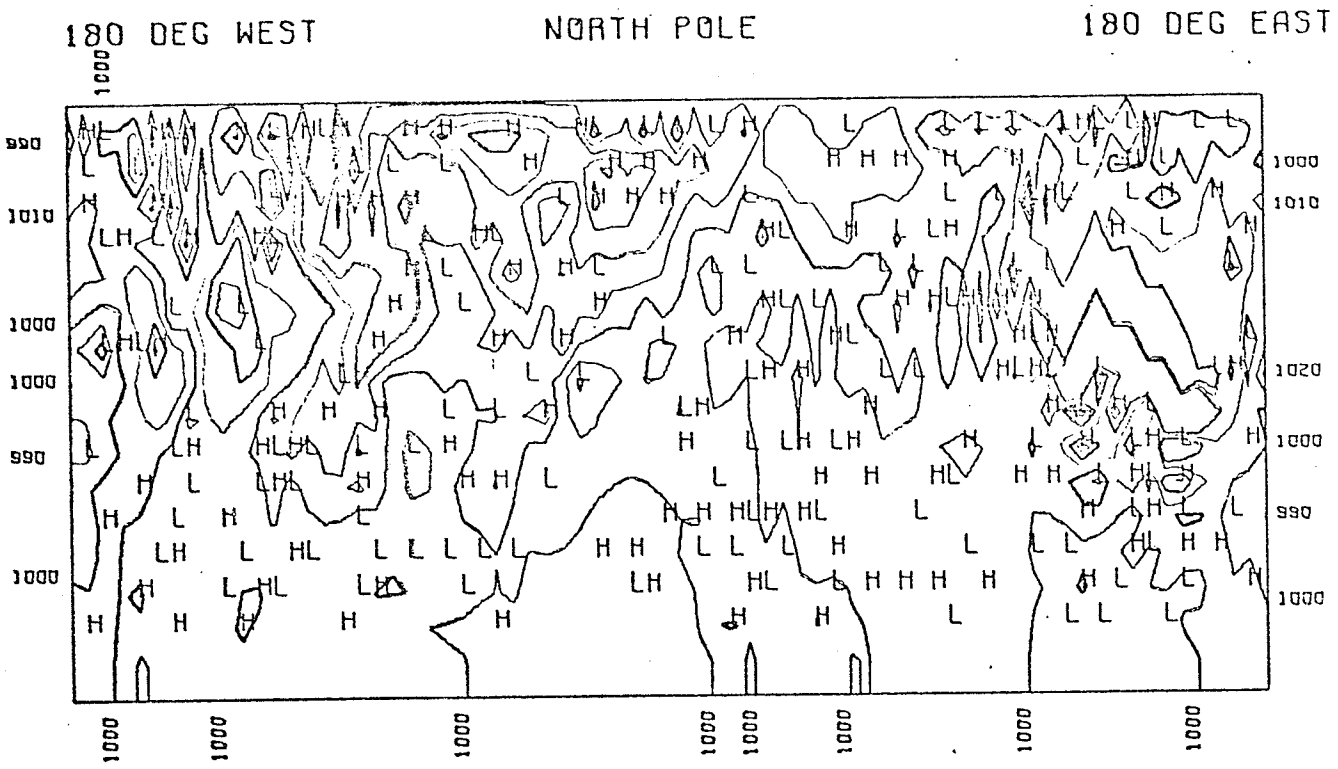

Figure 4.29: Surface Pressure (mb), model P3, 26 hour

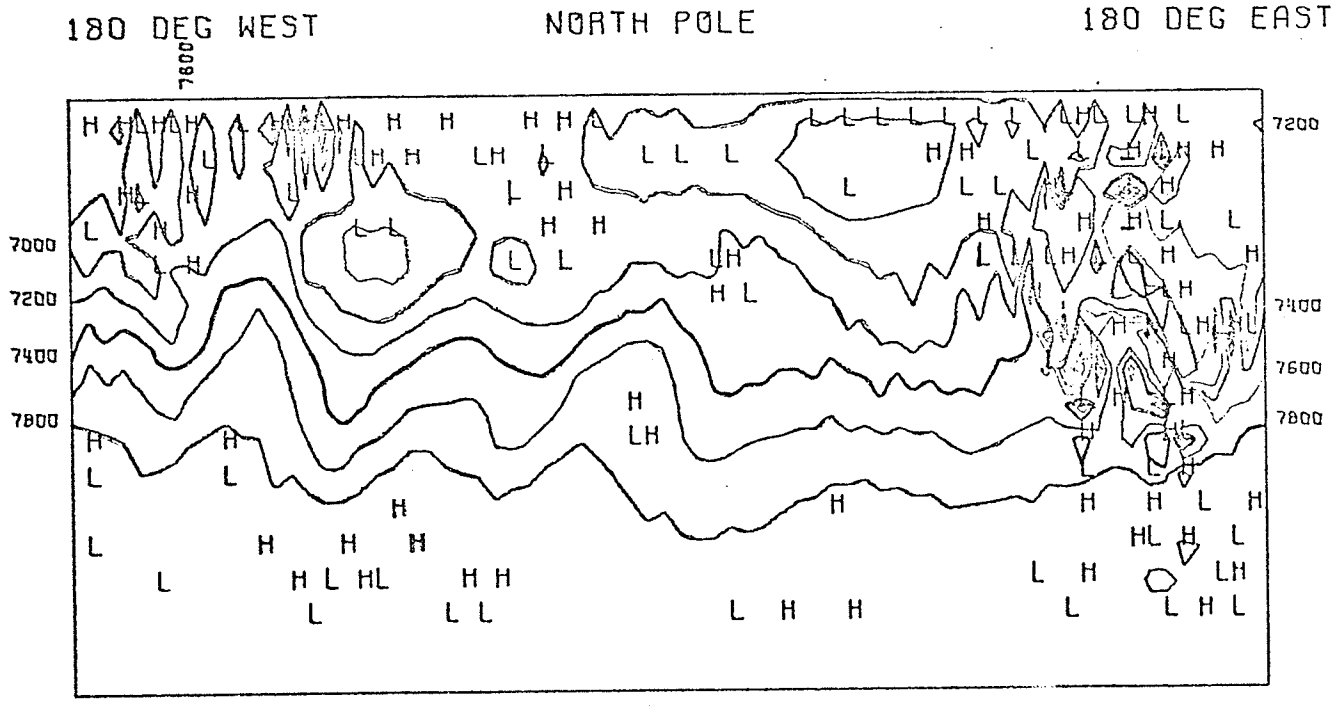

Figure: 4.30: 400 mb Geopotential (m), model P3, 26 hour

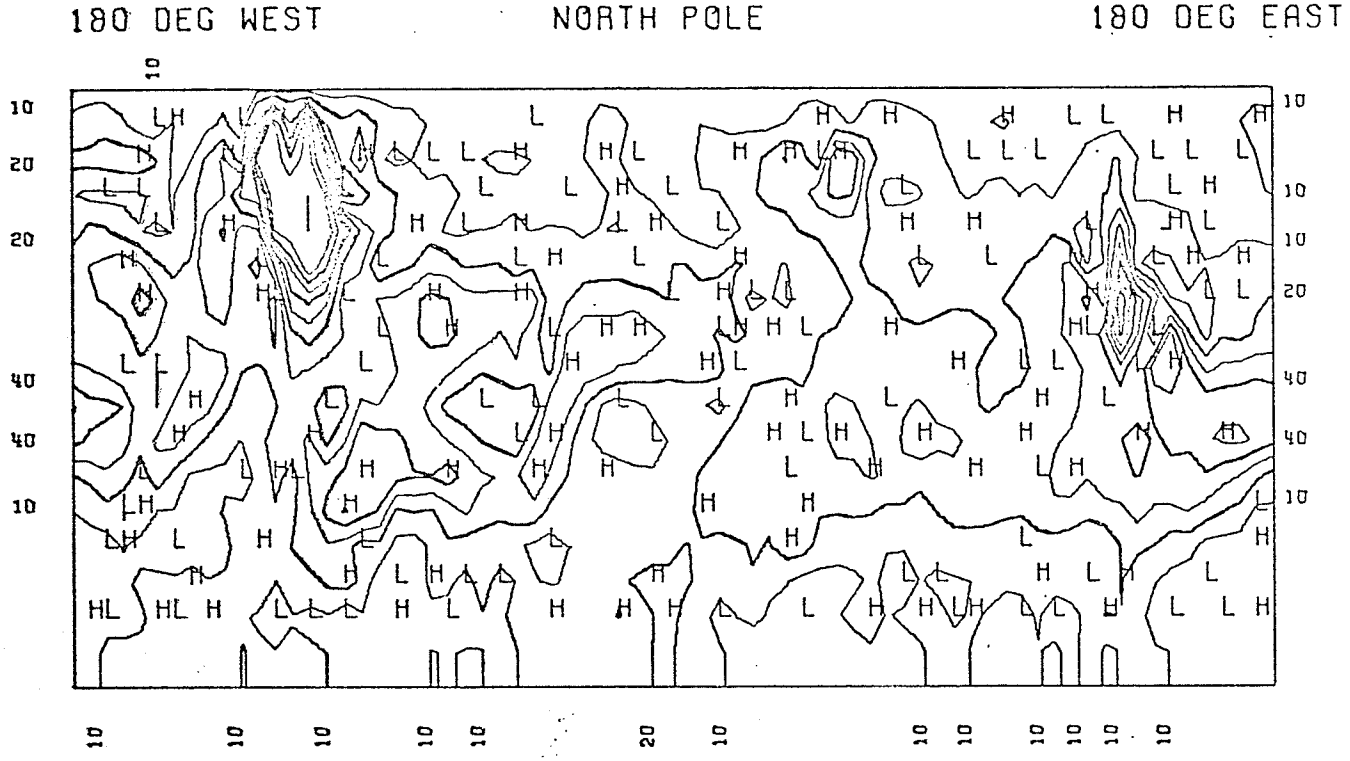

Figure 4.31: 400 mb Resultant Velocity Isotachs (m/sec), model P4, 36 hour

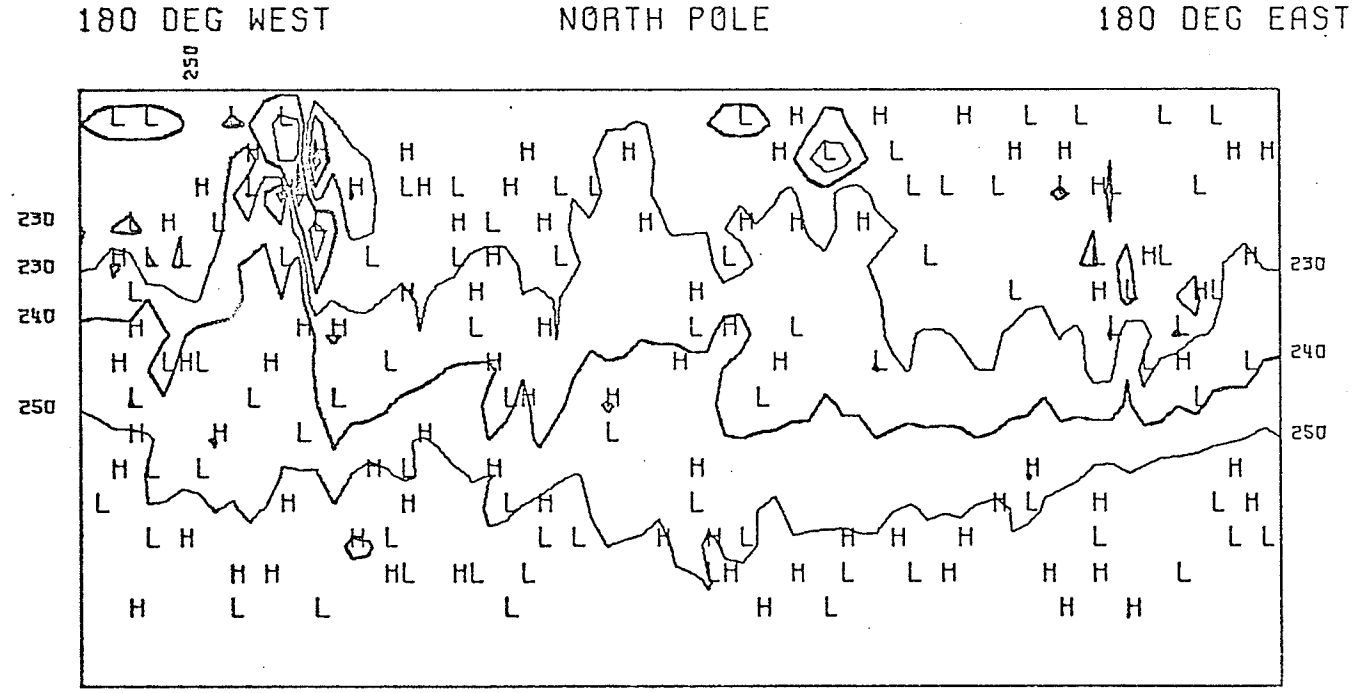

Figure 4.32: 400 mb Temperature (^{o}K), model P4, 36 hour

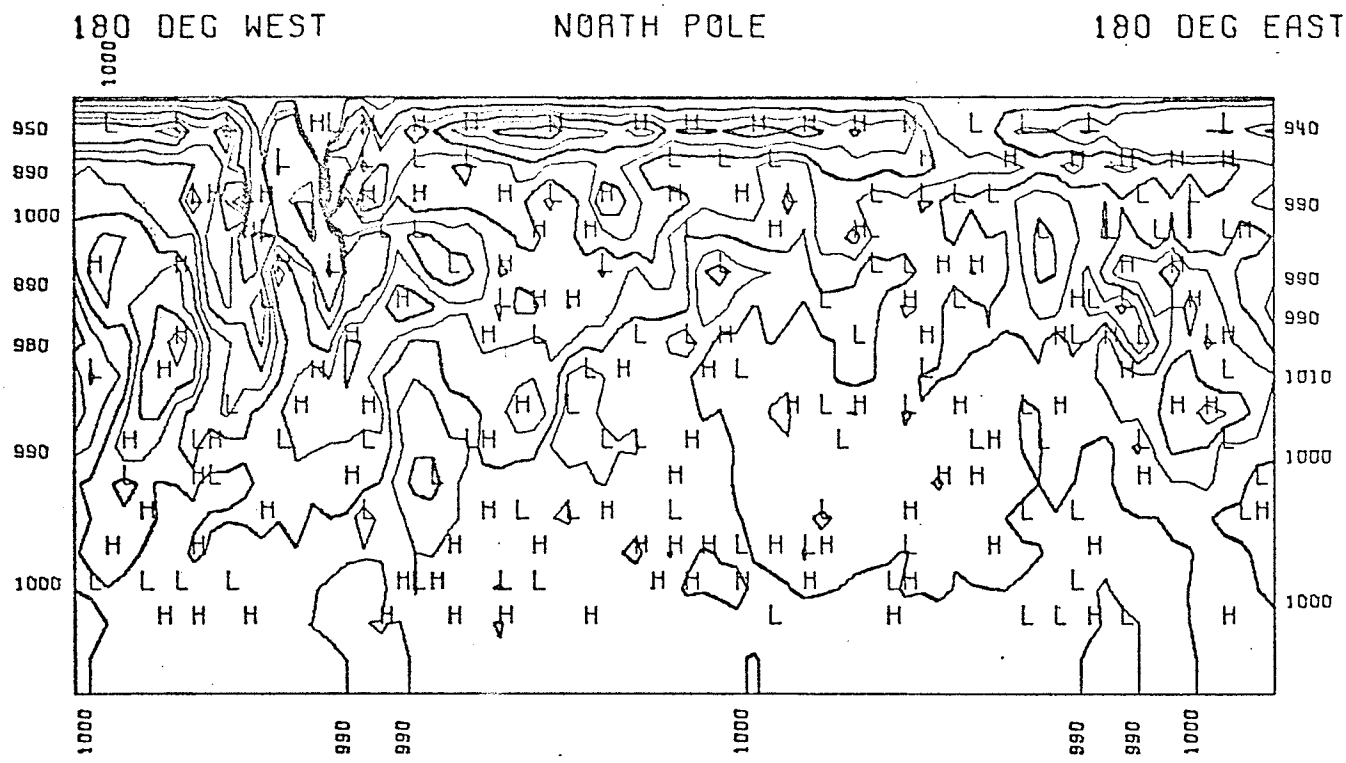

Figure 4.33: Surface Pressure (mb), model P4, 36 hour

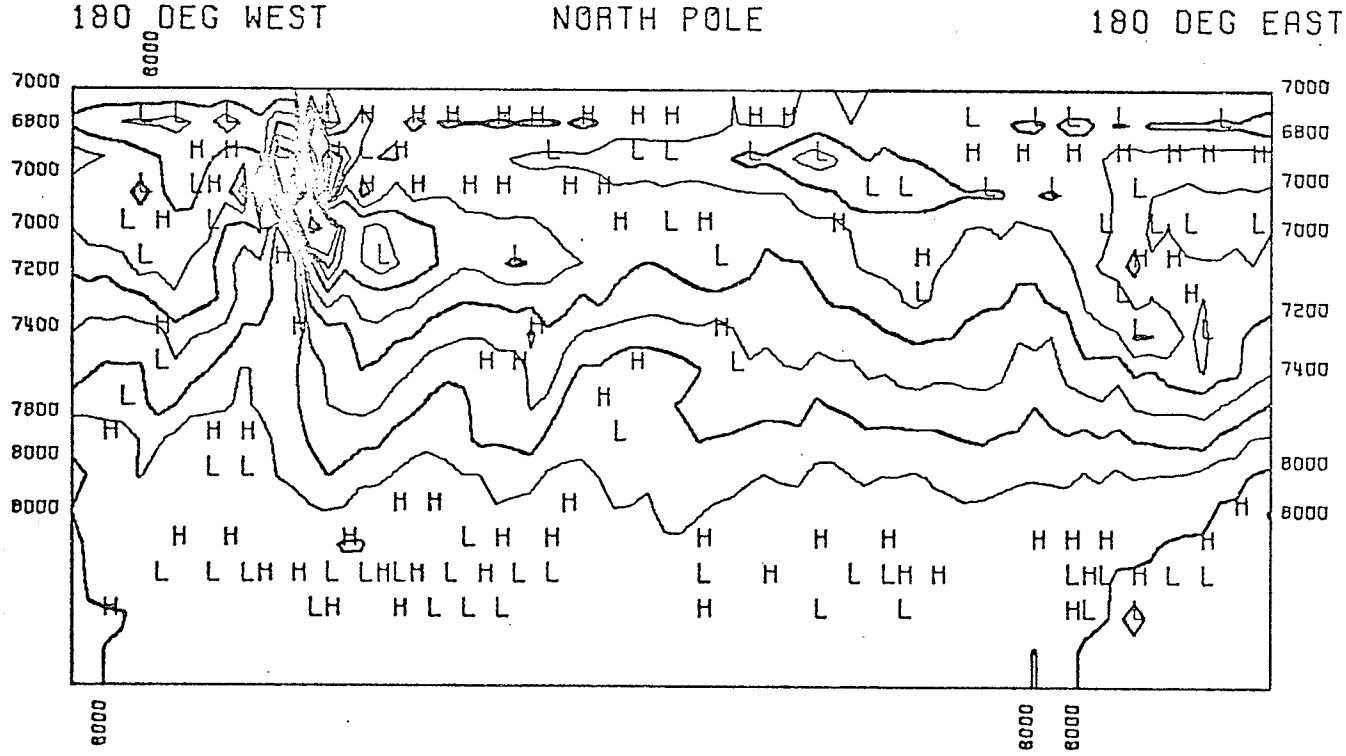

Figure 4.34: 400 mb Geopotential (m), model P4, 36 hour

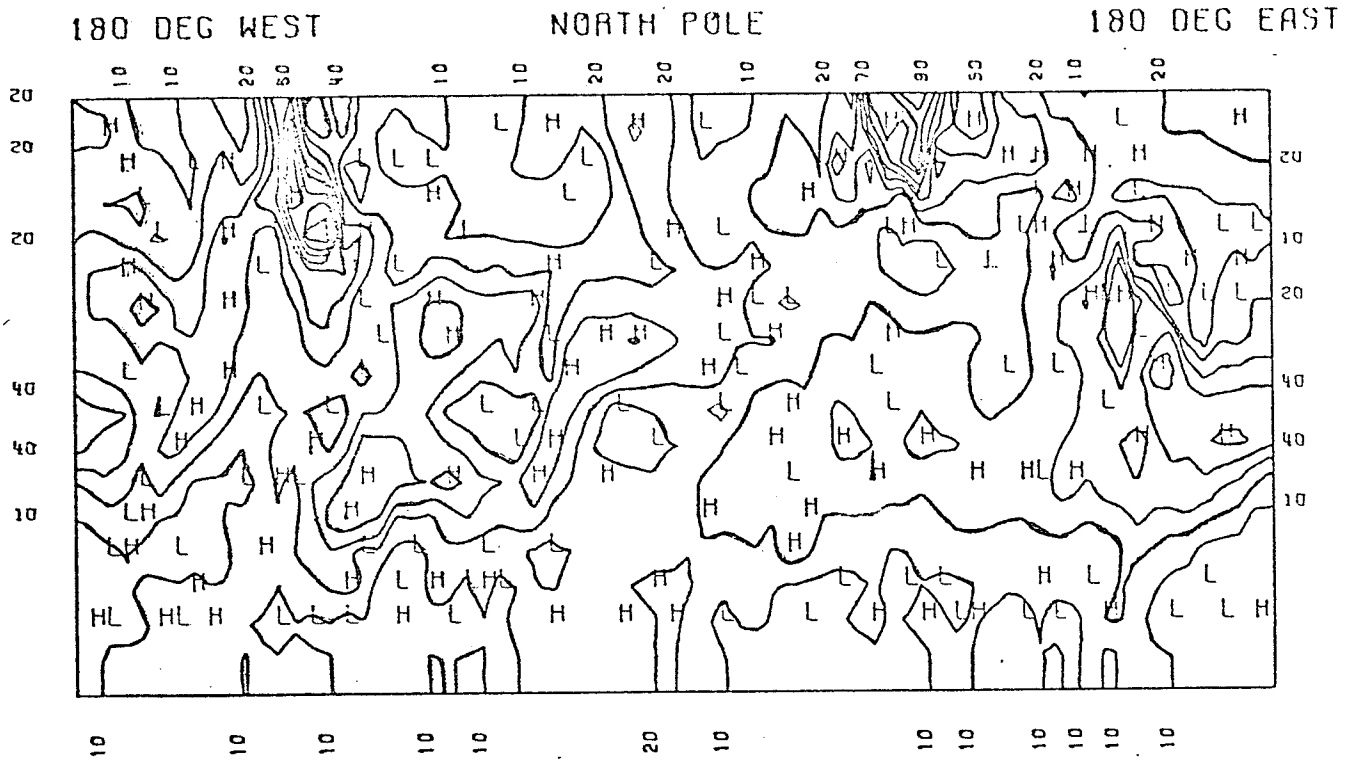

Figure 4.35: 400 mb Resultant Velocity Isotachs (m/sec), model P5, 36 hour

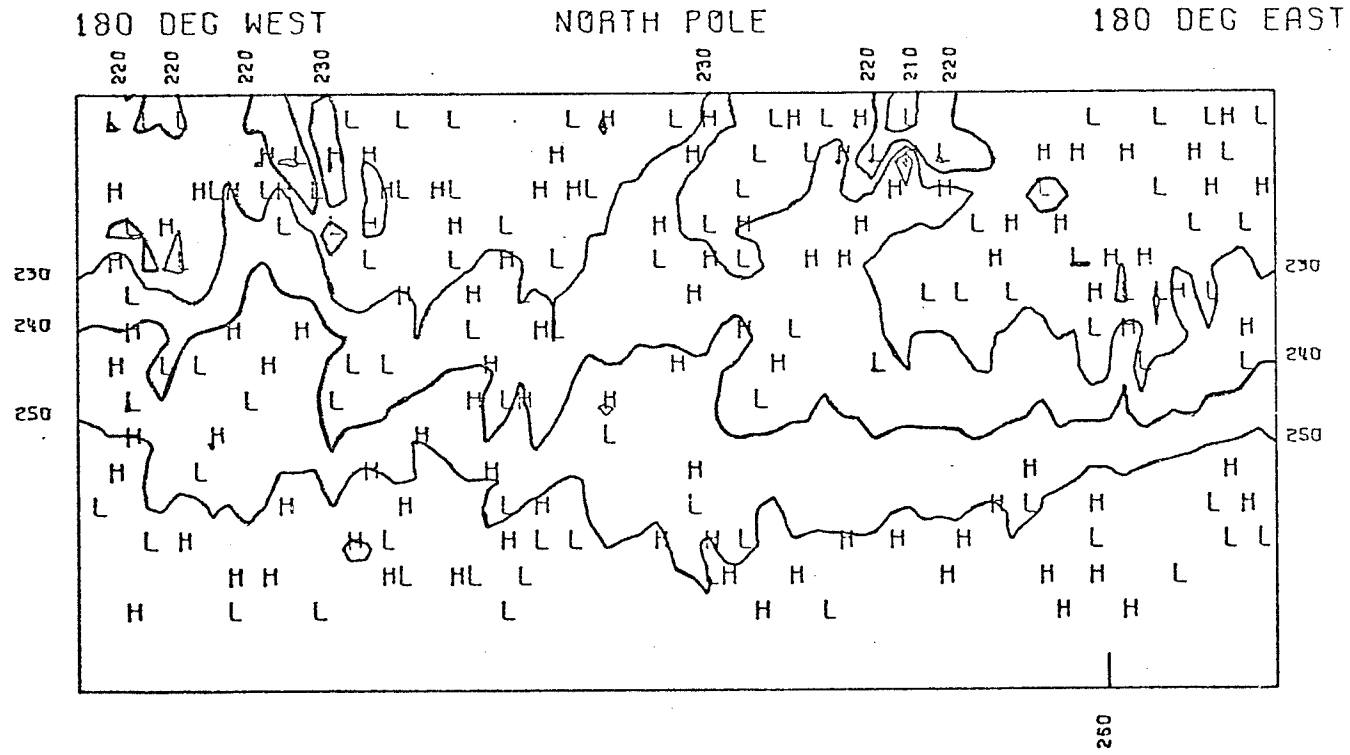

Figure 4.36: 400 mb Temperature (^{o}K), model P5, 36 hour

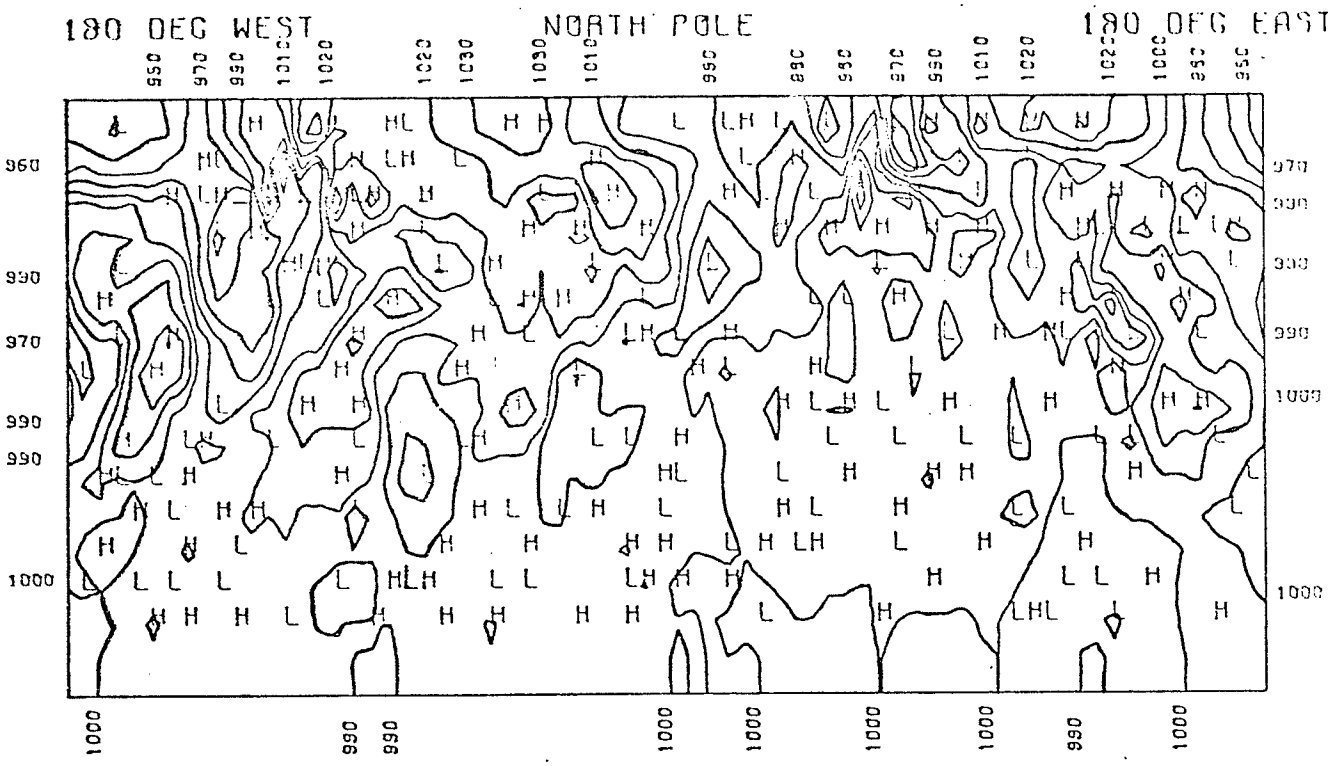

Figure 4.37: Surface Pressure (mb), model P5, 36 hour

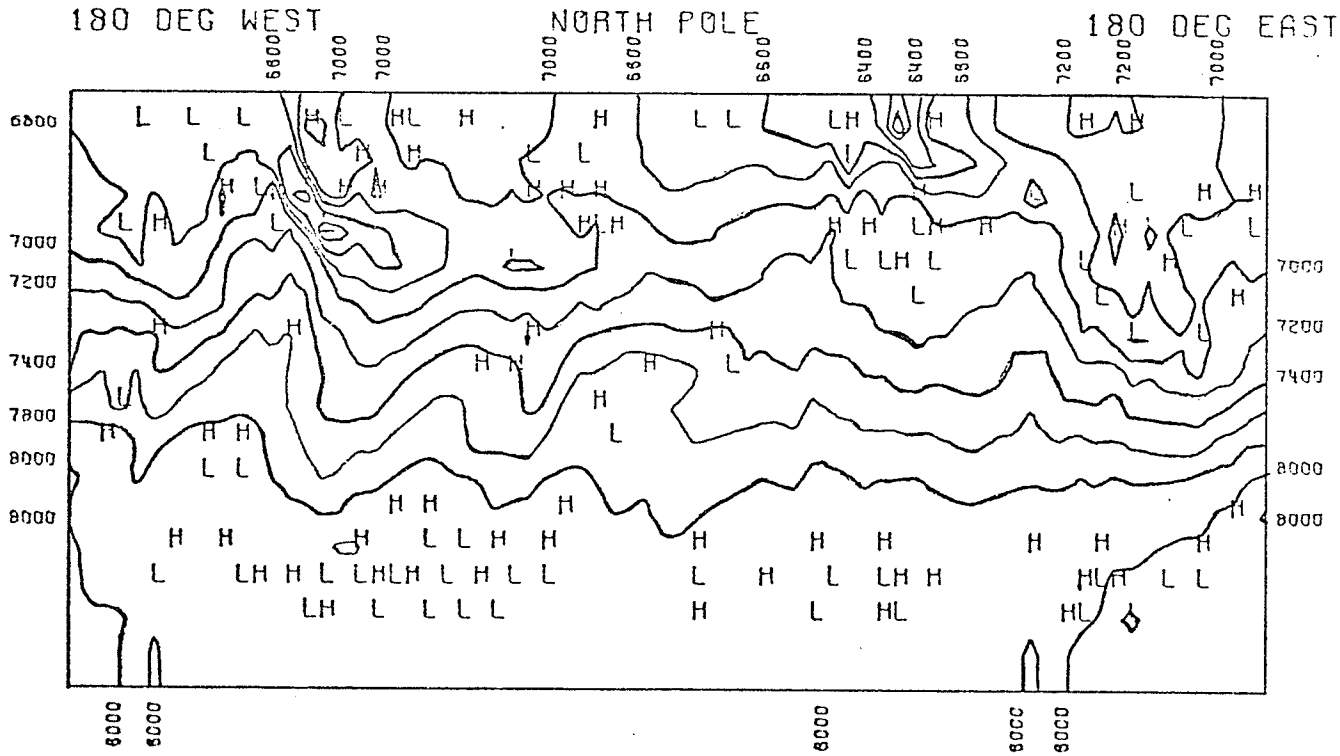

Figure 4.38: 400 mb Geopotential (m), model P5, 36 hour

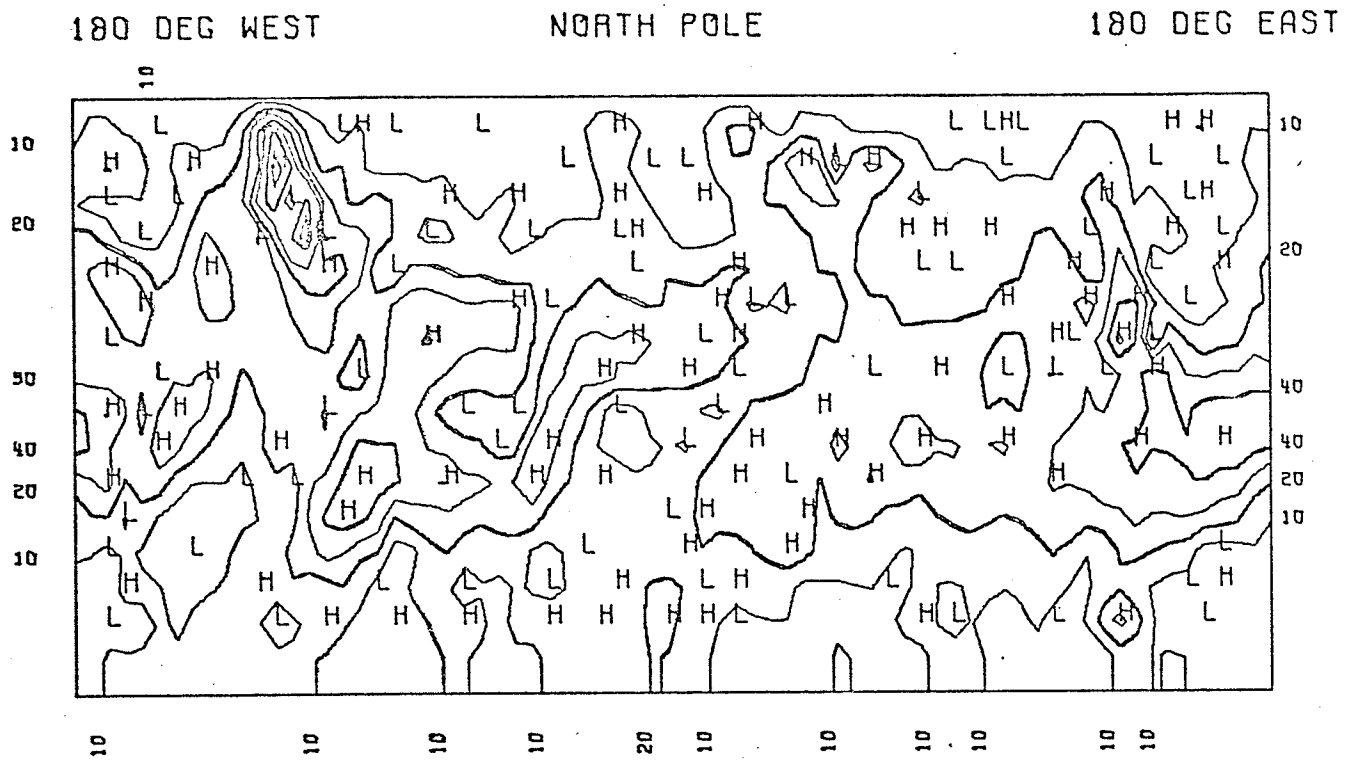

Figure 4.39: 400 mb Resultant Velocity Isotachs (m/sec), model P6, 36 hour

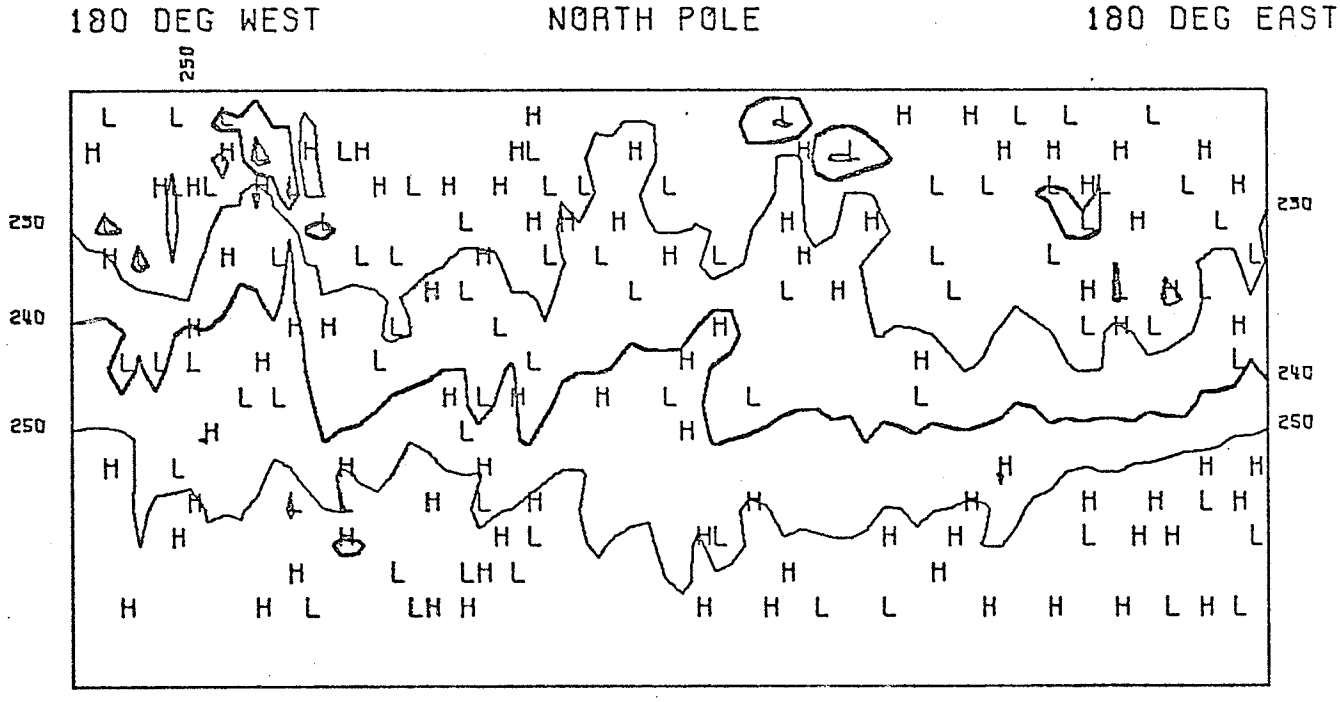

Figure 4.40: 400 mb Temperature (^{o}K), model P6, 36 hour

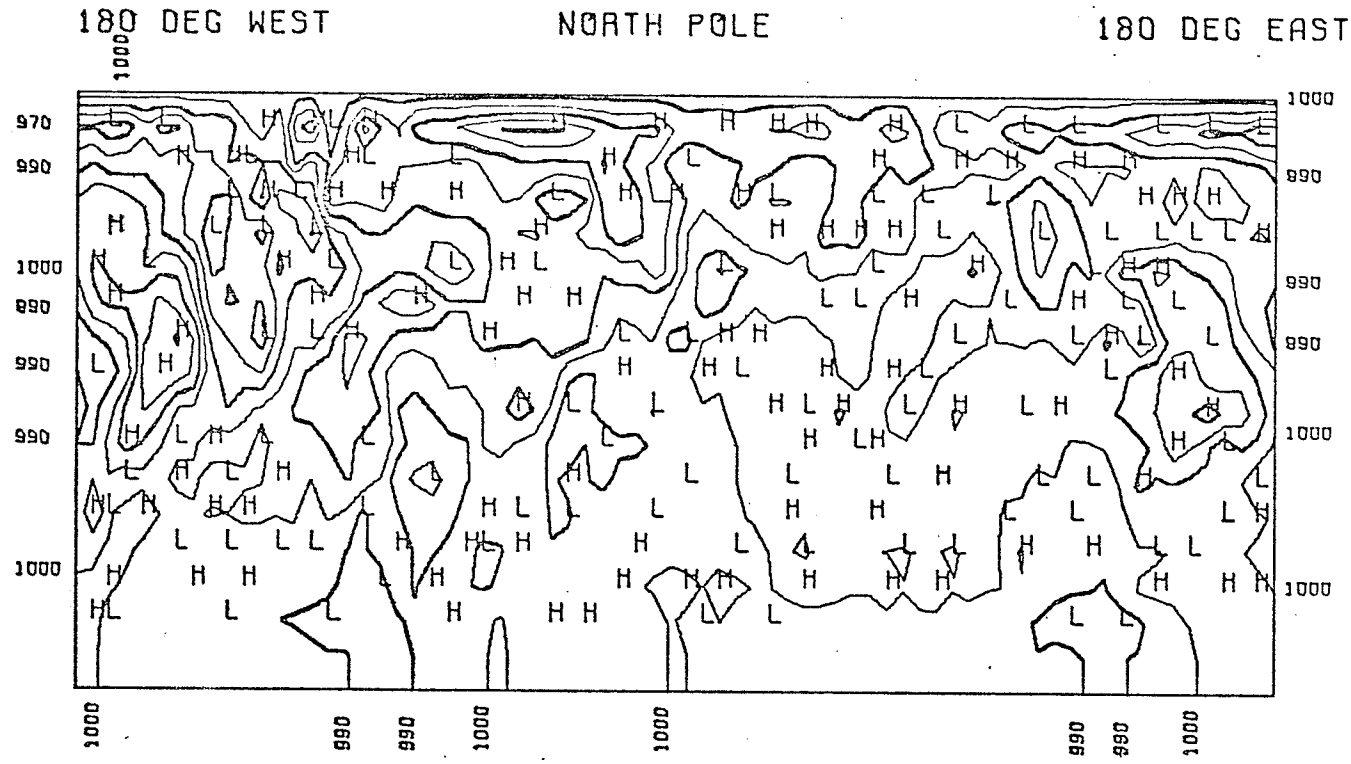

Figure 4.41: Surface Pressure (mb), model P6, 36 hour

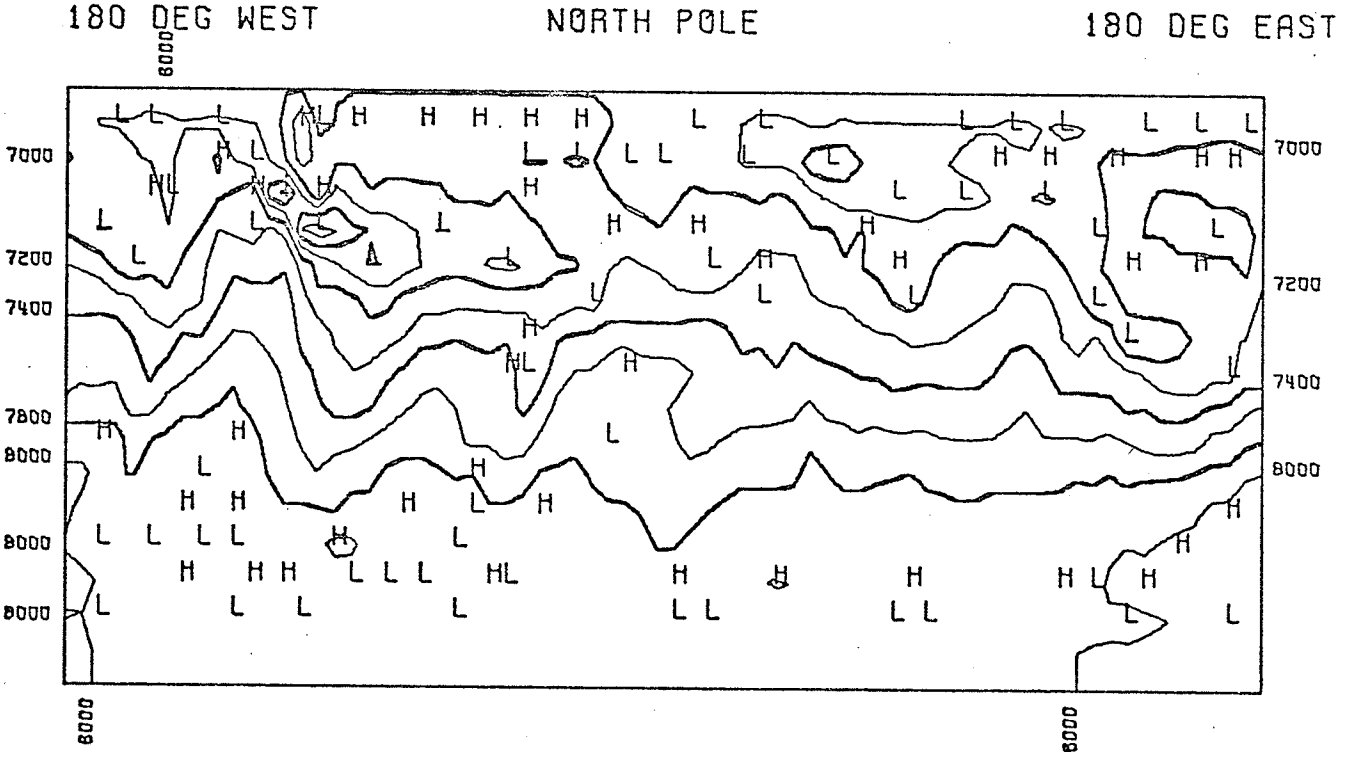

Figure 4.42: 400 mb Geopotential (m), model P6, 36 hour

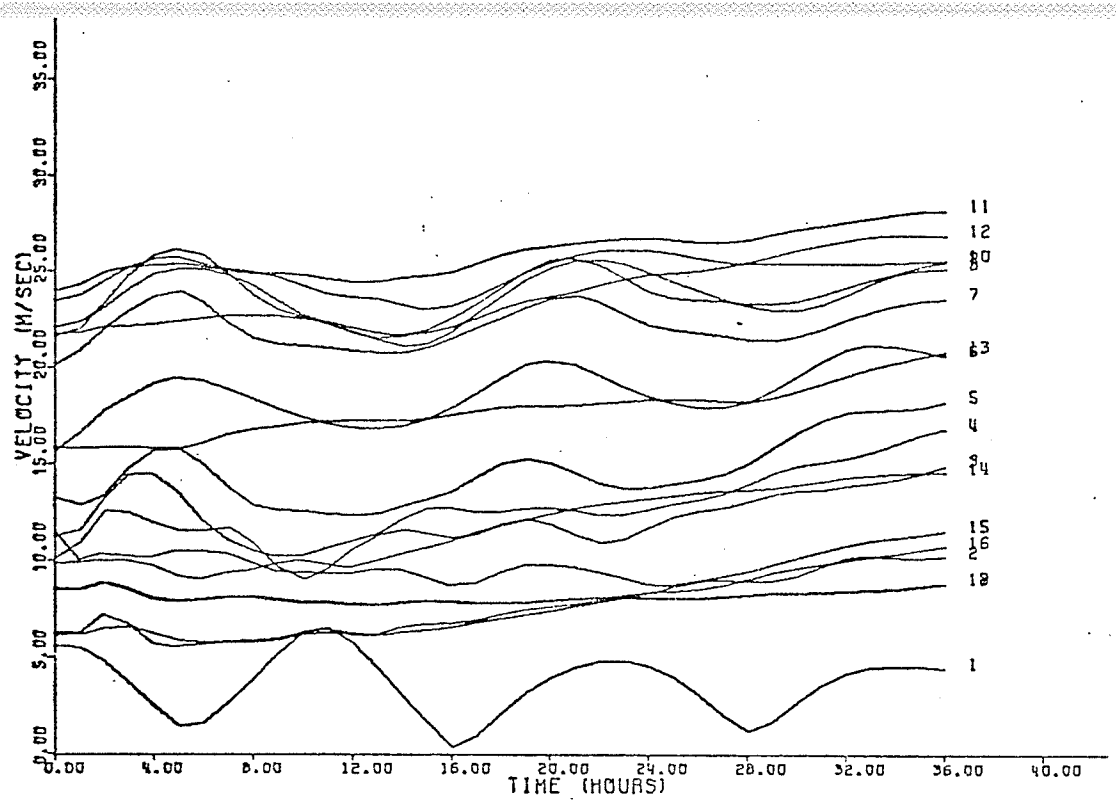

Figure 4.43: 400 mb Resultant Velocity Isotachs (m/sec), model P6, 0-36 hour zonal mean, numbers on the right denote the latitude circle, 1 denotes the north pole, 18 denotes the equator

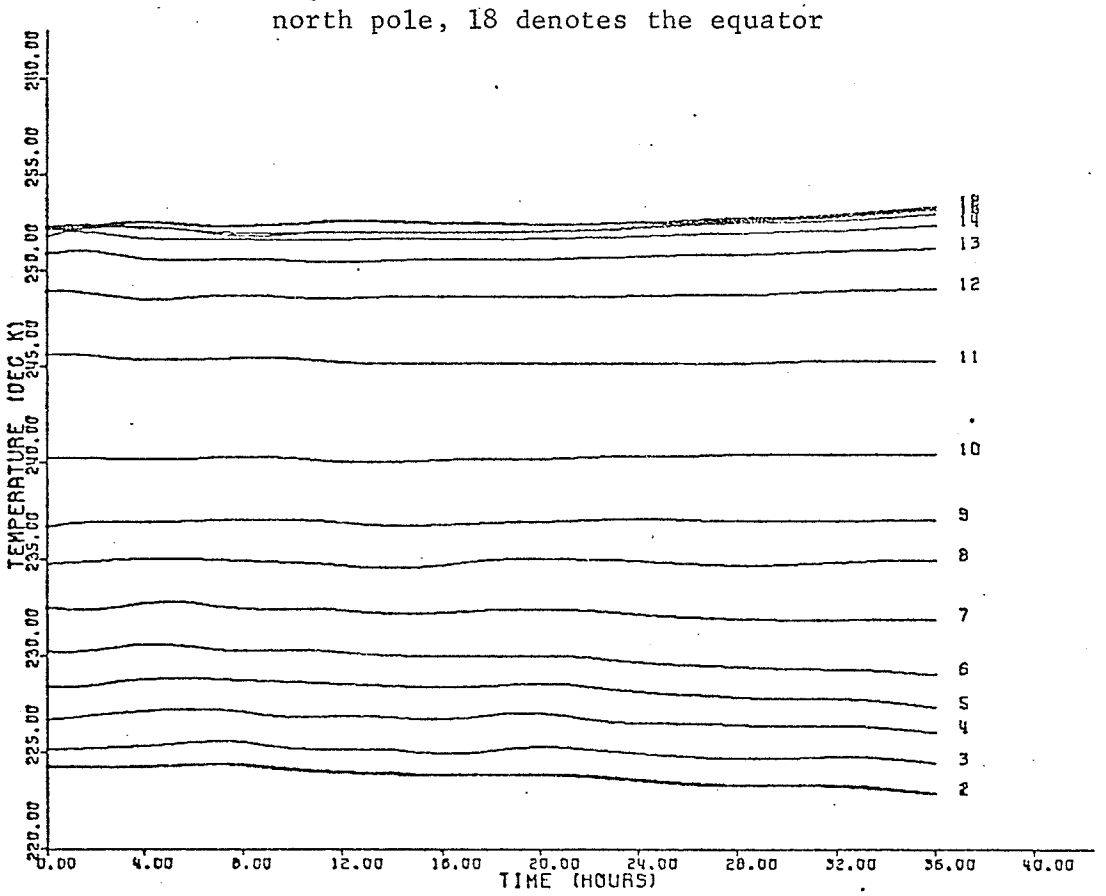

Figure 4.44: 400 mb Temperature (^{o}K), model P6, 0-36 hour zonal mean, numbers on the right denote the latitude circle, 1 denotes the north pole, 18 denotes the equator

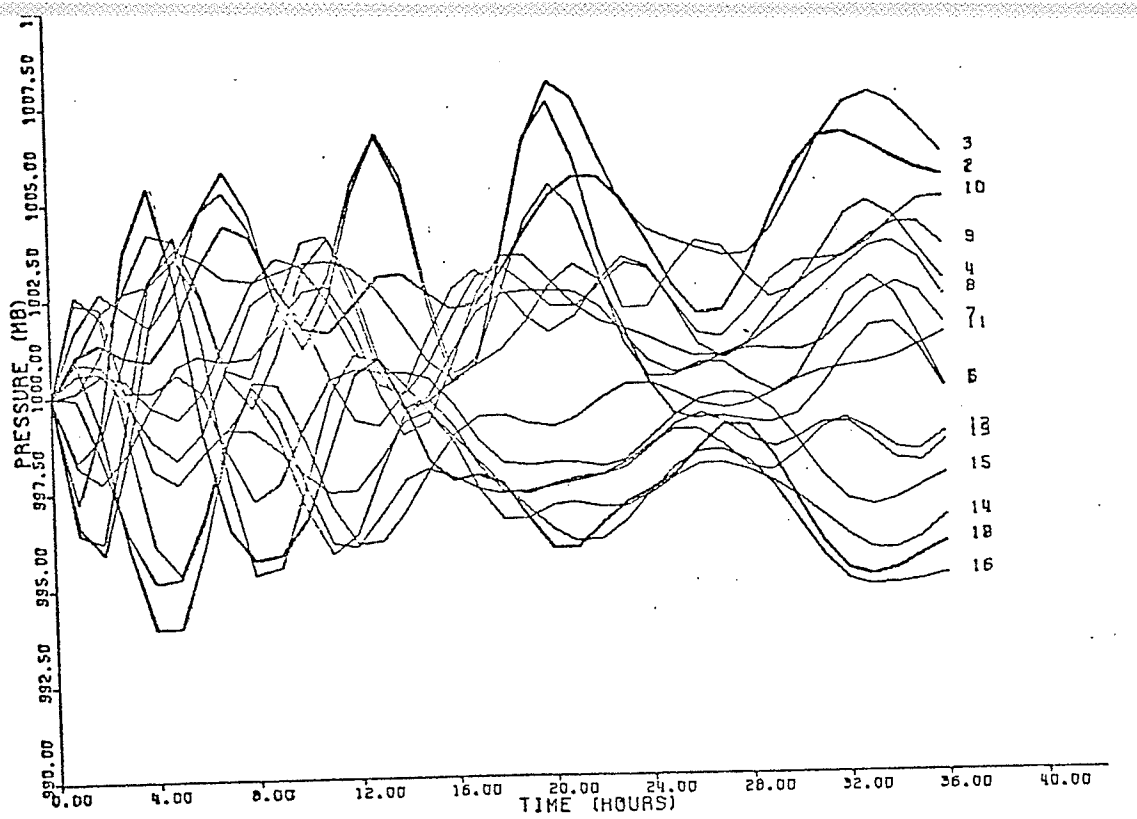

Figure 4.45: Surface Pressure (mb), model P6, 0-36 hour zonal mean, numbers on the right denote the latitude circle, 1 denotes the north pole, 18 denotes the equator

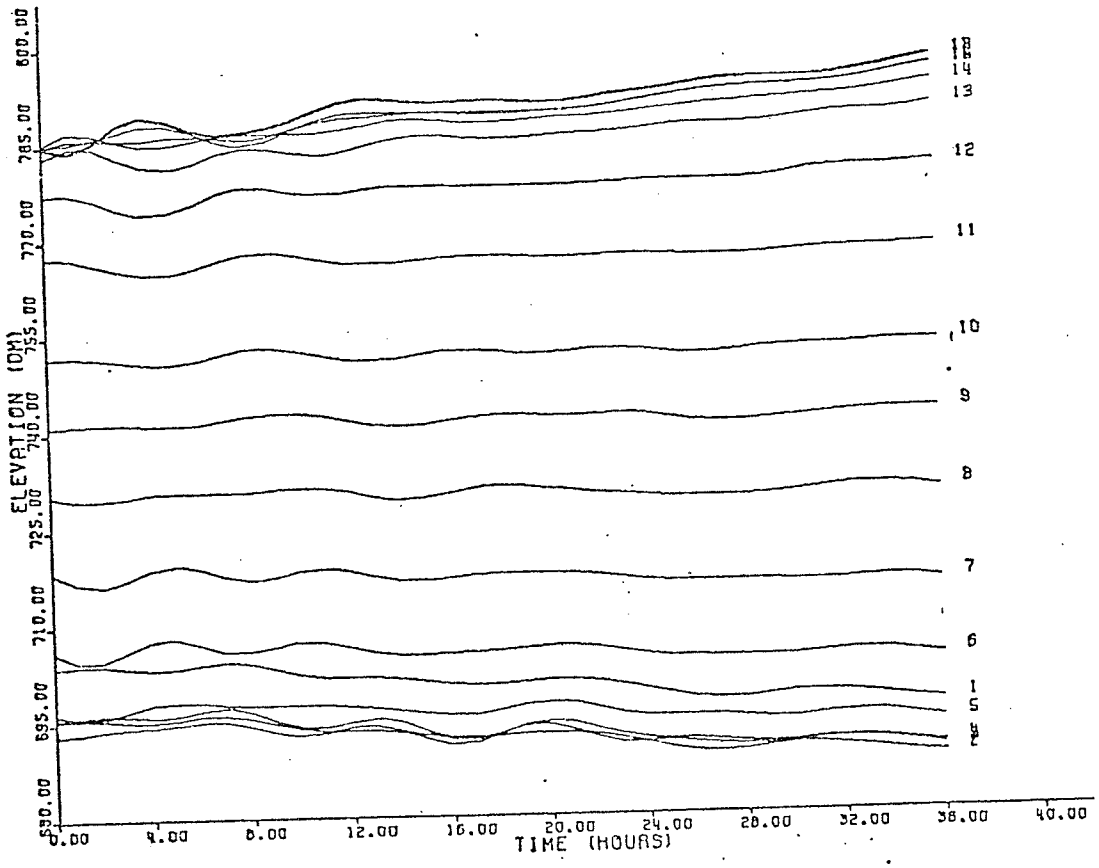

Figure 4.46: 400 mb Geopotential (dm), model P6, 0-36 hour zonal mean, numbers on the right denote the latitude circle, 1 denotes the north pole, 18 denotes the equator

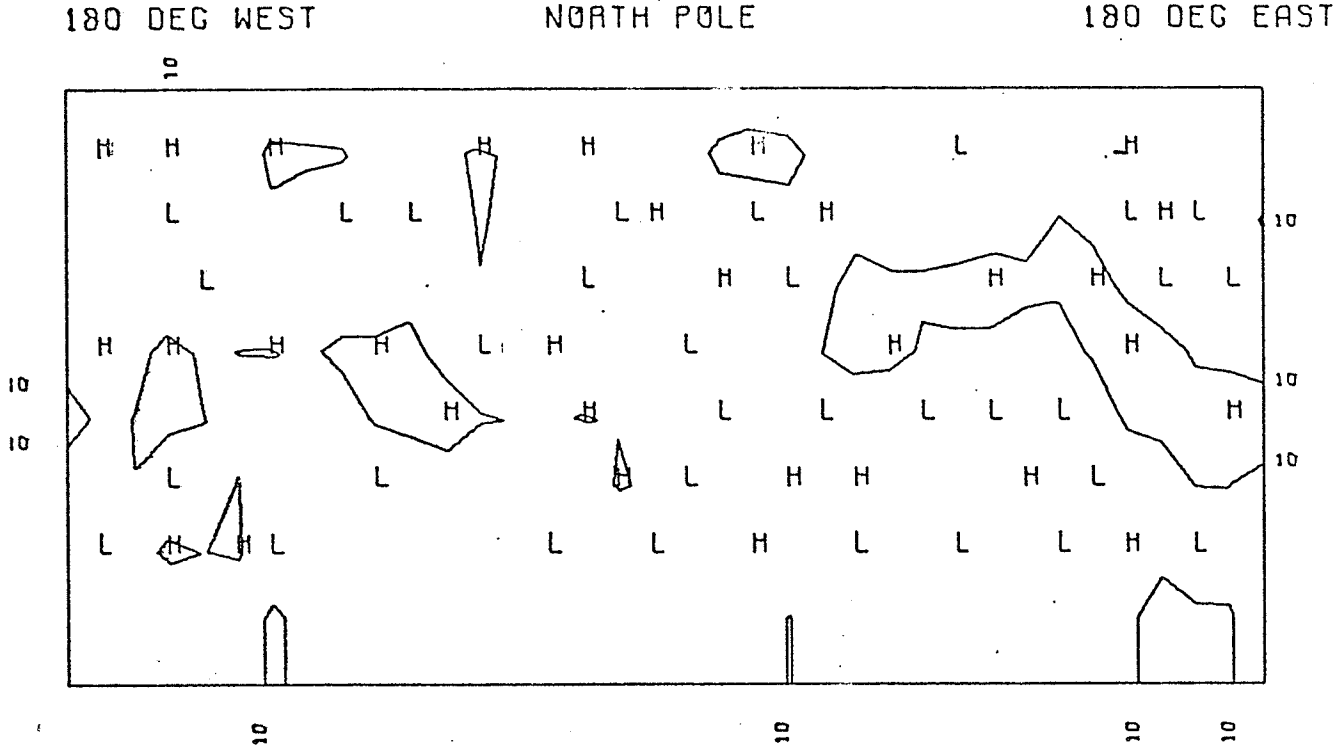

Figure 4.47: 800 mb Resultant Velocity Isotachs (m/sec), model P7, 36 hour

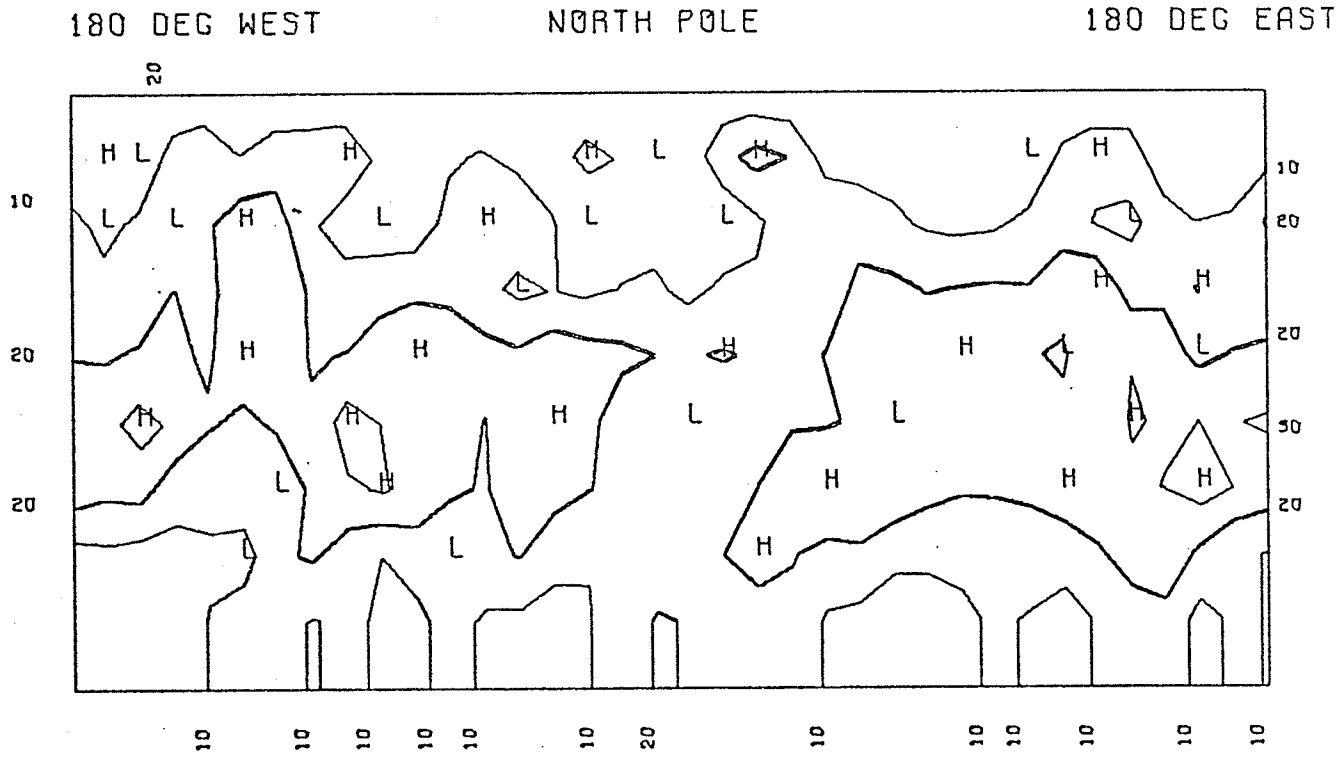

Figure 4.48: 400 mb Resultant Velocity Isotachs (m/sec), model P7, 36 hour

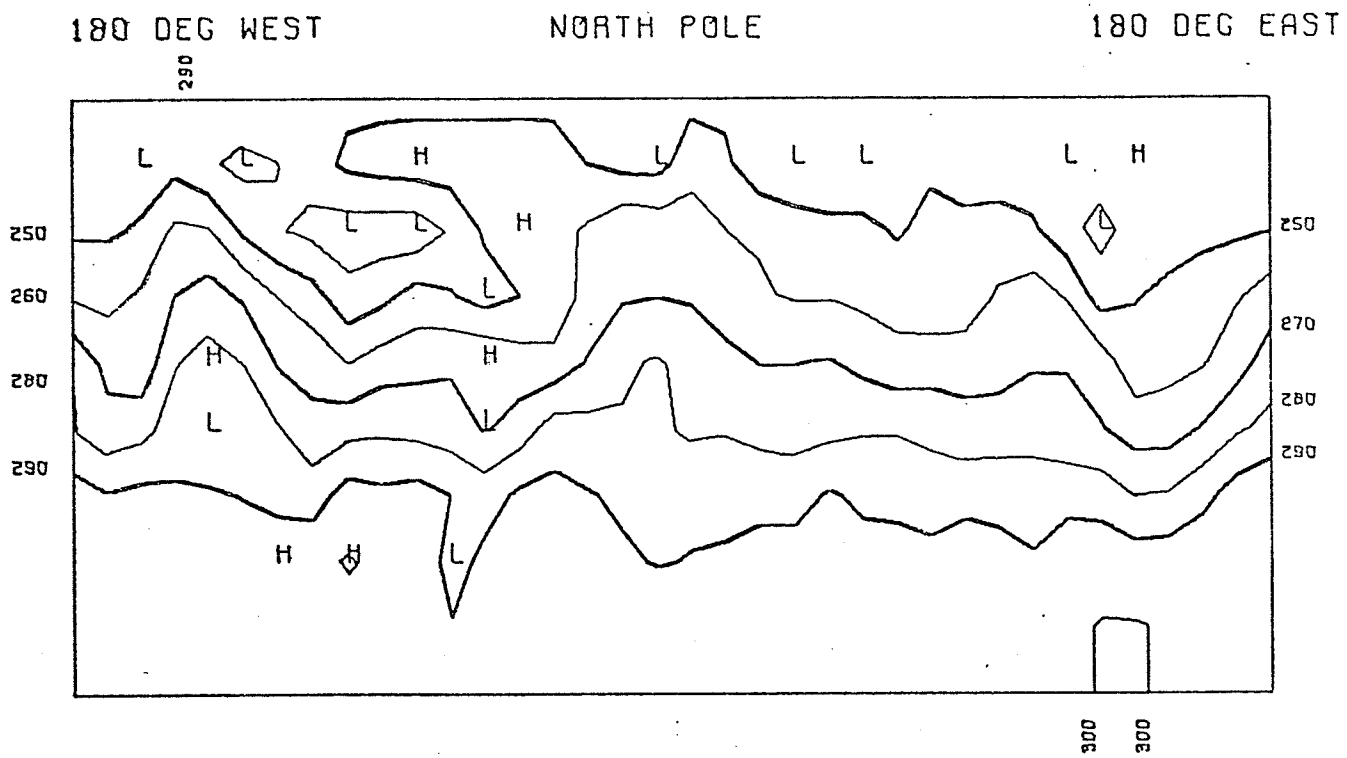

Figure 4.49: 800 mb Temperature (^{o}K), model P7, 36 hour

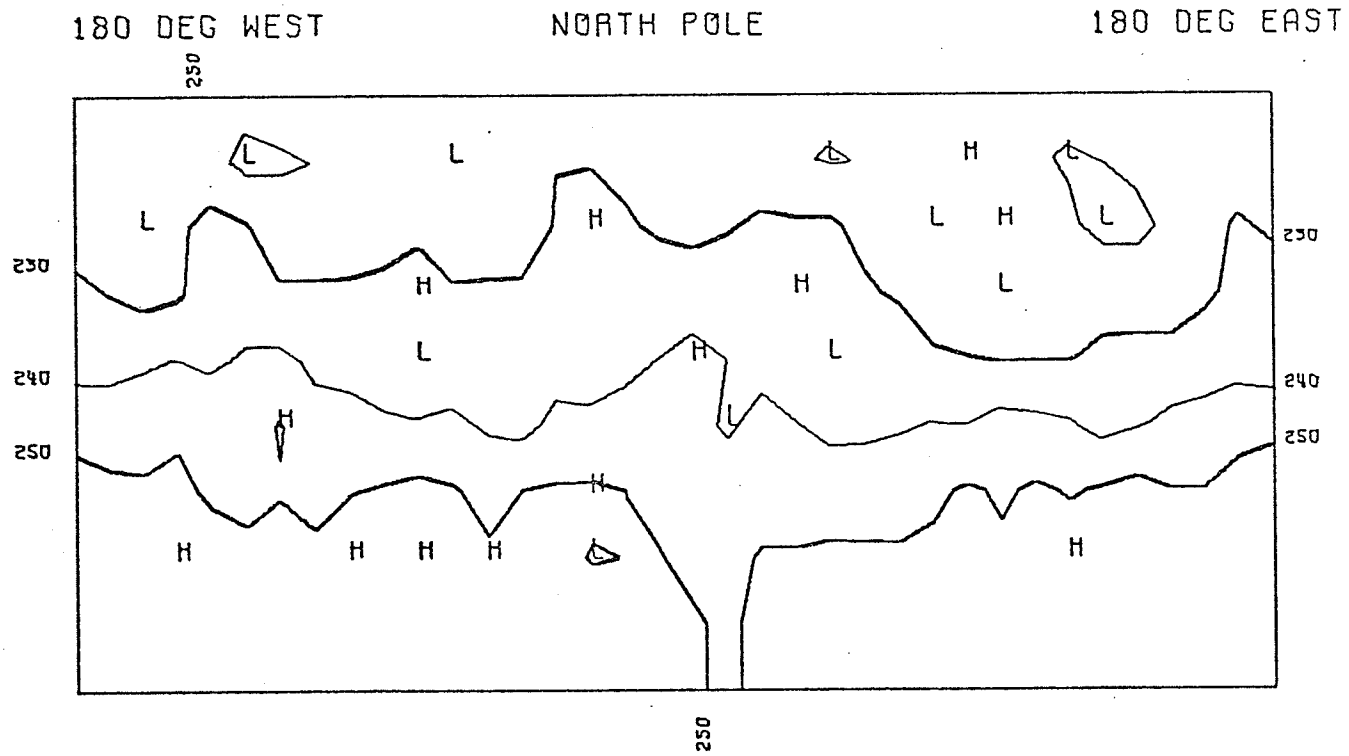

Figure 4.50: 400 mb Temperature (^{o}K), model P7, 36 hour

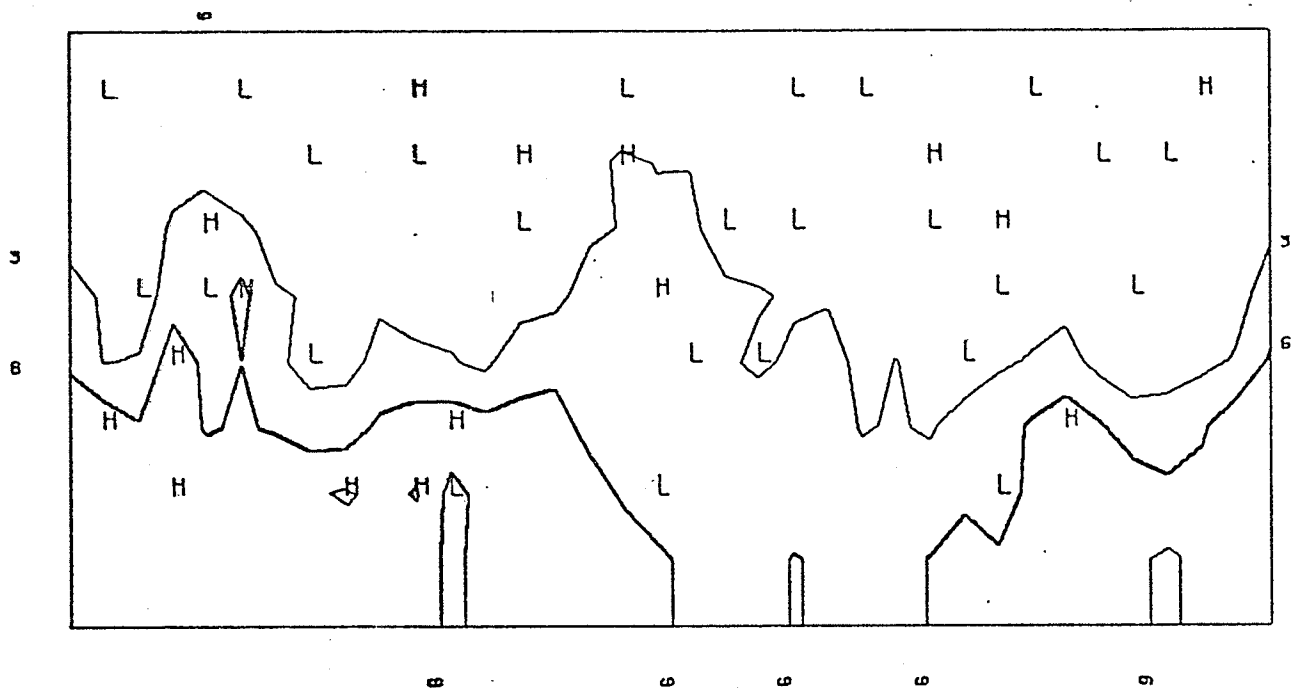

Figure 4.51: 800 mb Moisture (g H_2O/g dry air x 10^{-3}), model P7, 36 hour

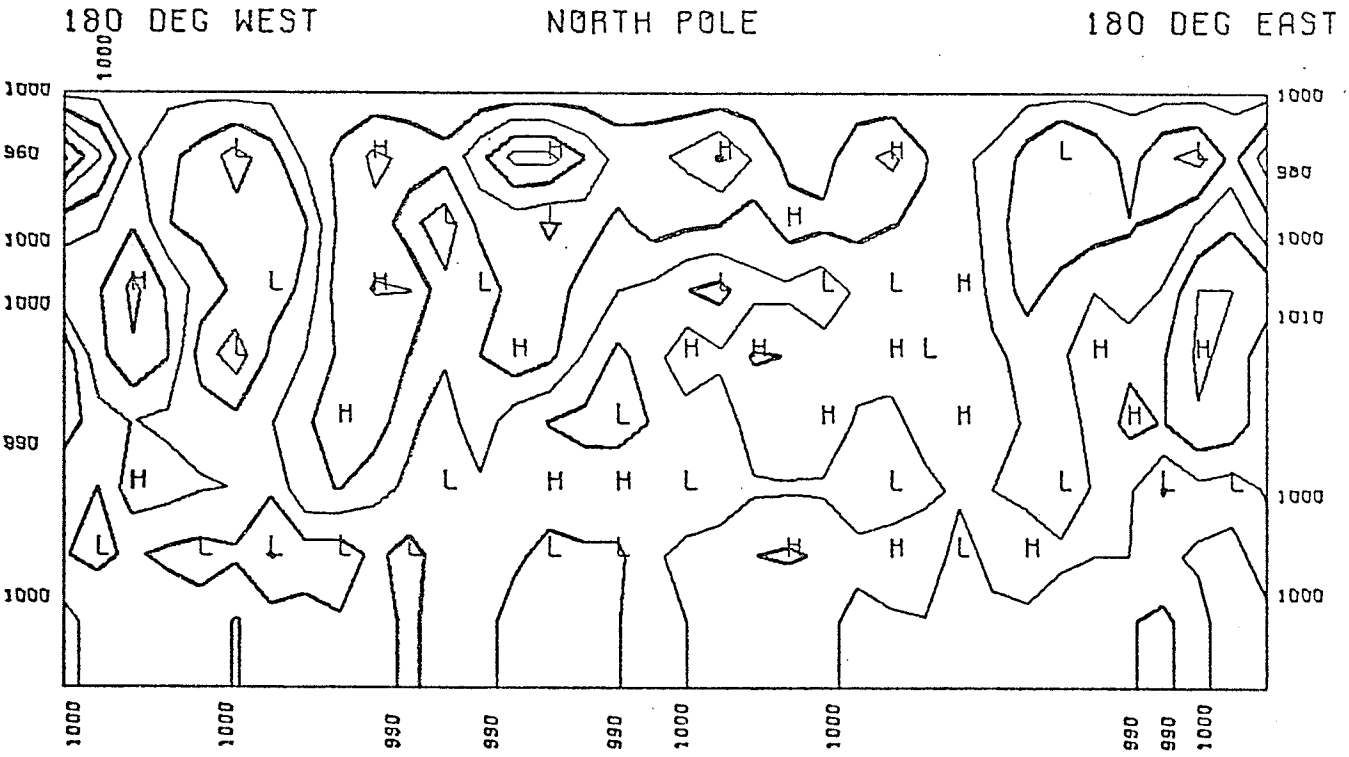

Figure 4.52: Surface Pressure (mb), model P7, 36 hour

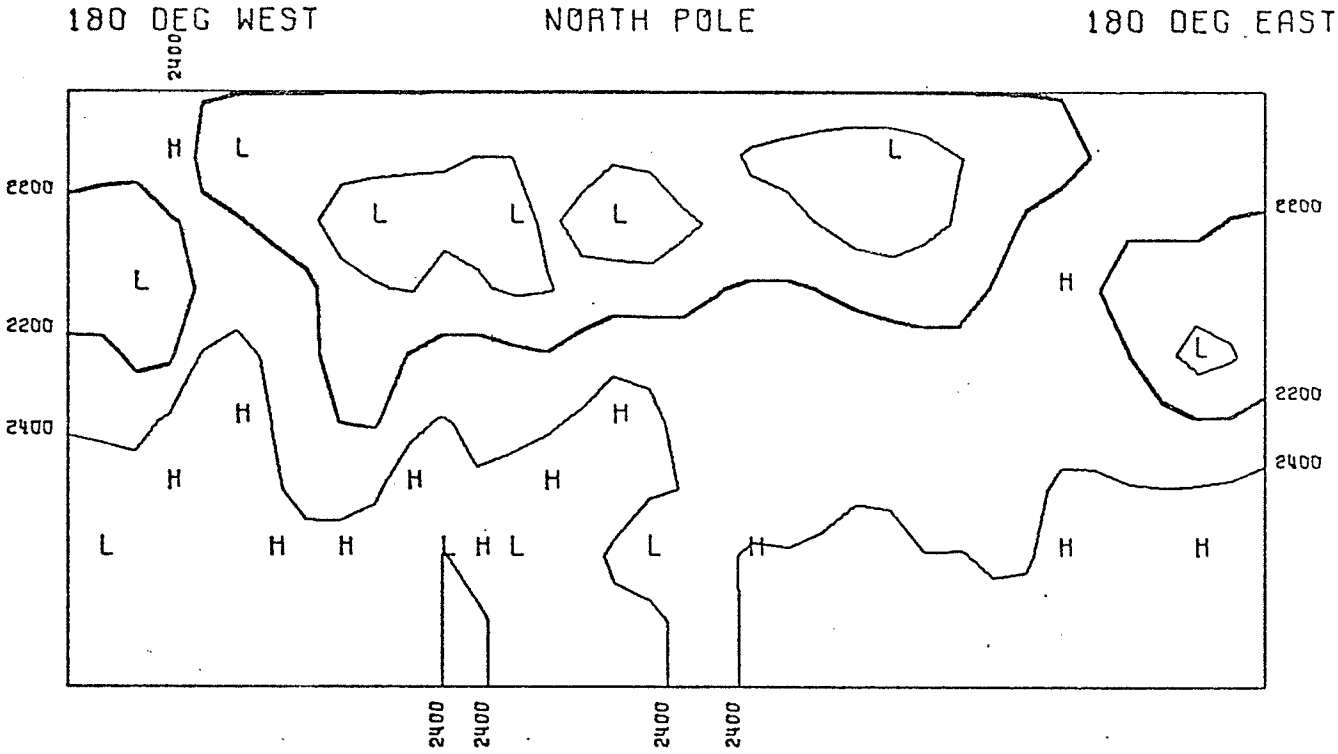

Figure 4.53: 800 mb Geopotential (m), model P7, 36 hour

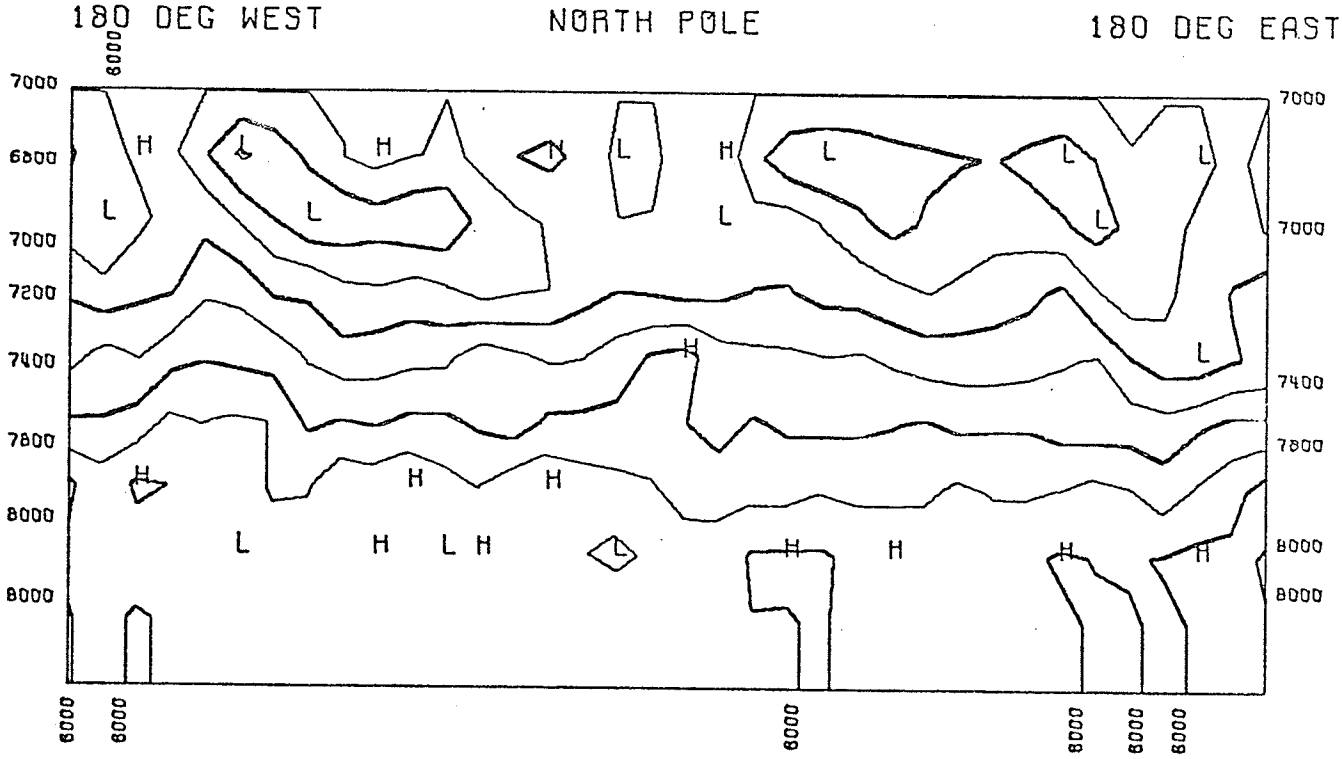

Figure 4.54: 400 mb Geopotential (m), model P7, 36 hour

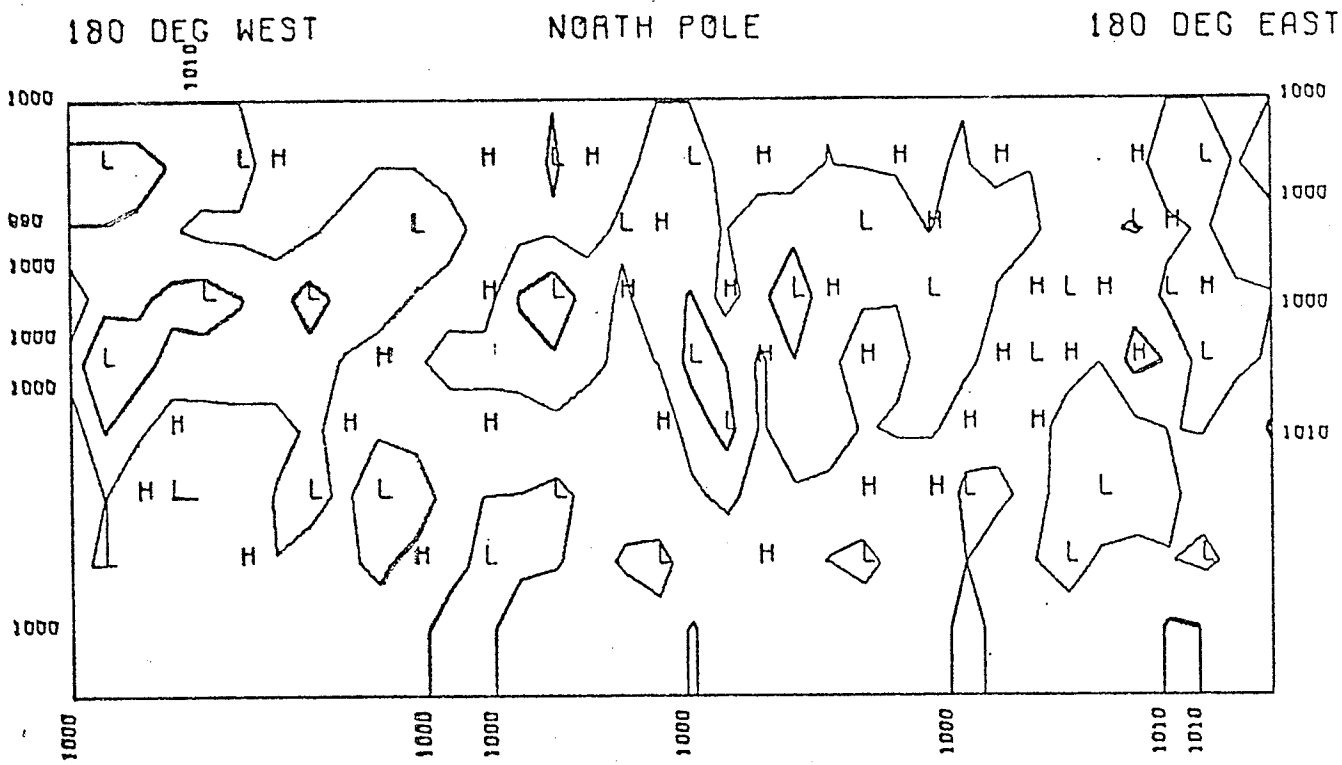

Figure 4.55: 800 mb Resultant Velocity Isotachs (m/sec), model P7, 36 hour error, 1000 represents zero error

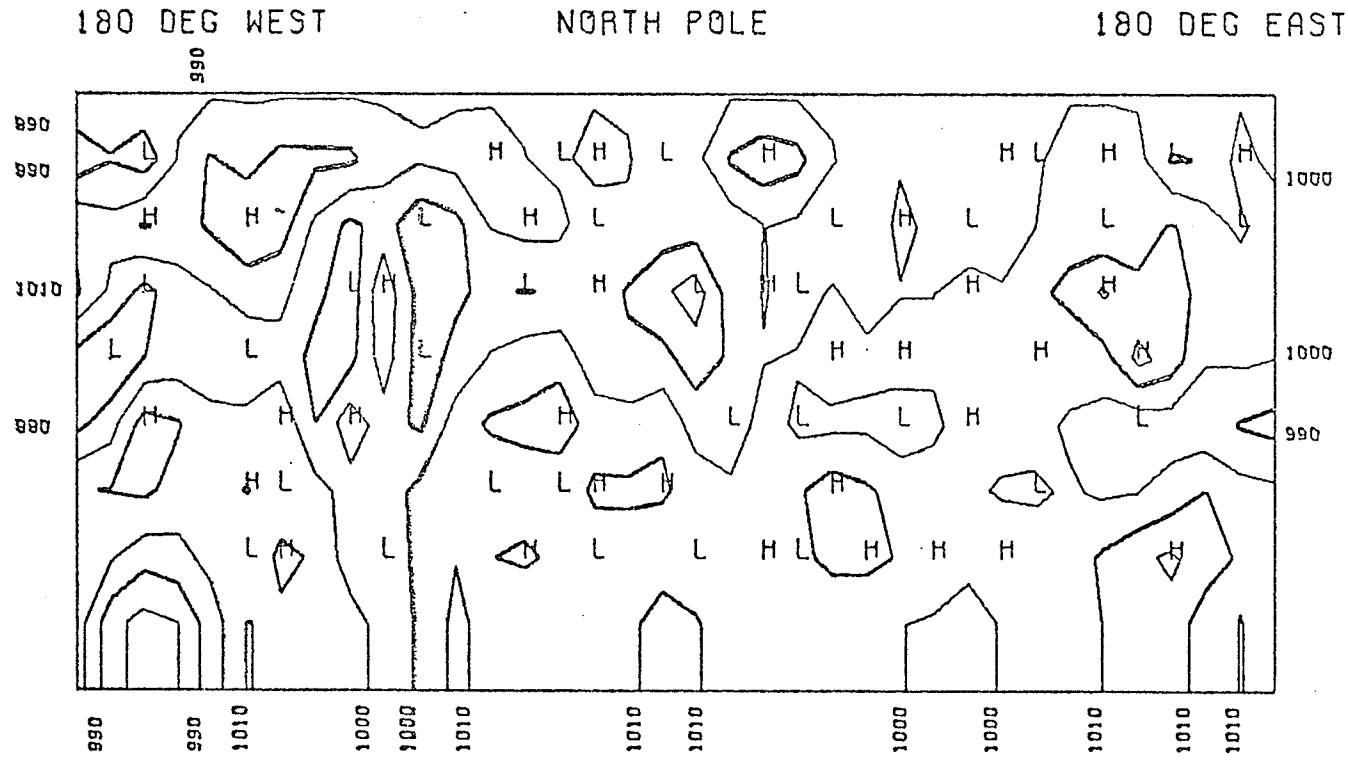

Figure 4.56: 400 mb Resultant Velocity Isotachs (m/sec), model P7, 36 hour error, 1000 represents zero error

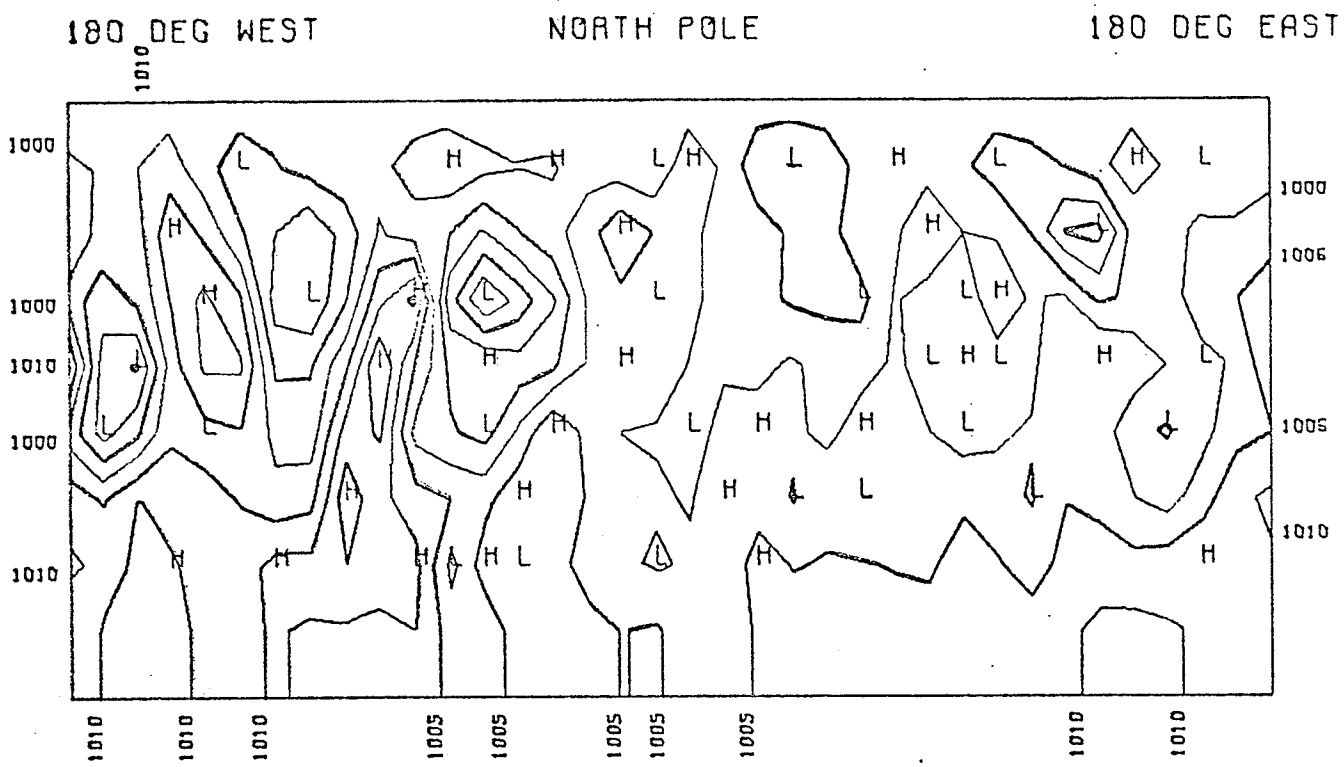

Figure 4.57: 800 mb Temperature (^{o}K), model P7, 36 hour error, 1000 represents zero error

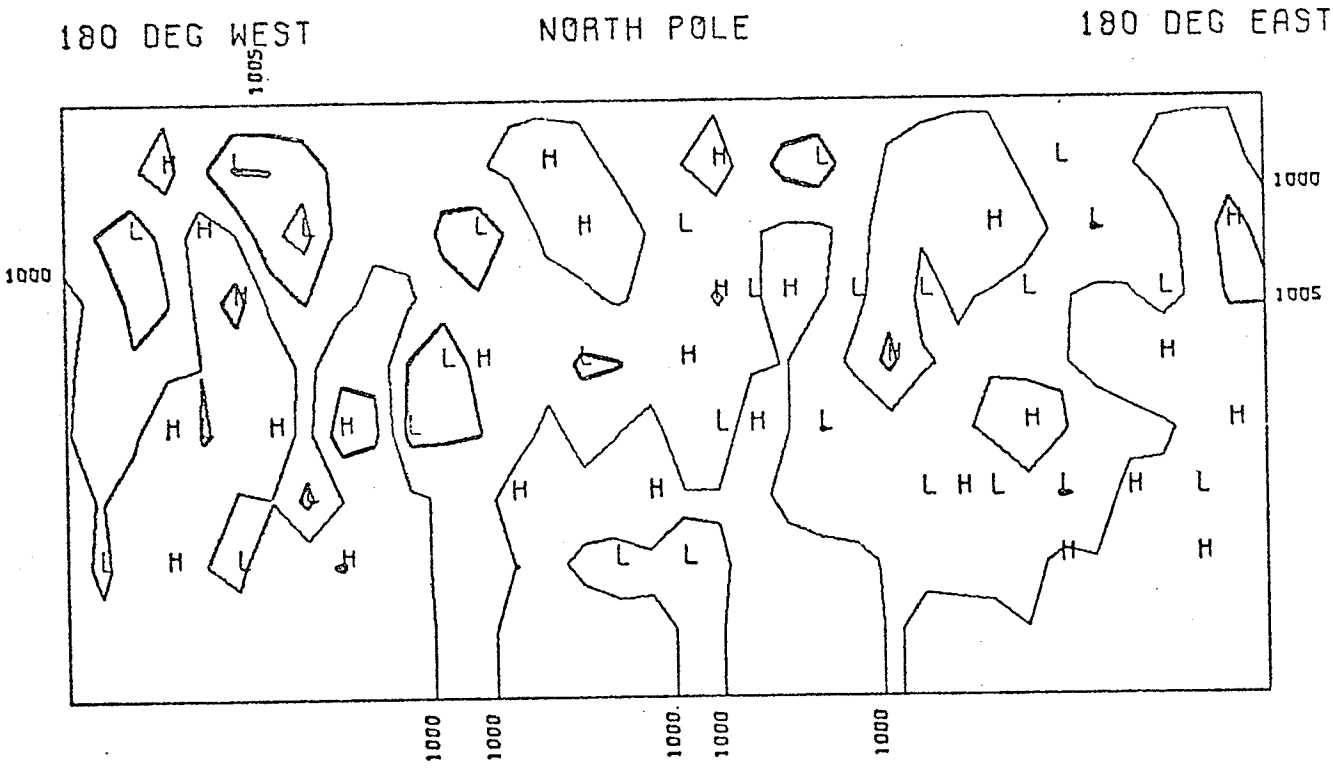

Figure 4.58: 400 mb Temperature (^{o}K), model P7, 36 hour error, 1000 represents zero error

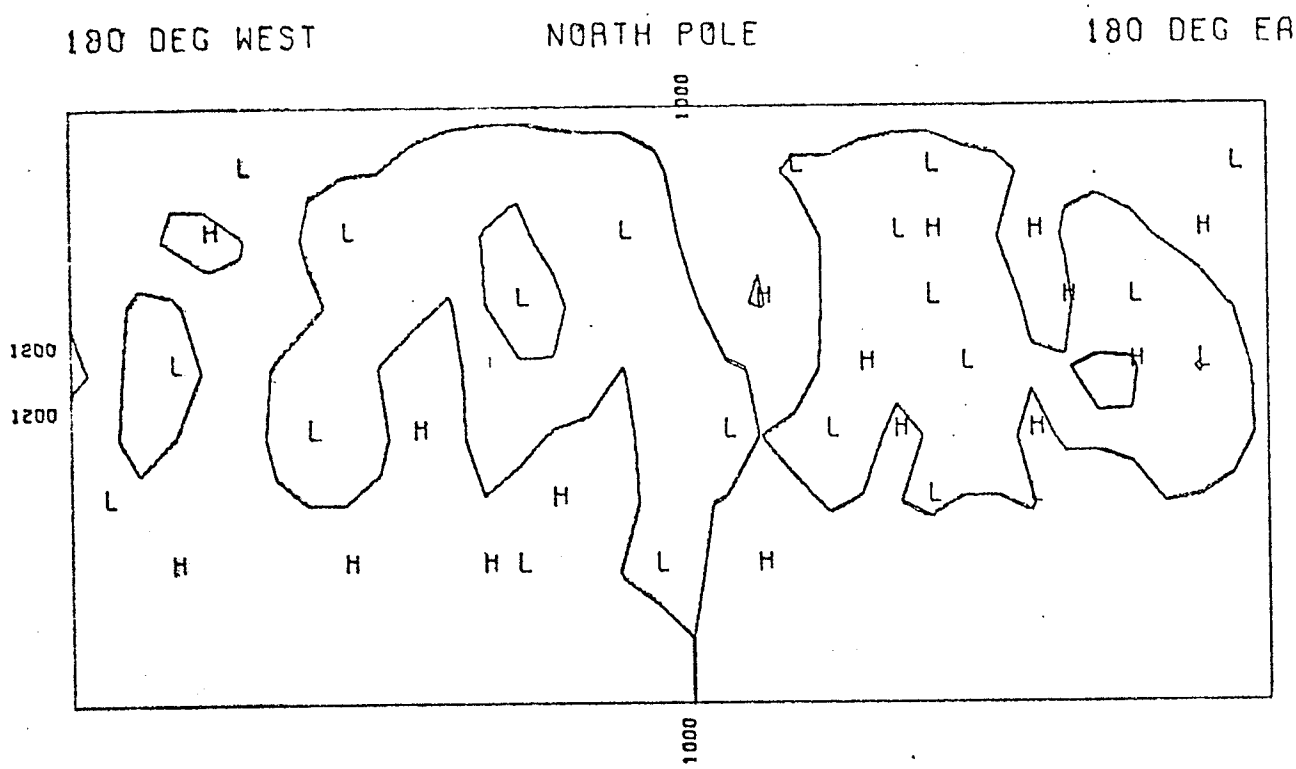

Figure 4.59: 800 mb Geopotential (m), model P7, 36 hour error, 1000 represents zero error

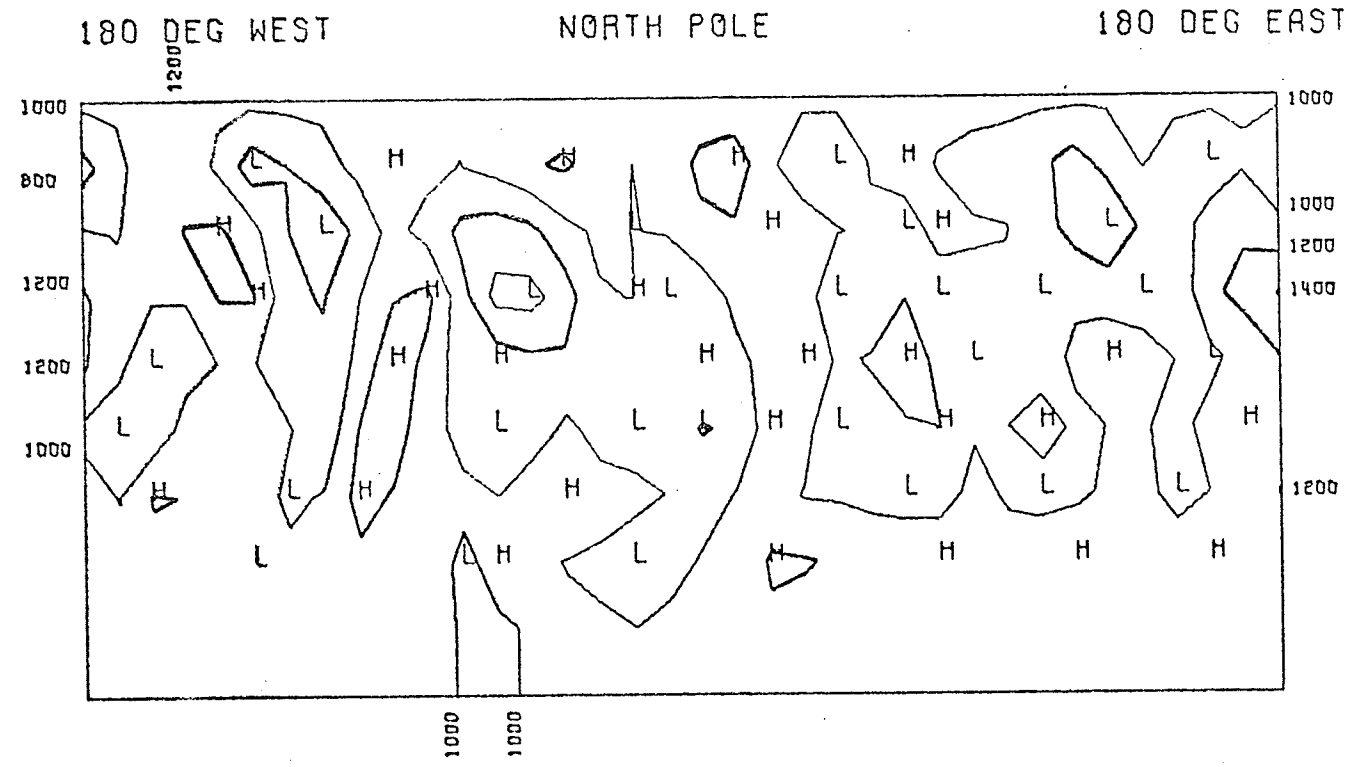

Figure 4.60: 400 mb Geopotential (m), model P7, 36 hour error, 1000 represents zero error

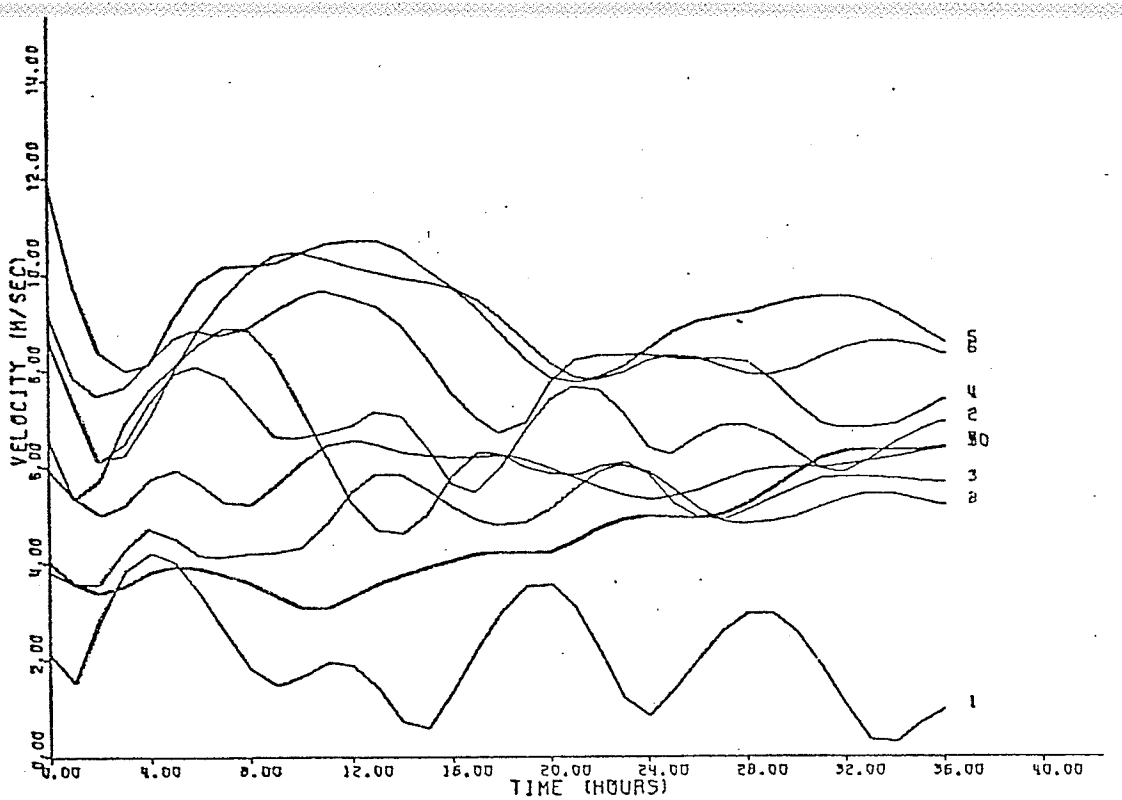

Figure 4.61: 800 mb Resultant Velocity Isotachs (m/sec), model P7, 0-36 hour zonal mean, numbers on the right denote the latitude circle, 1 denotes the north pole, 10 denotes the equator

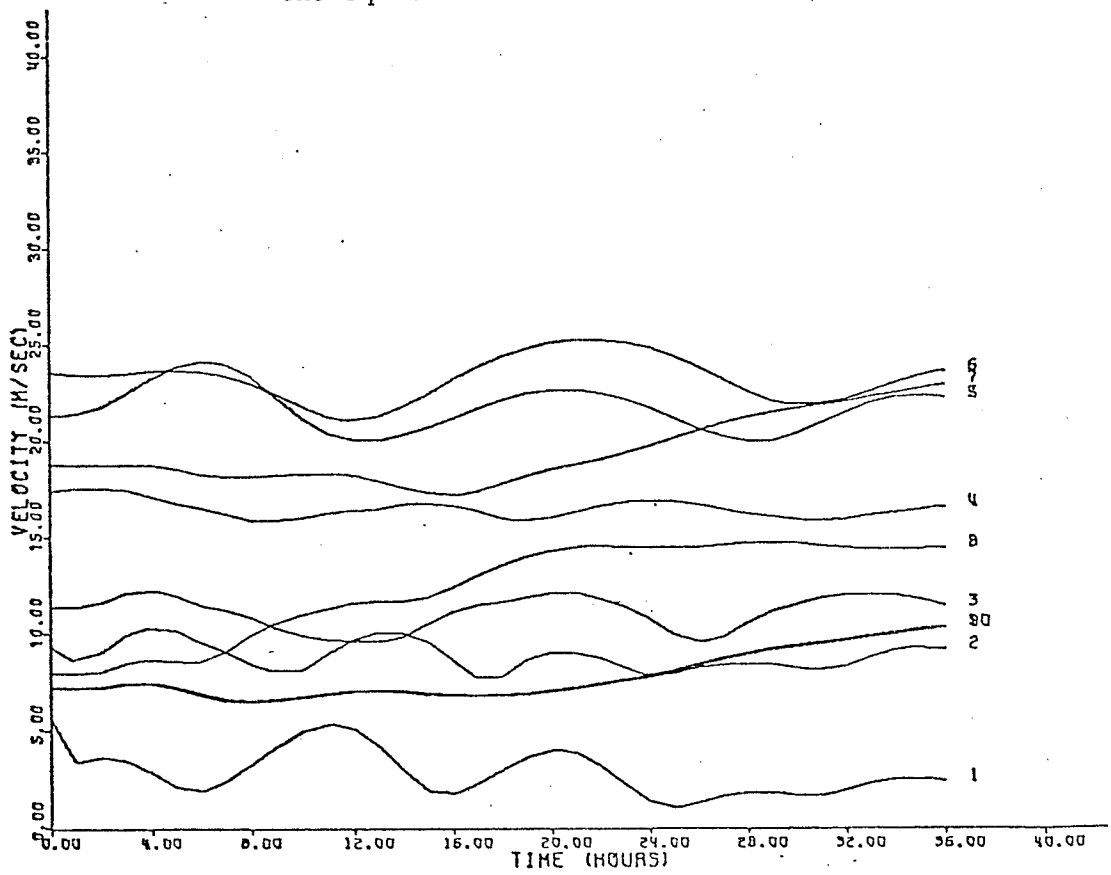

Figure 4.62: 400 mb Resultant Velocity Isotachs (m/sec), model P7, 0-36 hour zonal mean, numbers on the right denote the latitude circle, 1 denotes the north pole, 10 denotes the equator

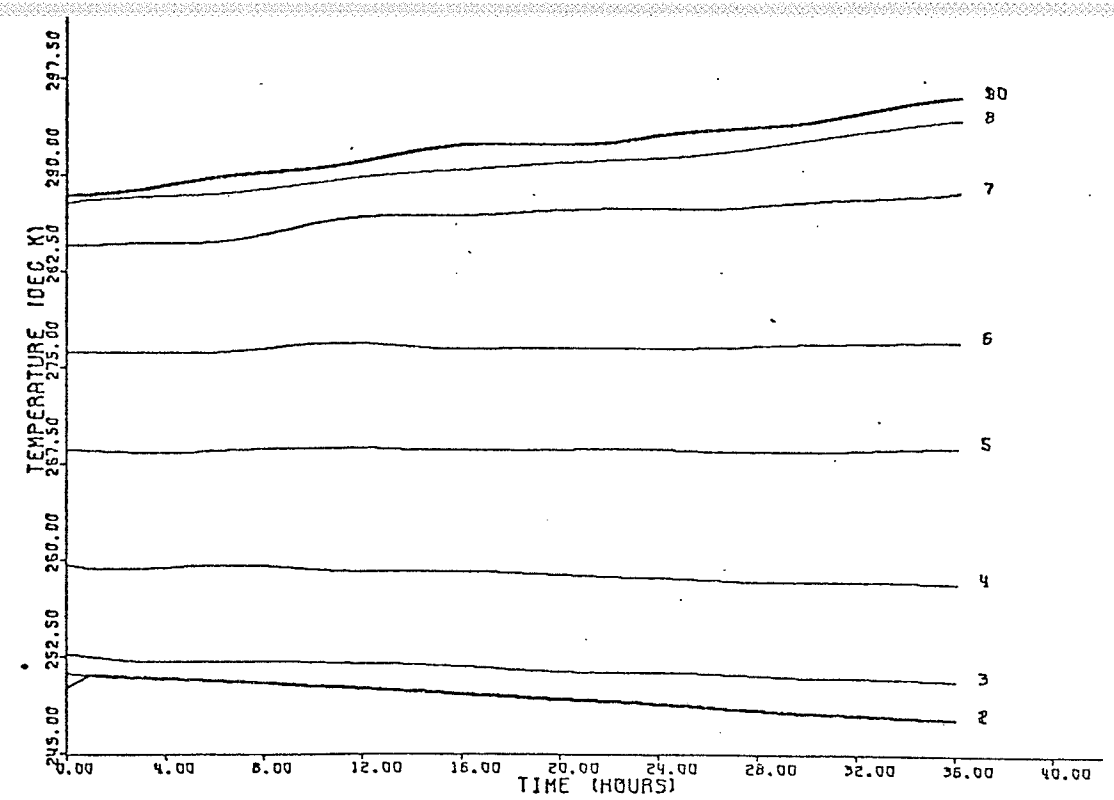

Figure 4.63: 800 mb Temperature (^{o}K), model P7, 0-36 hour zonal mean, numbers on the right denote the latitude circle, 1 denotes the north pole, 10 denotes the equator

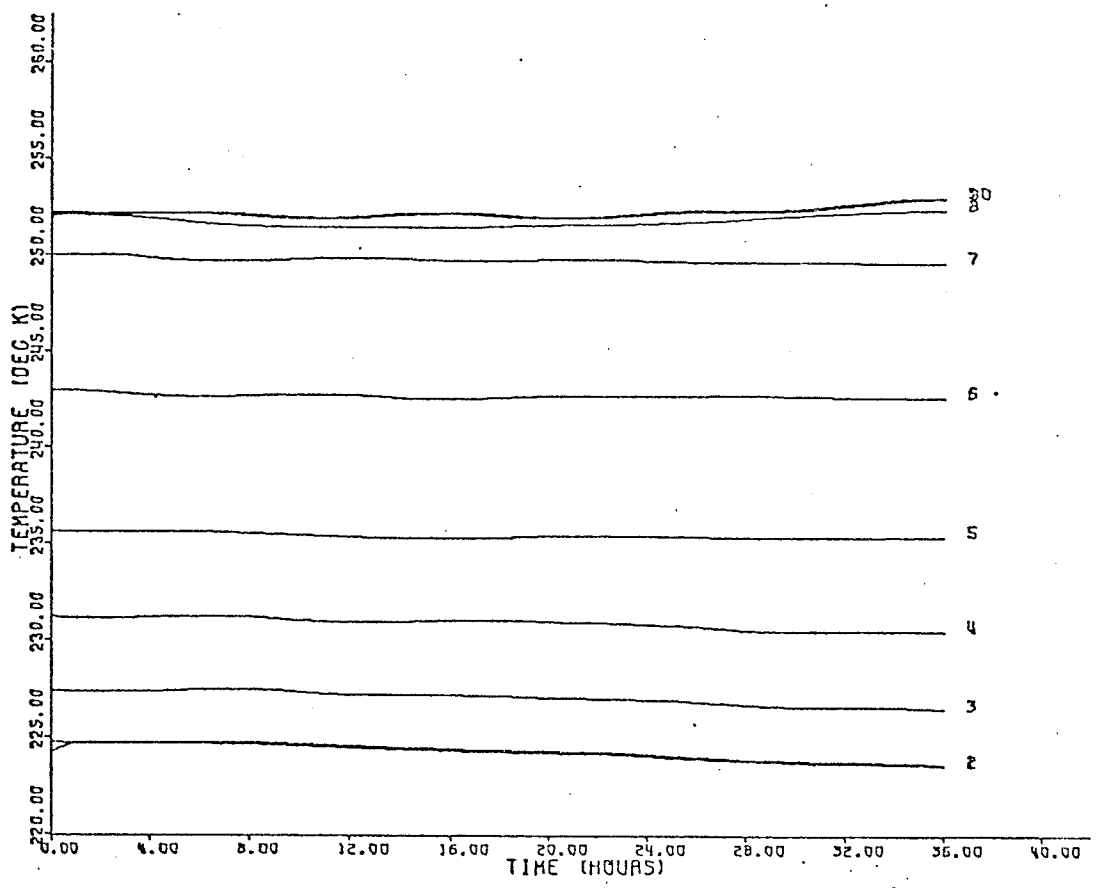

Figure 4.64: 400 mb Temperature (^{o}K), model P7, 0-36 hour zonal mean, numbers on the right denote the latitude circle, 1 denotes the north pole, 10 denotes the equator

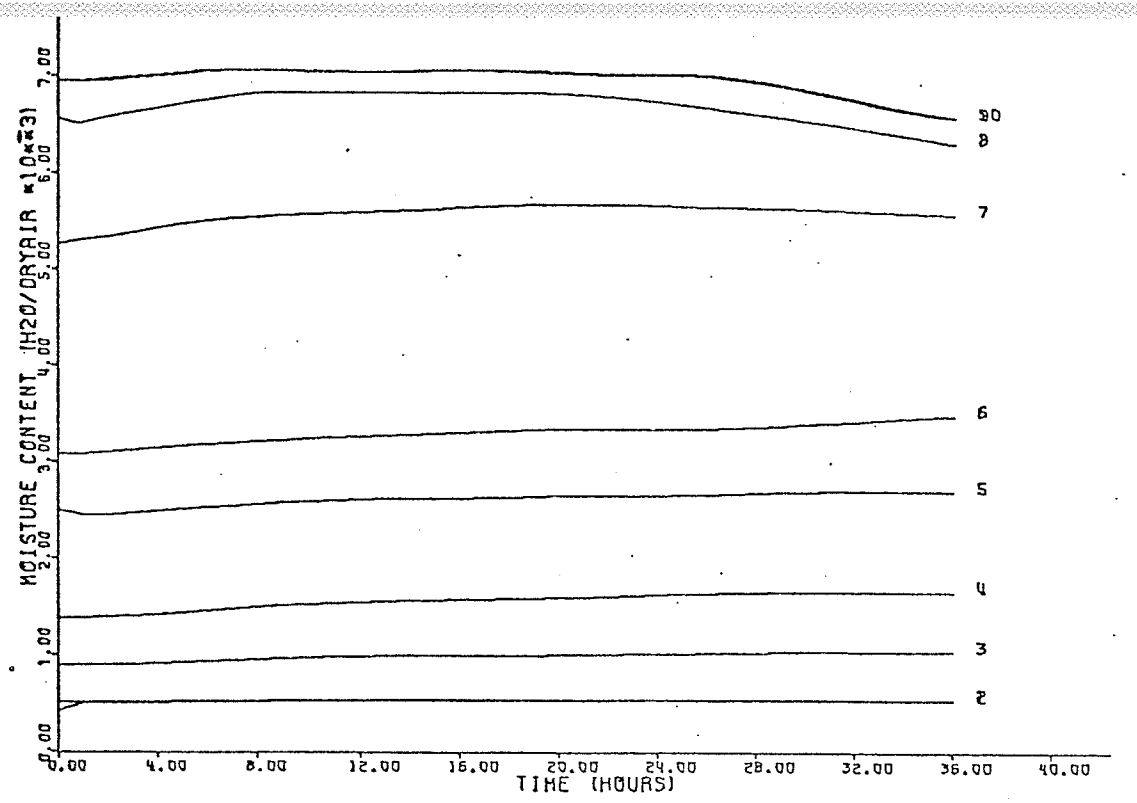

Figure 4.65: 800 mb Moisture (g H_2O/g dry air x 10^{-3}), model P7, 0-36 hour zonal mean, numbers on the right denote the latitude circle, 1 denotes the north pole, 10 denotes the equator

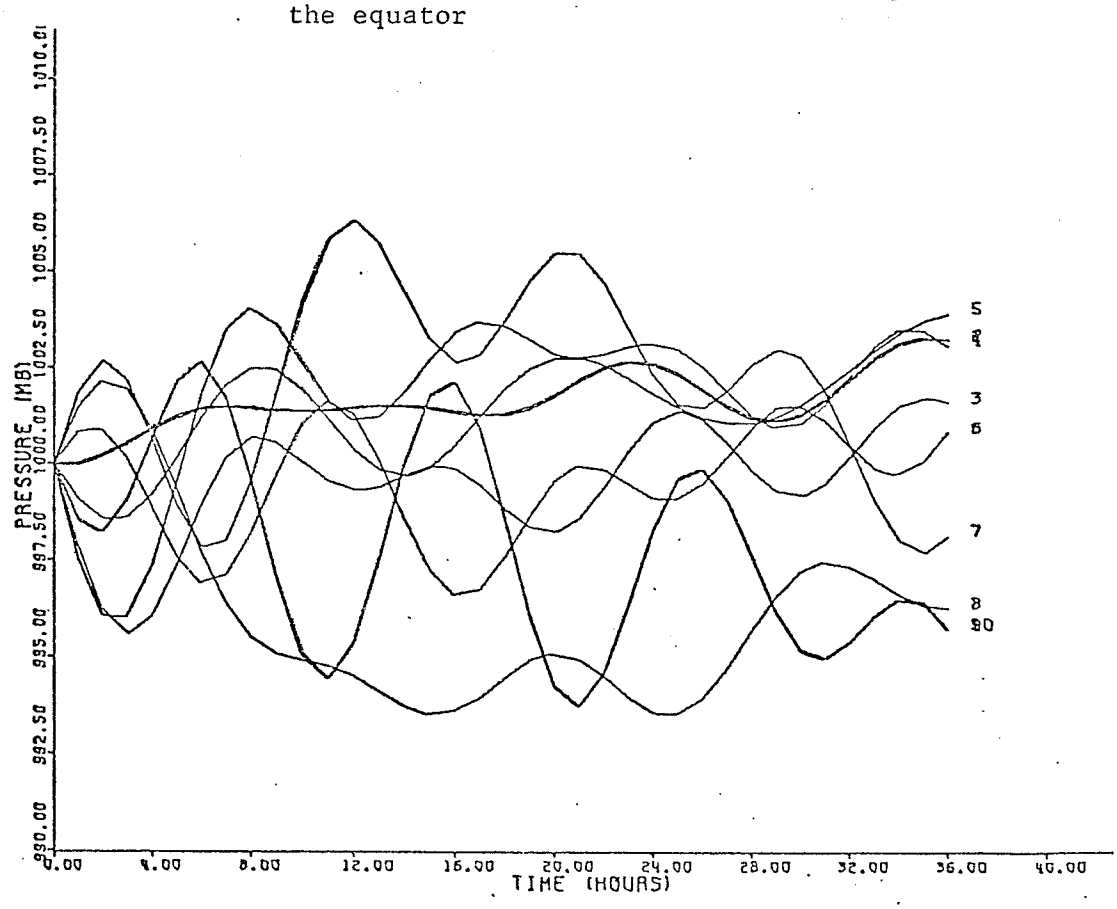

Figure 4.66: Surface Pressure (mb), model P7, 0-36 hour zonal mean, numbers on the right denote the latitude circle, 1 denotes the north pole, 10 denotes the equator.

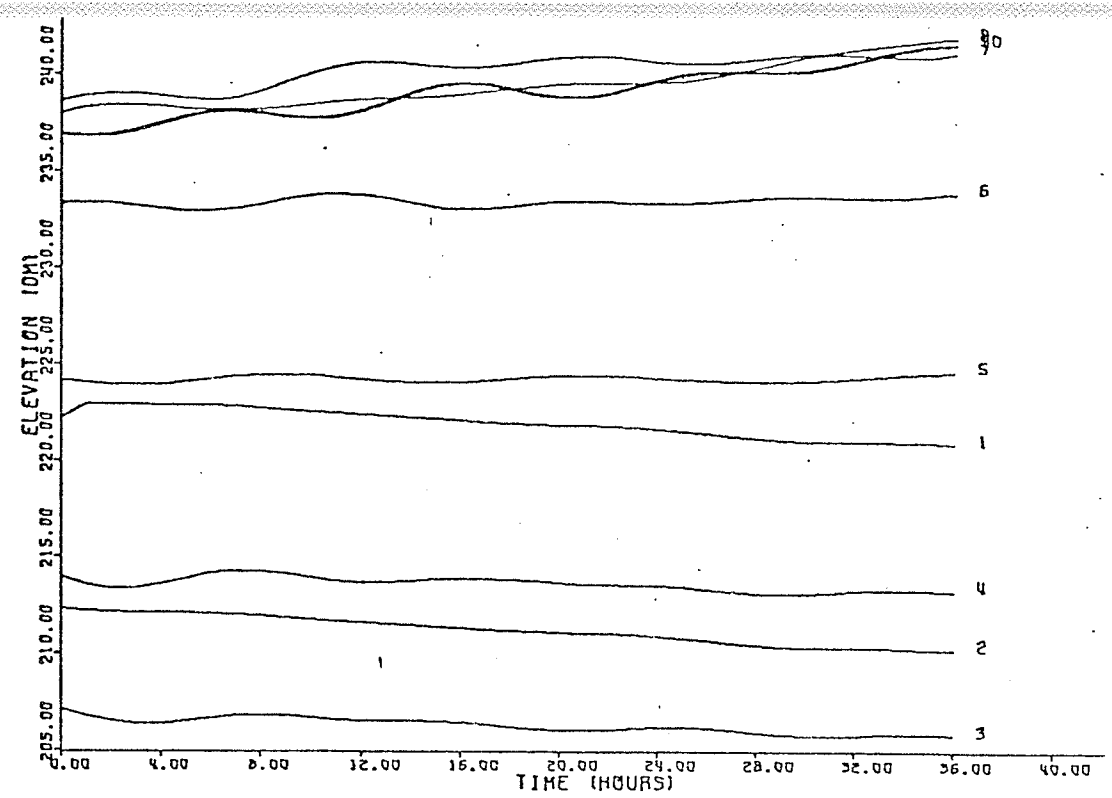

Figure 4.67: 800 mb Geopotential (dm), model P7, 0-36 hour zonal mean, numbers on the right denote the latitude circle, 1 denotes the north pole, 10 denotes the equator

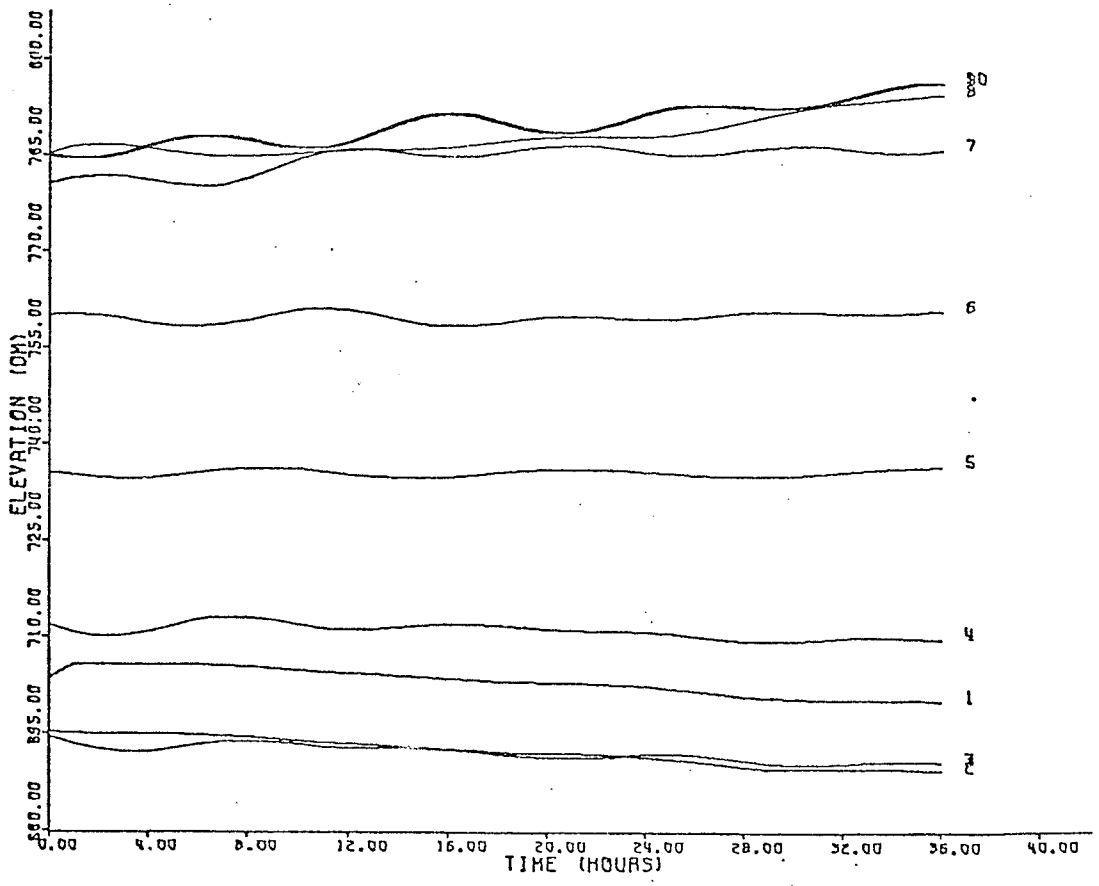

Figure 4.68: 400 mb Geopotential (dm), model P7, 0-36 hour zonal mean, numbers on the right denote the latitude circle, 1 denotes the north pole, 10 denotes the equator

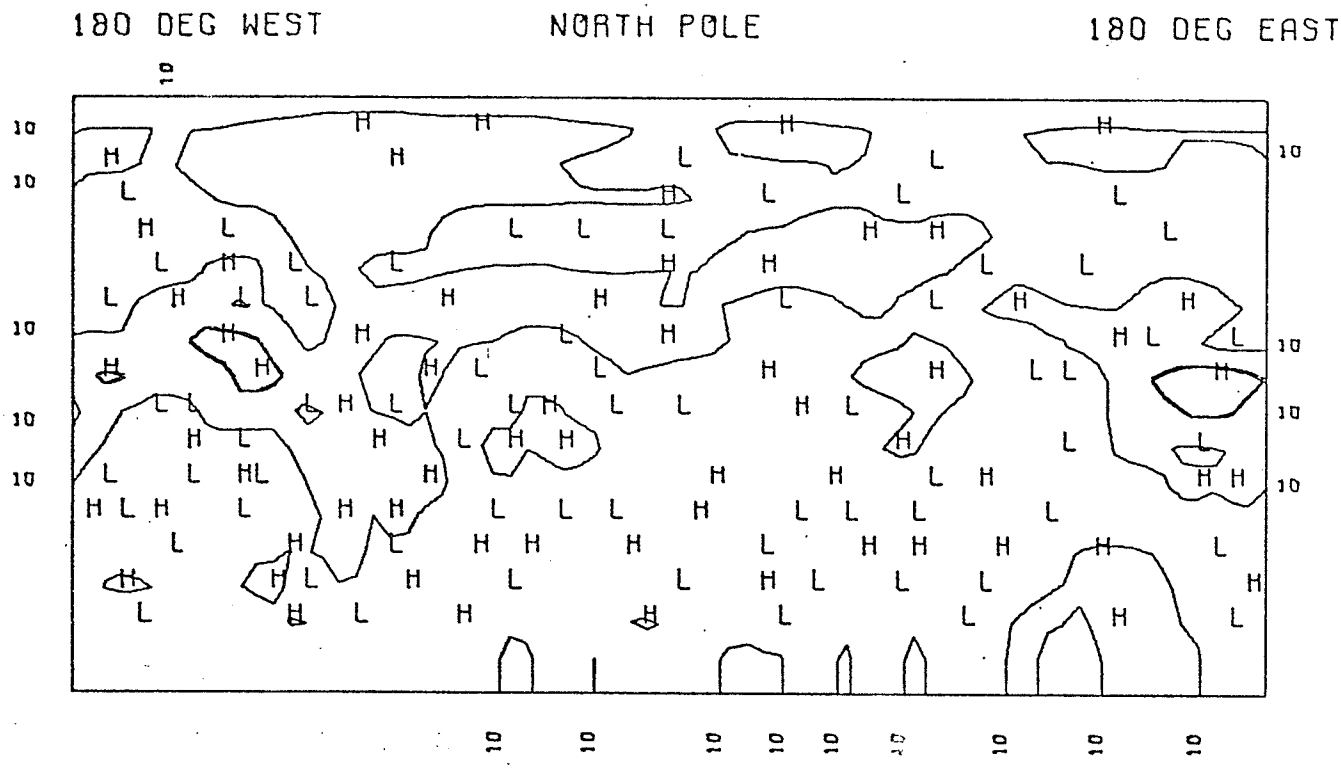

Figure 4.69: 800 mb Resultant Velocity Isotachs (m/sec), model S, 36 hour

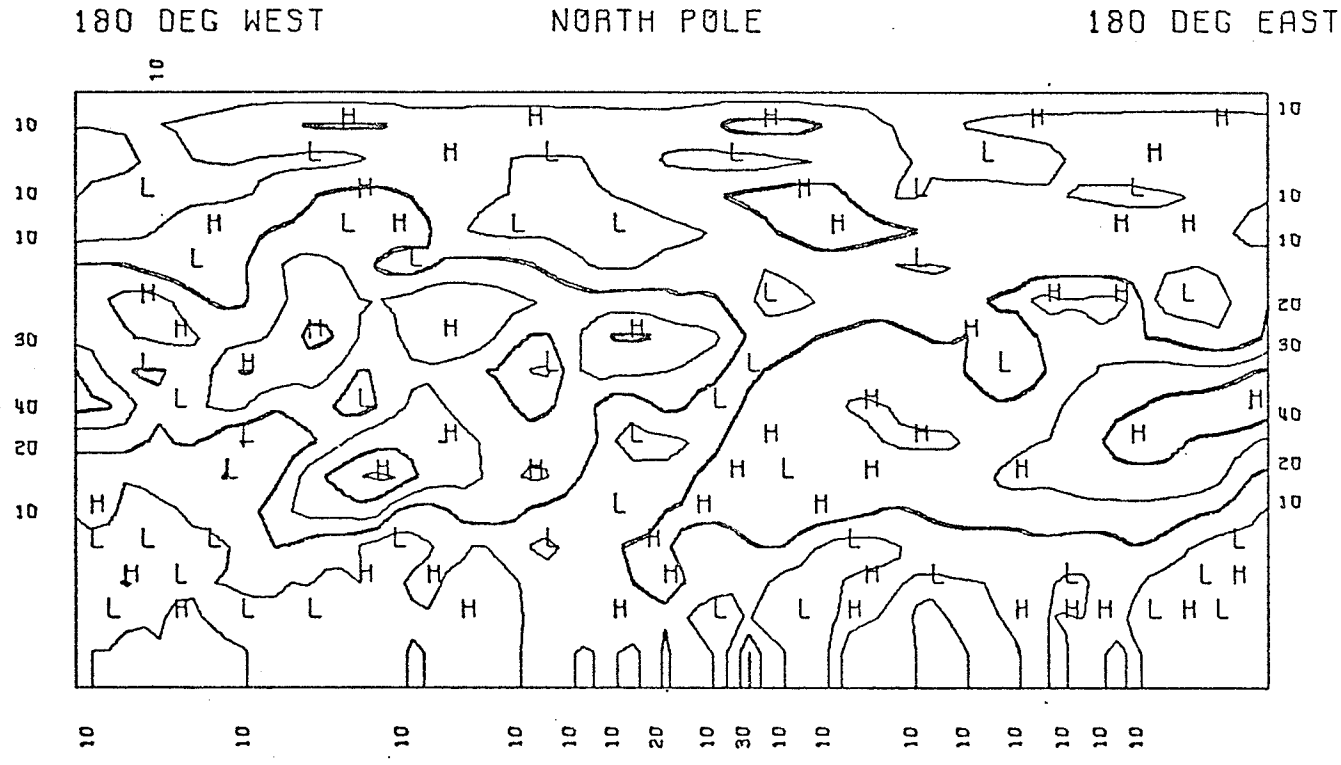

Figure 4.70: 400 mb Resultant Velocity Isotachs (m/sec), model S, 36 hour

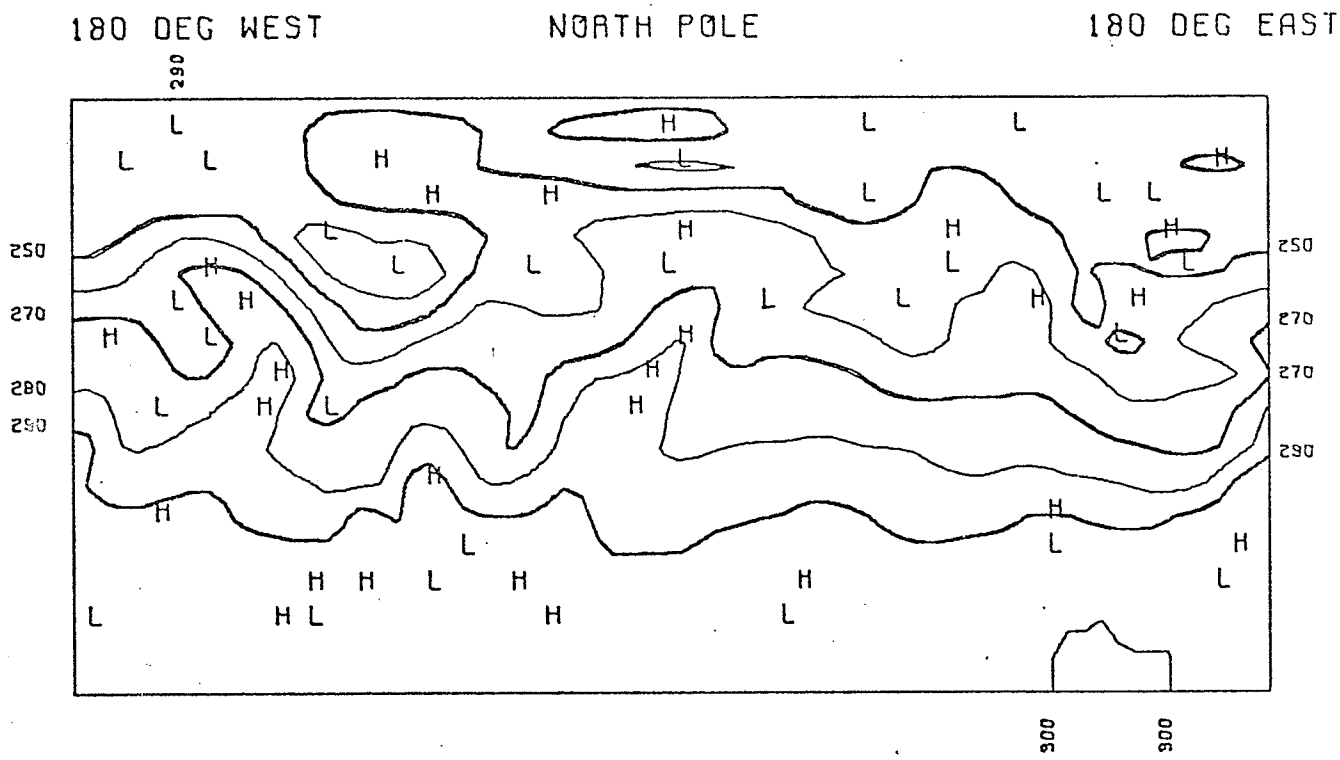

Figure 4.71: 800 mb Temperature (^{o}K), model S, 36 hour

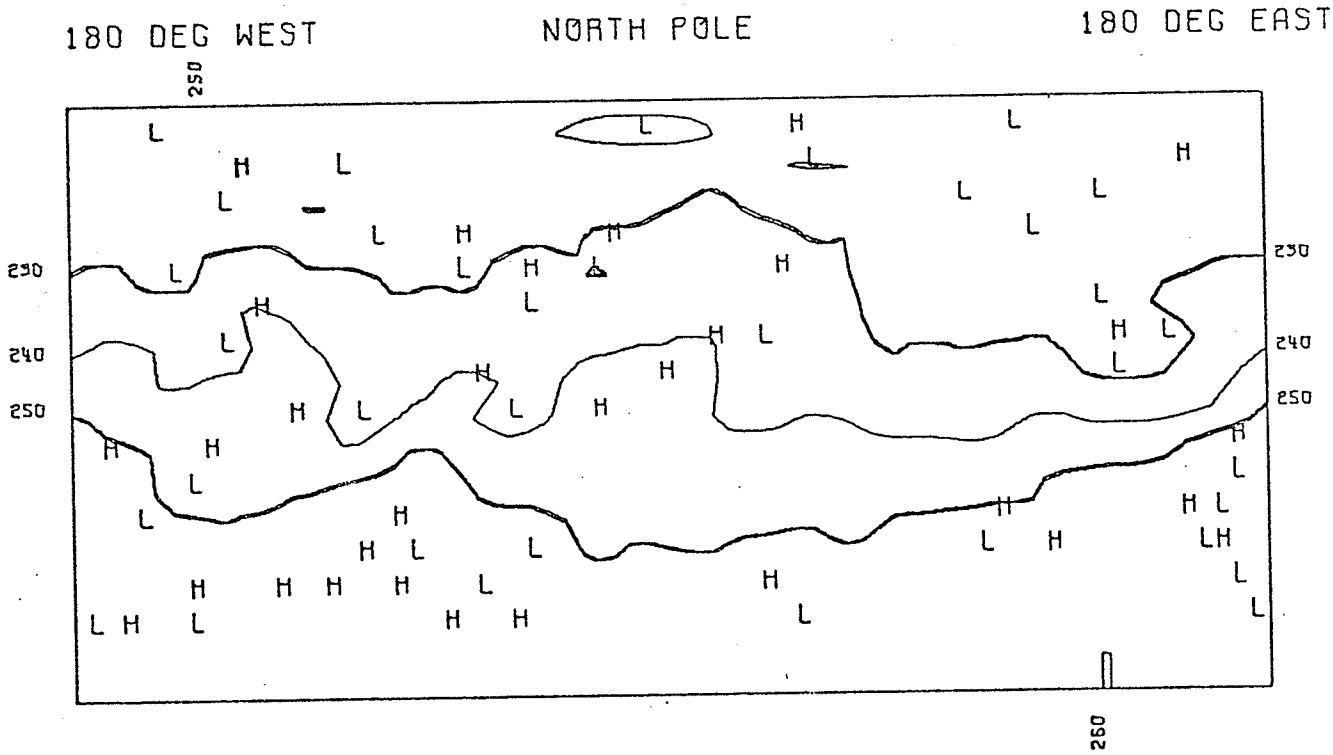

Figure 4.72: 400 mb Temperature (^{o}K), model S, 36 hour

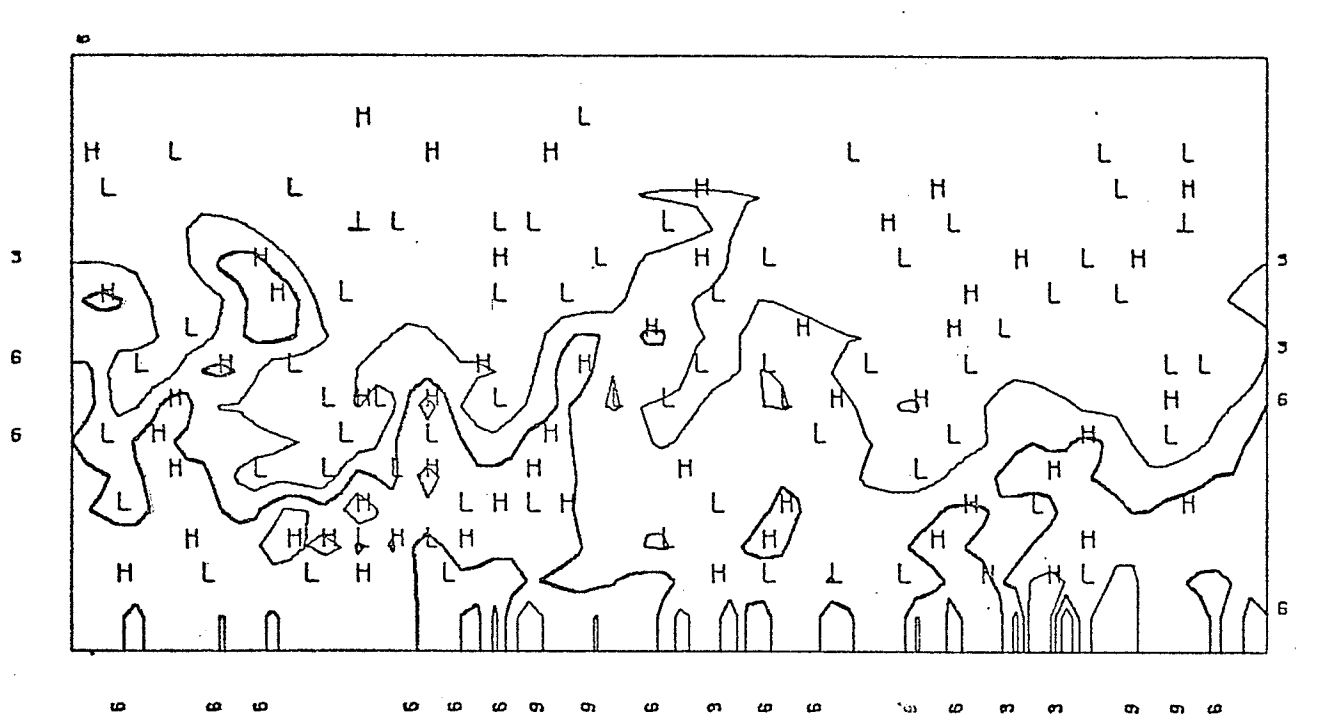

Figure 4.73: 800 mb Moisture (g H_2O/g dry air x 10^{-3}), model S, 36 hour

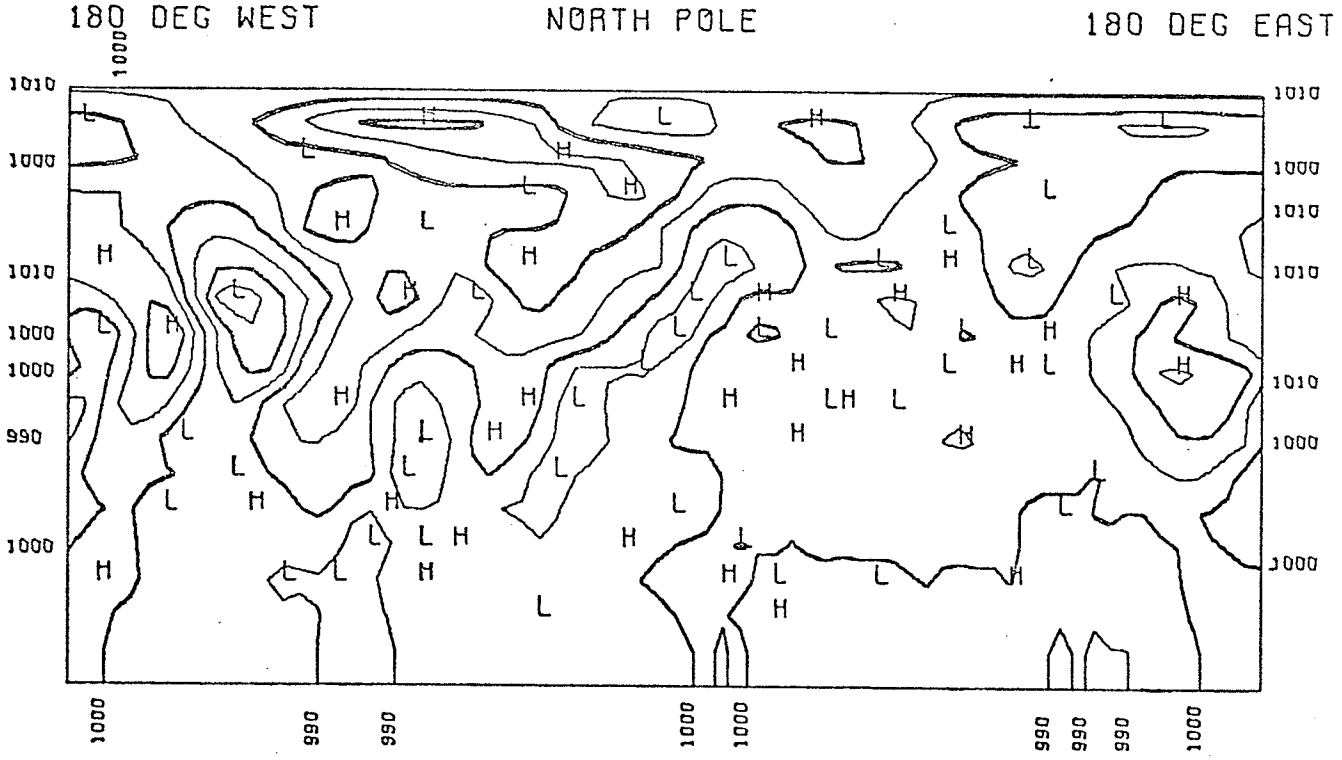

Figure 4.74: Surface Pressure (mb), model S, 36 hour

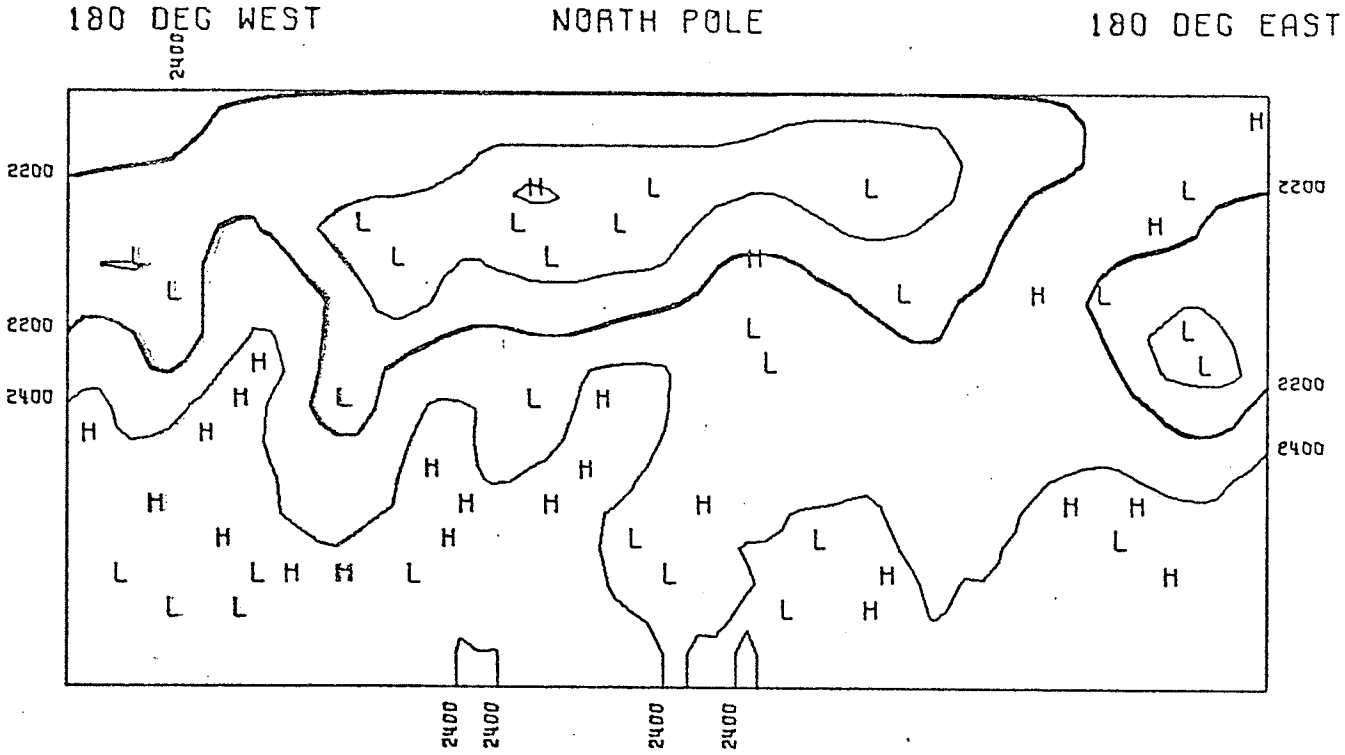

Figure 4.75: 800 mb Geopotential (m), model S, 36 hour

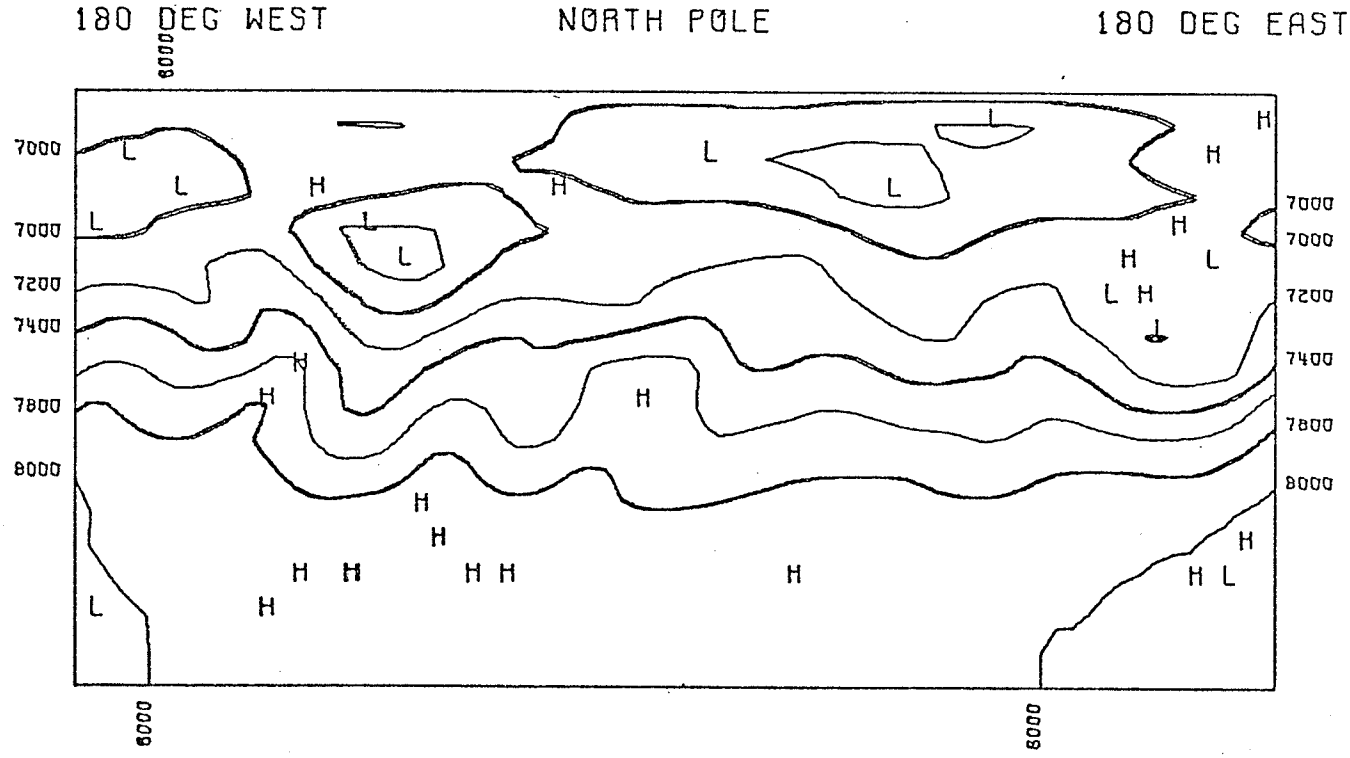

Figure 4.76: 400 mb Geopotential (m), model S, 36 hour

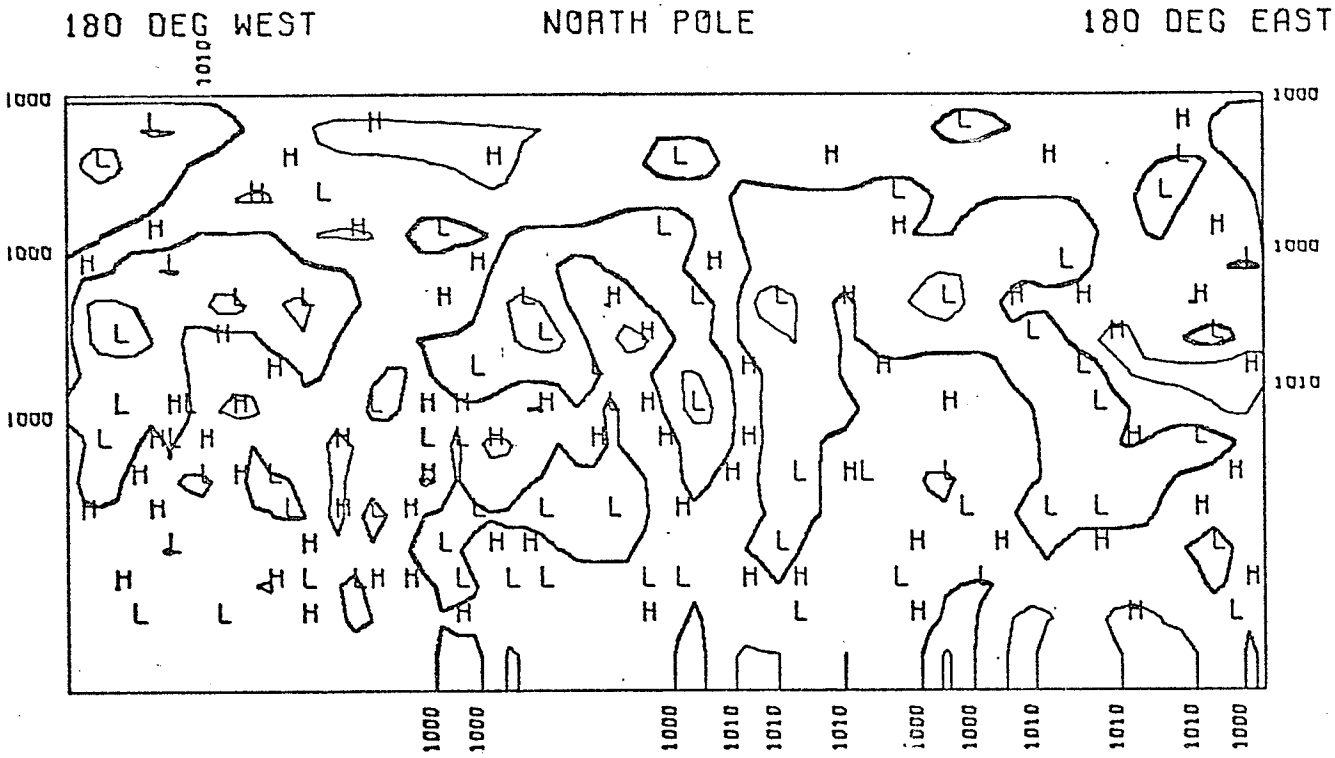

Figure 4.77: 800 mb Resultant Velocity Isotachs (m/sec), model S, 36 hour error, 1000 represents zero error

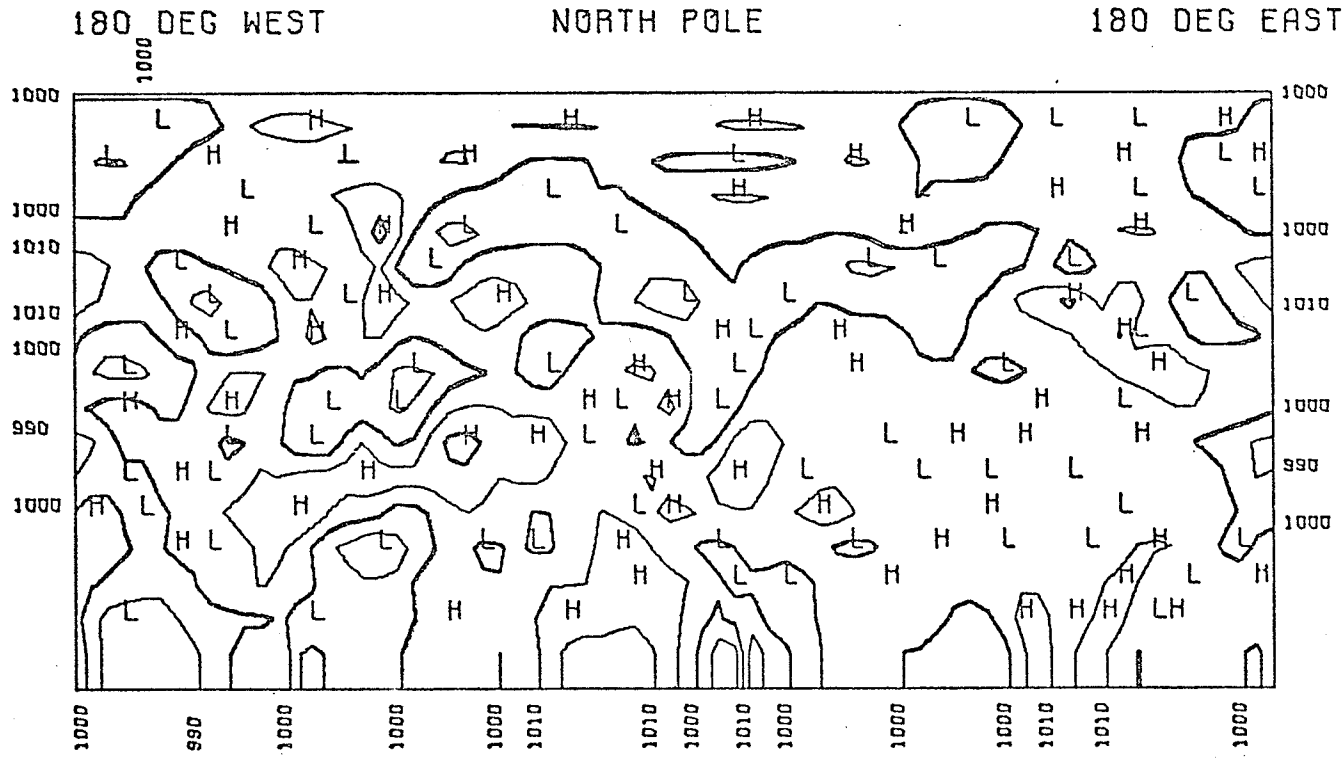

Figure 4.78: 400 mb Resultant Velocity Isotachs (m/sec), model S, 36 hour error, 1000 represents zero error

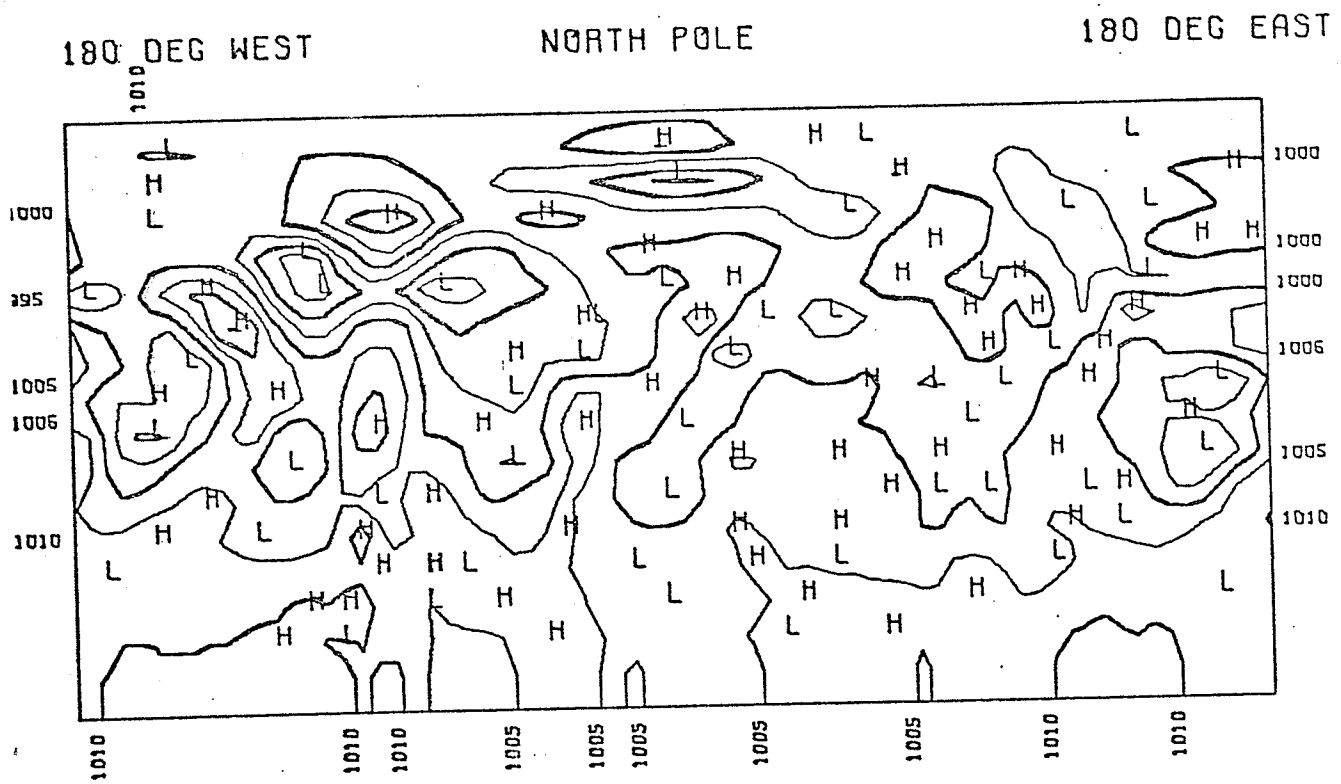

Figure 4.79: 800 mb Temperature (^{o}K), model S, 36 hour error, 1000 represents zero error

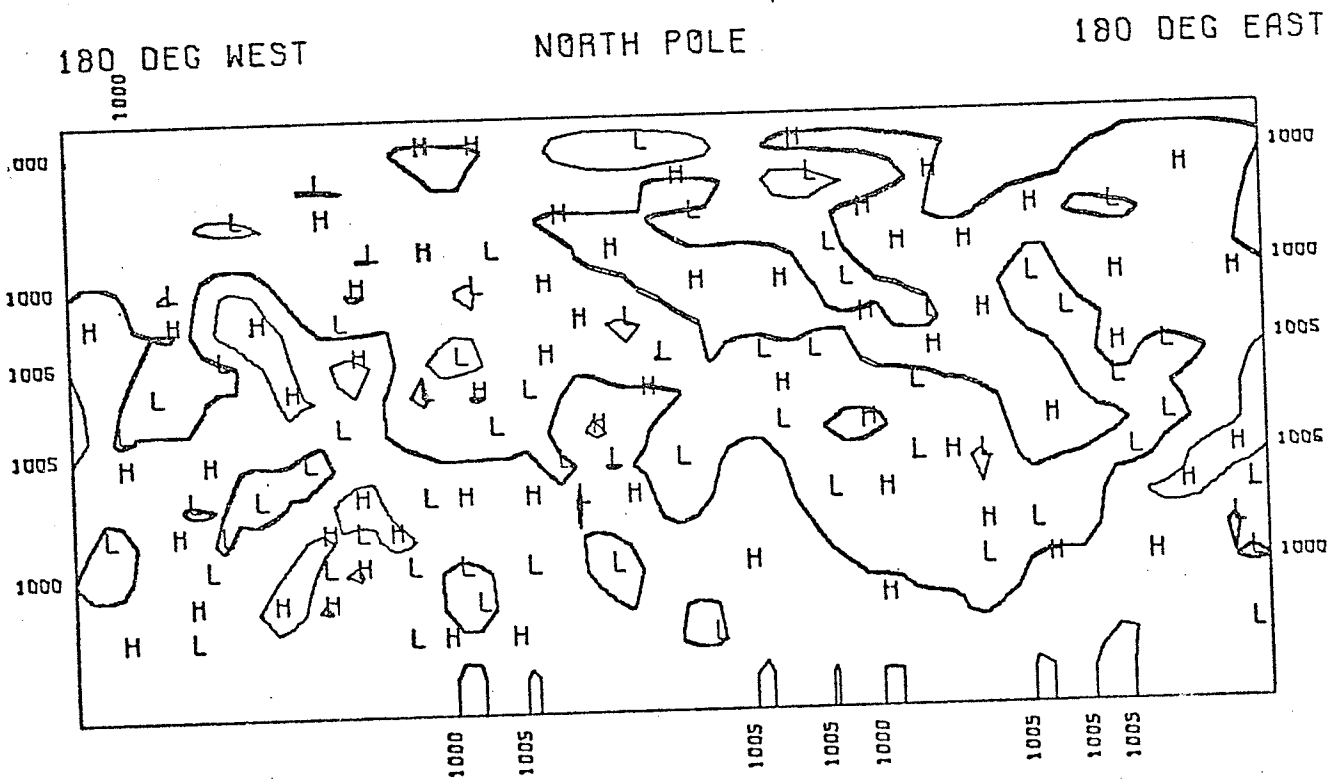

Figure 4.80: 400 mb Temperature (^{o}K), model S, 36 hour error, 1000 represents zero error

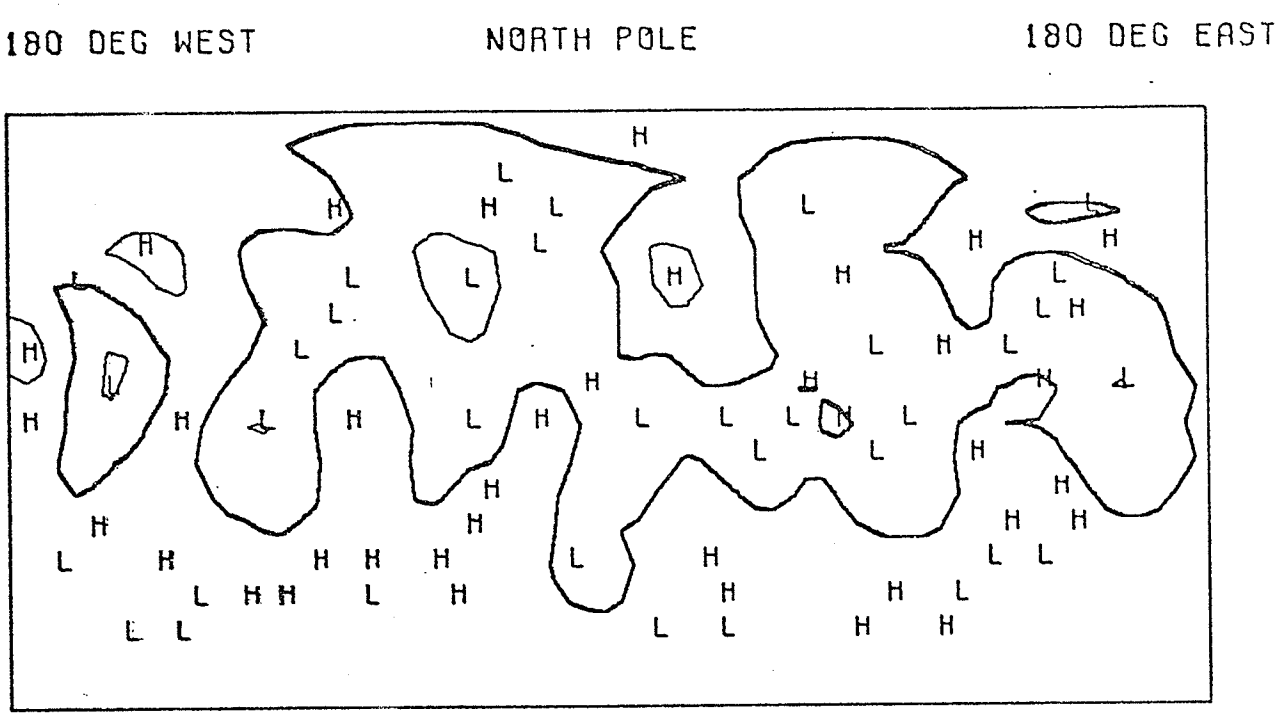

Figure 4.81: 800 mb Geopotential (m), model S, 36 hour error, 1000 represents zero error

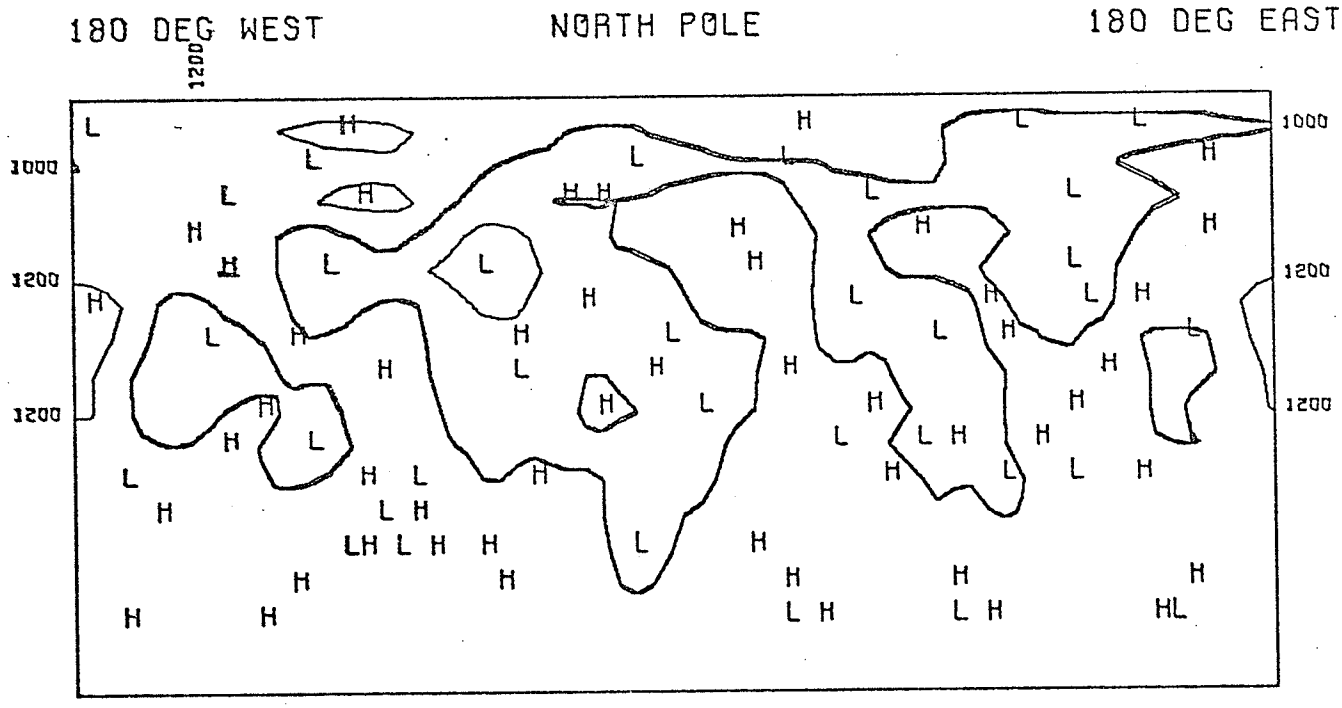

Figure 4.82: 400 mb Geopotential (m), model S, 36 hour error, 1000 represents zero error

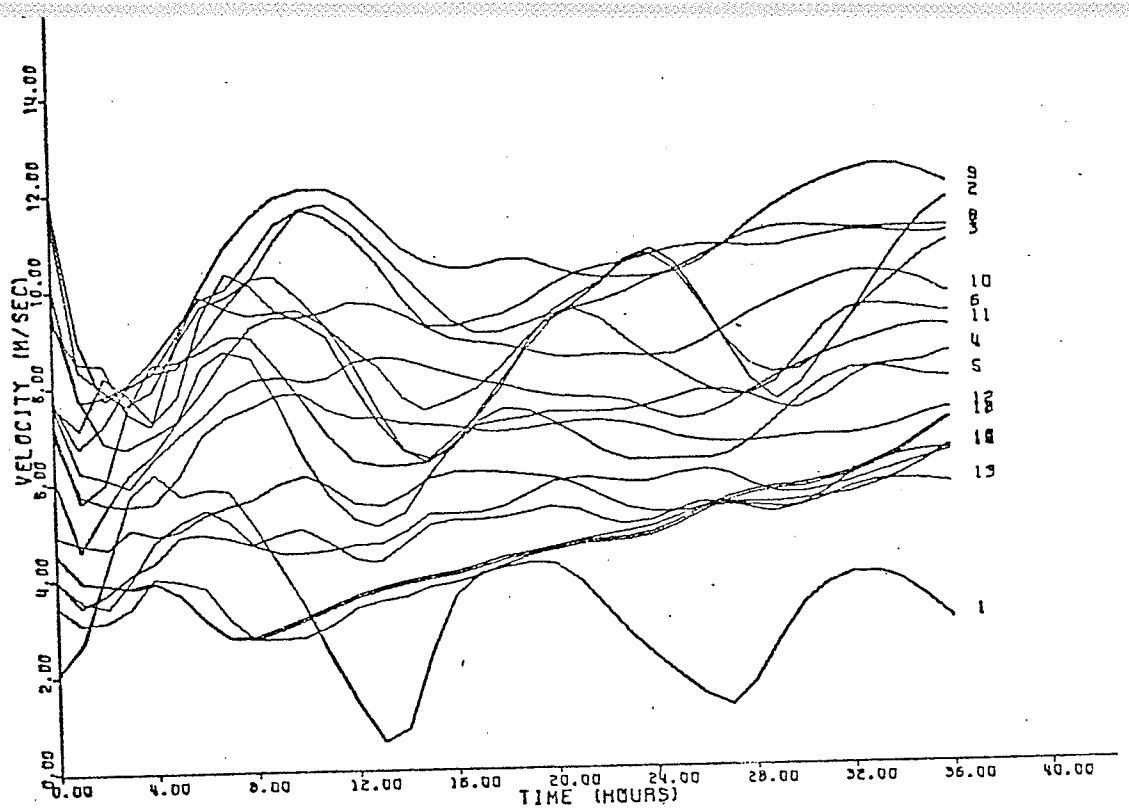

Figure 4.83: 800 mb Resultant Velocity Isotachs (m/sec), model S, 0-36 hour zonal mean, numbers on the right denote the latitude circle, 1 denotes the north pole, 18 denotes the equator

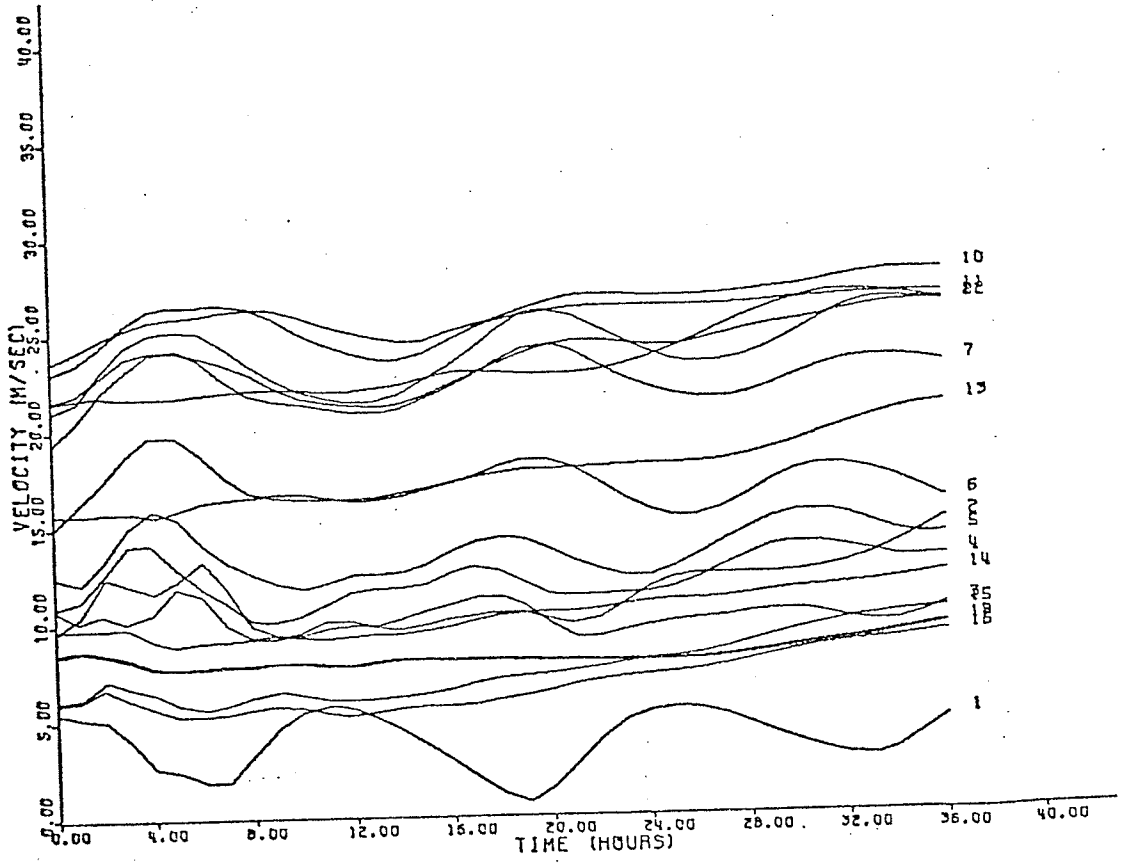

Figure 4.84: 400 mb Resultant Velocity Isotachs (m/sec), model S, 0-36 hour zonal mean, numbers on the right denote the latitude circle, 1 denotes the north pole, 18 denotes the equator

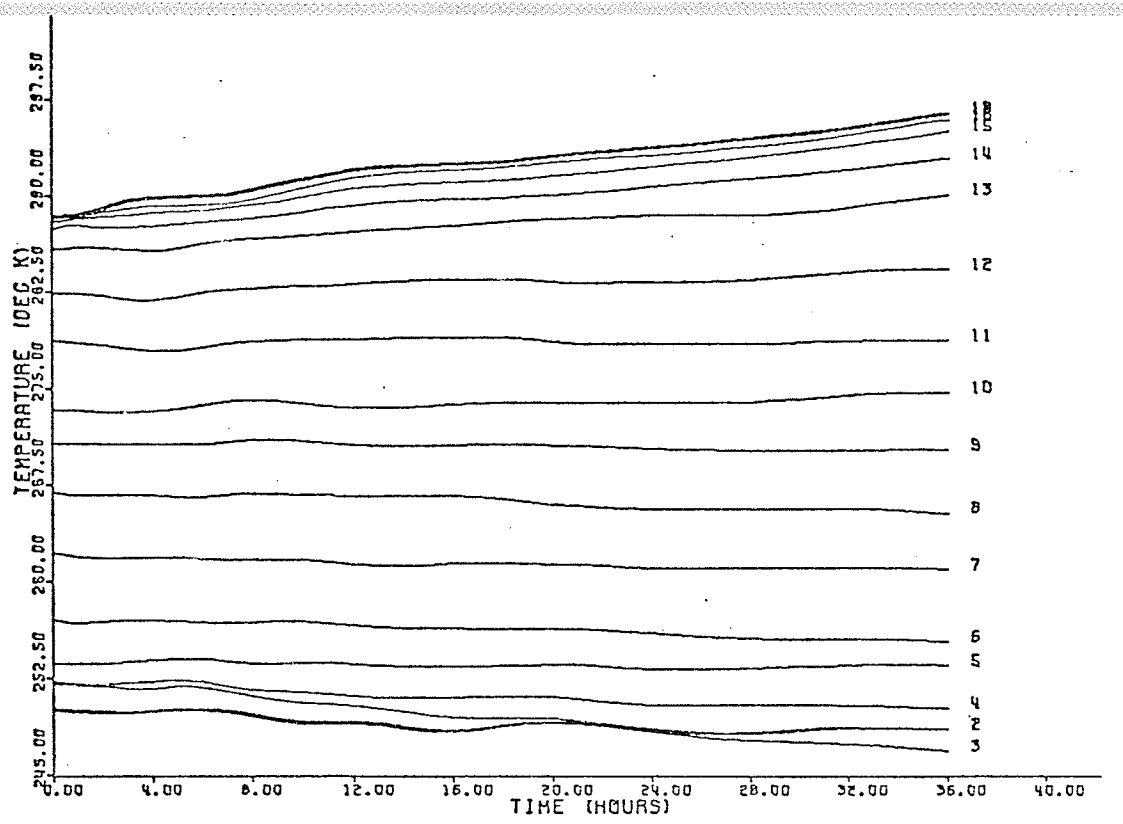

Figure 4.85: 800 mb Temperature (^{o}K), model S, 0-36 hour zonal mean, numbers on the right denote the latitude circle, 1 denotes the north pole, 18 denotes the equator

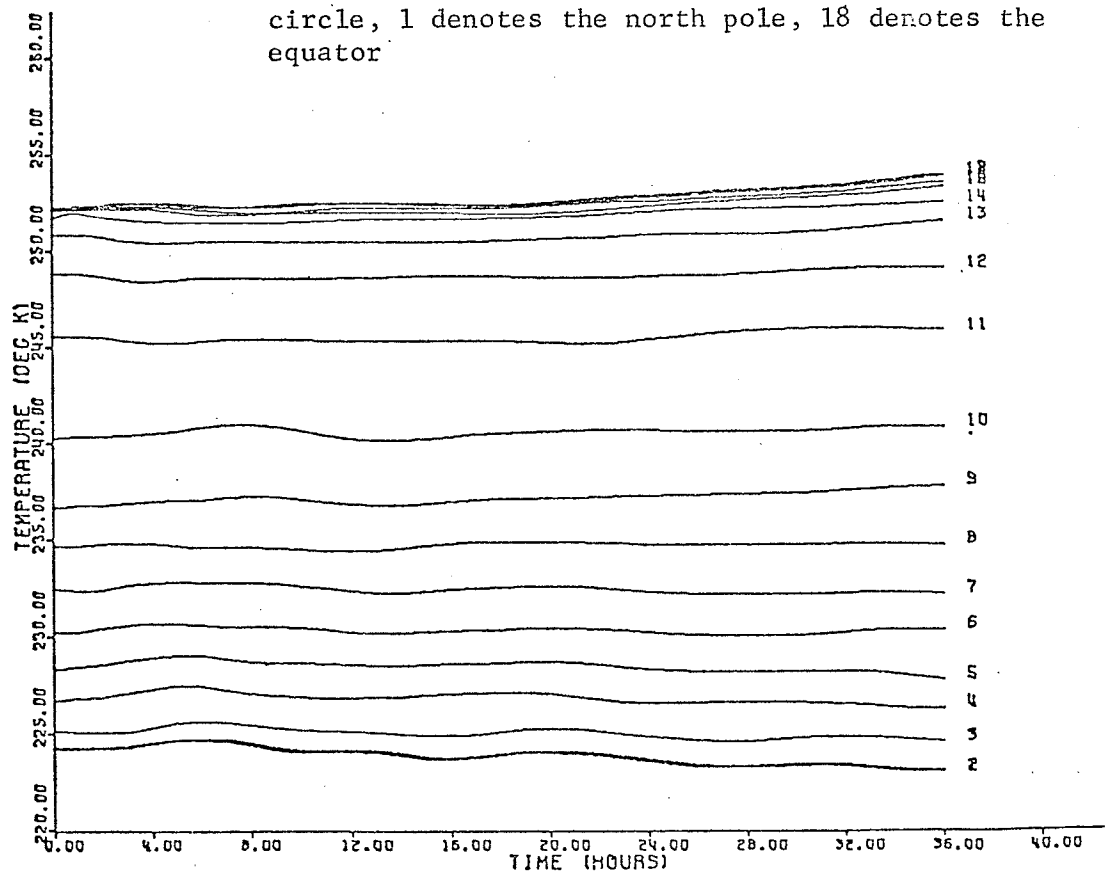

Figure 4.86: 400 mb Temperature (^{o}K), model S, 0-36 hour zonal mean, numbers on the right denote the latitude circle, 1 denotes the north pole, 18 denotes the equator

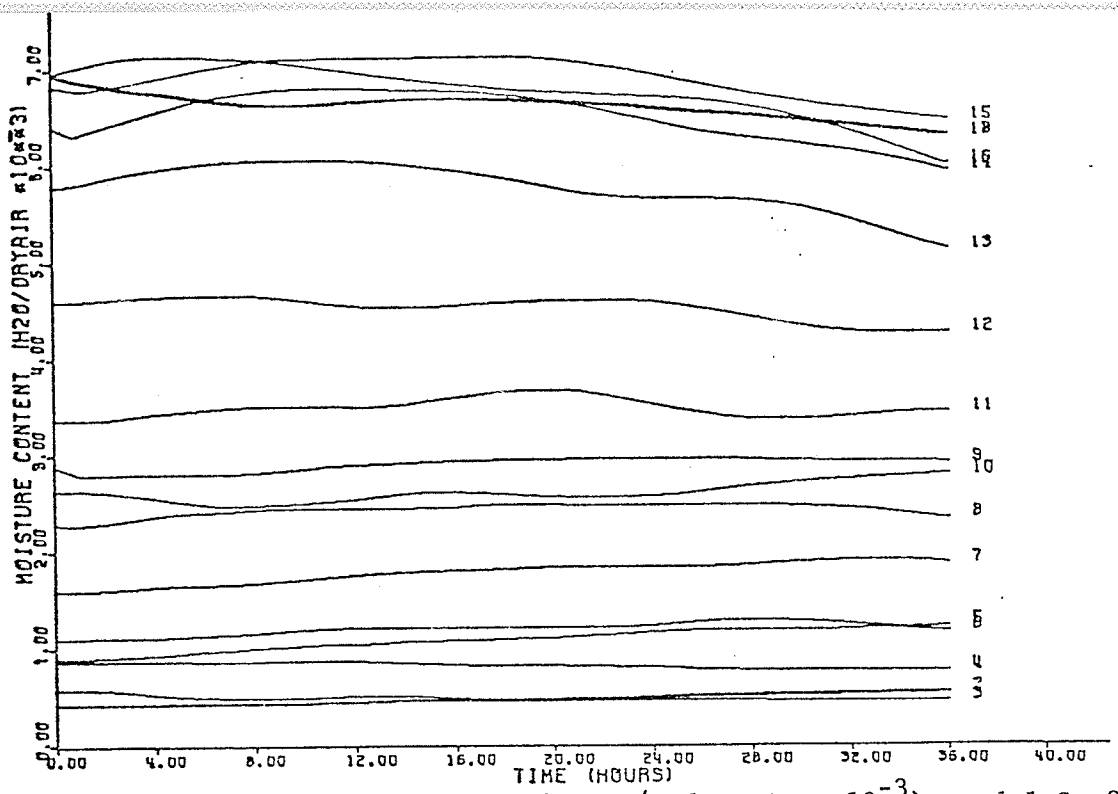

Figure 4.87: 800 mb Moisture (g H_2O/g dry air x 10^{-3}), model S, 0-36 hour zonal mean, numbers on the right denote the latitude circle, 1 denotes the north pole, 18 denotes the equator

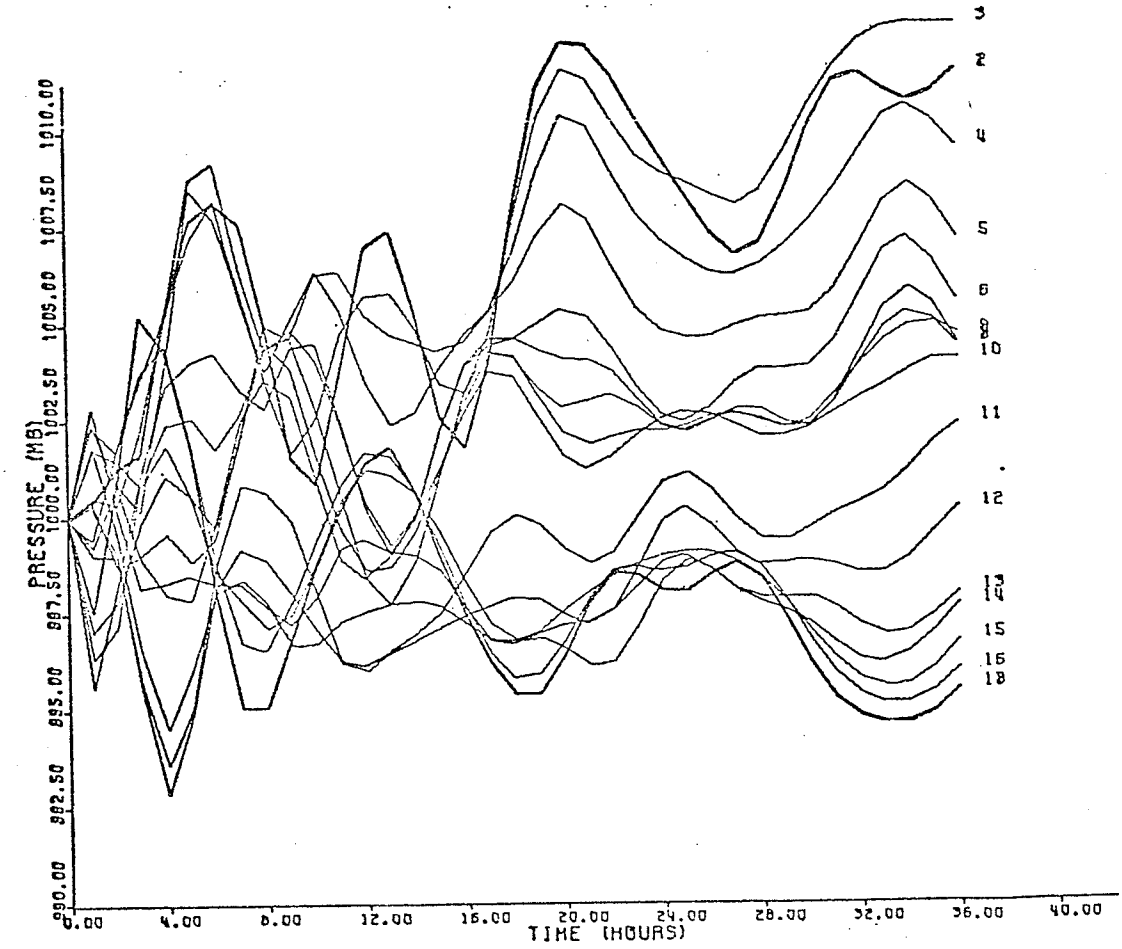

Figure 4.88: Surface Pressure (mb), model S, 0-36 hour zonal mean, numbers on the right denote the latitude circle, 1 denotes the north pole, 18 denotes the equator

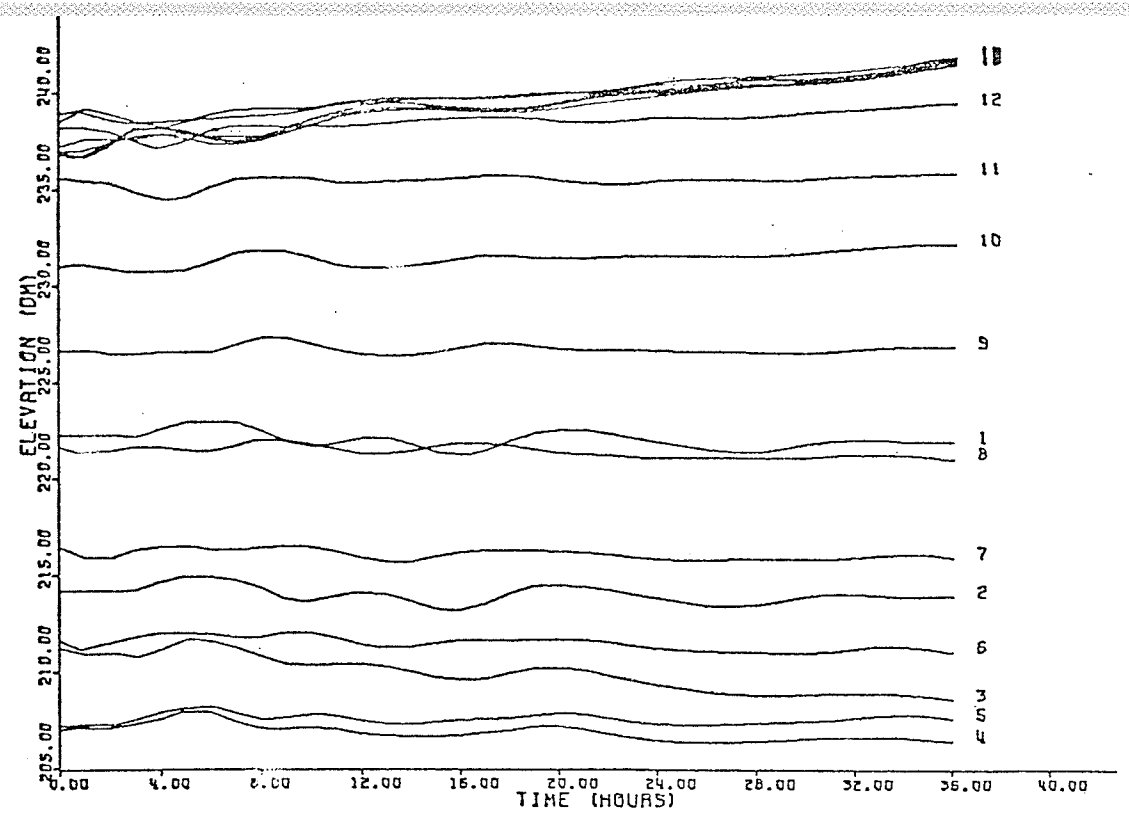

Figure 4.89: 800 mb Geopotential (dm), model S, 0-36 hour zonal mean, numbers on the right denote the latitude circle, 1 denotes the north pole, 18 denotes the equator

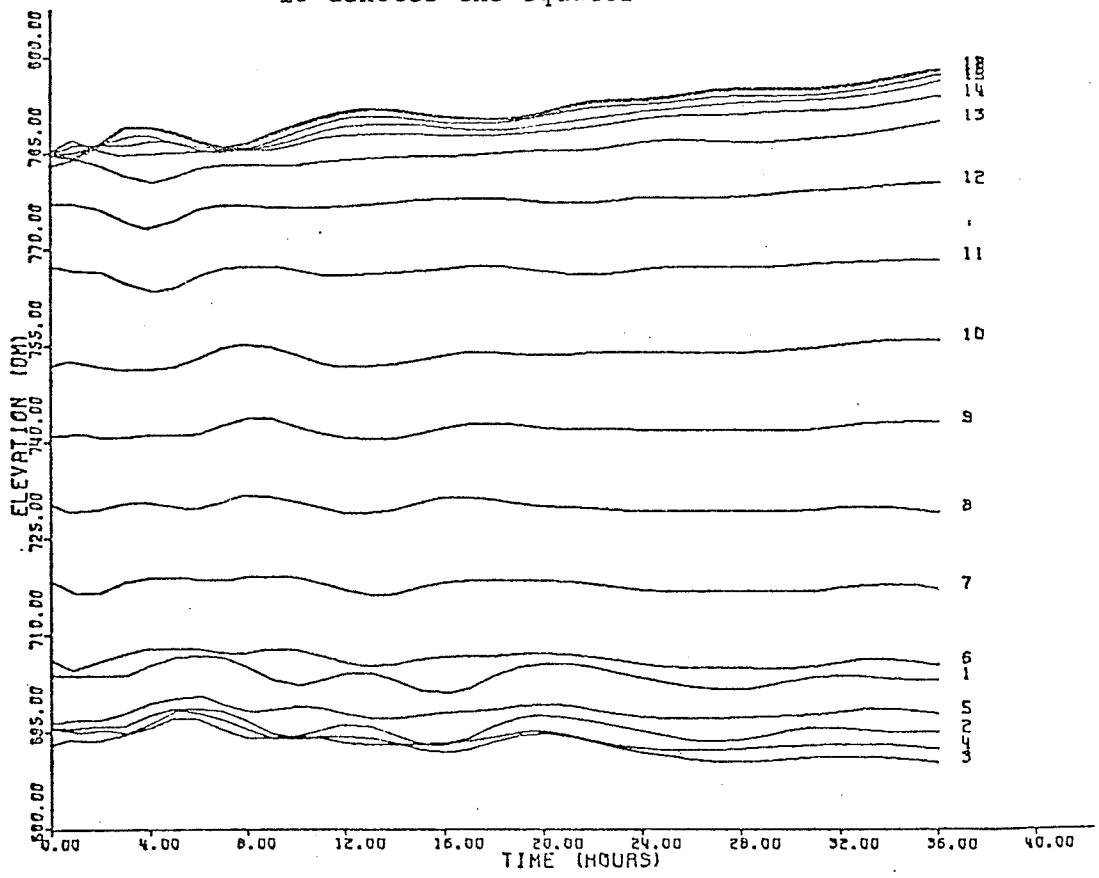

Figure 4.90: 400 mb Geopotential (dm), model S, 0-36 hour zonal mean, numbers on the right denote the latitude circle, 1 denotes the north pole, 18 denotes the equator

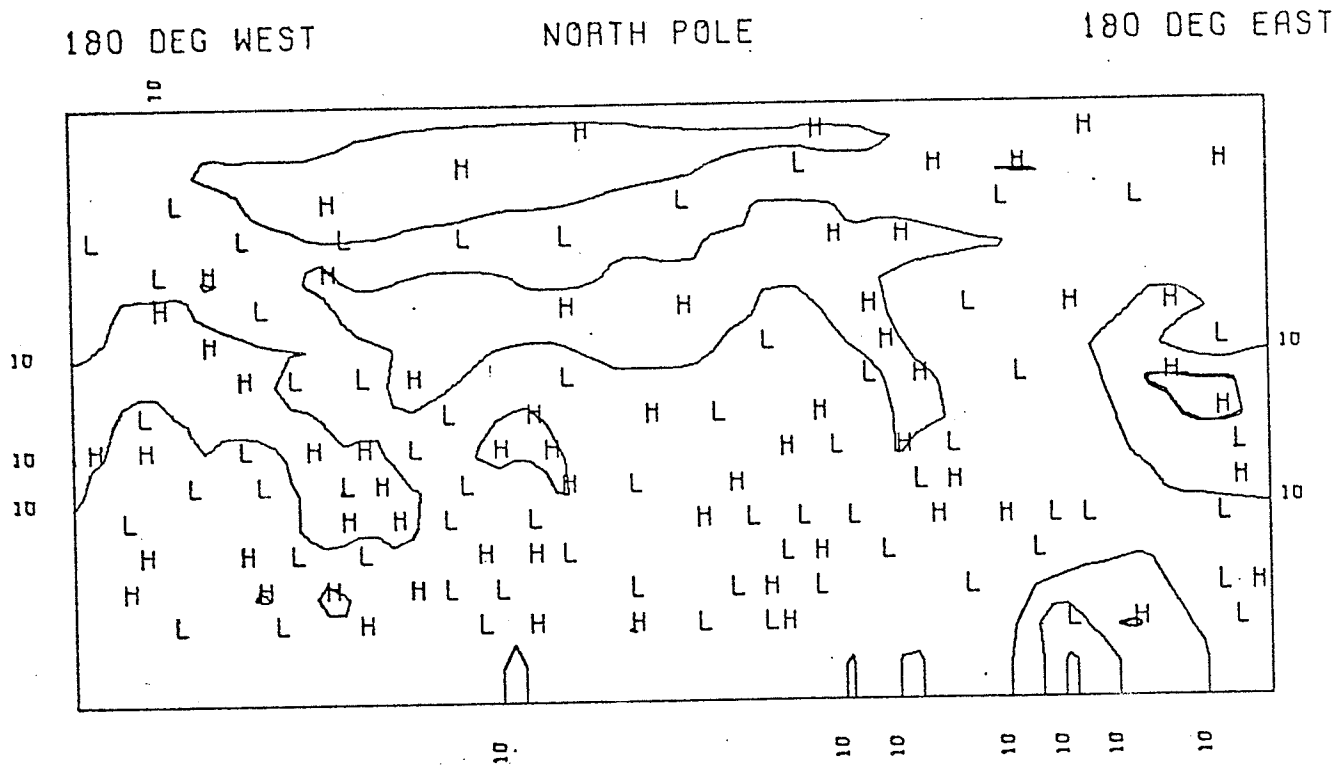

Figure 4.91: 800 mb Resultant Velocity Isotachs (m/sec), model F, 36 hour

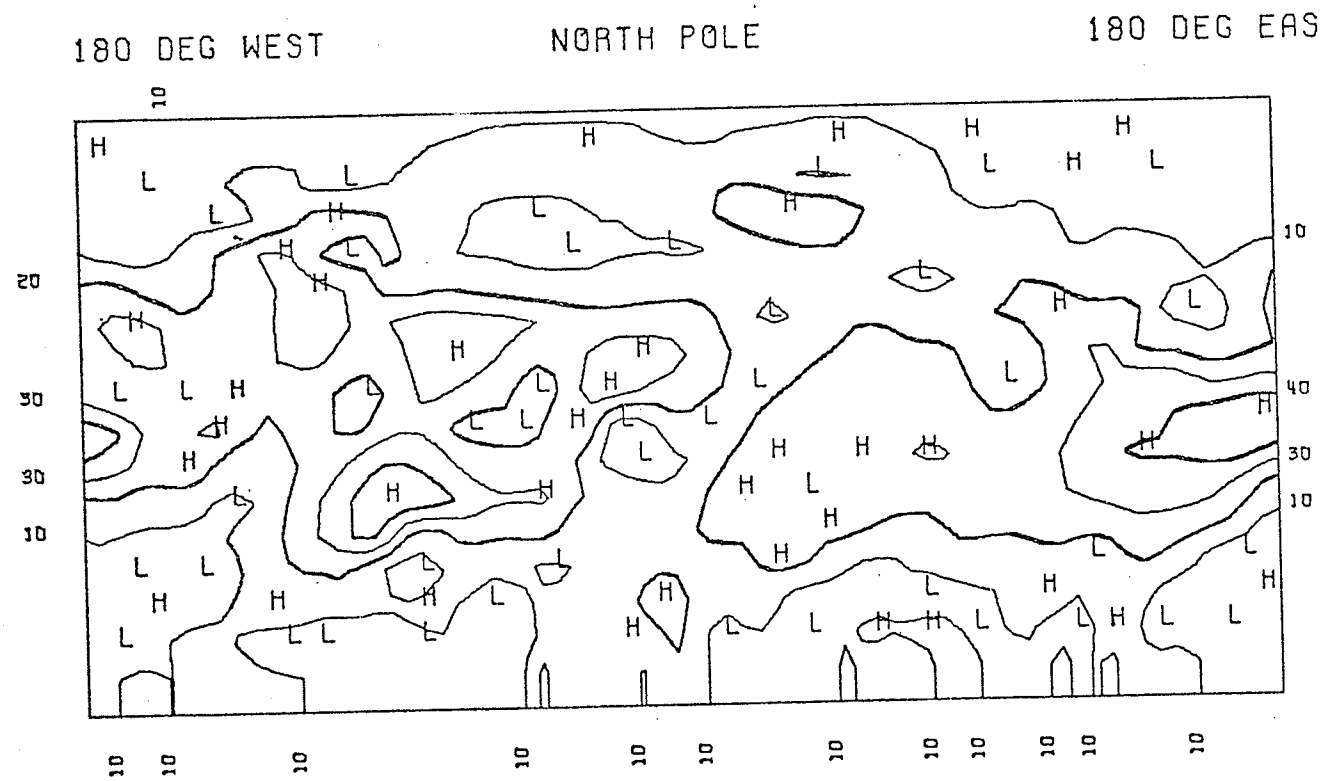

Figure 4.92: 400 mb Resultant Velocity Isotachs (m/sec), model F, 36 hour

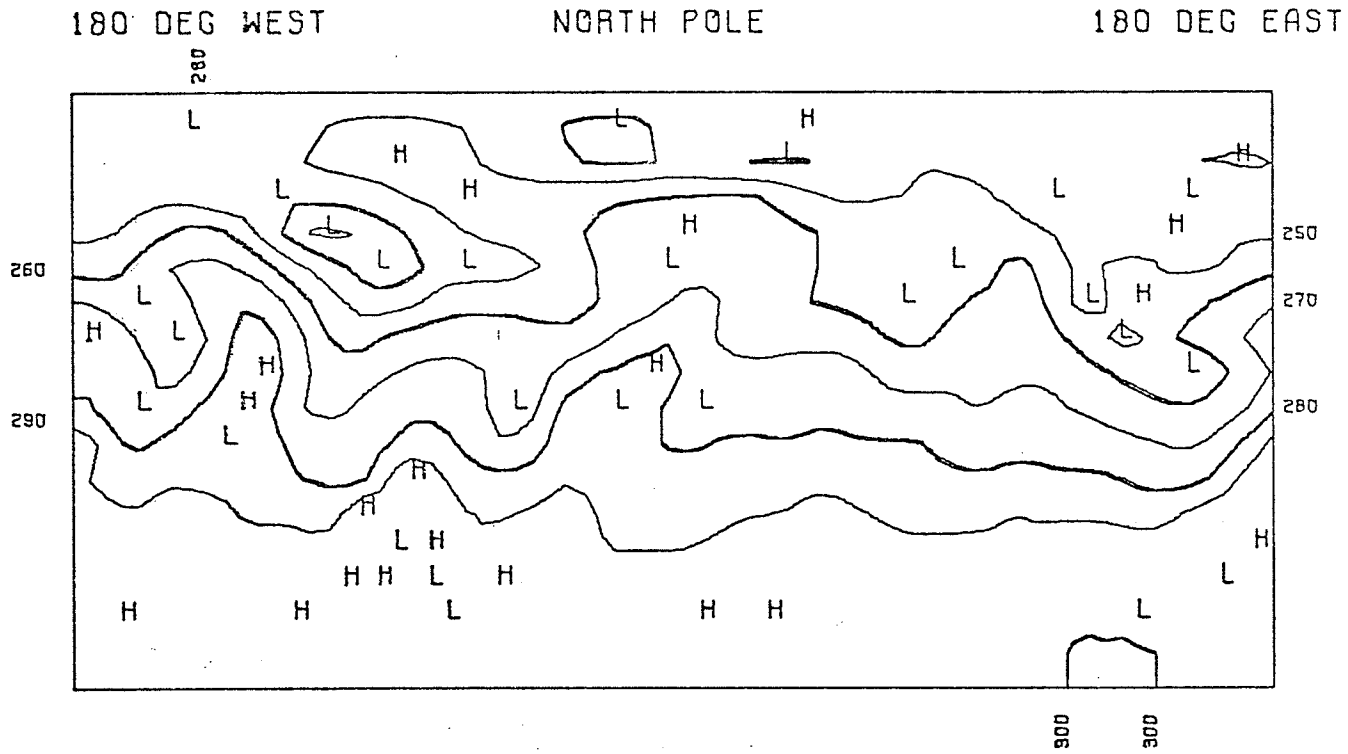

Figure 4.93: 800 mb Temperature (^{o}K), model F, 36 hour

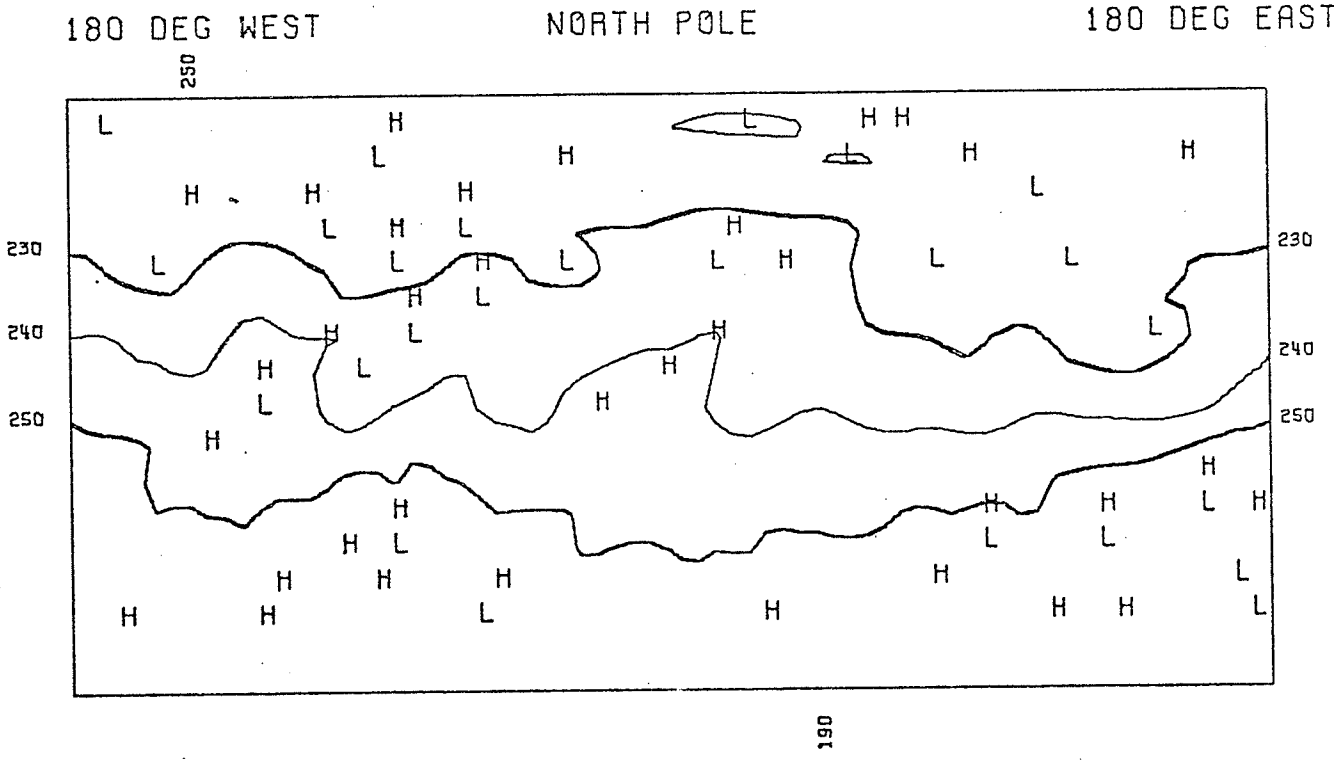

Figure 4.94: 400 mb Temperature (^{o}K), model F, 36 hour

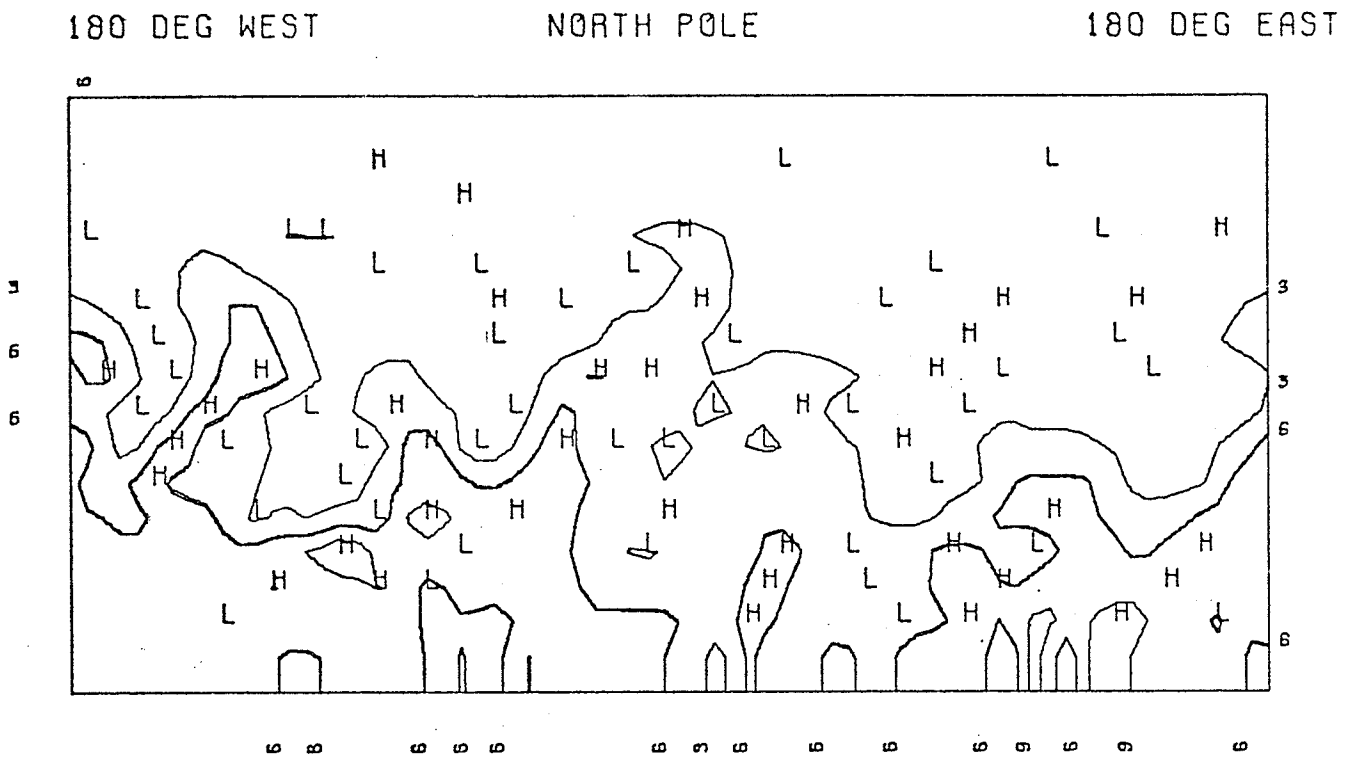

Figure 4.95: 800 mb Moisture (g H_2O/g dry air x 10^{-3}), model F, 36 hour

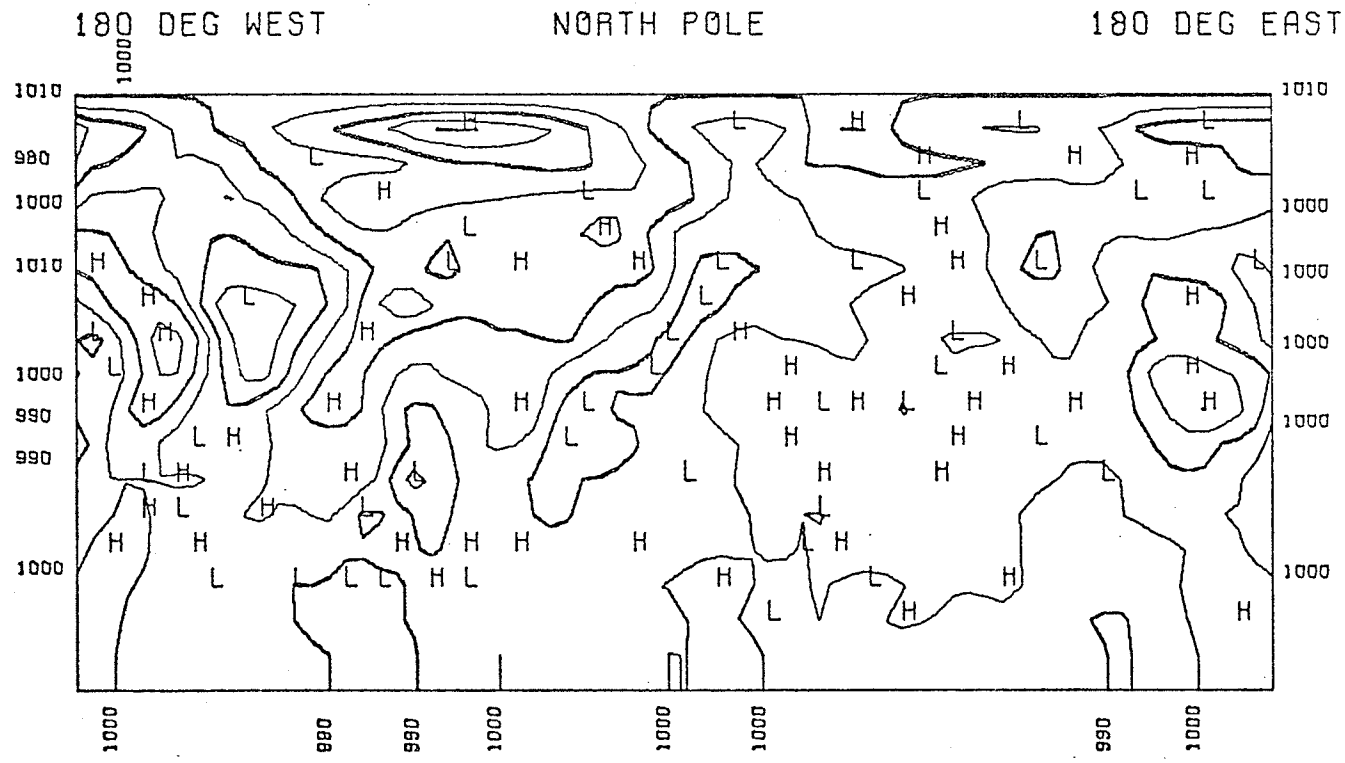

Figure 4.96: Surface Pressure (mb), model F, 36 hour

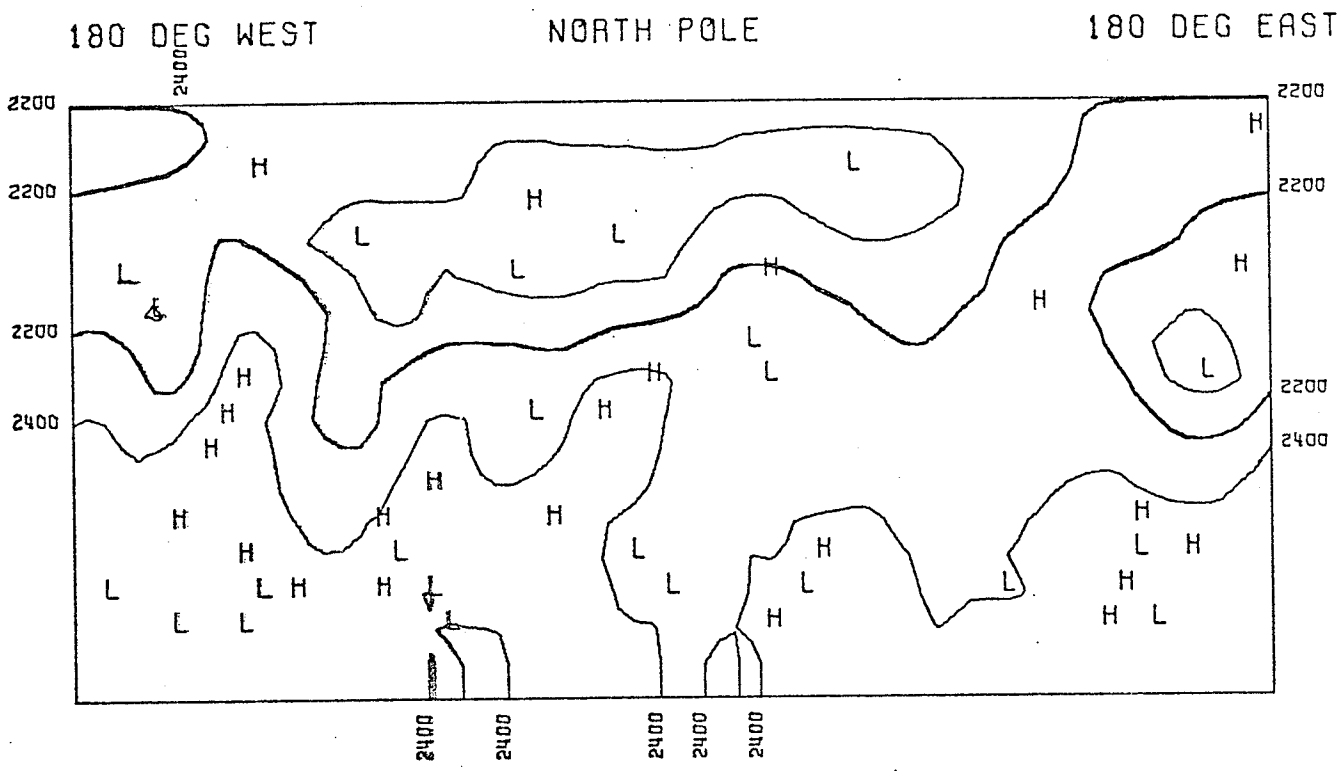

Figure 4.97: 800 mb Geopotential (m), model F, 36 hour

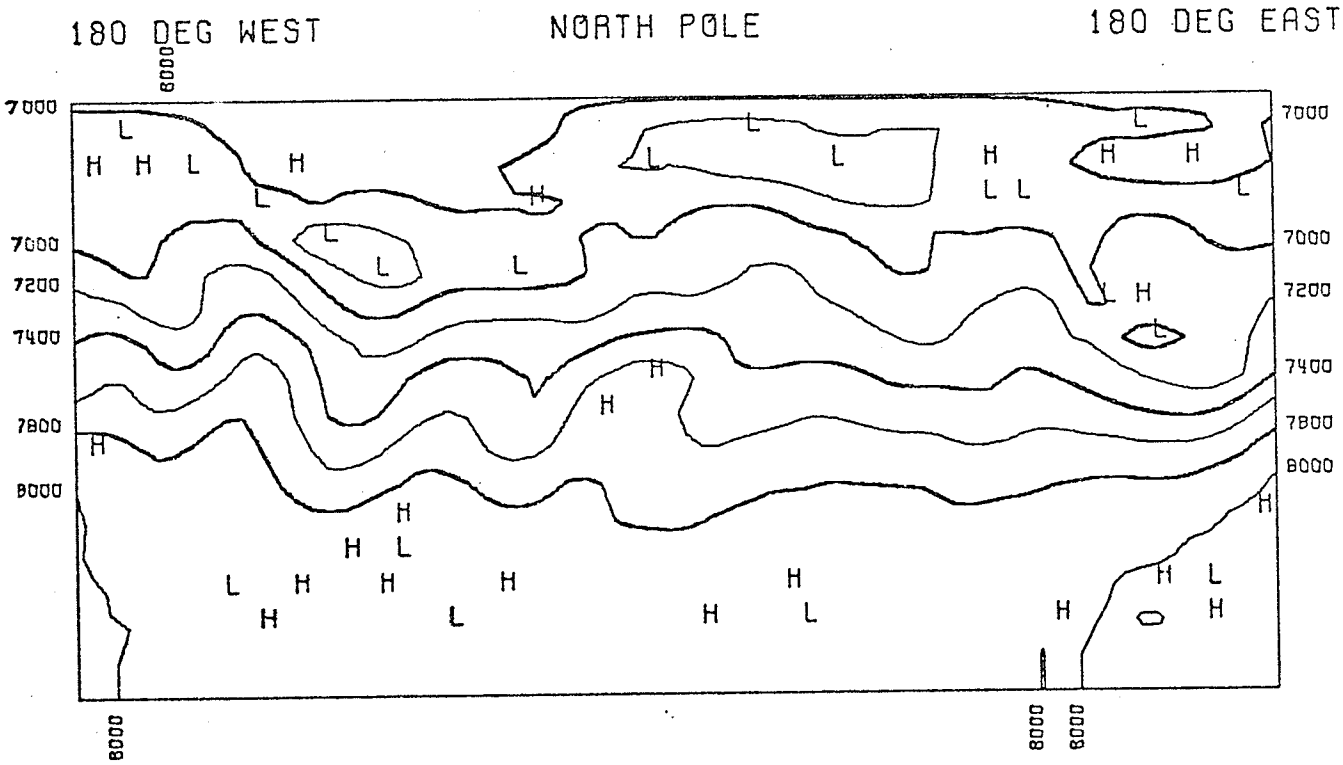

Figure 4.98: 400 mb Geopotential (m), model F, 36 hour

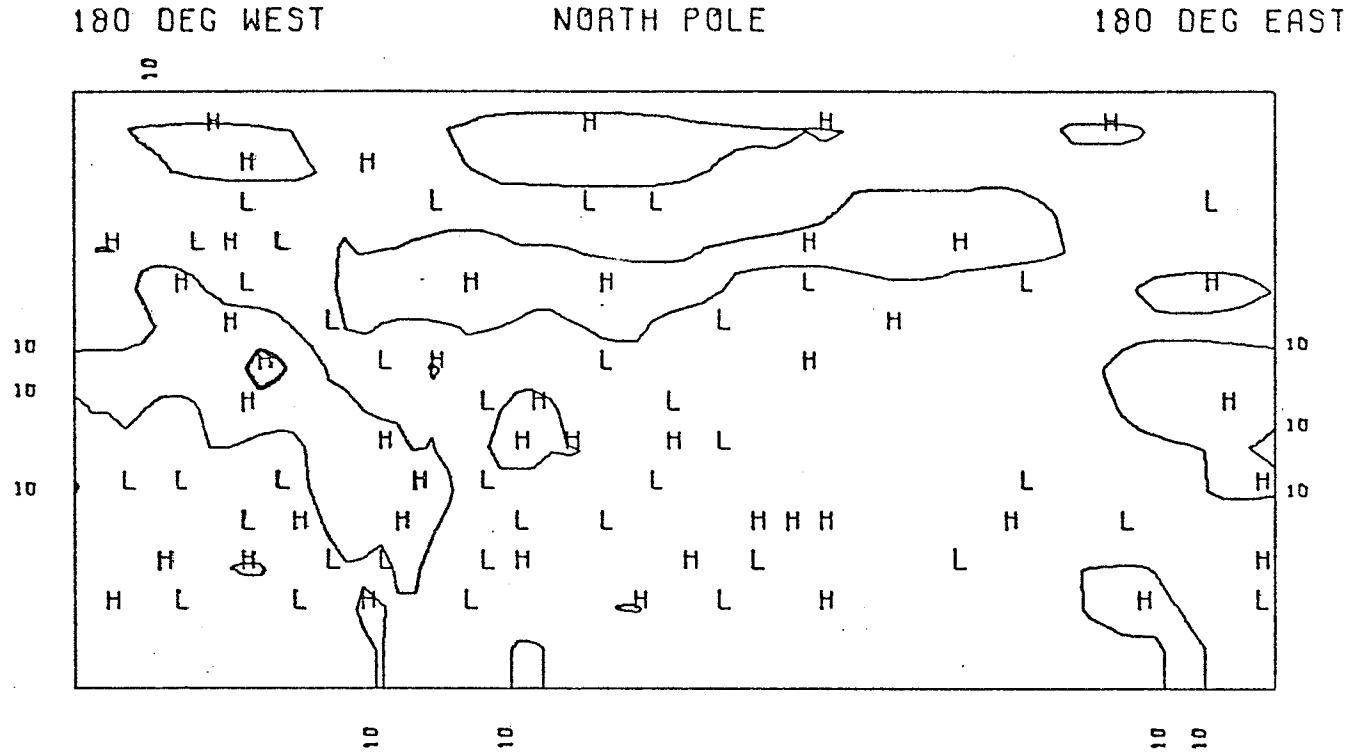

Figure 4.99: 800 mb Resultant Velocity Isotachs (m/sec), model ST, 36 hour

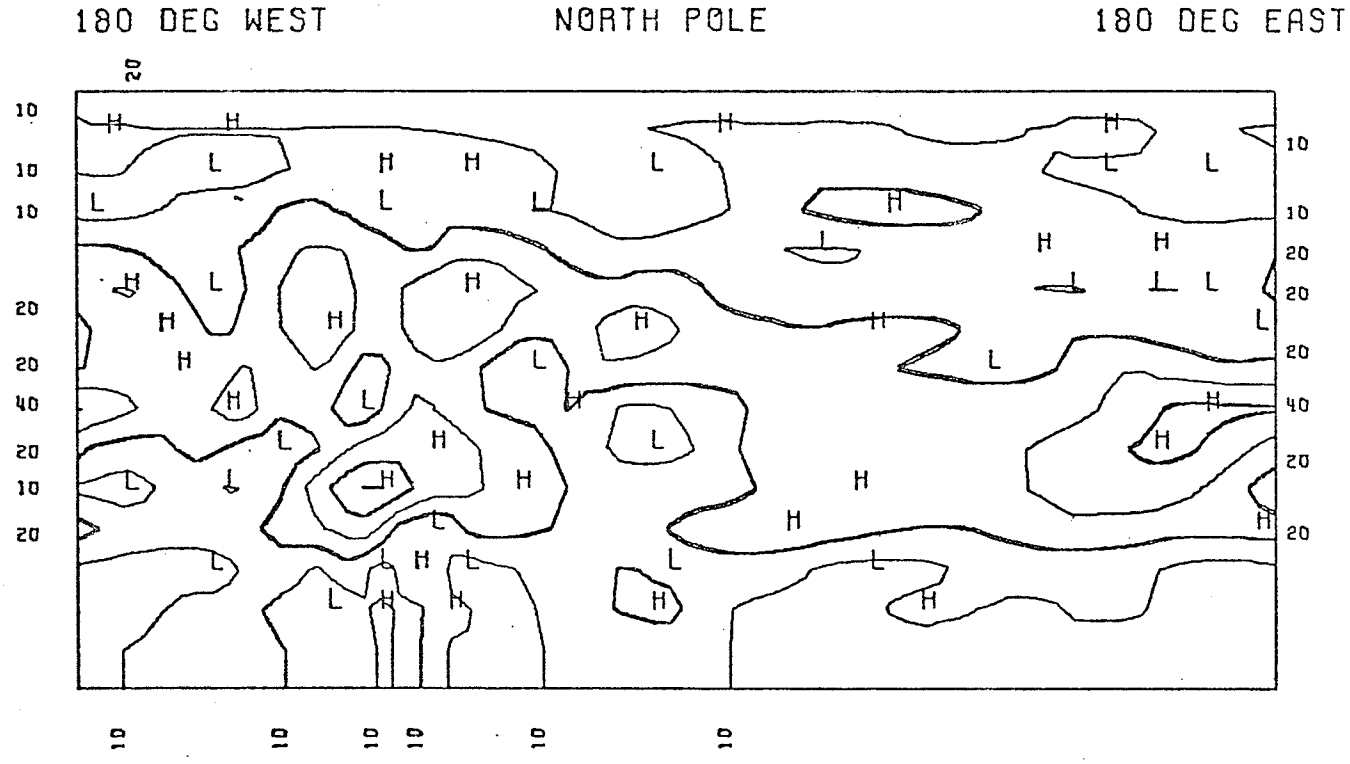

Figure 4.100: 400 mb Resultant Velocity Isotachs (m/sec), model ST, 36 hour

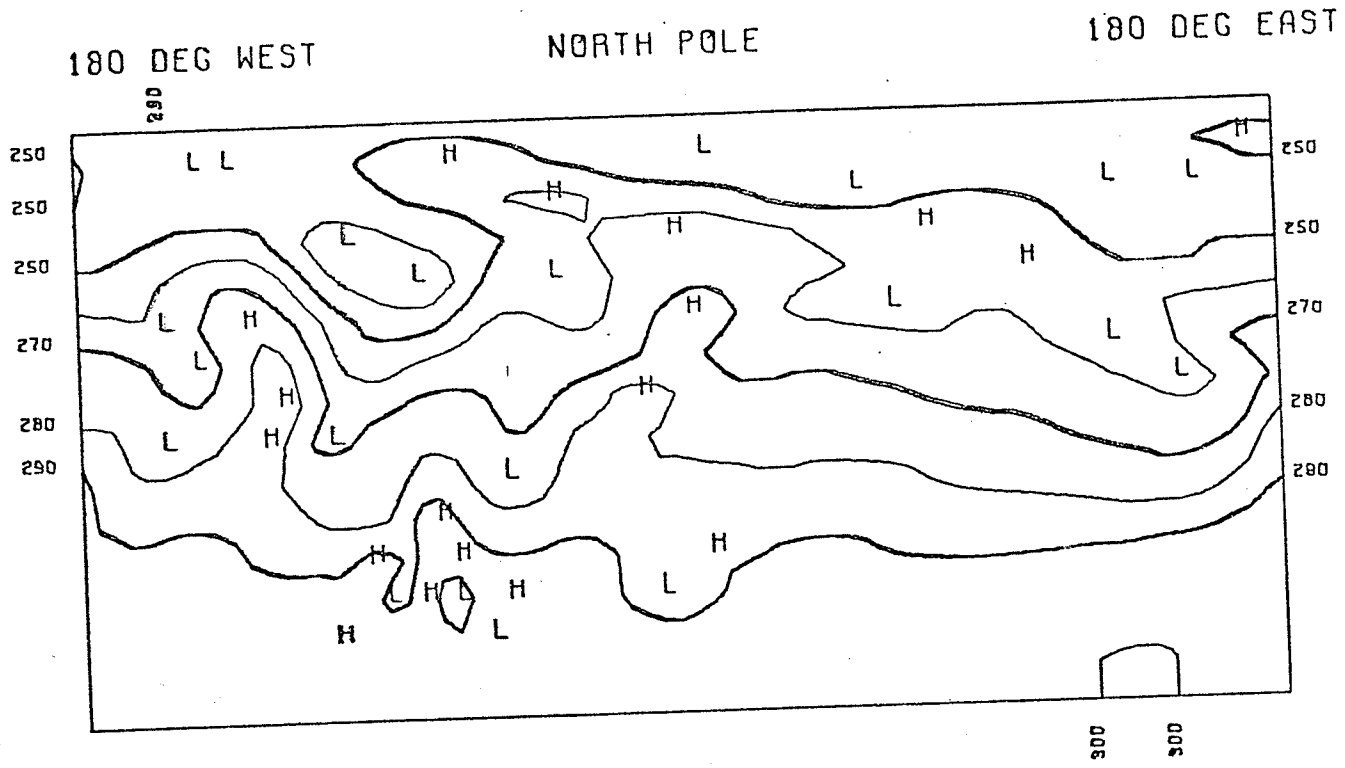

Figure 4.101: 800 mb Temperature (^{o}K), model ST, 36 hour

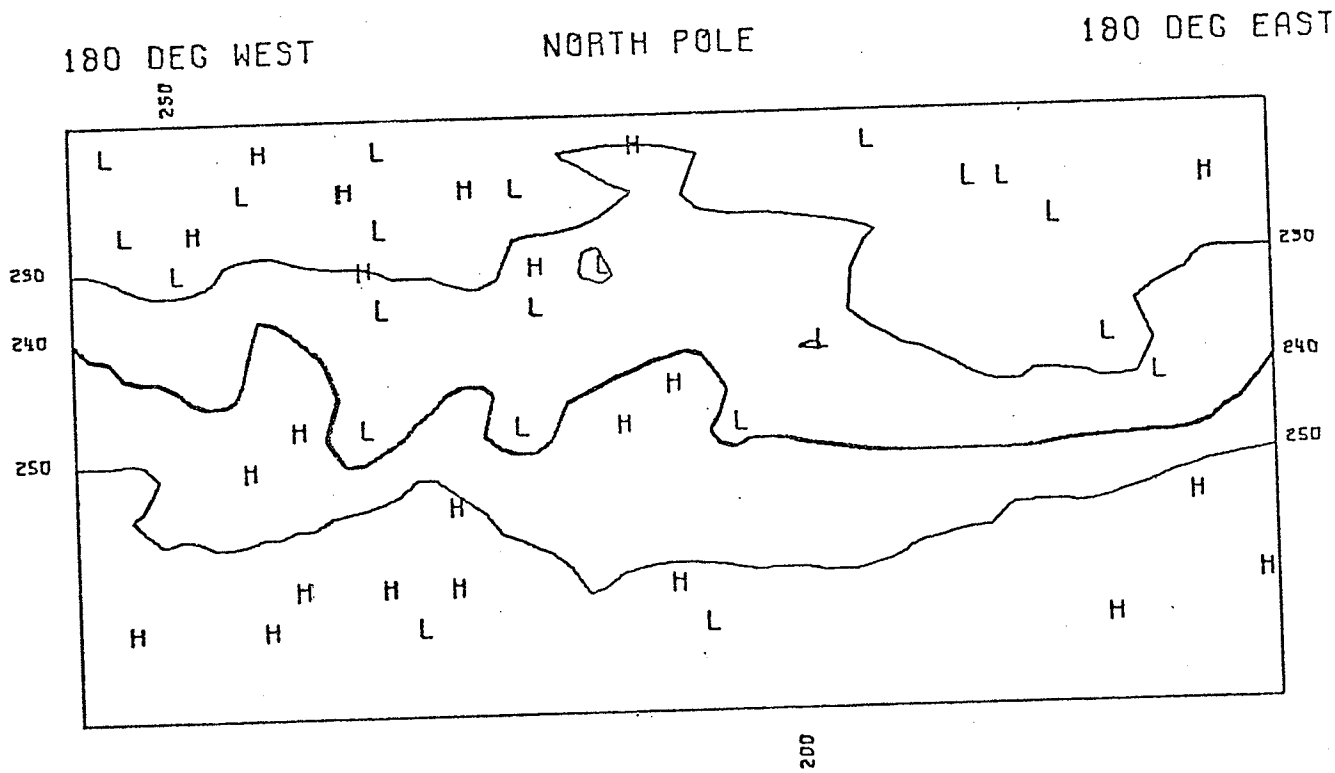

Figure 4.102: 400 mb Temperature (^{o}K), model ST, 36 hour

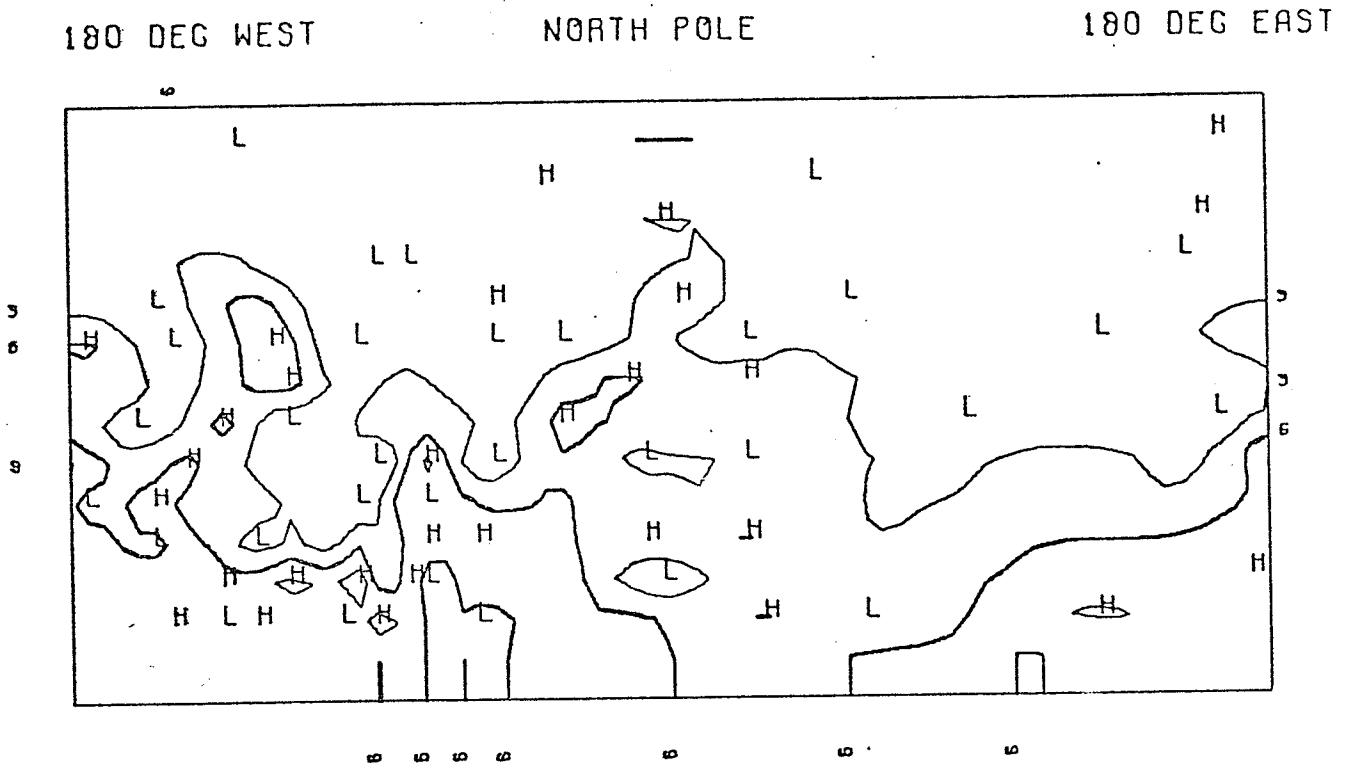

Figure 4.103: 800 mb Moisture (g H_2O/g dry air x 10^{-3}), model ST, 36 hour

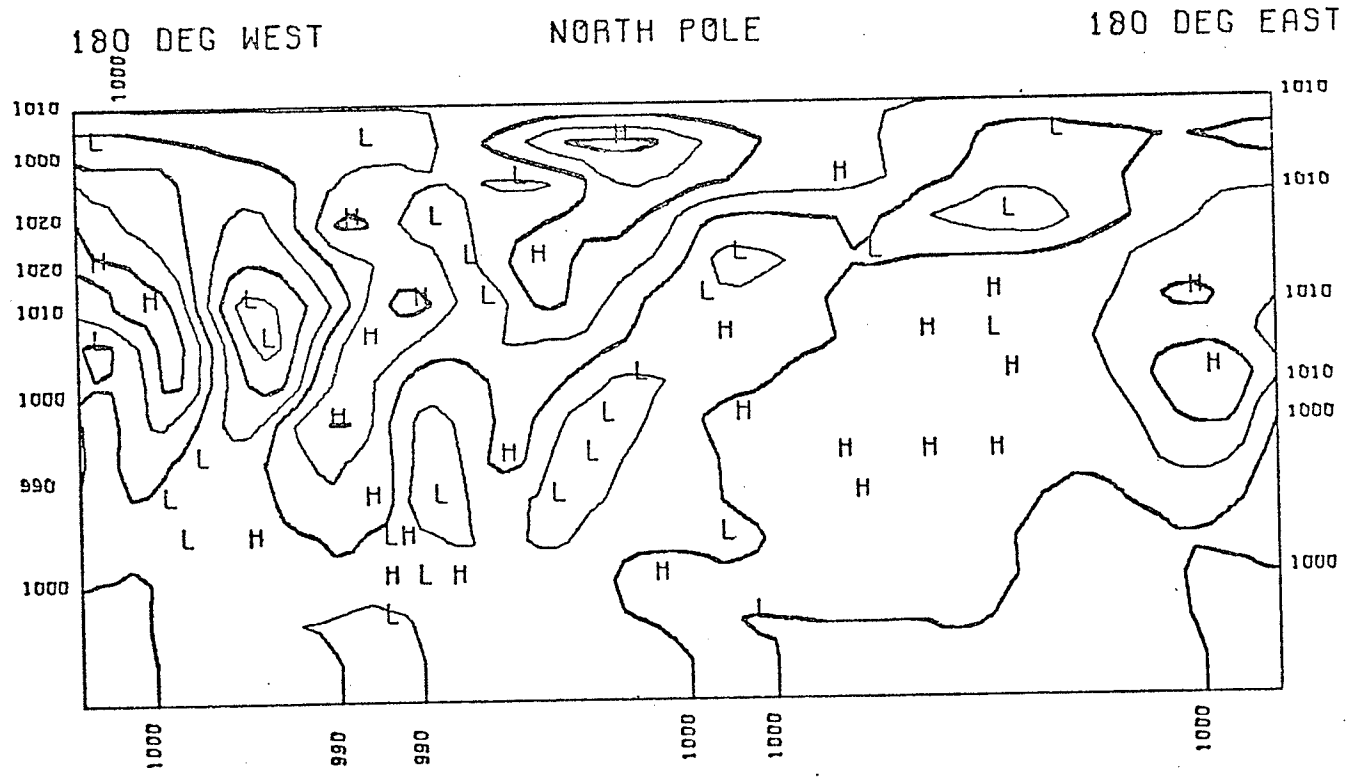

Figure 4.104: Surface Pressure (mb), model ST, 36 hour

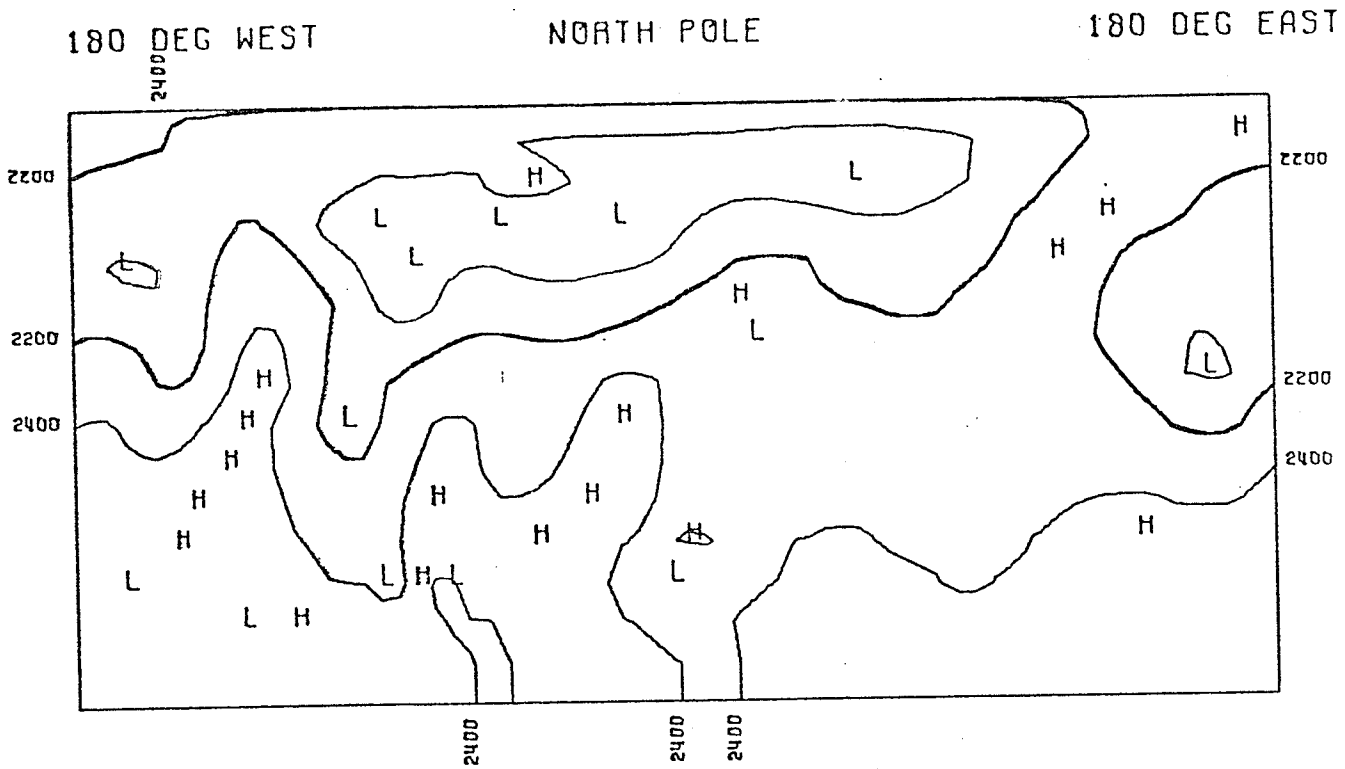

Figure 4.105: 800 mb Geopotential (m), model ST, 36 hour

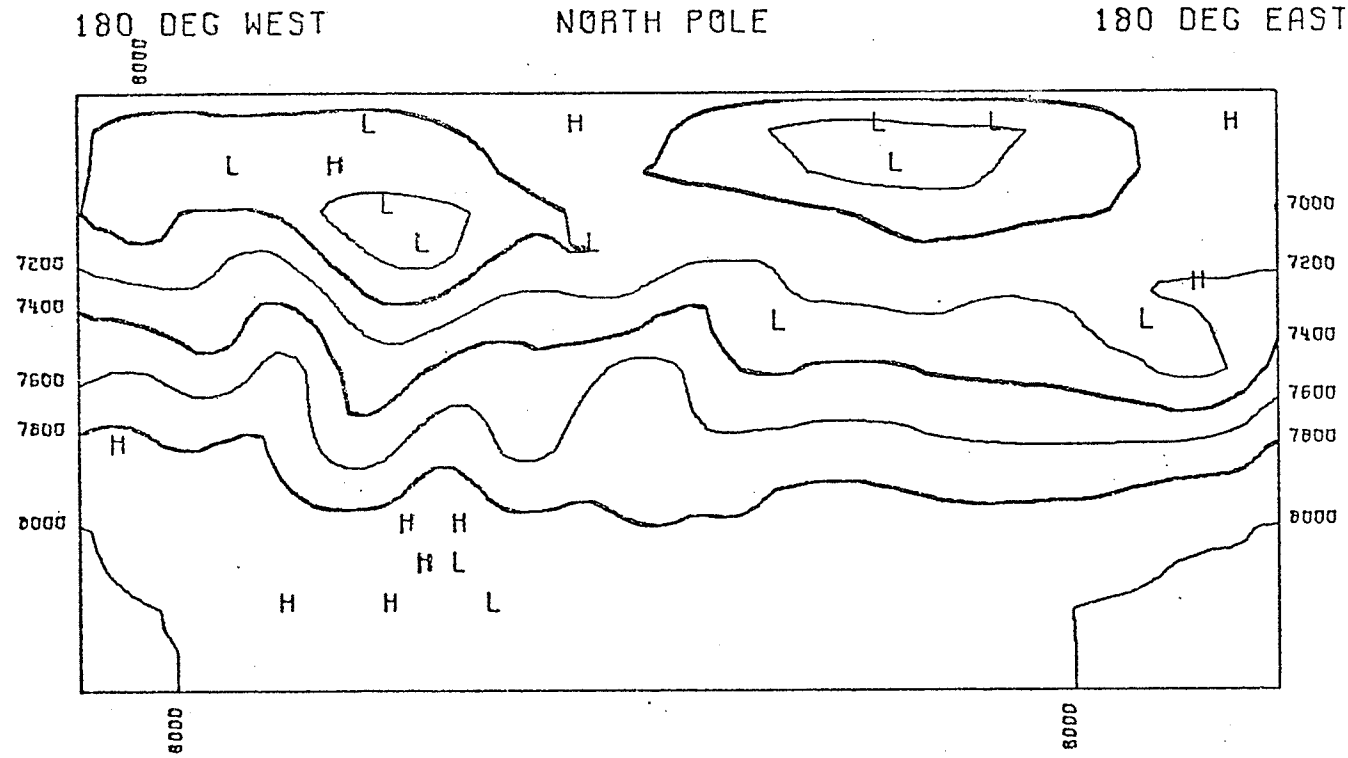

Figure 4.106: 400 mb Geopotential (m), model ST, 36 hour

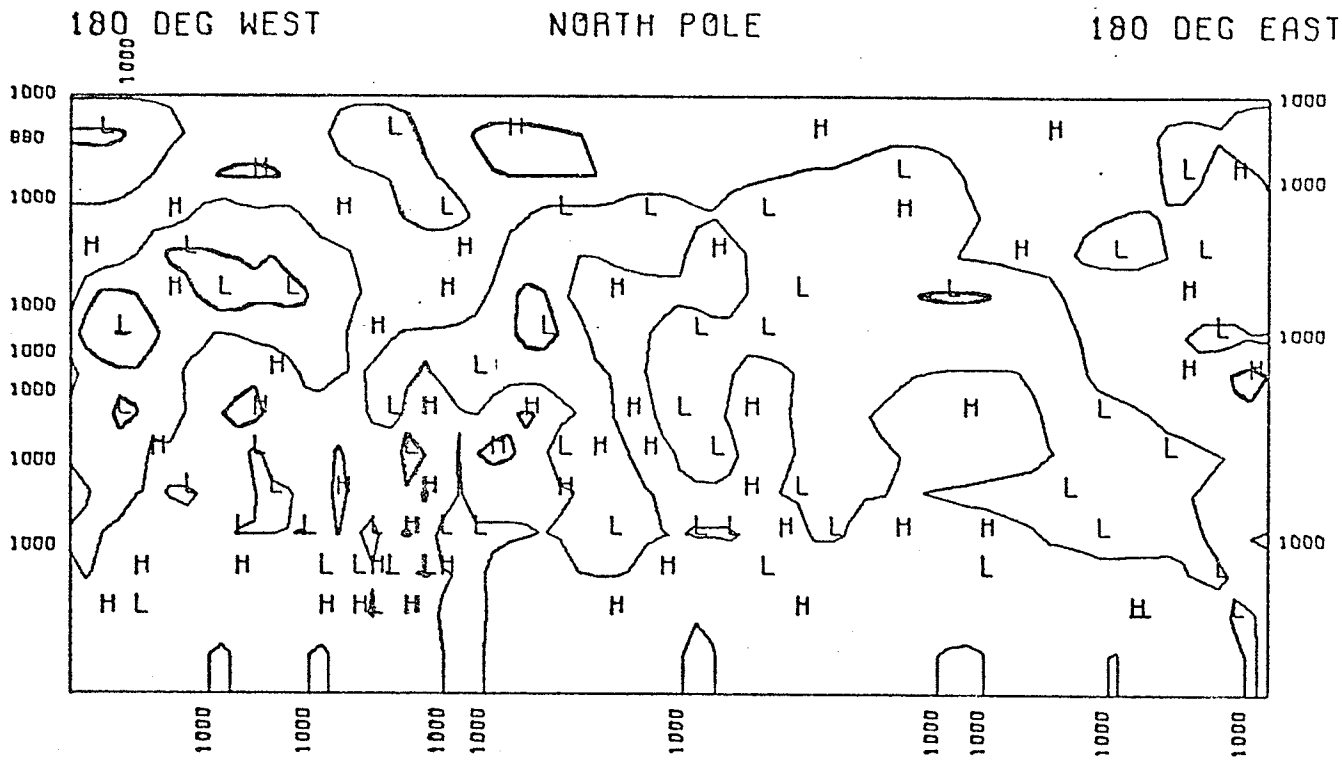

Figure 4.107: 800 mb Resultant Velocity Isotachs (m/sec), model ST, 36 hour error, 1000 represents zero error

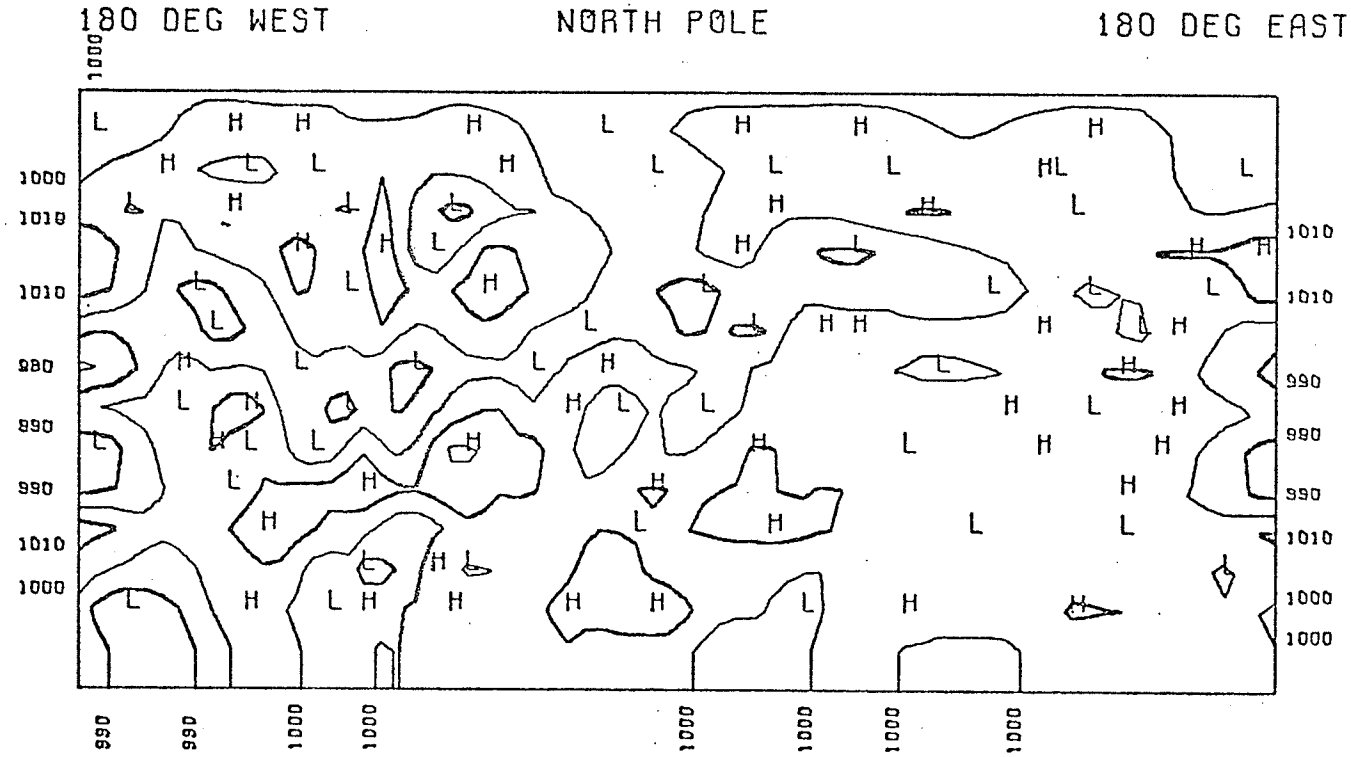

Figure 4.108: 400 mb Resultant Velocity Isotachs (m/sec), model ST, 36 hour error, 1000 represents zero error

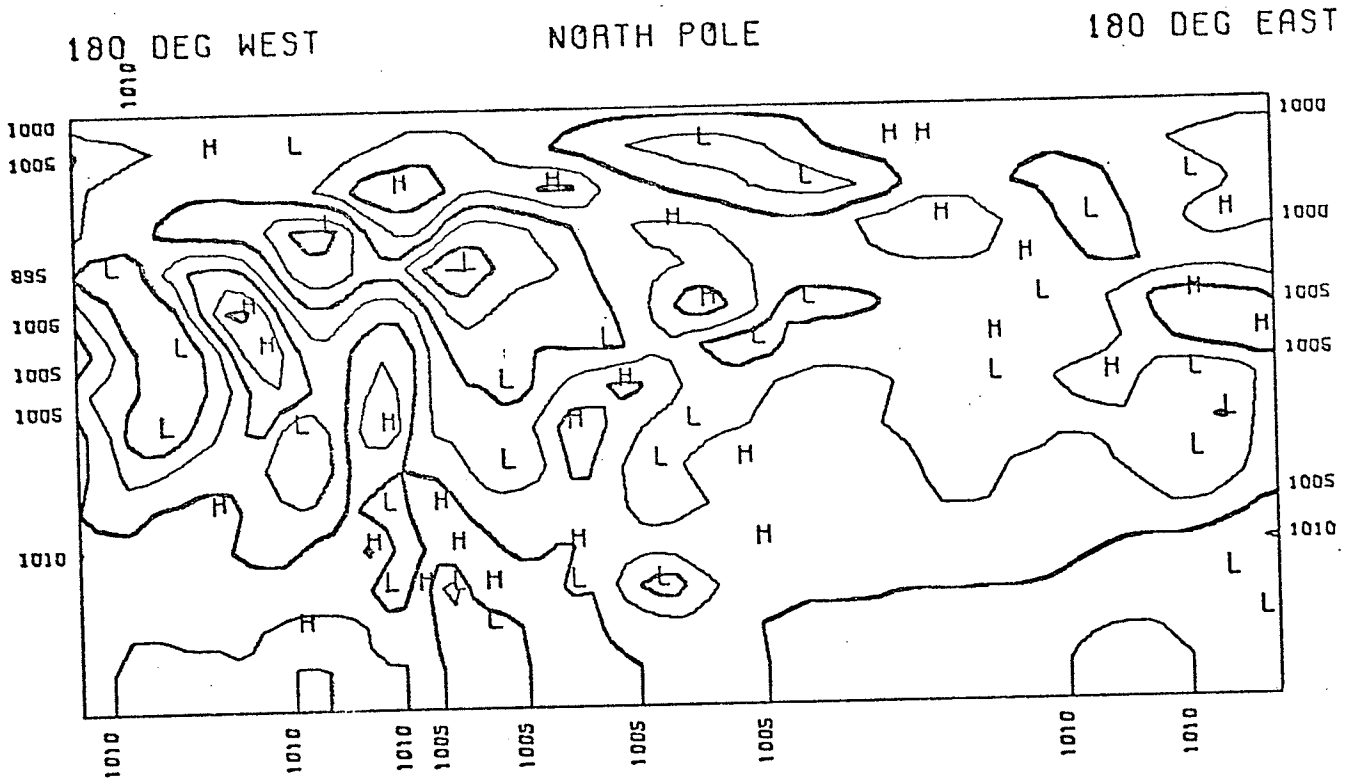

Figure 4.109: 800 mb Temperature (^{o}K), model ST, 36 hour error, 1000 represents zero error

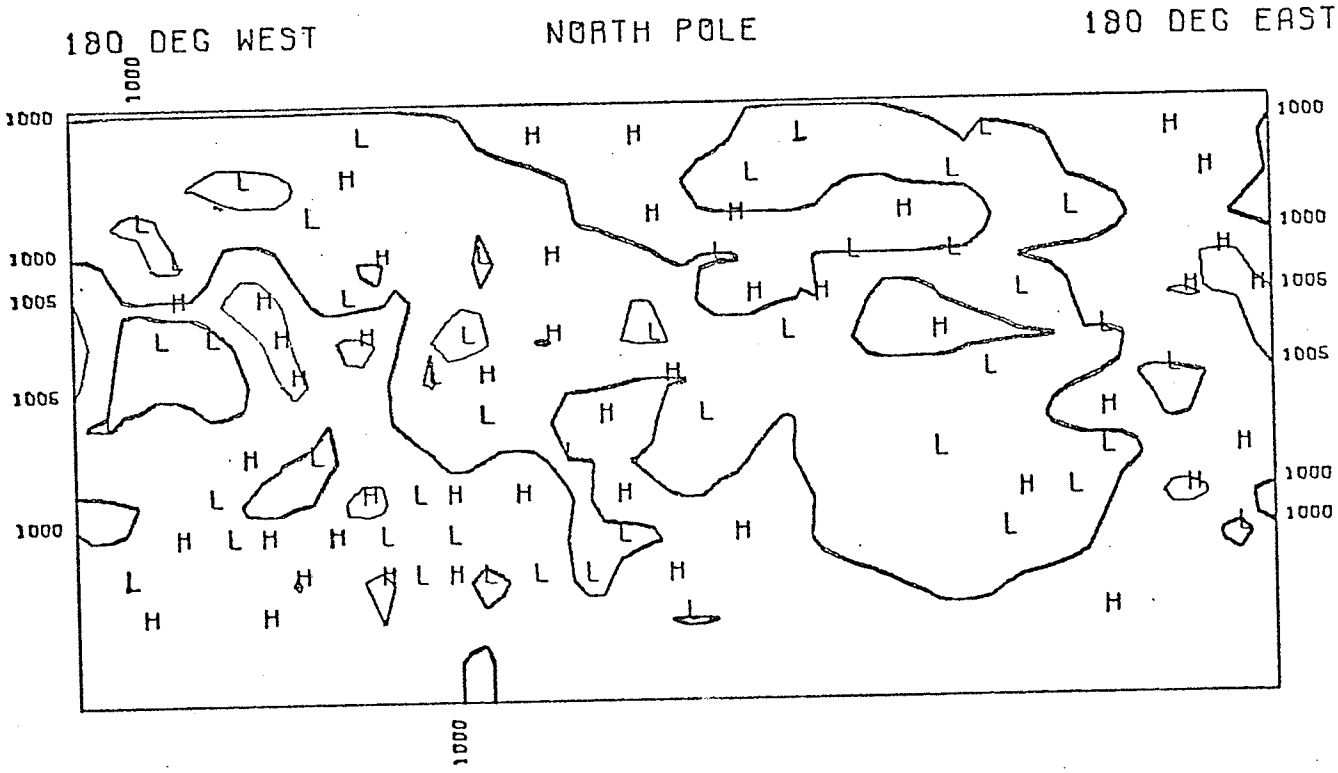

Figure 4.110: 400 mb Temperature (^{o}K), model ST, 36 hour error, 1000 represents zero error

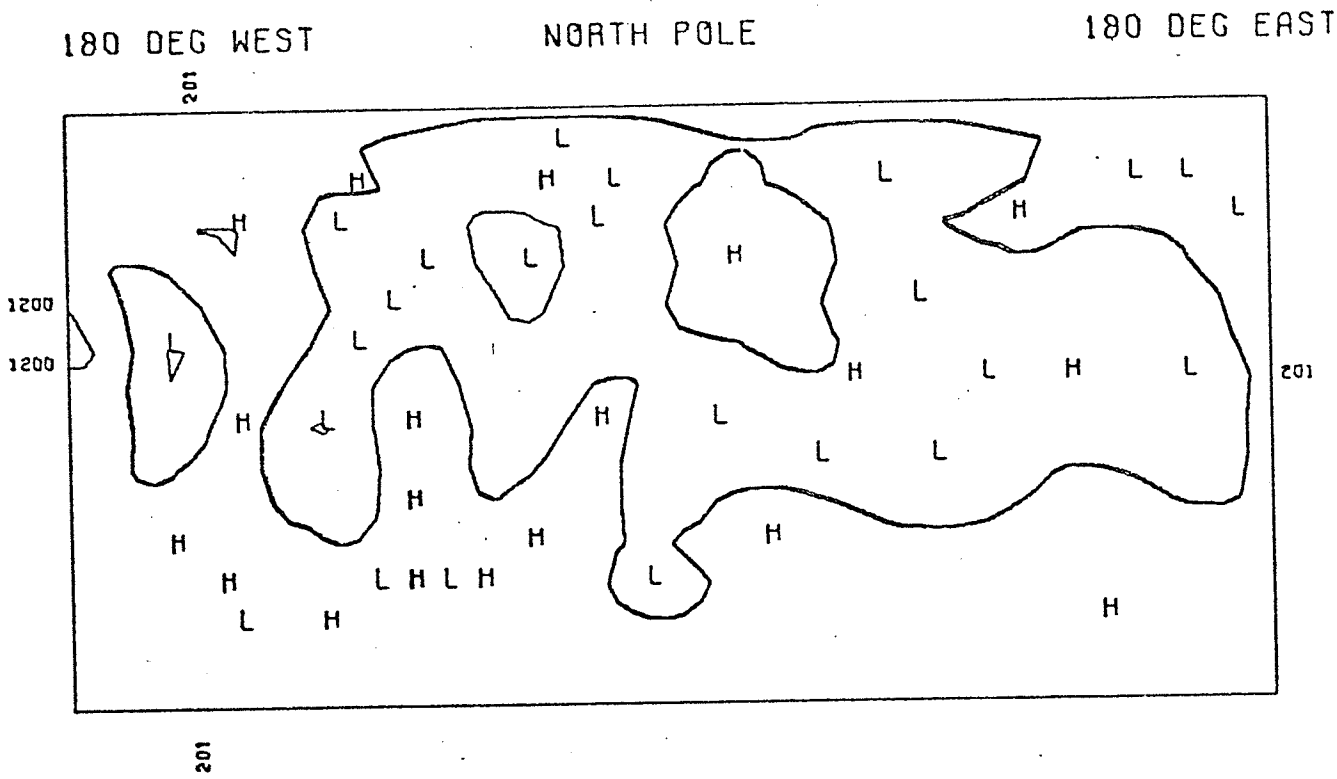

Figure 4.111: 800 mb Geopotential (m), model ST, 36 hour error, 1000 represents zero error

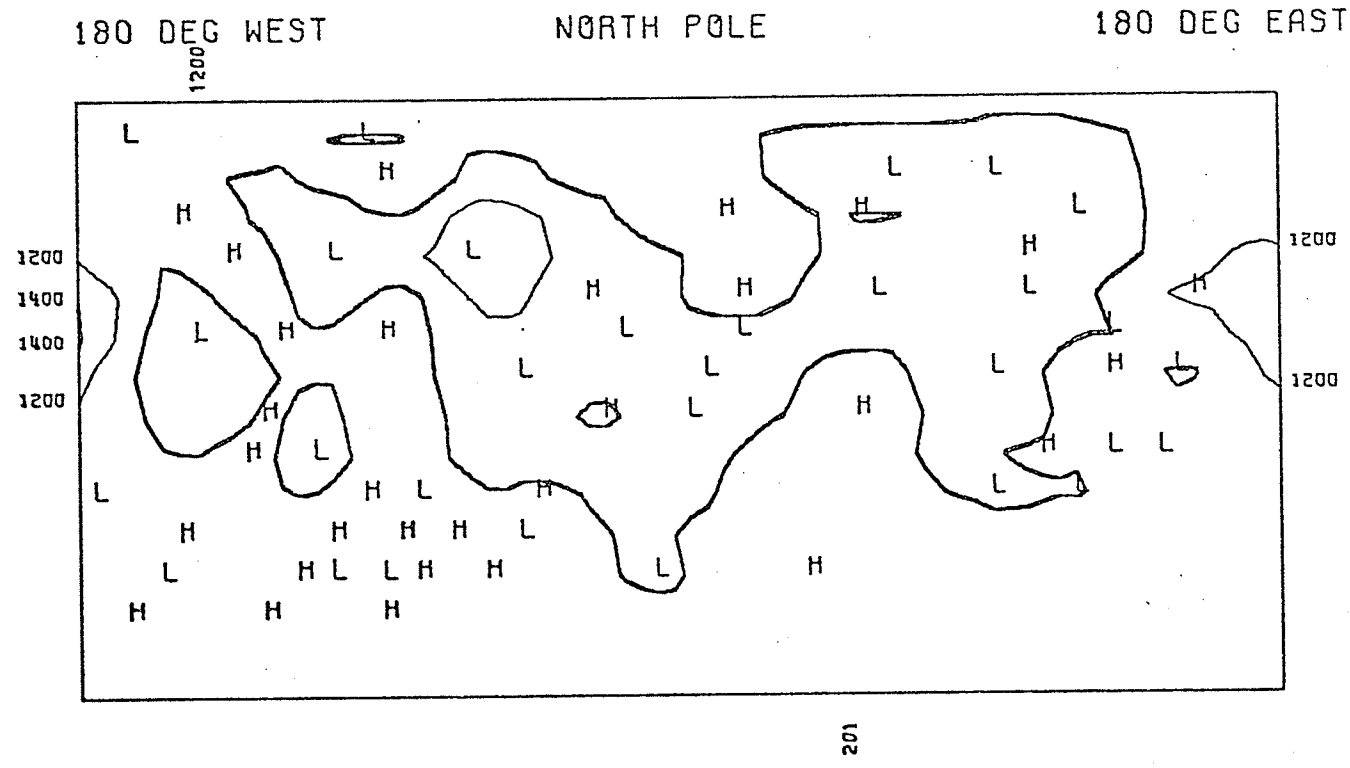

Figure 4.112: 400 mb Geopotential (m), model ST, 36 hour error, 1000 represents zero error

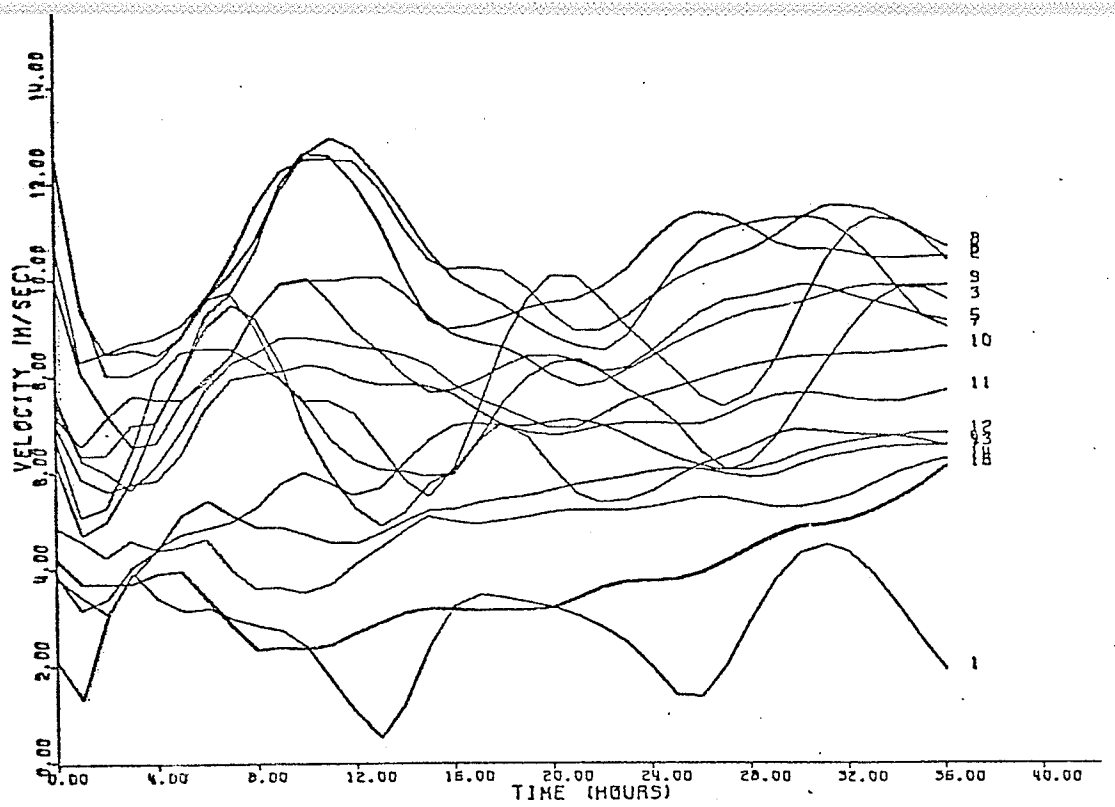

Figure 4.113: 800 mb Resultant Velocity Isotachs (m/sec), model ST, 0-36 hour zonal mean, numbers on the right denote the latitude circle, 1 denotes the north pole, 16 denotes the equator

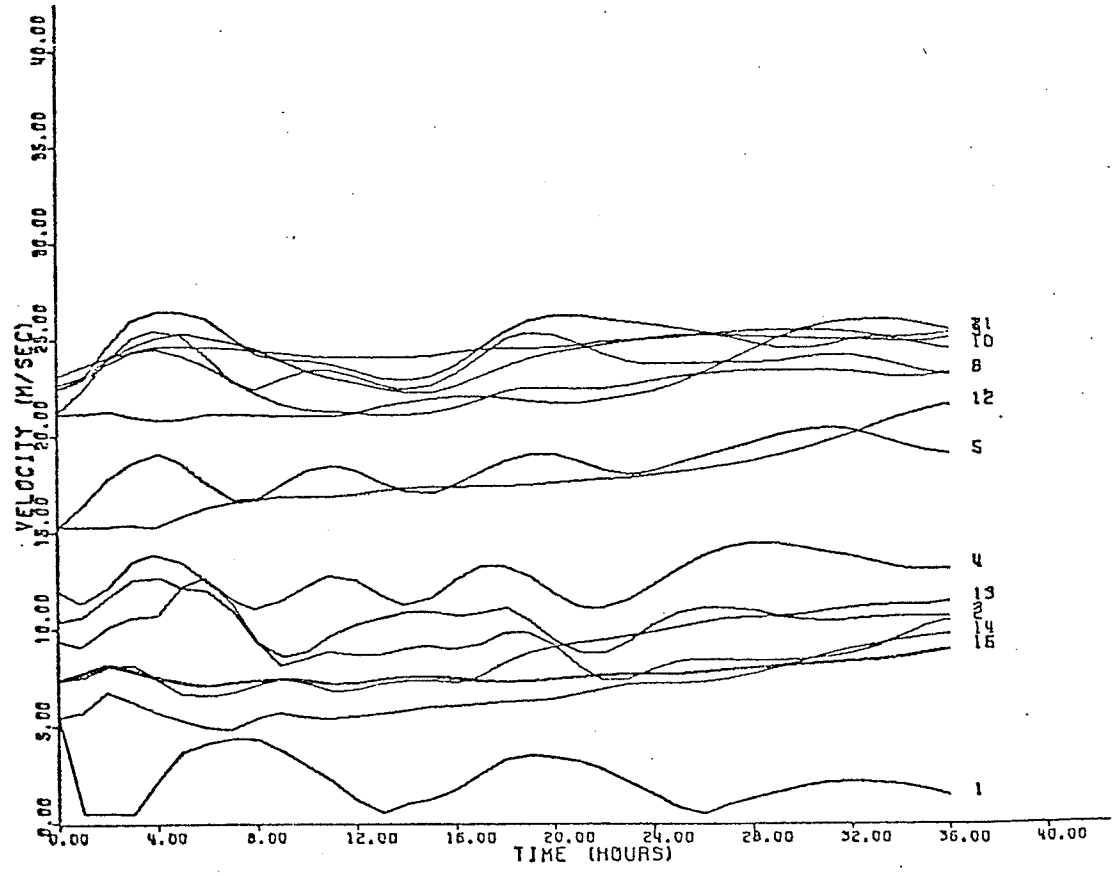

Figure 4.114: 400 mb Resultant Velocity Isotachs (m/sec), model ST, 0-36 hour zonal mean, numbers on the right denote the latitude circle, 1 denotes the north pole, 16 denotes the equator

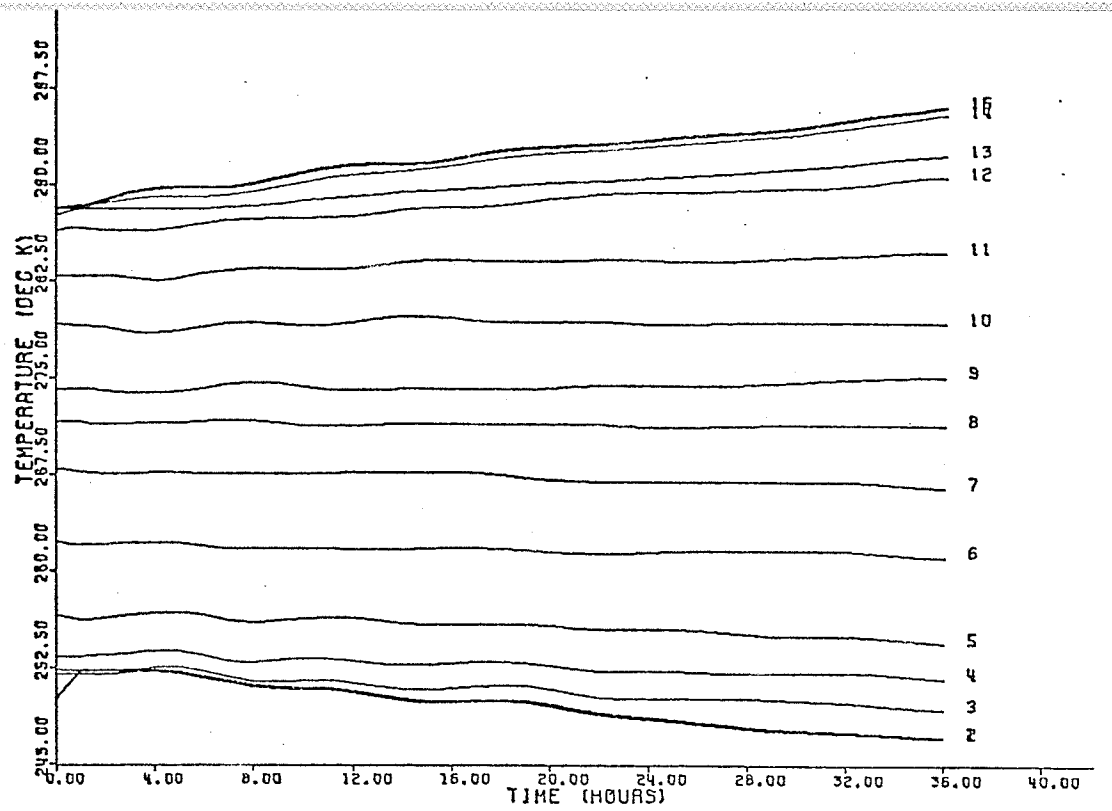

Figure 4.115: 800 mb Temperature (^{o}K), model ST, 0-36 hour zonal mean, numbers on the right denote the latitude circle, 1 denotes the north pole, 16 denotes the equator

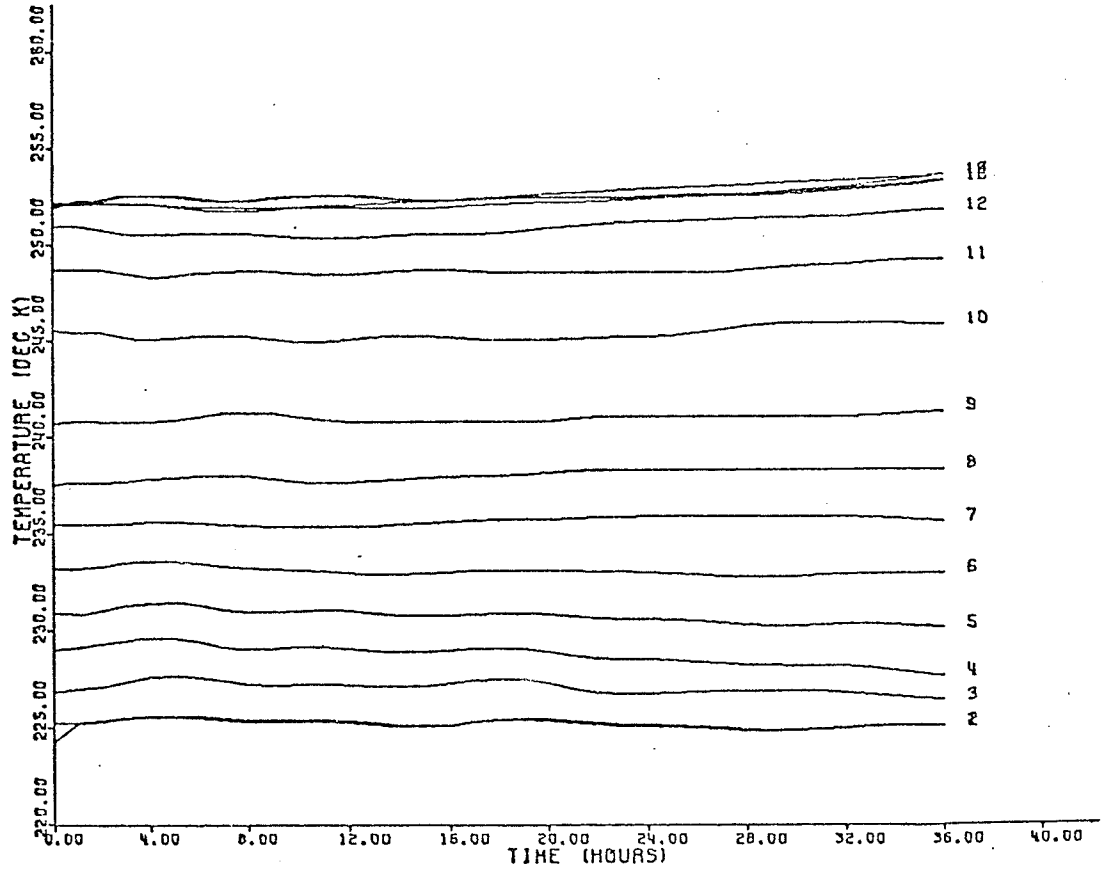

Figure 4.116: 400 mb Temperature (^{o}K), model ST, 0-36 hour zonal mean, numbers on the right denote the latitude circle, 1 denotes the north pole, 16 denotes the equator

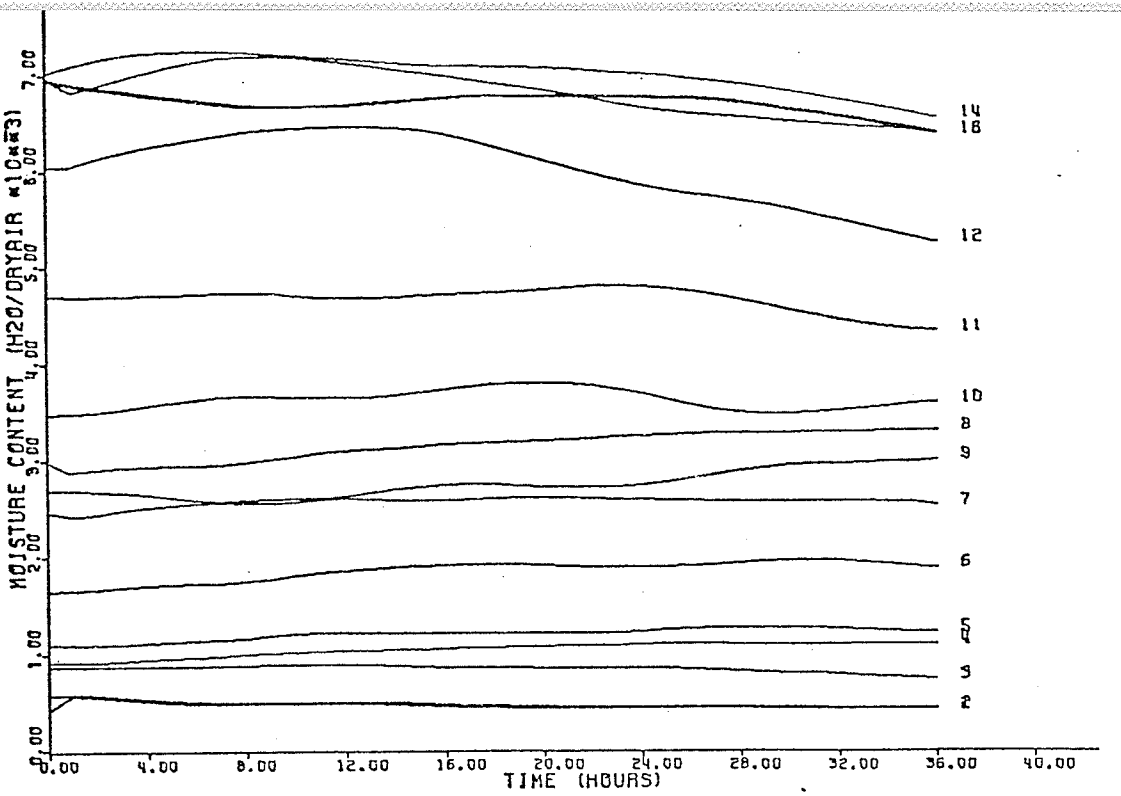

Figure 4.117: 800 mb Moisture (g H_2O/g dry air x 10^{-3}), model ST, 0-36 hour zonal mean, numbers on the right denote the latitude circle, 1 denotes the north pole, 16 denotes the equator

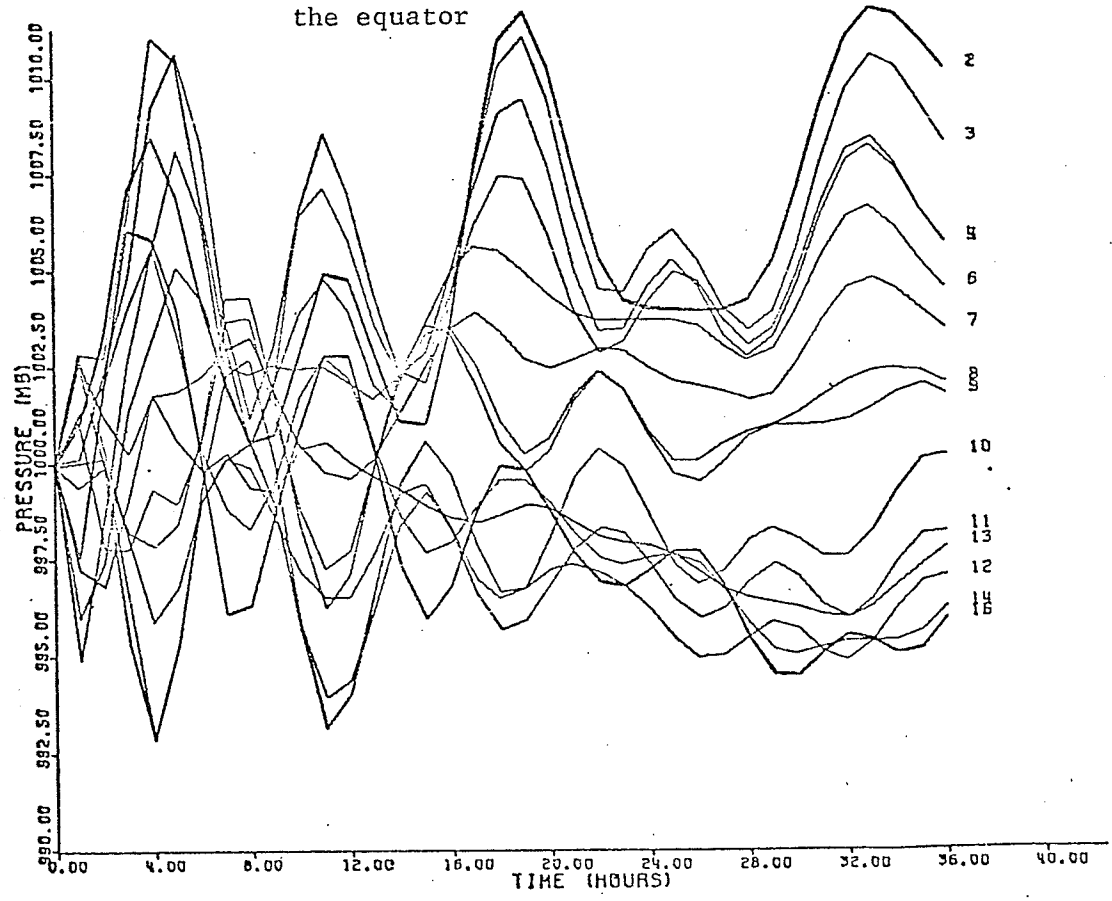

Figure 4.118: Surface Pressure (mb), model ST, 0-36 hour zonal mean, numbers on the right denote the latitude circle, 1 denotes the north pole, 16 denotes the equator

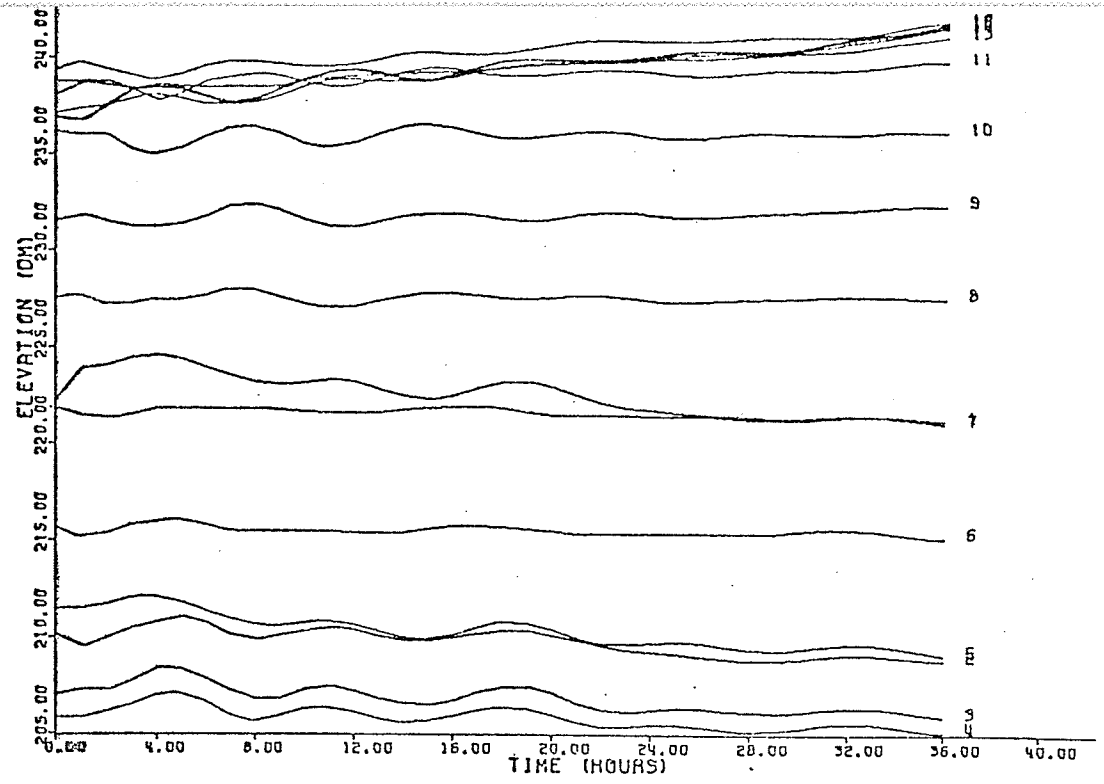

Figure 4.119: 800 mb Geopotential (dm), model ST, 0-36 hour zonal mean, numbers on the right denote the latitude circle, 1 denotes the north pole, 16 denotes the equator

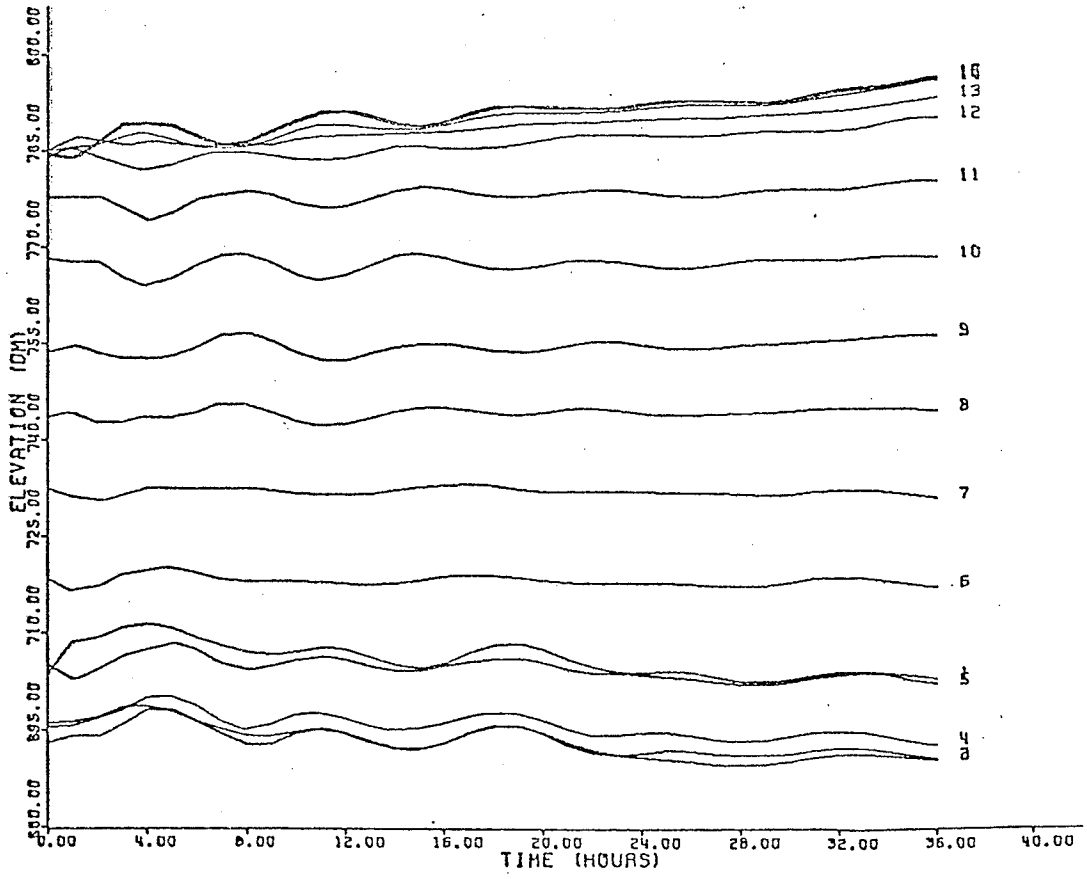

Figure 4.120: 400 mb Geopotential (dm), model ST, 0-36 hour zonal mean, numbers on the right denote the latitude circle, 1 denotes the north pole, 16 denotes the equator

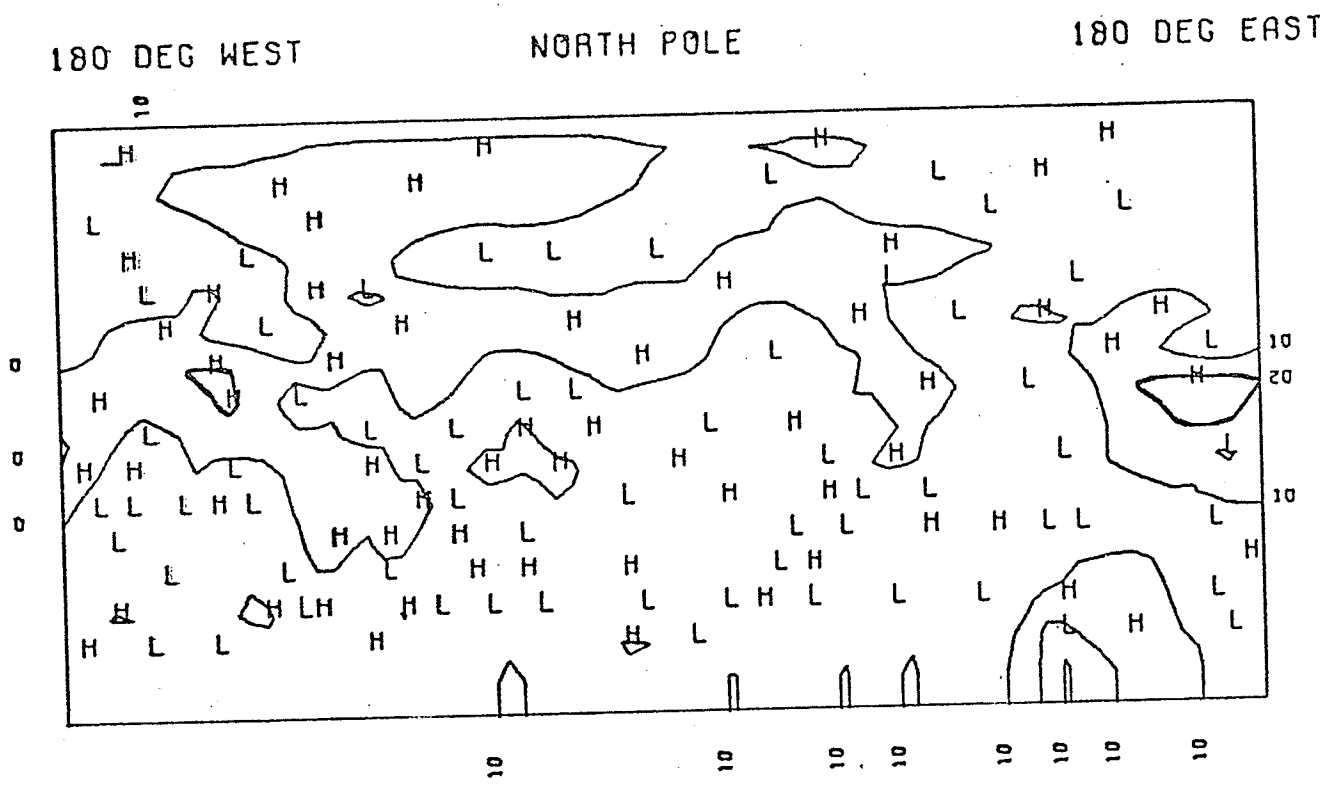

Figure 4.121: 800 mb Resultant Velocity Isotachs (m/sec), model C1, 36 hour

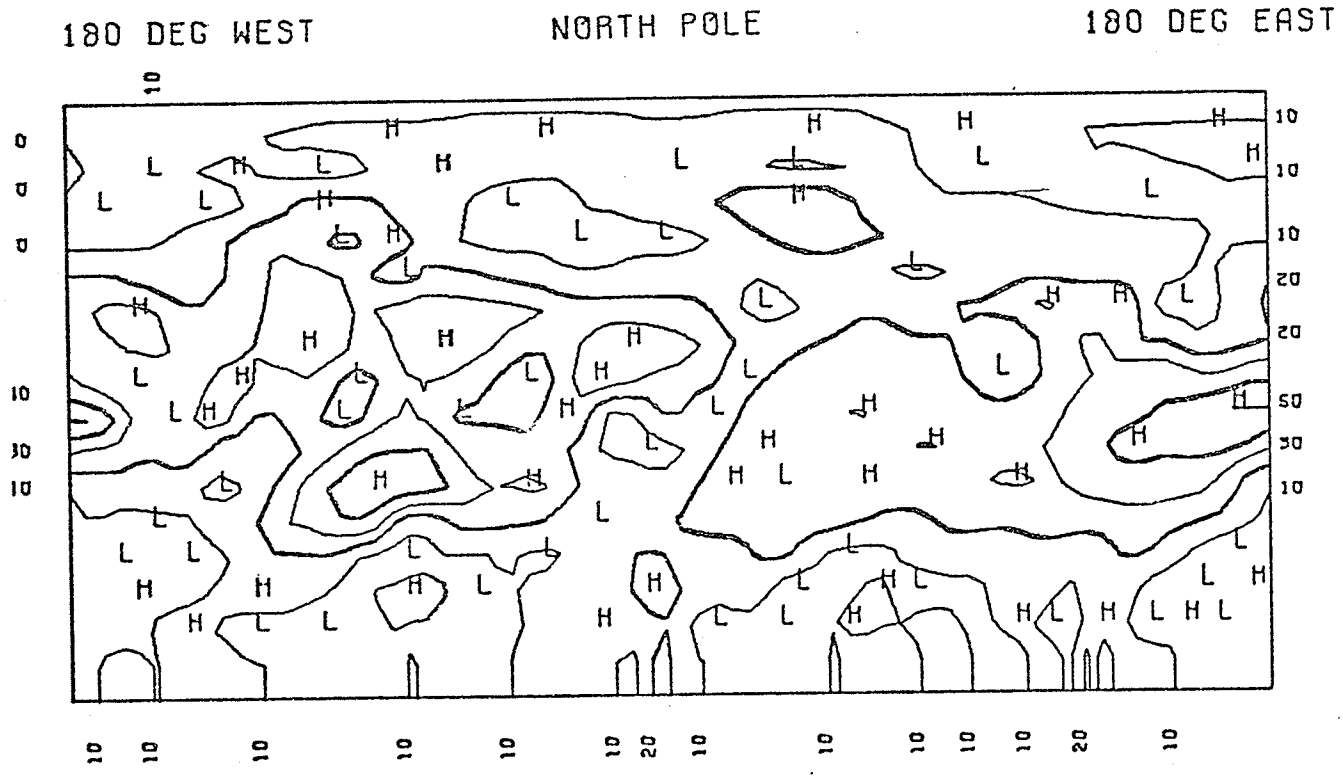

Figure 4.122: 400 mb Resultant Velocity (m/sec), model C1, 36 hour

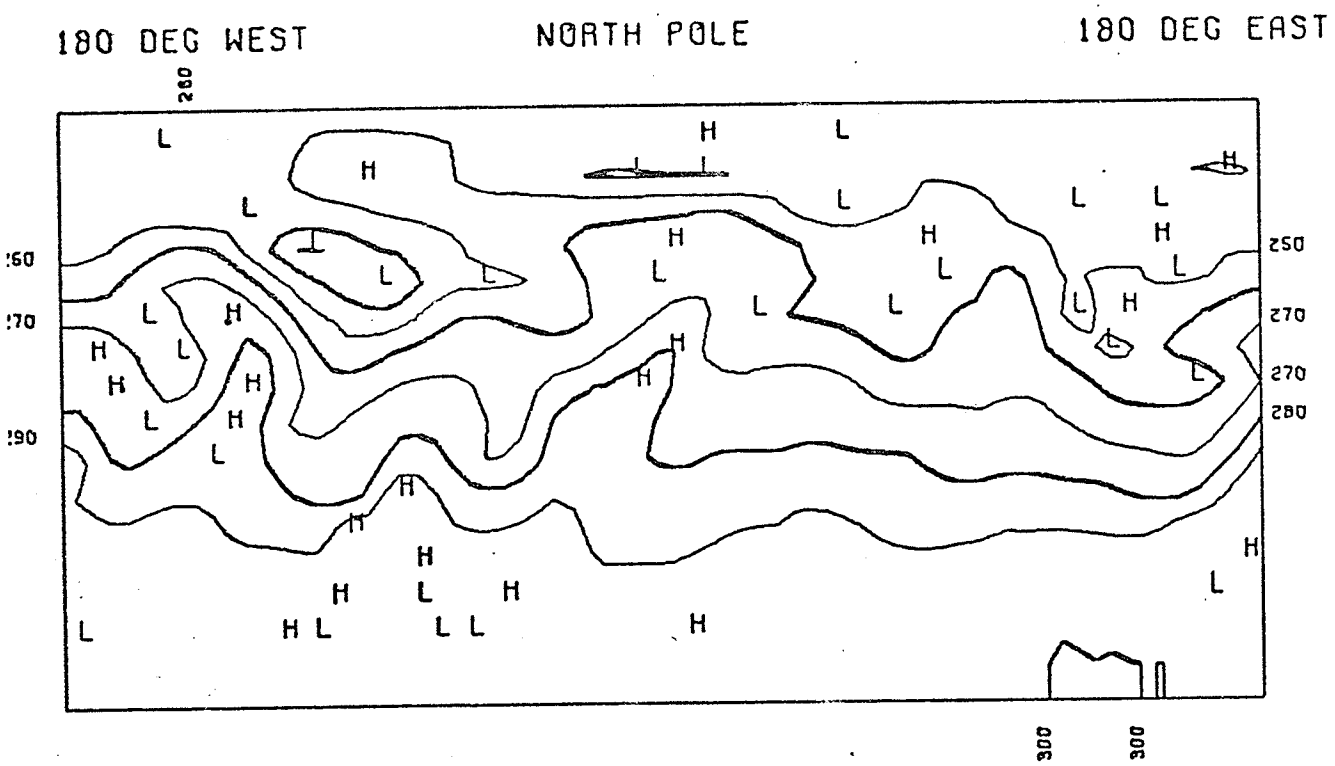

Figure 4.123: 800 mb Temperature (^{o}K), model C1, 36 hour

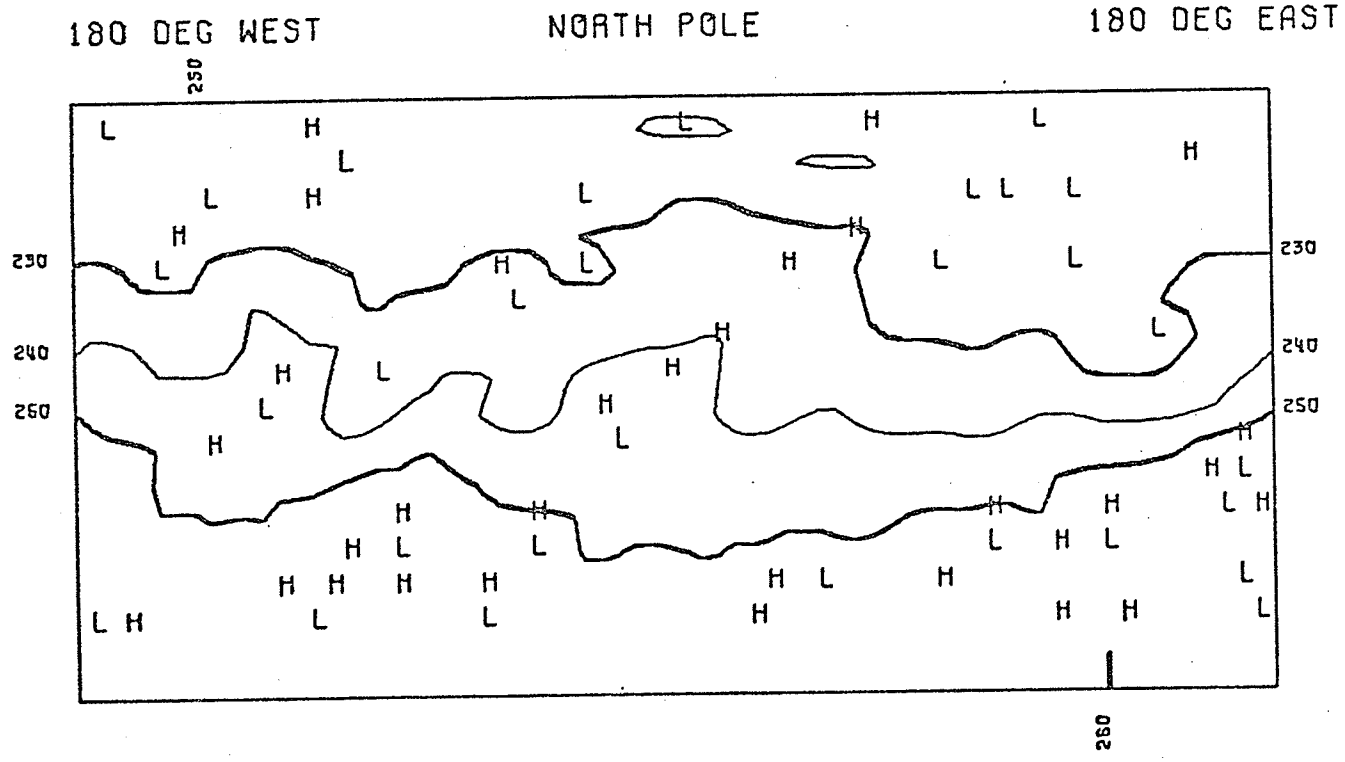

Figure 4.124: 400 mb Temperature (^{o}K), model C1, 36 hour

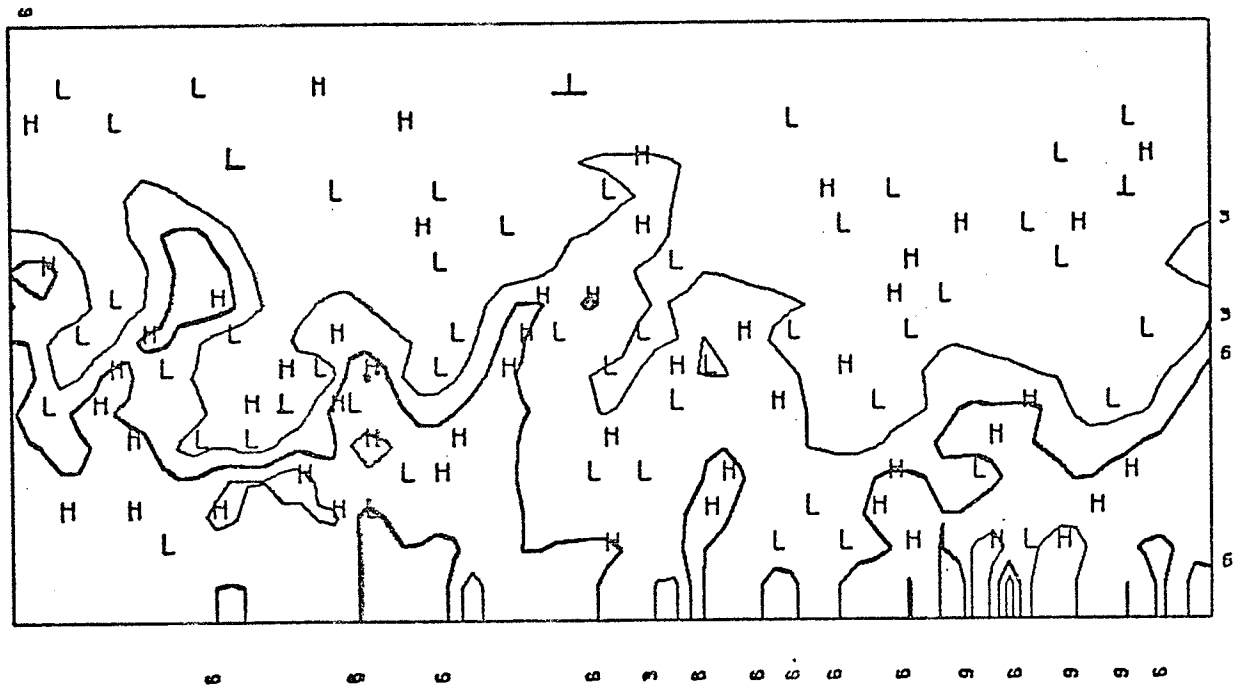

Figure 4.125: 800 mb Moisture (g H_2O/g dry air x 10^{-3}), model C1, 36 hour

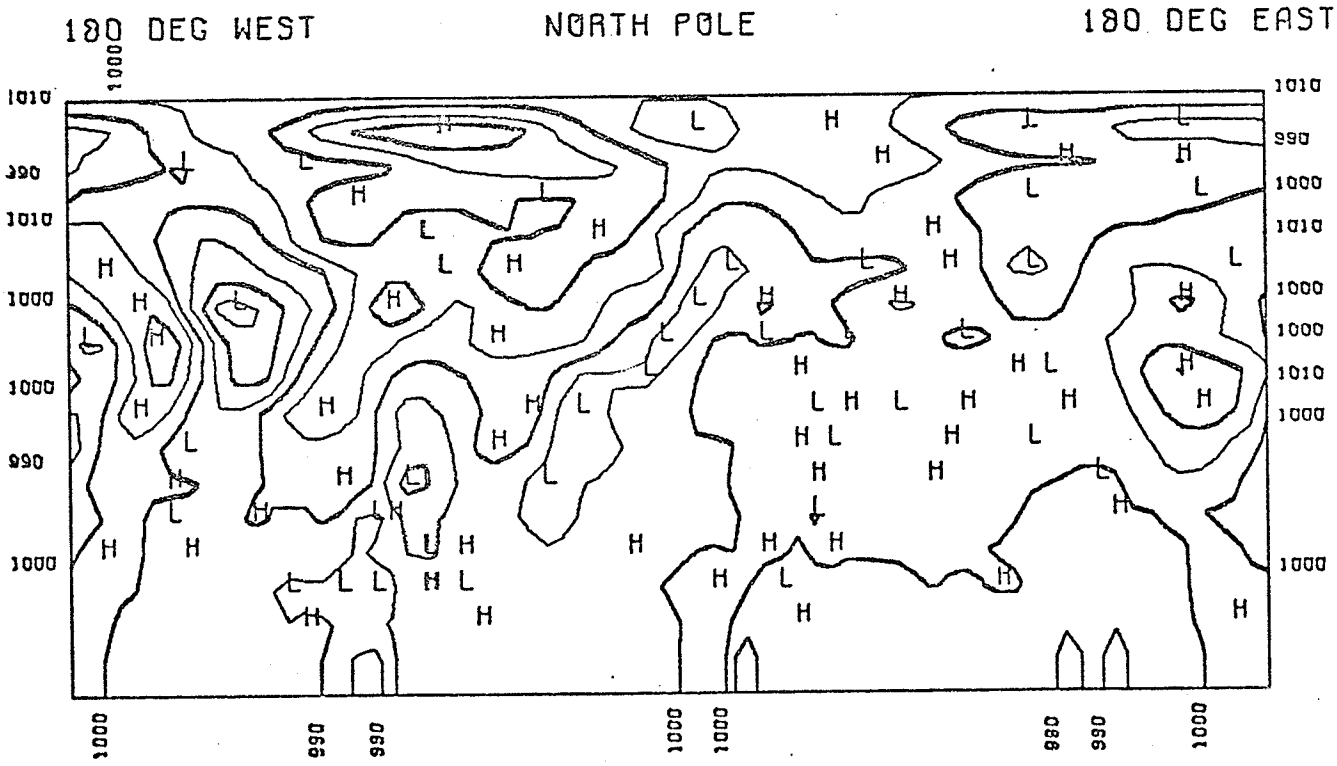

Figure 4.126: Surface Pressure (mb), model C1, 36 hour

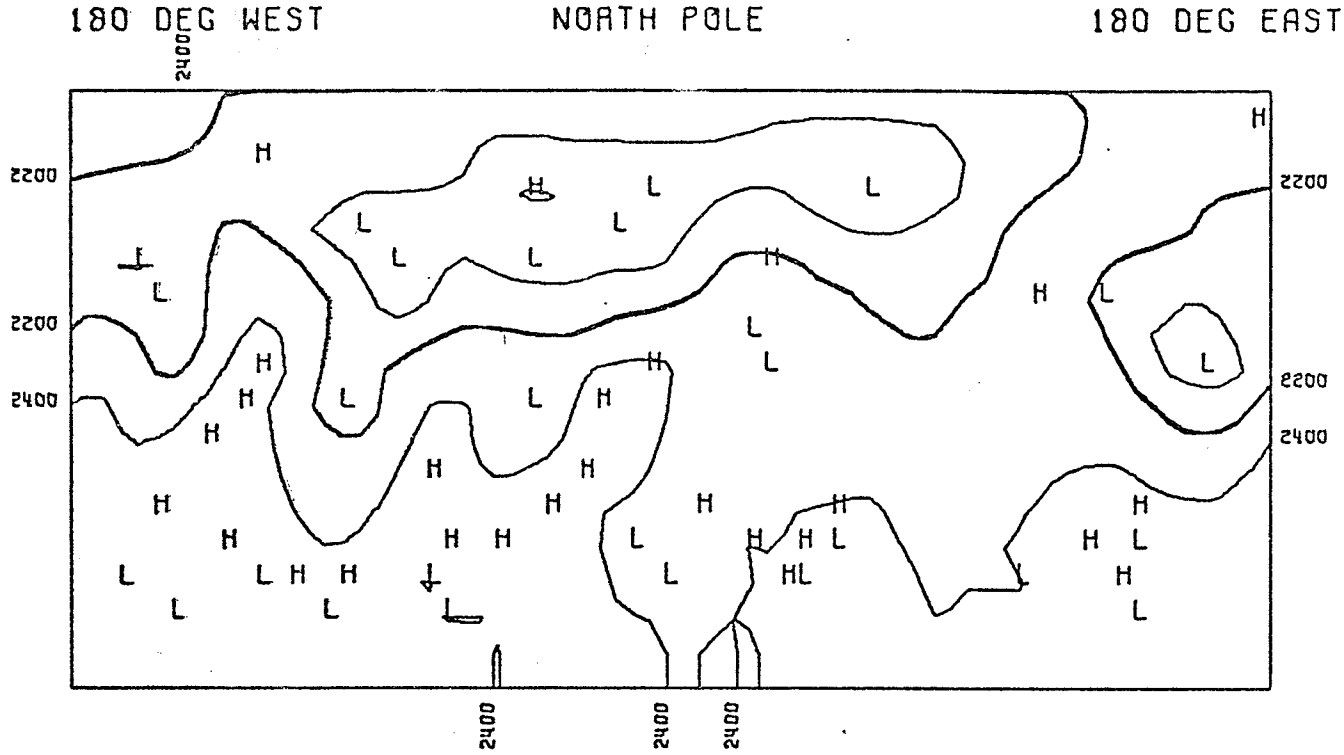

Figure 4.127: 800 mb Geopotential (m), model C1, 36 hour

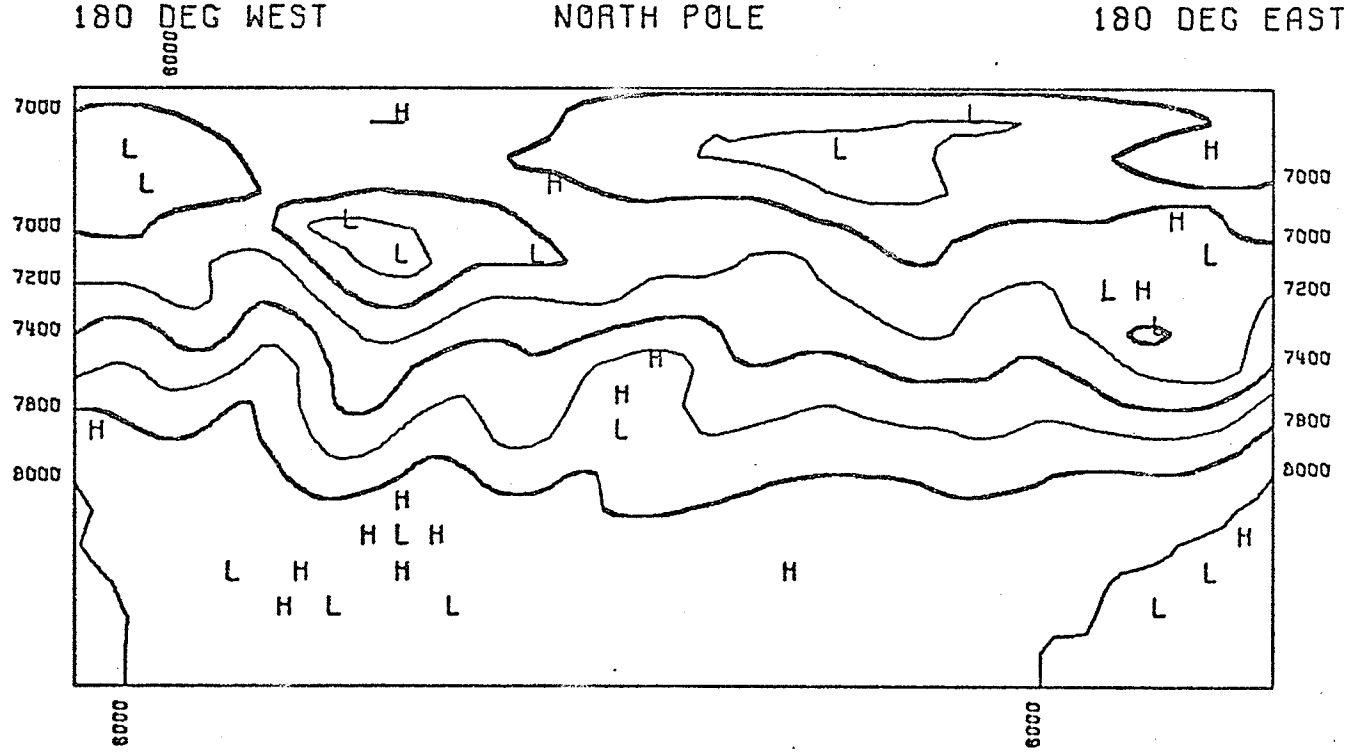

Figure 4.128: 400 mb Geopotential (m), model C1, 36 hour

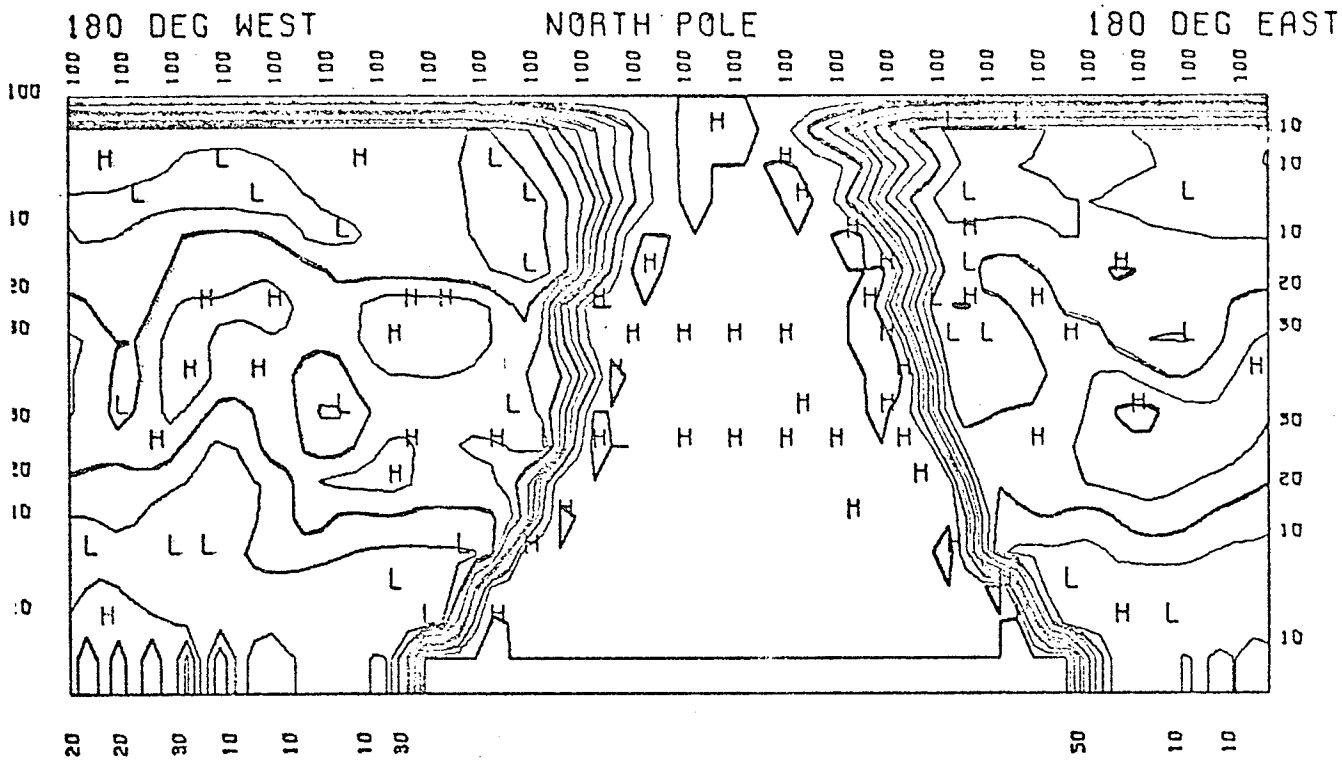

Figure 4.129: 400 mb Resultant Velocity Isotachs (m/sec), model C2, 7 hour

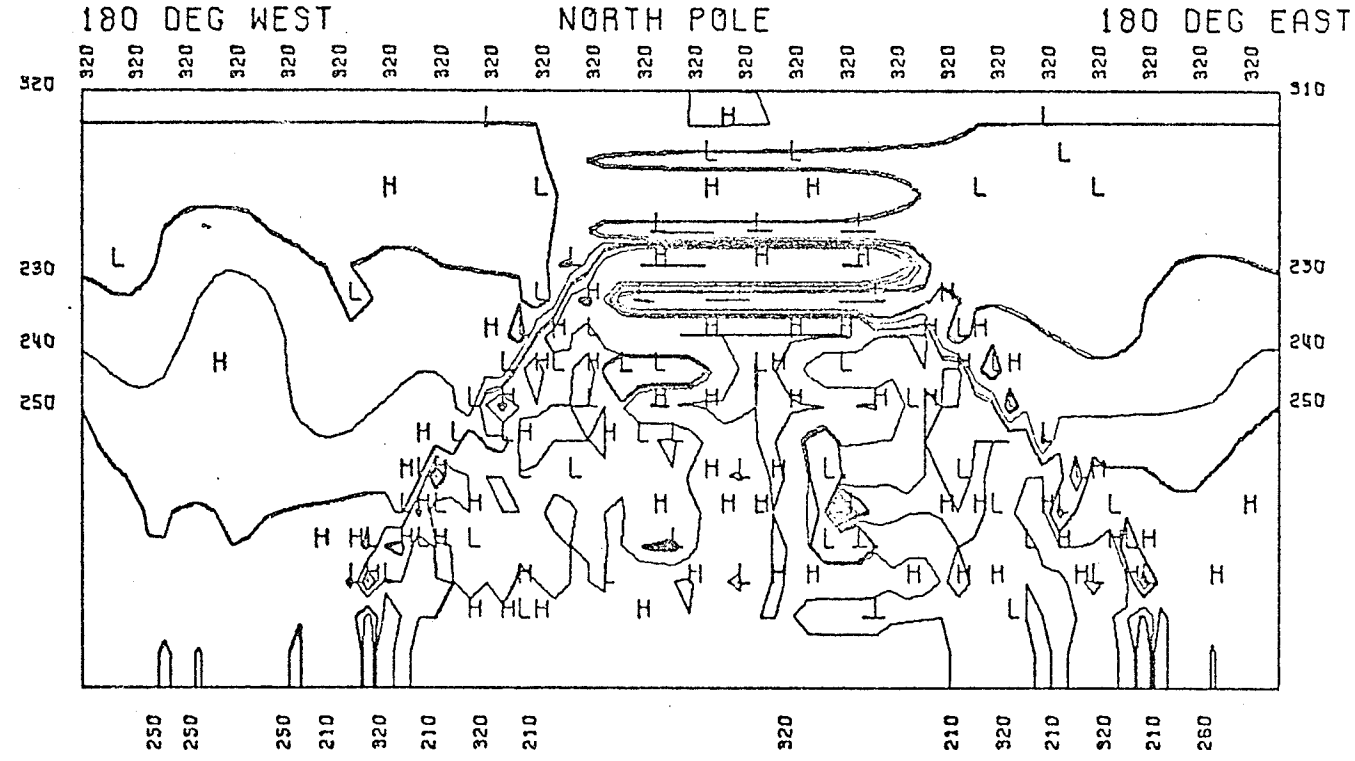

Figure 4.130: 400 mb Temperature (^{o}K), model C2, 7 hour

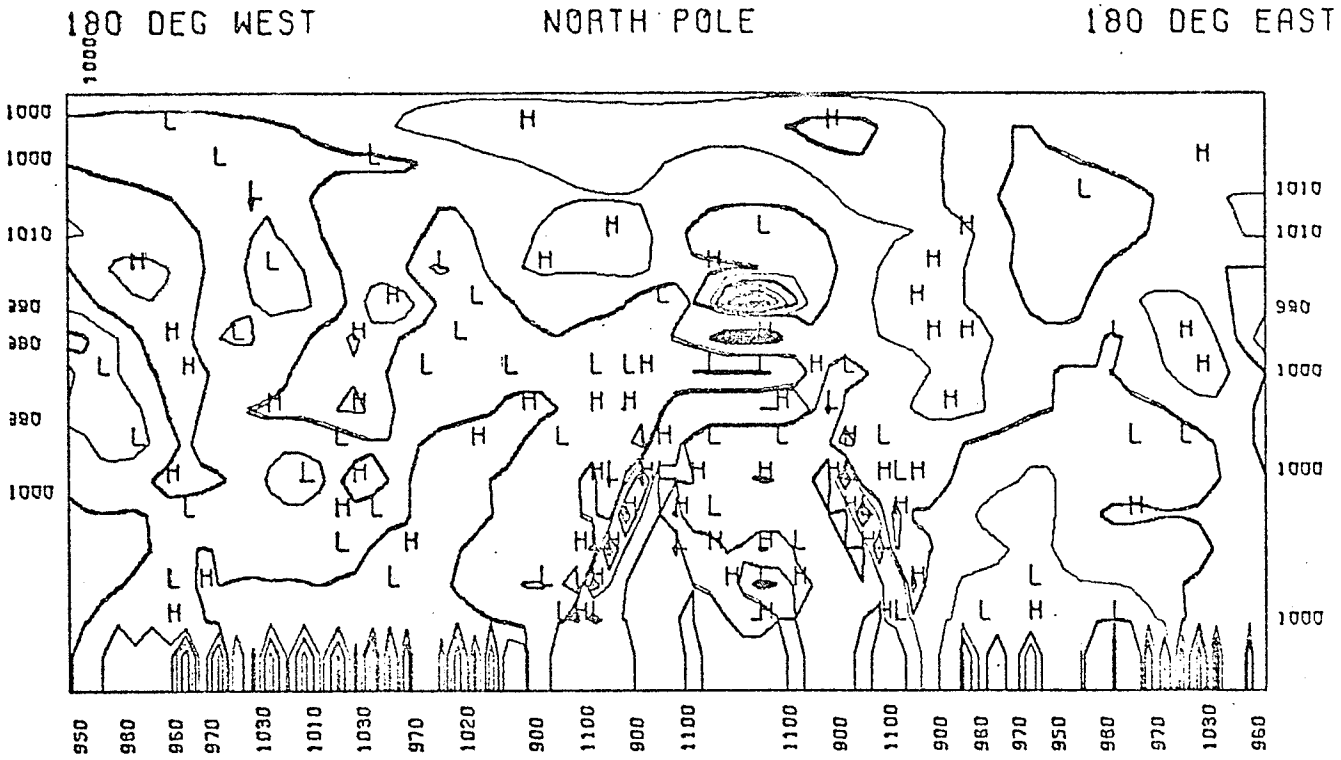

Figure 4.131: Surface Pressure (mb), model C2, 7 hour

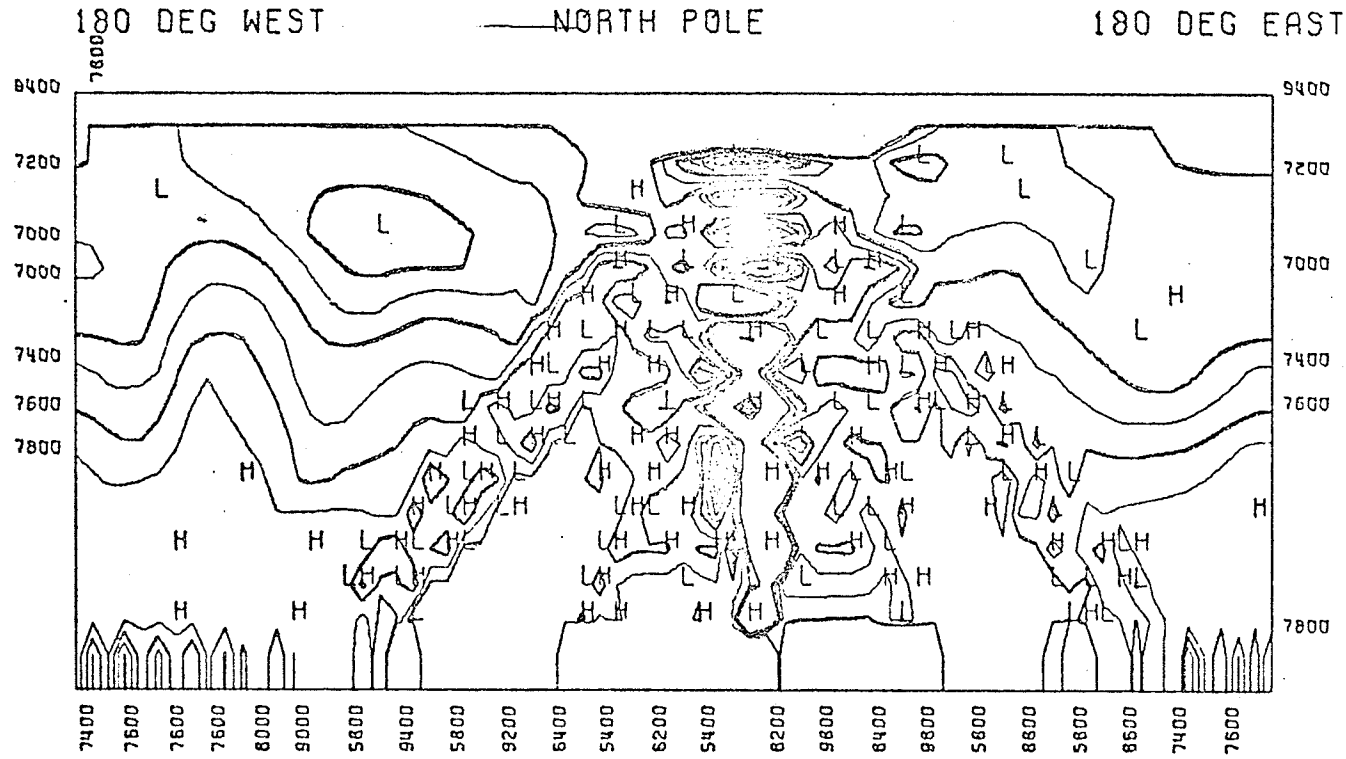

Figure 4.132: 400 mb Geopotential (m), model C2, 7 hour

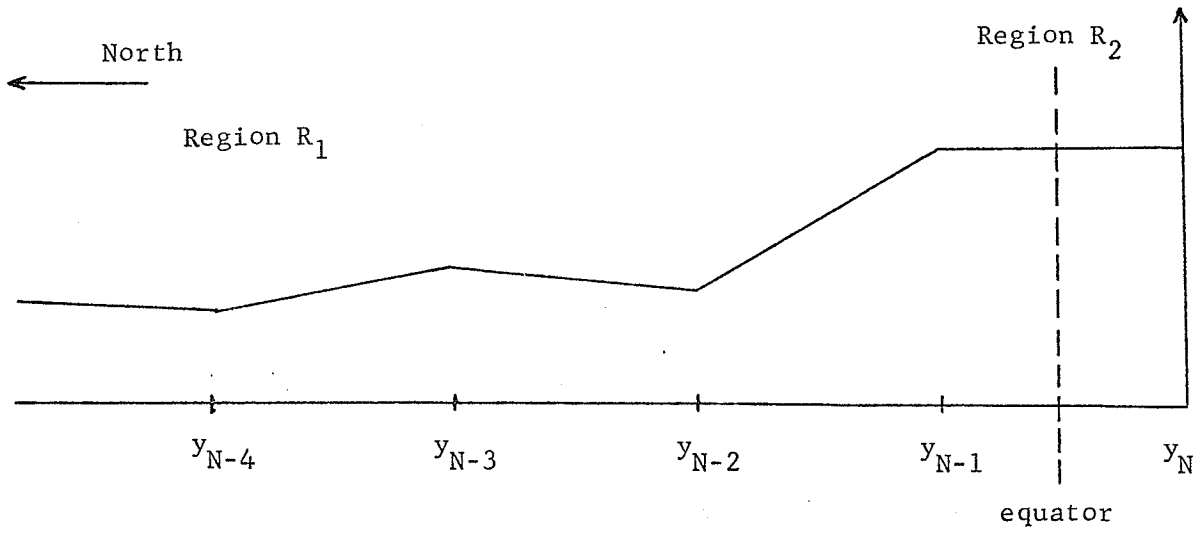

Figure 4.133: Equator Region in Model C2.

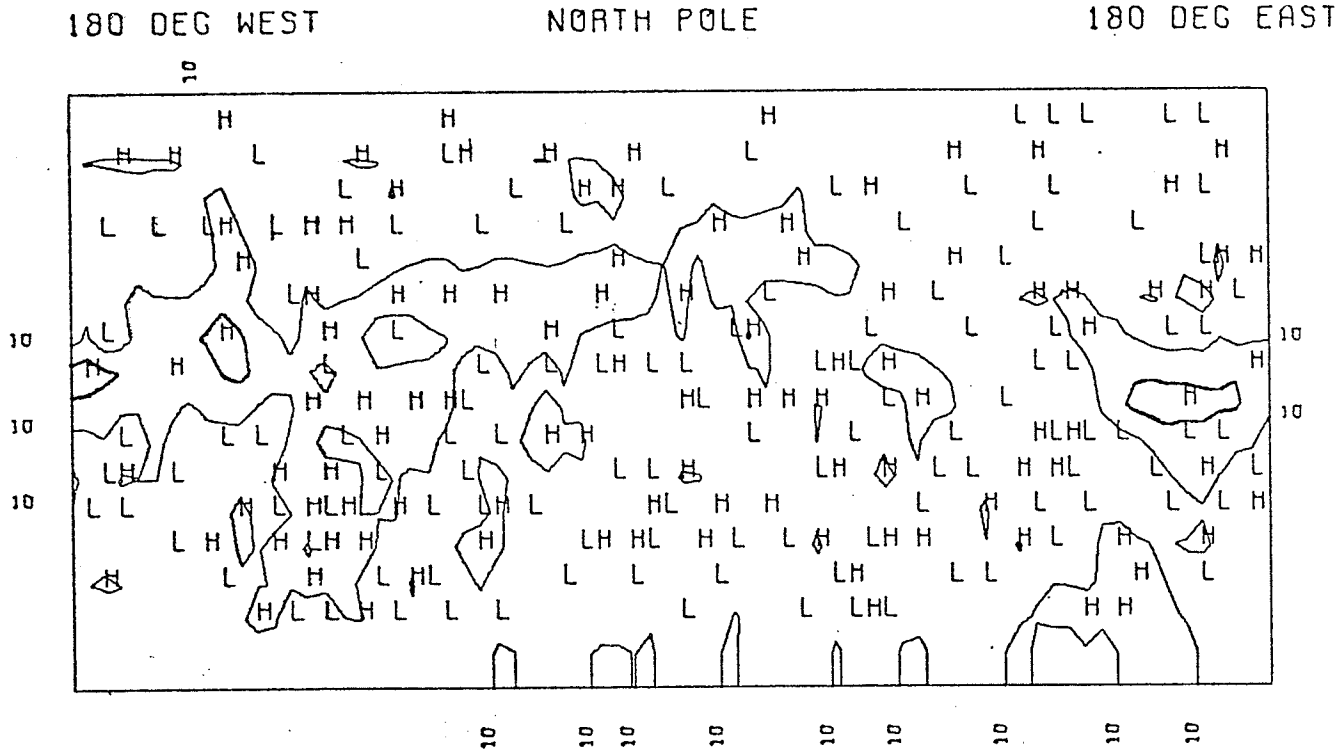

Figure 5.1: 800 mb Resultant Velocity Isotachs (m/sec), comparison model MA, 36 hour

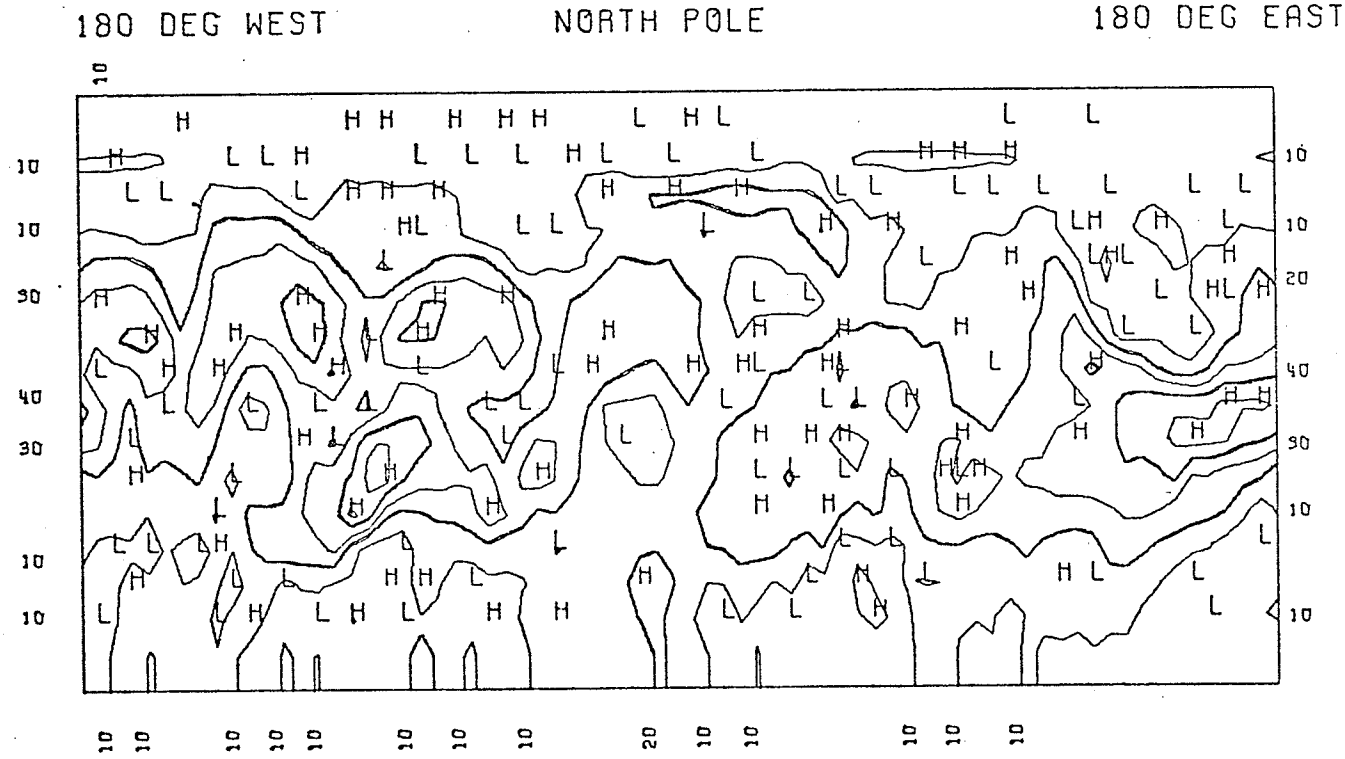

Figure 5.2: 400 mb Resultant Velocity Isotachs (m/sec), comparison model MA, 36 hour

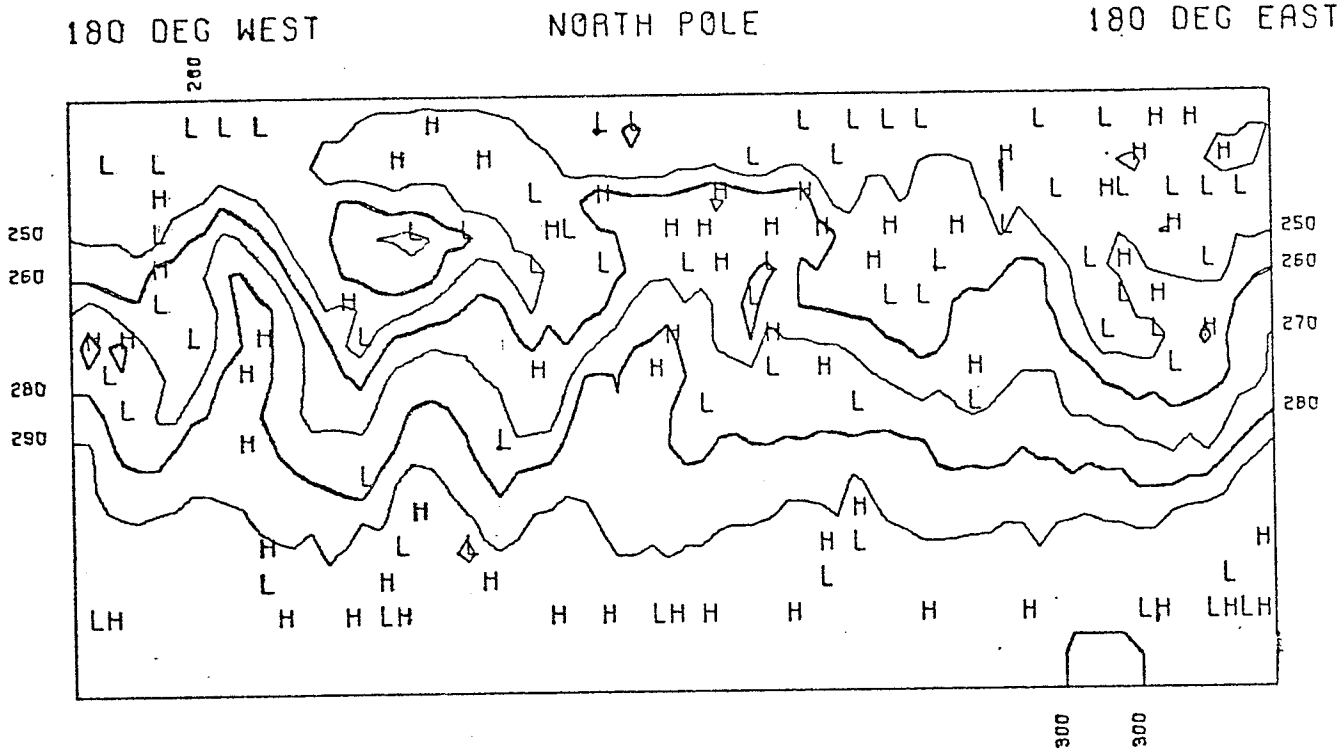

Figure 5.3: 800 mb Temperature (^{o}K), comparison model MA, 36 hour

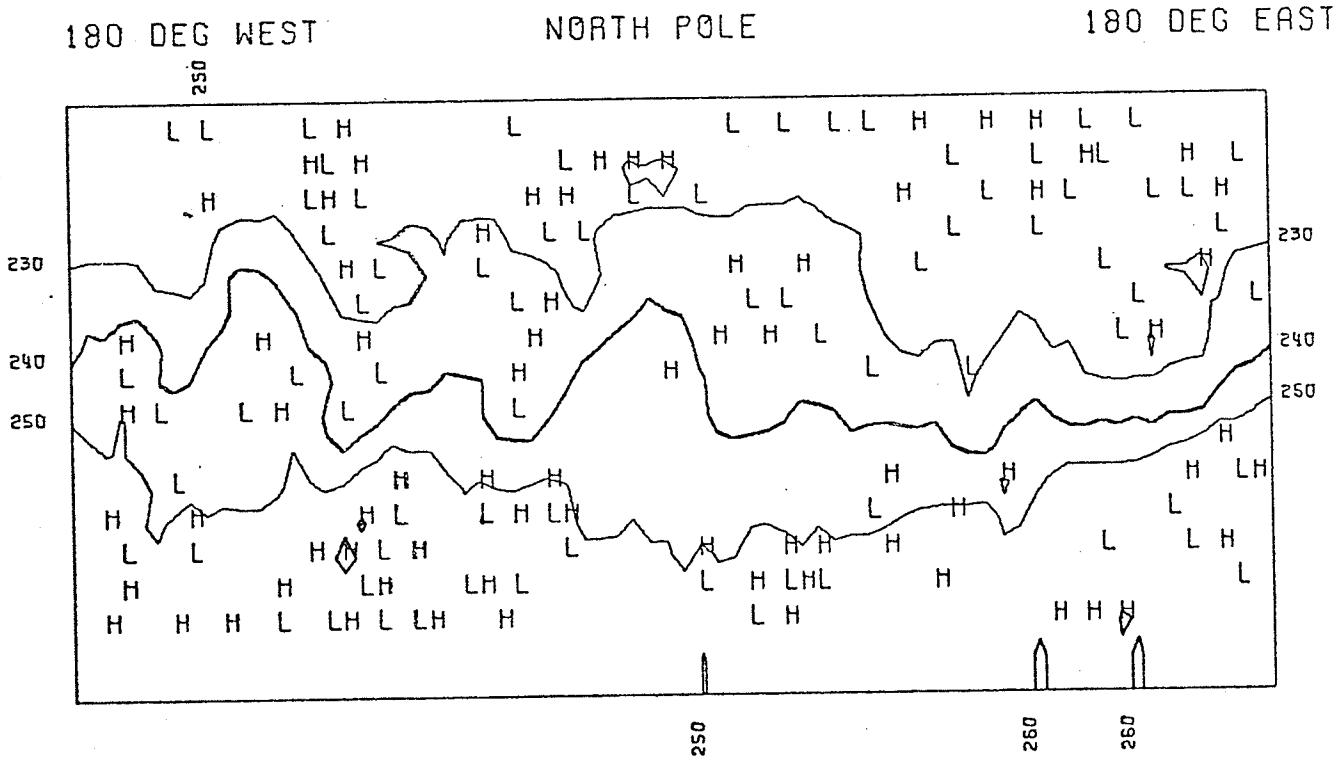

Figure 5.4: 400 mb Temperature (^{o}K), comparison model MA, 36 hour

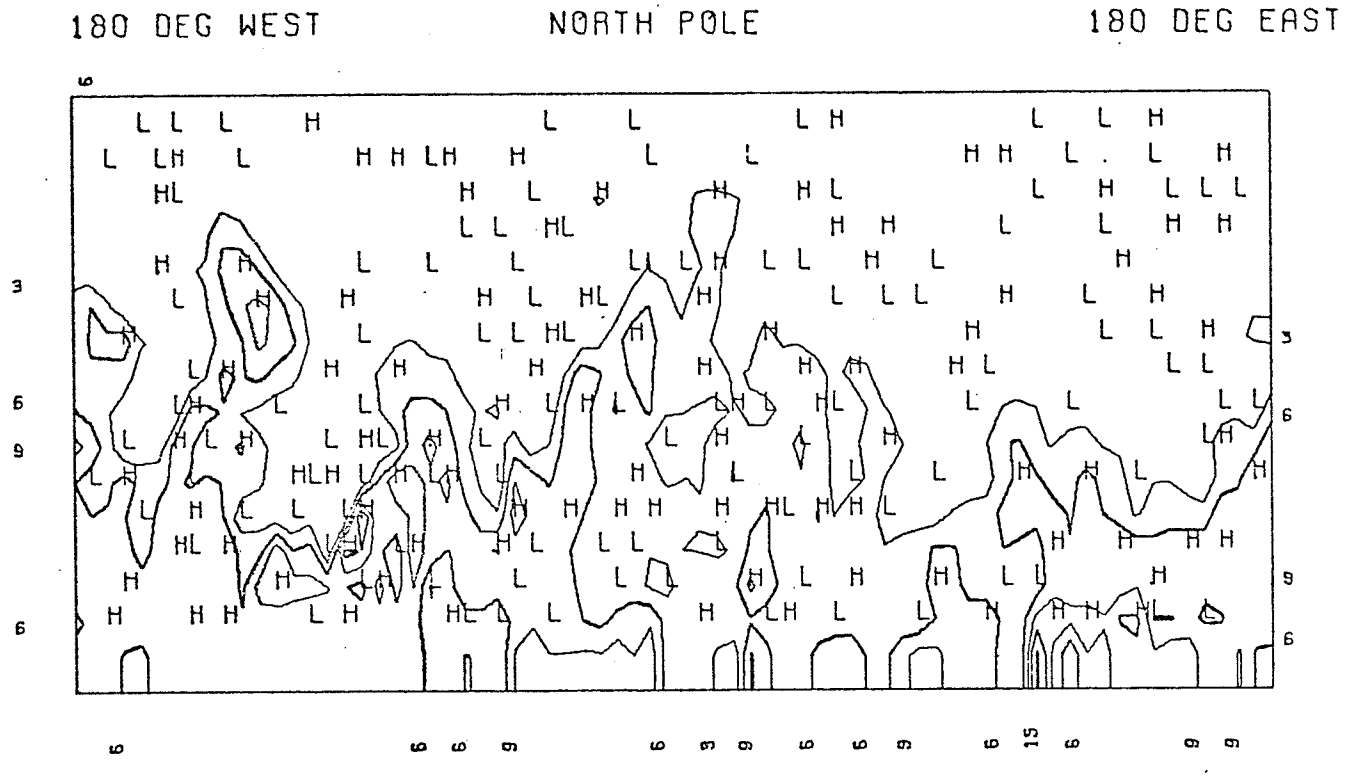

Figure 5.5: 800 mb Moisture (g H_2O/g dry air x 10^{-3}), comparison model MA, 36 hour

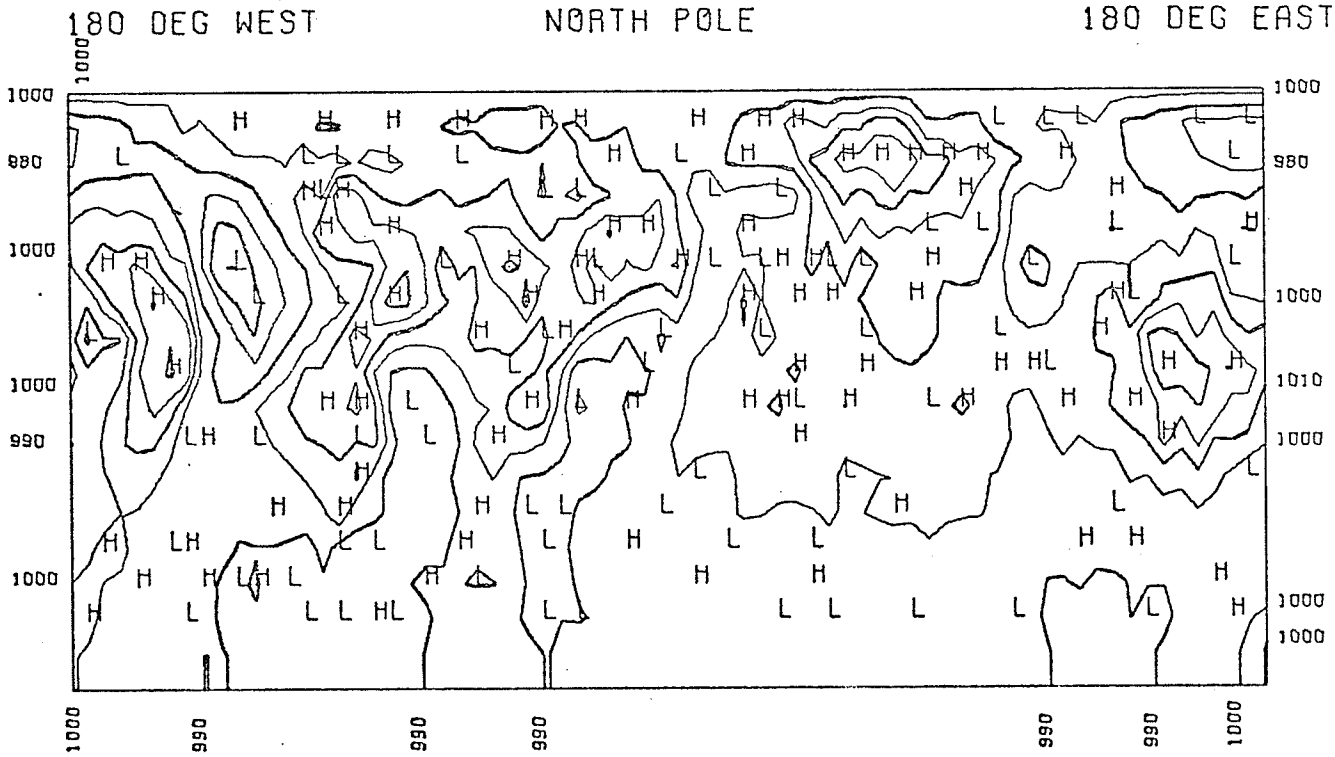

Figure 5.6: Surface Pressure (mb), comparison model MA, 36 hour

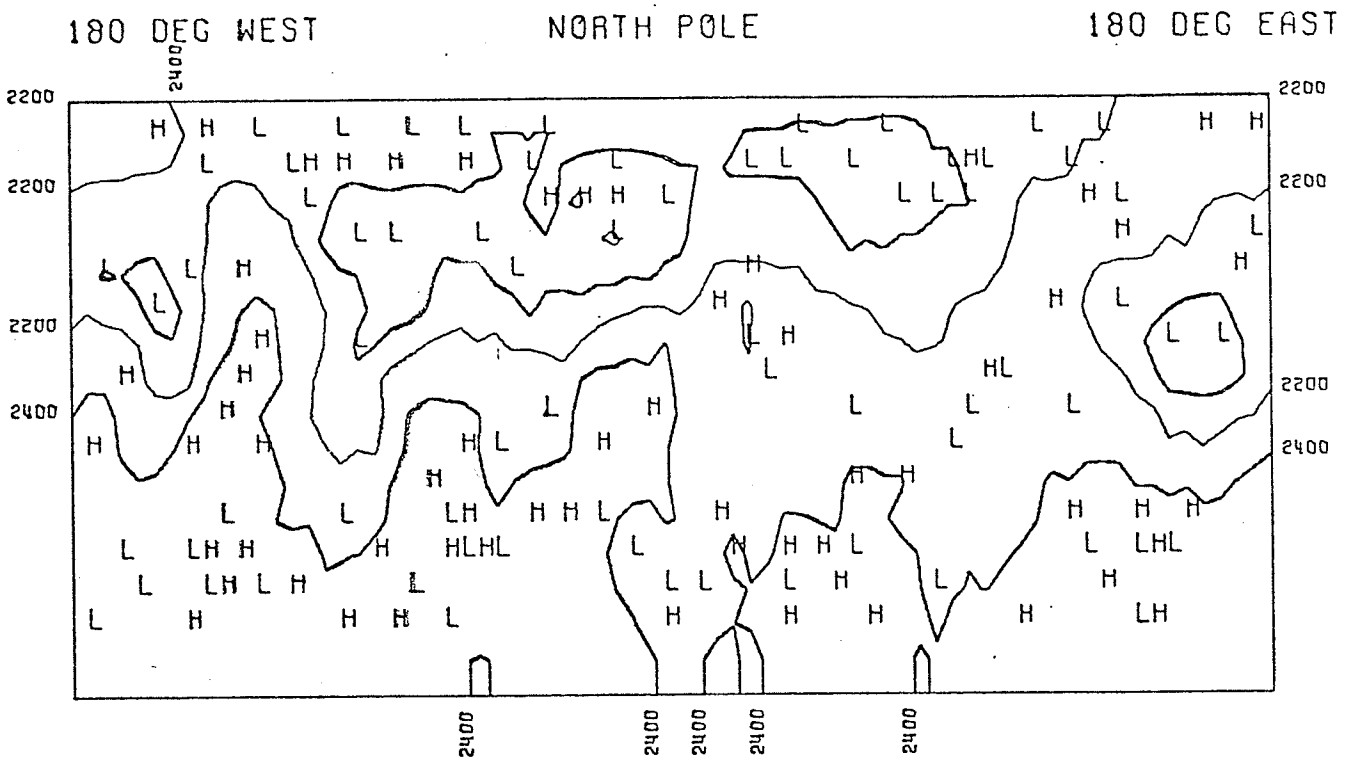

Figure 5.7: 800 mb Geopotential (m), comparison model MA, 36 hour

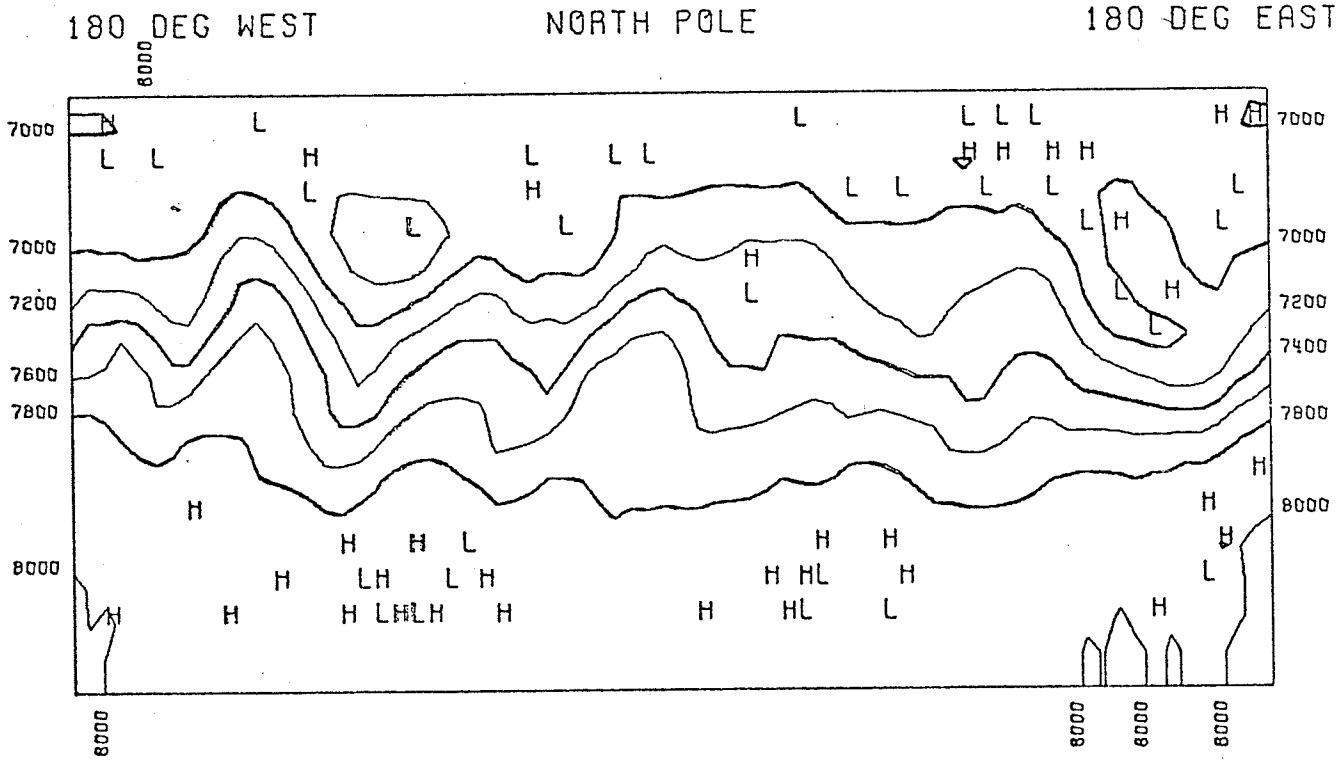

Figure 5.8: 400 mb Geopotential (m), comparison model MA, 36 hour

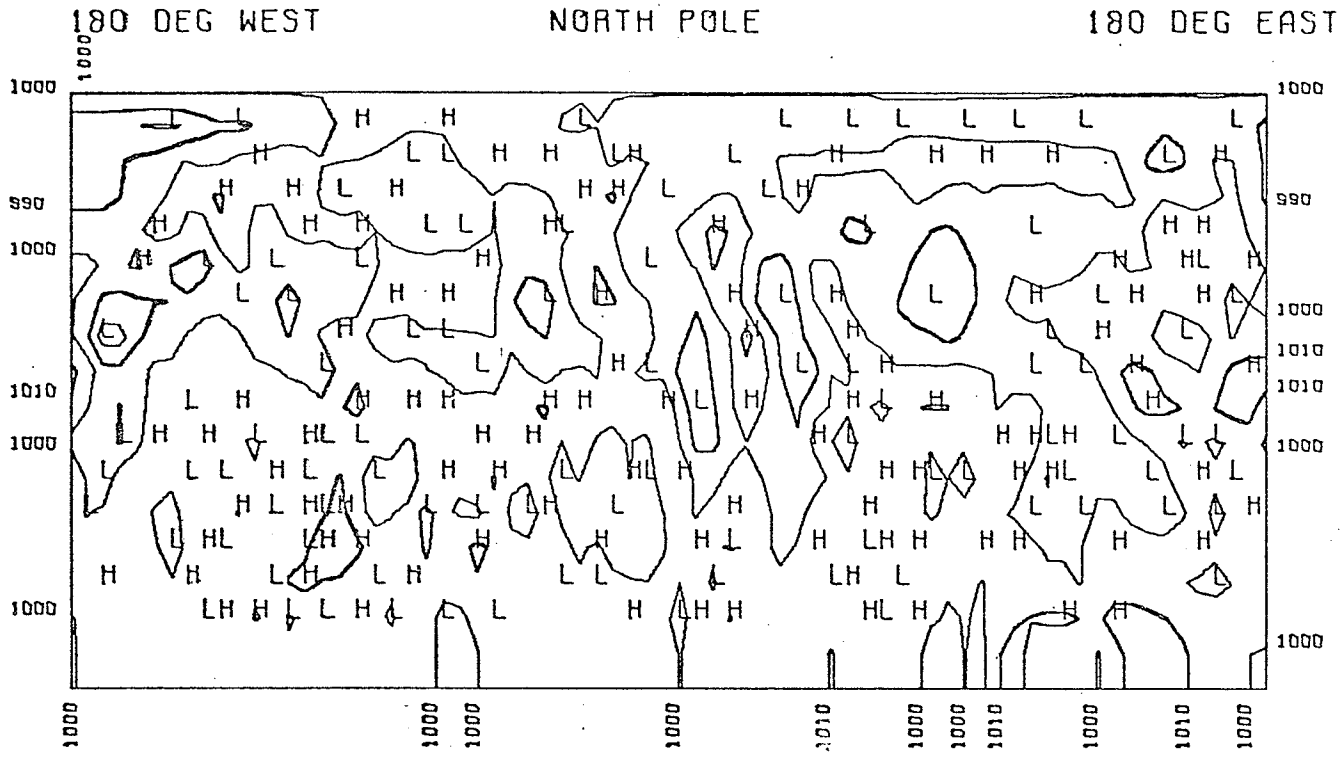

Figure 5.9: 800 mb Resultant Velocity (m/sec), comparison model MA, 36 hour error, 1000 represents zero error

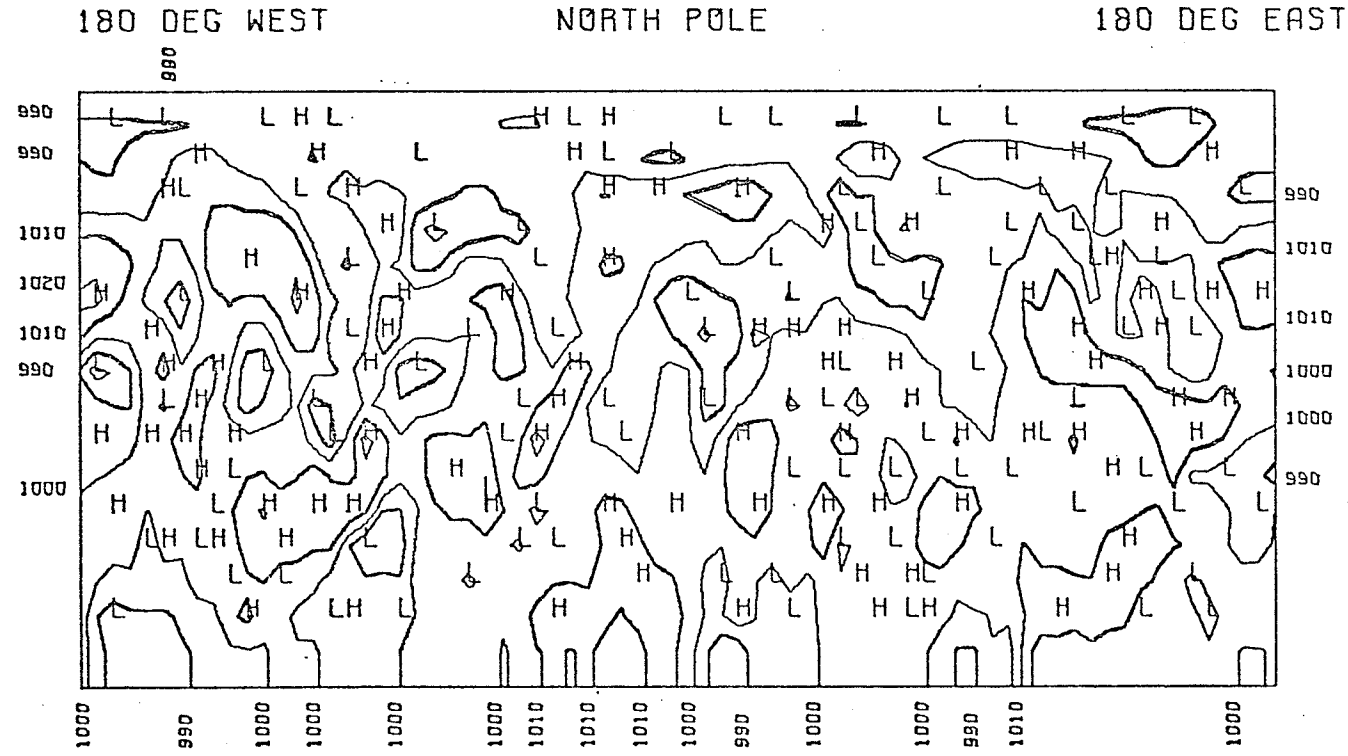

Figure 5.10: 400 mb Resultant Velocity (m/sec), comparison model MA, 36 hour error, 1000 represents zero error

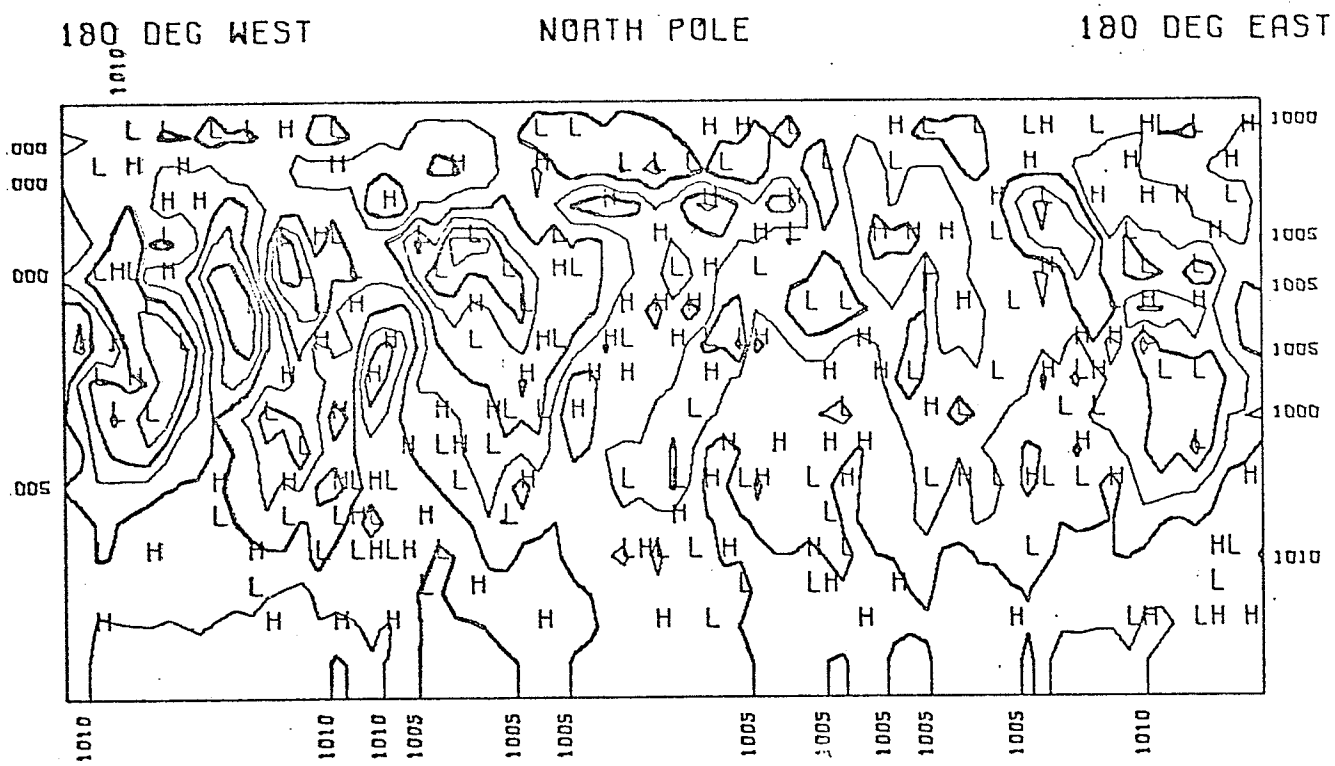

Figure 5.11: 800 mb Temperature (^{o}K), comparison model MA, 36 hour error, 1000 represents zero error

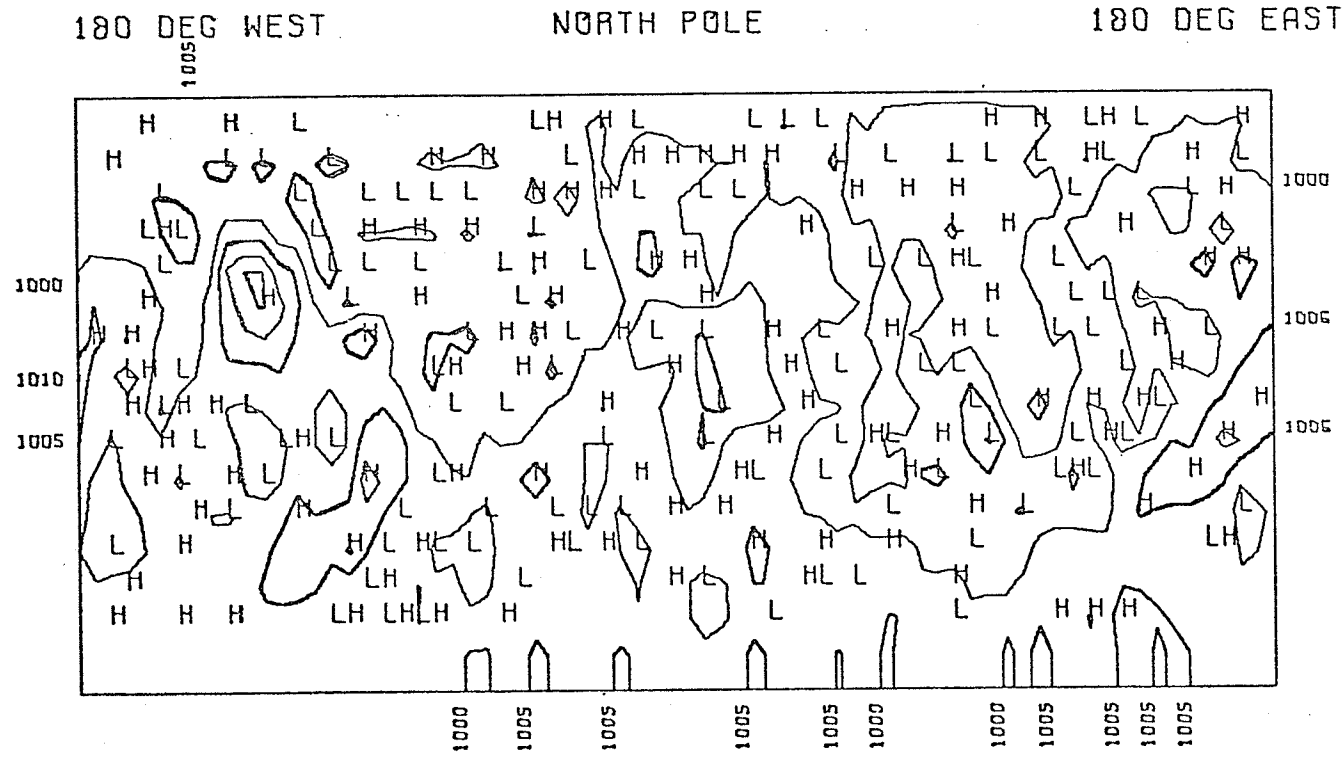

Figure 5.12: 400 mb Temperature (^{o}K), comparison model MA, 36 hour error, 1000 represents zero error

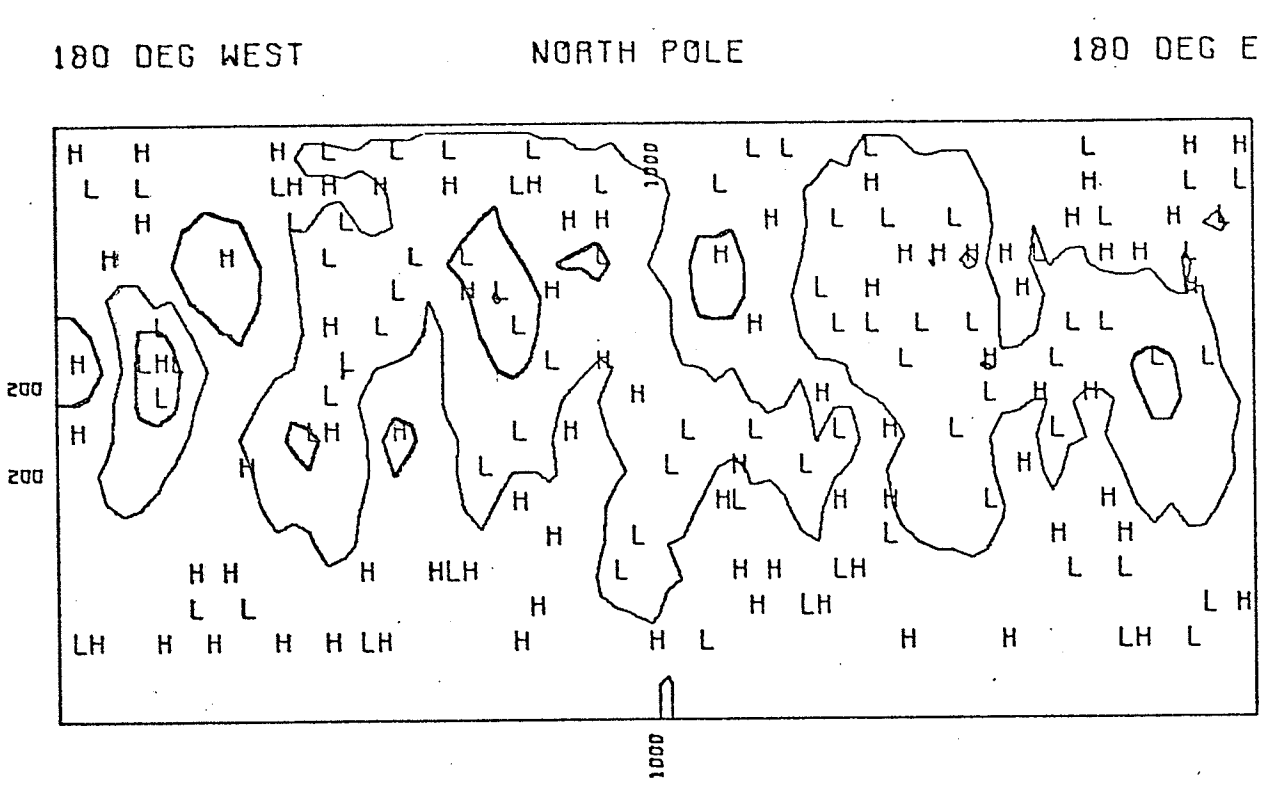

Figure 5.13: 800 mb Geopotential (m), comparison model MA, 36 hour error, 1000 represents zero error

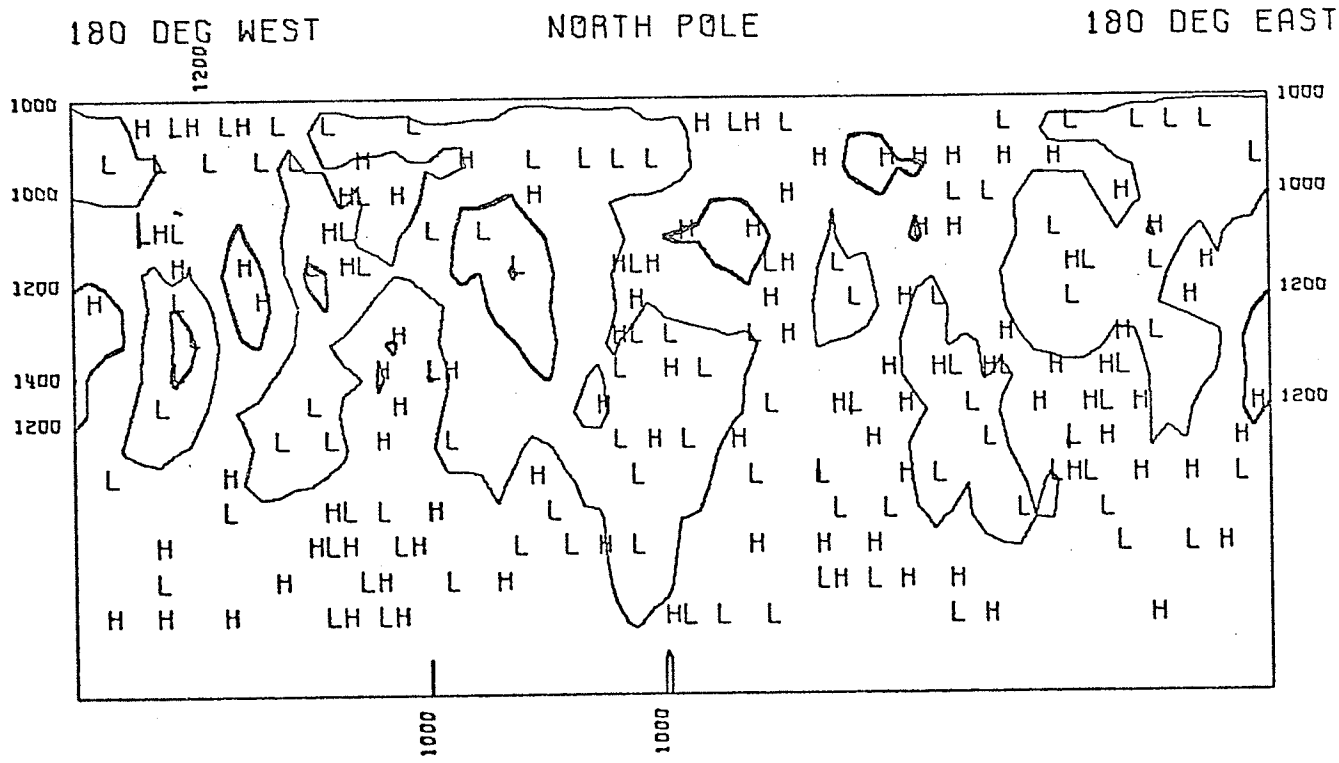

Figure 5.14: 400 mb Geopotential (m), comparison model MA, 36 hour error, 1000 represents zero error

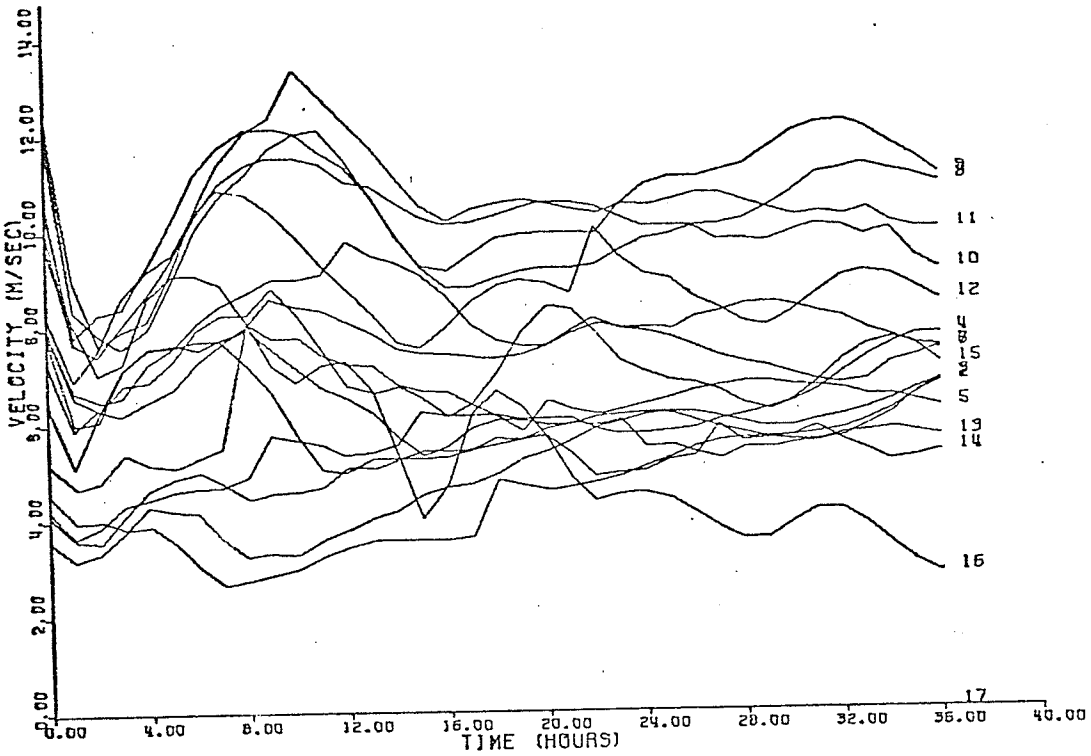

Figure 5.15: 800 mb Resultant Velocity Isotachs (m/sec), comparison model MA, 0-36 hour zonal mean, numbers on the right denote the latitude circle, 1 denotes the equator, 16 denotes the north pole

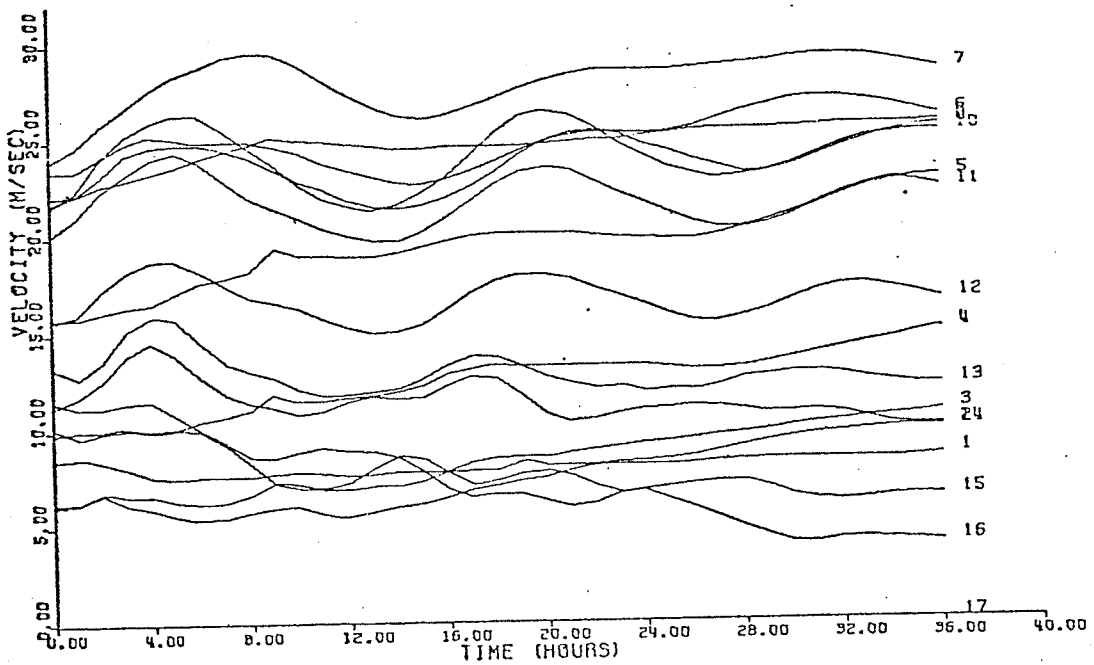

Figure 5.16: 400 mb Resultant Velocity Isotachs (m/sec), comparison model MA, 0-36 hour zonal mean, numbers on the right denote the latitude circle, 1 denotes the equator, 16 denotes the north pole

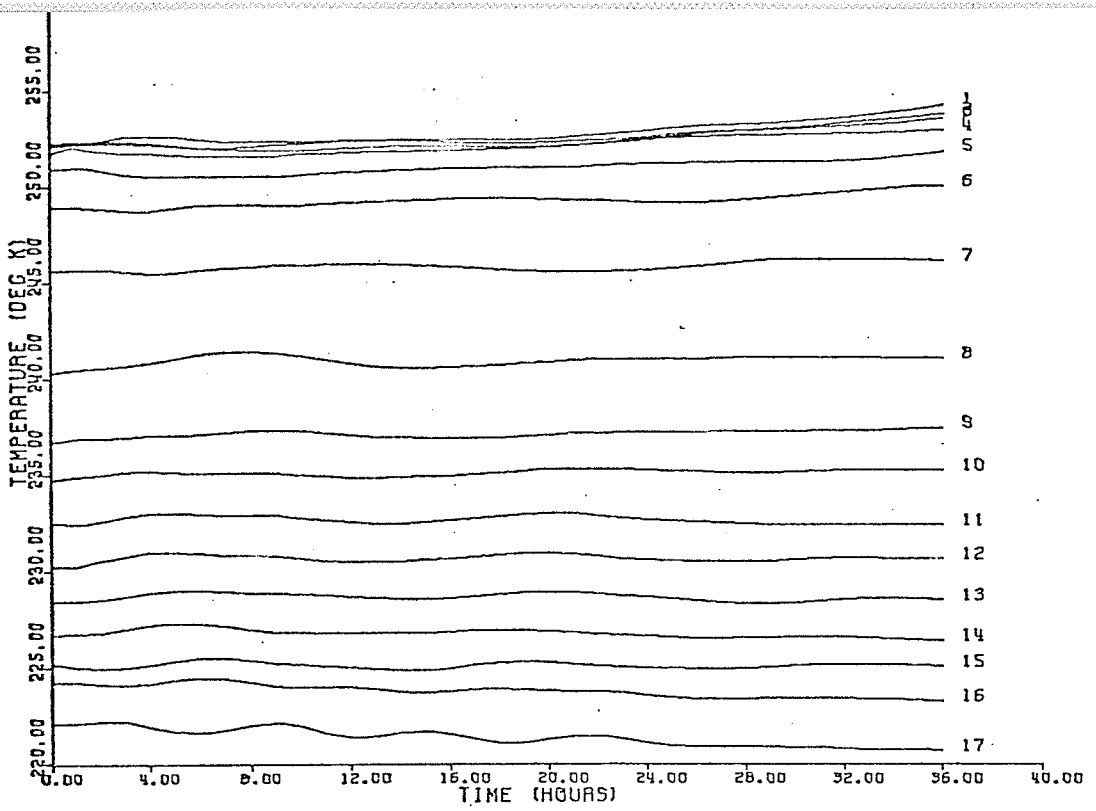

Figure 5.17: 400 mb Temperature (^{o}K), comparison model MA, 0-36 hour zonal mean, numbers on the right denote the latitude circle, 1 denotes the equator, 17 denotes the north pole

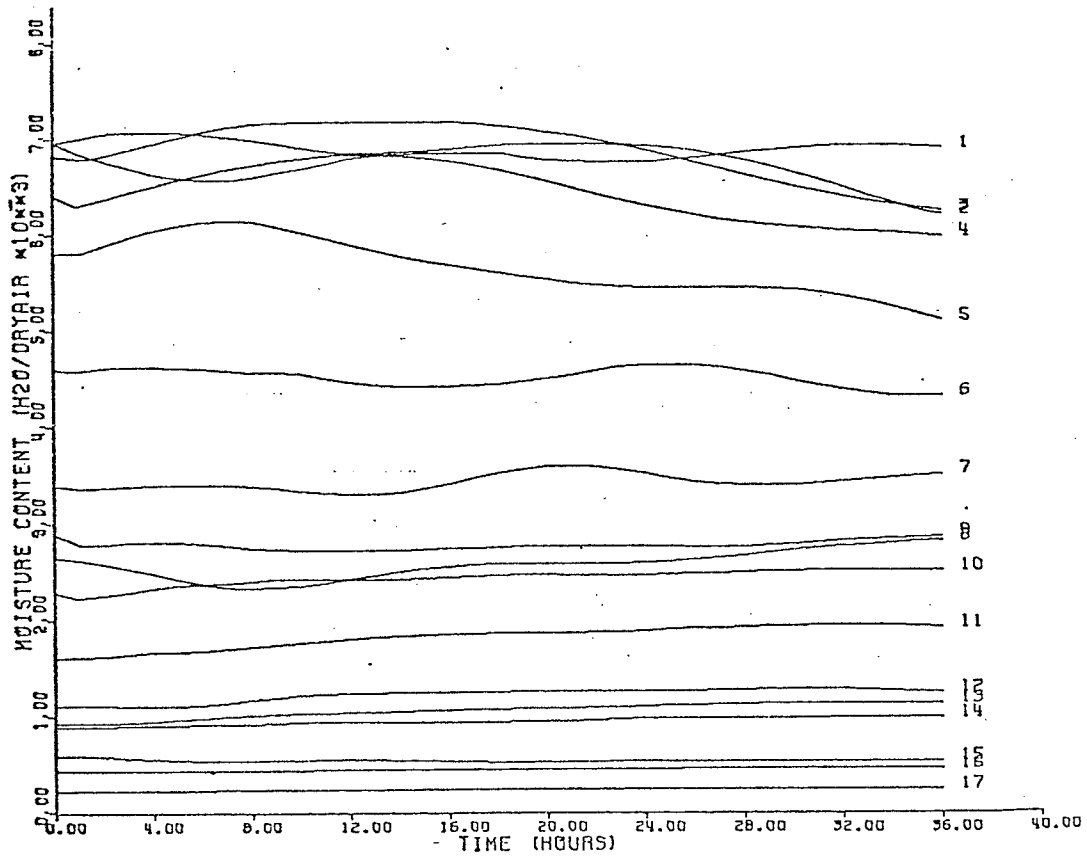

Figure 5.18: 800 mb Moisture (g H_2O/g dry air x 10^{-3}), comparison model MA, 0-36 hour zonal mean, numbers on the right denote the latitude circle, 1 denotes the equator, 17 denotes the north pole

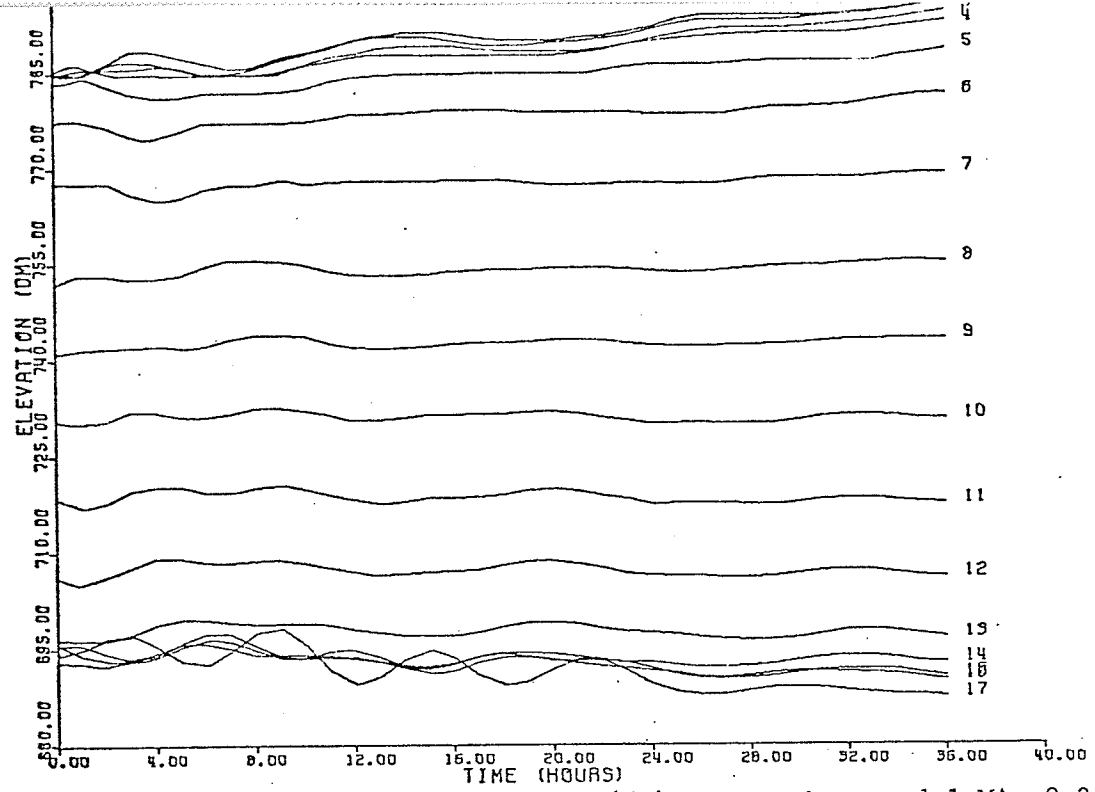

Figure 5.19: 400 mb Geopotential (dm), comparison model MA, 0-36 hour zonal mean, numbers on the right denote the latitude circle, 1 denotes the equator, 17 denotes the north pole

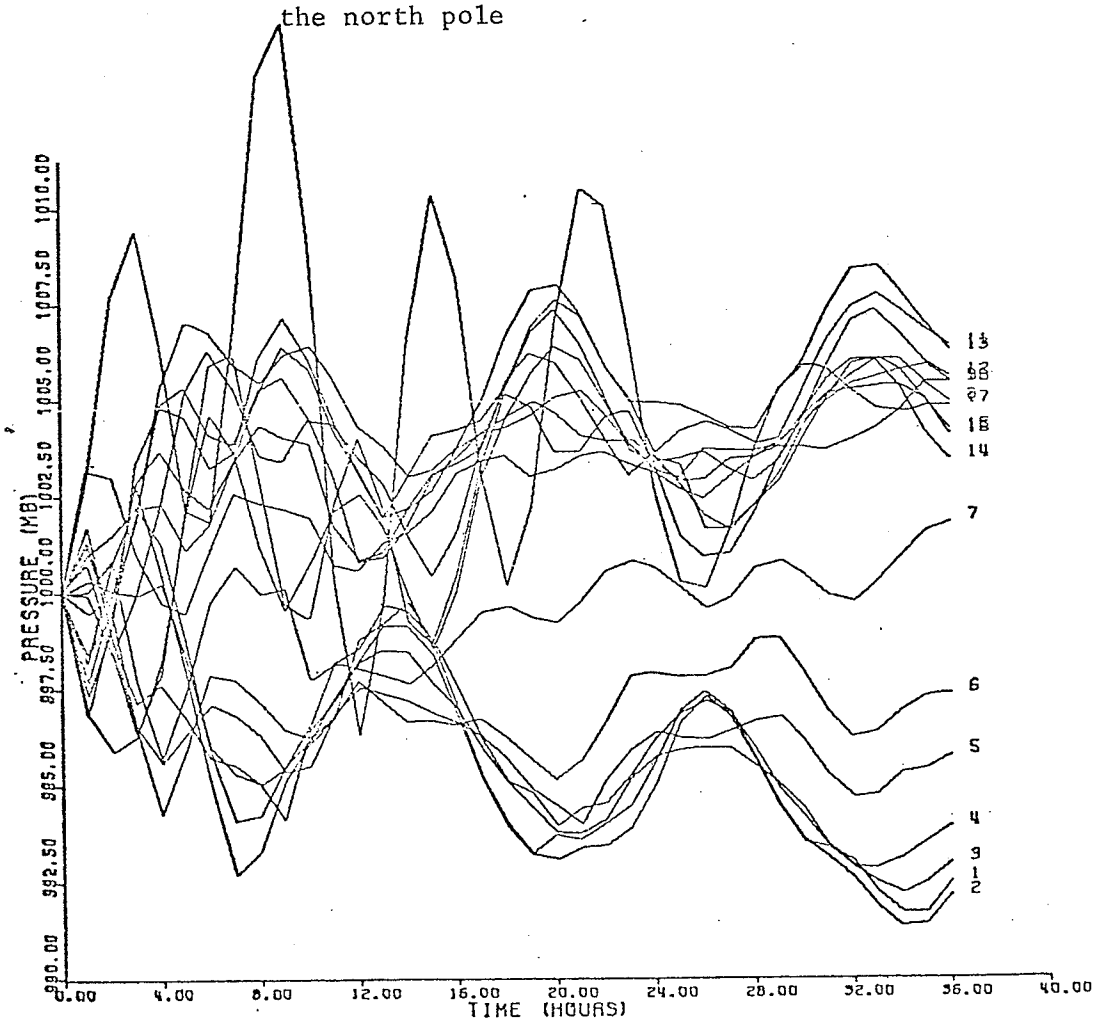

Figure 5.20: Surface Pressure (mb), comparison model MA, 0-36 hour zonal mean, numbers on the right denote the latitude circle, 1 denotes the equator, 17 denotes the north pole

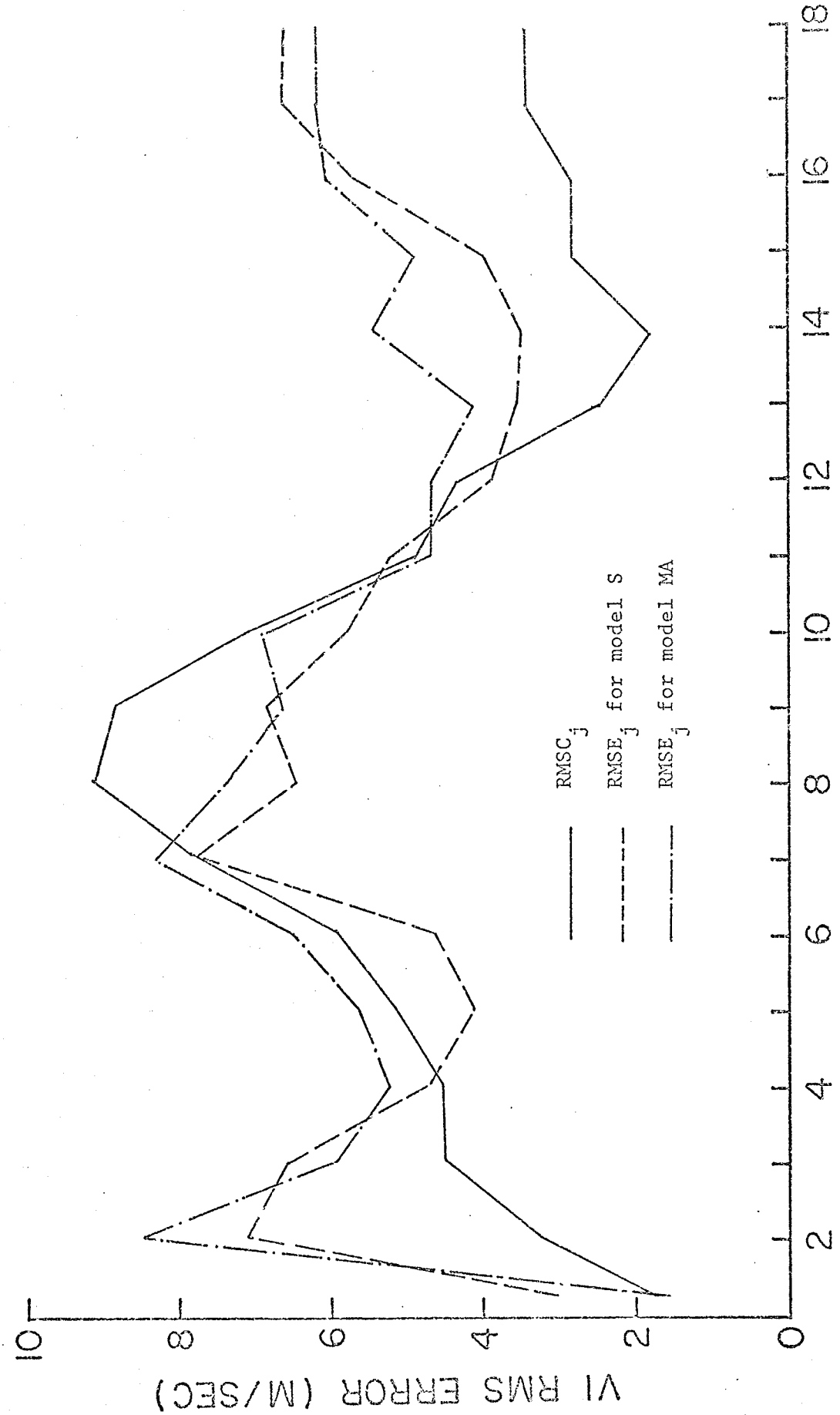

Figure 5.21: V1 RMSE$_j$ for models S and MA, and RMSC$_j$

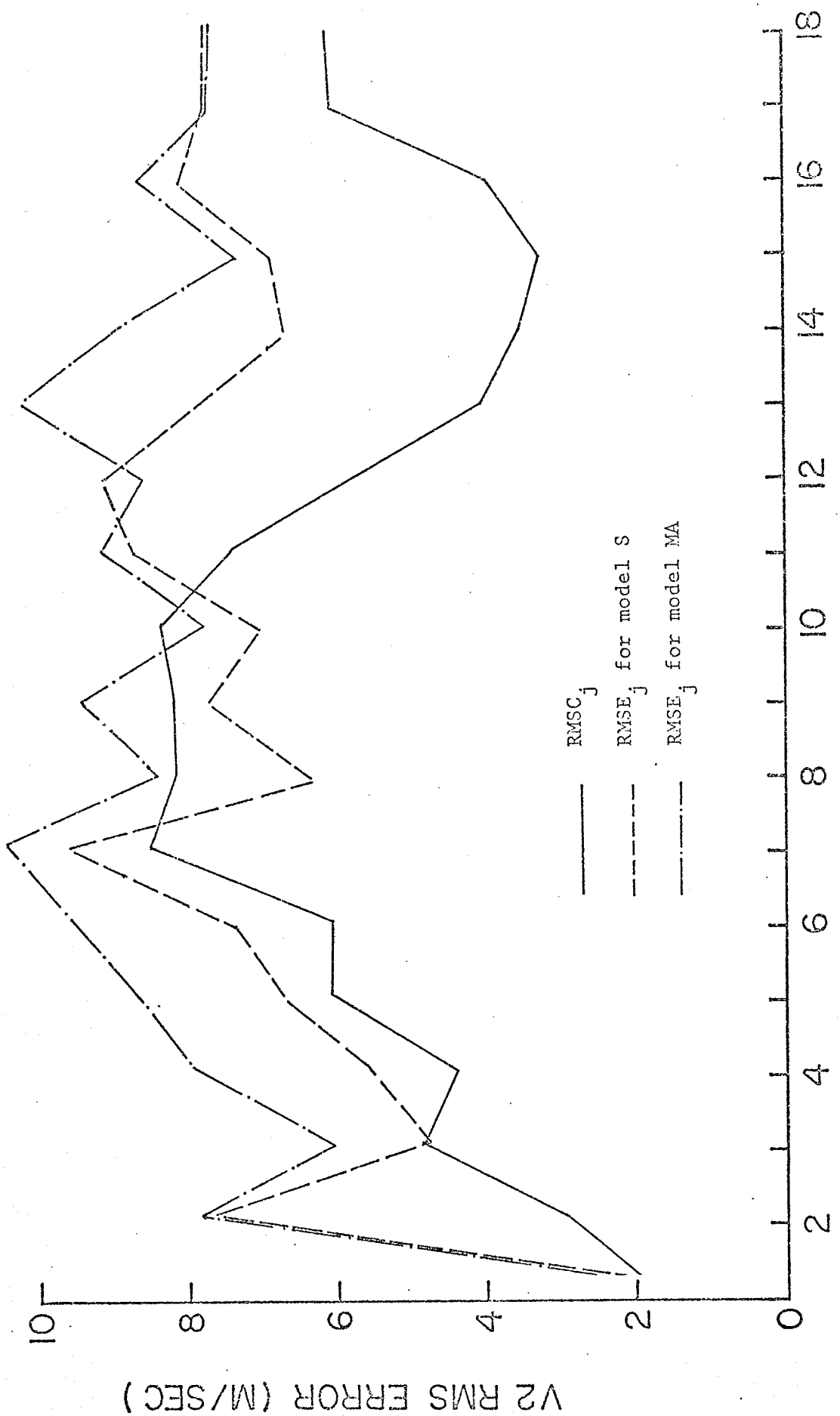

Figure 5.22: V2 RMSE$_j$ for models S and MA, and RMSC$_j$

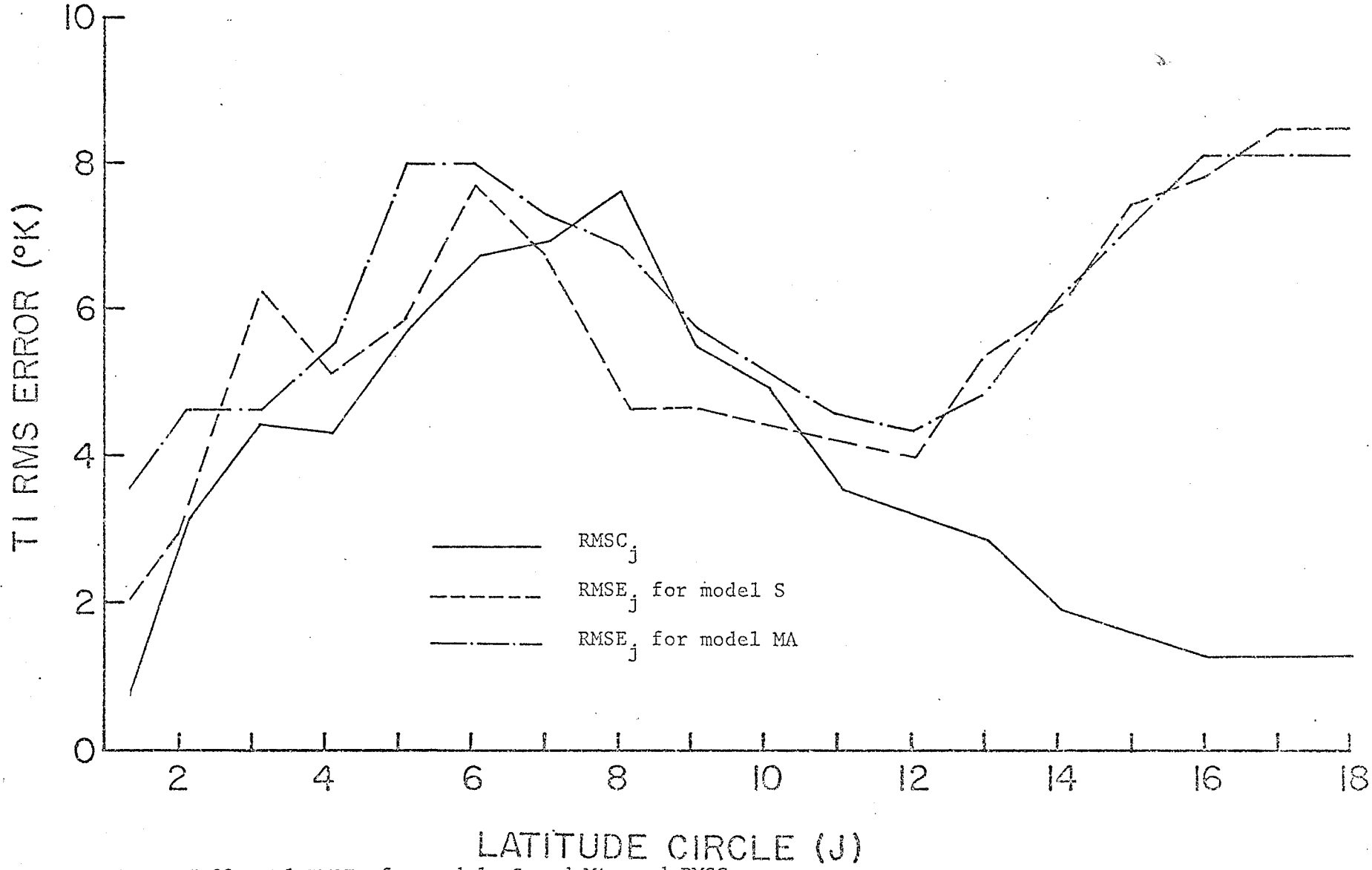

Figure 5.23: T1 RMSE$_j$ for models S and MA, and RMSC$_j$

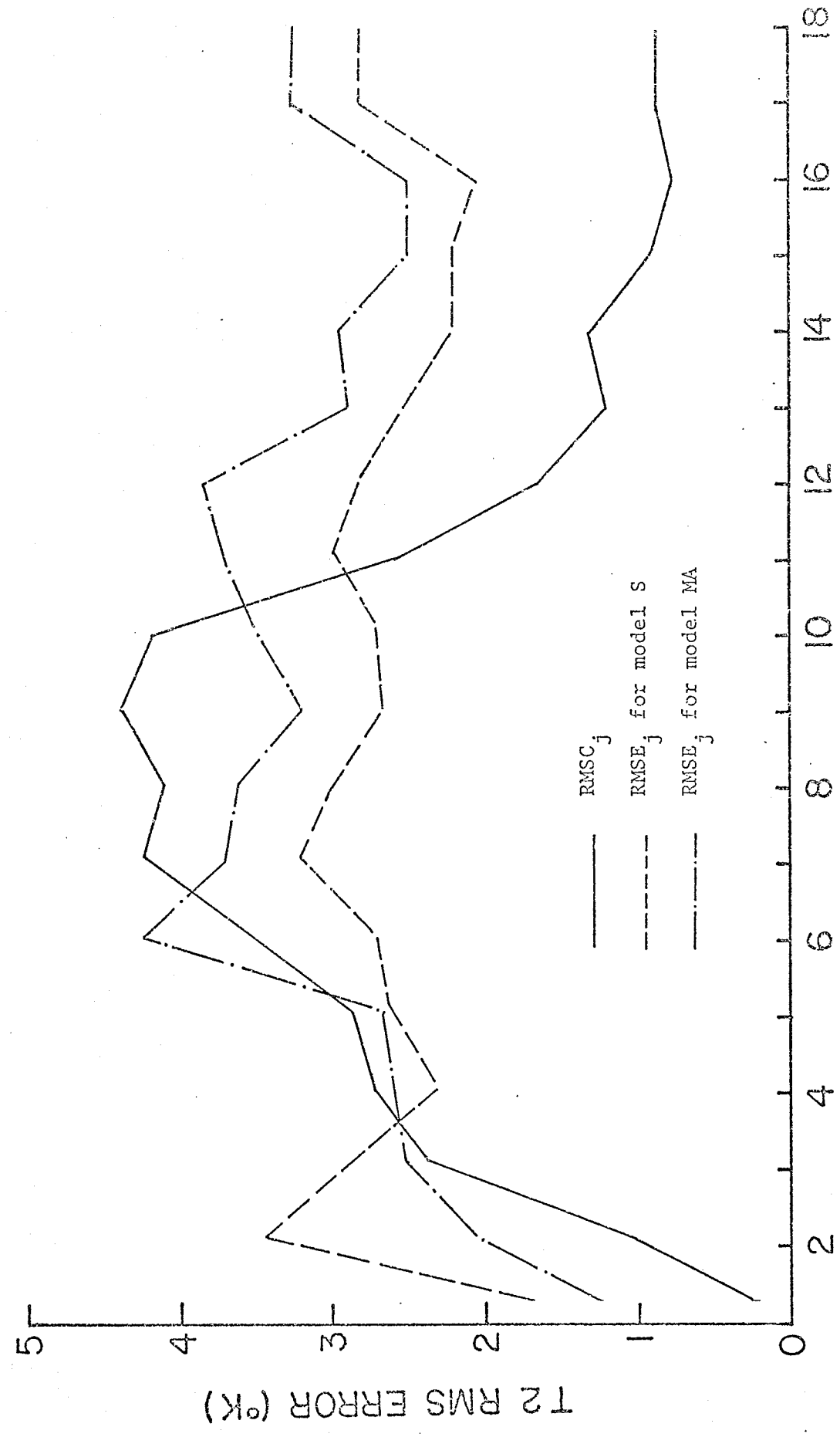

Figure 5.24: T2 RMSE$_j$ for models S and MA, and RMSC$_j$

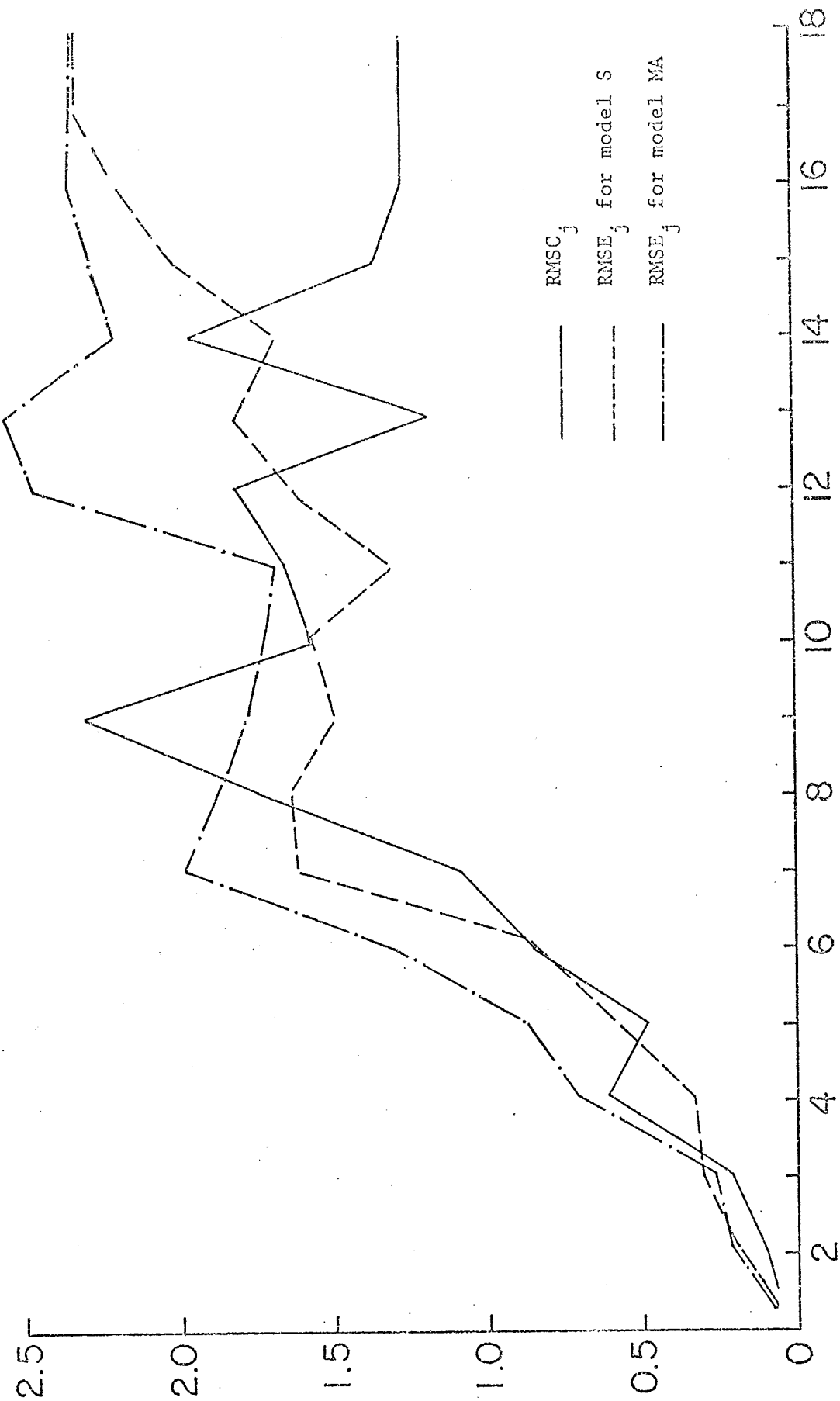

Figure 5.25: Q1 $RMSE_j$ for models S and MA, and $RMSC_j$

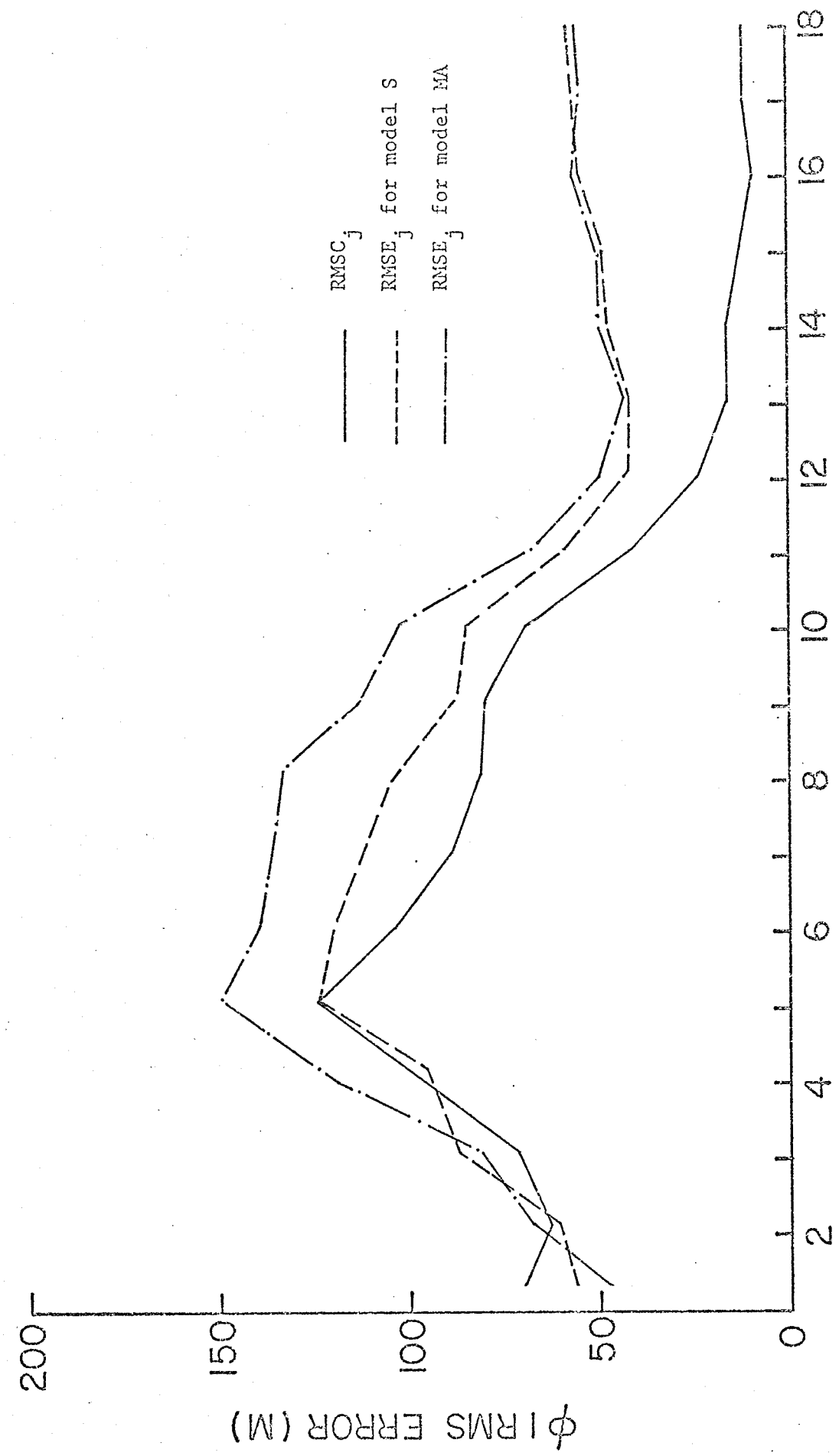

Figure 5.26: ϕ1 $RMSE_j$ for models S and MA, and $RMSC_j$

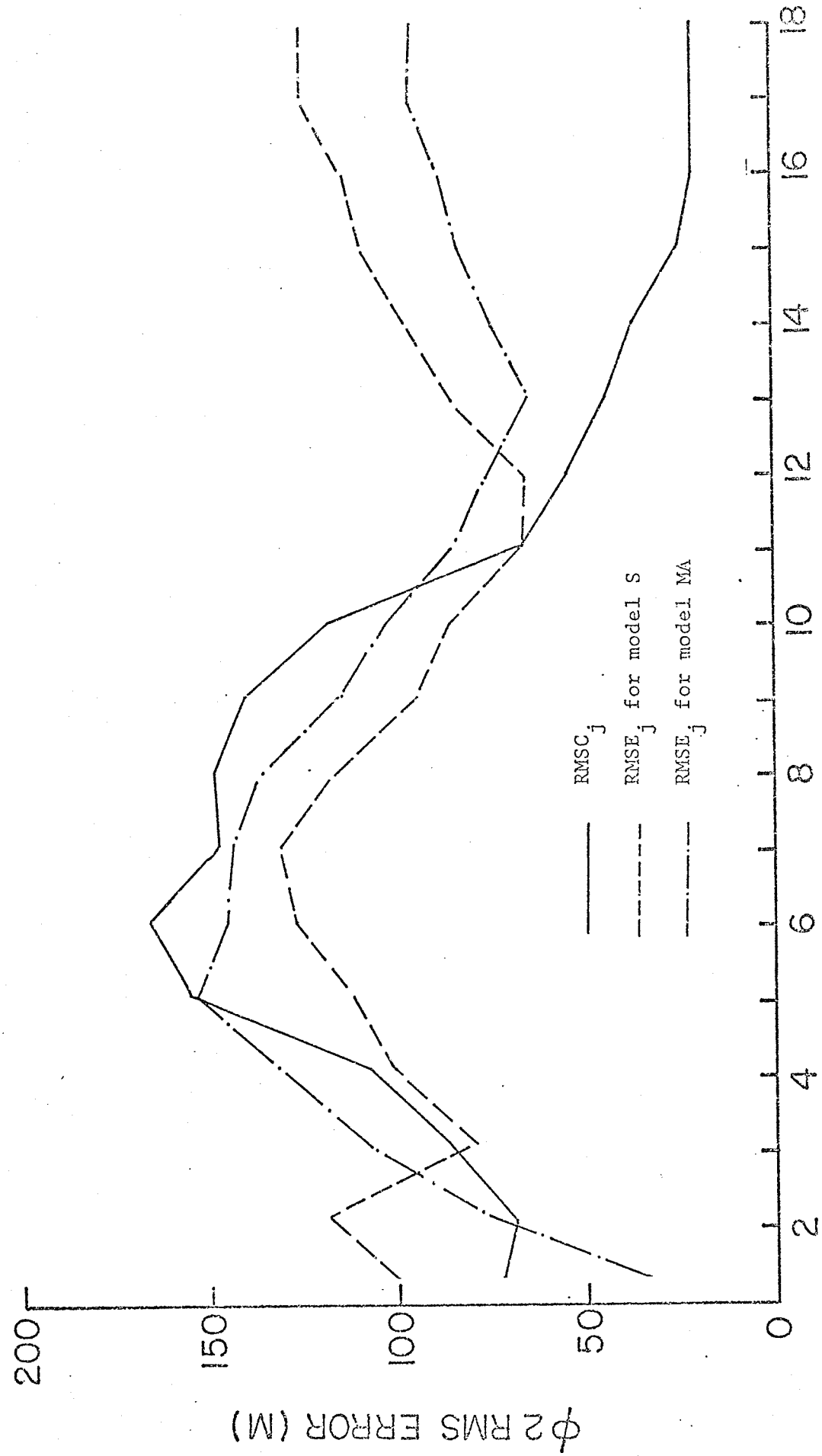

Figure 5.27: ϕ2 $RMSE_j$ for models S and MA, and $RMSC_j$

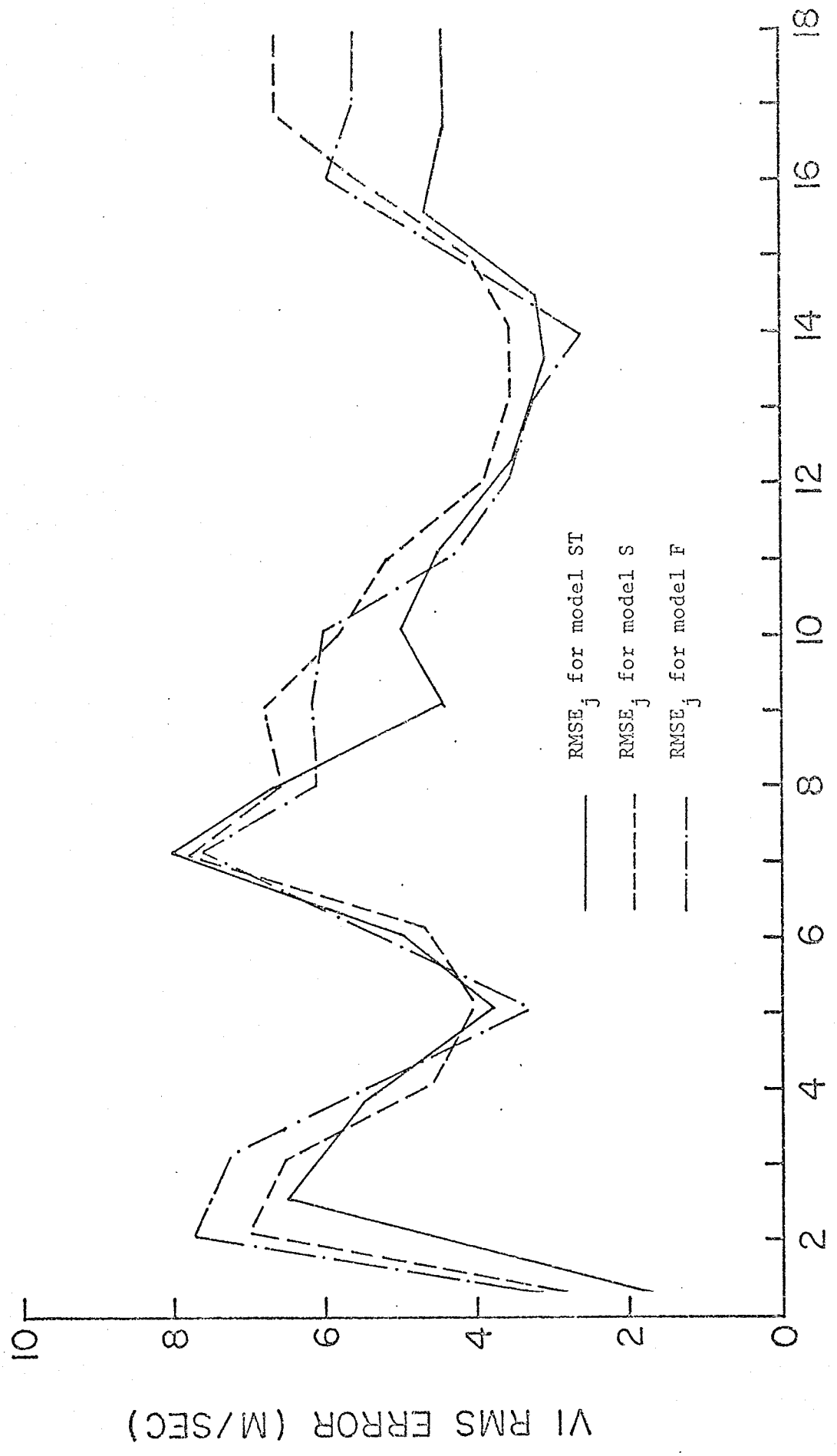

Figure 5.28: V1 RMSE$_j$ for models S, F, ST

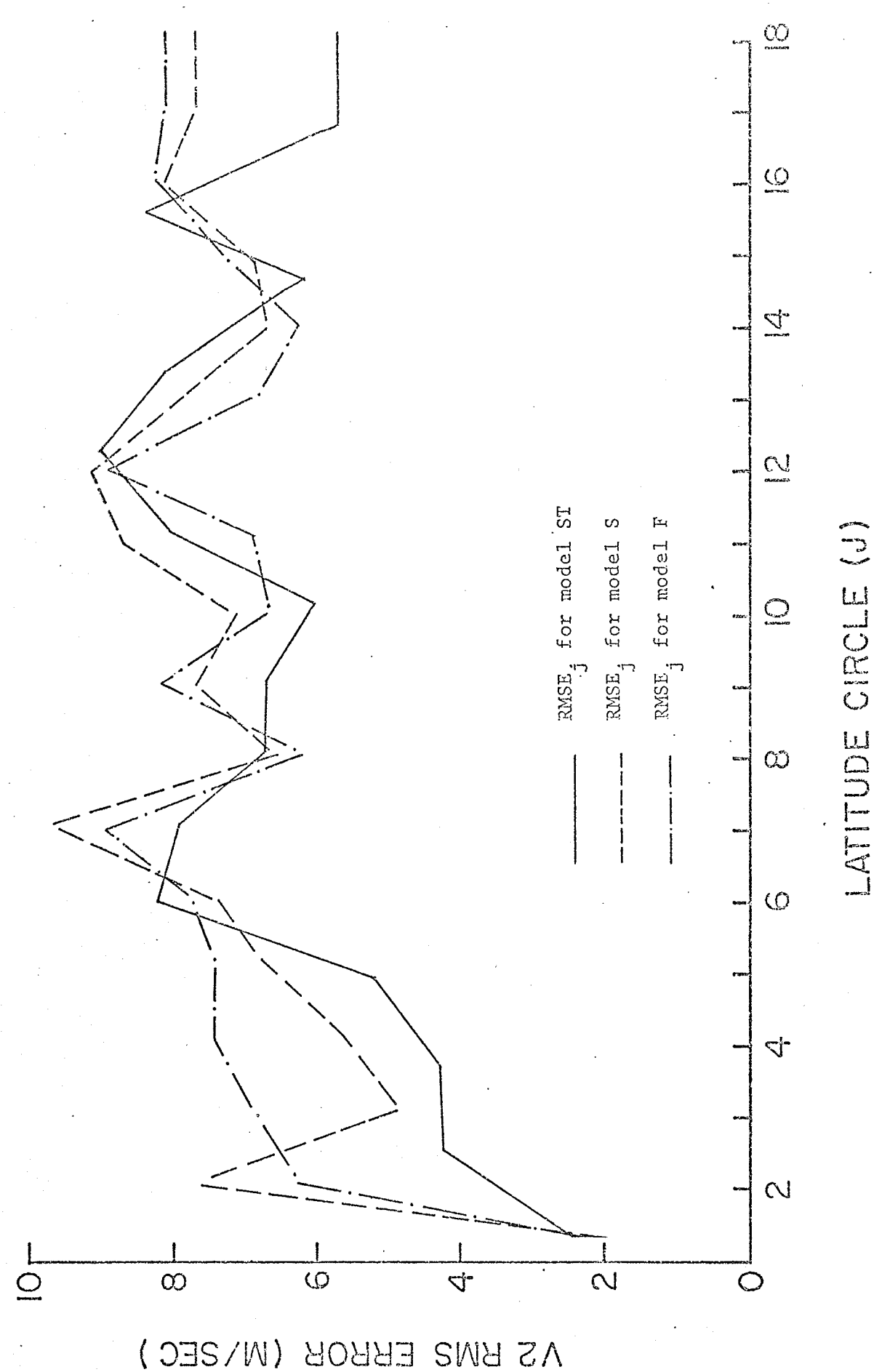

Figure 5.29: V2 RMSE$_j$ for models S, F, ST

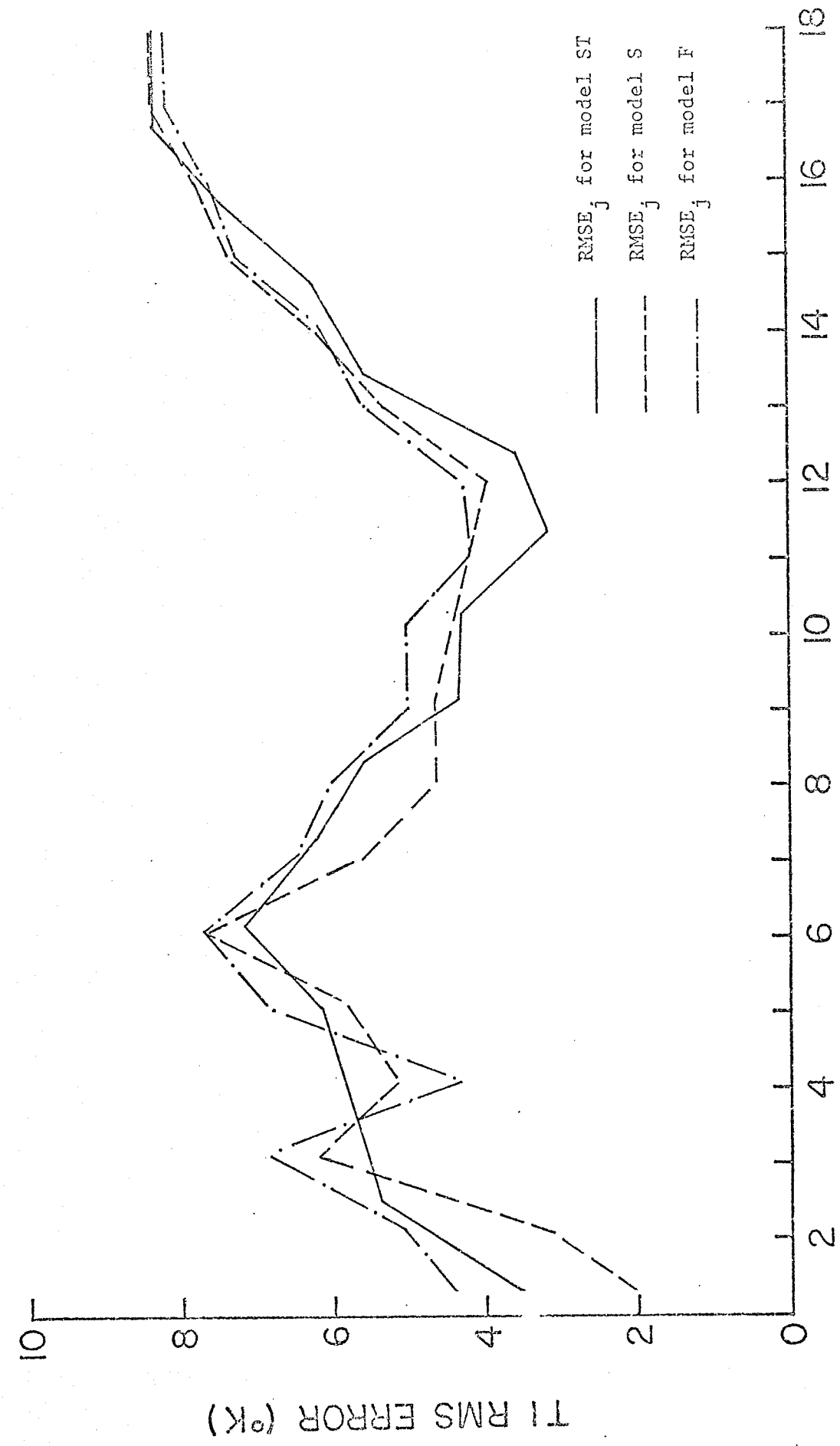

Figure 5.30: T1 RMSE$_j$ for models S, F, ST

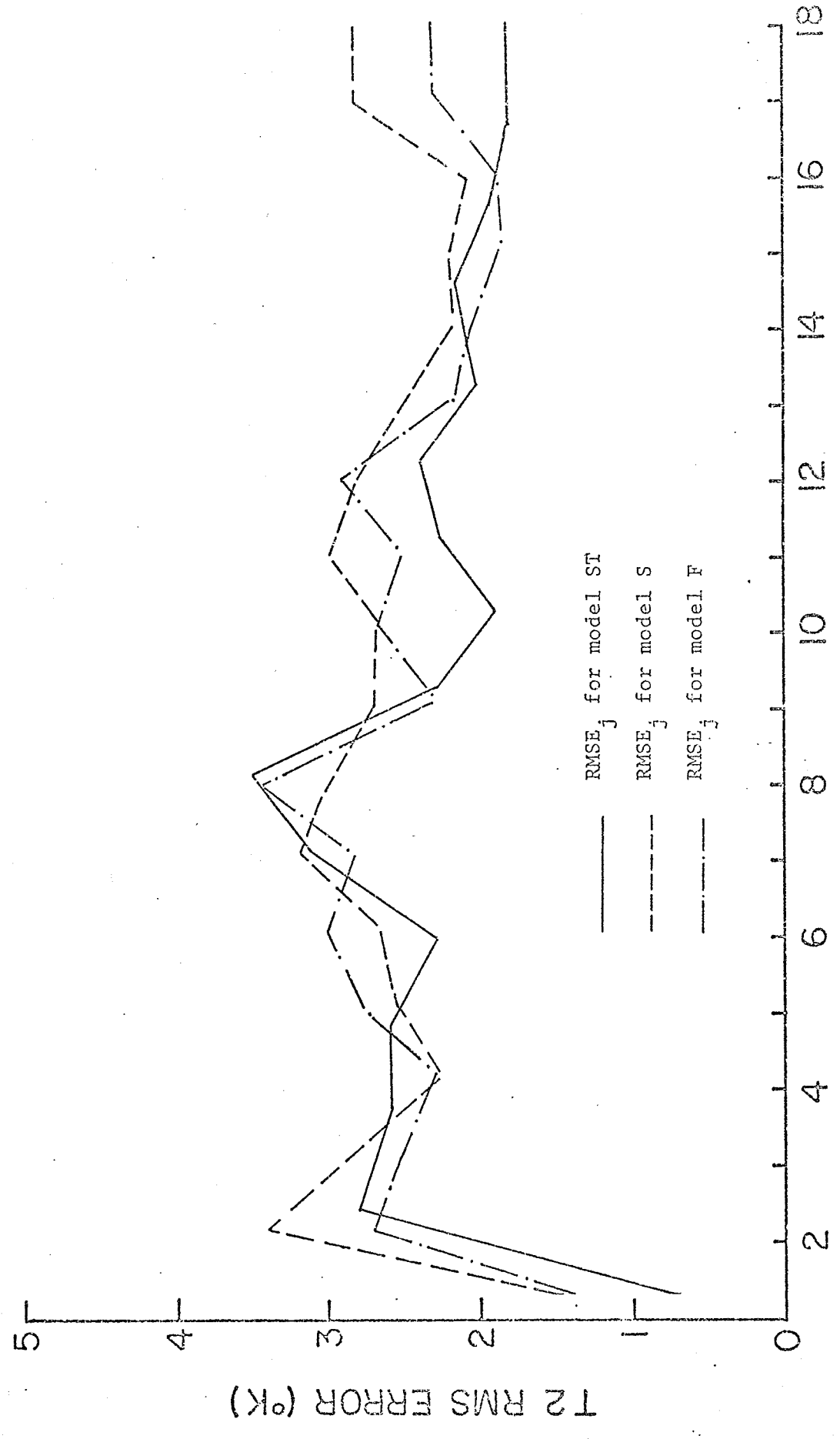

Figure 5.31: T2 RMSE$_j$ for models S, F, ST

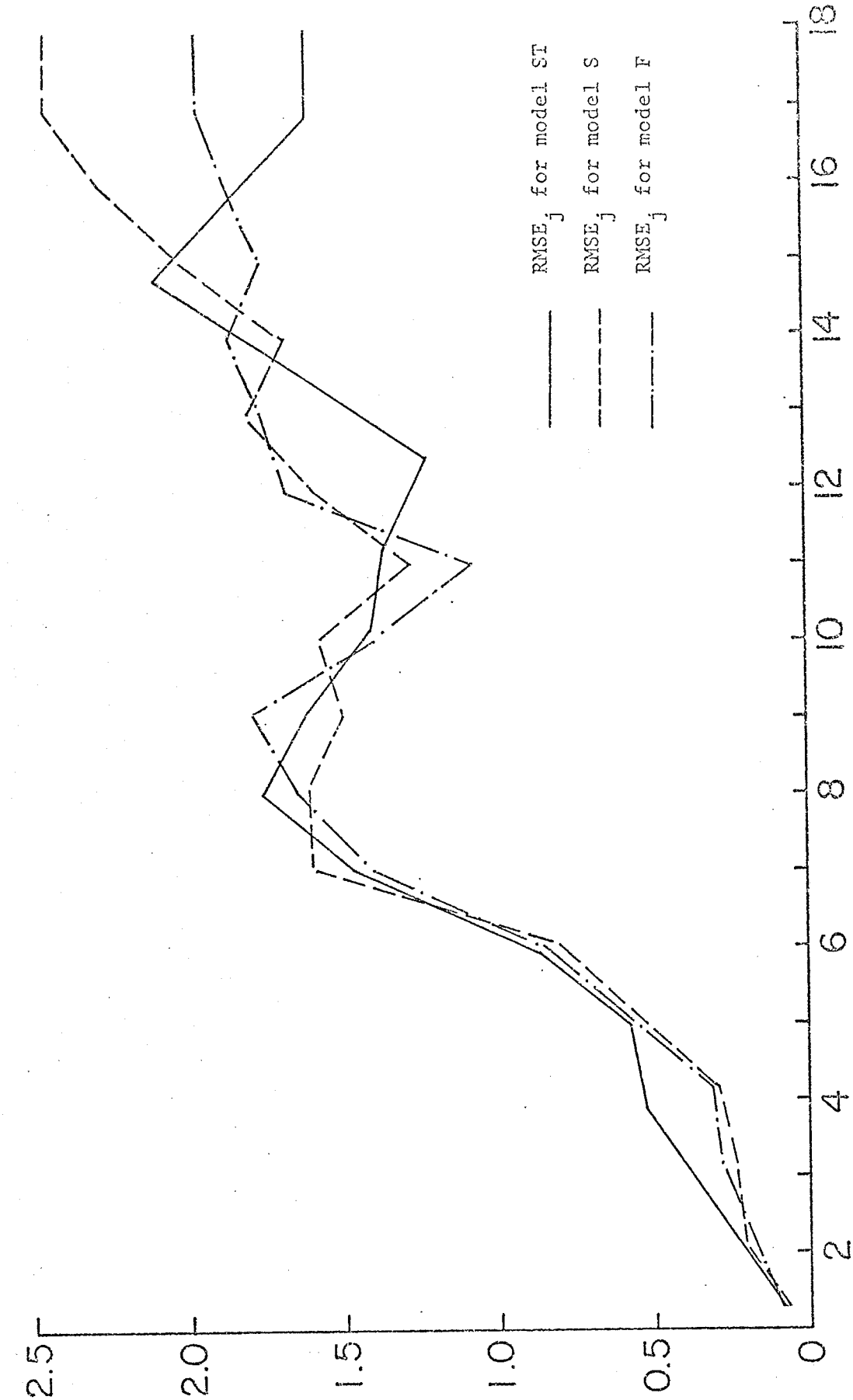

Figure 5.32: Q1 $RMSE_j$ for models S, F, ST

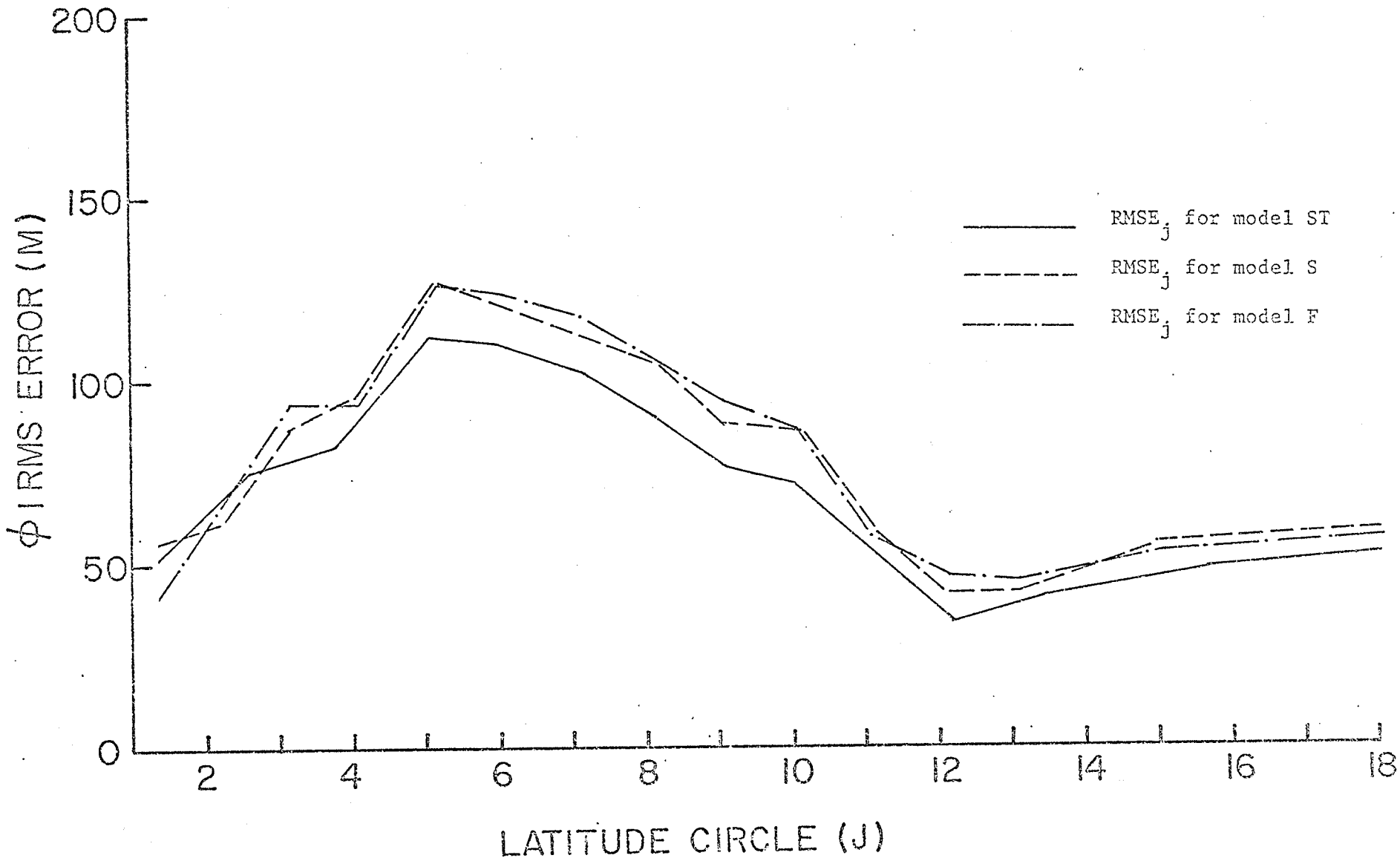

Figure 5.33: ϕ 1 RMSE$_j$ for models S, F, ST

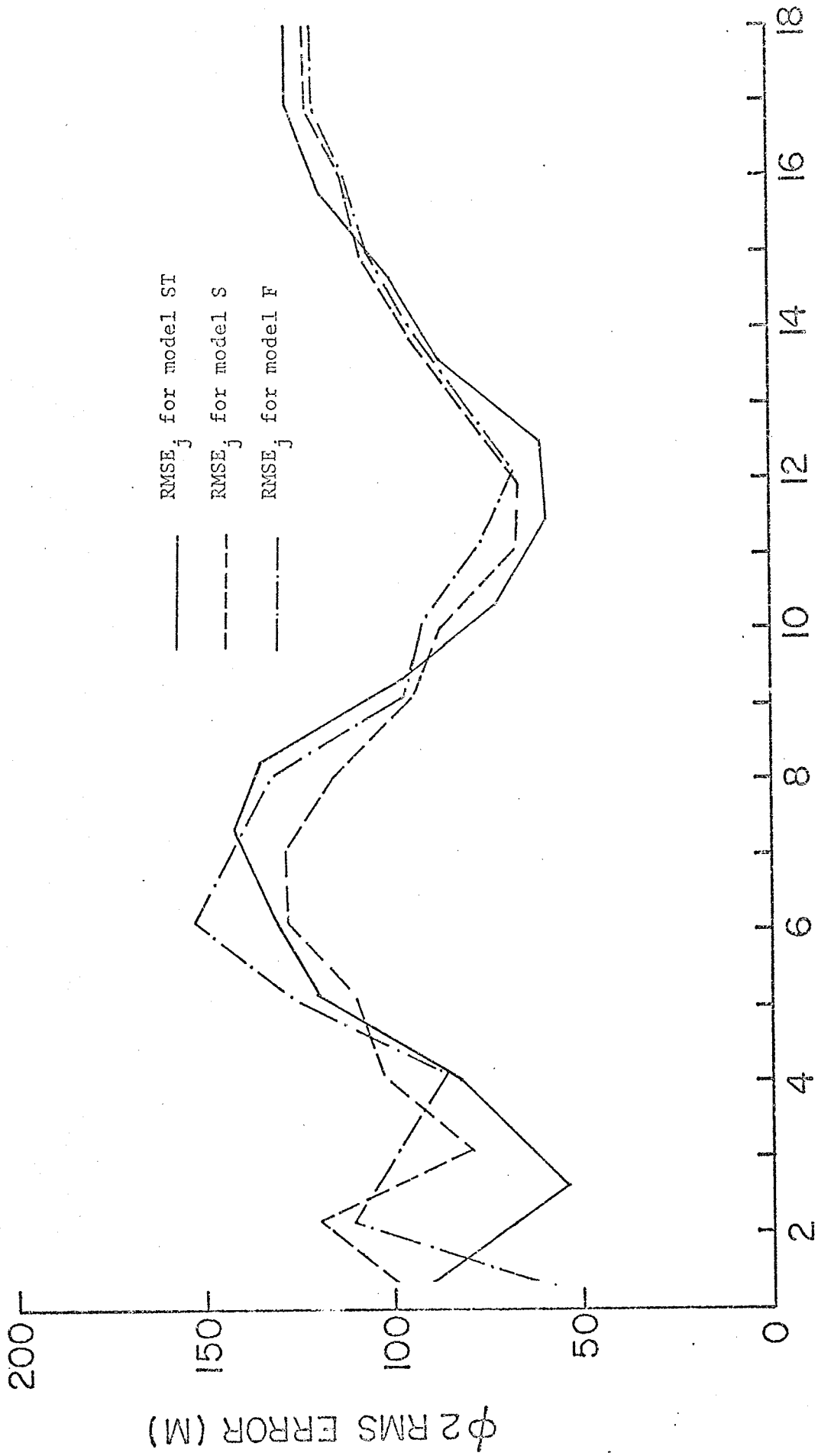

Figure 5.34 ϕ2 RMSE$_j$ for models S, F, ST

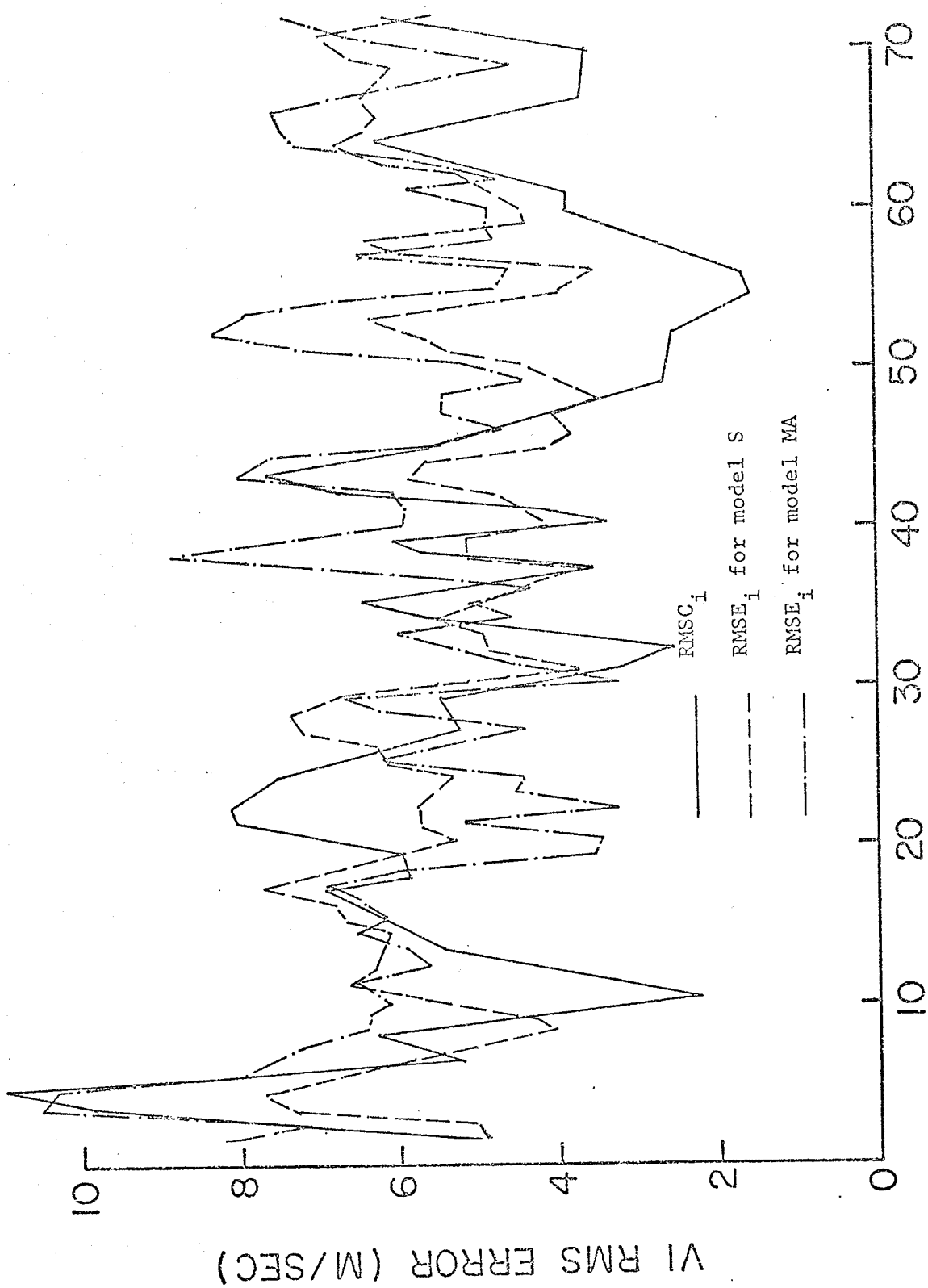

Figure 5.35: V1 RMSE$_i$ for models S and MA, and RMSC

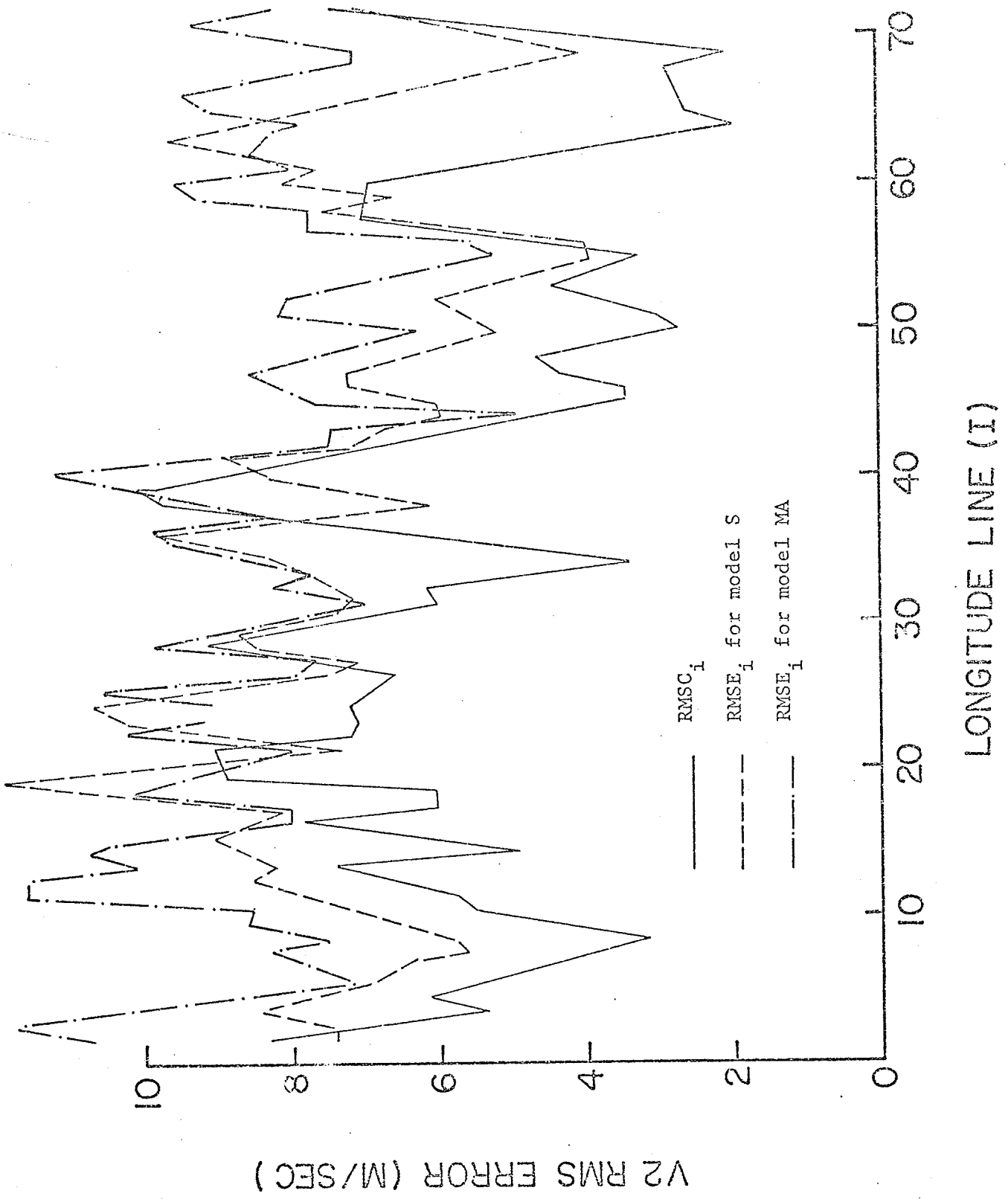

Figure 5.36: V2 RMSE$_i$ for models S and MA, and RMSC

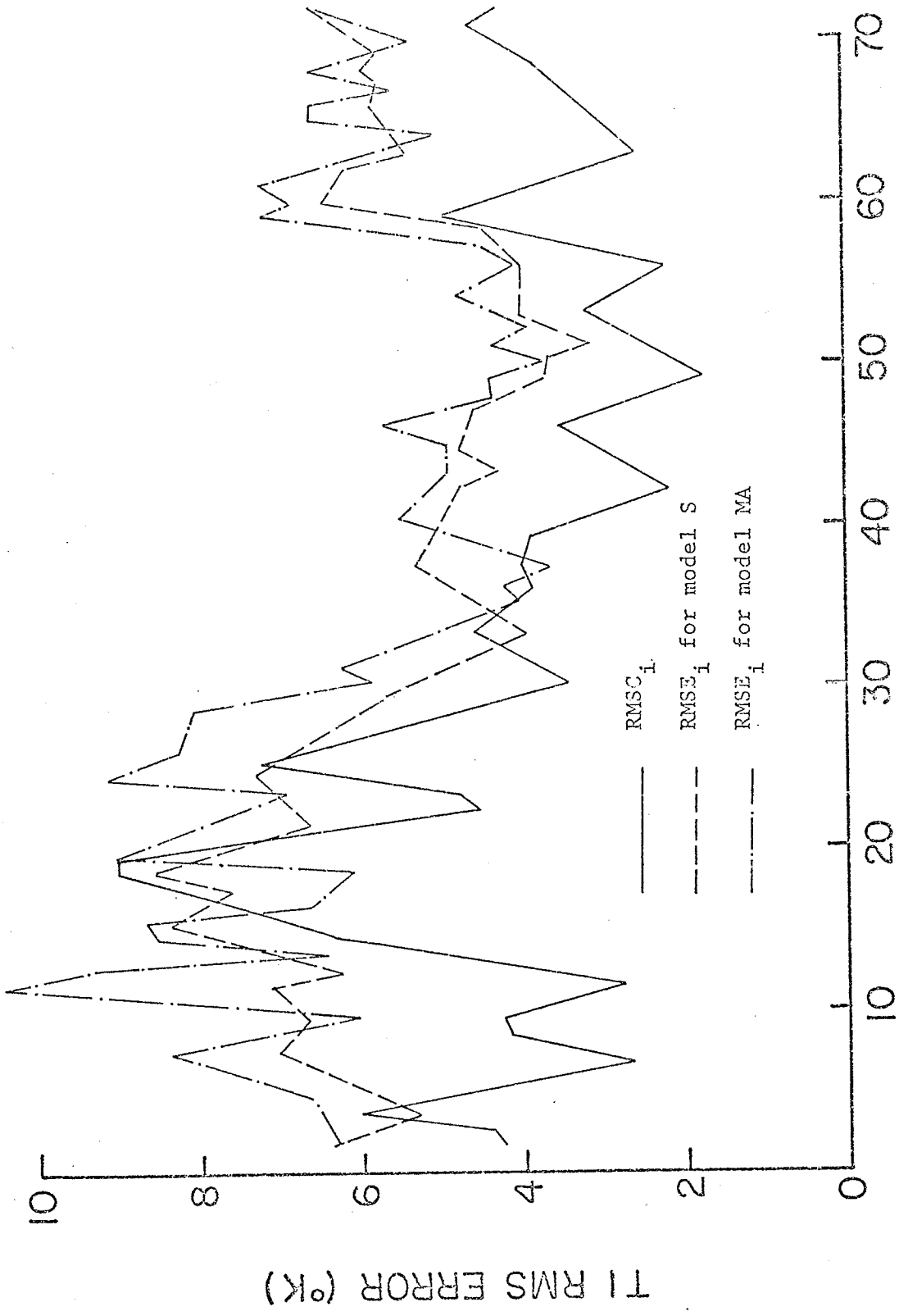

Figure 5.37: T1 RMSE$_i$ for models S and MA, and RMSC

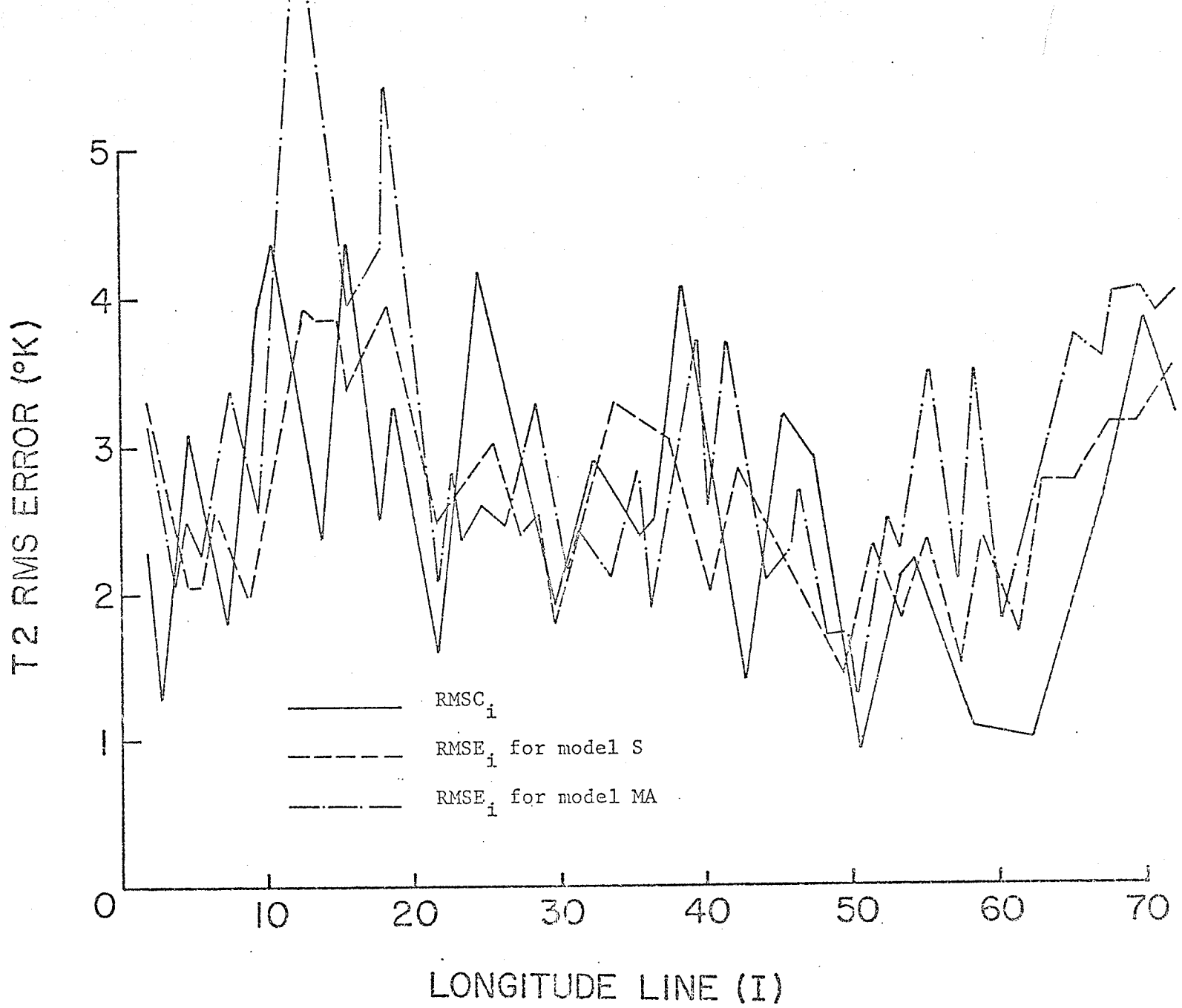

Figure 5.38: T2 RMSE$_i$ for models S and MA, and RMSC

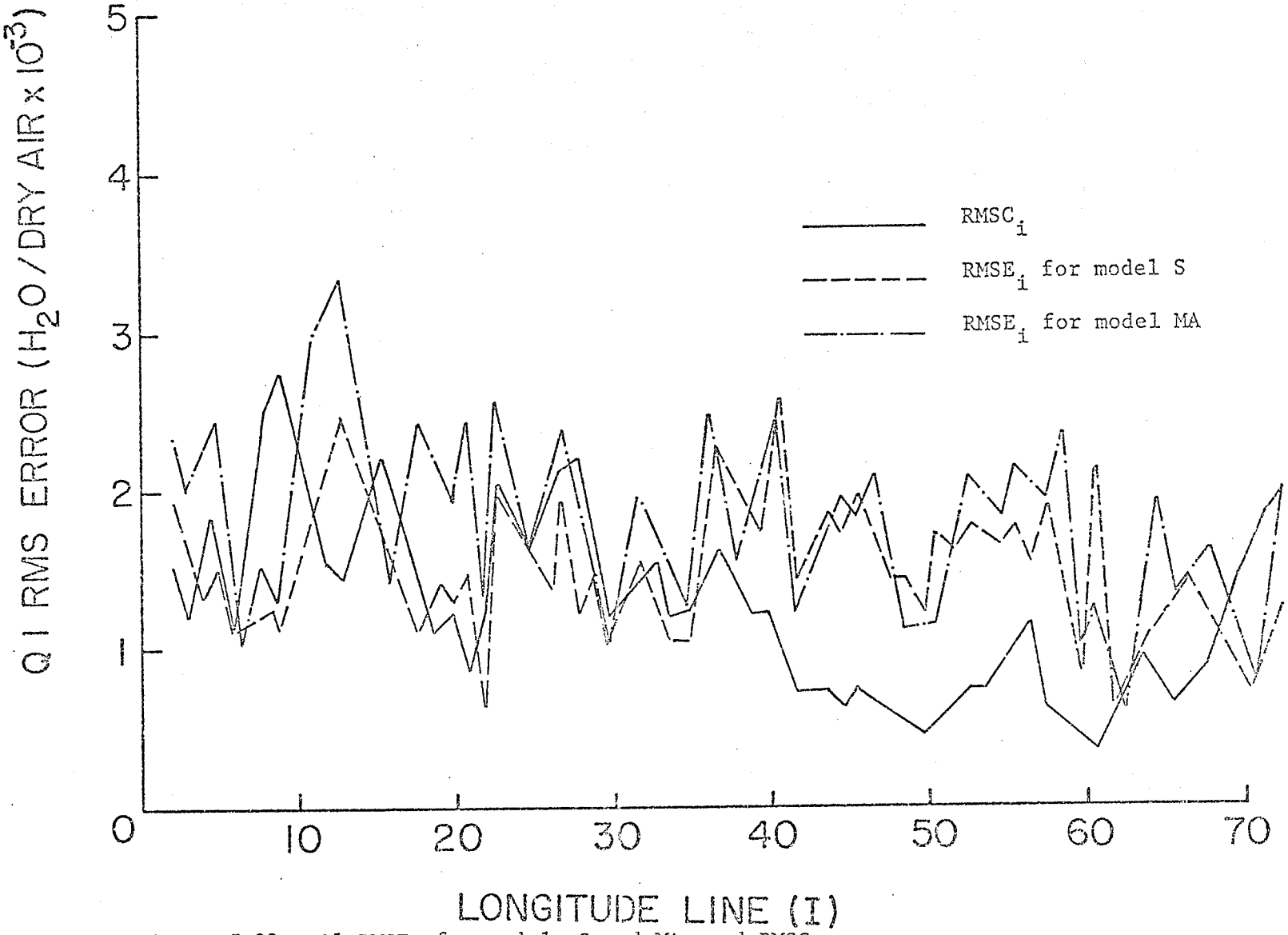

Figure 5.39: Q1 RMSE$_i$ for models S and MA, and RMSC

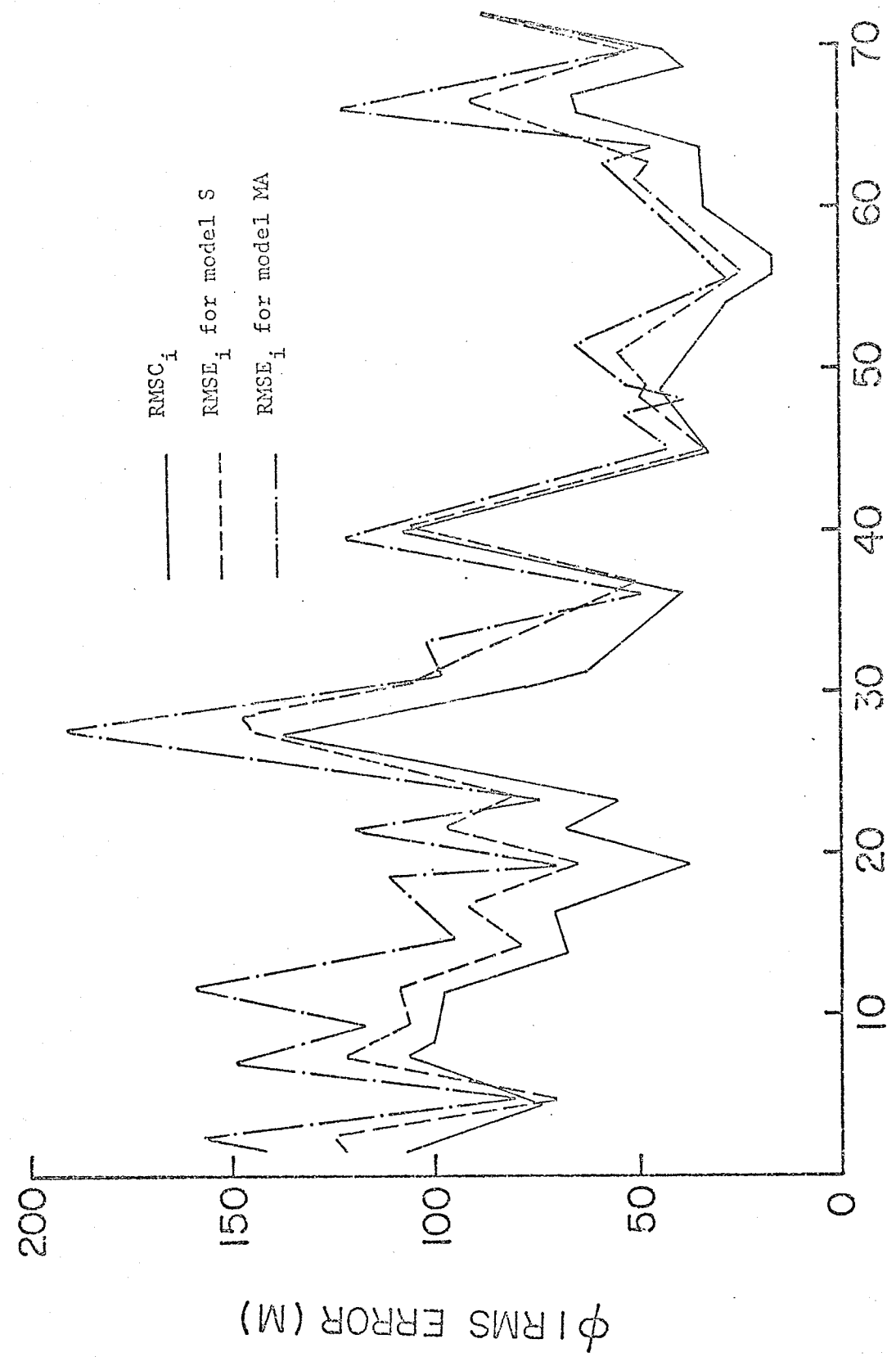

Figure 5.40: ϕ1 RMSE$_i$ for models S and MA, and RMSC

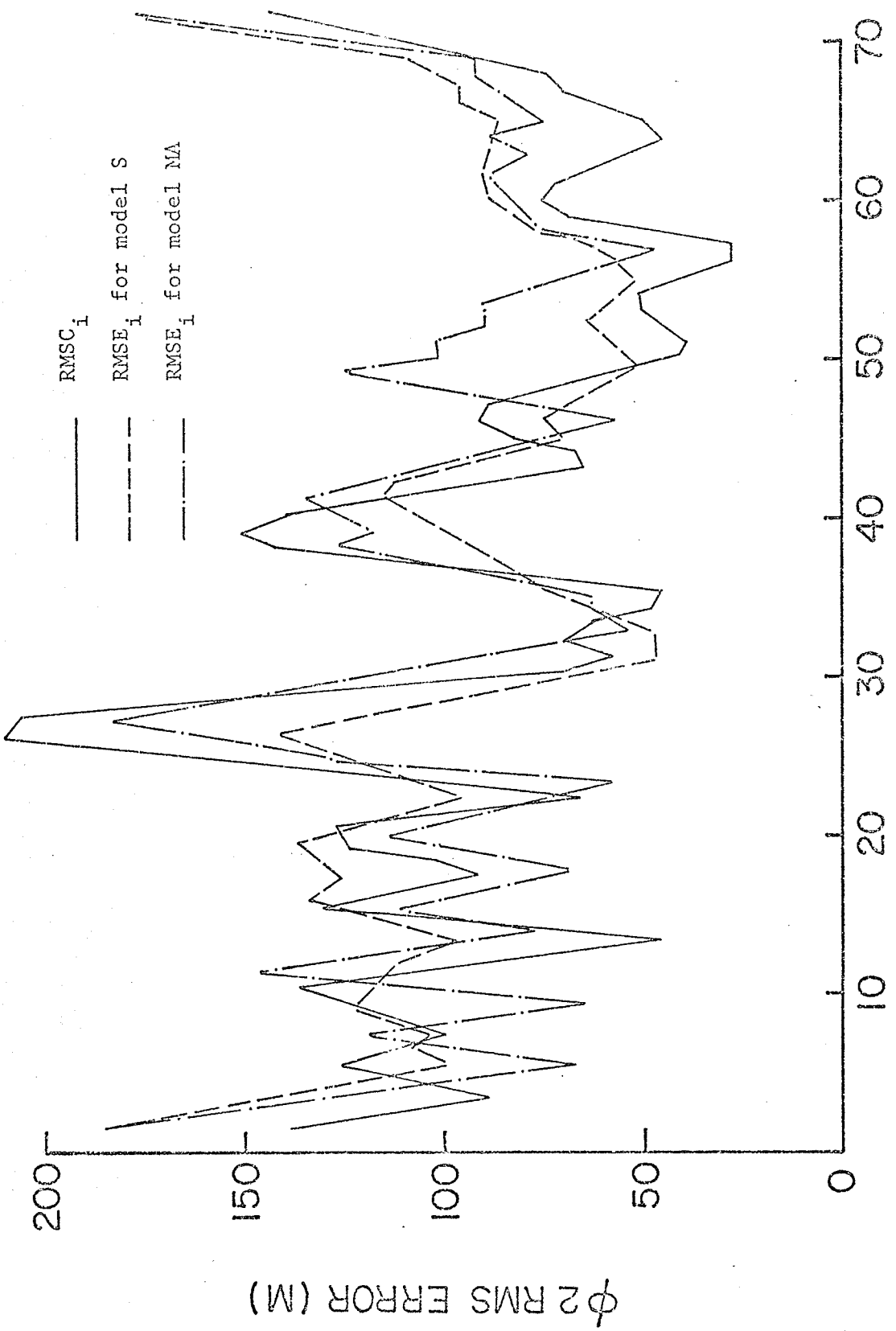

Figure 5.41: ϕ2 RMSE$_i$ for models S and MA, and RMSC

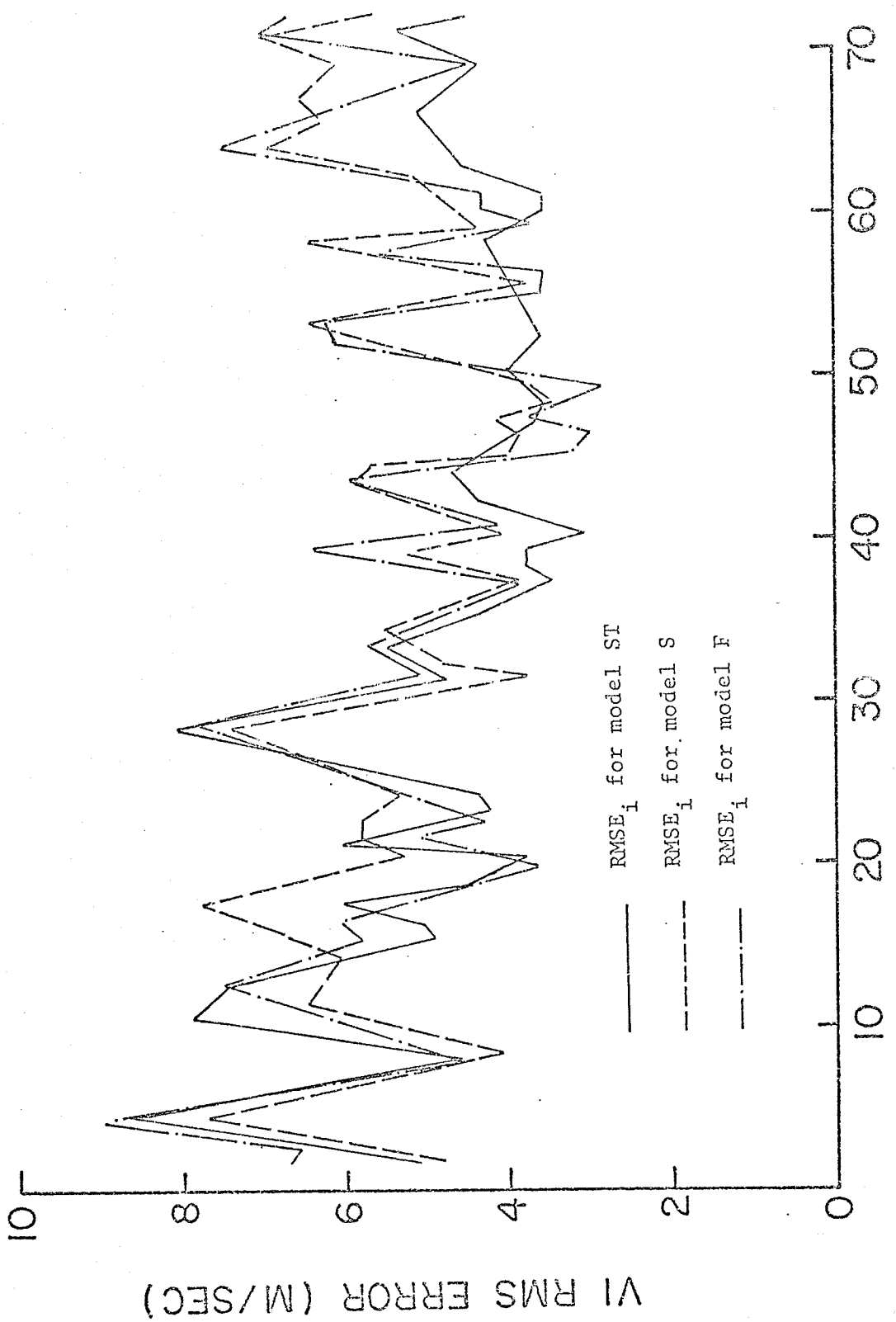

Figure 5.42: V1 RMSE$_i$ for models S, F, ST

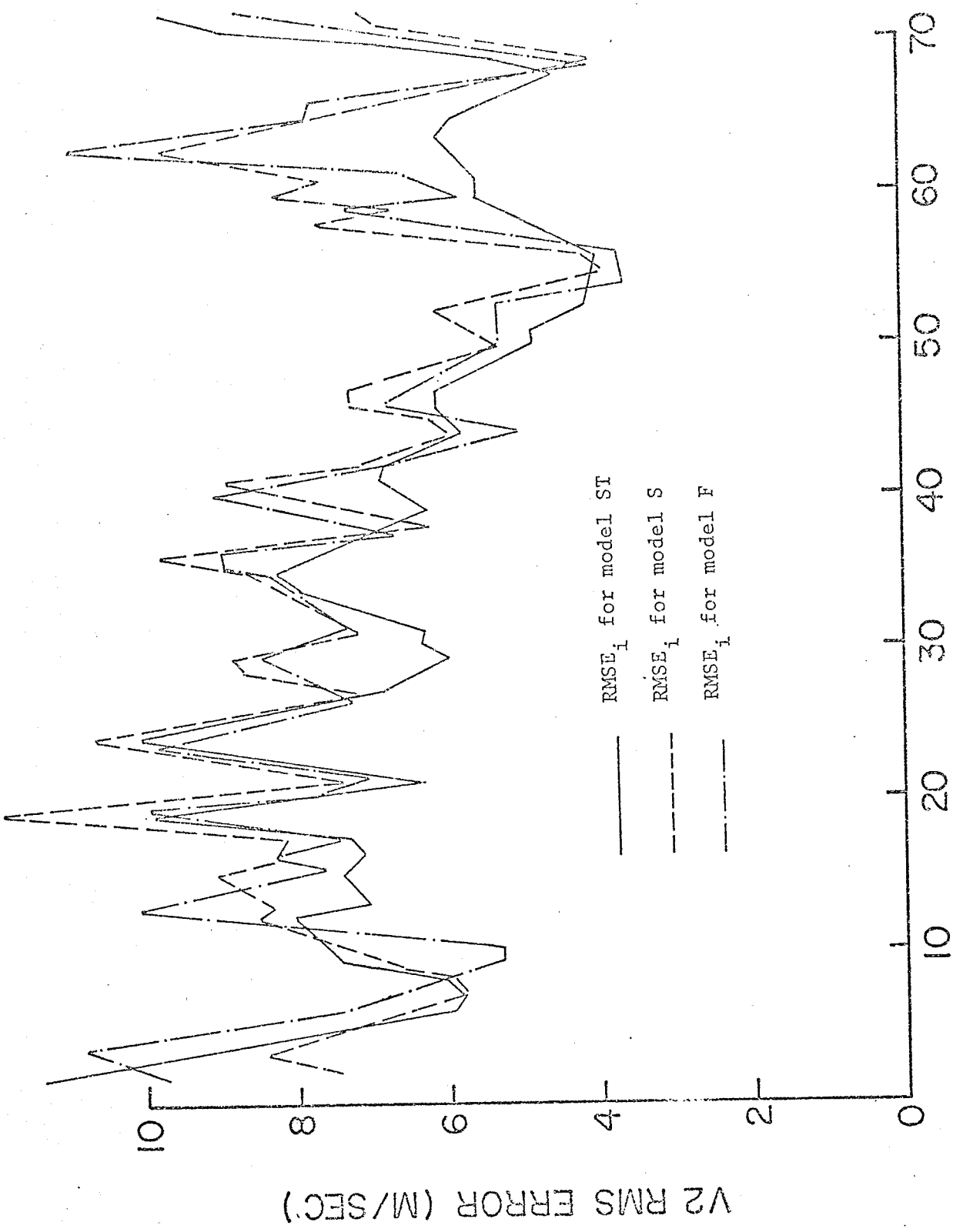

Figure 5.43: V2 RMSE$_i$ for models S, F, ST

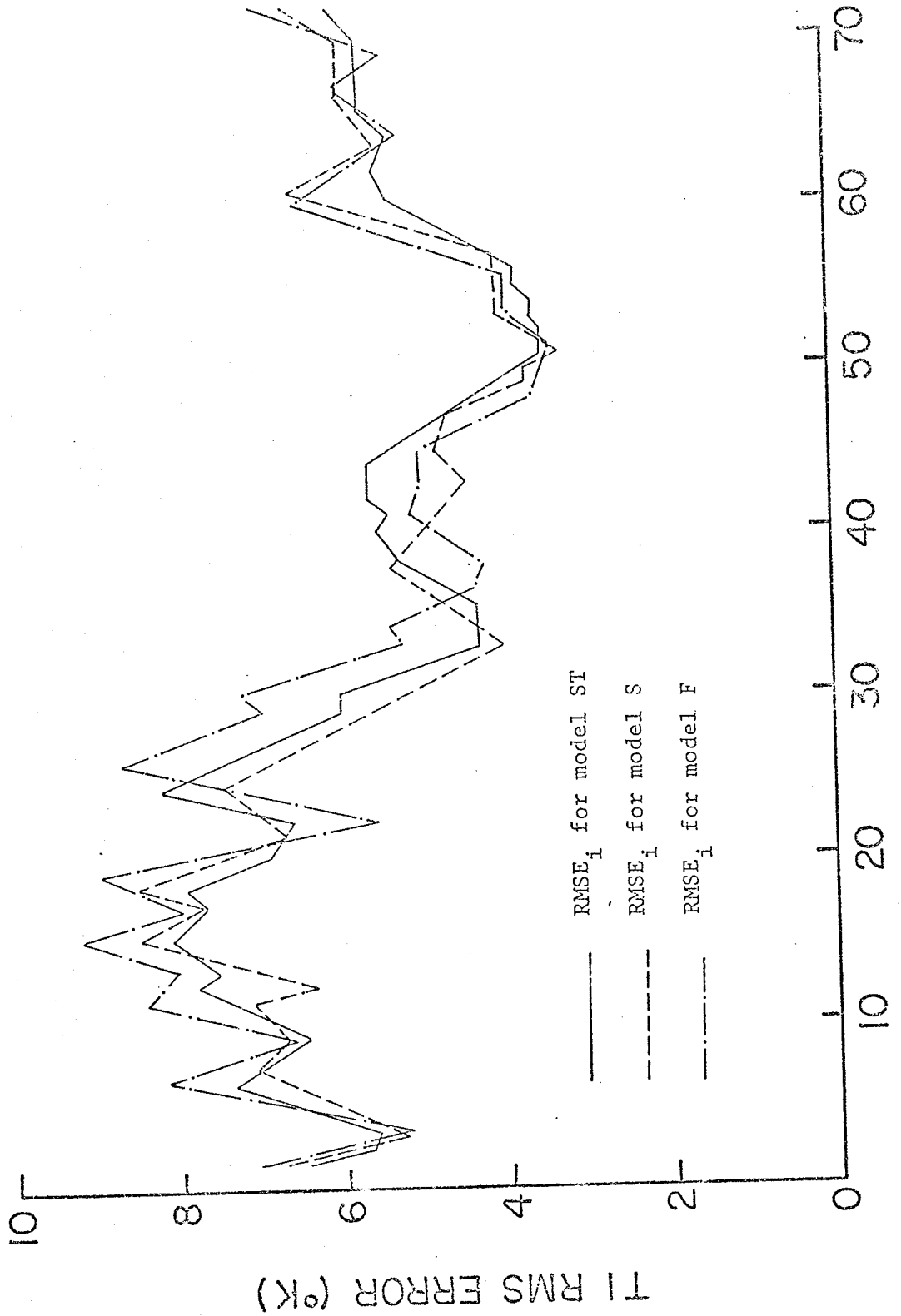

Figure 5.44: T1 RMSE$_i$ for models S, F, ST

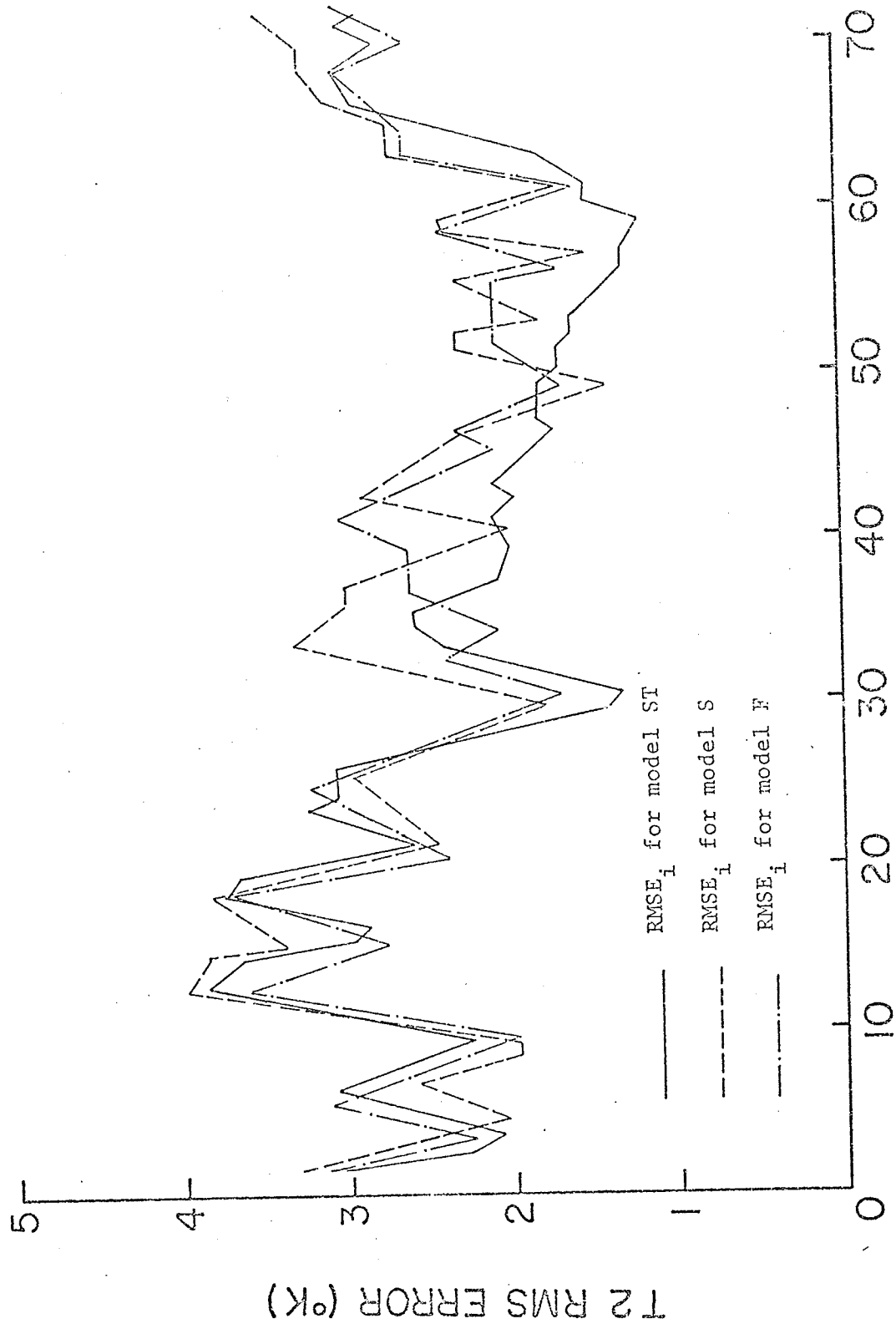

Figure 5.45: T2 RMSE$_i$ for models S, F, ST

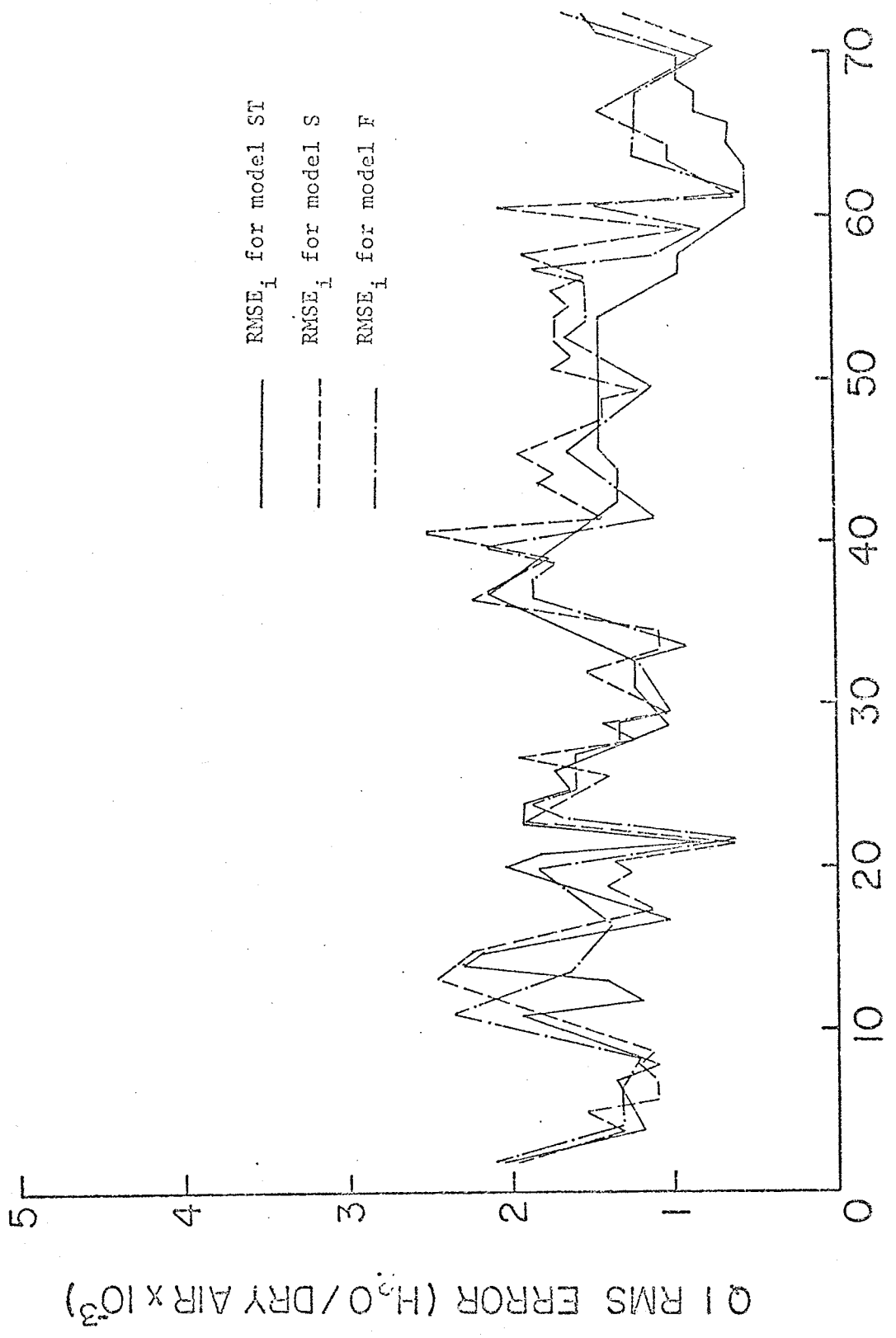

Figure 5.46: Q1 RMSE$_i$ for models S, F, ST

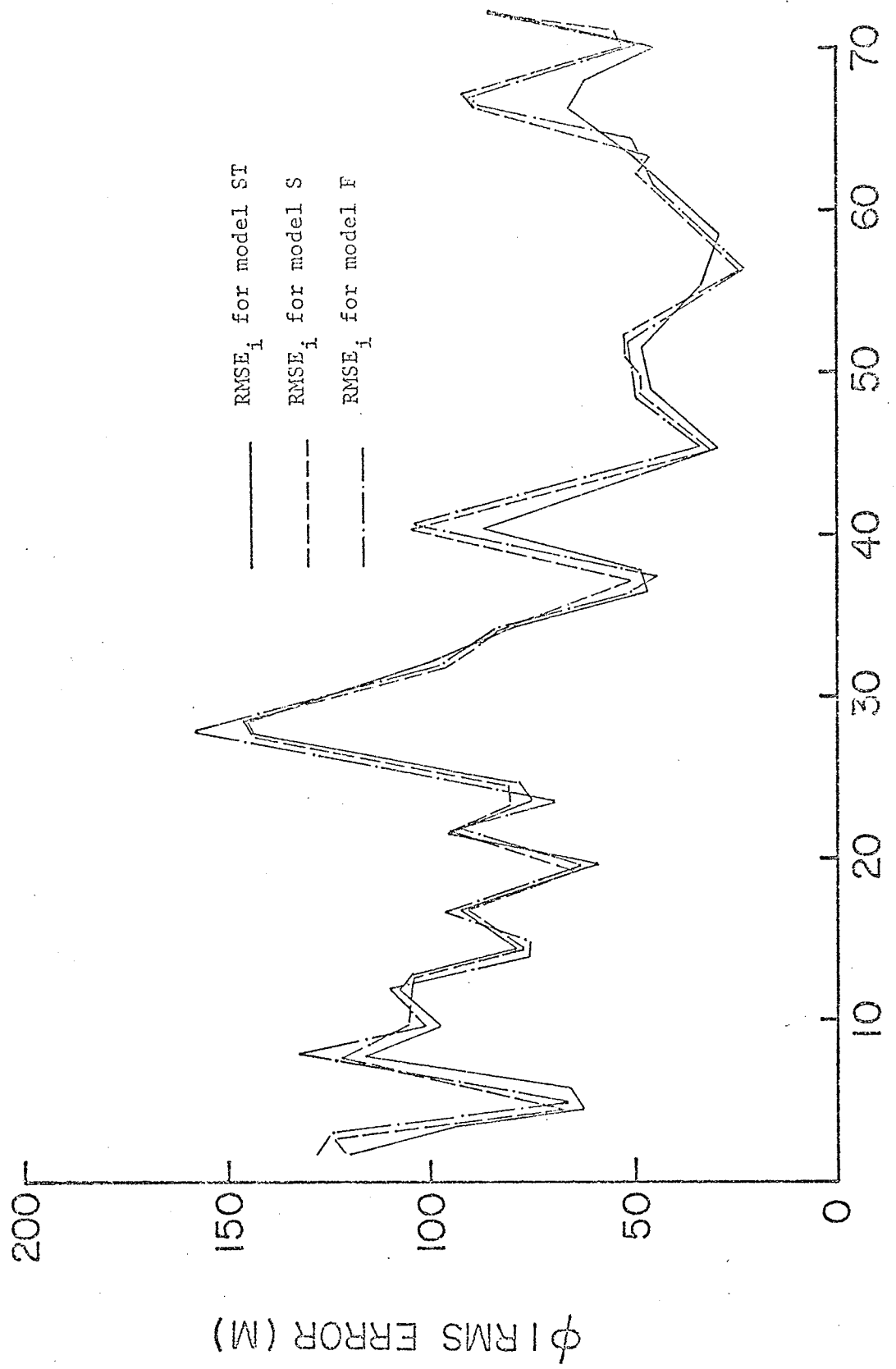

Figure 5.47: ϕI RMSE$_i$ for models S, F, ST

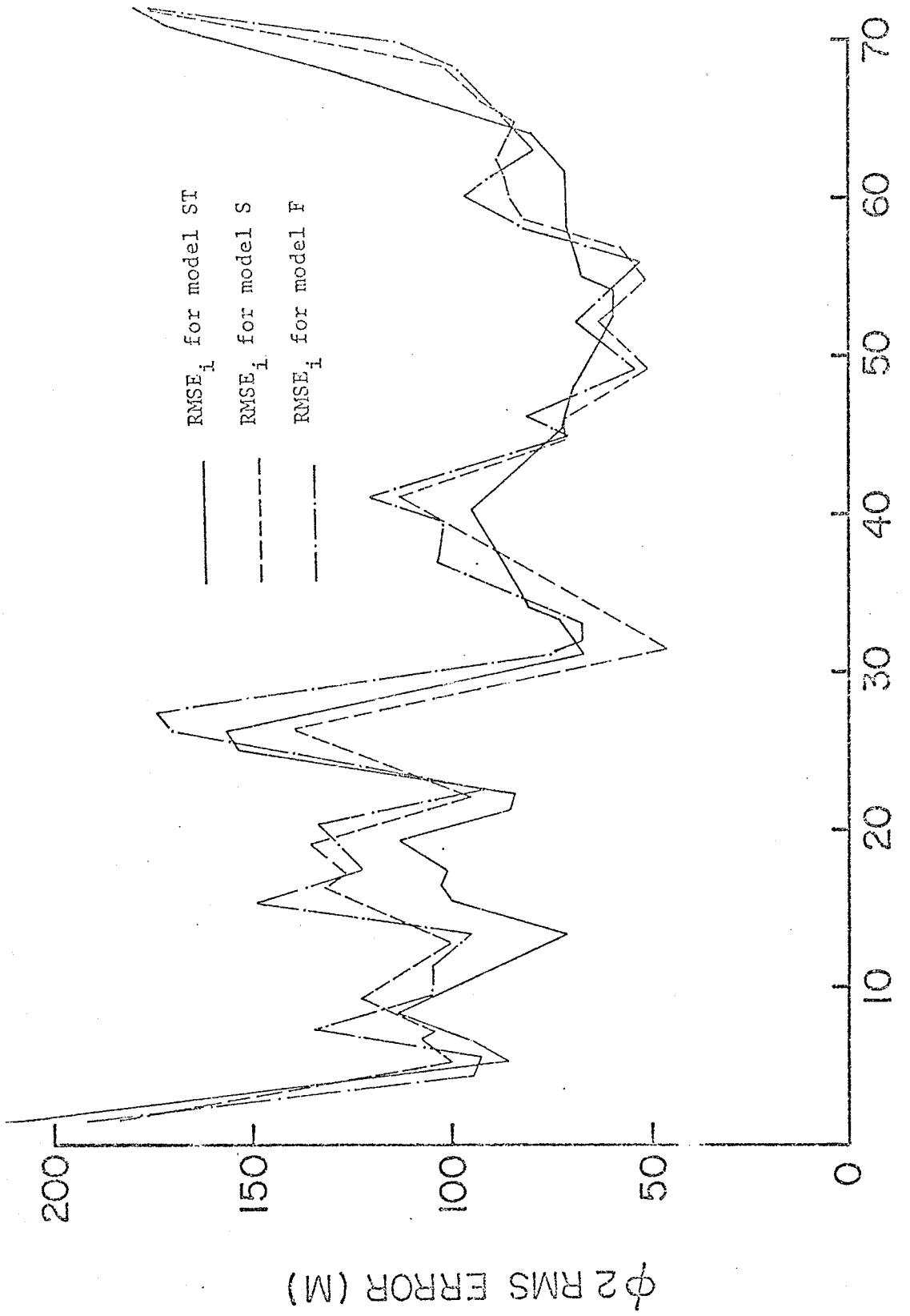

Figure 5.48: ϕ2 RMSE$_i$ for models S, F, ST

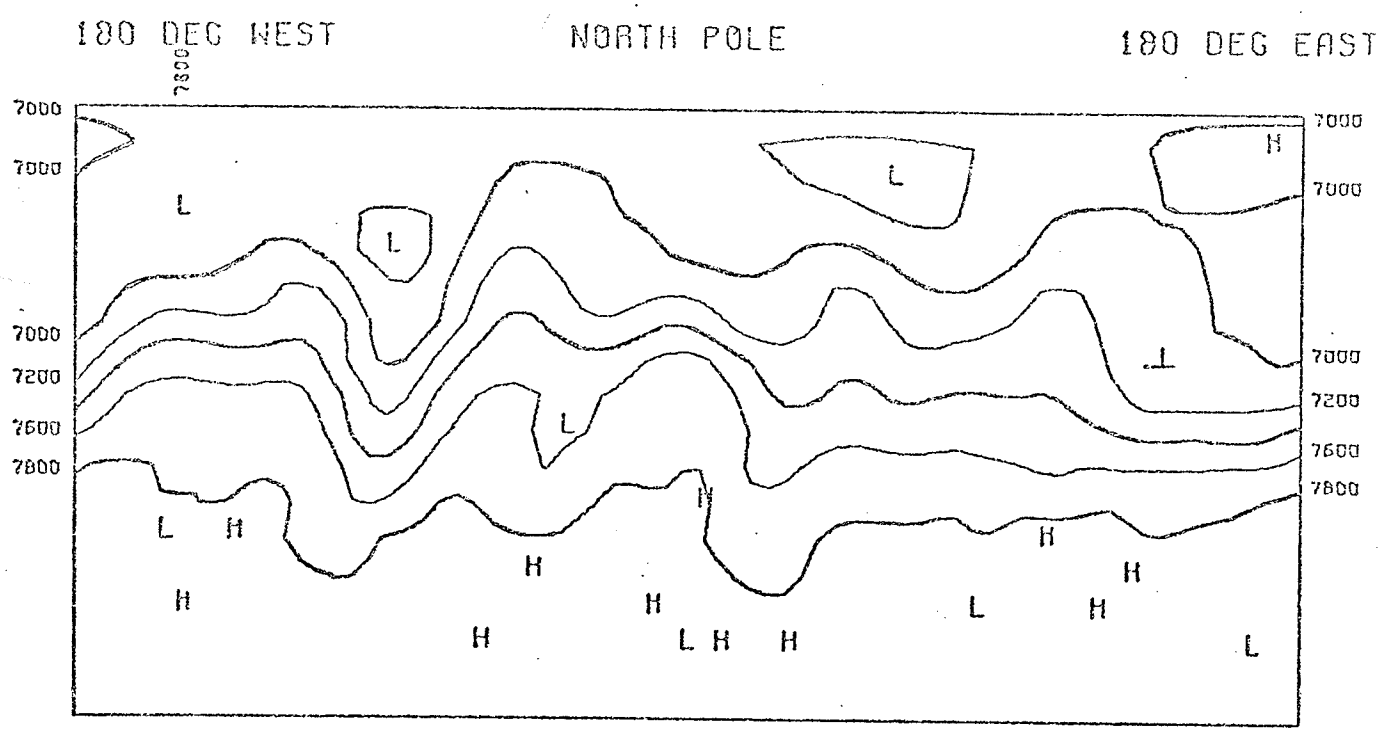

Figure 5.49: 400 mb Geopotential (m), 36 hour true

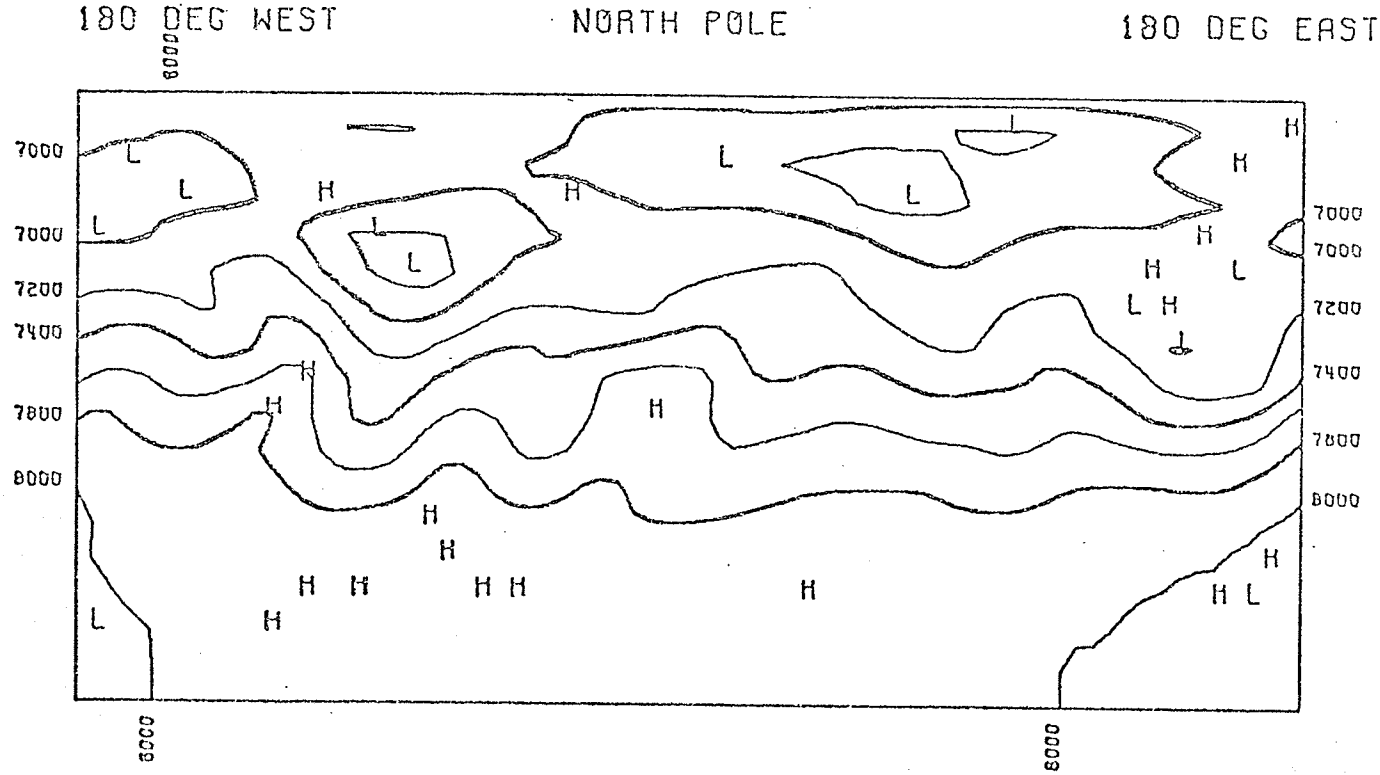

Figure 5.50: 400 mb Geopotential (m), model S, 36 hour

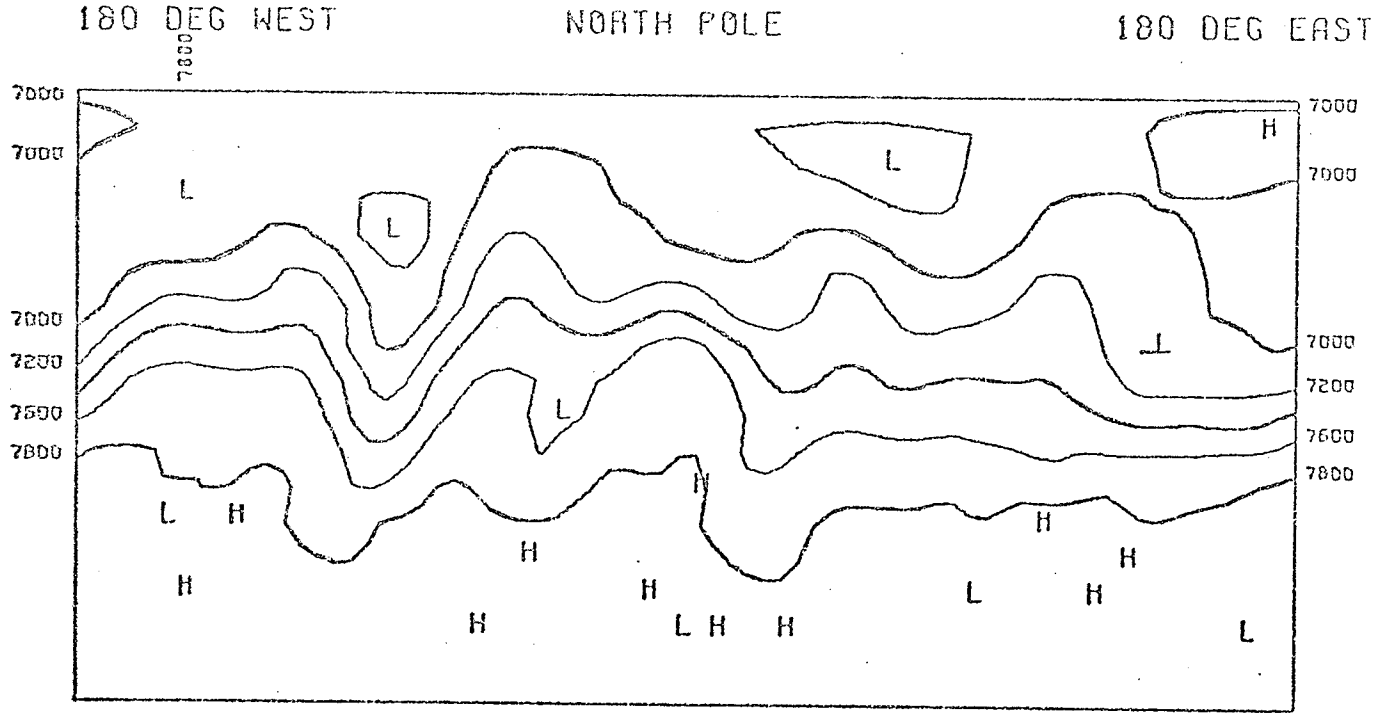

Figure 5.51: 400 mb Geopotential (m), 36 hour true

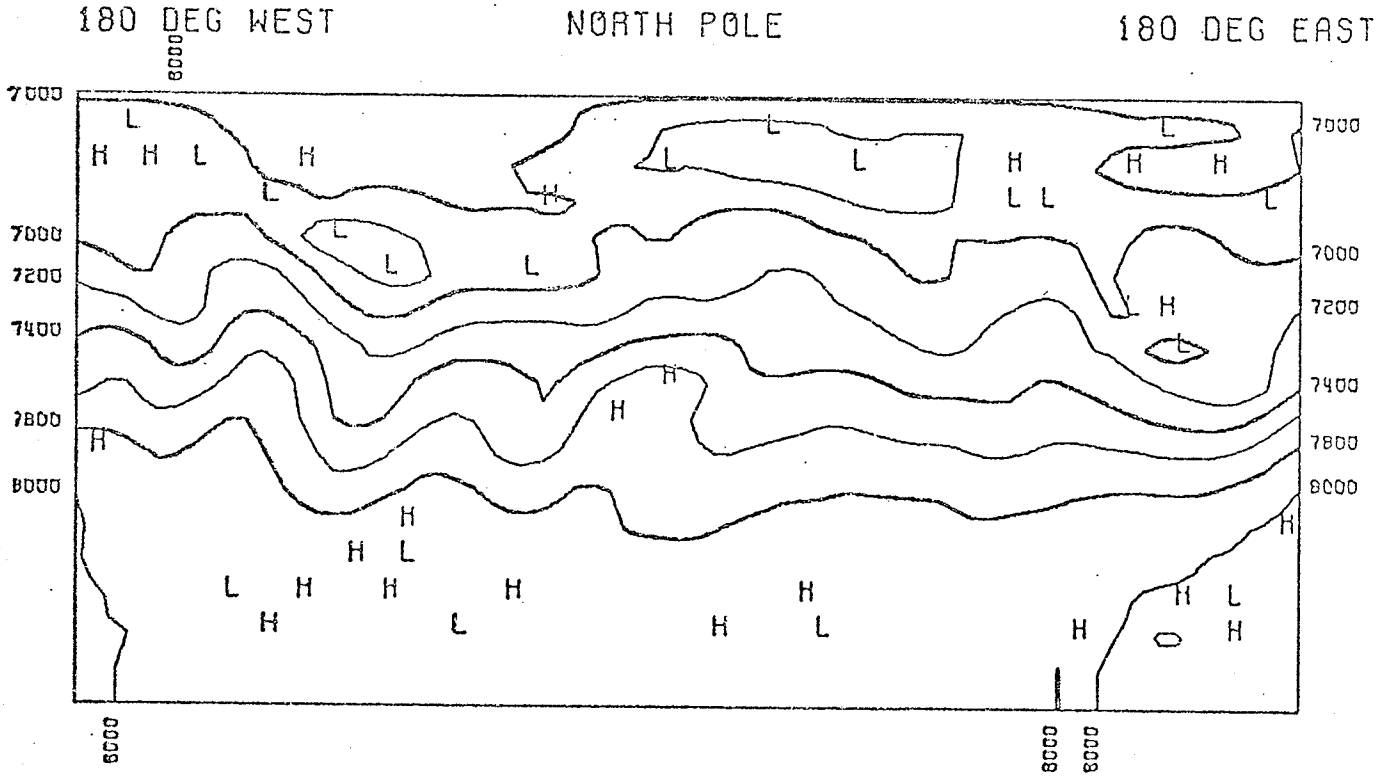

Figure 5.52: 400 mb Geopotential (m), model F, 36 hour

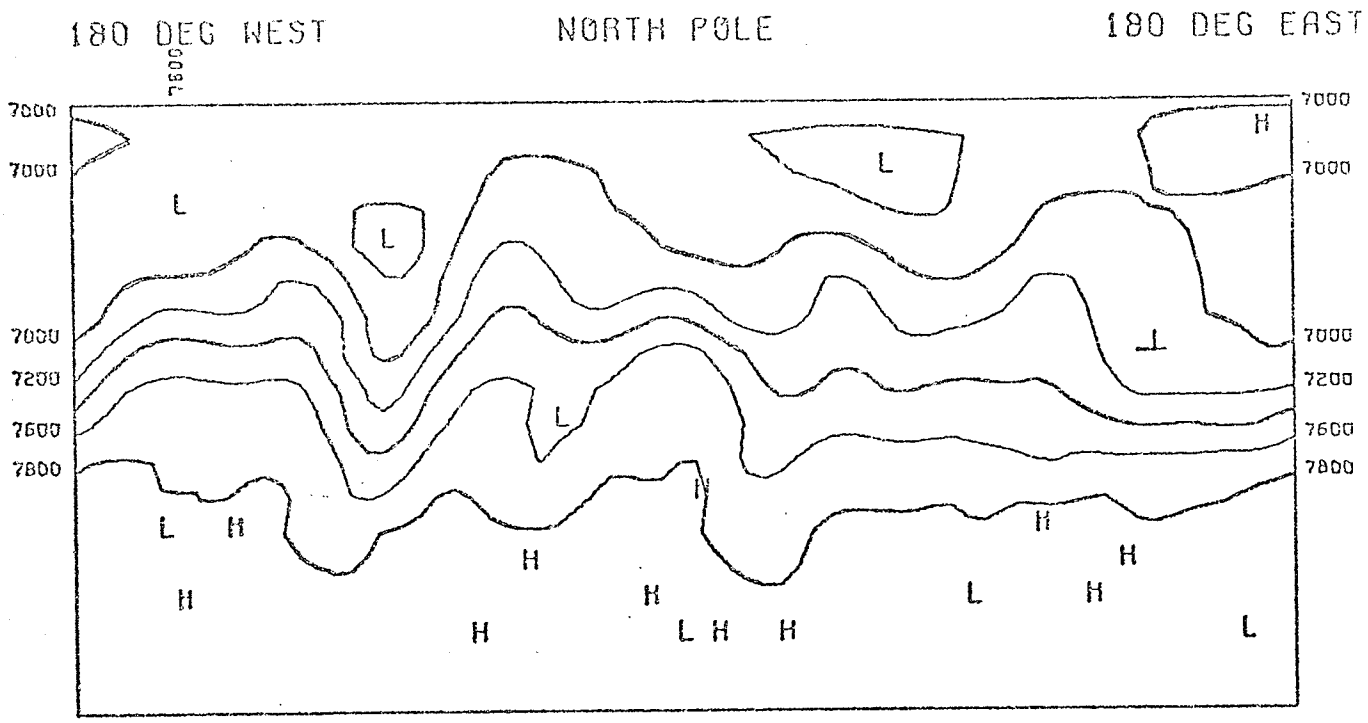

Figure 5.53: 400 mb Geopotential (m), 36 hour true

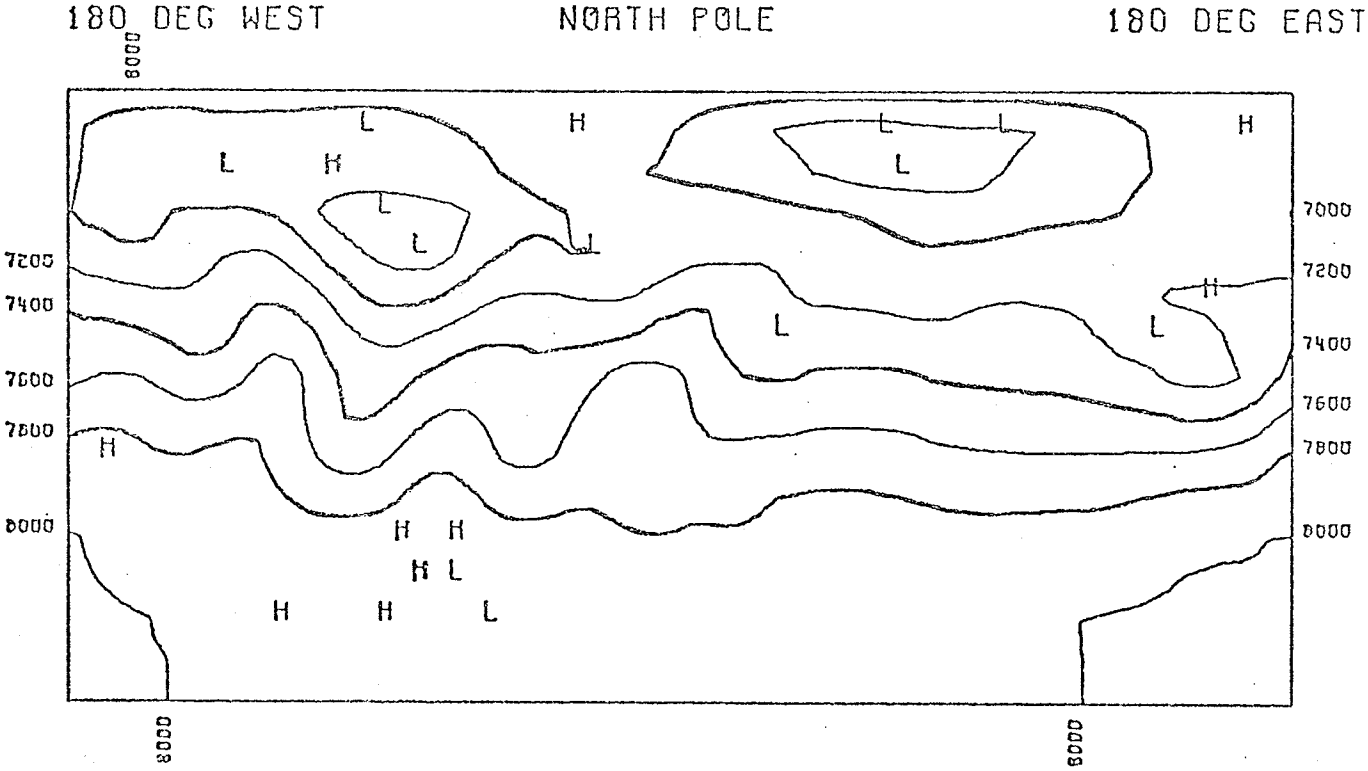

Figure 5.54: 400 mb Geopotential (m), model ST, 36 hour

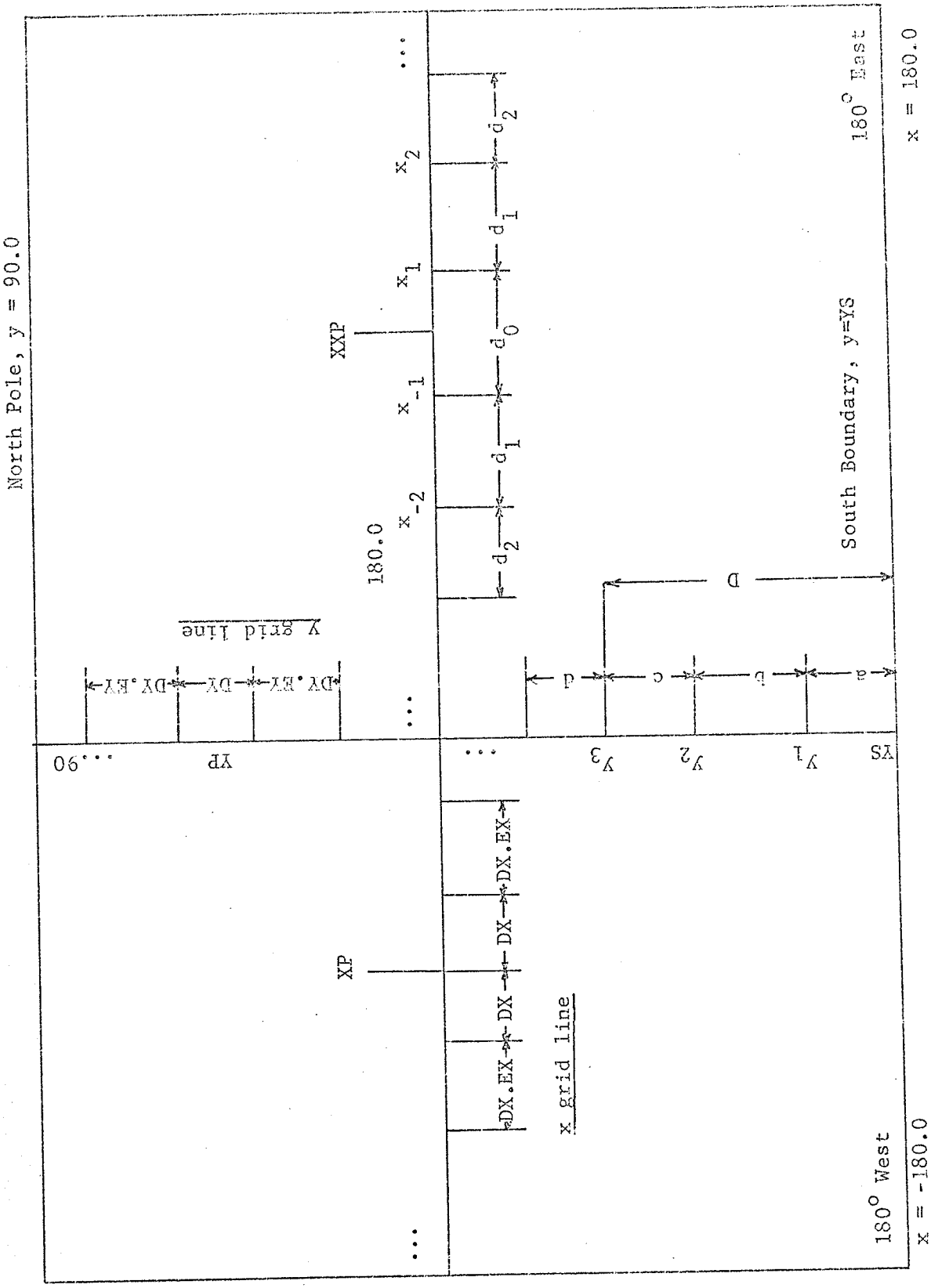

Figure A2.1: The preliminary grid